Modelling of Metal on Metal Hip Prostheses

Thesis submitted for the degree of Doctor of Philosophy

July 2015

Ali AL-SAFFAR

Abstract

Metal-on-metal (MOM) total hip replacement is an artificial hip joint has been used to replace damaged or diseased natural joints. MOM studies have demonstrated severe complications due to metal wear debris in tissues adjacent to the implants. Reducing the wear rate and operating with full film lubrication could reduce these problems; a better understanding of the lubrication mechanisms is also relevant to other hard bearing materials such as ceramics or new metal alloys.

Ball-in-socket MOM contacts were analysed using the Abaqus Finite Element package to simulate dry contact between the acetabular cup and the femoral head. Different cup thicknesses of 4, 6, 8, and 10 mm were considered using a polyurethane foam block support system.

Elastohydrodynamic lubrication (EHL) analyses were developed for the contacts using three different approaches to specify the contact. These were

(i) A simple model based on the radii of relative curvature,

(ii) An equivalent contact model developed so that its dry contact area and maximum pressure replicated the values obtained from the FE analysis, and

(iii) A modified version of (ii) that also ensured equivalence of the gap shape outside the contact area.

Published in vivo information for the hip joint contact forces over the walking cycle was used to specify the operating conditions for the EHL analysis.

This was achieved by developing techniques to transform the in vivo information to provide load direction and kinematic information relative to the nominal contact point between the components.

The analysis method was found to be effective for all points of the walking cycle for cases where the cup thickness exceeded 5 mm and modelling approach (ii) was identified as satisfactory. For a cup thickness of 4 mm, membrane action began to emerge in the FE analyses so that such contacts behaved in a different way.

Acknowledgements

I would really like to thank my supervisors. Prof. H P Evans and Prof. S Evans for their effort, many hours of advising and guidance, encouragement and proof-reading throughout the duration of this work.

I would also like to thank Dr. K. Sharif and Dr. H Umran for our useful discussions about the EHL software used in this project. I would also like to thank my friends and colleagues whom I have not mentioned here.

Finally I would like to thank my wife for her continuous support and patience over the past three years.

Contents

Nomenclature

a	Radius of contact area
c_d	Diametral clearance
d	Surface deflection
D	Femoral head diameter
$\acute{E}$	Reduced elastic modulus
E_1, E_2	Elastic modulus for bodies 1 and 2
F	Load
h	Film thickness
h_c	Central film thickness (when x=0, y=0)
h_m	Minimum film thickness
h_u	The undeformed geometry
M	Moment
P	Pressure
P_o	Maximum pressure
R	Principal radius of relative curvature
R_b	Radius of femoral head
R_c	Radius of cup

t	Time
W	Load
wt	Cup wall thickness
x, y, z	Cartesian coordinates
γ_1 , γ_2	Poisson's ratio for bodies 1 and 2
ω	angular velocity

Subscribe

h	Hertzian
f	Finite element
equiv	Equivalent model
mod	Modified model

Other symbols are defined in the text

Introduction

1.1 Introduction

The natural hip joint is one of the largest and strongest joints in the body. It is the place where the femur and the pelvic bones articulate with each other. The high stability of the hip joint comes from its ball and socket configuration which has a high degree of envelopment. It allows for a wide range of multi-axial movements required for normal daily activities like walking and sitting. Supporting the weight of the body represents the second function of the hip joint in both the static and dynamic positions. The hip joint comprises of the acetabulum (socket) in the pelvic bone and the femoral head, as shown in Figure 1. The head of the femur/ ball/ is the convex component of the hip joint, and it is covered with an articular cartilage. It forms two – thirds of a sphere reflecting the high degree of articulation provide by the joint. The acetabulum/ socket/ is the concave surface of the pelvis bone. The cavity of the acetabulum is also covered with a cartilage layer.

Large and strong muscles surround the articulation between the ball and the socket. The two cartilage layers in addition to a lubricant fluid, called synovial fluid, allow the femoral head to rotate freely with a range of motion in three directions. A healthy joint is expected to last a lifetime as a result of the high performance of the lubrication process preventing bone to bone contact occurring at the interface. There are a number of diseases such as arthritis, osteoarthritis and rheumatoid arthritis that cause degradation of the articular cartilage. These diseases affect the lubrication operation and lead to losing the

range of motion and experiencing bone–on–bone contact. Consequently, the joint often needs to be restored by hemiarthroplasty, hip resurfacing or total hip arthroplasty surgical procedures.

Different materials have been used instead of the damaged hip joint in replacement prostheses. There are four main types of hip replacements which are characterised by the material couples at the sliding interface, metal-on-metal (MOM), metal-on-polyethylene (MOP), ceramic-on-ceramic (COC), ceramic-on-polyethylene (COP). Details of the advantages and the limitations of each one of these material combinations will be discussed in the next sections of this chapter.

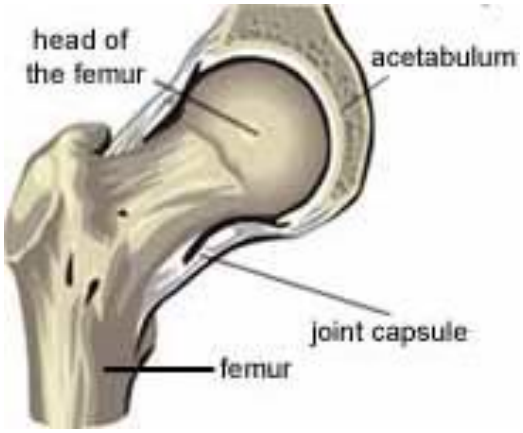

Figure. 1: The natural hip joint, reproduced from Pramanik [1].

Definitions of common terms

- Osteolysis: is the bone degeneration caused by the response of the immune system to wear debris.
- Impingement: when the femoral head moves at or around the boundary of the acetabular cup rim, sometimes resulting a dislocation.

1.2 Total Hip Arthroplasty

Artificial hip joints have been in existence for over 100 years, but the last 50 years have seen some remarkable developments [2]. The replacement of diseased natural joints by totally artificial joints is one of the most successful surgical procedures carried out today. Over 70,000 replacement joints are currently performed annually in patients in the United Kingdom [3] and more than one million hip joint replacements are carried out worldwide every year [4].

A Total Hip Arthroplasty (THA) is a biomechanical device used to replace the damaged, diseased or fractured, hip joint as shown in Figure 2. It is a cost effective surgical procedure undertaken to reduce pain and reintroduce function of the hip joint. A total hip replacement is comprised of a femoral component and an acetabular component.

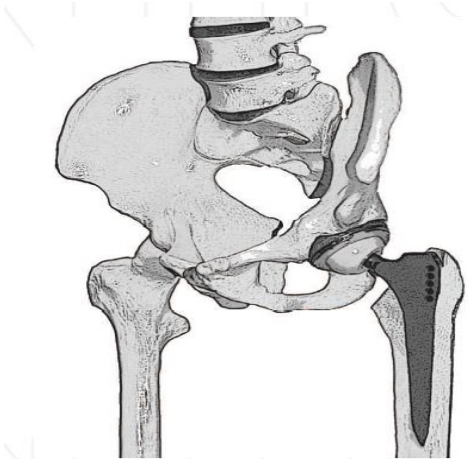

Figure 2: Left hip replacement, reproduced from Kluess [5]

Figure 3 shows a range of femoral components that are either of a modular or one piece design. The modular components consist of a shaft, a stem, which is inserted into the thigh bone, and a replaceable femoral head which is connected to the stem through a taper locking mechanism. Additional tapered sleeves make it possible to adjust the length of the neck during surgery.

(a) **(b)**

Figure 3 a) One piece femoral head, reproduced from Ramos [6], b) Modular femoral head, reproduced from Garbuz [7]

Similarly, the acetabular component, cup, is either a monoblock or of modular design, as shown in Figure 4. The modular component is composed of a liner and a shell where the shell is fixed to the concave surface of the acetabulum and the liner is fixed into the shell, while the monoblock cup is just one piece and is fixed directly to the acetabulum.

(a) **(b)**

Figure 4 (a) Monoblock acetabular cup, reproduced from [8], (b) Modular acetabular cup, reproduced from [9].

The fixation method between the stem and thigh bone and between the cup and the pelvic bone may be with or without cement and will be discussed later in this Chapter. The two articulating surfaces of the artificial hip joint comprise the inner bearing surface of the cup, which can be metal, ceramic or polyethylene, and the metal or ceramic femoral head.

1.3 Hip Resurfacing

Total hip arthroplasty is a successful operation for middle to late age with more than 90% to 95% survival rate at ten years. Implant survival after THA in younger patients is lower [10, 11]. Despite high wear characteristics with earlier generations, MOM hip resurfacing has been used for the treatment of younger patients [12]. A metallic acetabular cup is inserted into the acetabulum cavity without cement. The neck of the femur remains in place,

whereas the surface of the head of the femur is changed by a cemented metallic bearing surface as shown in Figure 5.

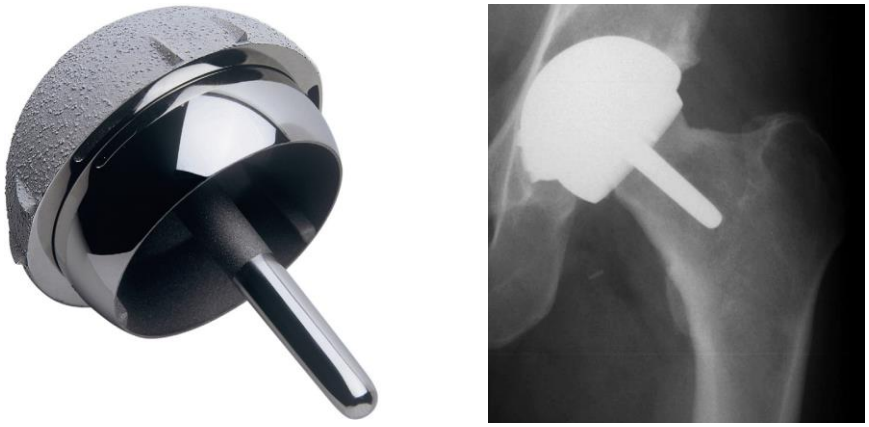

Figure 5: Hip resurfacing, reproduced from Ramakrishnan [13]

The advantages of hip resurfacing over total hip arthroplasty include proximal femoral bone preservation, optimization of stress transfer to the proximal femur and reproduction of normal hip biomechanics, greater implant stability, and perceived ease of revision. Clinical function is thought to be better with a large femoral head with patients reporting less postoperative limping [12, 14]. It is also found that there is a higher rate of activity, a greater range of motion and a lower rate of dislocation due to the large diameter bearing with the hip resurfacing than with total hip arthroplasty. It preserves much more of the femoral bone which allows replacement with a conventional THA later if needed.

On the other hand, there are potential disadvantages to resurfacing arthroplasty. It appears, in a proportion of cases, to require a greater resection of acetabular bone than conventional arthroplasty, and there is concern over the long-term survival of the femoral component. It is reported that men lose 18% and women 25% of bone mineral density in the femoral neck from age 30 to age 70. Thus, it is possible there will be more femoral neck fractures over time in resurfaced hips. Obviously, femoral neck fracture cannot occur after a conventional THA [7, 15].

Hip resurfacing is more likely to fail in female patients over 55 years old because of decreased bone density. Figure 6 shows the clinical results for 254 hips resurfaced, 154 male and 100 female hips. All patients were followed up for the time range 12-45 months [12]. Therefore there are age and gender limitations when hip resurfacing has been used.

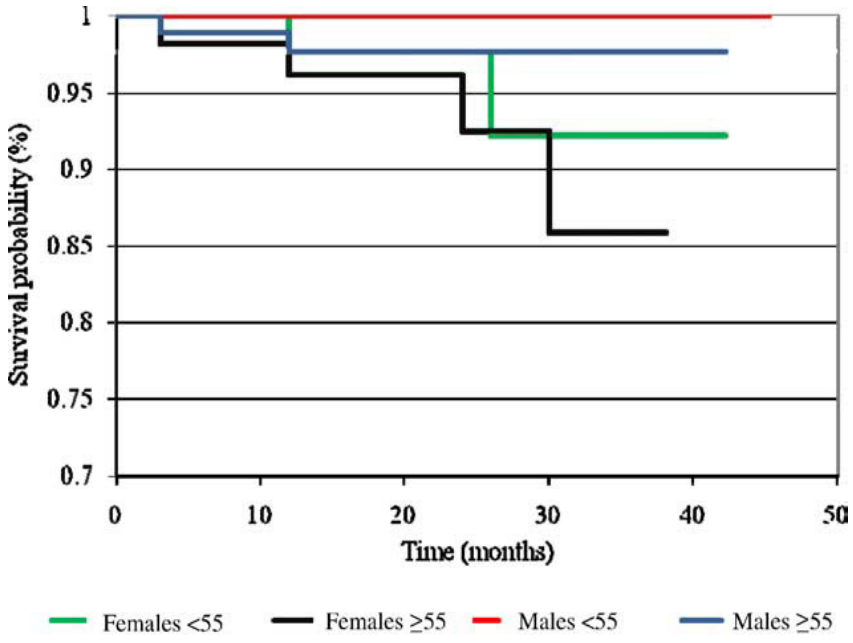

Figure 6: Male and Female survival probability of hip resurfacing, reproduced from Jameson [12].

1.4 Metal on Polyethylene Hip joint (MOP)

The metal femoral head on a polyethylene cup is the most common choice for the artificial hip joint. This combination of materials has acceptable articulation properties such as shock absorption, very low friction and is also inexpensive. Charnley introduced low-frictional torque arthroplasty of the hip (LFA) into routine clinical practice in November 1962 [16]. Charnley low-friction arthroplasty which, in its original form, consisted of a stainless steel femoral component with a 22.225 mm diameter femoral head rubbing against a polytetrafluoroethylene (PTFE) acetabular cup. The low friction came from two design features.

The first was the choice of PTFE as one component of the joint which ensured a very low coefficient of friction. The second feature was the use of a small diameter femoral head which ensured that any friction generated, acted at a small radius, hence reducing the frictional torque which Charnley felt was important for the longevity of the procedure [2]. It reduced the stresses across the interface between the implant and the bone, which is the weakest part of the construct.

Sliding properties, mechanical strength and biocompatibility of polyethylene have been improved by the development of cross-linked ultra-high molecular weight polyethylene (UHMWPE). Although Metal on Polyethylene (UHMWPE) has high success rates, the osteolysis, foreign body reactions and implant loosening as a result of the polyethylene wear particles are still long term major concerns in total hip arthroplasty. There are three different metallic femoral heads, which have been used to articulate

against the polyethylene (UHMWPE) acetabular cups in the total hip replacement:

- Cobalt – chromium – molybdenum.
- Titanium – aluminium – vanadium.
- Stainless steel.

1.5 Metal on Metal Hip joint (MOM)

First generation MOM hip bearings include prostheses developed in the 1960s. Some implants from this era survived for more than 25 years because of low wear rates and minimal osteolysis. However, alongside these encouraging durability results, first generation MOM studies also demonstrated metal wear debris in tissues adjacent to the implants, particularly in prostheses with loose components or impingement. The first generation MOM articulations were commonly used until the mid – 1970s. Most were then abandoned in favour of MOP articulation. The main reason for this change was the introduction of the Charnley low-friction arthroplasty.

Long-term results of MOM implants had boosted their popularity and led to the development of second generation MOM implants in the early 1980s. In addition, polyethylene wear from MOP implants was hypothesized to cause osteolysis around the implant. Second generation MOM implants have an improved bearing interface and are composed of alloys with an increased metal hardness, it was also much tighter tolerances and more accurate manufacturing. Although medium and long term clinical results with MOM bearings appeared to have demonstrated excellent durability, recent studies have shown that MOM bearing systems are not resistant to osteolysis. The widespread

acceptance of MOM articulations has been tempered by concerns regarding increased metal ion production from these devices. Within the cells of tissues, nanoparticles are exposed to a series of oxidative mechanisms designed to destroy the foreign body, which leads to the generation of metal ions [17].

By the use of MOM bearings, significantly lower wear is experienced, 0.19 mm^3/year for MOM compared to 0.98 mm^3/year for MOP. The amount of volumetric wear was reduced; but the number of particles produced increased 100-fold. These bearings have raised new problems associated with small metal particles and their relationship to the local and systemic environment within the body. Furthermore, with increased numbers of small metal particles the surface area available for corrosion is also increased. Nano-sized particles could be absorbed more easily than micro-particles and can cause more DNA damage [18].

Metal particles and ions may spread throughout the body by blood and lymphoreticular dissemination and potentially have harmful effects on the immune system, the kidneys and the nervous system [19]. Serum cobalt levels are the most frequently reported metal ion concentrations, and they were found to be 5–6 fold higher in patients after MOM implantation than preoperatively [20].

1.6 Ceramic on Polyethylene Hip Joint (COP)

In the mid-1970s, a total hip replacement in the form of a ceramic femoral head and a polyethylene acetabular cup was introduced in order to reduce the volume of polymeric wear debris. In more recent years ceramic femoral heads

have been mounted on metallic stems in modular constructions in increasing numbers in order to provide an inert, very hard, smooth counterface for polyethylene acetabular cups as a means of reducing wear. Laboratory and clinical data strongly confirm that wear is considerably reduced with the ceramic femoral head penetrating into the acetabular cup at a rate of fifty percent, or less, of the rate for comparable metallic heads [21].

For a period of time high purity alumina (Al_2O_3) has been used for femoral heads of hip joint implants due to its excellent immunological biocompatibility, longevity, corrosion resistance and wear resistance. The mid 1980s marked the entry of zirconia into the orthopaedic field. Zirconia is a ceramic that offers higher strength and higher fracture toughness associated with similar biocompatibility when compared to alumina.

Today hip joint implants made of a titanium stem, ceramic ball head, ceramic or polyethylene inlay and titanium acetabular cup are considered the most reliable. In the 1970s, failure rates of implanted ceramic heads of up to 13.4% were reported. The most recent studies report failure rates in the range of 0.004 – 0.05%. This includes all causes of fracture including impingement, combinations of head with damaged metal tapers or non-approved tapers, entrapped debris in the stem – ball interface, material flaw, incorrect surgical use, wrong cup position and mishandling. Even though the probability of failure is very low nowadays, all possible measures should be considered to decrease it further.

Despite the excellent material properties of ceramics noted above, their fracture toughness is low compared to metals. The presence of contaminants

or scratches can yield a non-uniform load transfer which induces stress concentrations in the ball head, thus increasing the risk of failure [22].

1.7 Ceramic on Ceramic Hip Joint (COC)

Aluminium oxide and zirconium oxide are the most widely used ceramics on both bearing surfaces, as shown in Figure 8. Ceramics were introduced in total hip arthroplasty because of their high wear resistance and low friction.

Figure 8: Ceramic-on-ceramic hip joint Replacement, reproduced from [23]

With the increasing number of prostheses implanted, audible squeaking has arisen as a new complication. The incidence of squeaking varies considerably, ranging from less than 1% to 21%. The exact mechanism for squeaking remains unclear [24].

Ceramics are known to be brittle materials with no ductility and limited bending strength. As the material has no possibility to deform, implants break without warning. Several factors have been reported to increase the risk of failure of ceramic heads including increased body weight, high activity level,

and entrapment of a foreign body between the taper and the ball, but the most important factor is material quality. Although COC bearings have proven their efficacy in the long term, concern remains over some risk of fracture and the cost of the prosthesis [25].

The clinically relevant alumina COC particles are less toxic than the cobalt-chromium MOM particles relative to the equivalent particle volumes. This emphasises the fact that the nature, size and volume of particles is important in assessing the biological effects of wear debris on cells in vitro [26]. Figures 9 and 10 illustrate the volumetric wear rate for different bearing surfaces [27].

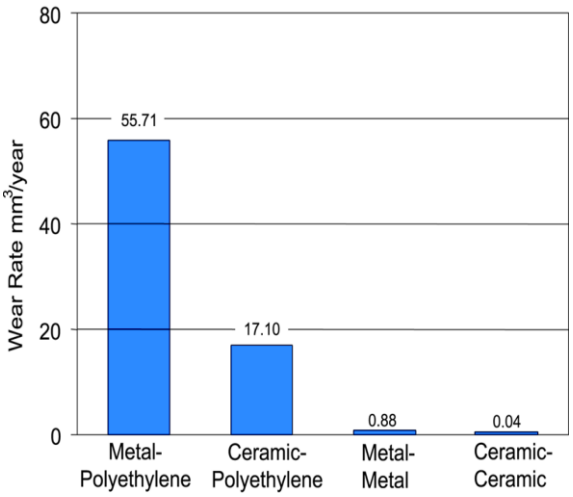

Figure 9:Wear rate of bearing couples[27]

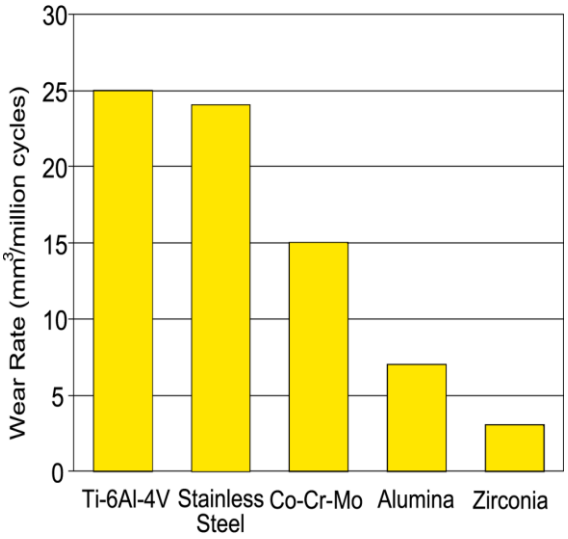

Figure 10: Wear rates of polyethylene when used against various orthopaedic materials [27]

1.8 Fixation of the prosthesis

Fixation of the artificial hip joint is accomplished either with or without cement. The two components of the implant, stem and cup may or may not be cemented to the thigh bone and the acetabulum respectively. Both ideas have significant support and the surgeons have several preferences.

1.8.1 Cemented fixation

The use of cemented hip prostheses has given excellent clinical results. The success of cemented implants depends on many factors. Fatigue failure of the cement mantle interfaces, stem-cement and cement-bone, have each been identified as a possible loosening mechanism of the prosthesis. A cement thickness higher than 2 mm does not apparently affect the mechanical behaviour of the cement mantle [6].

Due to the high physical loading, use of cemented fixation is not recommended for active and young patients. Studies concluded that cement crack failures begin in the cement bone interface with formation of micro-cracks [28, 29]. Other authors have indicated that the most critical success factor is the interface between stem and cement, where localized high strains occur in the cement mantle due to the difference between cement and stem stiffness values [30].

1.8.2 Cementless fixation

Concepts of cementless fixation involve screwing or press-fitting the components into the bone to provide initial stability. The long-term fixation is then achieved by subsequent bone growth into the porous coating or rough surface of the implant over time, to provide what is referred to as biological fixation [31]. There are other methods to achieve additional cementless fixation. Various shapes and cross–sections, rectangular or taper, of the femoral stem are commonly used to fix the femoral component. Furthermore, spikes and fins may be included on the outer surface of the cup or the shell to locate them firmly into the concave surface of the acetabulum.

1.9 Discussion

MOM total hip replacements have been used widely due to their low wear rate comparing to the conventional MOP prostheses. High wear rate and wear particles of the MOP have been considered to be the reason for developing the osteolysis and the aseptic loosening and they are still long term major concerns in total hip arthroplasty. This is particularly the case with younger patients who tend to be more active than older patients and have longer life expectancy. For such patients the MOP prosthesis is not attractive and more appropriate solutions are required. COC hip replacements have very low surface roughness and high wear resistance, both of which are highly desirable characteristics. However their mechanical properties are not ideal as they are brittle materials with limited bending strength and have been found to break without warning.

MOM bearings could emerge as a good choice for replacing the diseased or damaged natural hip joint, particularly in younger patients. They present a different design challenge and a means to conduct a detailed analysis of the lubrication mechanism taking into account the true shape of the components is a necessary step in building a comprehensive understanding of their operation. They are known to generate large numbers of very small wear particles. There have been examples that have functioned extremely well in patients, and others where their performance was less satisfactory. Both of these considerations need a robust accurate lubrication analysis as a basis for further investigation. This is therefore the main focus of the research reported in the thesis.

Literature Review

The term bio-tribology was introduced by Dowson and Wright in 1973 to cover all aspects of tribology related to biological systems. The best known examples of the subject are the numerous studies of natural synovial joint lubrication and the design, manufacture and performance of various forms of total joint replacements [32]. Eliminating wear and operating with fluid film lubrication could one day allow the artificial hip joint to reproduce the tribological performance and function of the natural synovial hip joint.

In engineering there are three distinct lubrication regimes: fluid film lubrication, mixed lubrication and boundary lubrication. The main problem associated with the long term survival of ultra-high molecular weight polyethylene (UHMWPE) hip joint replacement is loosening believed to be caused by the adverse tissue reaction to wear particles. The film thickness is generally thought to be much smaller than the surface roughness of the UHMWPE bearing surface, consequently leading to a mixed or boundary lubrication regime and generation of wear particles [33]. MOM bearings for total hip arthroplasty are an alternative to polyethylene bearing surfaces. Hip simulators demonstrate that MOM bearings have lower wear rate volume than MOP bearings. However, clinical reports have identified concerns related to metal ion release and hypersensitivity type lymphocytic reaction. The hypersensitivity reaction often leads to the formation of large complex fluid/soft tissue collections around the hip joint which can be clinically asymptomatic [34-35].

An efficient lubrication system between the ball surface of the femoral head and the inner surface of the acetabular cup of the artificial hip joint is a crucial factor for enhancing the long-term survival of these biomedical implant components. A large number of clinical, experimental and theoretical studies of the hip joint replacement have been reported in the literature, where different problems and theories investigated. In this chapter a number of each category of these research areas will be reviewed.

MOM bearings are being used increasingly in total hip arthroplasty for treatment of arthritis of the hip in younger and active patients. The advantages of this approach include increased stability and decreased wear as compared to metal-on-plastic bearing surfaces. However, there have been reports of metal debris generated from wear being detectable in the blood, tissue and urine. The localized effect of metal debris produces groin pain and soft-tissue lesions that are termed *Pseudotumors* around the hip, which should be taken seriously as they identify a metal reaction. These reactions can cause progressive soft tissue necrosis leading to instability [36-41].

A comparison study for 144 patients using MOM large diameter femoral head of total hip arthroplasty was carried out between April 2006 and November 2008 by Lavigne et al [42]. The purpose of this study was to compare the amount of metal ion release (chromium and cobalt) from four different types of prostheses supplied by four different implant manufacturers (Biomet, DePuy, Smith & Nephew, and Zimmer). The femoral head and acetabular component were both made of high-carbon-content cobalt-chromium alloy in each of the four types of prostheses. For chromium ion levels, no significant differences were found between the four groups at all follow up time periods. For cobalt ion

levels a significant difference was found between the groups at three, six, twelve and twenty four months with the Zimmer implant showing the highest levels and the Biomet implant the lowest. The source of metal ion is hypothesized to be wear and corrosion at the junction between the adapter sleeve and the femoral stem may be responsible for elevated ion levels. There are limitations in this study, as the in vivo measurements of whole blood ion levels do not always reflect the local ion load around the implant and do not allow discrimination between ion release from wear of articulating surfaces and other sources.

It was found that the concentration of metal ions may affect bone cell health and contribute to the bone-related complications of the prostheses. Many authors have reported elevation of metal ions for patients who had MOM total hip arthroplasty. Short period studies and follow-up for twelve months in 29 patients and longitudinal follow-up in 44 patients for a minimum of 7 years postoperatively showed higher ions levels. Circulating physiological levels of cobalt and chromium are normally less than 0.25 μg/l, while the mean serum chromium and cobalt levels in these patients were 1.3 and 2.2 μg/l at 12 months. Although there was a consistent increase in the mean serum chromium level until 3 years after implantation, there was little difference in the levels from years 3 to 7 postoperatively. It has also been demonstrated that the addition of a sleeve with modular junctions causes more ion release than bearing surface wear [43-45].

COC and MOM hip arthroplasty have been compared in many different studies. Porat et al [46] in 2012 reviewed records of 2907 total hip arthroplasty implanted between 1996 and 2009; 1697 (58%) had COC and 1210 (42%) MOM bearing surfaces. Femoral head sizes ranged from 28 to 36 mm for the COC cases and from 28 to 60 mm for the MOM cases. The minimum follow-up for the COC cases was 6 months (mean, 48 months; range 6-97 months) and for the MOM cases was 24 months (mean, 60 months; range, 24-178 months). The overall COC revision rate was 2.2% (38 of 1697) with aseptic loosening accounting for 55% of revisions. The overall MOM revision rate was 5.4% (65 of 1210) with adverse tissue reactions accounting for 26% of revisions.

In 2011 Bernasek et al [47] identified the incidence of "squeaking" in modular MOM prostheses in total hip arthroplasty and studied whether males or females were more likely to experience squeaking. They reviewed the patient records and radiographs of 539 patients (542 hips) from three independent centres who underwent a MOM arthroplasty between February 2001 and December 2005. The minimum follow-up was 36 months (mean, 76 months; range, 36-119 months). The acetabular cup and femoral stem were made from titanium alloy with a porous surface coating, whereas the femoral heads and acetabular inserts were cobalt-chromium alloy. They identified squeaking in eight of the 542 hips; five were in women and two were in men (one patient had bilateral squeaking). No hips with 45^{o} or less acetabular inclination squeaked (291 hips); eight of 251 hips with inclination angles greater than 45^{o} squeaked. In this research there was no information about the number of male patients of the total (539) to specify the percentage. So the occurrence for male and female patients is not clear.

Contact forces and friction moments were measured in vivo during walking in eight patients by Damm et al [48] in 2013. Instrumented hip implants with 32 mm diameter heads were used. In vivo measurements were taken 3 months post operatively. Peak contact forces of 248% of the bodyweight and peak friction moments of 0.26% bodyweight times meter were determined, as shown in figure 2.1(a) and (b). A telemetry circuit, 6 strain gauges with an accuracy of 1-2%, and a secondary induction coil were placed in the hollow neck, which was closed by welding. The strain gauge signals were transferred via an antenna in the implant head to the external receiver. A coil around the hip joint powered the inner electronics inductively. The equations used to calculate the friction coefficient were;

$$\mu_x = \frac{M_x}{(F_{yz} * R)} \ldots\ldots (2.1)$$

$$\mu_y = \frac{M_y}{(F_{xz} * R)} \ldots\ldots (2.2)$$

$$\mu_z = \frac{M_z}{(F_{xy} * R)} \ldots\ldots (2.3)$$

where F_{yz}, F_{xz} and F_{xy} are the measured forces in the sagittal, frontal and horizontal planes respectively.

$M_{x,}$ M_y and M_z are the measured moments.

R is the radius of the head, the results of these equations are shown in Figure 2.1 (c).

The friction force, can be calculated by:

$$F_{friction} = \mu * F_{res} \quad \ldots\ldots (2.4)$$

The friction moments increased during the extension phase of the joint. The average coefficient of friction also increased during this period, from 0.04 at toe off to 0.06 at heel strike. During the flexion phase the friction coefficient increased further to 0.14 at toe off. The large increase of the friction could be caused by the synovial fluid being squeezed out under load. In this investigation the number of patients was small, and only one implant type was used at only one speed of walking and one time after implantation which are limitations of this interesting work.

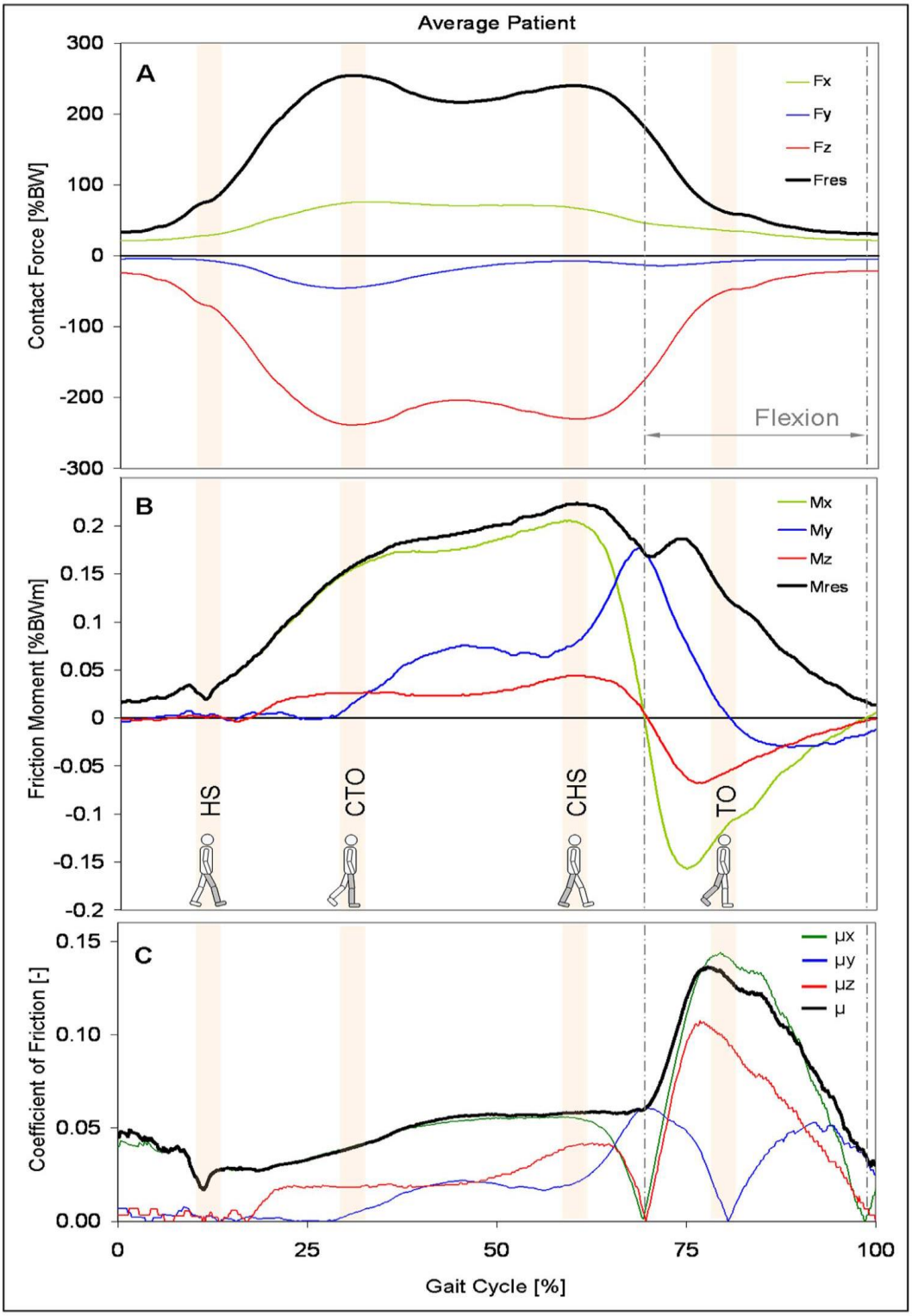

Figure 2.1 (a) measured contact force and its components, (b) measured friction moments and its components, (c) coefficient of friction from 3D calculation. The data are for an average subject during level walking at approximately 1 m/s [48].

In 2005 Liu et al [49] employed the finite element method using the Abaqus package (Version 6.4-1) to compare the contact mechanics at the bearing surfaces between a MOM hip resurfacing 50 mm diameter prosthesis and a 28 mm diameter total hip replacement with similar bearing material combination. The nominal diametrical clearances between the femoral head and acetabular cup for the hip resurfacing and total hip replacement prostheses were 145 and 120 μm, respectively. All implants were manufactured from high-carbon cobalt-chromium alloy. A fixed resultant contact load of 3200 N was applied to both models. A significant reduction in the predicted contact pressure by over 53% as well as a corresponding increase in the contact area by approximately 220% was found in the hip resurfacing prosthesis, in comparison to the total hip replacement. The predicted maximum contact pressures were 22 MPa for the resurfacing bearing and 47 MPa for the THA. The corresponding predicted contact area for the hip resurfacing and THA were 237 and 74 mm^2 respectively. The reduced contact pressure and increased contact area were due to the combination of the larger bearing size and increased elastic deflection of the metallic cup and the underlying bone support. A better understanding could be obtained from this study by using surgical and patient parameters within the simulation procedures.

The deformation of metallic acetabular cups for MOM hip resurfacing was investigated theoretically using the finite element method in 2006 by Yew et al [50]. Three representative cups, characterised by the cup wall thickness as thin, intermediate and thick were considered, as shown in Figure 2.2. Both two-dimensional axisymmetric and three-dimensional finite element models were developed to examine the important parameters during and after the press-fit

procedure, and in particular the deformation of the metallic cup. All cups were specified as high-carbon cobalt-chromium alloy. Two different methods of simulating the press-fit, multiple- displacement and multiple-load, were examined to simulate the procedure as realistically as possible without increasing the computational overheads.

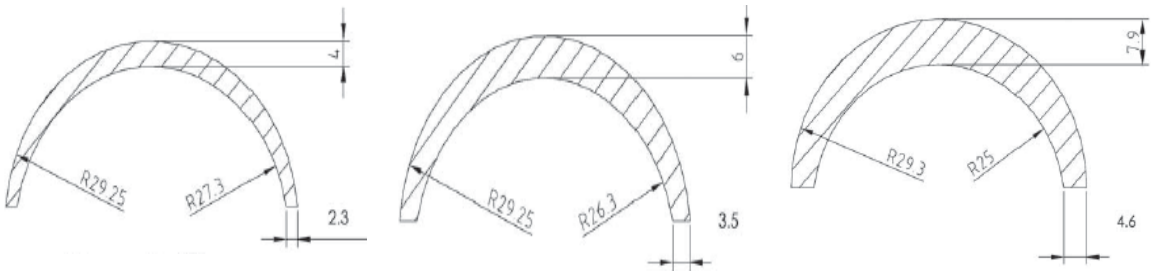

Thin cup intermediate cup thick cup

Figure 2.2 Cross-sections of three cup design [50].

The Abaqus package was used to simulate contact of the surfaces in this study using the contact pair option of master and slave surfaces. Different cup sizes (diameter between 46 and 70 mm) and various interferences between 0.25 and 1 mm were used. Simulation of the cup deformation behaviour was carried out using a two-point pinching model with a modified spherical cavity of polyurethane foam, as shown in Figure 2.3. The results were validated against classical Hertzian contact mechanics. The most significant factor influencing the cup deformation was the cup wall thickness. The cup deformation was found to increase as the cup wall thickness decreased, the interference increased, and the size increased.

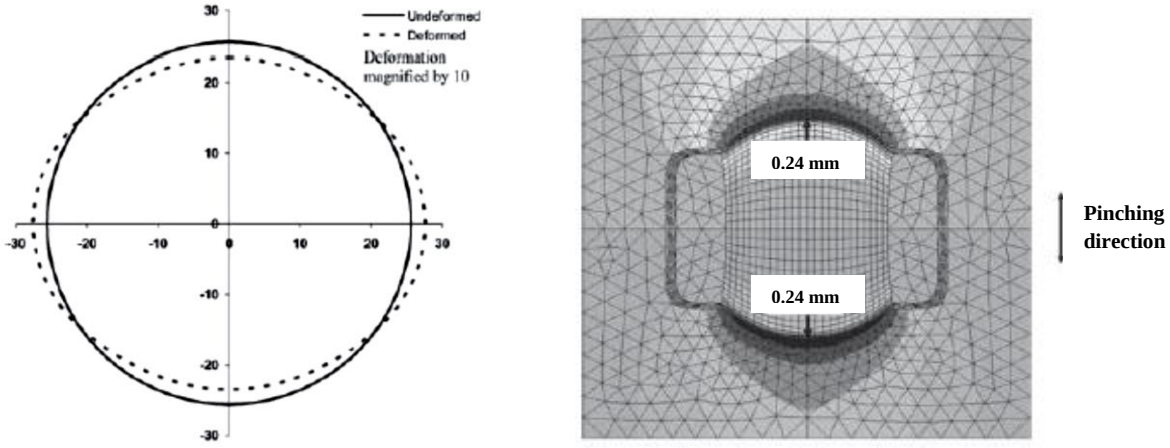

(a) (b)

Figure 2.3 (a) Original and deformed cup with a diametral interference of 0.5 mm under the punching action caused by press fitting of the cup. (b) Displacement of the foam in pinching direction [50].

The effect of the press-fitting on the cup deformation has been investigated by other researchers [51-54]. However, Yew and his group were only researchers to use the polyurethane foam with rectangular cut-outs to represent the in vivo situation, and they found a good agreement between the finite element simulation and experimental work using cadaveric specimens. The author of thesis has adopted the same polyurethane foam block approach in the research.

The combined influence of head lateral micro-separation and the acetabular cup abduction angle on the contact pressure were investigated by Sariali et al [55] in 2012. A 32 mm ball with a radial clearance 30 μm total hip arthroplasty was analysed using a finite element model. The cup was positioned with an abduction angle ranging from 45^{o} to 90^{o}. The medial-lateral micro-separation varied from 0 to 500 μm. A load of 2500 N was applied through the head centre.

Complete edge loading was obtained for a 60 µm medial-lateral separation, as shown in Figure 2.4. Under the case of centred loading, the maximum contact pressure was found to be 66 MPa, which is very close to the theoretical value predicted by the Hertz theory (64.4 MPa).

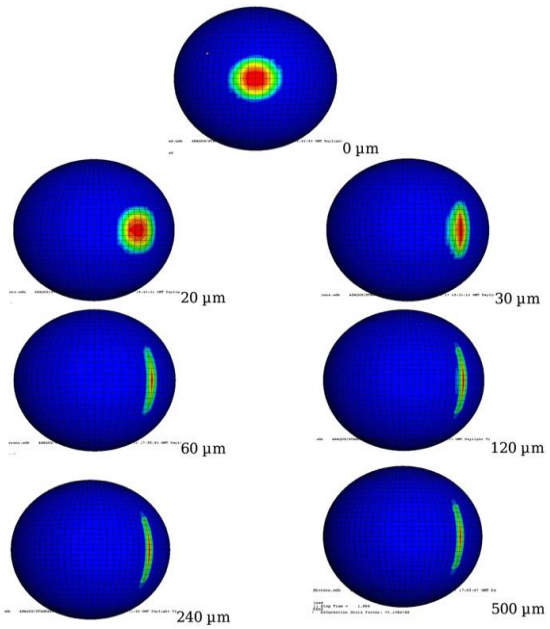

Figure 2.4 Results of FE contact analyses with medial lateral micro-separations between 0 and 500 µm showing changing contact area shape as the micro-separation increased [55].

Under edge loading conditions, the contact area was found to be elliptical. Both cup abduction and lateral micro-separation displacement induced a large increase in the contact pressure. Indeed, above 240 µm the contact pressure reached an asymptotic value of about 200 MPa as shown in figure 2.5. This

model did not take into account the surrounding bone, it modelled only the bearing surfaces. Furthermore, it did not take into account the effects of lubrication. A further limitation is that the load used was higher than the reported in vivo values.

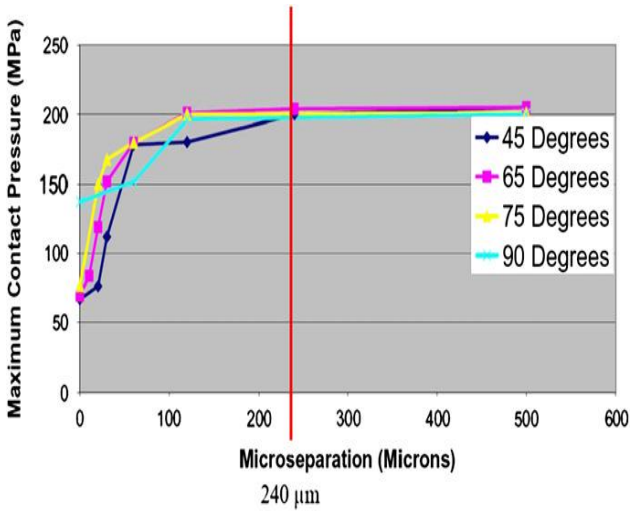

Figure 2.5 Variation of contact pressure according to the cup abduction angle and head lateral microseparation values [55].

In 2003 Udofia and Jin [56] highlighted the importance of the design and manufacturing parameters on the tribological performance of MOM hip prostheses. An Elastohydrodynamic Lubrication (EHL) analysis was carried out under a simple steady state rotation ω, of 2 rad/s to represent the flexion and extension motion. The Reynolds and elasticity equations were coupled and solved numerically. A constant vertical load of 2500 N was considered with the acetabular cup assumed to be positioned horizontally. The effect of radial clearance on the predicted film thickness and pressure distribution was investigated. Under realistic physiological walking conditions a decrease in the

radial clearance from 150 to 50 μm resulted in a 137% increase in the predicted minimum film thickness from 19 to 45 nm.

That could be used to obtain the ratio of the theoretical film thickness to the composite roughness of the surfaces

$$\Lambda = \frac{h_{min}}{\sqrt{R_{q1}^2 + R_{q2}^2}} \dots\dots (2.5)$$

where R_{q1} and R_{q2} are root mean square roughness height of surfaces 1 and 2, respectively.

Λ is an indicator of the lubrication regime with Λ > 3 corresponding to full film conditions and Λ < 1 indicating significant asperity interaction and boundary lubrication conditions.

Consequently, given a surface roughness of 0.01 μm for both contacting surfaces, the predicted mixed lubrication regime for the larger clearance was changed to a full fluid film lubrication regime for the smaller clearance. In this research of Udofia and Jin, it would be necessary to consider the variation of the cup thickness and the anatomical position of the cup on the predicted film thickness. As it is known that a decrease in the cup thickness would result in a significant increase in the elastic deformation, this factor could influence the lubrication behaviour.

Also in 2004 Dowson et al [57] studied the variation of clearance and head diameter of MOM hip implants on the wear rates both experimentally in simulator tests, and theoretically in terms of film thickness and lambda ratio (Λ). Head diameters ranging from 16 – 54 mm and diametral clearance from 53 –

307 μm were studied. Effective mixed-film lubrication achieved through careful design and manufacture greatly reduced wear.

Heads and cups were manufactured from cobalt chromium alloy. A constant load, 2500 N, and angular velocity, 1.5 rad/s, were used. The running-in wear volumes were very low for larger diameter heads and smaller clearance, as shown in Figures 2.6 and 2.7. Where the volumetric wear increased relatively and almost linearly for both 16 mm and 22 mm diameter joints as can be seen in Figure 2.6 for points (a), this is indicative of a full boundary mode of lubrication. On the other hand, steady low wear rates were established earlier as the head diameter increased from 28 mm to 36 mm and then 54.5 mm, as shown in the same figure for points (b) and (c). The results have shown that head diameters should be as large as possible and the diametral clearances as low as practicable to ensure that the joints operate well into the mixed lubrication regime. Effects of the variation of the diametral clearance and the head diameter on the lubrication system and wear rate were investigated by other researchers [58-59]. They found that increasing the diameter of the head and reducing the radial clearance of the MOM hip replacement will transfer the lubrication system from boundary to mixed lubrication with a consequential reduction in the wear rate. These results emphasize what Dowson et al found, although the computational wear model of Feng Liu et al [60] in 2012 showed that an opposite result was obtained if the material of the cup was UHMWPE. Feng found that the calculated wear rate of the PE bearing based on their wear model can be decreased by twofold by increasing the bearing clearance from 0.02 to 0.35 mm, and a larger diameter generally resulted in a higher wear rate.

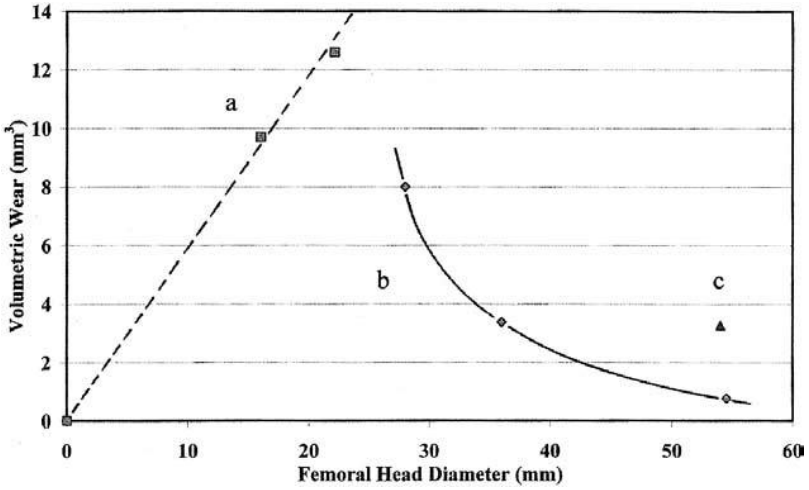

Figure 2.6 The influence of femoral head diameter on volumetric running-in wear. (a) boundary lubrication, 16 and 22 mm diameter; (b) mixed lubrication, 28 mm c_d (55-70) µm, 36 mm c_d (76-78) µm, 54.5 mm c_d (83-129) µm; (c) 54 mm c_d (254-307) [57].

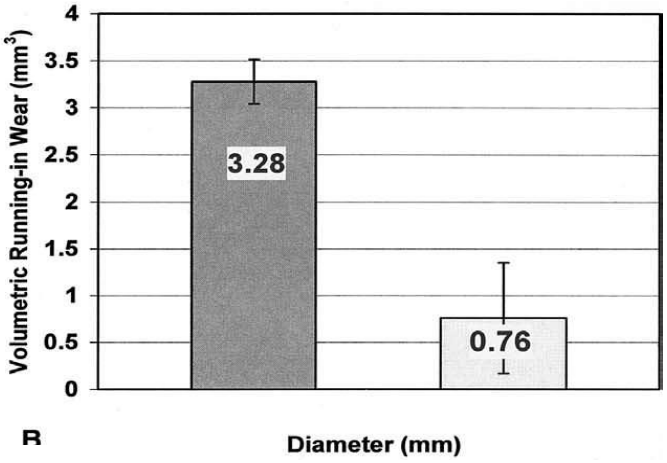

Figure 2.7 Influence of diameter clearance on running-in wear for 54 mm c_d (254-307) µm and 54.5 mm c_d (83-129) µm [57].

In 2006 Liu et al [61] analysed the performance of EHL for a typical MOM bearing employing a polyethylene backing underneath a metallic cup inlay under dynamic operating conditions of load and speed representative of normal walking. The major load component in the vertical load direction and the major flexion / extension motion were considered in the study. The radius of the femoral head was 14 mm with a nominal radial clearance of 60 μm between the head and cup. A Newtonian and iso-viscous lubricant model was assumed. It was found that the polyethylene backing employed in the MOM hip, combined with dynamic squeeze film action, significantly improved the transient lubrication film thickness under cyclic walking and consequently a fluid film lubrication regime was possible for smooth bearing surfaces provided that the average roughness was less than 0.005 μm. The hip joint is generally subjected to dynamic load and speed in three directions during walking, whereas, only the major components of load and speed were adopted in this work. A better result could be obtained from this work if the three components of load and speed were used. Gao et al [62] found that the lubrication in the MOM hip implant was improved under 3D physiological loading and motion.

A novel MOM hip implant employing a specific aspherical bearing surface, Alpharabola, as the acetabular surface was investigated in 2010 by Meng et al [63]. Dry contact and Elastohydrodynamic lubrication under steady state conditions were analysed. The alpharabola surface defined in equation (2.6) was employed as the internal bearing surface of an acetabular cup.

$$\frac{x^2}{R_2^2/\alpha} + \frac{(y-R_2+R_2/\alpha)^2}{R_2^2/\alpha^2} + \frac{z^2}{R_2^2/\alpha} = 1 \quad \text{.....(2.6)}$$

Here *x*, *y* and *z* are Cartesian coordinates defined in figure 2.8, R_2 is the desired minimum radius of curvature of the Alpharabola surface, and α is the parameter to control the variation rate of the radius of curvature.

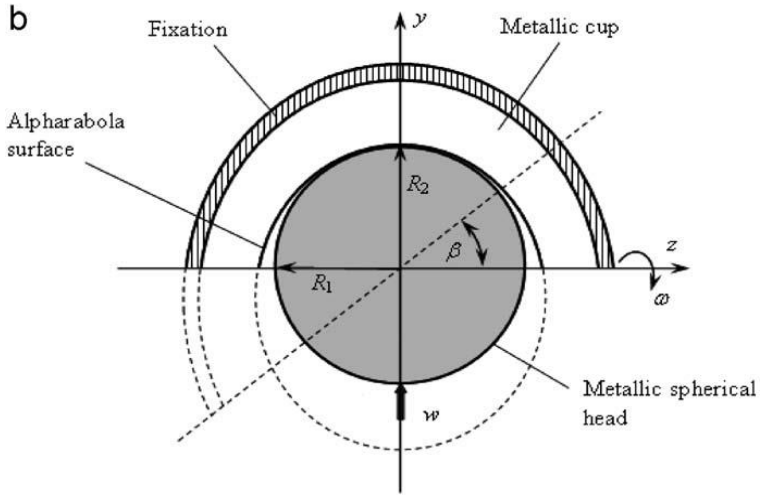

Figure 2.8 The MoM hip implant using Alpharabola as the cup surface [63].

Both femoral head and acetabular cup were specified as cobalt chromium alloy. The cup thickness of 9.5 mm for a typical 28 mm MoM hip implant was adopted. The bone and the fixation of the cup were represented by an equivalent support layer 2mm thick with appropriate mechanical properties. The vertical load was chosen as 3000 N and only the angular velocity around z-axis was considered with a value 2 rad/s. The results compared with the conventional spherical bearing surfaces showed that a more uniform pressure distribution and a thicker lubricant film thickness within the loaded conjunction were predicted for this novel hip implant. However, the manufacturing of the Alpharabola cup can be potentially more challenging due to the local non-spherical surface. The manufacturing errors and the angles of inclination and anteversion produced during the implantation operation could also affect the sensitivity of the lubrication performance of the Alpharabola cup surface.

In 2010 Gao et al [64] simulated the surface texture with simple cylindrical dimples numerically under steady state and walking conditions. A MOM hip replacement made from cobalt chromium alloy was assumed using a ball-in-socket model. A cylindrical dimple profile was numerically generated as shown in Figure 2.9. The radius (r) and the depth (d) of the dimples were chosen to be 0.2 mm and 1 μm respectively. The dimples were distributed over the bearing surface with a uniform spatial interval (L) of 2 mm.

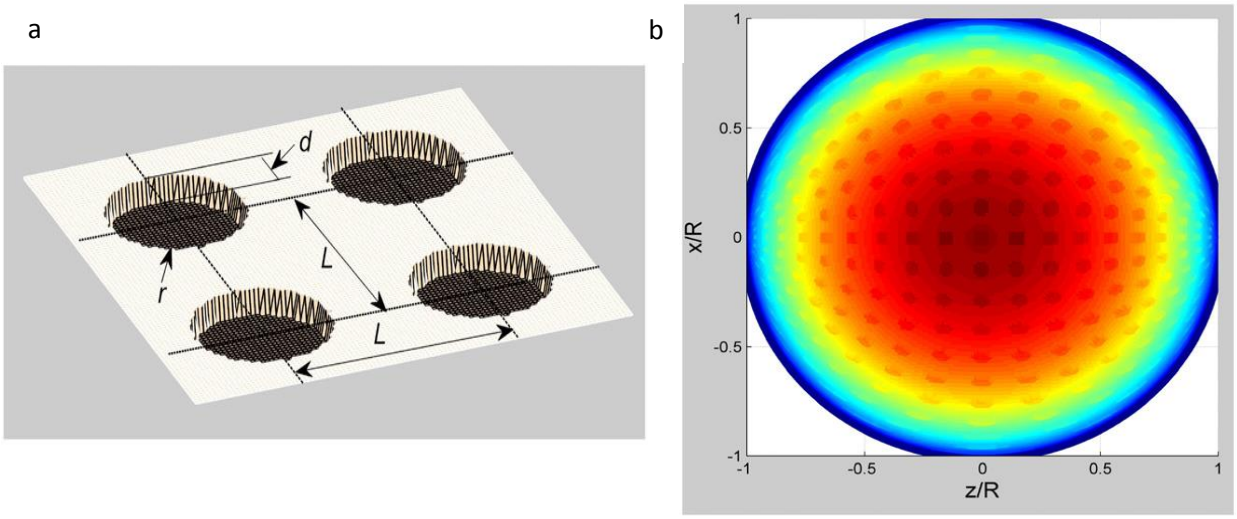

Figure 2.9 Illustration of dimple surface texturing [64] showing (a) geometry of virtual dimples, and (b) their distribution on the bearing surface.

The results showed that surface texturing may have a potentially beneficial effect on the lubrication performance of MOM hip replacements. The average film thickness of the dimpled surface model was found significantly increased, mainly due to the contribution of dimpled surface texture. For example, the average film thicknesses of the dimpled and smooth surfaces were 0.053 μm and 0.04 μm respectively.

Friction moments of the hip joint in various bearings under simulated physiological joint conditions were measured using custom test apparatus by Bishop et al [65] in 2008. One sample each of nine different bearing pairs was available for testing. The surface finish of all implants was measured with a surface scanner and the arithmetic average of the absolute values, R_A, ranged from 0.01 to 0.03 μm for all implants with the exception of the polyethylene cup which had a mean roughness of 0.25 μm. MOM, MOP, MOC and COC bearings were tested. Diameters ranged from 28 to 55 mm and diameter clearances from 0.053 to 0.235 mm were used. Distilled water alone and distilled water with 17% foetal calf serum were used as lubricant at room temperature. The largest moments in serum were measured for large diameter MOM bearings, followed by MOP and the lowest moments were for small diameter COC and MOC combinations. Water as a lubricant was found to double the moments in comparison with serum. In this work there was only one sample of each bearing type used so that any variations in manufacture or test set-up could not be tested and statistical evaluation was limited.

Summary

Literature regarding hip prostheses, in general, and MOM types, in particular, has been reviewed in this Chapter. The functional behaviour of MOM joints is not fully understood and is the subject of this investigation. The emphasis taken is that of examining the mechanical action of these joints with particular reference to their capability in forming lubricating films to separate the contacting components. Key questions to be examined in the research are

1- What is the relationship between the contact area and pressure in the prosthesis joint and what are the results of applying the Hertzian contact equations to the configuration?

2- How does the contact area and pressure vary as a result of the cup thickness and the means by which the cup is restrained?
3- Can EHL analysis techniques be used for the contacts, and how can they be utilised if the contacts do not behave in accordance with the Hertz equations?
4- Can the appropriate loading and kinematic conditions of the contact be obtained from the patient measurement information made available to researchers in the field?
5- Can a transient EHL analysis of the walking cycle be constructed based on the considerations given above?
6- What are the synovial fluid film thickness levels that can be expected in MOM prostheses, and can design choices be identified to optimise this?

The Governing Equations of the Elastohydrodynamic Lubrication of Point Contact

3.1 Introduction

In this thesis point contact EHL analyses have been carried out using available software. The author's contribution to the modelling has been to introduce surface gap corrections to the problem as part of establishing the most appropriate EHL model specifications for analysis of the MOM prosthesis contacts. The fundamental equations to be solved in the analysis are briefly reviewed in this Chapter for completeness.

The main governing equations of the (EHL) problem for point contacts will be described. The two contacting surfaces are assumed to be smooth and steady state conditions are adopted. The Hertzian theory for two contacting bodies will be used to obtain the maximum contact pressure and the radius of the contact area. The results of the dry contact finite element analysis (FEA) of this project will be compared with the Hertzian theory analysis. The gap outside the contact area zone from the Hertzian theory will be calculated and compared with the gap obtained from the FEA. From the principles of the Hertzian theory, when the principal radii of relative curvature of the contacting bodies are equal then the contact area shape is circular. Consequently, a circular point contact will be adopted due to the symmetry of the geometry used. The governing equations of the EHL analysis of the contact point are:-

- Film thickness equation for elastic surfaces.
- Reynolds equation for hydrodynamic lubrication.

The lubricant pressure within the contact area zone is related to the film thickness by the Reynolds equation, and it is considered that this pressure is sufficient to deform the two contacting bodies. Deformation of the bearing surfaces of MOM hip implants under load within the contact zone caused by representative contact pressure is typically of micron proportions, while the calculated film thicknesses are only a few tens of nanometres. The ratio of elastic deformation to film thickness can thus be of the order of 10^3 [63, 66].

3.2 Hertzian contact of two elastic bodies

The maximum contact pressure and the dimension of the contact area of the two elastic contacting bodies can be calculated using the geometry, the material properties and the applied load of the bodies, which are illustrated in Figure 3.1 for a general case. In engineering applications concentrated contacts may be line or point contacts according to whether the zero load contact takes place along a line (e.g. two cylinders with parallel axes) or at a point (e.g. a ball on a plane). Line contacts can occur between gear teeth but this involves edge effects with stress concentrations that are often controlled by crowing of the teeth to result in an elliptical point contact. For the research in this thesis the basic configuration is that of a ball in a hemispherical cup, which is a nominally circular point contact. The conventional presentation of elliptical point contacts is in terms of convex bodies and that approach is used here without loss of generality.

When the contact situation occurs with different principal radii of relative curvature $R_x \neq R_y$ then the resulting contact area is elliptical. If they are equal $R_x = R_y$ then the contact area is a circle. The Hertz theory for two contacting surfaces is based on a number of assumptions:

- The contacting surfaces are frictionless.
- The contacting bodies are treated as elastic half-spaces.

- The surfaces are continuous and non-conforming.
- The strains are small.

For contacting bodies whose principal axes of curvature coincide as illustrated in figure 3.1 the principal radii of relative curvature, R_x and R_y, can be calculated as follows [67]:

$$\frac{1}{R_x} = \frac{1}{R_{x1}} + \frac{1}{R_{x2}} \quad \text{.....(3.1)}$$

$$\frac{1}{R_y} = \frac{1}{R_{y1}} + \frac{1}{R_{y2}} \quad \text{.....(3.2)}$$

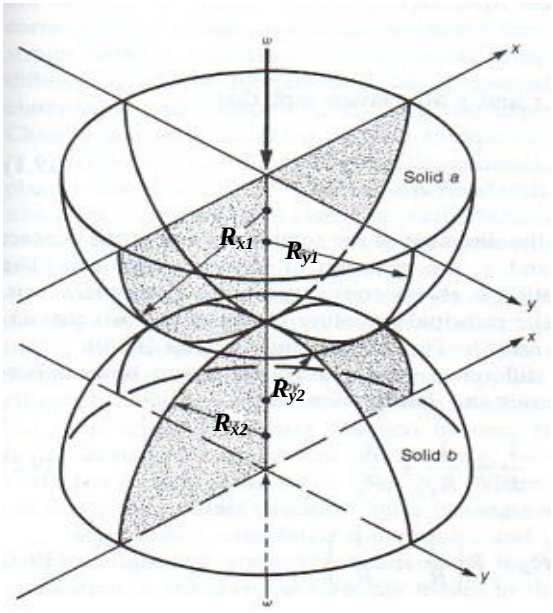

Figure 3.1 Contact of two elastic bodies [68].

when $R_{x1}=R_{y1}=R_1$ and $R_{x2}=R_{y2}=R_2$ the contact area is circular and the radius of relative curvature is the same in all directions and is given by;

$$\frac{1}{R} = \frac{1}{R_1} + \frac{1}{R_2} \quad \text{.....(3.3)}$$

If one of the bodies is concave, as in the current case where the ball is convex and the cup is concave, then a negative radius of curvature is applied in Equation (3.3) to obtain;

$$\frac{1}{R} = \frac{1}{R_1} - \frac{1}{R_2} \quad \text{.....(3.4)}$$

For a circular point contact the maximum Hertzian contact pressure is;

$$P_{o(h)} = \sqrt[3]{\frac{3}{2}\frac{W\,É^2}{\pi^3\,R^2}} \quad \text{.....(3.5)}$$

Where, suffix h indicates the results from Hertz's Equations.

The pressure distribution is in the form of an ellipsoid, and is given by;

$$P = P_{o(h)}\sqrt{1 - \frac{r^2}{a_h^2}} \quad \text{.....(3.6)}$$

where $r = \sqrt{x^2 + y^2}$

The radius of the contact area and the reduced elastic modulus are:

$$a_h = \sqrt[3]{\frac{3}{2}\frac{RW}{É}} \quad \text{.....(3.7)}$$

$$\frac{2}{É} = \frac{1-\gamma_1^2}{E_1} + \frac{1-\gamma_2^2}{E_2} \quad \text{....(3.8)}$$

An improvement to the Hertz theory for the case of a sphere in contact with a cup has been provided by Goodman and Keer [96]. This suggests that the contact is stiffer than that predicted by the Hertz equations and has a contact dimension that is approximately 3% smaller than the corresponding Hertzian result for the case illustrated which has radii in the ratio 1.01. The radius ratio for the contacts analysed in the current work is 1.004 and so the difference can be expected to be bigger.

The contact results obtained from the FEA analysis presented in chapter 7 have contact dimensions that are smaller than the Hertzian result and are therefore in closer agreement with the Hertzian analysis than with that of Goodman and Keer [96]. However, as the approach to the EHL analysis adopted in the current research is to generate Hertzian contacts that have the same contact dimensions as the actual FEA results, there is no advantage to be gained by relating the FEA contact analyses to the Goodman and Keer model. Furthermore, as the elastic deflection analysis embedded in the EHL approach is for plane semi-infinite bodies and is entirely compatible with the Hertzian contact model this is the best analytic contact model to adopt in this modelling role.

3.3 Lubrication of the Contact

The circular point contact can be considered as the contact of a sphere with a plane where the radius of the sphere is the radius of relative curvature given in equation (3.4). Furthermore, the plane may be regarded as rigid with the elastic deflection of the sphere being that for a body with reduced elastic modulus as given in equation (3.8). The nature of this elastic deflection is given in equation (3.30). This situation is illustrated in figure 3.2 which shows a schematic section of the equivalent contact in the entrainment direction of the EHL contact.

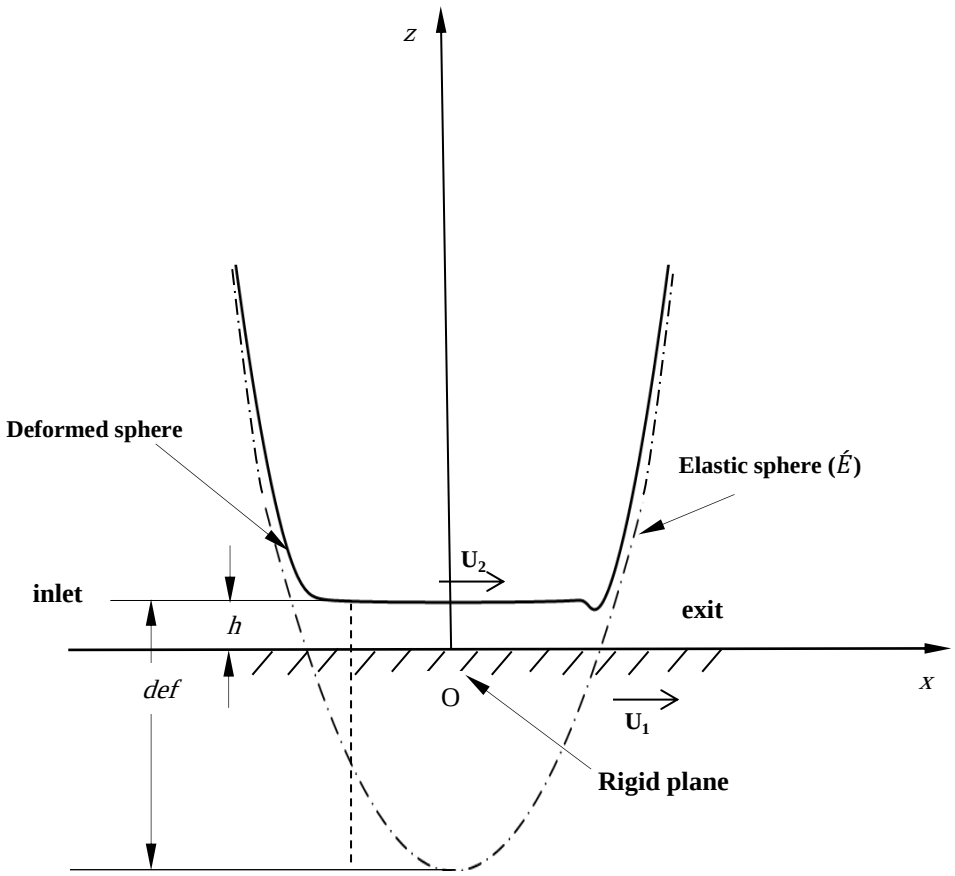

Figure 3.2 Schematic section of the EHL contact in the entrainment direction, *x*,

The figure illustrates the main features of an EHL contact. The elastic deflection results in a near parallel lubricant film in the entrainment direction in the area corresponding to the Hertzian contact. The lubricant film thickness, *h*, has a restriction at the exit of the contact. The lubricant is drawn into the contact area by the motion of the surfaces relative to the contact point, i.e. due to the surface velocities U_1 and U_2. The z axis is drawn at a larger scale than the x axis so that the undeformed sphere (chained) appears as a parabola. The elastic deflection, def, is large compared to the film thickness which is a characteristic of EHL.

The lubricant is contained between the two surfaces which are near parallel in the contact region including the inlet and exit zones. The way in which the lubricant moves and its varation of pressure is described by Reynolds equation which is derived in the next section.

3.4 Reynolds Equation

The governing equation to predict the hydrodynamic pressure of the oil film lubricant is known as Reynolds equation and it was obtained by Reynolds in 1886. It can be derived from the equilibrium of a small fluid element under the action of the viscous shear stresses and the fluid pressure. There are a number of assumptions that should be considered for deriving this equation which are listed below [69];

1- Body forces are neglected.
2- The pressure is considered to be constant through the film thickness.
3- There is no slip at the boundaries.
4- The lubricant is Newtonian.
5- The flow is laminar.
6- The fluid inertia can be neglected.
7- The lubricant density is constant through the film thickness.
8- The viscosity is taken as constant through the thickness of the film.

Consider the problem of the equilibrium of a small element of lubricant, as shown in Figure 3.3, with sides of length *dx*, *dy* and *dz* on which pressures and shear stresses act.

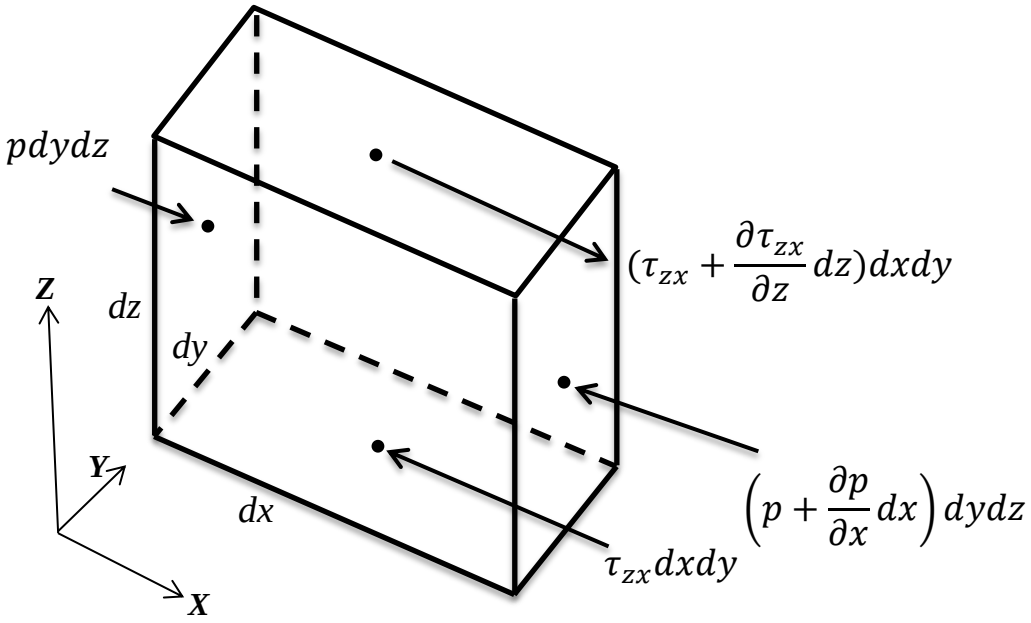

Figure 3.3 Equilibrium of an element

For equilibrium the forces acting in the, x-direction must balance so that;

$$pdydz + (\tau_{zx} + \frac{\partial \tau_{zx}}{\partial z} dz)dxdy = \tau_{zx} dxdy + \left(p + \frac{\partial p}{\partial x} dx\right) dydz \quad \ldots(3.9)$$

Multiplying out and cancelling,

$$\frac{\partial \tau_{zx}}{\partial z} dzdxdy = \frac{\partial p}{\partial x} dxdydz \ldots\ldots (3.10)$$

so that

$$\frac{\partial \tau_{zx}}{\partial z} = \frac{\partial p}{\partial x} \ldots. (3.11)$$

In the same way, summation of forces in the y-direction must be balanced to obtain;

$$\frac{\partial \tau_{zy}}{\partial z} = \frac{\partial p}{\partial y} \ldots. (3.12)$$

From the Newton's law of viscous flow

$$\tau_{zx} = \eta \frac{\partial u}{\partial z} \ldots (3.13)$$

and

$$\tau_{zy} = \eta \frac{\partial v}{\partial z} \ldots . (3.14)$$

where *u* and *v* are the velocities in the x and y directions respectively. Substituting these equations into the pressure gradient equations leads to;

$$\frac{\partial p}{\partial x} = \eta \frac{\partial^2 u}{\partial z^2} \ldots . (3.15)$$

$$\frac{\partial p}{\partial y} = \eta \frac{\partial^2 v}{\partial z^2} \ldots . (3.16)$$

From the basic assumptions, the pressure and the viscosity are constant through the film thickness, z-direction. So equation (3.15) can be integrated twice with respect to z to give;

$$\frac{\partial u}{\partial z} = \frac{1}{\eta}\frac{\partial p}{\partial x} z + C_1 \ldots . (3.17)$$

$$u = \frac{1}{\eta}\frac{\partial p}{\partial x}\frac{z^2}{2} + C_1 z + C_2 \ldots . (3.18)$$

where C_1 and C_2 are the integration constants. Two boundary conditions are required to determine the constants. From assumption 3;

when $z = h$, $u = U_1$

and when $z = 0$, $u = U_2$

where U_1 and U_2 are the surface velocities. Putting these boundary conditions into equation (3.18) gives;

$$u = \frac{1}{\eta}\frac{\partial p}{\partial x}\frac{(z^2 - zh)}{2} + (U_1 - U_2)\frac{z}{h} + U_2 \ldots . (3.19)$$

In the same way and with the boundary conditions $z = h$, $v = V_1$, and $z = 0$, $V = V_2$, the velocity v in the y-direction becomes;

$$v = \frac{1}{\eta}\frac{\partial p}{\partial y}\frac{(z^2 - zh)}{2} + (V_1 - V_2)\frac{z}{h} + V_2 \ldots . (3.20)$$

The lubricant flow rate per unit width in the x-direction, q_x, can be calculated by the integration $\int_0^h u\, dz$ and similarly the lubricant flow rate in the y-direction, q_y, is $\int_0^h v\, dz$.

Therefore

$$q_x = \int_0^h u\, dz = \frac{1}{2\eta}\frac{\partial p}{\partial x}\left|\frac{z^3}{3} - \frac{z^2 h}{2}\right|_0^h + \left|(U_1 - U_2)\frac{z^2}{2h}\right|_0^h + |U_2 z|_0^h \ldots (3.21)$$

giving

$$q_x = -\frac{h^3}{12\eta}\frac{\partial p}{\partial x} + (U_1 + U_2)\frac{h}{2} \ldots . . (3.22)$$

and in the same way

$$q_y = \int_0^h v\,dz = \frac{1}{2\eta}\frac{\partial p}{\partial y}\left|\frac{z^3}{3} - \frac{z^2 h}{2}\right|_0^h + \left|(V_1 - V_2)\frac{z^2}{2h}\right|_0^h + |V_2 z|_0^h \ldots (3.23)$$

$$q_y = -\frac{h^3}{12\eta}\frac{\partial p}{\partial y} + (V_1 + V_2)\frac{h}{2} \ldots\ldots (3.24)$$

For continuity of flow in steady state conditions equation (3.25) must be satisfied;

$$\frac{\partial q_x}{\partial x} + \frac{\partial q_y}{\partial y} = 0 \ldots\ldots (3.25)$$

It is possible to write $\bar{U} = \frac{U_1 + U_2}{2}$, and in most cases there is no surface movement in y-direction, therefore $V_1 = V_2 = 0$

Substituting equations (3.22) and (3.24) into (3.25) then leads to;

$$\frac{\partial}{\partial x}\left(\frac{\bar{U}h}{2} - \frac{h^3}{12\eta}\frac{\partial p}{\partial x}\right) + \frac{\partial}{\partial y}\left(-\frac{h^3}{12\eta}\frac{\partial p}{\partial y}\right) = 0 \ldots\ldots (3.26)$$

Re-write equation (3.26)

$$\frac{\partial}{\partial x}\left(\frac{h^3}{12\eta}\frac{\partial p}{\partial x}\right) + \frac{\partial}{\partial y}\left(\frac{h^3}{12\eta}\frac{\partial p}{\partial y}\right) = \frac{\partial}{\partial x}\left(\frac{\bar{U}h}{2}\right) \ldots\ldots (3.27)$$

Equation (3.27) is the steady state Reynolds equation in two dimensions used in this thesis and *x* is the entrainment direction.

3.5 The film thickness equation

The lubricant film thickness between the two contacting surfaces in the EHL analysis can be calculated by;

$$h(x,y) = h_u(x,y) + d(x,y) + S_e \dots\dots (3.28)$$

where h_u is the undeformed geometry and is calculated as;

$$h_u = \frac{x^2}{2R_x} + \frac{y^2}{2R_y} \dots\dots (3.29)$$

S_e is the separation between the two contacting surfaces.

and d is the surface deflection. For contacting bodies that are assumed to be semi-infinite the deformation of the elastic body is perpendicular to the contacting surface, and the pressure applied will cause a deflection at all points of the contacting surface of the semi-infinite body. This deflection is obtained by the integration of the pressure distribution applied to the surface using the equation given by Timoshenko and Goodier [70] as shown below;

$$d(x,y) = \frac{2}{\pi \grave{E}} \iint_{area} \frac{p(s,b)\, dsdb}{\sqrt{(x-s)^2 + (y-b)^2}} \dots\dots (3.30)$$

The integration term can be evaluated in a differential form which was given by Evans & Hughes [71], and for numerical calculations the deflection at any mesh point is given by

$$\nabla^2 d(x_i, y_j) = \frac{2}{\pi \grave{E}} \sum_{allk,alll} f_{k-i,l-j}\, p_{k,l} \dots (3.31)$$

where $f_{i,j}$ is the differential influence coefficient, and more detail about this coefficient can be found in Evans and Hughes [71].

3.6 The load equation

The predicted load from the EHL of the two contact bodies can be calculated by double integration of the pressure distribution over the computing domain;

$$W = \iint_{area} p\, dxdy \ldots\ldots (3.32)$$

3.7 The fluid properties model

The viscosity and density of the lubricant are both taken to be pressure dependent in the EHL model. The viscosity is assumed to be given by the commonly adopted equation due to Roelands (1966)

$$\eta = \eta_0 \exp\left\{\ln(\eta_0/\kappa)\left[(1+\chi p)^Z - 1\right]\right\} \qquad \ldots\ldots (3.33)$$

Constants κ and χ in this equation have the values $\kappa = 63.15 \times 10^{-6}$ Pa.s, and $\chi = 5.1$ GPa^{-1} Pa.s, and constant Z is chosen so as to have the specified pressure viscosity coefficient at ambient conditions by ensuring that the slope of ln(η) plotted against p is equal to α when p = 0, resulting in

$$Z = \frac{\alpha_0}{\chi \ln(\eta_0/\kappa)} \qquad \ldots\ldots (3.34)$$

The density is assumed to be given by the formula introduced by Dowson and Higginson (1966)

$$\rho = \rho(p) = \rho_0\left(\frac{1+\gamma p}{1+\lambda p}\right) \qquad \ldots (3.35)$$

with $\gamma = 2.266$ GPa^{-1} and $\lambda = 1.683$ GPa^{-1}

The lubricant in an artificial hip joint is peri-prosthetic synovial fluid in hip joint replacement patients (in vivo) and bovine serum diluted to various concentrations is generally used for simulator testing (in vitro). Synovial fluid, SF, is a viscous fluid that has lubrication, metabolic, and regulatory functions within synovial joints. SF contains lubricant molecules, including proteoglycan-4 (PRG4, also known as lubricin and a superficial zone protein) and hyaluronan. SF is an ultrafiltrate of plasma with secreted contributions from cell population linings and from within the synovial joint space, that include chondrocytes and synoviocytes. A major component of SF composition is proteins derived from plasma. Total protein concentration in normal human SF is 19–28 mg/ml, nearly one-third of that in plasma.

The rheological and tribological properties of SF have been characterized through measurements of viscosity, viscoelasticity, and friction. Normal SF is a viscous, non-Newtonian fluid. It behaves as a viscous material at low frequencies of oscillation, and as an elastic material at high frequencies.

The majority of investigative work determining the composition of synovial fluid has been carried out on bovine synovial fluid mainly because large quantities of it are available. Synovial fluid is a plasma dialysate modified by constituents secreted by the joint tissues. The major difference between synovial fluid and other body fluids derived from plasma is the high content of hyaluronic acid in synovial fluid.

Synovial fluid is believed to have two main functions: to aid in the nutrition of articular cartilage by acting as a transport medium for nutritional substances, such as glucose, and to aid in the mechanical function of joints by

lubrication of the articulating surfaces. Articular cartilage has no blood, nerve, or lymphatic supply. Glucose for articular cartilage chondrocyte energy is transported from the periarticular vasculature to the cartilage by the synovial fluid. Under fasting conditions, the glucose concentration of synovial fluid is usually approximately equal to that of blood. A decreased amount of synovial fluid glucose may be associated with articular diseases, particularly septic and immune-mediated arthritis [91-93].

Laboratory measurements of viscosity at various shear rates for the synovial fluid have shown powerful non-Newtonian shear thinning characteristics under relatively low shear rates. However, this shear thinning declines significantly at high shear rates [74]. Thus, it is usually appropriate to approximate the non-Newtonian synovial fluid with reasonable accuracy as a Newtonian fluid at the very high shear rates, which are likely to be experienced in hip joint replacement under steady walking conditions [59, 74].

3.8 Discretisation and method of solution

The deflection given in equation (3.30) means that the gap between the surfaces when pressure is developed that acts on them is given by

$$h(x,y) = h_u(x,y) + \frac{2}{\pi E'} \sum_{all\ k,all\ l} f_{k-i,l-j}\ p_{k,l} \quad .....(3.36)$$

where $h_u(x,y)$ is the shape of the undeformed gap between the surfaces.

This is stated in the differential form proposed by Evans and Hughes (2000) so that it may be included as a second differential equation to the EHL problem rather than in the integral form of equation (3.30). This becomes

$$\nabla^2 h = \nabla^2 h_u + \frac{2}{\pi E'} \sum_{all\ k,all\ l} f_{k-i,l-j}\ p_{k,l} \quad \ldots(3.37)$$

where $f_{i,j}$ are the differential influence coefficients and the pressures $p_{k,l}$ are those at the nodes of a finite difference grid with mesh size Δx and Δy.

The Reynolds equation is discretized using 2nd order central differences on the mesh illustrated in figure 3.4.

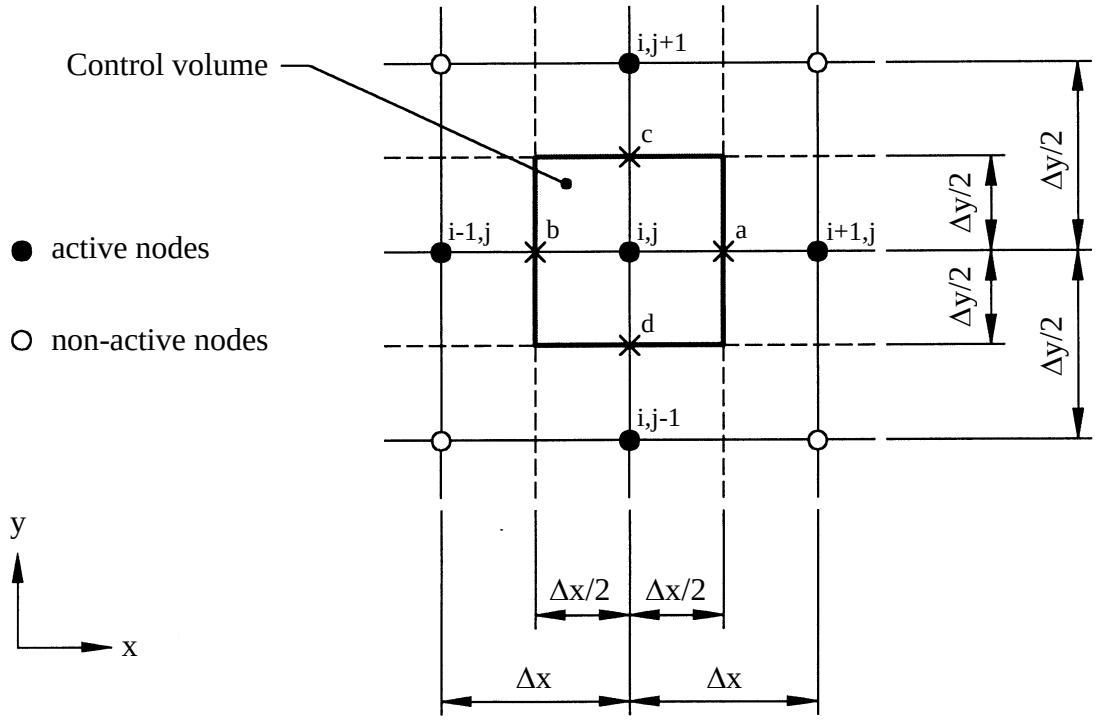

Figure 3.4 Detail of finite difference grid used to discretize the EHL problem.

For the equation applied at mesh point (i,j) the Reynolds equation becomes

$$- p_{i,j}\left(-\frac{\sigma_a+\sigma_b}{\Delta x^2}+\frac{\sigma_c+\sigma_d}{\Delta y^2}\right)+p_{i+1,j}\left(\frac{\sigma_a}{\Delta x^2}-\frac{\overline{U}h}{2\Delta x}\frac{\partial\rho}{\partial p}\right)+p_{i-1,j}\left(\frac{\sigma_b}{\Delta x^2}+\frac{\overline{U}h}{2\Delta x}\frac{\partial\rho}{\partial p}\right)$$
$$+p_{i,j+1}\left(\frac{\sigma_c}{\Delta y^2}\right)+p_{i,j-1}\left(\frac{\sigma_d}{\Delta y^2}\right)+h_{i+1,j}\left(-\frac{\overline{U}\rho}{2\Delta x}\right)+h_{i-1,j}\left(\frac{\overline{U}\rho}{2\Delta x}\right)=0 \qquad (3.38)$$

where $\sigma=\dfrac{\rho h^3}{12\eta}$.

The elastic equation is discretised on the same mesh to the form

$$\left(\frac{h_{i+1,j}+h_{i-1,j}-2h_{i,j}}{\Delta x^2}\right)+\left(\frac{h_{i,j+1}+h_{i,j-1}-2h_{i,j}}{\Delta y^2}\right)=\nabla^2 h_u+\frac{2}{\pi E'}\sum_{all\ k,all\ l} f_{k-i,l-j}\ p_{k,l} \qquad (3.39)$$

Where $\nabla^2 h_u$ is obtained analytically as 2/R.

Equations (3.38 and 3.39) are solved as a coupled pair of equations in the variables h and p. Equation 3.38 is nonlinear as terms ρ and η are dependent on pressure, and equation (3.39) involves all the pressures in the solution zone. Both equations are linearised in order to solve the problem and the solution to the non-linear problem is obtained at the end of a series of iterations that progressively develop distributions of pressure and film thickness satisfying all the equations. Equation (3.38) has an outer loop pressure which is used to find the values of ρ and η so that the terms in brackets are fixed for each mesh point during the coupled solution. For equation (3.39) only the eight points that are immediate neighbours to point (i,j) are included in the summation and the contribution of the remainder of the points is obtained from the outer loop pressure for those that are far away, and by using previous cycle inner loop pressures for those at an intermediate distance.

In this way the pair of equations involve pressures and film thickness at the nodes shown in figure 3.4. For the current study the method of solution was semi implicit with each row of n mesh points in the entrainment direction giving 2(n-2) equations in 2(n-2) unknowns $p_{i,j}$ and $h_{i,j}$, where j is fixed and p and h values on the neighbouring rows $j\pm1$ are fixed for the row j calculation. The additional values of the variables at i=1 and i=n were supplied by the appropriate boundary conditions. During development by Holmes et al [97] the problem was formulated as an alternating direction implicit method (ADI) but it was found that solutions were obtained more quickly by repeating the flow direction row calculations, rather than by solving the transverse rows alternately. This is a reflection of the fact that the flow is almost entirely in the entrainment direction within the Hertzian zone.

The boundary condition adopted for the film thickness was that its value at the inlet boundary on the entrainment centreline was given the value h_{con}, and

the remaining boundary points were given consistent values based on the undeformed film thickness variation h_u, and the deflection along the boundary as determined by using equation (3.30) for the current outer loop pressure to find the deflection at each point around the boundary.

The load was obtained for the outer loop pressure by using Equation (3.32) and this was assessed against the required load for the problem. In the initial iterative cycles the value of value h_{con} was kept constant, but as the outer loop pressure approached convergence, the value of h_{con} was adjusted periodically in order to obtain a final converged solution that supported the required load.

The author was not concerned with developments of the solution method other than those relating to the specification of the undeformed gap for the equivalent Hertzian models described in Chapter 6. The EHL solution routine was available as a package developed by other researchers at Cardiff, and the author was able to use it successfully for the research carried out in this project.

Development of FEA Contact Models

4.1. Introduction

In this chapter modelling the dry contact problem between two elastic bodies using the ABAQUS FEA system will be described. The nature of the contact shape, line, circular or elliptical, and the maximum contact pressure can be obtained by specifying the load, material properties, geometry of the contacting bodies and carrying out a contact analysis. To develop a technique for making such analyses between 3D bodies, a ball on plane contact as shown in Figure 4.1, was used as the first stage to simulate the contact in the hip joint. Representing the contact in the hip joint anatomically was regarded as a second stage to be proceeded when the contact analysis technique had been developed and validated with the ball on plane contact for which an analytical solution is available.

At the start of the investigation the FEBio software was used as a finite element analysis solver method to simulate the contact. After three months it was found that the tools available within this package to simulate the geometry and obtain detailed results of the contact pressure distribution were limited and did not allow the software to be used for the intended purpose.

As a result of this experience it was decided to use the commercially available Abaqus 6.12 software package for the contact analyses. A brief description of the Abaqus software and its contents is given in the Appendix. Defining the geometry of the contacting components and carrying out the dry contact between the two elastic bodies will be described in section 4.3. The results obtained for contact pressure distribution and the radius of contact area from the finite element analysis

will be compared with the theoretical Hertzian results to validate the contact modelling approach used in section 4.4.

Finally, in section 4.5 different boundary conditions for supporting the cup have been used to investigate the effect of the fixation process. The results of the changing of boundary conditions on the value of the contact pressure distribution are also reviewed.

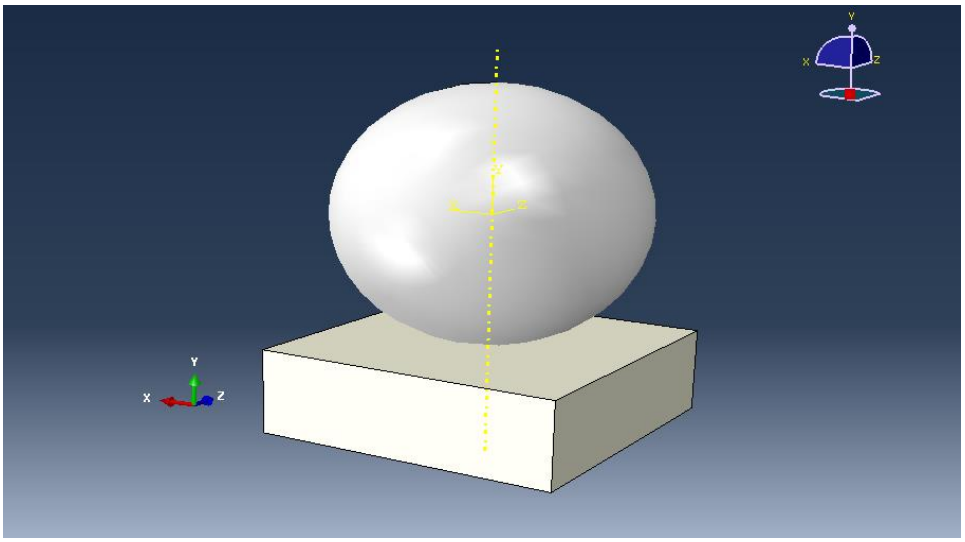

Figure 4.1, Dry contact of the ball on plane

4.2. Finite Element Analysis

The finite element method (FEM) is a numerical technique for solving a wide range of complex physical phenomena, particularly those exhibiting geometrical and material non-linearities (such as those that are often encountered in the physical and engineering sciences). It is used most frequently to tackle problems

that aren't readily amenable to analytical treatments. The premise is simple; continuous domains (geometries) are decomposed into discrete, connected regions (or finite elements). An assembly of element-level equations is subsequently solved, in order to establish the response of the complete domain to a particular set of boundary conditions. There are several finite element methods. These are the *Direct Approach*, which is the simplest method for solving discrete problems in 1 and 2 dimensions; the *Weighted Residuals* method which uses the governing differential equations directly (e.g. the Galerkin method), and the *Variational Approach*, which uses the calculus of variations and the minimisation of potential energy (e.g. the Rayleigh-Ritz method).

FEA uses a system of points called nodes which make a grid called a mesh. This mesh is programmed to contain the material and structural properties which define how the structure will react to certain loading conditions. Nodes are assigned at a certain density throughout the material depending on the anticipated stress levels of a particular area. Regions which will receive large amounts of stress, or have rapid spatial variation in stress, usually have a higher node density than those which experience little or no stress or near constant stress. Points of interest may consist of: fracture point of previously tested material, fillets, corners, complex detail, and high stress areas. The mesh acts like a spider's web in that from each node, there extends a mesh element to each of the adjacent nodes. This web of vectors is what carries the material properties to the object, creating many elements.

Nodes are located at each end of the element, a bar element for example, each of which can have displacements in the x and y directions. The displacements are denoted u_1, u_2, u_3, and u_4. Corresponding forces due to these displacements are F_1, F_2, F_3, and F_4. The bar has a uniform cross-sectional area and Young's Modulus.

The general relationship between force and displacement is $F_i = k_{ij} * u_j$, where F_i is the force in direction i, u_j is the displacement in direction j, and k_{ij} is the "stiffness" coefficient relating F_i to u_j. In the current example of a bar element confined to the *xy* plane, the force, displacement and stiffness system of equations are [94, 95]:

$$F_1 = k_{11}u_1 + k_{12}u_2 + k_{13}u_3 + k_{14}u_4 \qquad (4.1)$$

$$F_2 = k_{21}u_2 + k_{22}u_2 + k_{23}u_3 + k_{24}u_4 \qquad (4.2)$$

$$F_3 = k_{31}u_1 + k_{32}u_2 + k_{33}u_3 + k_{34}u_4 \qquad (4.3)$$

$$F_4 = k_{41}u_1 + k_{42}u_2 + k_{43}u_3 + k_{44}u_4 \qquad (4.4)$$

Alternatively, in matrix form:

$$\{F\} = [k]\{u\} \qquad (4.5)$$

The matrix k_{ij} is called the element stiffness matrix. It is the matrix which defines the geometric and material properties of the bar. Element stiffness matrices are a fundamental part of FEA. These matrices always define inherent properties of the system being studied at the element level.

For a more complex system, a 'global' stiffness matrix is required – i.e. one that describes the behaviour of the complete system, and not just the individual element bars. The global system of equations for the unknowns (for example the displacements u_{ij}) in the finite element analysis, takes the following form:

$$[K]\{u\} = \{F\} \qquad (4.6)$$

Global Stiffness Matrix

Nodal displacements (unknowns)

Nodal forces

To obtain {u} then

$$\{u\} = \{F\}\,[K]^{-1} \qquad (4.7)$$

Different methods can be used to calculate the inverse global stiffness matrix. For the linear system there are *n* equations to be solved with *n* unknowns, where n is the number of distinct nodal freedoms. The global stiffness matrix is an *n* by *n* array and solution of equation (4.6) is a complex problem when there are a large number of degrees of freedom, and many sophisticated mathematical techniques are used to obtain accurate solutions. This process is not problem dependant because of the general way in which the finite element system discretises the problem and so the FE method is particularly suitable to be packaged in a general purpose solution tool such as the Abaqus package used in this research.

4.3. **Finite Element Analysis of Contact Modelling**

A steady state contact mechanism was used to simulate the contact in the MOM hip joint replacement. All materials that have been defined in this simulation were assumed to be linear elastic. Different element shapes were employed to mesh the parts involved in this work. Results of the contact, the pressure distribution and the area of contact have been reviewed.

4.3.1 **Creating the Parts**

At the first stage of the contact simulation the model was divided into the two parts that are to be created, the ball is “part1”, and the plane is “part2”. Due to the symmetry of the geometry (ball on plane) and to reduce the total time to run the model only one quarter of the geometry was modelled as shown in Figure 4.2, with suitable boundary conditions to ensure that the quarter model behaves as if it was part of the full model. The part was created by drawing a two dimensional profile

and then manipulating it to obtain a three dimensional solid model. To form the entire model the two parts were assembled later.

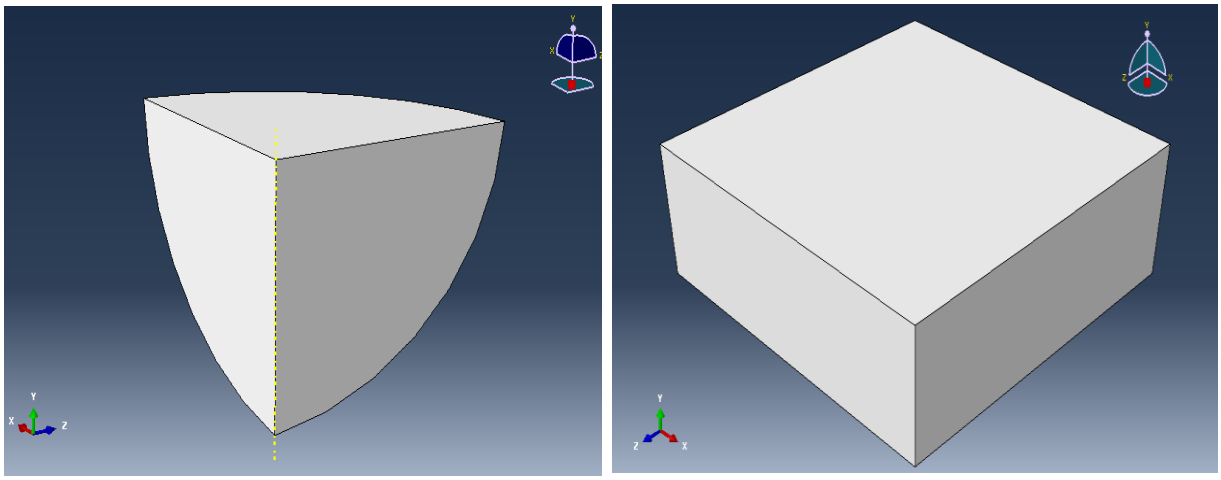

(a) The quarter ball (Part1) **(b) the plane (Part2)**

Figure 4.2 Creating 3D elastic solid geometry

4.3.2 **Properties**

The most popular MOM total hip arthroplasty is manufactured from cobalt chromium, CoCr, alloy which was taken as the material to be used in this research. The material parameters [72] of the two contacting bodies are shown below:-

- Modulus of Elasticity = 210 GPa
- Poisson's ratio = 0.3

The deformation between the two contacting bodies, part1 and part2, was considered to be elastic.

4.3.3 **Assembly**

The assembly process includes moving one instance relative to the second one in the global coordinate system and manipulating them together, so the quarter ball is the upper instance and the plane is the lower. To ensure that the two instances are in the correct position, two constraints were made to the two faces of the quarter ball to be parallel with the two faces of the plane, as shown in Figure 4.3. Nodes on these surfaces were constrained so they can only move within the respective planes. This ensured that deflection under load was the same as that which would occur in the complete model.

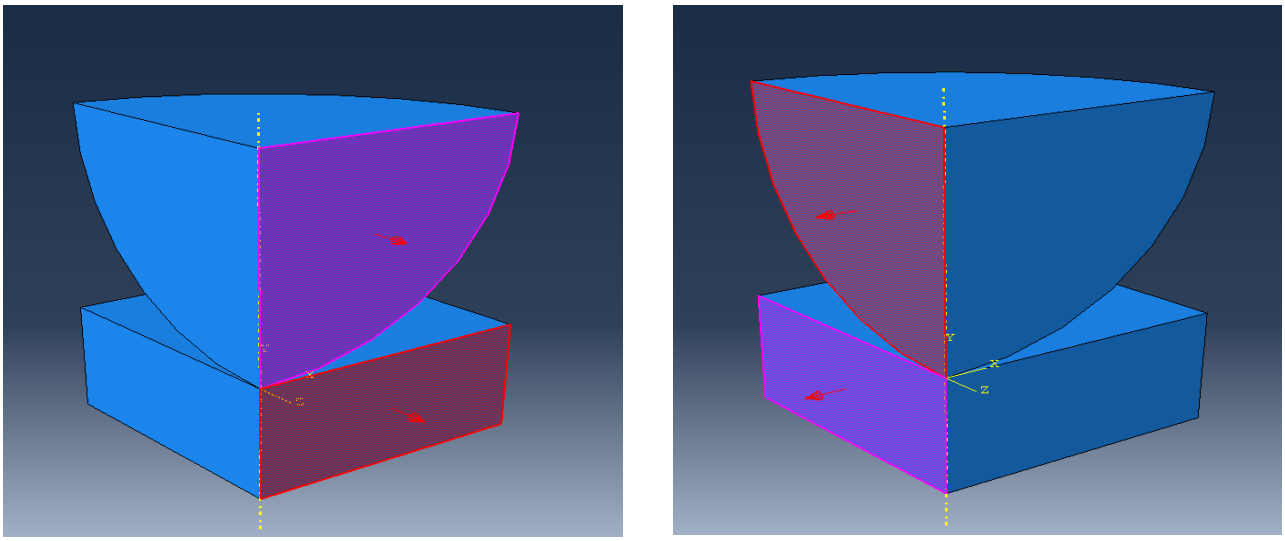

(a) **(b)**

Figure 4.3: Parallel faces constraint for instances of the quarter ball and the plane

4.3.4 **Step and Interaction**

In this contact problem there were steps, the **making contact** step and the **applying load** step, which were specified together with the ***initial*** step which the software generates automatically. The initial step is used for applying the boundary conditions only and no analysis was carried out in this step. In the first step, making contact, a ***static analysis*** was used to apply the contact mechanism between the two surfaces, the curved surface of the quarter ball instance, **surface1,** and the top surface of the plane instance, **surface2**, as shown in Figure 4.4.

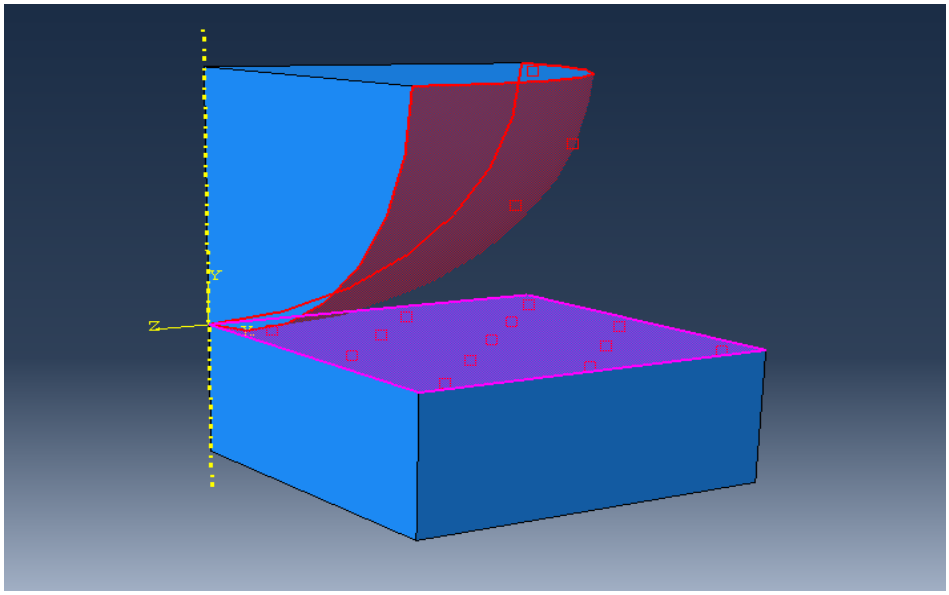

Figure 4.4: Surface-to surface contact.

The coefficient of friction between the two surfaces was assumed to be zero. A ***surface-to-surface*** contact was used as a contact analysis method, discretization method. When using surface-to-surface contact, it is necessary to specify which

surface is the ***Master*** surface and which one is the ***slave*** surface. At this stage the curved surface, **surface1**, of the quarter ball was selected to be the master and the top surface of the plane, **surface2**, was selected as the slave surface. The choice of which surfaces are to be the master and the slave surface within the Abaqus/CAE software depends on three factors:

- The mesh density of the parts in terms of relative fineness of mesh.
- Whether the bodies are ***rigid*** or ***deformable*** bodies.
- The relative stiffness of the material from which the bodies are made.

If any one of the two contacting bodies has a coarse mesh, relatively stiff material properties or is a rigid body, then the contact surface of this body must be the master surface.

In the current contact simulation the two contacting bodies, the quarter ball and the plane, are both deformable bodies and have the same material properties. The only difference between them is the mesh resolution. Therefore as the quarter ball was meshed with a coarse mesh and the plane meshed with a fine mesh the ball was selected as the master surface. More details about the meshing process can be found in section 4.3.6.

4.3.5 Loads and Boundary conditions

In this simulation a **concentrated force** was applied in the downwards direction (negative Y direction) to the vertex at the top surface corner of the quarter ball instance. The load was applied during the second static analysis step, created using the **Step** module. In the current model the bottom surface of the plane instance is constrained completely and thus cannot move in any direction. The two faces of the

quarter ball instance and also the two faces of the plane in the **x** and **z** directions, as shown in Figure 4.5, had zero displacement during the simulation in the normal directions. Within these boundary conditions the quarter ball was free to move in the **y**-direction only under the action of the applied load.

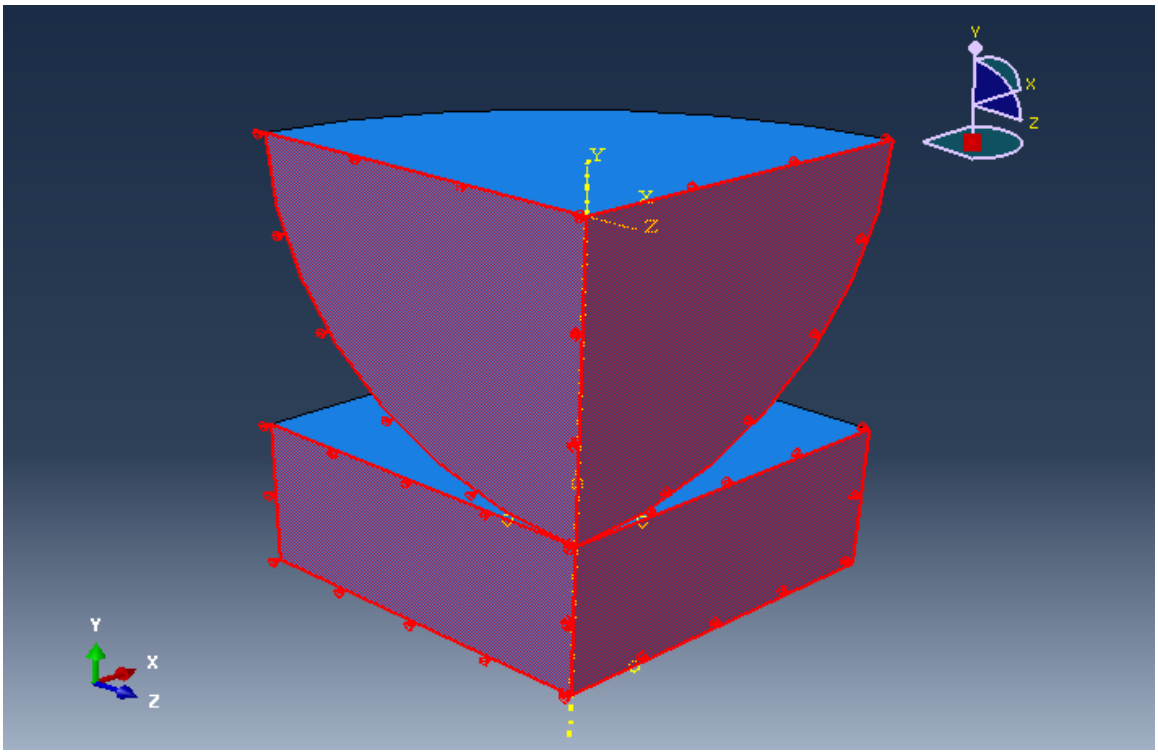

Figure 4.5 Four faces have been specified to have zero displacement in the normal directions

4.3.6 Mesh

Abaqus/CAE supplies a variety of tools for managing mesh characteristics. Mesh density can be specified by the seeding process. There are two ways to seed the geometry of the model, the global seed and the local seed. The global seed has been used to specify the element size of the body as a whole, as shown in Figure 4.6.

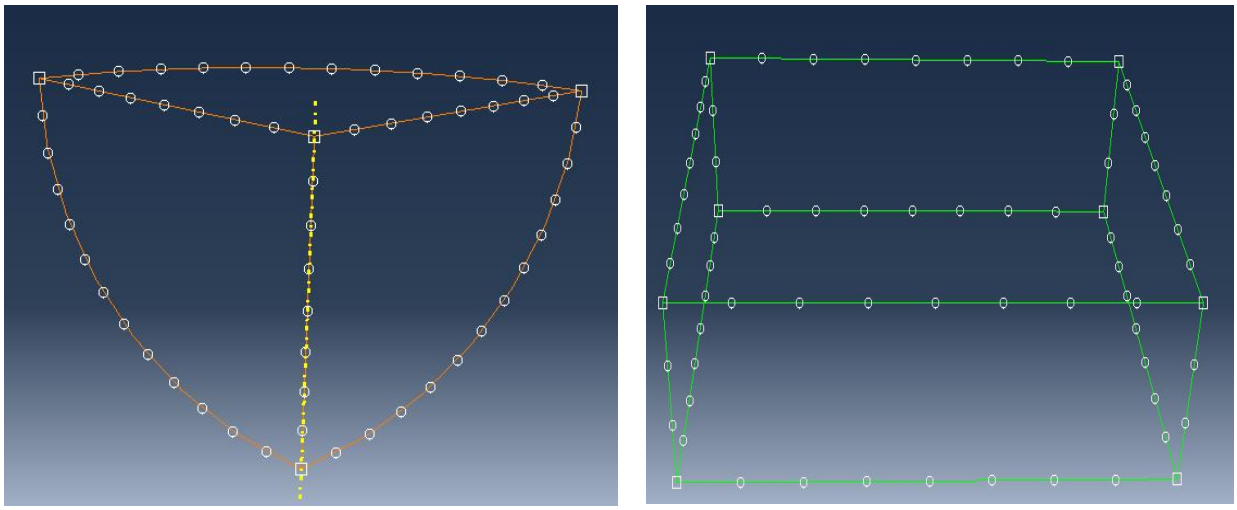

(a) **(b)**

Figure 4.6: Global seed, (a) part1 seed, (b) part2 seed

The uniform sized element specified using the global seed allows the automatic meshing tools to create a smooth mesh. Two of the three different elements shapes were possible for use in meshing the two instances, the brick and the tetrahedral elements, as shown in Figure 4.7. Wedge elements were not available for automatic meshing.

There are two aims that should be achieved in using the mesh module. Firstly, a coarse resolution of the global model permitted the contact simulation of the whole volume to be accomplished with only moderate computational time. It was carried out by using the global seed. Secondly, it is well known from the principles of the theory of contact mechanics that a small contact area will be produced as a result of the contact between the two non-conformal bodies. To meet the requirement of a high enough resolution within the contact area in the model, a local seed must be used.

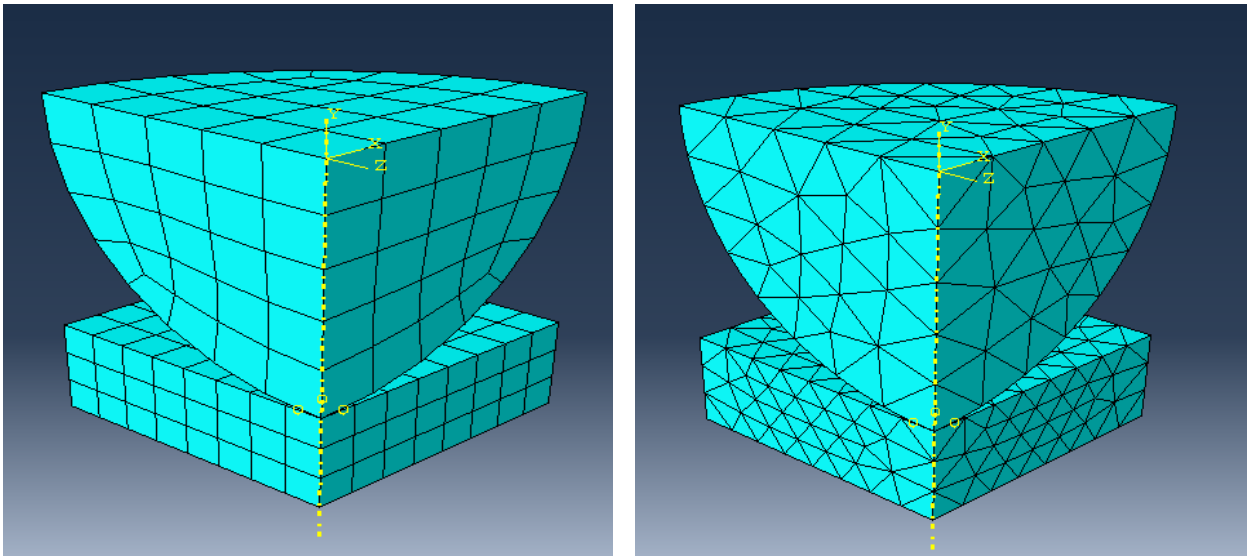

(a) **(b)**

Figure 4.7: global mesh, (a) brick element, (b) Tet element

There are two ways to use the local seed. The first method represents increasing the number of elements in one direction by using very small element size. On the other hand, a coarse mesh was used in the opposite direction as shown in Figure 4.8. This method is called **bias** seeding.

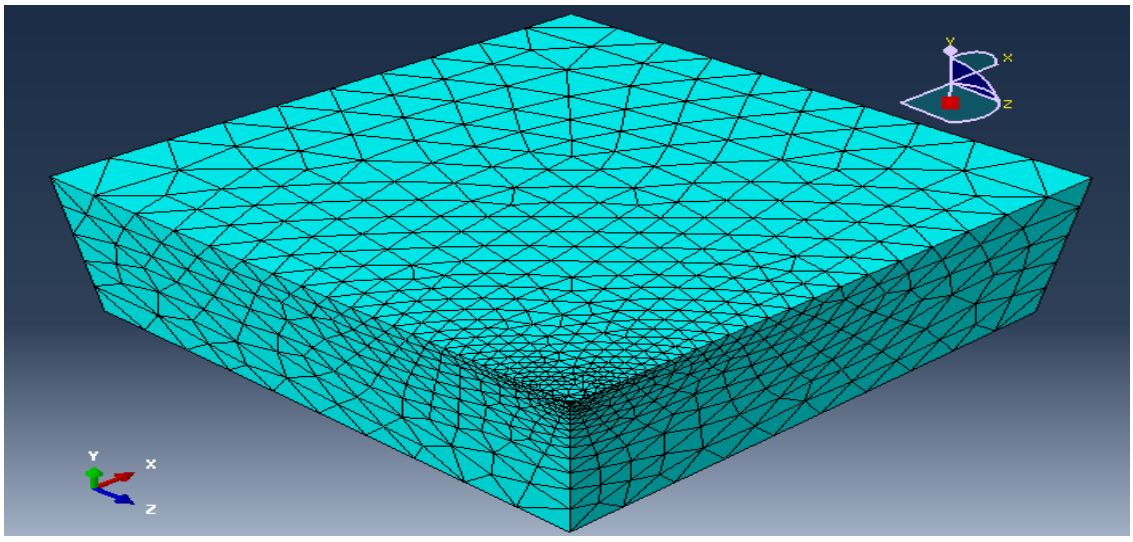

Figure 4.8: Bias seed for the slave surface, surface2, of the plane

The second way to gain a high resolution at and near the contact area can be attained by making a **Partition**. The Abaqus package provides the partition toolset to divide the part into regions. Partitions may be used, where it is essential to make a change in the material properties, to indicate a location of the load, or to specify a mesh boundary for these regions, for example. The result of the partition around the contact area to obtain a fine mesh is shown in Figure 4.9.

It is important to know that the output data which is obtained by Abaqus as a result of the contact analysis of the two surfaces, **CPRESS**, **COPEN**, **COORD**, can be extracted from the slave surface, **surface2**. Where;

CPRESS is the contact pressure at surface nodes.

COPEN is the contact opening at surface nodes.

COORD provides the coordinates at nodes.

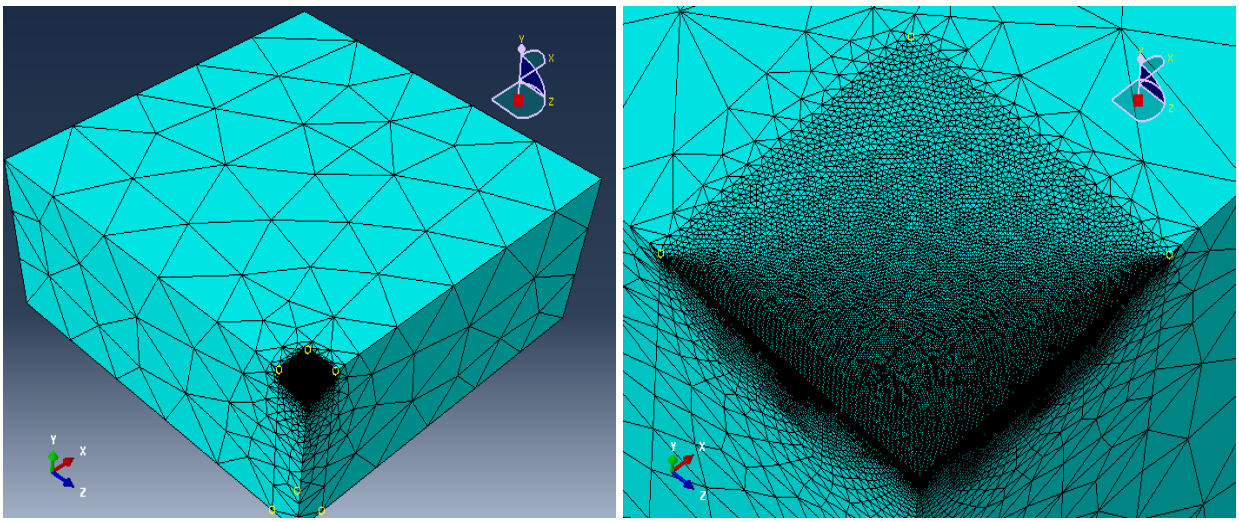

(a) **(b)**

Figure 4.9: Seeding of model, (a) partition and local seed, (b) zoomed local area

It was found that using the local seed with the partition process was more flexible for meshing the contact area than the bias seed and generated a mesh where the element size distribution was relatively uniform. A good finite element mesh can be achieved when its resolution can be modified without impacting the results. This is the case regardless of the refinement method used to seed the geometry.

4.3.7 Job and Visualisation

By creating the analysis job the model becomes ready for submitting for solution. When data is incorrect or missing the submitting process will stop to show an appropriate error message. With practice the analysis of the model is usually carried out normally. The output data is written to the output database when the full analysis is complete. The visualisation module of Abaqus/CAE, also called Abaqus Viewer, was used to view the analysis results and to read the output database. The contour of contact pressure and the boundary of the contact area for the contact simulation between the quarter ball and the plane is shown in Figure 4.10 for the case when the parts were meshed using tetrahedral elements.

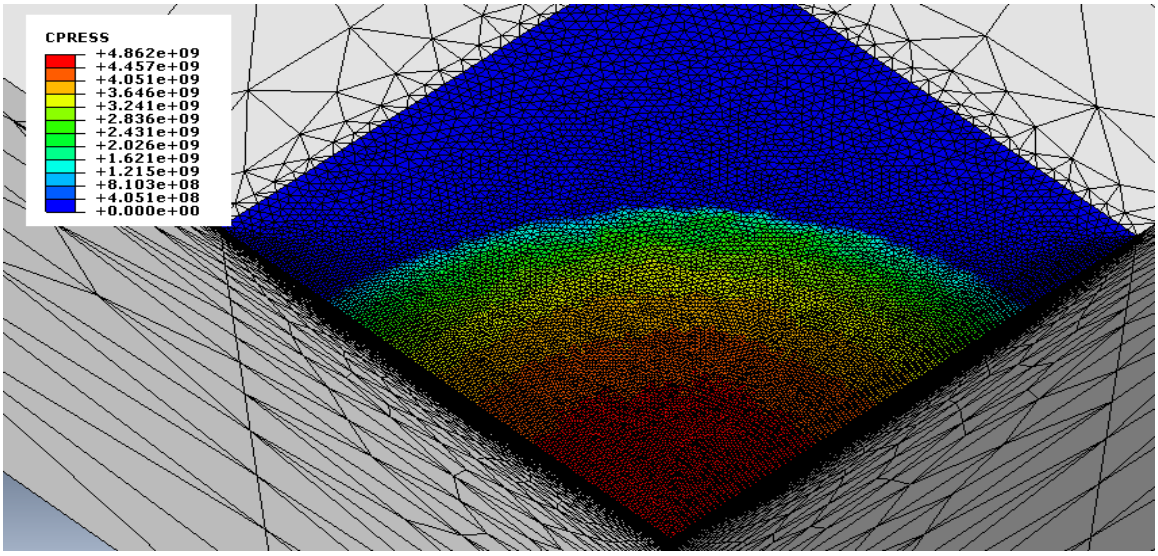

Figure 4.10: Contours of contact pressure (Pa) on the slave surface partition

Figure 4.14 compares the result of using tetrahedral elements with that of using hexahedral elements. It can be seen, that the pressure variation in the contour of the contact pressure is more uniform in Figure 4.11 (b) than in Figure 4.11 (a). The reason for this comes from using a tetrahedron element shape in the meshing module in (a) while the element shape in (b) was hexahedron. The result for the tetrahedral elements is different on different radial planes and this illustrate that the results for contact pressure were inaccurate in spite of the fine resolution. In addition, the unstructured distribution of surface nodes with the tetrahedron element is not useful in terms of extracting the output data to reuse it with other software. However, the tetrahedron element is the most flexible element shape and can be used with any complicated geometry. At this stage the hexahedron element was adopted for meshing the slave surface for any contact simulation on the basis that it maintains uniformity in the solution on different radial planes.

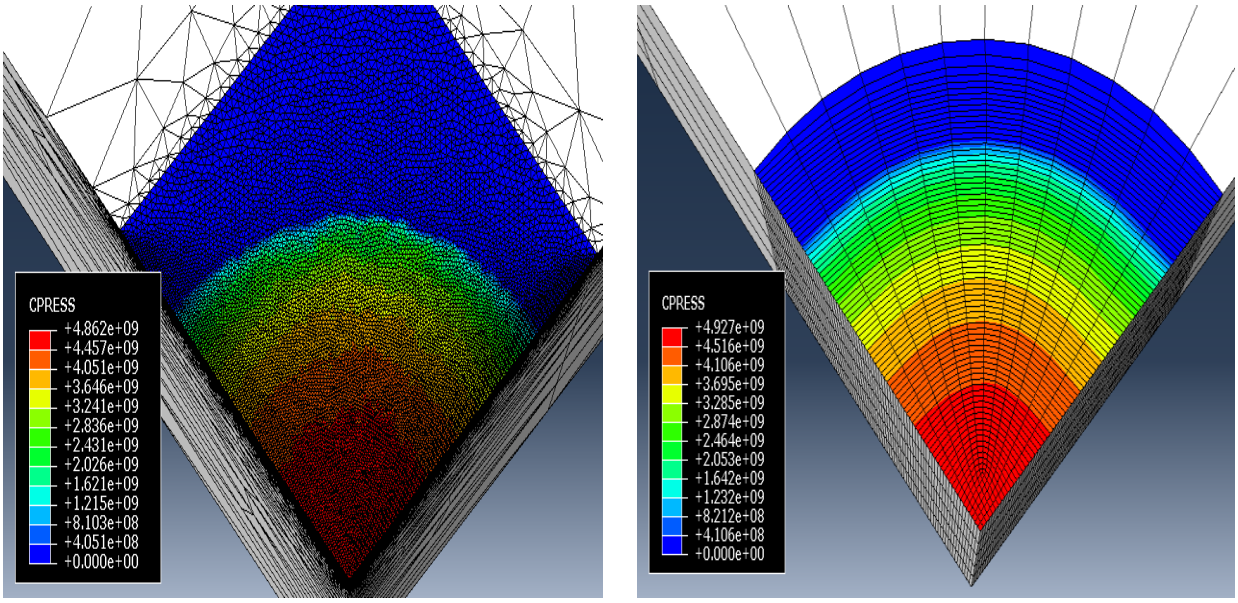

(a) (b)

Figure 4.11: Contour of contact pressure / Pa for, (a) tetrahedral element mesh, (b) hexahedral element mesh.

4.4. Verifying the Results

The results obtained from the finite element software were verified to investigate the results sensitivity to the length and type of the element. A large number of models were investigated using same geometry, load and boundary conditions, and material properties. The only difference between them was the element sizes and shapes, for example two models were compared as shown in figures 4.12 and 4.13. In these two models the element length was 0.003 m for both, while the element type was tetrahedral for figure 4.12 and hexahedral for figure 4.13. The number of nodes in these two models was 5820 and 1022 for the tetrahedral and hexahedral element types, respectively.

It can be seen from these figures that there is a variation of 34% in the maximum contact pressure, although all the parameters and convergence criteria are the same for these two models. This suggest that the finite element results vary relative to the element type and length. In general, using finer element dimensions leads to more accurate results than those for a coarse mesh size, regardless the element shape as can be seen from figure 4.11 where there is an only 1.3% variation in the maximum contact pressure for that two different element shape models relative to each other.

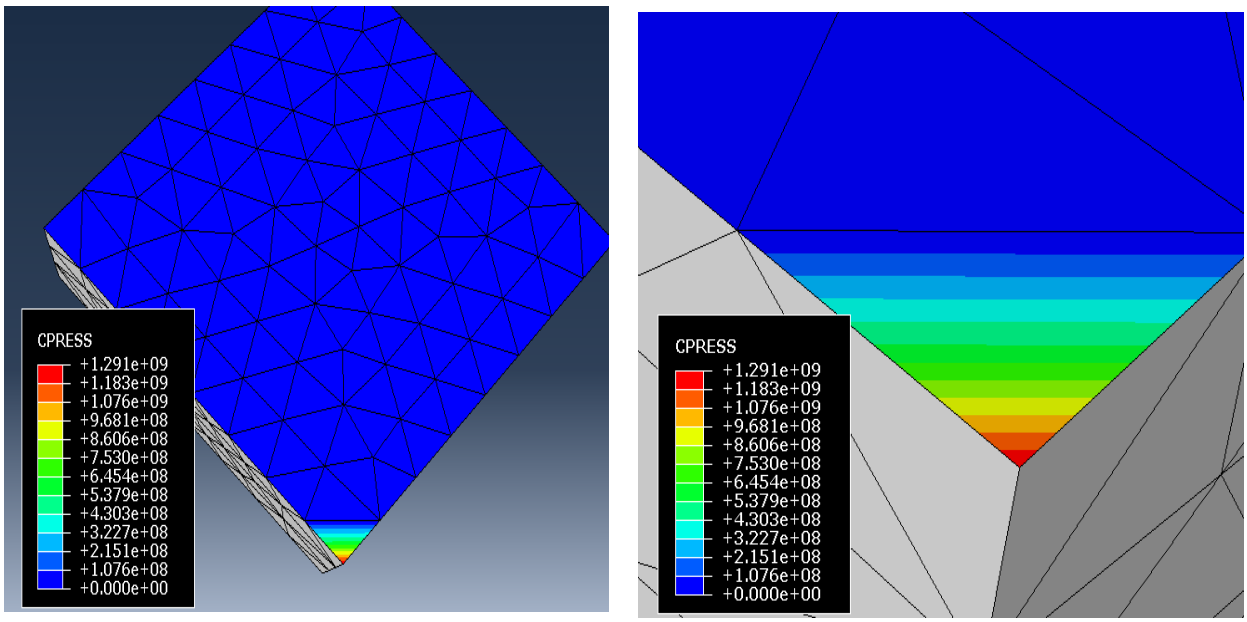

(a) (b)

Figure 4.12 (a) tetrahedral element mesh, (b) zoomed local area.

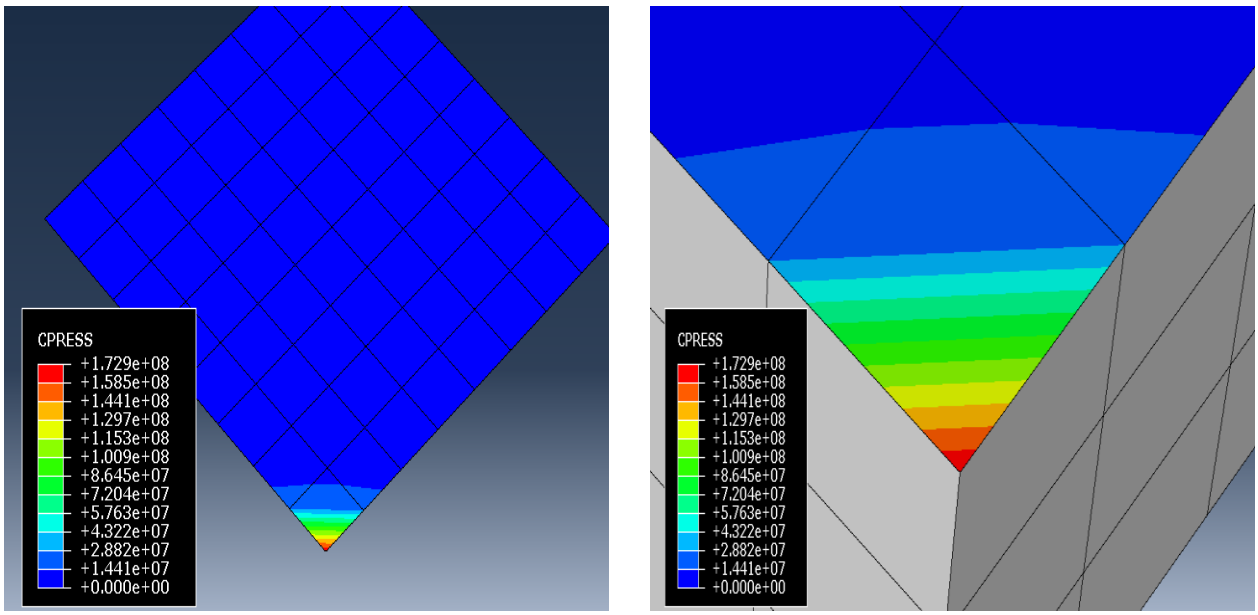

(a) (b)

Figure 4.13 (a) Hexahedral element mesh, (b) zoomed local area.

Verifying the results of the finite element analysis was also carried out by comparing them with the results obtained from the theoretical equations of Hertzian theory. A comparison between the contact pressure distributions from the Hertzian equations of contact mechanics with the finite element analysis, FEA, results is shown in Figure 4.14.

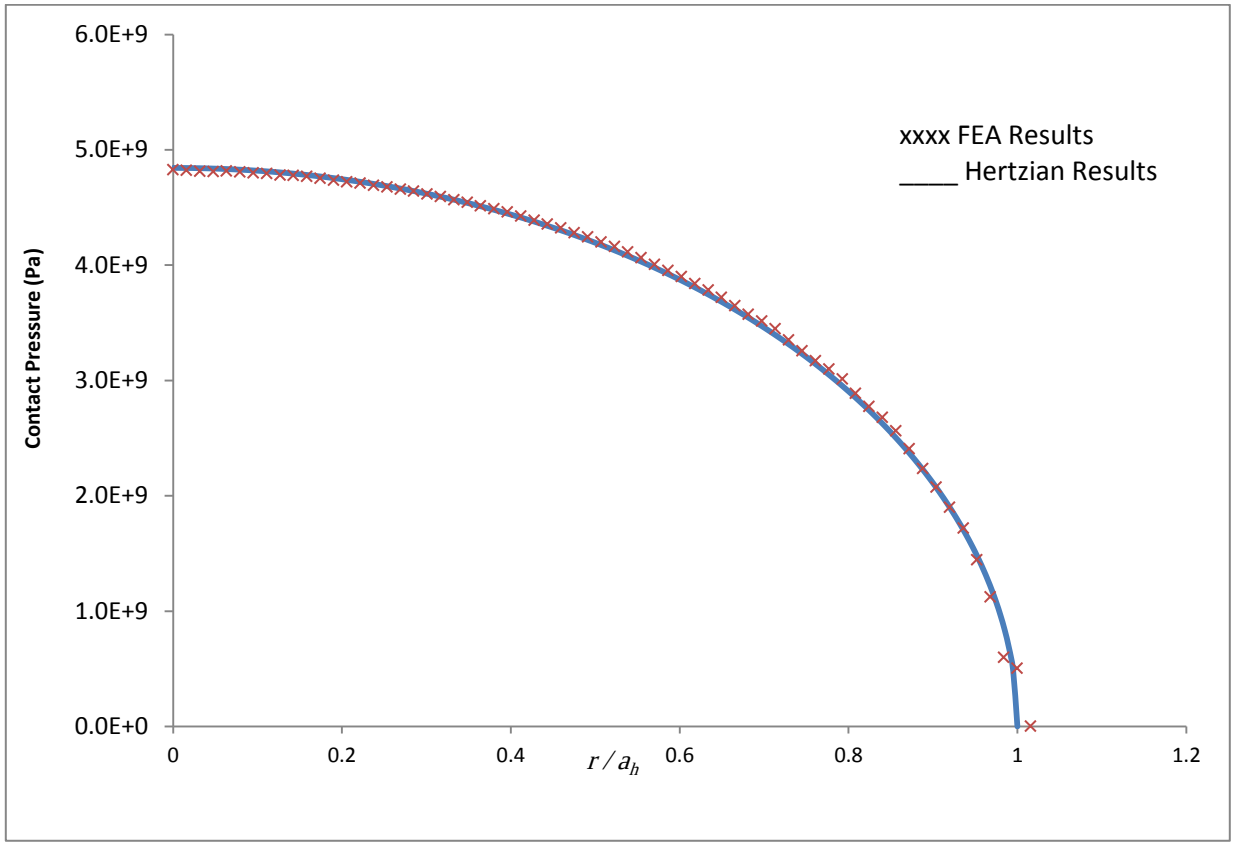

Figure 4.14: Pressure distribution of quarter ball-on-plane

It is quite clear from Figure 4.14 that the contact pressure distribution between the quarter ball and the plane is a good approximation to the Hertzian pressure, but it was not able to follow the analytical result to the accuracy that might be expected from the spatial resolution allowed by the mesh at the edge of the contact area.

Extensive experiments were carried out using different approaches within the options available but this minor discrepancy could not be eliminated and seems to be a characteristic of the contact model. It is interesting to note that in the software documentation the Hertzian contact problem is covered and illustrated using a relatively coarse mesh where the edge discrepancy is not apparent.

4.5 Full Ball–Cup Simulation

Reducing the computational running time and verifying the results with the theoretical Hertzian equations were the aims of adopting the simple geometry, quarter ball-on-plane. After obtaining the results of the simple geometry, a full ball–on–cup model was created to simulate the MOM total hip replacement.

Three different boundary conditions have been used as follows;

1- The outer cup surface was constrained completely.

2- A circumferential stiffening ring was added to the cup periphery to restrain the ball-cup system.

3- A band supporter was attached to the outer cup surface along its mid plane to fix the cup.

Each one of these supporting systems will be dealt with in more detail later. The purpose of using these suggested fixation methods was to examine the effect of

fixing on the pressure distribution, radius of contact area and the value of maximum contact pressure.

The ball and the cup modelled in the three systems had the same dimensions, material properties, applied load, shape and size of the element mesh. The geometric and the material parameters are listed in Table 4.1:-

Table 4.1

Radius of the ball	0.025 m
Radial clearance	0.0001 m
Cup thickness	0.008 m
Modulus of Elasticity	$210*10^9$ Pa
Poisson`s ratio	0.3

A concentrated load of 3 kN was applied in the direction of the central axis of the ball. The load value used in this simulation represents four times an average body mass, 75 kg [73] to cover the variation in multiples of the body weight that is applied to the hip joint during the normal walking cycle.

The contact between the full ball–on–cup is shown in Figure 4.15. There were 17779 tetrahedral elements and 25668 nodes for the ball, and the cup was modelled using 8208 linear hexahedral elements with a total of 9733 nodes. Within the surface-to-surface contact method the ball surface was selected to be the master surface, while the inner cup surface was used as the slave surface.

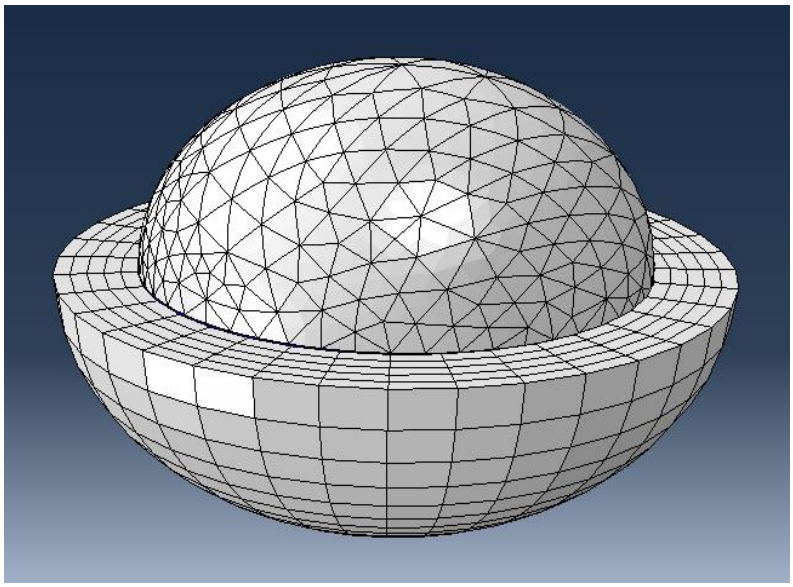

Figure 4.15: Contact simulation of ball-on-cup.

For the first model the outer surface of the cup was fully constrained in the three directions. Two analysis steps were carried out with this contact simulation job as well as the initial step. The finite element analysis result of the contact pressure is shown in Figure 4.16.

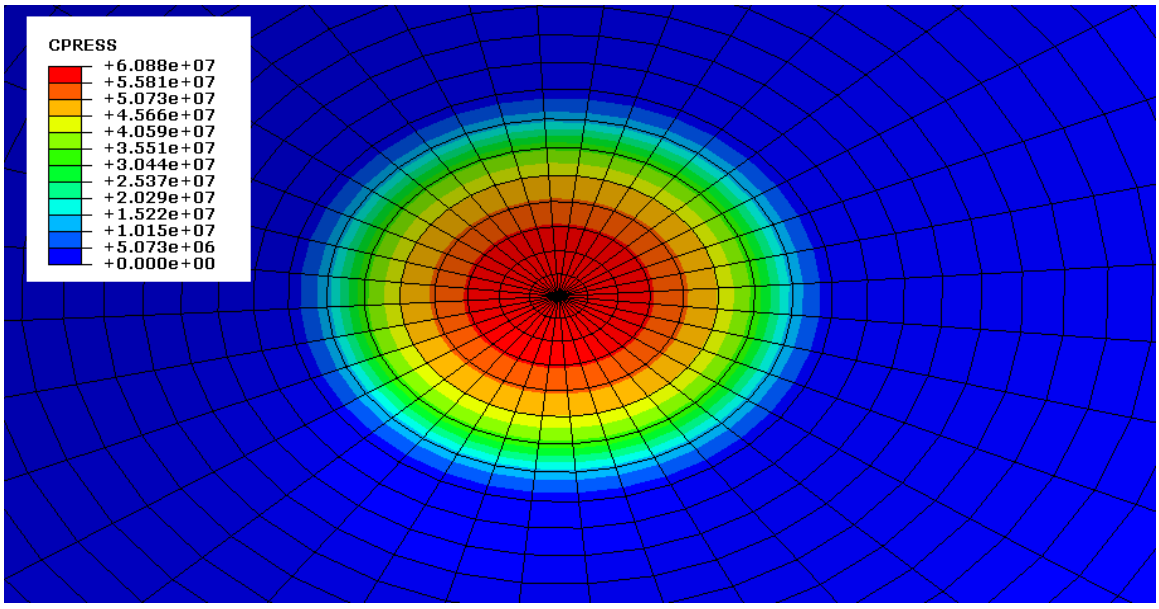

Figure 4.16: Contour of the contact pressure (Pa) of the slave, cup, surface

The assembly module of the circumferential ring system is shown in Figure 4.17. The material properties of the ring were similar to the ball and cup. The thickness of the ring was 1mm and the width was 8 mm. The inner surface of the ring was joined to the cup, while the outer surface was constrained to have zero displacement in the x, y, z directions.

A tie constraint was applied to join the inner surface of ring with the outer cup surface. The tie constraint allows the user to connect two regions together even though these two different regions have dissimilarity in the meshes created on the surfaces.

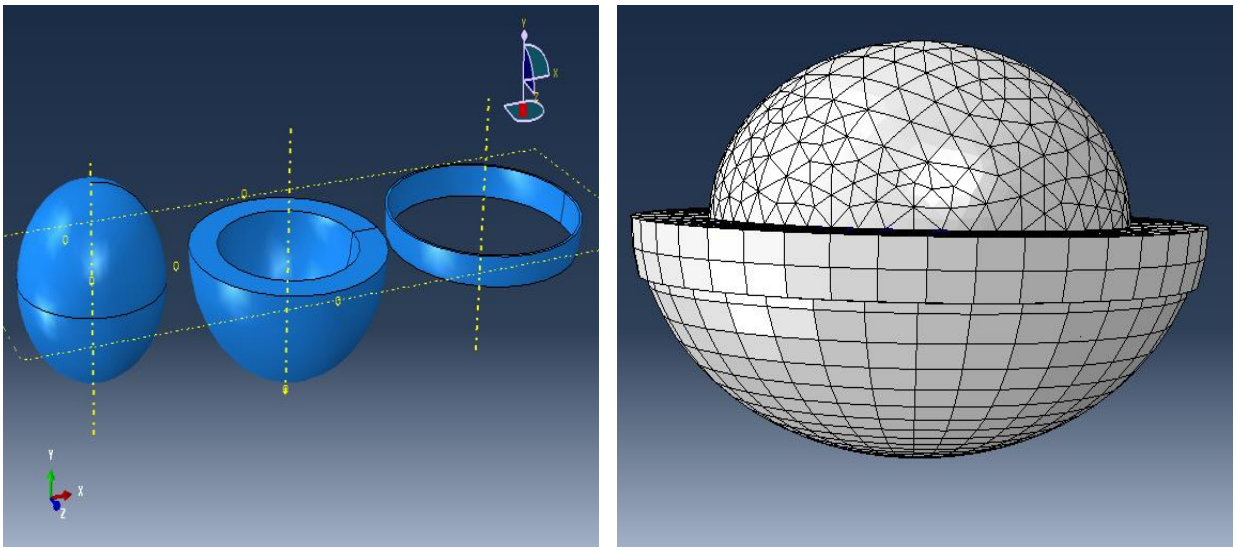

(a) (b)

Figure 4.17: (a) Ball-cup-ring parts, (b) Assembly model.

By using the tie connection there will not be any relative motion between the joined bodies. Figure 4.18 shows the pressure contours of the contact area on the inner cup surface.

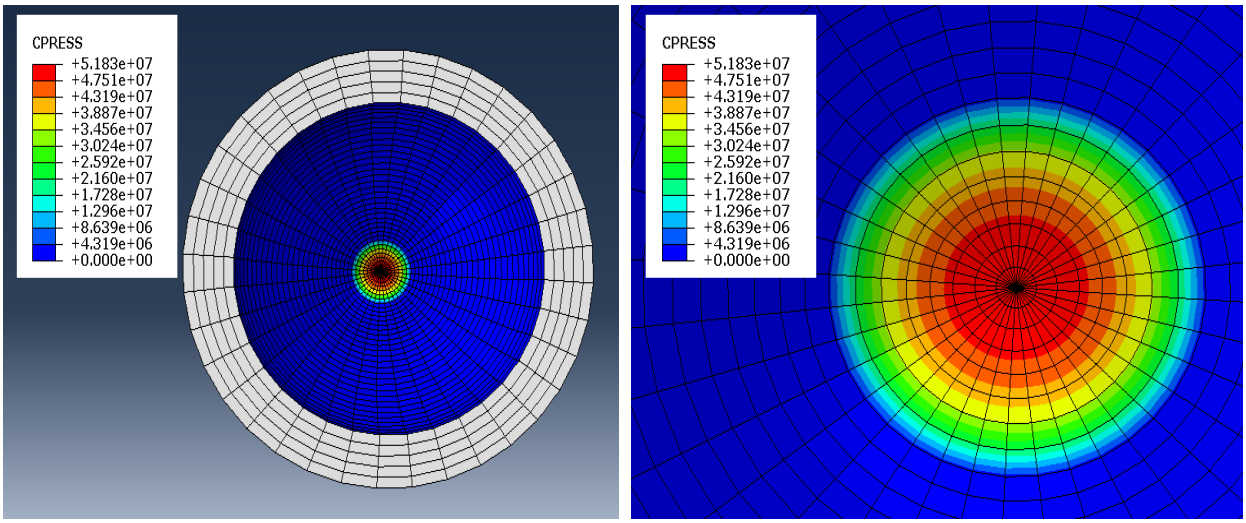

(a) (b)

Figure 4.18 Contours of contact pressure / Pa, (a) for whole cup (b) for the contact area

The band supporter was used to restrain the ball-cup system, as shown in Figure 4.19. It has a 15 mm width and 1 mm thickness. The tie constraint has been used to connect the band and the cup. It also has the same material properties as ball-cup system and its outer surface was restrained.

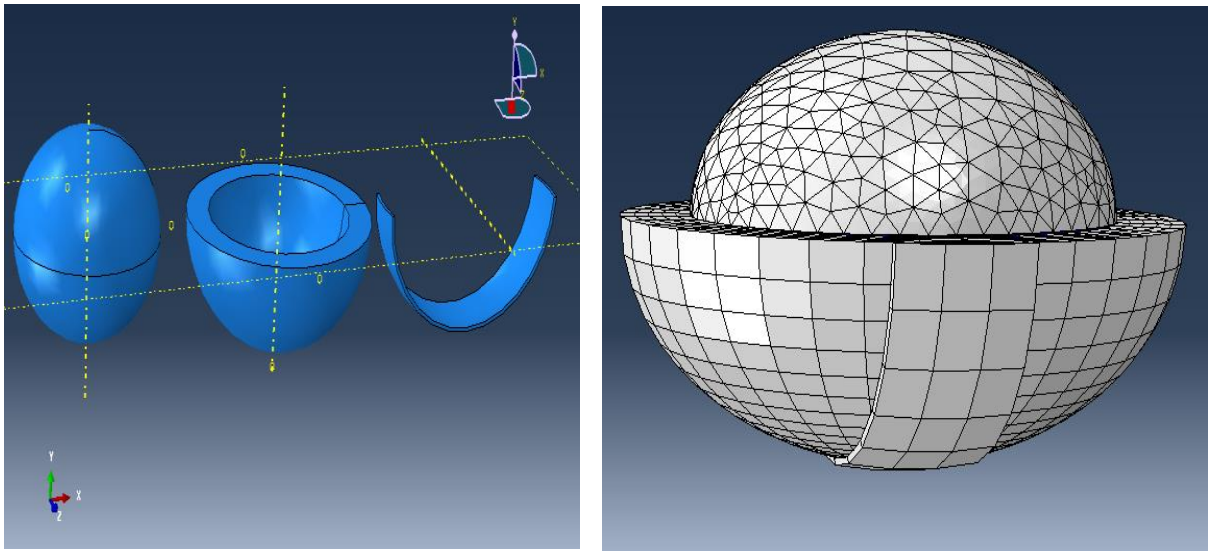

(a) (b)

4.19: (a) Ball-cup-band supporter parts, (b) Assembly model.

The results of the contact pressure distribution for the three different supporting systems are shown in Figure 4.20.

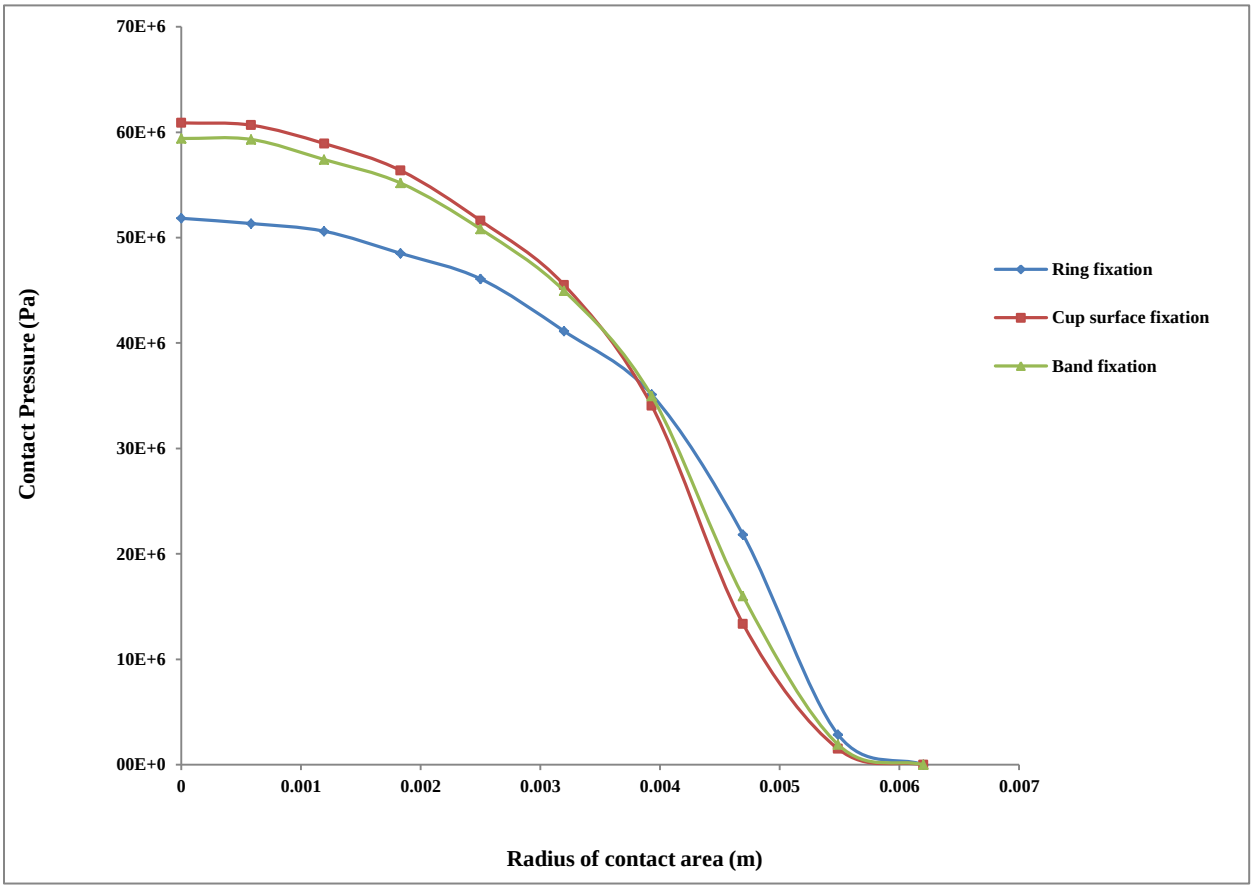

Figure 4.20: Contact pressure distribution of ball-on-cup for 8mm cup thickness

It can be seen from Figure 4.20 that regardless of the way used to restrain the ball-cup system with 8 mm cup wall thickness, the radius of the contact area was similar. On the other hand, there was a 20% difference in the maximum contact pressure due to the dissimilarity in the fixation conditions. To see if this case is a general or it was specific to 8 mm cup thickness, further investigation was carried out by using a 5 mm cup wall thickness with the same set of boundary conditions as discussed above, and the results are shown in Figure 4.21.

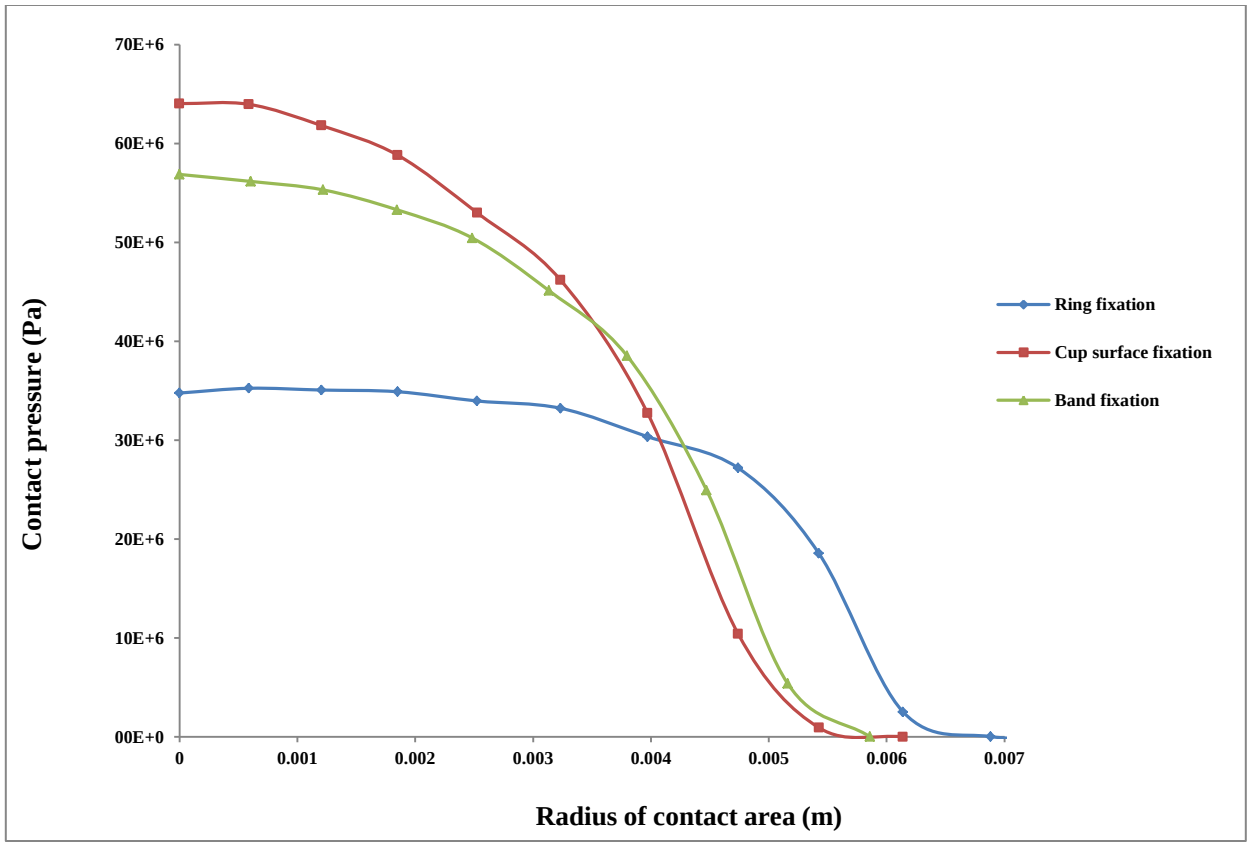

Figure 4.21: Contact pressure distribution of ball-on-cup for 5mm cup thickness

In general, in Figure 4.21, the trend of the pressure curves for the band and full cup surface fixation are still parabolic and similar to the trend of curves with the 8 mm cup thickness, while the ring fixation curve had an approximately horizontal trend within the contact area and a bigger contact area radius than the other two fixation structures with the 5 mm cup thickness. A reduction in the maximum contact pressure of 46% and 11% were found for the ring and band fixation methods respectively relative to the full outer cup surface supported model.

From Figures 4.20 and 4.21, it is clear that using various systems of fixation to support the ball-cup MOM hip joint might vary the contact pressure and radius of

the contact area. This could affect the performance of the artificial hip joint. As a result of that variation, the contact analysis of MOM prostheses is required to be more representative of the in vivo situation. This will be covered and described in some detail in the next chapter.

FEA Contact Analyses and Equivalent Hertzian Models

5.1 Introduction

Finite element analysis has been used considerably in implant development, and to provide assistance to resolve clinically complicated problems. In this thesis ball-in-socket MOM contacts were analysed using the Abaqus software package to simulate the dry contact between the acetabular cup and the femoral head as discussed in Chapter 4. Hexahedral and tetrahedral element shapes were used to mesh the cup and the ball respectively. Three different constraints of the ball-in-socket system: ring, band and full outer cup surface were examined with various cup thicknesses. Significant variations in the value of the contact pressure and the contact area were found due to using the various support systems.

Developing models where the stress field is similar to the in vivo situation led to a search for the most appropriate boundary condition to support the ball-in-socket system. Consideration of the numerical method used to simulate the in vivo situation of the boundary condition and the fixation of the MOM hip joint replacement is the objective of the next two sections.

5.2 The Sawbones polyurethane foam block

Due to the limitations of using cadaveric specimens of pelvis bone experimentally, “Sawbones” polyurethane foam blocks have been widely used in vitro. The Sawbones blocks are available with a range of material properties. Consequently, they should be able to represent various bone densities.

Grimes [75] and Fritsche et al [76] used Sawbones blocks to simulate the insertion and the deformation behaviour of the acetabular cup. Jin et al [74] found that a hemispherical cavity in a Sawbones polyurethane block with

rectangular cut-outs as shown in Figure 5.1 gave the best approximation to the in vivo situation. They used both cadaver and polyurethane foams to investigate the interference press fit of a metallic one –piece acetabular cup employed for MOM hip resurfacing. The diametral cup deformation as a result of the press fit was measured on different foam cavity models and grades, and it was found that the deformation measured from a two- point pinching cavity model was consistent with the cadaveric test. Other researchers, Ong et al [77] and Schmidig et al [78] have also used a hemispherical cavity with cut-outs in their studies to simulate the bony acetabulum. The foam in the deformed model had a further cavities machined to create two recesses and promote shell deformation by removing the supporting material from the superior and inferior aspects of the acetabular rim area. By removing the foam support, this simulated a pelvis with dense bone at the ischial and ilium columns of the acetabulum that would cause compression of the cup during insertion.

In the current work, a polyurethane foam block was added to the ball-in-socket artificial joint model to represent the structure of the total hip replacement anatomically. It was important to select the appropriate material properties for the polyurethane block so that the model represented the pelvic bone as closely as possible.

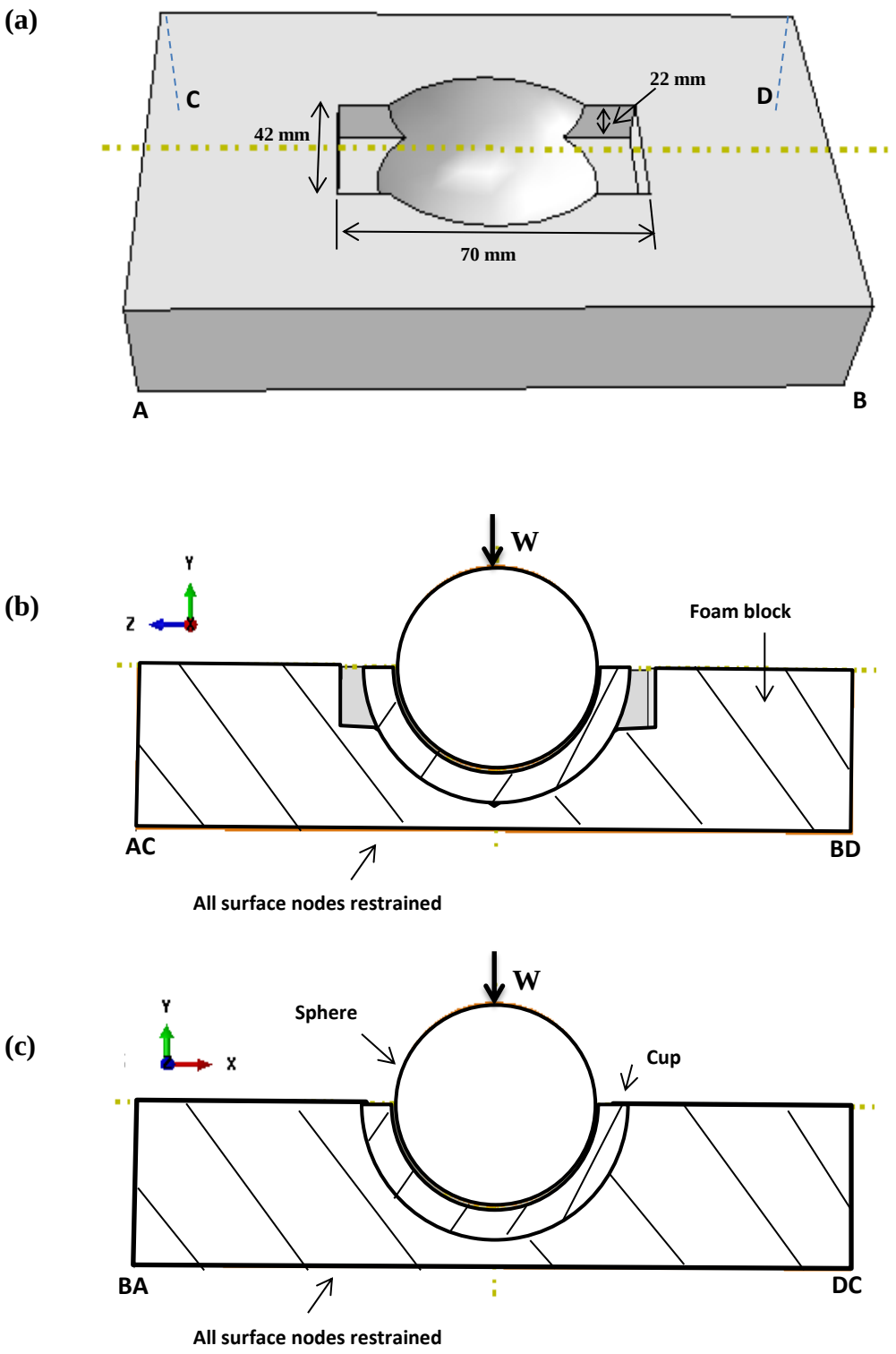

Figure 5.1 (a) Polyurethane foam block used to restrain cup, (b) longitudinal and (c) transverse section of the foam, cup and sphere.

The density of the foam varies from 80 – 800 kg/m^3 (5 – 50 pounds per cubic foot, pcf) and the compressive modulus of elasticity range is 16 – 1148 MPa as shown in Figure 5.2.

DENSITY		COMPRESSIVE		TENSILE	
		STRENGTH	MODULUS	STRENGTH	MODULUS
pcf	g/cc	MPa	MPa	MPa	MPa
5	0.08	0.60	16	1.0	32
10	0.16	2.2	58	2.1	86
15	0.24	4.9	123	3.7	173
20	0.32	8.4	210	5.6	284
30	0.48	18	445	12	592
40	0.64	31	759	19	1000
50	0.80	48	1148	27	1469

Figure 5.2 Material properties of Sawbones blocks [79]

From the literature the polyurethane foam with density 480 kg/m^3 (30 pcf) is the most commonly used to simulate the pelvic bone. According to ASTM F-1839 the block with a density of 480 kg/m^3 (30 pcf) has similar properties to cortical bone [76], Fritsche et al analysed the deformation behaviour of threaded and press-fit acetabular cup designs during insertion and extraction with regard to the possibility of cup failure. Jin et al [74] employed grades with densities of 240, 480 and 640 kg/m^3 (15, 30, 40 pcf) to simulate different bone properties. They found that the grade with density 480 kg/m^3 (30 pcf) gave results that agreed with cadaveric tests. Therefore a Sawbones block with 480 kg/m^3 (30 pcf) density, 445 MPa modulus of elasticity, was simulated in the current study.

5.3 Assembly of the ball-cup-block

A three dimensional assembly process for the (ball, cup and block) was carried out by applying a frictionless dry contact between the ball surface and the inner cup surface. Spears et al [80] investigated the amount of friction occurring between the cup – bone surfaces during the press-fitting. A range of friction coefficients (0.1 – 0.5) was assigned to the cup-bone interface using finite element model. They found that the intermediate values of friction (0.2-0.3) gave the best results because a high friction coefficient (0.5) restricted the penetration of the cup during load application, while a low friction coefficient (0.1) resulted in unrestricted rebounding during load removal.

In this work a frictional contact with a friction coefficient of 0.3, was used between the outer cup surface and the hemispherical cavity of the Sawbones block. The polyurethane block was meshed using a four node linear tetrahedral element shape with a free meshing technique as shown in Figure 5.3. In this simulation a concentrated force was applied to the vertex at the top surface of the ball. The lower surface of the polyurethane block was fixed in the x, y, z directions for both translation and rotation, and this was the only boundary condition adopted to support the ball-cup-block system.

The contact results data calculated by the Abaqus software for each node on the contact surfaces were the contact pressure, the gap between the contacting surfaces and the coordinates. This data was appended to a file so that for each node it was possible to obtain the node label and pressure value or node label and the coordinate value and so on. These files were then manipulated to tabulate all variables in terms of the node label in a single file. This was achieved by writing a Fortran language code.

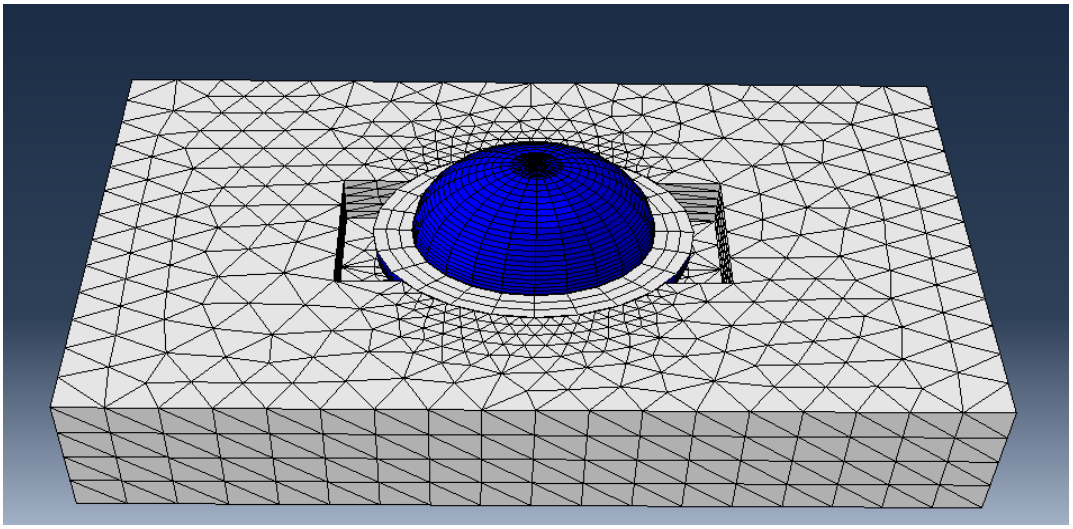

Figure 5.3 Assembly of Ball, Cup and Block

In section 4.5 of Chapter 4, selecting the master and the slave surfaces for modelling the surface to surface contact was carried out as follows; the ball surface was chosen to be the master surface, while the inner cup surface was used as a slave surface. In the current model the master and slave surfaces were reversed in comparison with Chapter 4, so that the ball surface became the slave and the inner cup surface was the master. The reason for this exchange operation was that during the walking cycle the rotation of the ball relative to the cup would need to be taken into account. To obtain contact pressure and gap data between the surfaces it was judged appropriate to use the ball's structured mesh to extract the information from the Abaqus system, by rotating the ball so that the origin of the radial mesh lines corresponded to the contact point. This data would be available on a structured mesh to feed into subsequent EHL models without introducing interpolation errors.

The ball (slave) surface, which was used to extract the data, was divided into 24 radial lines, as shown in Figure 5.4. For each line it was possible to obtain data for every mesh point on that line.

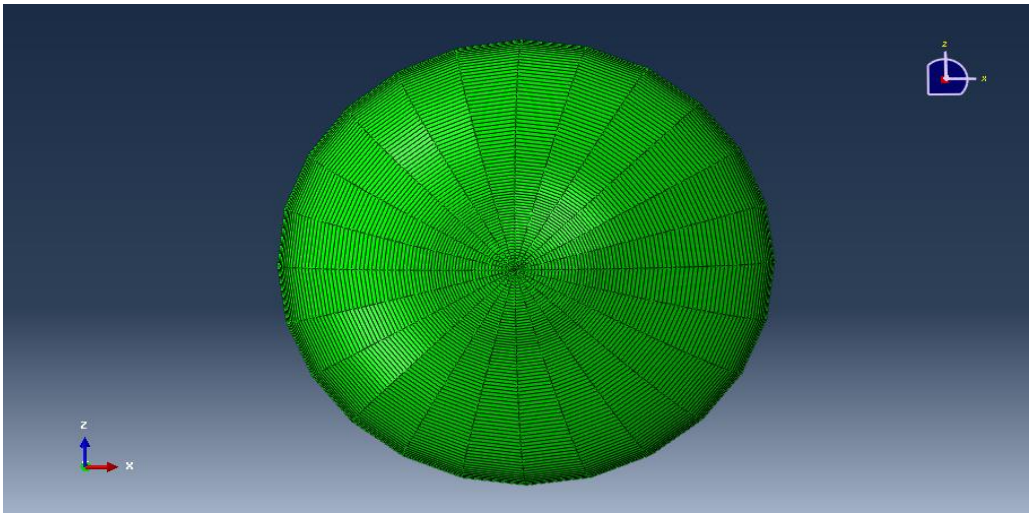

Figure 5.4 Slave surface with 24 radial lines

Choosing the 24 radial lines was specified with consideration of two factors. Firstly, the total time required to run the analysis of the finite element job. Secondly, from the Hertzian theory the contour plot of the contact pressure should be circular when the two contacting bodies are solids of revolution, as in the current geometry. Figure 5.5 shows the computer running time for the analysis of the job against different numbers of radial lines, 10, 12, 18, 24 and 26.

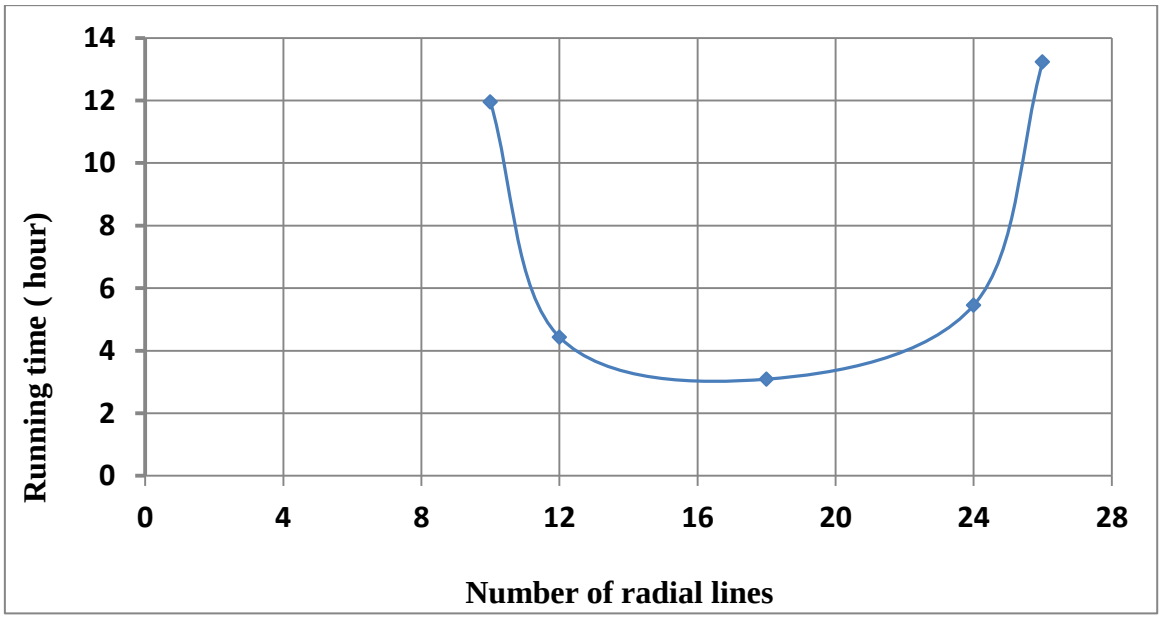

Figure 5.5 Different numbers of radial lines of slave surface against the PC running time

From Figure 5.5, it seems that the minimum running time occurs at 18 radial lines and this is consistent with the first condition. The pressure distribution for these variations of using different numbers of radial lines at the 0^{o} angular position is shown in Figure 5.6. It can be seen that the variation in the pressure value is quite small and it does not affect the accuracy of the results.

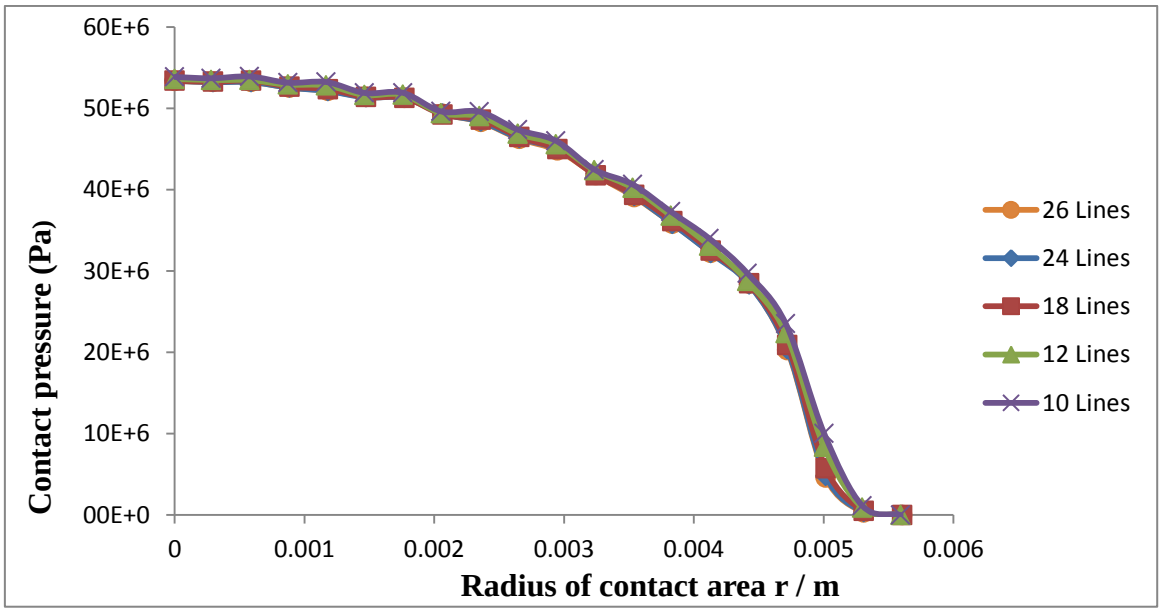

Figure 5.6 pressure distribution with different radial lines of slave surface

Generally, choosing eighteen curved lines or less did not satisfy the circular contour of contact pressure as shown in Figure 5.7. These contours are closer to polygons rather than circles. It is evident that with an increase in the number of radial lines of the slave surface a more circular shape can be obtained. However, the time required to analyse the job was multiplied due to the larger number of elements and nodes that were used. It should be noted that linear elements were used in accordance with the advice given by Abaqus. Trials with quadratic elements had confirmed that they did not give any advantages and indeed produced contact pressure profiles where pressures at mid side and corner nodes

followed two parallel curves with an inter node oscillation. The choice of 24 radial lines is to some extent aesthetic for symmetrical problems, but gives enhanced resolution for cases encountered later in the study where circumferential asymmetry is a feature of the results.

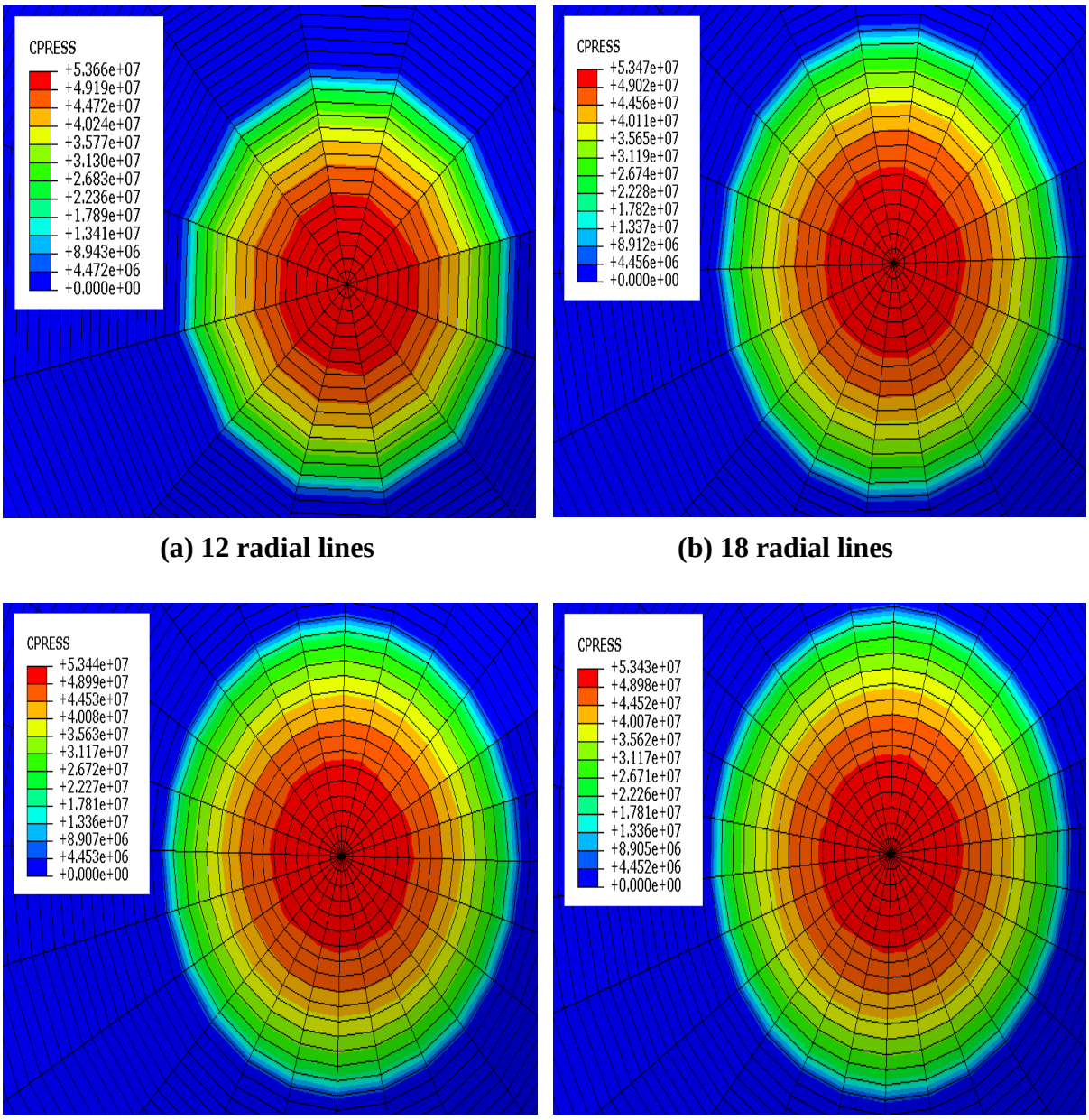

(a) 12 radial lines **(b) 18 radial lines**

(c) 24 radial lines **(d) 26 radial lines**

Figure 5.7: ball (slave) surface with different numbers of radial lines

For all of the results presented in the remainder of this thesis 24 radial lines were chosen for the FE contact analyses. These were at 15° increments from the sphere's *x* axis whose orientation depends on the direction of the contact force as discussed in section 6.4.

In sectional figures of contact pressure and gap between the surfaces the sections in each of the 24 radial directions are superimposed for comparison. The key in such figures labels the individual sections in terms of their angular positions (0°, 15°, 30°….345°). Figure 5.11 in the next section is the first figure of this type.

5.4. Radius of the contact area edge (*a*)

In this investigation it was necessary to calculate, r and θ. The radius, r, which represents the curved distance from the centre of the contact area to the particular node measured along the ball surface as shown in Figure 5.8.

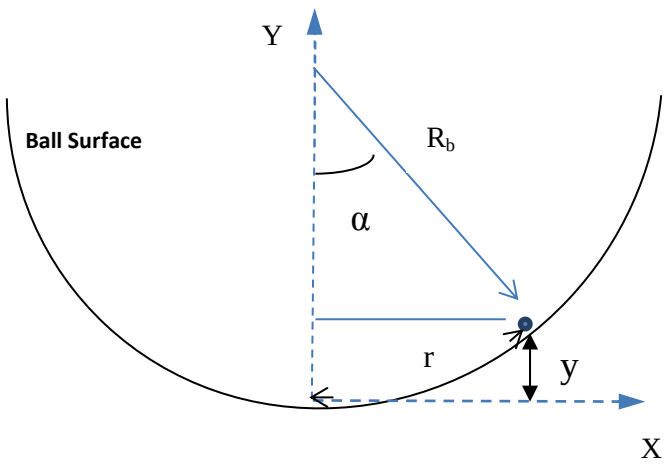

Figure 5.8 Radius of contact area (r)

R_b is the radius of the ball

$$r = R_b * \alpha \qquad \ldots\ldots\ldots\ldots(5.1)$$

$$\therefore r = R_b * \cos^{-1}\left(1 - \frac{y}{R_b}\right) \qquad \ldots\ldots\ldots..(5.2)$$

The angle (θ) is the measured angle from the X- axis of the finite element analysis geometry to the selected node on the slave surface, the ball surface, as shown in Figure 5.9. The difference in the angle (θ) between each line of the 24 radial lines of the slave surface is 15^{o}. The first line of the 24 radial lines is the x- axis and was taken as θ = 0 while the second line was θ = 15^{o} and so on.

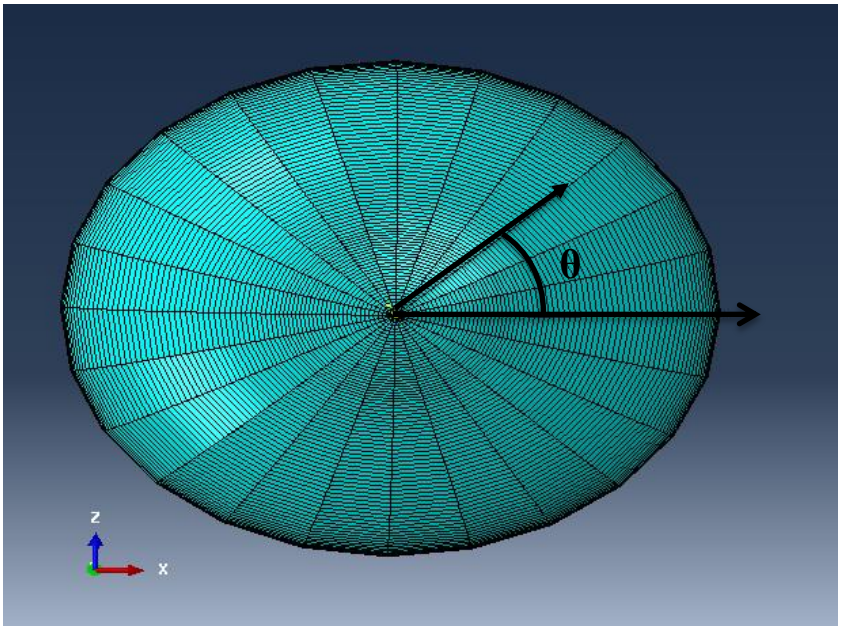

Figure 5.9: the measured angle, θ, relative to the slave surface

The radius of contact (r) and the angle (θ) were calculated for each mesh point using its Cartesian coordinates. The node label was employed so it was possible to sort the contact pressure and the gap value for each node on the contact surface. All the calculations and sorting the data were carried out by writing a computer program using the Fortran language software.

The finite element results of the ball-cup-block system, the contact area and the pressure distribution are shown in Figures 5.10 and 5.11 respectively where the load was applied in the direction of the cup's axis of rotational symmetry. It can be noted from these Figures that the results are quite similar to the Hertzian theory, where the contact area is circular and the contact pressure distribution is semi-elliptical.

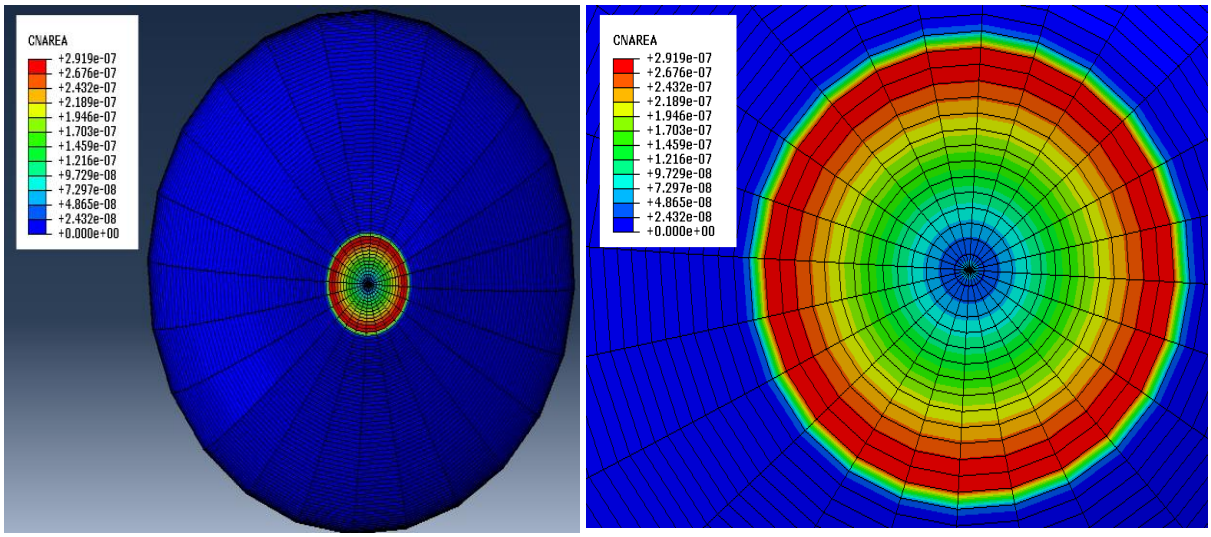

(a) (b)

Figure 5.10: (a) contact area of slave surface, (b) zoomed local area

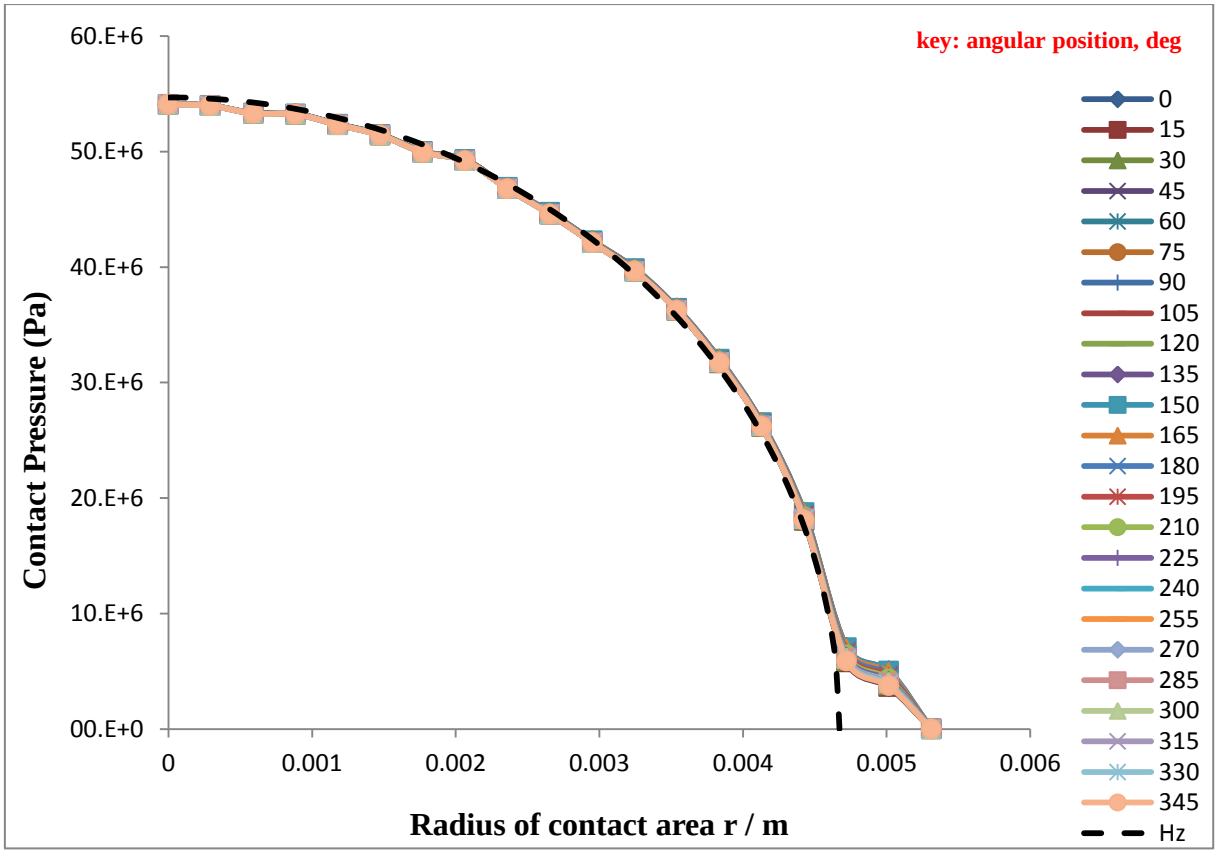

Figure 5.11 Pressure distributions at each radial line of the slave surface

In Figure 5.11, the black dashed line is the Hertzian pressure distribution based on load, relative radius of curvature and material elastic properties. The numbers from 0–345 represent the 24 radial lines of nodes which are used to obtain data from Abaqus at every 15^{o} angle increment. It is clear that there is a numerical error in the pressure value at the point immediately before the first zero pressure point. This error point occurred in all the contact models that have been developed in this study, regardless as to whether the model used a fine mesh resolution, a coarse mesh, the linear element type, the quadratic element type, hexahedron, tetrahedron or wedge element shapes. To investigate this error a plot of pressure and gap against contact radius for one case study was drawn as shown in Figure 5.12.

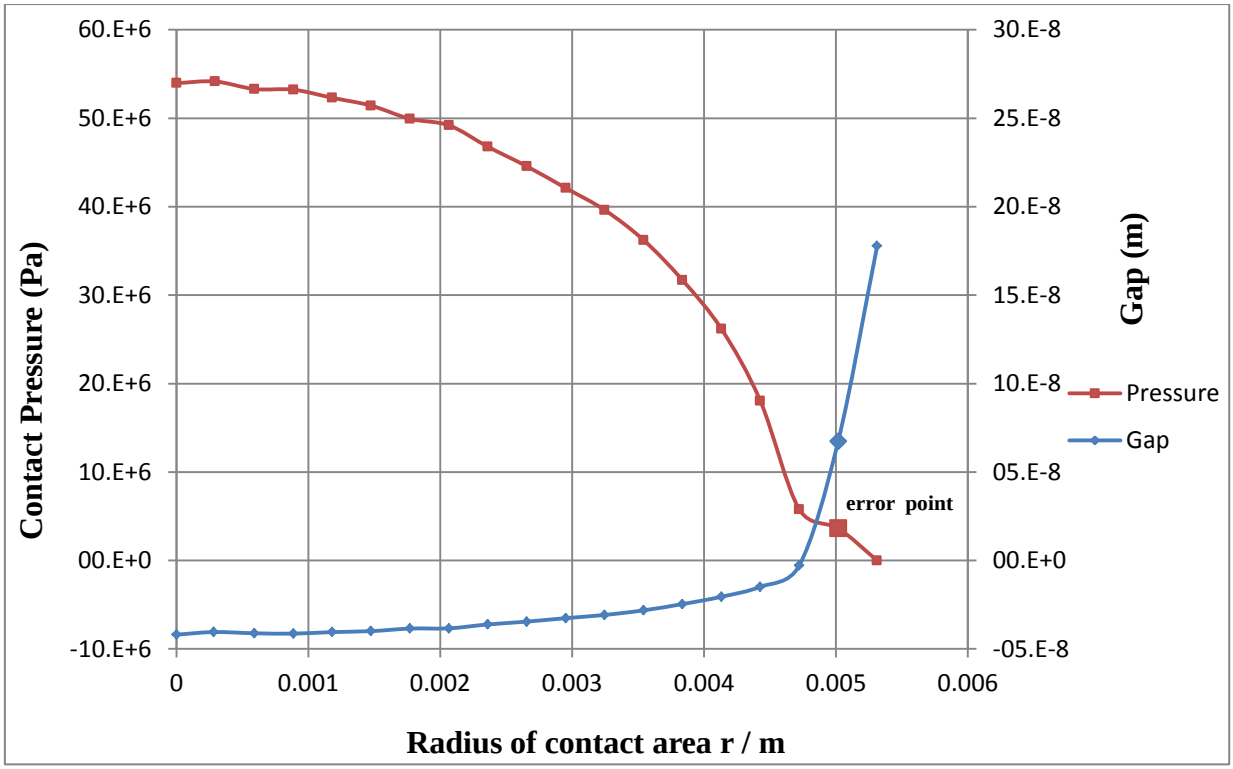

Figure 5.12: Pressure and Gap distribution from FE analysis

The solution to a contact problem consists of a contact area zone where:

$P \geq 0$ and $Gap = 0$ at $r \leq a$

Also a non- contact area zone where:

$P = 0$ and $Gap > 0$ at $r > a$

In the contact analysis with a finite element discretised approach, it is not possible to insist that the gap $\equiv 0$ in the contact zone, the approach adopted by the Abaqus package for contact analyses is:

(i) $P \geq 0$ and $-pt < Gap \leq 0$ in the contact zone and

(ii) $P = 0$ and $Gap > 0$ elsewhere

where (pt) is the penetration tolerance of the surfaces.

Condition (ii) is violated at the error point as can be seen in Figure 5.12. The error point at r = 5 mm has a pressure value greater than zero and a positive gap

value at the same time which is in conflict with the contact conditions. Therefore this error point has been disregarded from the calculations. The dimension of the contact radius when the pressure value equals zero is calculated by using a curve fit for the last two or three points just before the error point.

A linear curve fit using the last two points, and a quadratic curve fit using the last three points were carried out to compare them and select the most appropriate result as shown in Figure 5.13. It was found that the quadratic curve fit for the last three points had a closer value to the theoretical calculations for the Hertzian pressure value. The slope of the quadratic curve is also steeper than the slope of the line curve fit which is consistent with the Hertzian pressure where the slope becomes infinite at the edge of the loaded region. As a result, it was judged that the quadratic curve was the more accurate of these two options.

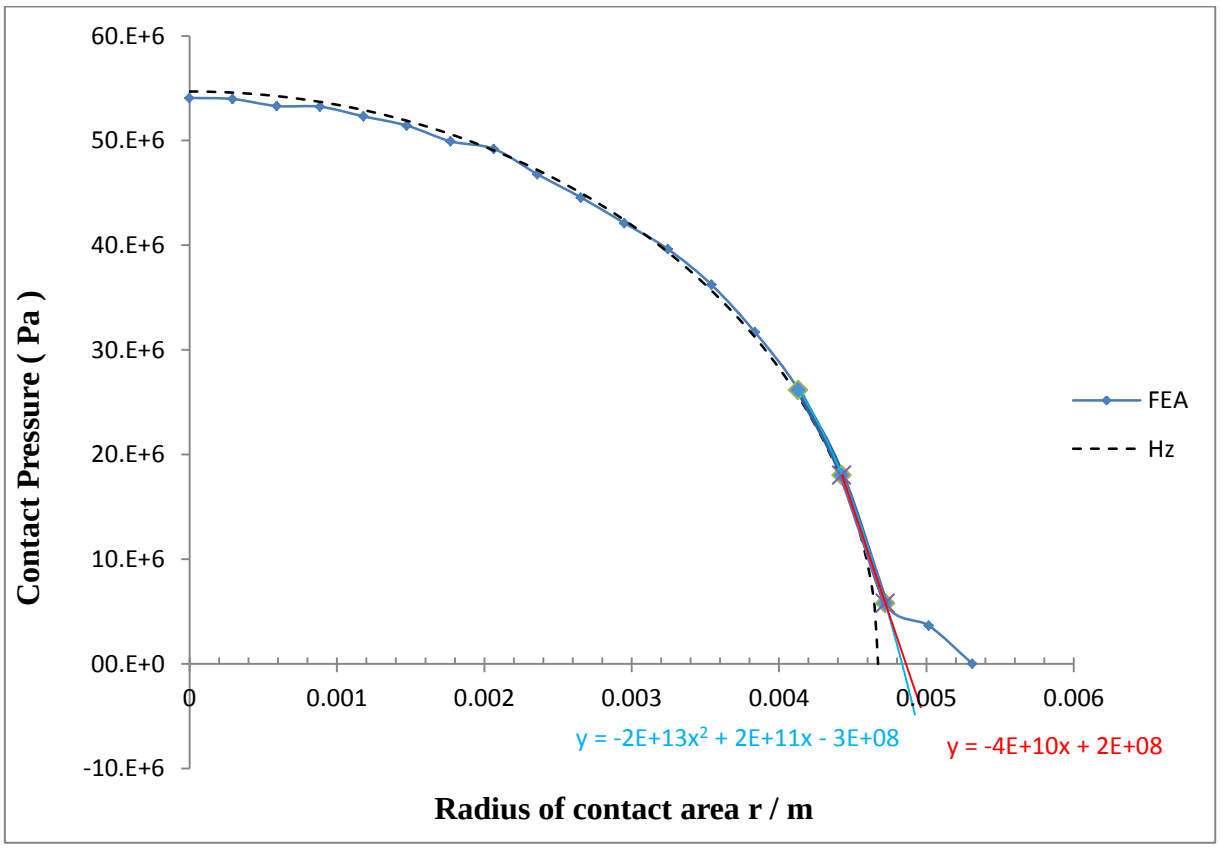

Figure 5.13 showing the curve fit to last two and three points

Another way to obtain the most accurate value of the radius of contact was assumed by using a parabola Equation to curve fit the last two points as follows:

$$a - r = kp^2 \qquad \text{……..(5.3)}$$

This is a parabola whose axis of symmetry is in the negative direction passing through the point r = ***a*** with infinite slope.

There are two unknown constants, ***a*** and k in this Equation. Substituting the last two points before the error point of the pressure curve in Equation 5.3, where these two points are referred to as (r_1, p_1) and (r_2, p_2), gives:

$$a - r_1 = kp_1^2 \qquad \text{…….(5.4)}$$

$$a - r_2 = kp_2^2 \qquad \text{…….(5.5)}$$

From Equations 5.4 and 5.5, k equals:

$$k = \frac{r_1 - r_2}{p_2^2 - p_1^2} \qquad \text{…..(5.6)}$$

Then ***a*** can be calculated by:

$$a = r_1 + (r_1 - r_2)\frac{p_1^2}{(p_2^2 - p_1^2)} \qquad \text{……(5.7)}$$

Comparison of the calculated values of contact radius, *a*, obtained from quadratic three points (*a* from 3p) and parabola two points (*a* from 2p) for the 24 radial lines are given in table (5.1). It can be seen from this table that the average value of *a* calculated from the two points parabola is less than the *a* value from three points quadratic and it is also closest to the Hertzian *a* value. As a result, the two points parabola of Equation (5.3) was adopted to calculate the radius of the contact area in this research. The average value of *a* from the 24 lines was taken as the radius at the edge of the contact area.

Table (5.1) values of radius of contact for the 24 radial lines.

angle	***a* from 2p**	***a* from 3p**	angle	***a* from 2p**	***a* from 3p**
0	0.0047558	0.004835	195	0.0047649	0.004852
15	0.004756	0.004835	210	0.0047631	0.00485
30	0.0047572	0.004838	225	0.0047615	0.004846
45	0.004759	0.00484	240	0.0047601	0.004842
60	0.0047609	0.004845	255	0.0047591	0.00484
75	0.0047629	0.00485	270	0.0047588	0.00484
90	0.0047651	0.004854	285	0.0047592	0.004842
105	0.0047676	0.004859	300	0.0047596	0.004843
120	0.0047698	0.004862	315	0.0047594	0.004842
135	0.0047709	0.004864	330	0.0047582	0.00484
150	0.0047706	0.004863	345	0.0047567	0.004837
165	0.004769	0.00486	Average	0.0047622	0.004847
180	0.0047669	0.004857			

5.5. Equivalent Semi-Infinite Body Contact

For the case study used at this stage the mechanical properties of the geometry applied in the FE analysis, the Abaqus software, and in calculations with the Hertz Equations are listed in Table (5.2). The load applied to the head of the prosthesis was 2500 N which represents approximately three times body weight of 750 N [74]. To the author's knowledge, most researchers use 3- 4 times body weight to represent the applied load in the hip joint during normal walking activity. In other words, the employed forces in their laboratory tests or calculation procedures for simulation the hip joint are between 2 kN to 3 kN as a maximum load value. This range of forces is not only an assumed value, it has also been measured experimentally as will be shown in Chapter 6.

Table (5.2) geometry properties

E_1 (Young Modulus for body 1)	210 GPa
E_2 (Young Modulus for body 2)	210 GPa
γ_1 (Poisson's ratio)	0.3
γ_2 (Poisson's ratio)	0.3
R_b (ball radius)	25 mm
R_c (cup radius)	25.1 mm

The Hertz Equations that were used to calculate the maximum contact pressure $P_{o(h)}$ and the radius at the edge of contact a_h were given in Chapter 3, equations 3.4 to 3.8: The results then become

$P_{o(h)}$ = 54.689 MPas, and a_h = 4.67 mm.

A comparative study for different cup thicknesses has been carried out using 4, 6, 8, 10 mm thicknesses. The effect of cup thickness variation on the pressure generation between the ball and the cup is shown in Figure 5.14.

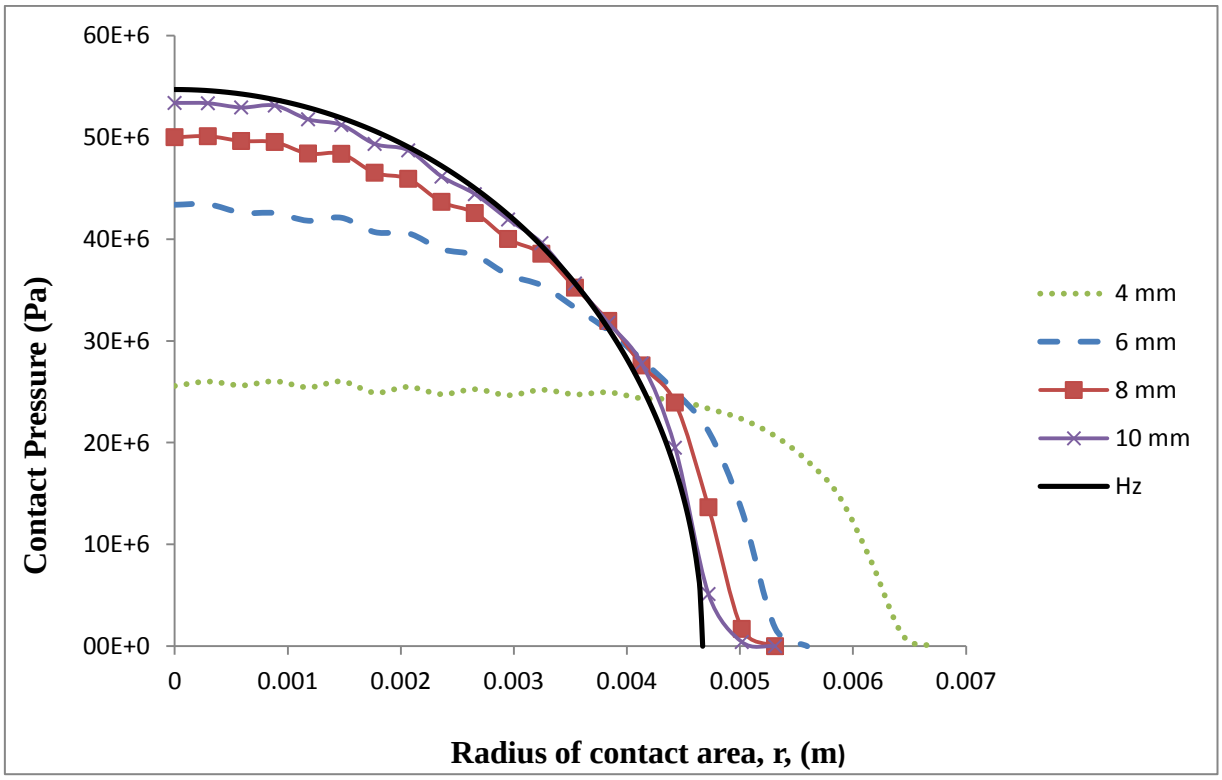

Figure 5.14: Contact pressure for one radial line of different cup thickness

The pressure distribution from 10 mm, 8 mm and 6mm cup thickness will be compared with the equivalent Hertzian pressure later. It can be seen from Figure 5.14 that the contact pressure for the 4mm cup thickness does not look like the semi-elliptical pressure Hertzian distribution. It has an almost constant pressure within the contact area falling to zero over the last 20% of the contact radius.

The results obtained from the FE analysis with 10 mm cup thickness were

$P_{\mathrm{o(f)}}$ = 54.077 MPa and a_{f} = 4.762 mm, where

suffix f indicates the FEA results.

The difference between the FEA results and Hertzian theory may occur because the FEA contact is not semi-infinite, this is clearly the case when the cup thickness is 4mm. It is also because the FEA load is the resolved contact pressure and this takes into account the slope of the contact interface.

Because the EHL analysis assumes that the surface deflection corresponds to that of a semi – infinite body, it was necessary to determine an equivalent Hertzian problem that has the same characteristics as the FEA model results. Equivalence is taken as a Hertzian contact that has the same maximum pressure and the same contact radius.

Modifying the Hertzian contact pressure, $P_{\mathrm{o(h)}}$, and the Hertzian contact radius, a_{h}, to be the equivalent contact pressure, $P_{\mathrm{o(equiv)}}$, and the equivalent contact radius, a_{equiv}, from the FE analysis was achieved by changing the reduced elastic modulus, $\acute{E}$, to be an equivalent elastic modulus, $\acute{E}_{\mathrm{equiv}}$, and changing the applied load, W, to be an equivalent load, W_{equiv}.

The requirement is that

$a_{\text{equiv}} = a_{\text{f}}$ …….. (5.8)

$P_{\text{o(equiv)}} = P_{\text{o(f)}}$ …..(5.9)

where suffix ‘equiv’ indicates the Hertzian results equivalent to the FEA results.

Equations 3.5 and 3.7 can be re-written as,

$$\acute{E}_{equiv} = \frac{\pi R P_{0(h)}}{a_h} \quad \text{…. (5.10)}$$

$$w_{equiv} = \frac{2\pi P_{o(h)} a^2{}_h}{3} \quad \text{….. (5.11)}$$

by substitution of Equations 5.8 and 5.9 into Equations 5.10 and 5.11 the necessary values of $\acute{E}$ and W are found to be

$$\acute{E}_{equiv} = \frac{\pi R P_{0(f)}}{a_f} \quad \text{…….(5.12)}$$

$$w_{equiv} = \frac{2\pi P_{o(f)} a^2{}_f}{3} \quad \text{…….(5.13)}$$

Equations 5.12 and 5.13 were employed to evaluate the equivalent load and reduced modulus of elasticity. These values make the contact pressure and the radius of contact area from Hertz Equations equivalent to the real joint as evaluated by FE analysis of the joint components. The results of these calculations for 10, 8 and 6 mm cup thickness are shown in Figure 5.15 – 5.17, and the values of P_{o}, a, $\acute{E}_{\text{equiv}}$ and W_{equiv} are given in table (5.3).

Table 5.3. Contact parameters for semi-infinite contact and for equivalent semi-infinite contacts for the cup thicknesses of 10, 8 and 6 mm.

	W (N)	$\acute{E}$ (GPa)	a (mm)	P_o (MPa)
Semi-infinite	2500	230.77	4.67	54.689
10 mm cup	2492	217.23	4.76	52.475
8 mm cup	2451	203.67	4.84	49.99
6 mm cup	2381	166.94	5.12	43.39

A good agreement was found between the pressure curve trend of the finite element results and the equivalent Hertzian results for the 10 and 8 mm cup thickness, with a small deviation for the 6 mm cup.

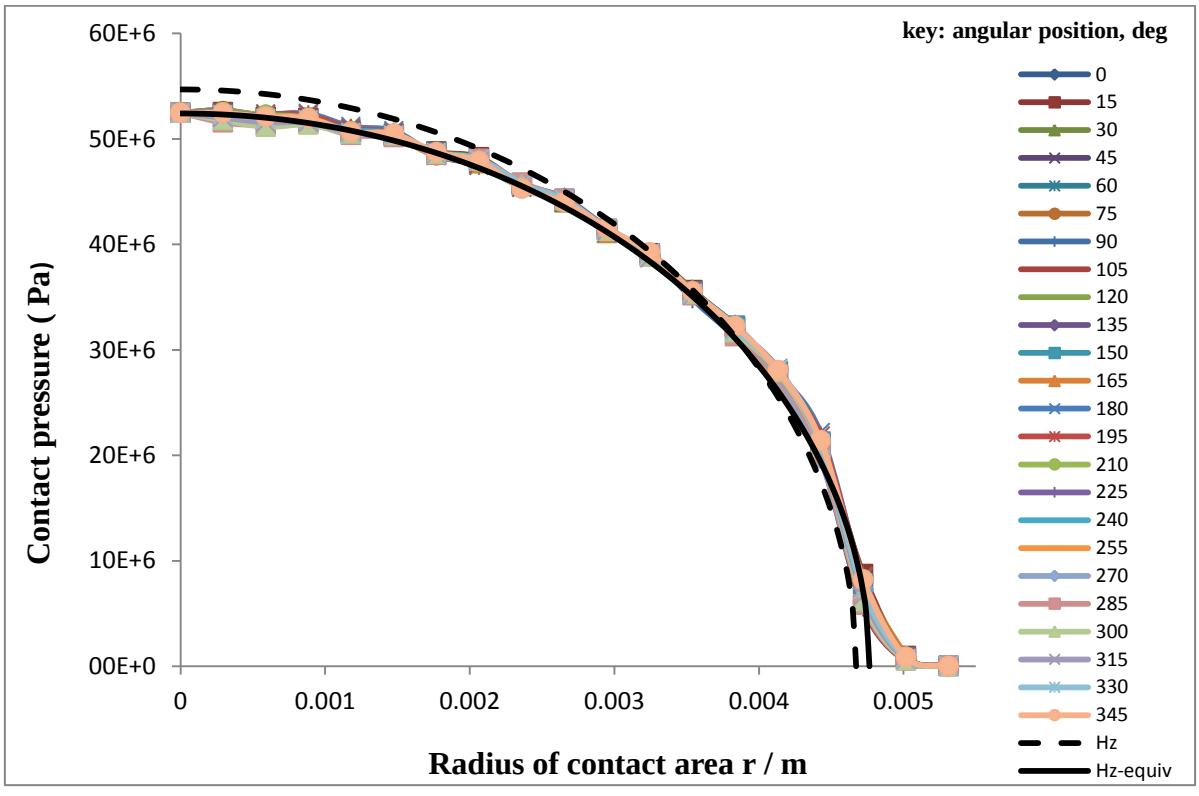

Figure 5.15 Hertz equivalent, Hertz theory and the FEA pressure sections for 10 mm cup.

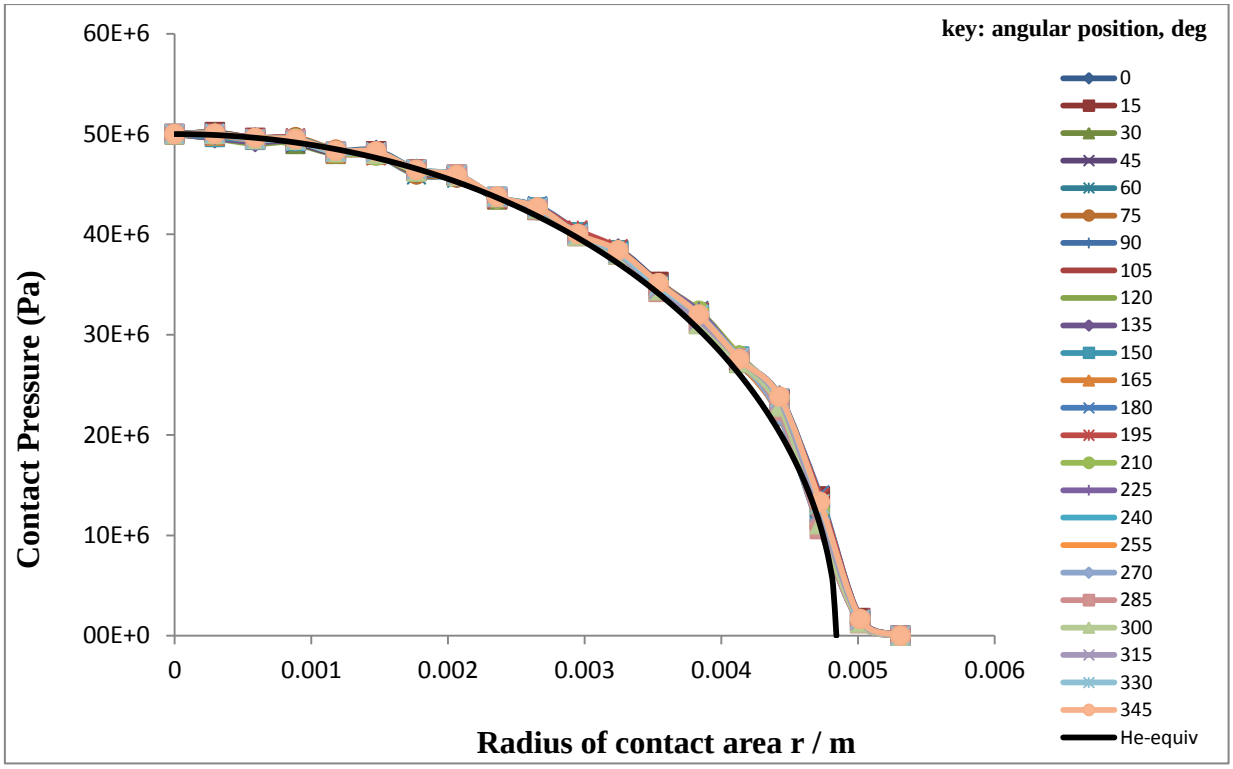

Figure 5.16: Hertz equivalent and the FEA pressure sections for 8 mm cup

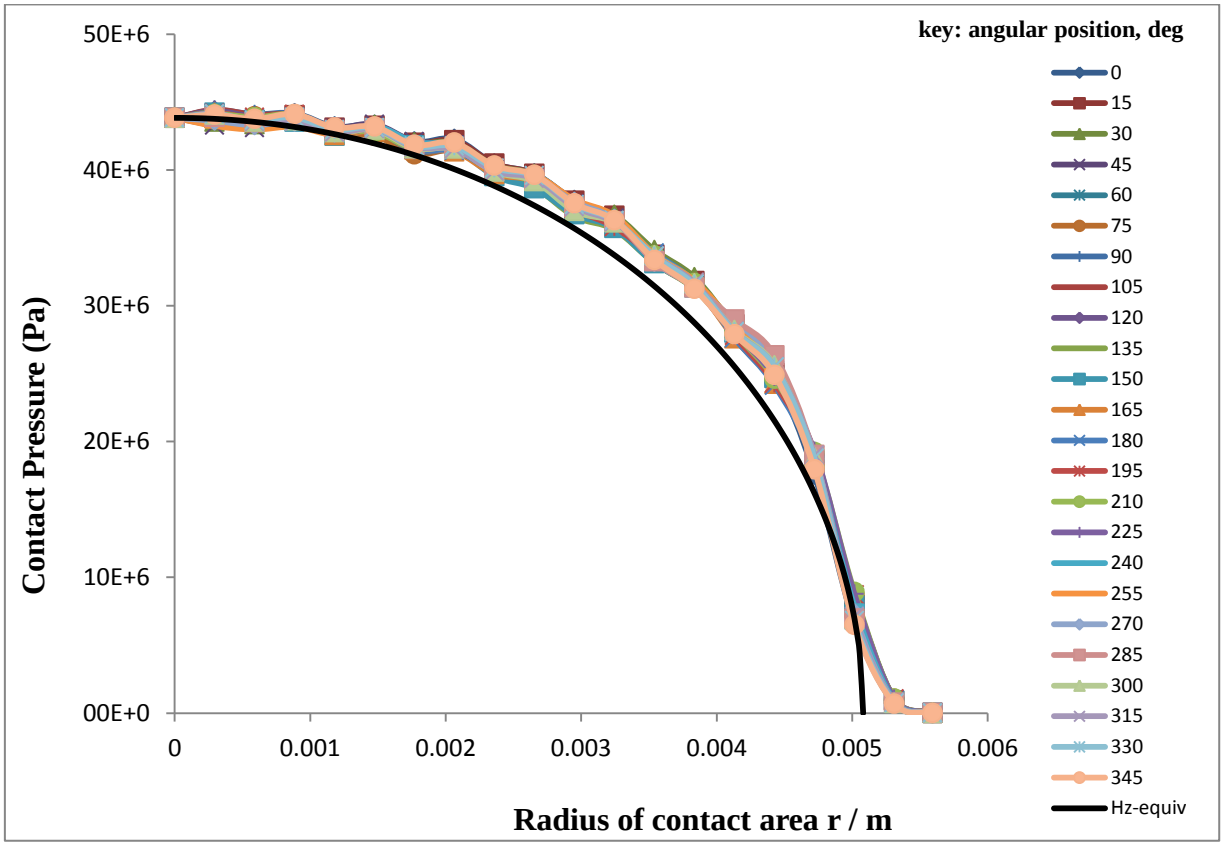

Figure 5.17: Hertz equivalent and the FEA pressure sections for 6 mm cup

5.6 Gap Outside the Contact Area

The gap outside the contact area is equal to the distance between the two contacting bodies outside the contact zone, as shown in Figure 5.18.

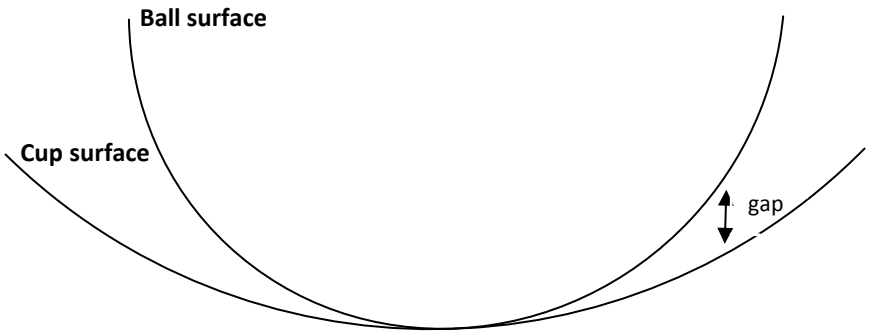

Figure 5.18: The gap between two contacting geometries

From the numerical analysis of the Abaqus software, the gap at every 15^{o} angle for all the 24 radial lines, Gap_f, is as shown in Figure 5.19.

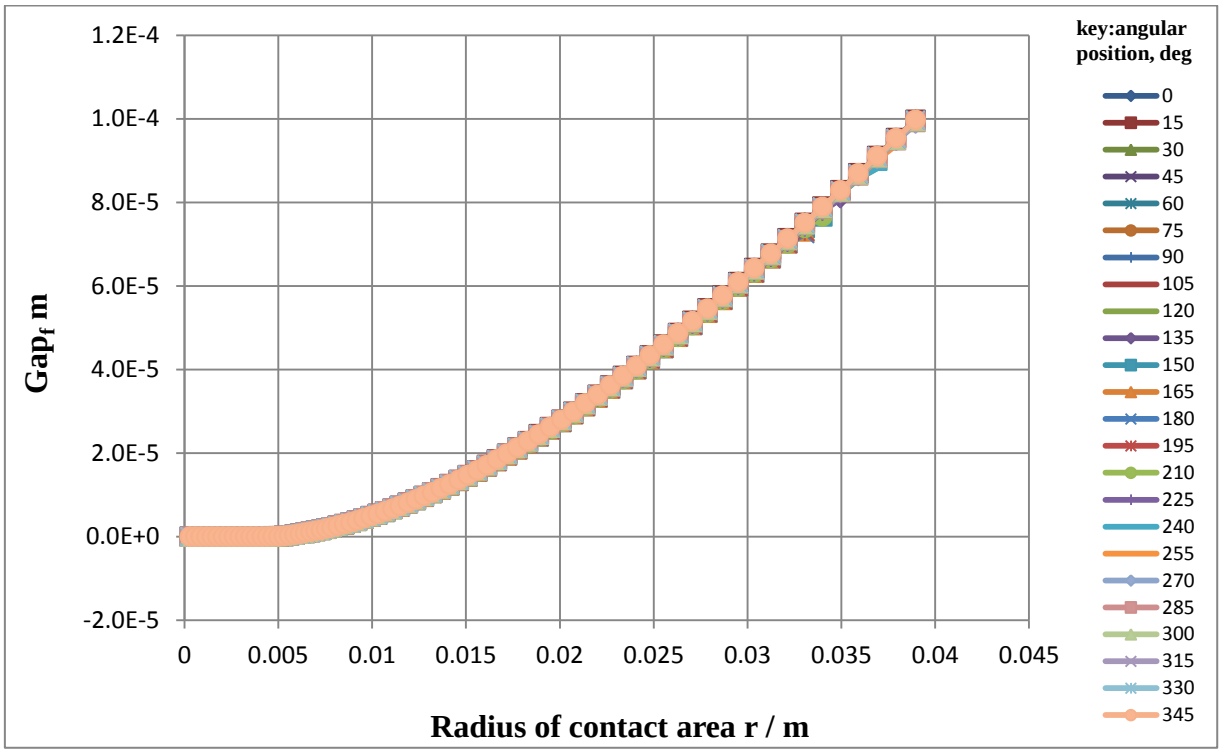

Figure 5.19: Gap values of the FEA, Gap_f, for the 24 radial lines

The gap outside the contact zone for the equivalent Hertzian contact, Gap_h, is given by Johnson [67]:

$$Gap_h = (r^2 - 2a^2)/ (2R)+(1/ \pi R)[(2a^2 - r^2)\sin^{-1}(a/r) + ar(1-(a^2/r^2)^{0.5})] \quad (5.14)$$

The difference between the gap from the FE analysis and the gap from the semi- infinite equivalent contact will be called the gap factor, as shown in Figure 5.20.

Gap factor = finite element gap – Hertzian gap

Then

Finite element gap = Hertzian gap + gap factor

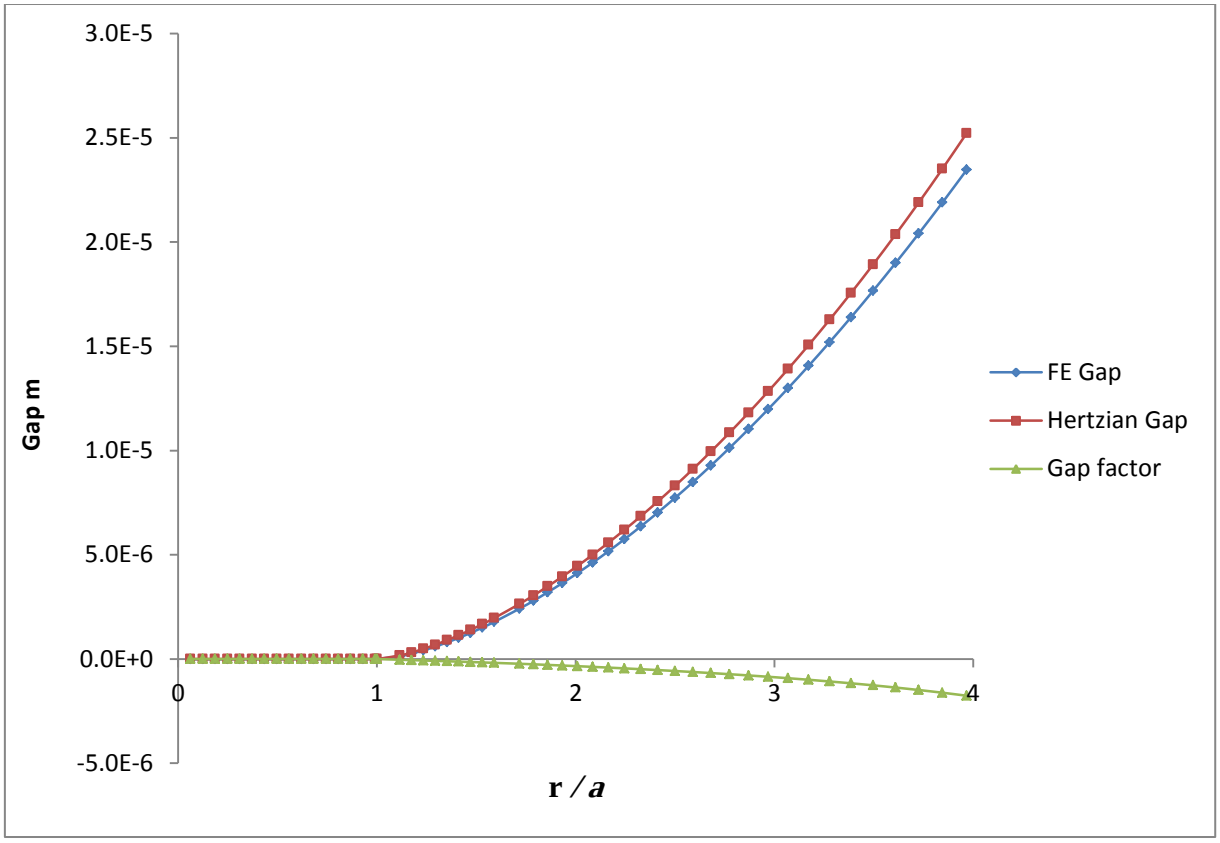

Figure 5.20: Gap_f, Gap_h for one of the radial lines with the corresponding gap factor

5.7 Elastohydrodynamic Lubrication

The long-term success of hip joint arthroplasty can be extremely affected by the performance of the lubrication process. Wear debris are generated normally by direct surface contact between the femoral head and the acetabular cup, causing abrasive and adhesive wear. Reducing wear particles can be promoted by using high wear resistance bearing materials and forming a good lubricant film in the joint capsule after total hip replacement. From a fluid film lubrication point of view, separating the contacting surfaces as much as possible can reduce the portion of the load carried by asperity contacts.

Lubrication of the contacts is by the synovial fluid whose pressure viscosity coefficient is of the order α = 16.5 GPa^{-1} as discussed in section 3.7. The reciprocal of α is 66.6 MPa so that piezo viscous effects became significant for contact pressures of this order. Lubrication analysis of hip prostheses is usually based on an Elastohydrodynamic model as is the case for the work described in [61-64], for example. The gap outside the contact needs to be the same in the equivalent model as in the FEA model. This is because the film is formed in the entry region to the contact so that must also be equivalent. Therefore, it was necessary in this research to investigate the effect of the gap factor in the lubrication of the MOM artificial hip joint.

The gap factor value was added to the undeformed geometry of the Semi-infinite equivalent gap in the EHL analysis so that the total is equal to the FE analysis gap. The gap factor values were calculated relative to the mesh of the FE analysis geometry, the 24 radial lines mesh nodes. Transferring the gap values from the FE coordinate system to the EHL coordinate system, as shown in the Figure 5.21, was accomplished by arranging an interpolation method as follows;

The rectangular coordinate system, (i, j), represents the EHL coordinate, while the circular coordinate, (r, θ), system represents the slave surface node of the finite element analysis.

Where

i varies from $-2.5a$ to $2a$

j varies from $-1.5a$ to $1.5a$

and m and n are the number of the nodes spacing in the half width of the Hertzian contact in the x and y directions respectively.

r varies from Hertzian half width value, a, to about $2.5a$.

θ varies from 0^o, radial line 1, to 345^o, radial line 24.

For each point in the EHL mesh outside the dry contact area the two radial lines, θ_1 and θ_2 closest to the point were found.

Linear interpolation formulas were then used,

$$Gap(r, \theta_1) = (((r - r_1) * gap(r_2, \theta_1)) + ((r_2 - r) * gap(r_1, \theta_1))) / (r_2 - r_1) \quad \text{……...(5.15)}$$

$$Gap(r, \theta_2) = (((r - r_1) * gap(r_2, \theta_2)) + ((r_2 - r) * gap(r_1, \theta_2))) / (r_2 - r_1) \quad \text{…..…(5.16)}$$

$$Gap(i,j) = (((\theta - \theta_1) * gap(r, \theta_2) + ((\theta_2 - \theta) * gap(r, \theta_1)) / (\theta_2 - \theta_1) \quad \text{….....….(5.17)}$$

This process is illustrated in Figure 5.21 A and B

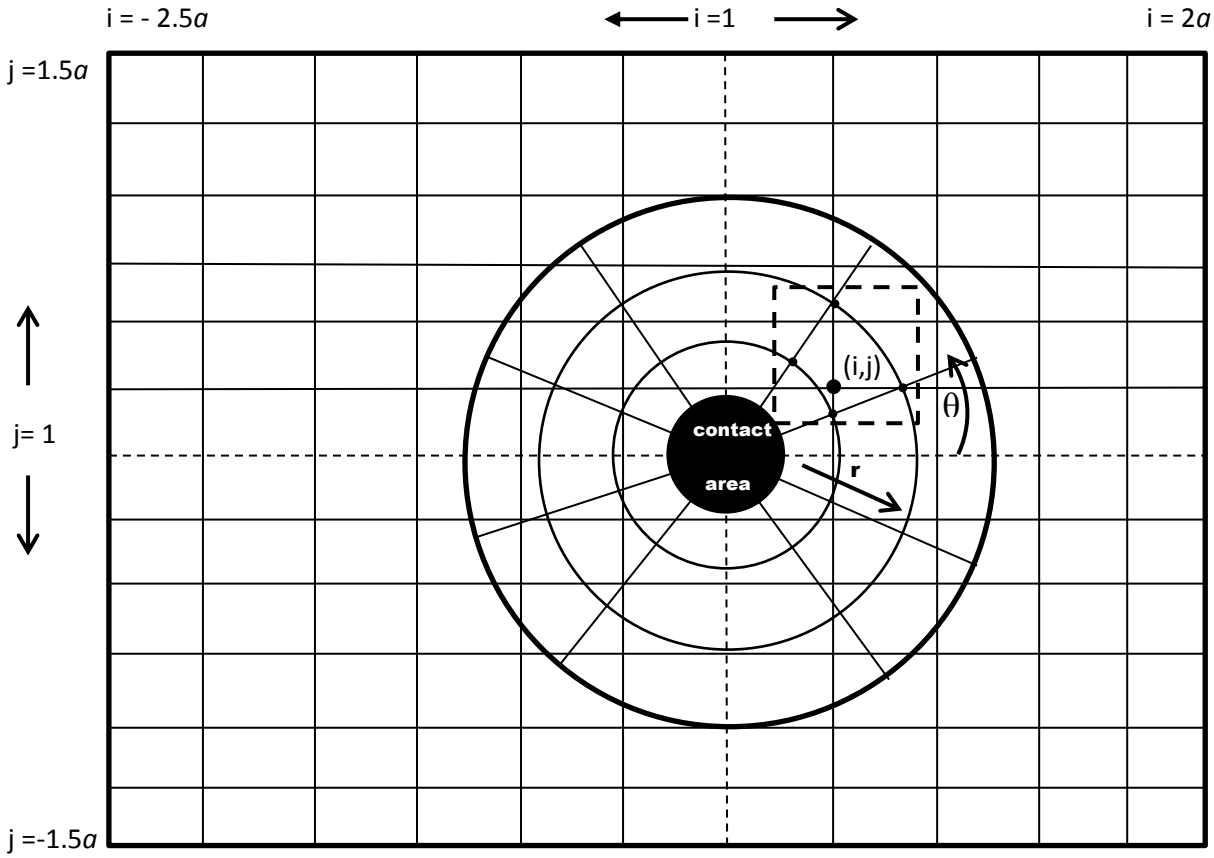

(a)

(b)

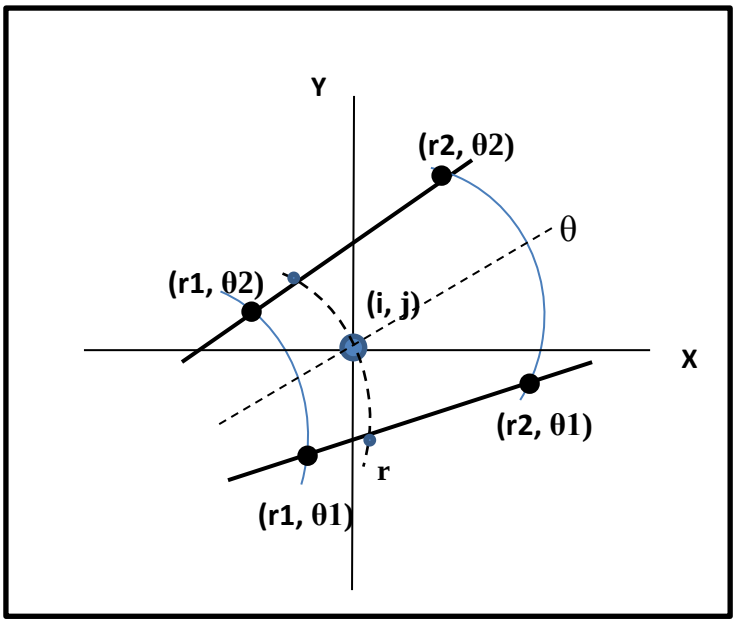

Figure 5.21 (a) and (b) Coordinates and mesh points used for transferring the gap value from FE to EHL coordinate systems

Changing the contact point position of the ball-cup system relative to the acetabular cup in the MOM prosthetic hip may lead to poor lubrication performance. Saikko et al [82] showed that a steep contact position of the cup exceeding a critical value of 60^{o} leads to an asymmetric contact area, boundary lubrication at best, and considerably higher wear rate. Clarke et al [83] also showed a non-linear relationship between inclination angle and indicative wear depth, whilst wear was clearly at its highest at the steepest inclination angle.

Clinically it is observed that the optimum inclination angle is in the region of $40–45^{o}$. It is becoming evident that socket-cup placement outside of a recommended range of 30^{o} to 50^{o} abduction angle (inclination angle) can lead to a greater amount of metal release particularly in small diameter components [84].

In order to investigate the influence of the contact area position on the contact pressure value, the radius of contact area and gap factor values, three models were generated. In the first model a central contact area was obtained when the load applied in the vertical, y-axis, direction as shown in Figure 5.22. In the second model as illustrated in Figure 5.23 the slave surface, the ball surface, was inclined 30^{o} to the vertical line. In the third model a 45^{o} inclination angle was used with the polar axis of the ball and the vertical axis of the cup as shown in Figure 5.24.

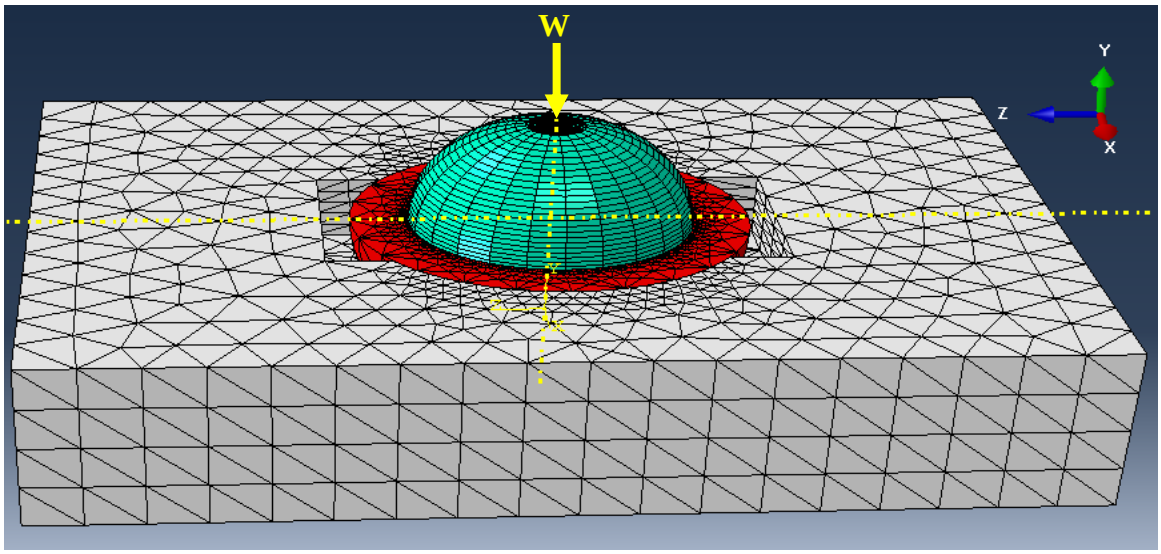

Figure 5.22: a central contact of the ball – cup system.

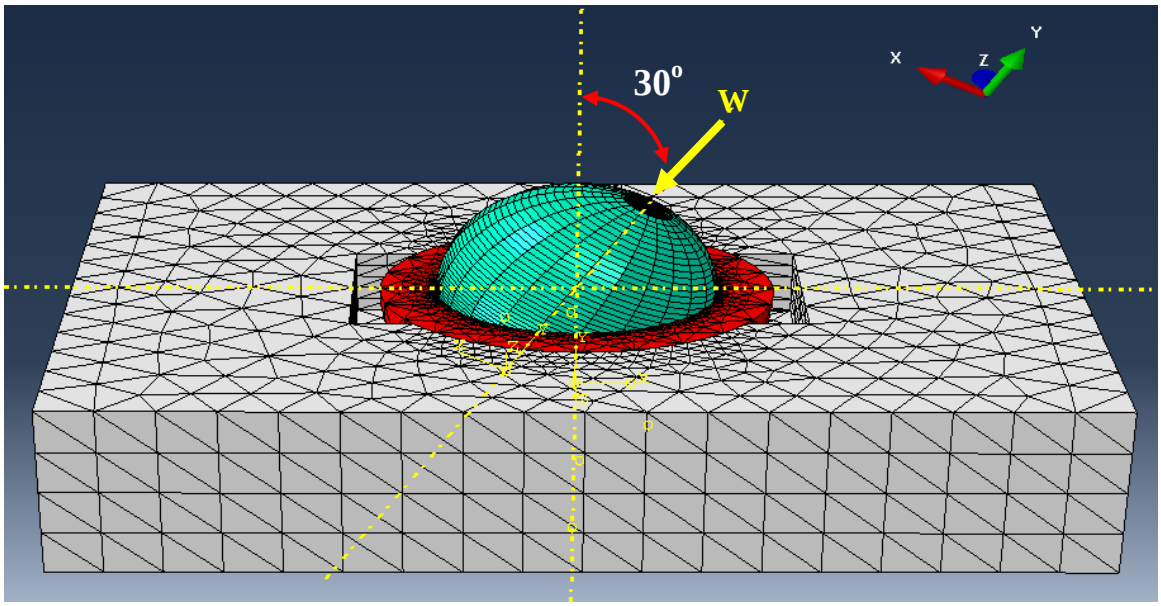

Figure 5.23: a 30° inclination angle between ball – cup system

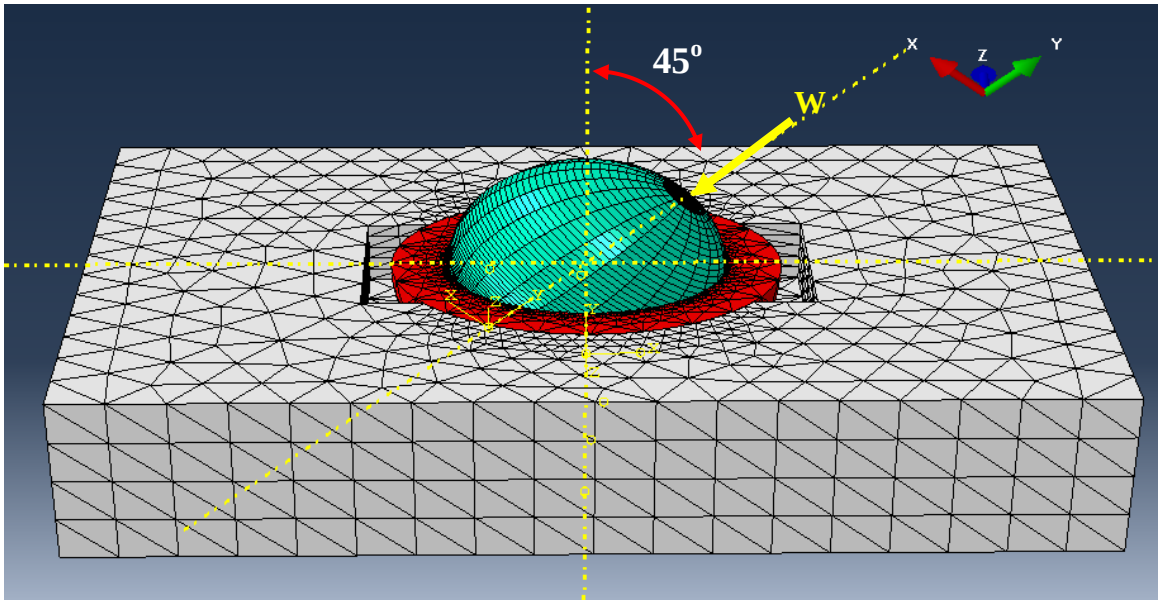

Figure 5.24: a 45° inclination angle between ball – cup system

The distribution of the equivalent contact pressure for the three different inclination angle cases is shown in Figure 5.25. Comparing these sections it can be seen that there is only a 0.8% reduction in the maximum contact pressure between the central contact case and the (30°) inclined case, and (1.63%) pressure reduction between the (0°) case and the (45°) case.

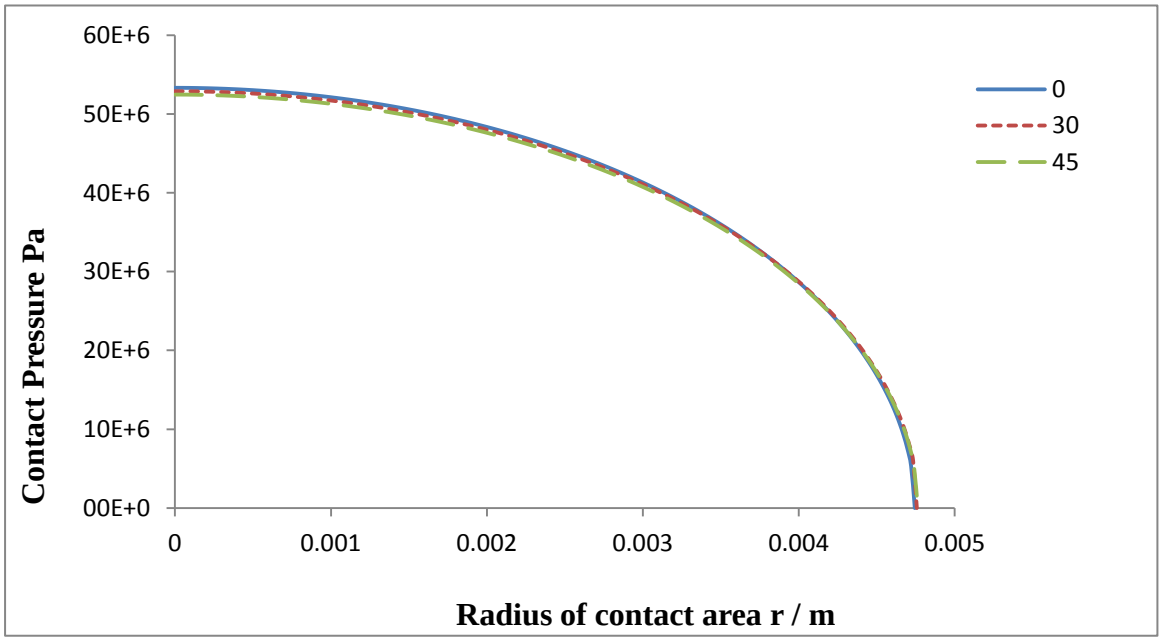

Figure 5.25: Equivalent contact pressure for 0°, 30° and 45° inclination angle

The gap factor values for the 24 radial lines of the three models are shown in Figures 5.26 to 5.28. Only very small differences were found in the gap factor values for the different radial lines when the contact between the ball and the cup was symmetrical about the vertical axis, i.e at 0^o inclination angle. The maximum gap factor value was about ($-0.2*10^{-6}$ m) at r/*a* =2.4 as shown in Figure 5.26.

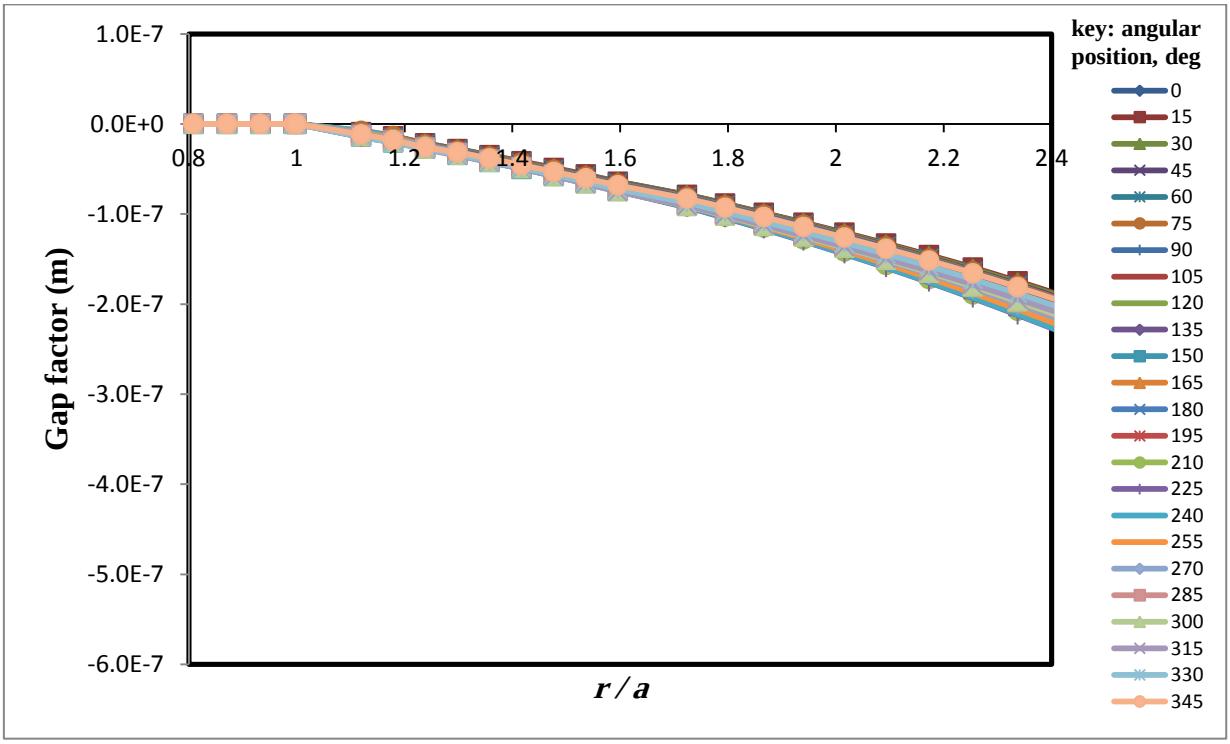

Figure 5.26 Gap factor of 10 mm cup thickness with 0^o inclination angle for the 24 radial lines

Relatively larger variations were found between the 24 radial lines when the ball surface was inclined at 30^o and 45^o about the vertical axis of the cup surface than the 0^o angle. The maximum gap factor was approximately ($0.45*10^{-6}$) for 30^o angle and ($0.5*10^{-6}$) for 45^o as shown in Figures 5.27 and 5.28. The gap factor was approximately double when there was a changing of the contact area position, which means specifying the correct contact position is essential to obtain accurate results.

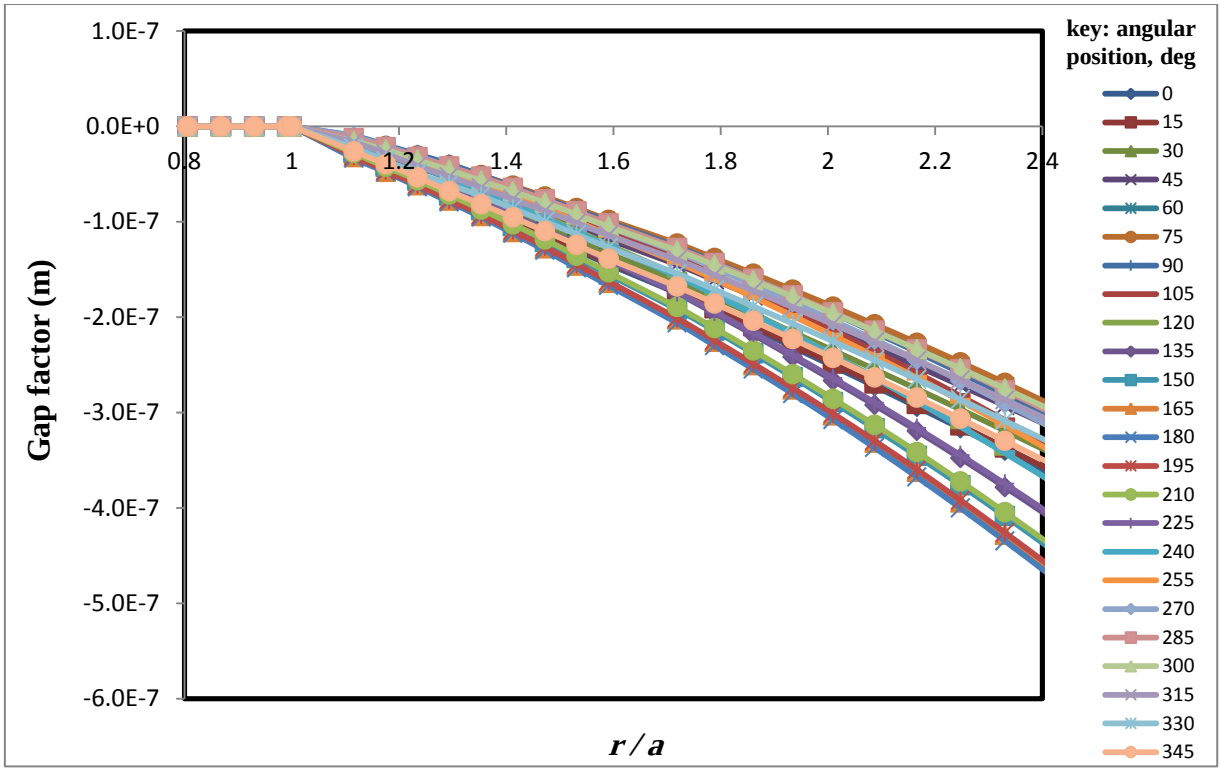

Figure 5.27 Gap factor of 10 mm cup thickness with 30° inclination angle for the 24 radial lines

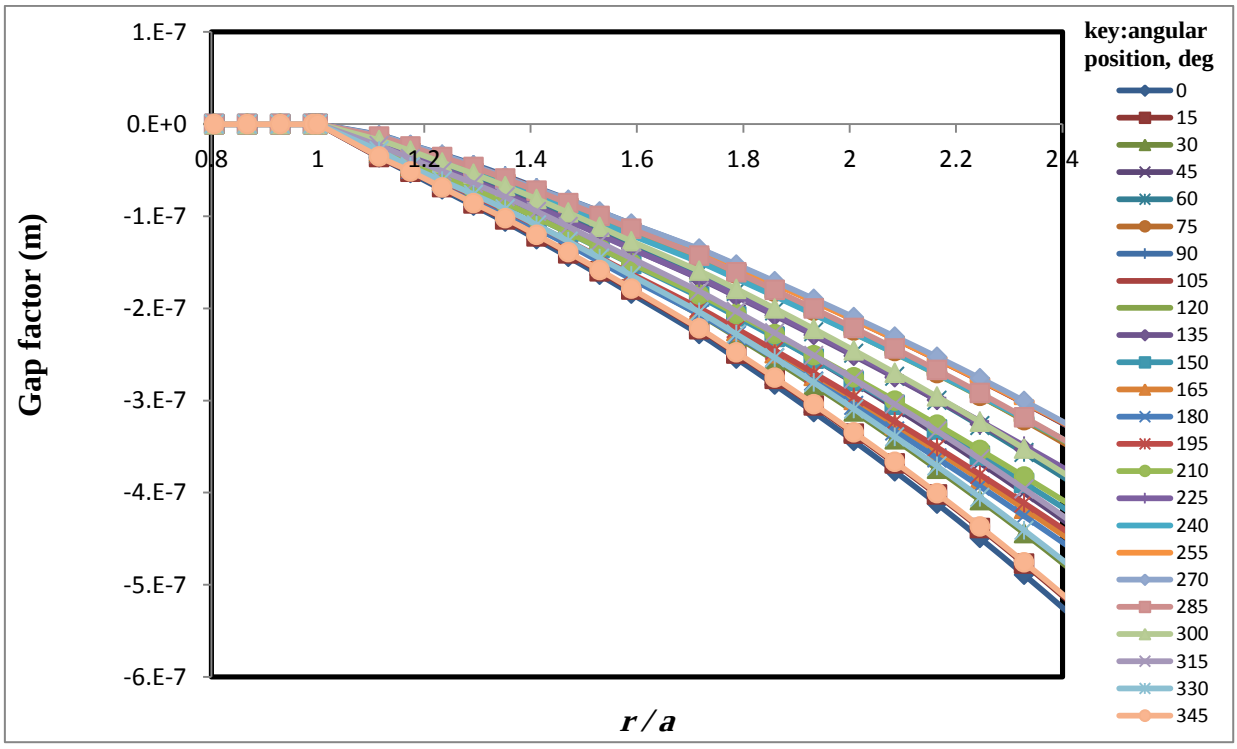

Figure 5.28 Gap factor of 10 mm cup thickness with 45° inclination angle for the 24 radial lines

5.8 Summary

This chapter has presented the developed form of the FEA contact analysis. The sensitivity of results to the restraint mechanism of the cup component was observed in Chapter 4. This was addressed by adopting the foam block approach introduced by Jin et al [74]. In this method a foam block with a hemispherical recess provides restraint of the cup through contacting surfaces with a specified friction coefficient. To replicate the asymmetrical nature of the cup support provided by the acetabulum, two additional recesses were specified in the foam block where there was no contact and therefore, no restraint.

The ball model was finalised by choosing an ordered radial structure for the finite element mesh. There were two reasons for this choice. It led to symmetric contact results for cases where the restraint system was also symmetric, whilst variations were observed when an unstructured mesh was used. It also provided a regular surface coordinate system for the ball which maximised the accuracy obtained for transferring information from the FEA model to the lubrication analysis. By orienting the polar axis of the ball in the load direction, the coordinate system became a polar system centred on the contact point, which was the ideal configuration as this was also the origin for the rectangular coordinates used for the EHL analysis.

The resolution of the mesh adopted was finalised by comparing results obtained with different angular resolution so as to optimise the symmetry of the results obtained and the computational time required.

The contact results obtained using Abaqus displayed an unexplained feature for all the analysis. This was an inconsistency between the results obtained and the contact conditions at the boundary of the contact area. This gave a constant error point at the last node on each radial line which had a contact pressure,

although it was not in contact. This is thought to be related to the convergence of the contact process within the software. The difficulty was overcome by disregarding this point as far as determining the contact area was concerned and adopting a parabolic curve fit based on the two closest mesh points to the error point.

The contact area and pressure results were developed into an equivalent Hertzian model. Whereby the elastic properties and the load were adjusted so as to provide a contact with the same contact dimension and maximum contact pressure as had been obtained from the FE model.

The difference between the shape of the gap between the surfaces obtained using the equivalent Hertzian and FEA models was quantified and procedures developed to make this available for subsequent EHL analyses based on the equivalent Hertzian model.

To complete the EHL analysis, kinematic information was required. Instead of estimating the position of the contact point, published measured data from different patients was used which was available in the form of a dataset [88]. Specification of the correct position of the contact point between the ball and the cup during normal walking activity was accomplished. The method developed to define the coordinates of the contact point position relative to the cup surface and the ball surface will be discussed in Chapter 6.

Gait Analysis

6.1 Introduction

Contact forces in the artificial hip joint should be known for experiments on wear and friction, durability and fixation of prostheses for optimising their design. It is also important to draw a clear picture for physiotherapists and patients who need to make decisions as to which activities must be avoided after hip replacement surgery. The contact forces acting in vivo in the total hip replacement during normal walking, stair climbing and other activities have been measured for an age group of patients between 55 and 76 years old [85]. Friction induced polyethylene wear and wear related aseptic loosening are the most frequent reasons for revisions of hip joint prostheses.

Other bearing combinations such as MOM type which are the focus of the current study have much lower wear rates but still retain the problem of aseptic loosening. The friction in the joint and thus the wear of the implants can be determined from measured joint contact forces and moments [86]. Lenaerts et al [87] analysed the effect of modelling of the hip geometry on the quantification of hip joint moments, muscle moments and hip contact forces during gait using musculoskeletal modelling.

In the current investigation the in vivo data for the hip joint contact forces and synchronous analysis of gait patterns from the **Orthoload** website [88] were adopted. In the Orthoload experimental program the three dimensional hip forces were measured in vivo with instrumented implants for four different patients. Telemetric data transmission was used for the four patients during the most frequent activities of daily living. All the data are available to researchers as a software program which is called HIP98. A new version of this software measurement data released in 2011 has been used in the current work.

6.2 Orthoload

The main window of the HIP98, version 2011, is shown in Figure 6.1. The data is presented as videos, force vectors, numerical data and video images of the patients. From the Orthoload database, it is possible to select an activity, one or several trials and a patient. Numerical data files of the contact forces can be downloaded and then used, for example in joint simulators or finite element analyses. Measured forces of the hip joint in this program are shown as a percentage of body weight, %BW. Consequently, it is possible for researchers to recalculate the forces by using the patients' body weight.

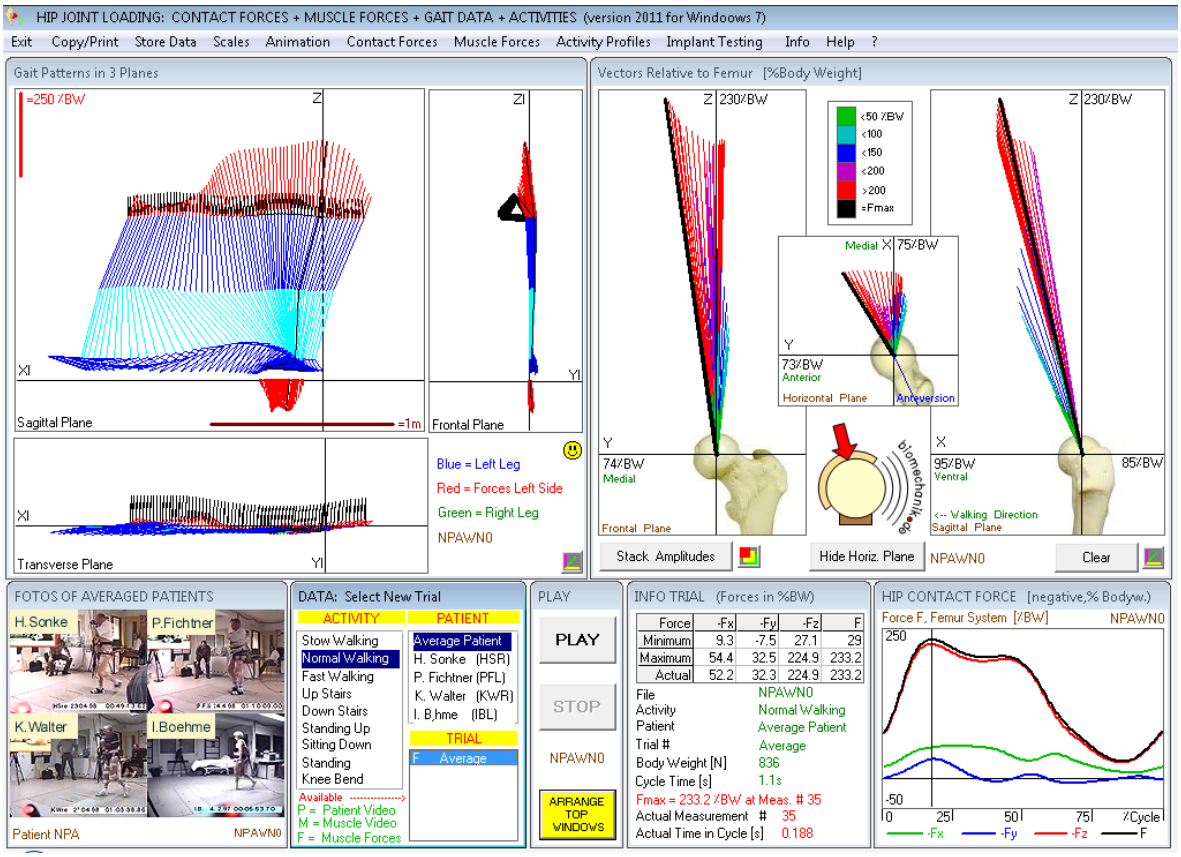

Figure. 6.1 Components of the main window of HIP98

All forces reported in HIP98 are relative to the left femur coordinate system, where the centre of the femoral head is chosen to be the centre of the femur system. A particular method of averaging was used to calculate average gait data and hip contact forces from a number of trials for the same patient. Averages from the four patients were averaged again to obtain data for a "typical" patient. The implant hip was made of an alumina ceramic head, a titanium stem and a polyethylene cup. Three of the four patients received non-cemented hip implants while the fourth patient had a cemented prosthesis. The patients were 51-76 years old. Measurements were taken between 11 and 31 months after hip replacement.

The resultant force of the hip joint, F, has three components F_x, F_y, F_z as shown in Figure 6.2. The angles of the resultant force in the three planes are referred as A_x, A_y, A_z. In order to investigate strength or fatigue of the implant, it is important to transfer the force components from the femur coordinate system to the implant system. Two angles are required for the transformation of forces, the anteversion angle AV of the implant and the angle S between the shaft axis of the implant and the z axis of the bone. There are individual values of the angles S and AV for each one of the four patients.

The resultant contact force, F, produces a three directional moment M about the intersection point of the neck and the shaft axes of the implant. This implant moment is composed of three components M_{xi}, M_{yi} and M_{zi}, where these components act about the implant system axes X_i, Y_i and Z_i in the RH screw sense as shown in Figure 6.2. The torsional moment M_{zi} is the important component for the implant fixation as it trends to rotate the implant about the shaft axis.

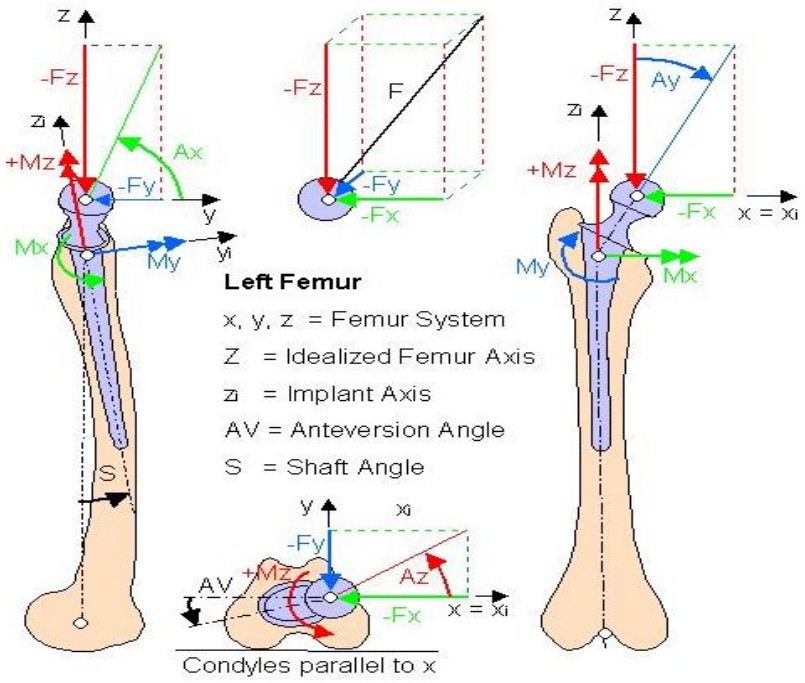

Figure 6.2 femur and implant coordinate system, [88]

In the Orthoload data, nine different activities were tested that were assumed to take place frequently in daily living. Each patient carried out most exercises between 4 and 6 times during the trials. A small number of trials could not be evaluated due to data errors. For stair climbing and walking, the instants of foot contact (heel strike) were selected to be the start of the activity cycles.

6.3 Hip Contact Forces

In this work the average case study of the four patients, the typical patient, was adopted. The resultant contact force, F, and its three components, F_x, F_y, F_z relative to the femur coordinate system for normal walking, which is the most frequent activity, are charted in Figure 6.3.

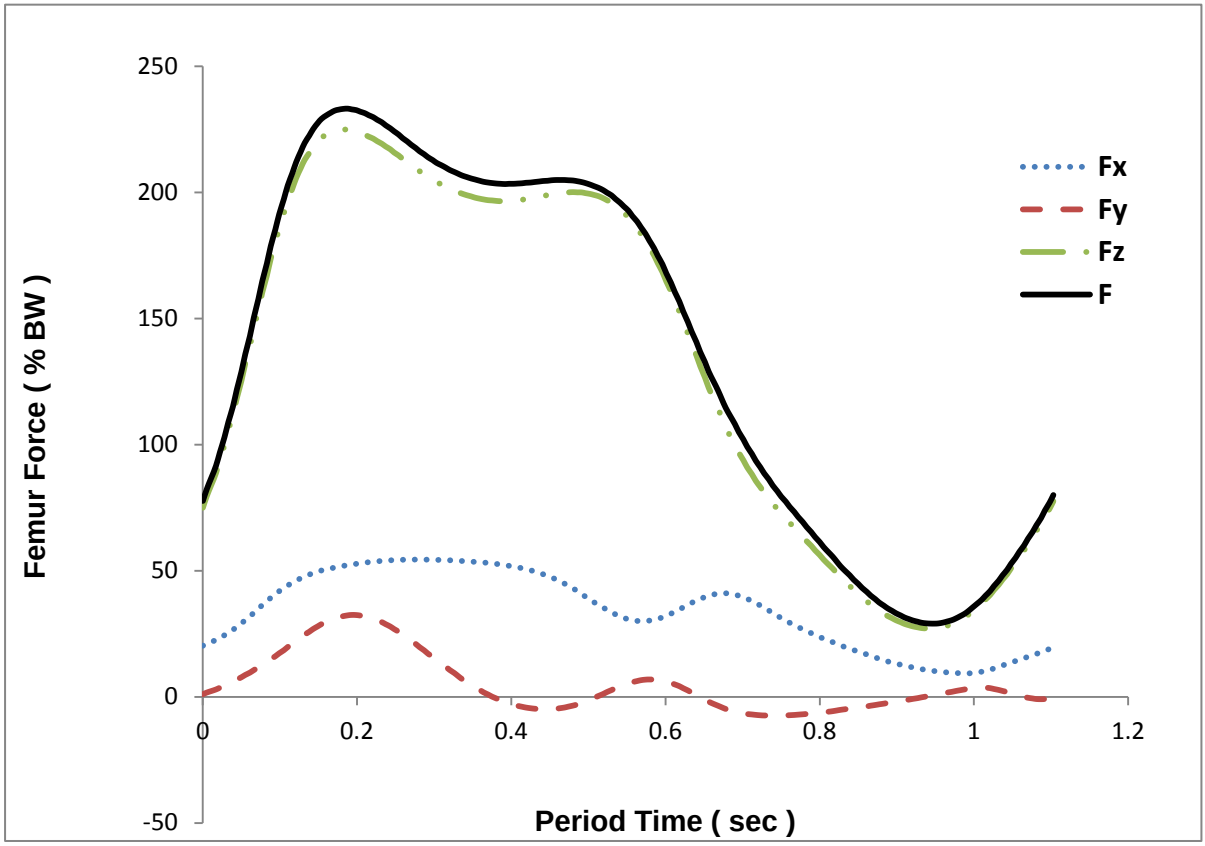

Figure 6.3 the measured contact force for one cycle of normal walking referred to the femur axis system

The cycle time of 1.103 s was divided into 200 time steps for numerical simulation. The data available in the HIP98 package are the three force components, F_x, F_y, F_z and the resultant force, F, relative to the following coordinate systems:

- The Femur coordinate system as previously shown in Figure 6.2.
- The Pelvis coordinate system illustrated in Figure 6.4.
- The Cup coordinate system illustrated in Figure 6.5.

Moreover, the ground reaction forces, implant moments, flexion and abduction angles are also included in the data.

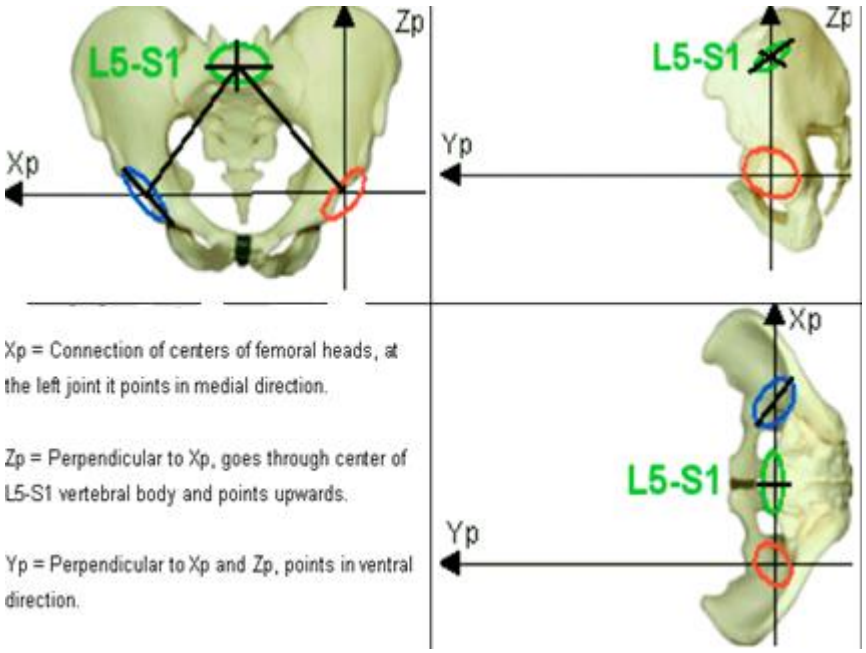

Figure 6.4 Pelvis coordinate system, [88]

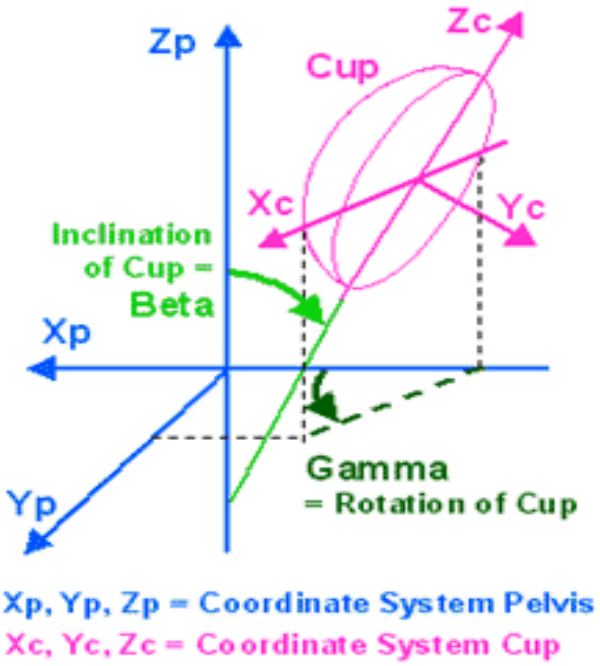

Figure 6.5 Cup coordinate system, [88]

The resultant contact force and its three components relative to the cup and pelvis coordinate systems are shown in Figures 6.6 and 6.7. It is clear from these Figures that the resultant force, *F*, has the same values relative to the three different coordinate systems, femur, pelvis and cup, whereas the three components in the x, y, z directions vary depending on the various coordinate systems. In addition, the force component in the z-direction (F_z) has the biggest value and it is nearly equal to the resultant force especially for the femur and pelvis coordinate systems.

Meng et al [89] and Liu et al [90] employed only the vertical load component and the major velocity component in the flexion – extension direction in their studies. Gao et al [62] showed that under walking conditions, the horizontal load components had a significant impact on the lubrication film due to the squeeze film effect. During the whole walking cycle both the average and central film thickness were found to increase to a range of 40-65 nm, compared with the range of 25-55 nm under a single, vertical, load and one motion condition, flexion – extension, which suggested the lubrication in the MOM hip implant was improved under 3D physiological loading and motion. In the current work the physiological loading and motion gait cycle in all three directions have been taken into account.

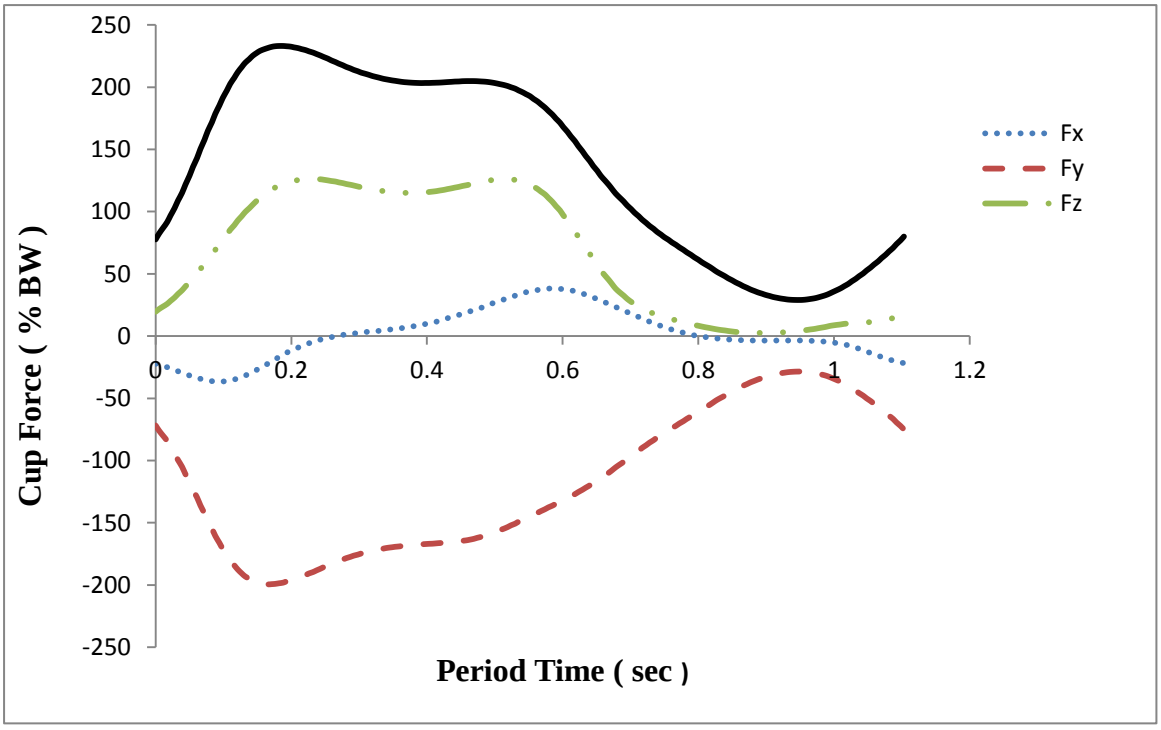

Figure 6.6 the measured contact force for one cycle of normal walking referred to the Cup coordinate system

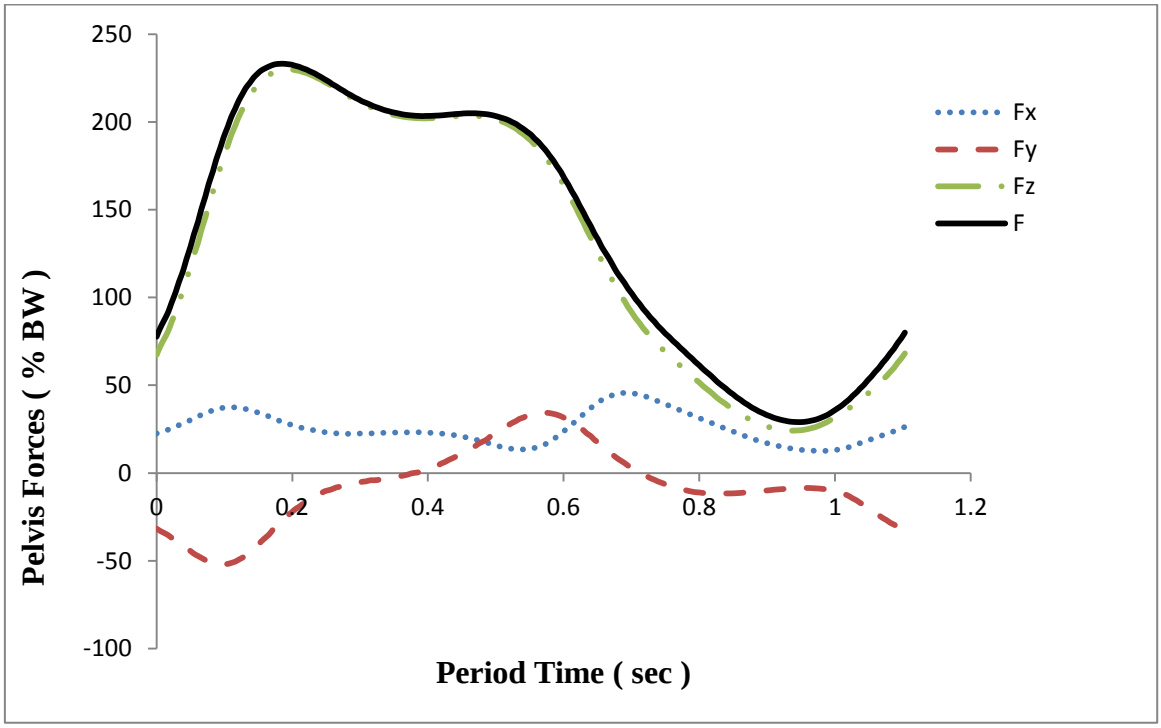

Figure 6.7 the measured contact force for one cycle of normal walking referred to the Pelvis coordinate system

6.4 Coordinates of the Contact Points

The coordinates (x, y, z) of the contact points relative to the femur or the cup system were not available from the data in HIP98. In addition, there was no information about the relative velocity between the contacting surfaces, the femur surface and the cup surface, which are essential for the EHL analysis. The only data available for normal walking was the average speed of the four patients which was 1.09 m/s.

Evaluation of the coordinates of the contact point position at each time step of the walking cycle have been carried out. As mentioned previously, the table of force components F_x, F_y and F_z for each time step relative to the cup coordinate system is available from the data of the HIP98 system. Consequently, the coordinates K_x, K_y, K_z of the general contact point K was calculated by using vector algebra. It was assumed that the contact points are located at the position that the resultant force vector from the ball centre intersects the ball and the cup surfaces, i.e at the vectorial position .

$$\overrightarrow{\boldsymbol{K}} = \frac{\vec{F}}{|F|} R \qquad \text{.....(6.1)}$$

The results from Equation (6.1) for the cup surface are shown in Figure 6.8. It can be seen from this Figure that all the contact points, the 200 steps, are located in the upper half of the cup. The distance between the farthest contact point and the centre of the cup is approximately 16 mm in this projection. However, the radius of the cup was 25 mm which means that there is no contact between the femoral head and the acetabular cup at or around the rim of the cup. Figure 6.9 shows this trace superimposed on a plan view of the cup viewed in the negative Y_c direction.

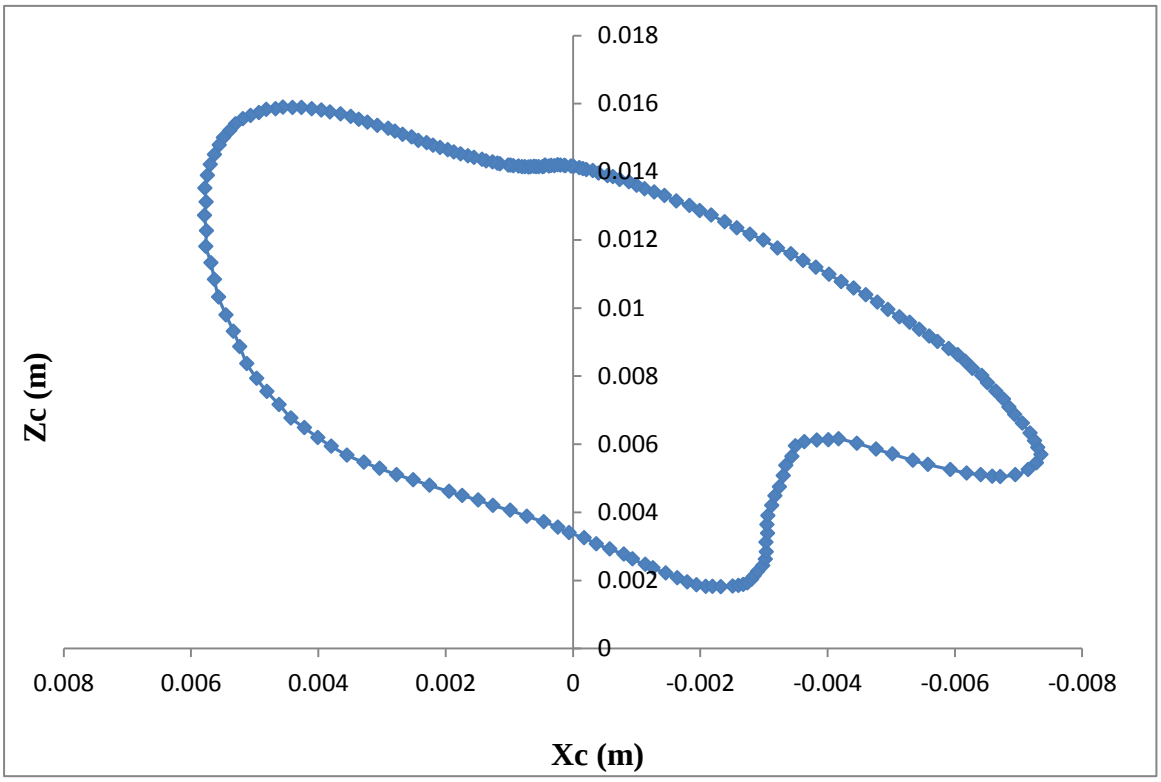

Figure 6.8 the contact point's positions relative to the cup coordinate system projected onto the X_c Z_c plane

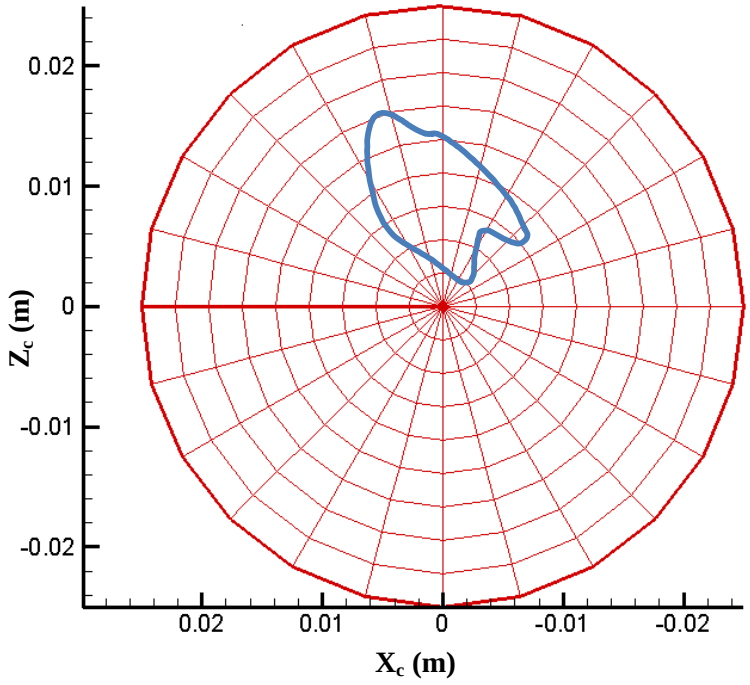

Figure 6.9 Contact points trace relative to the cup size

The same procedure as was used to specify the coordinates of the contact points relative to the cup system was repeated to calculate the coordinates of the contact points relative to the femur system as shown in Figure 6.10. The HIP98 software does not provide information concerning the contact point postion but does indicate it by means of a video showing its motion over the walking cycle. These videos can be viewed in the femur coordinate system or in that of the cup. The contact points illustrated by the videos can be seen to agree closely with the current evaluations shown in Figures 6.9 and 6.10.

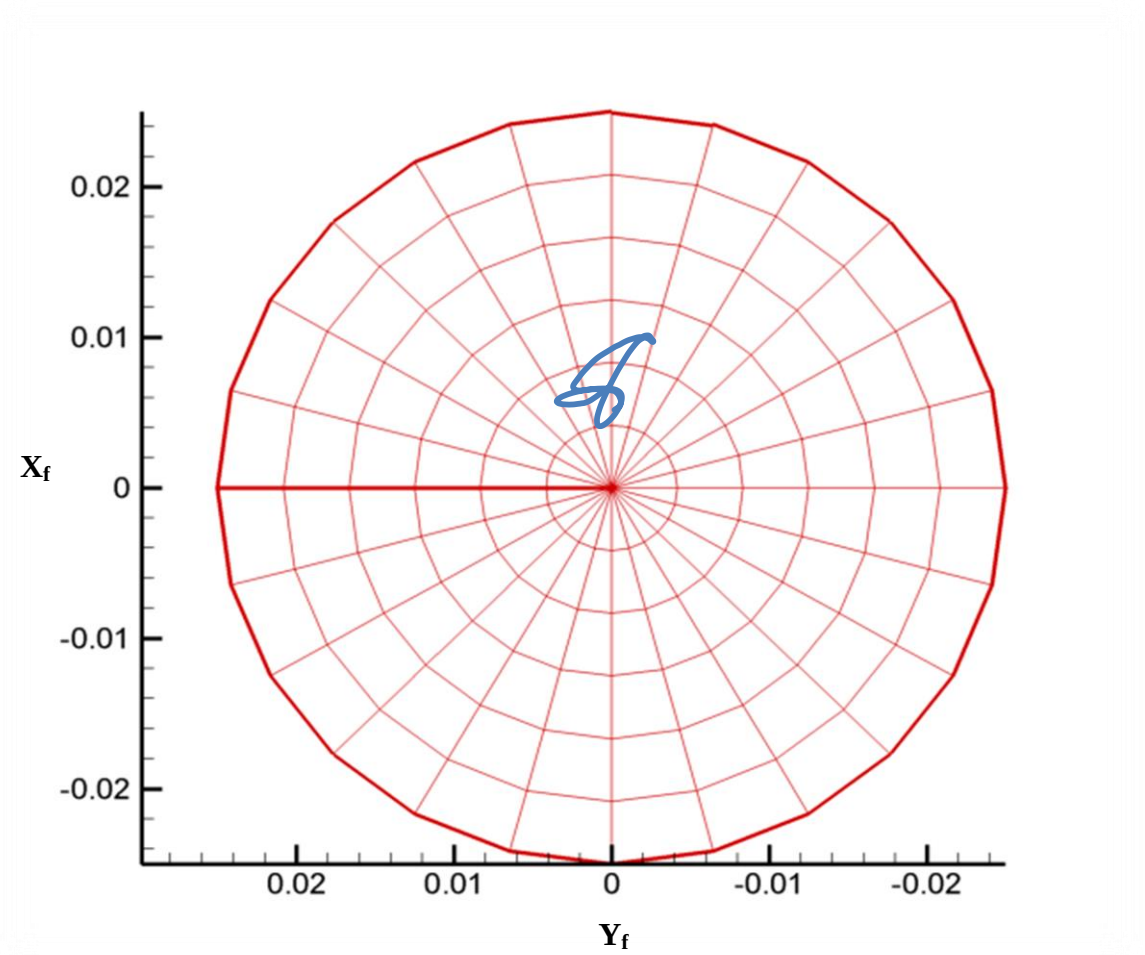

Figure 6.10 Contact points trace relative to the femur coordinate system

Two angles, α_1 and α_2, were used to specify the position of the general contact point *K* on the cup surface. Plane AA contains point *K* and the Y_c-axis and α_1 is the angle that the plane makes with the X_c-axis as shown in Figure 6.11.

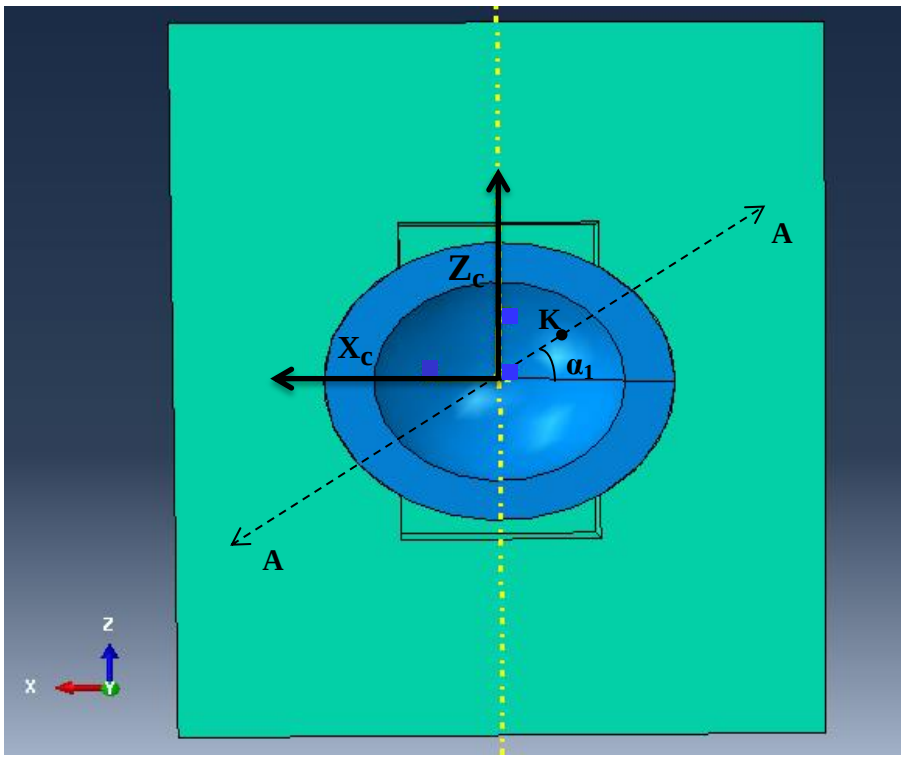

Figure 6.11 General contact point *K* on plan of cup viewed in negative Y_c direction

Figure 6.12 shows the cup sectioned on the plane AA and indicates the meaning of angle α_2 which is the angle between OK and the negative Y_c-axis.

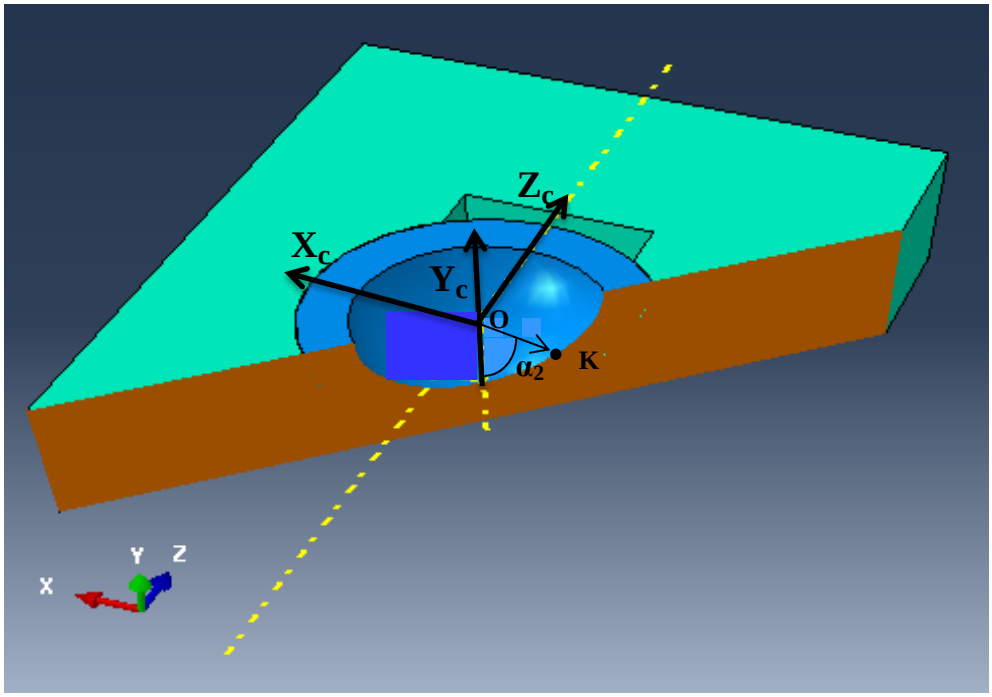

Figure 6.12 Section of cup on AA plane showing general contact point, *K*, and angle α_2

By calculating the contact point position as a vector for all the contact points within the walking cycle trace relative to the cup system, it was possible to calculate α_1 and α_2 as follows:

From Figures 6.11and 6.12;

$$K_y = -R\cos\alpha_2 \qquad \text{.....(6.2)}$$

$$K_x = -R\sin\alpha_2\cos\alpha_1 \qquad \text{.....(6.3)}$$

$$K_z = R\sin\alpha_2\sin\alpha_1 \qquad \text{.....(6.4)}$$

Dividing Equations (6.4) and (6.3) gives;

$$\alpha_1 = \tan^{-1}\frac{-Kz}{Kx} \qquad \text{..... (6.5)}$$

and re-writing equation (6.2) gives;

$$\alpha_2 = \cos^{-1}\frac{-Ky}{R} \qquad \text{.....(6.6)}$$

Using equations (6.5) and (6.6) the values of α_1 and α_2 for the 200 steps of the walking cycle were obtained, as shown in Figure 6.13. These two angles are necessary to specify the contact point for the finite element contact analysis. Simulating the contact between the femur and the cup using the Abaqus software for particular contact points within the walking trace was carried out by rotating the ball in directions of α_1 and α_2. The measured contact load was applied through the polar centre line of the ball component finite element mesh.

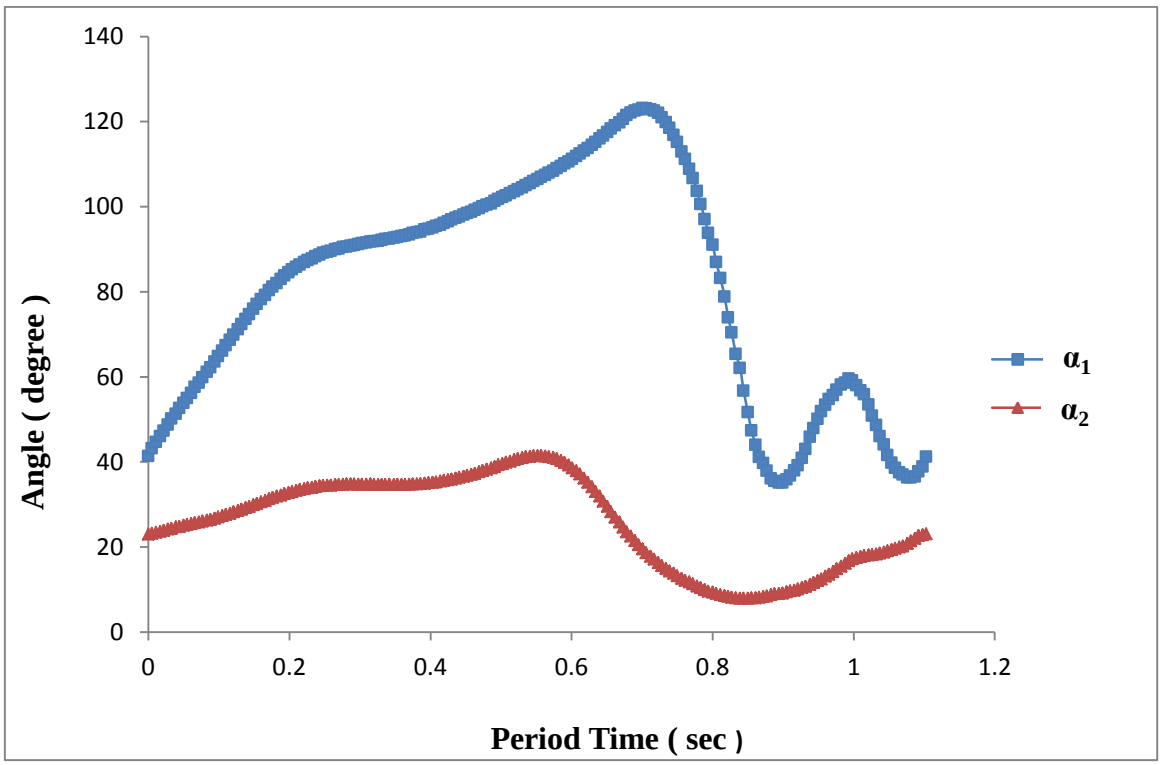

Figure 6.13 Variation of the angles α_1 and α_2 within the walking cycle

6.5 Transformation between coordinate systems

It was important to transform vector variables such as force, velocity and position from one coordinate system to another for calculation purposes. Furthermore, transformation can also be useful for comparison or verifying accuracy of the results. One of the main parameters which needed to be transformed from the femur coordinate system to the cup coordinate system was the velocity. The entrainment velocity, which is essential in the EHL analysis, equals to the average velocity value of the two contacting surfaces relative to the contact point. Both of these velocities must be obtained in the same coordinate system either the femur coordinate system or cup coordinate system.

The transformation matrices from the femur coordinate system, C_{E1}, and the pelvis coordinate system, C_{E2}, to the laboratory coordinate system are available from the data of the HIP98 for all the points in the walking cycle. These transformation matrices are different in each of the time steps because the position and orientation of the femur and pelvis system are continually changing as the patient moves. In contrast, there is no transformation matrix from the cup coordinate system to the laboratory system. The only information available about the cup coordinate system that it is fixed relative to the pelvis system and the transformation between them can be obtained by using the two available angles, γ (Gamma) and β (Beta), as shown in Figure 6.5. These angles are fixed for each patient and given in the database.

As a result, the transformation of the femur surface velocity from the femur coordinate system to the cup coordinate system was achieved as follows:

- Transformation from the femur coordinate system to the laboratory system, as shown in Figure 6.14, using a transformation matrix C_{E1}.

- Transformation from the laboratory system to the pelvis coordinate system using the transpose of the transformation matrix C_{E2}, C_{E2}^{T}.
- Rotating the pelvis coordinate system about the pelvic z and x axes to obtain the cup coordinate system using the trigonometric functions and the two available angles, γ (Gamma) and β (Beta). For the average patient γ and β are 70.3^{o} and 49.4^{o} respectively.

These steps can be written as;

$$\vec{U}_{fp} = C_{E2}^{T} * C_{E1} * \vec{U}_{f} \quad \ldots\ldots (6.7)$$

In equation (6.7) U_f is the surface velocity of the femur, which was established depending on the change of the contact point position with time as shown later, U_{fp} is the femur surface velocity relative to the pelvis coordinate system, and C_{E1} and C_{E2} are the transformation matrices. The nine elements of each matrix are available from HIP98 at each point of the walking cycle. The matrices have the general form:

$$C_E = \begin{pmatrix} C_{xx} & C_{yx} & C_{zx} \\ C_{xy} & C_{yy} & C_{zy} \\ C_{xz} & C_{yz} & C_{zz} \end{pmatrix} \quad \ldots\ldots (6.8)$$

To transform $\vec{U}_{fp}$ to the cup coordinate axes the rotation illustrated in figure 6.5 needs to be taken into account. Figure 6.5 is taken from the database information and needs to be interpreted in terms of the description of β and γ. To obtain the cup axis set firstly a rotation β takes place about the X_p axis and a further rotation through an angle γ then takes place about the Z_p axis. If the

unit vectors in the pelvic axis system are $\underline{I}$, $\underline{J}$ and $\underline{K}$, and in cup axis system $\underline{i}$, $\underline{j}$ and $\underline{k}$, the equations that give the transformation are

$$\left.\begin{aligned} \underline{i} &= \cos\gamma\,\underline{I} + \sin\gamma\,\underline{J} \\ \underline{j} &= -\cos\beta\sin\gamma\,\underline{I} + \cos\beta\cos\gamma\,\underline{J} - \sin\beta\,\underline{K} \\ \underline{k} &= -\sin\beta\sin\gamma\,\underline{I} + \sin\beta\cos\gamma\,\underline{J} + \cos\beta\,\underline{K} \end{aligned}\right\} \quad \text{.....(6.9)}$$

Equations (6.7) and (6.9) can be used to transform a vector of load, velocity, contact point position or any other vector between the femur and pelvis coordinate systems. Tests were conducted on the contact force vector given in the database whereby the femur force was transformed to the cup coordinate system in this way. This confirmed that the componenets were then as stated in the database. This gave confidence that the transformation process was correctly implemented.

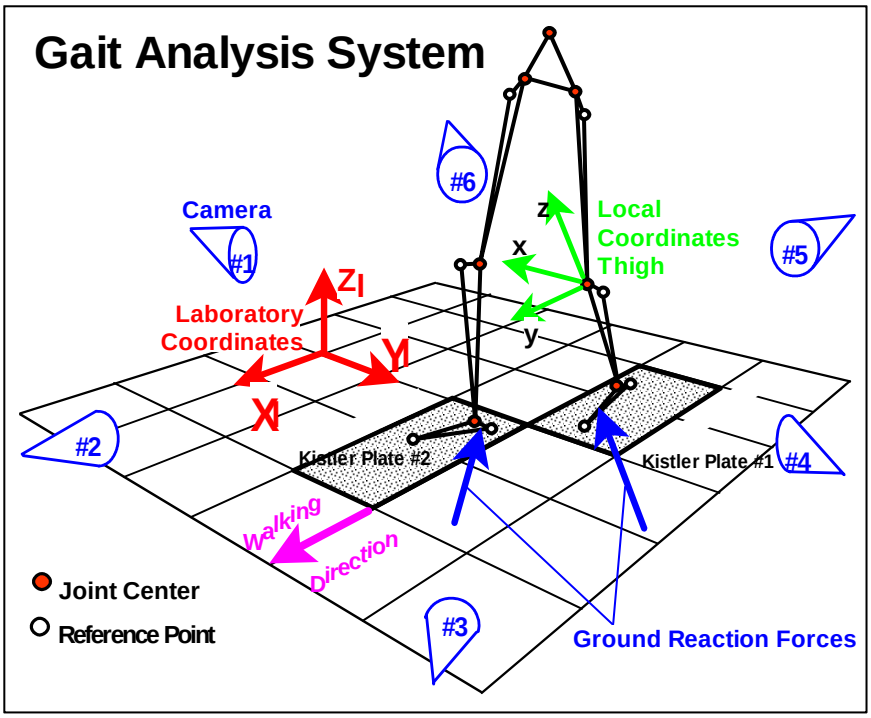

Figure 6.14 Laboratory coordinate system, [88]

The surface velocity of the femur relative to the contact point, U_{fi}, is the velocity of the contact point in the femur system with opposite sign.

U_{fi} = - velocity of contact point in the femur system.

The velocity of the contact point was established by utilisation of the coordinate values K_f (K_x, K_y, K_z) of the contact point at different times using backward differences, therefore

$$\vec{\mathbf{U}}_{\mathbf{fi}} = -\frac{\vec{\mathbf{K}}_{\mathbf{f(i+1)}} - \vec{\mathbf{K}}_{\mathbf{f(i-1)}}}{\mathbf{t_{i+1} - t_{i-1}}} \quad \text{.....(6.10)}$$

The only component of the surface velocity, $\vec{\mathbf{U}}_{\mathbf{fi}}$, that contributes to the entrainment velocity for the EHL analysis is tangential to the surface, and it can be determined by:

$$\vec{\mathbf{U}}_{\mathbf{fTi}} = \vec{\mathbf{U}}_{\mathbf{fi}} - \left(\frac{\vec{\mathbf{U}}_{\mathbf{fi}} \cdot \vec{\mathbf{K}}_{\mathbf{fi}}}{\mathbf{R}}\right) \frac{\vec{\mathbf{K}}_{\mathbf{fi}}}{\mathbf{R}} \quad \text{.....(6.11)}$$

In equation (6.11) the vector $\vec{K}_{fi}$ has magnitude R, and is normal to the surface at the contact point. The term in the bracket is thus the magnitude of the velocity in the normal direction and it is multiplied by the unit vector in the normal direction. The subtraction therefore removes the normal velocity from $\vec{U}_{fi}$ to establish the tangential velocity.

The same procedure was used to calculate the tangential component of the surface velocity of the cup in the cup coordinate system relative to the contact point. Using the corresponding notation, the relative velocity is

$$\vec{\mathbf{U}}_{\mathbf{ci}} = -\frac{\vec{\mathbf{K}}_{\mathbf{c(i+1)}} - \vec{\mathbf{K}}_{\mathbf{c(i-1)}}}{\mathbf{t_{i+1} - t_{i-1}}} \quad \text{..... (6.12)}$$

and its normal component is removed in the same way to give the tangential velocity vector of the surface relative to the contact point.

$$\vec{\mathbf{U}}_{\mathbf{cTi}} = \vec{\mathbf{U}}_{\mathbf{ci}} - \left(\frac{\vec{\mathbf{U}}_{\mathbf{ci}} \cdot \vec{\mathbf{K}}_{\mathbf{ci}}}{\mathbf{R}}\right) \frac{\vec{\mathbf{K}}_{\mathbf{ci}}}{\mathbf{R}} \quad \text{……..(6.13)}$$

Then the mean surface velocity relative to the contact point for the two surfaces is the mean of $\vec{\mathbf{U}}_{\mathbf{cTi}}$ and $\vec{\mathbf{U}}_{\mathbf{fTci}}$. To evaluate this it is necessary for both terms to be evaluated in the same coordinate system. The appropriate system is the cup system as that is used for the contact analysis.

$\vec{\mathbf{U}}_{\mathbf{fTc}}$ is the tangential component of the femur surface velocity relative to the contact point expressed in terms of the cup coordinate system, which can be obtained from the transformation matrices via equations (6.7 and (6.9). The entrainment velocity is then

$$\vec{\mathbf{U}}_{\mathbf{i}} = \frac{\vec{\mathbf{U}}_{\mathbf{cTi}} + \vec{\mathbf{U}}_{\mathbf{fTci}}}{\mathbf{2}} \quad \text{……..(6.14)}$$

To check the accuracy of the procedure and the transformation from the femur to the cup systems it was confirmed that $\vec{U}_{fTc}$ was perpendicular to $\vec{K}_{fi}$ for each time step.

A Microsoft excel spreadsheet was developed and used to transform the tangent femur surface velocity to the cup coordinate system through the laboratory and pelvis coordinate systems as described previously. The entrainment velocity, U_i, and its three components are shown in Figure 6.15.

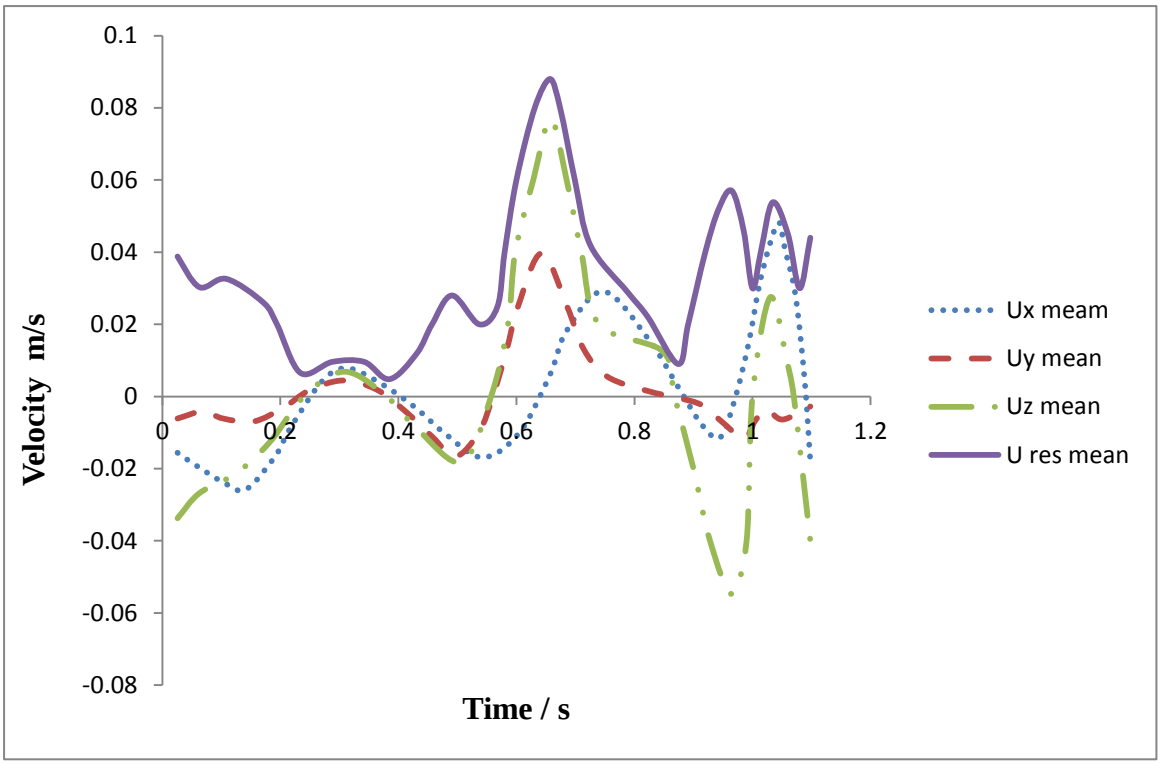

Figure 6.15 The entrainment velocity and its components over the walking cycle.

6.6 Steady State Analysis of the EHL

Nine points were selected from the trace of the gait cycle for futher investigation of EHL behaviour, as shown in Figure 6.16. The points were selected taking the location of the contact point relative to the centre of the cup into account so as to cover the range of positions in the cycle. In addition the variation of the contact force values were taken into account, as shown in Figure 6.17. The direction of the inlet and outlet of the lubricant flow was assumed in accordance with the EHL mesh direction.

These points in the walking cycle were used to develop steady state elastohydrodynamic lubrication analyses using the in vivo measured contact force, mean velocity and contact point position for the nine cases selected which are denoted by letters A to I.

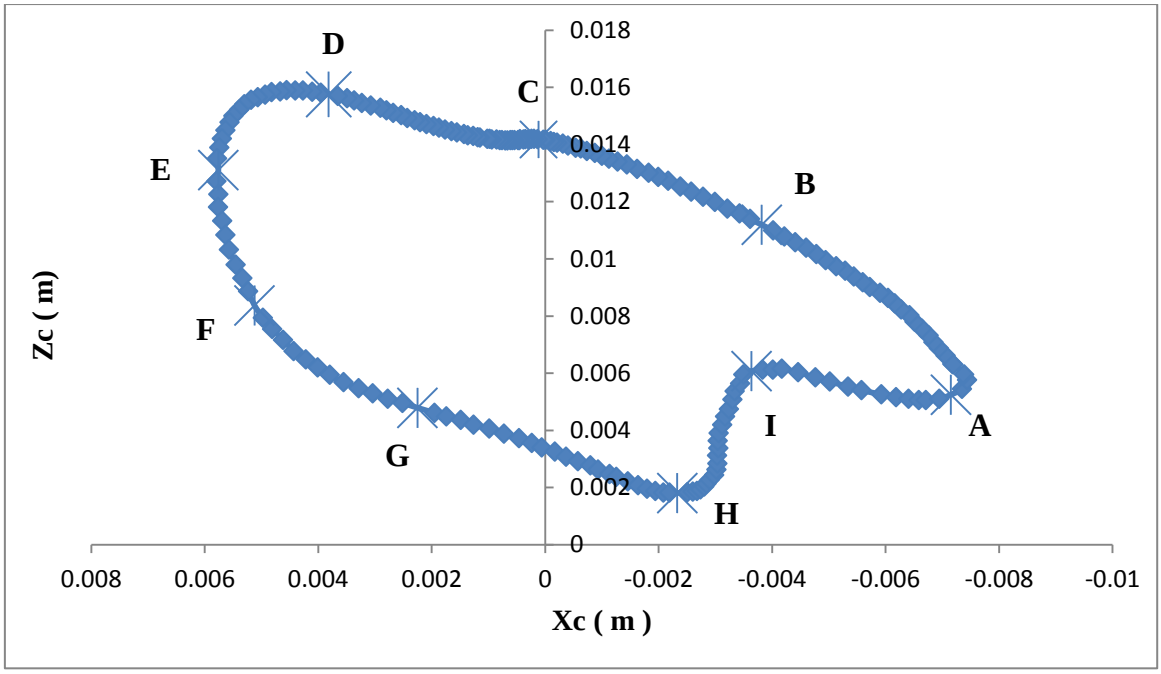

Figure 6.16 the nine selected contact points of the gait cycle

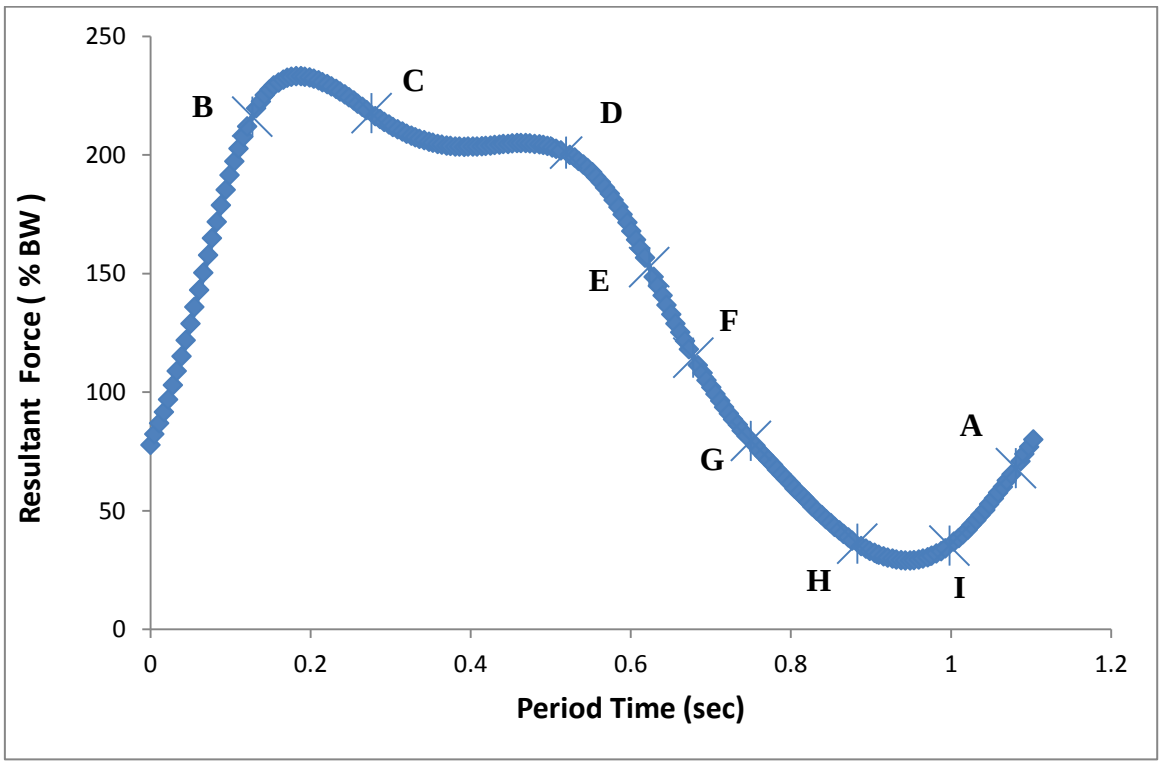

Figure 6.17 Different loads values for the selected nine points.

6.7 Discussion

This chapter has presented the method by which the variation of load and kinematic conditions at the contact has been established. This has not been by use of idealised walking cycles as often seen in the literature, but by use of a public database of experimental results obtained from patients whose hip prostheses have been instrumented to allow direct measurement of the contact load and its direction. The data made available in this way does not provide the necessary information for the EHL analysis directly and consequently calculation procedures have been developed to process the data in a robust and accurate way for all the time steps in the database. The database contains data for individual patients over a series of trials and also an averaged dataset and thus the process can give rise to several sets of experimentally accurate walking cycles for EHL analyses. For the results reported in the thesis the average database cycle information was used.

The load and kinematic conditions were all obtained from the contact load data. At each time step the contact load is given relative to both the femur coordinate system and the cup coordinate system. To proceed, it was necessary to transform the relevant information for the cup and femur components to a common axis set, and the cup axis set was chosen for this function. Transforming the vectorial information from the femur to the cup coordinate system was a complicated process that involved two intermediate coordinate systems. These were the laboratory coordinate system which was a fixed reference set, and the pelvis coordinate system. Both femur and pelvis coordinate systems moved continuously over the walking cycle and transformation matrices were provided in the dataset linking each to the laboratory coordinate system. There was no transformation matrix given in the database for the cup coordinate system which was offset from the pelvic system and rotated in a fixed general way so that none of the axes in the cup system was parallel to any of those in the pelvic system. Transferring

information from the femur to the cup systems involved two time step dependent matrix transformations to reach the pelvic system via the laboratory system, and a further fixed origin offset and compound rotation to reach the cup system.

The measured force vectors in the two systems were compared when both were expressed as components in the cup system and found to agree closely confirming that the measurements given were in agreement and that the implementation of the transformation process was accurate. This information allowed the coordinates of the contact point to be determined as the force vector from the cup system origin scaled to have magnitude equal to the ball radius gave the coordinates of the contact point. This information could then be used directly to form the FEA models of contact at any particular time step.

The kinematic information required is the entrainment velocity which is the mean surface velocity relative to the moving contact point. For each component (cup and femur) this was obtained in the component system as (minus) the difference in the contact point vectors at successive time steps divided by the time separation. These vectors were both brought to the cup system and their components normal to the contact removed to leave the tangent plane relative velocities. These were then averaged to obtain the entrainment vector for the time step. The checking operation on transferring the force vector between the systems gives assurance that no errors have been introduced in this process.

The entrainment velocities were found to vary in magnitude and direction relative to the axes to be used for the EHL analyses. This provides the necessary information to conduct a transient EHL analysis of the walking cycle including the entrainment reversals that take place. However, due to pressure of time it was not

possible to include this in the work reported and it remains an objective for further work. Within the time constraints of the research project it was decided to carry out steady state EHL analyses at a series of representative points over the meshing cycle, and these are reported in Chapter 7.

Results

7.1 Introduction

In this chapter a comparison between the results of the dry contact of the equivalent Hertzian theory and the results of the finite element analysis were carried out as a first stage. The results of the EHL of the Hertzian theory, the equivalent model, and the modified model were also investigated as a second stage, where the modified model equals to the equivalent model after adding the gap factor. A new system for calculating the contact point coordinates and relative velocity between the two contact surfaces was developed depending on the three dimensional forces using vector algebra. The 3D force information was obtained from **Orthoload** [88]. The procedure used to investigate the effect of the gap factor on the lubrication process was carried out for the nine contact points of the walking gait cycle as follows:

- Extracting the measured force and calculating the position of the contact point and the mean velocity relative to the contact point of the two contacting surfaces, the femur surface and the cup surface from the HIP98 program.
- Utilisation of the measured force and the position of the contact point in the Abaqus software to obtain the maximum contact pressure, radius of the contact area and gap value from the FE analysis.
- Using the maximum pressure and the contact area radius of the Abaqus software to modify the Hertzian maximum contact pressure and the radius of the contact area. As a result, an equivalent load and Modulus of Elasticity were produced.

- Determining the gap value of the Hertzian equivalent contact theory, and comparing it with the gap from the Abaqus software to obtain the gap factor values.
- Adding the gap factor value to the undeformed shape of the equivalent model.
- Running the EHL program to determine the differences between the Hertzian model pressure distribution and film thickness, the equivalent contact model pressure distribution and film thickness, the modified equivalent contact model pressure distribution and film thickness after adding the gap factor.
- Repeating the procedure for all the steps above with different cup thicknesses 4, 6, 8, and 10 mm.

7.2 FEA Pressure distribution

Figures 7.1 – 7.4 represent the pressure distribution of the dry contact between the ball surface and the cup surface. The finite element results of the Abaqus software version 6.12 were compared with the equivalent Hertzian theory results, (the black line). Different cup thicknesses of 4, 6, 8, 10 mm were investigated.

For the 4 mm cup thickness results presented in figure 7.1, it can be seen that the pressure distribution is non-Hertzian for contact points B, C, D, E and F. Consequently, the EHL analysis will be applied to only the Hertzian pressure distribution points that are A, G, H and I. The reason for some contact points to be Hertzian or otherwise is connected to the variation of the hip joint load. As it can be seen that points B, C and D have the largest deviation

from the Hertzian curves and it is known from Figure 6.17 that these three points have the maximum measured joint loads. On the other hand, the measured load for A, G, H, and I contact points are less than 30% of the maximum load value within the gait cycle which suggests that with the low load the contact pressure is Hertzian in form. Points E and F have intermediate load values and they show less deviation than points B, C and D, but they are still non-Hertzian.

Figures 7.2 to 7.4 show the corresponding results for cases where the cup thickness was 6, 8, and 10 mm, respectively. For these results the equivalent Hertzian model results is a good fit to the radial variation of pressure obtained from the FE analysis. The results for the 6 mm cup have a marginally greater deviation than these for 8 and 10 mm cups so it is clear that by increasing the cup thickness the contact pressure trend is to be closer and closer to a Hertz pressure distribution.

A significant variation in the hip joint load between the maximum value, 1819 N at point C, and the minimum value, 295 N at the point I, occurred in this research. The contact pressure variation for the 4 mm cup thickness was limited to the range 24.5 MPa (case I) to 29.3 MPa (case F), which represents a 19.5% variation. For the 6, 8, 10 mm cup thickness the variations are 56.7%, 72.4% and 78.5 % respectively over the contact sequence. Clearly, with the thin cup the results obtained have been less affected by varying the applied load, because the higher load values were not analysed due to their non-Hertzian behaviour.

Regardless of the cup thickness used for the lowest hip joint load, such as contact points H and I, a small variation was found in the pressure developed between the ball and the cup. For points H and I the maximum contact pressures are 25.19 MPa and 24.5 MPa respectively at 4 mm cup thickness, and 27.6 MPa and 27 MPa at 10 mm cup thickness. However, increasing the cup thickness from 4mm for points B, C and D where the contact pressures are 28.8 MPa, 28.9 MPa and 28.6 MPa respectively, to 10 mm leads to pressures of 48.2 MPa, 48 MPa and 46.8 MPa, respectively, despite the fact that the load for each point was the same. In general, increasing the cup thickness produces higher contact pressures and smaller contact areas as the cup becomes stiffer.

Table 7.1 shows the measured hip joint load, the calculated contact pressure from the FE analysis, the equivalent contact radius, the Hertzian contact radius, the entrainment velocity and the cup thickness to the Hertzian radius ratio for the nine contact points and four cup thicknesses. It was found from the ratio of the cup thickness to the Hertzian radius of contact, t/a_h, that when this ratio is unity or less the pressure distribution from the FE analysis is non Hertzian. This is apparent from the results for contact points B, C, D, E and F with the 4 mm cup thickness, as shown in figure 7.1 and Table 7.1.

Pressure distribution of 4 mm cup thickness

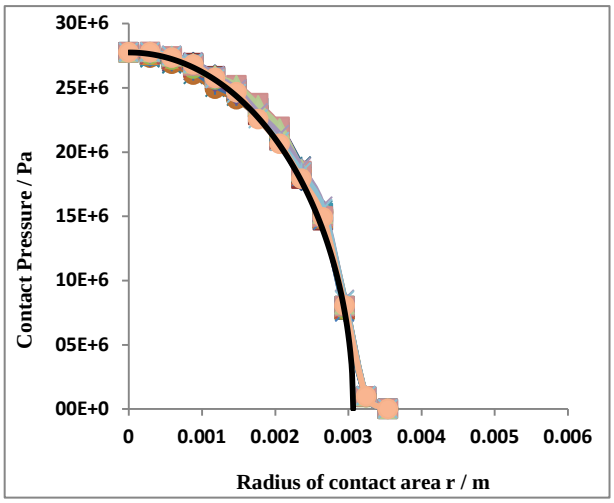

A

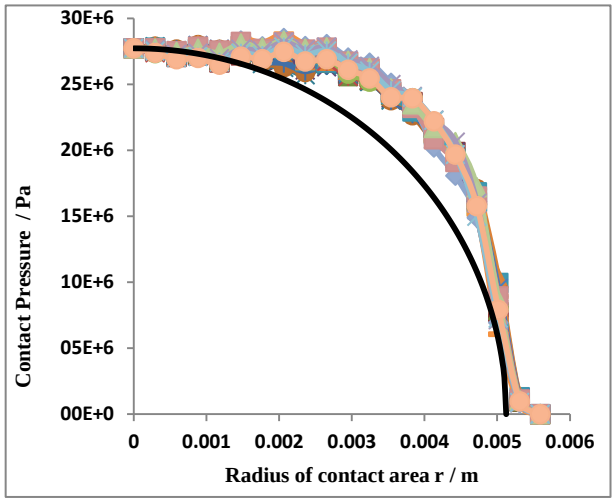

B

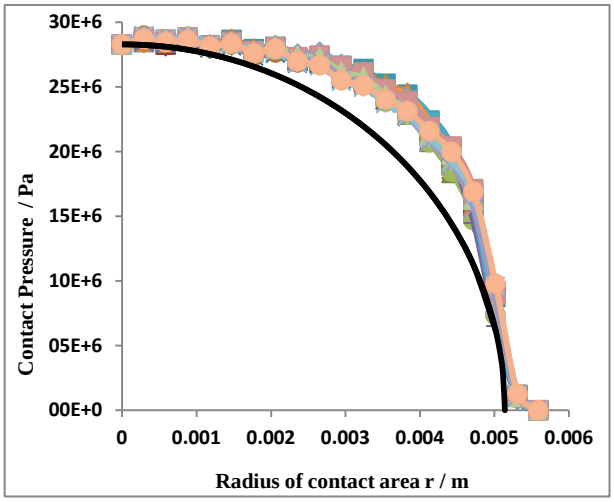

C

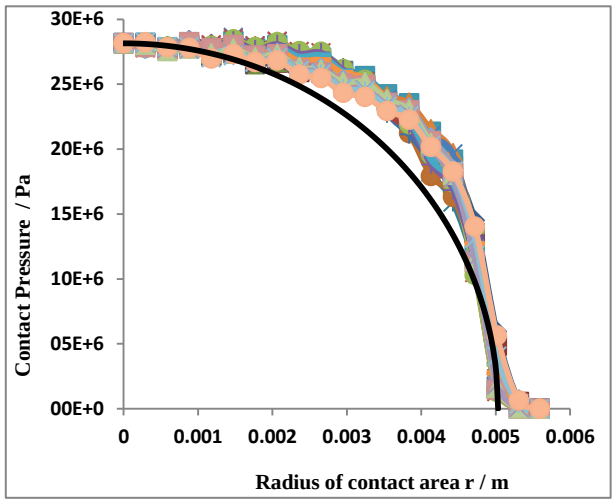

D

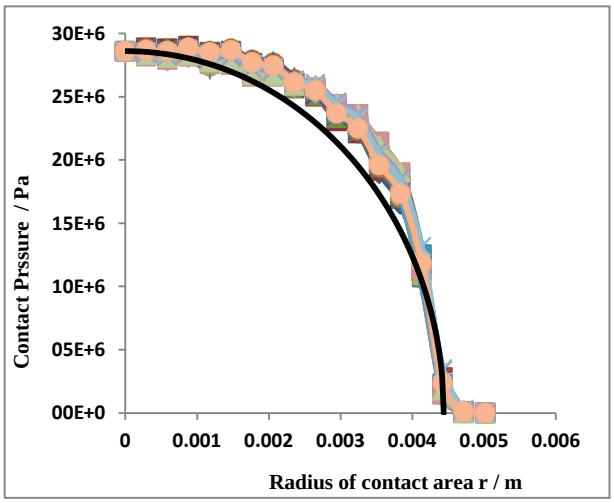

E

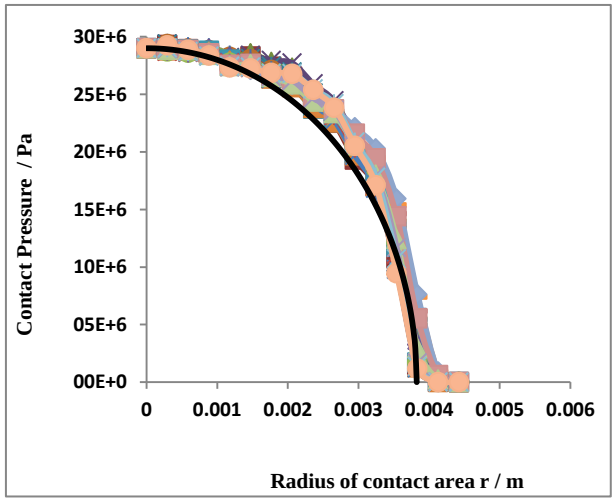

F

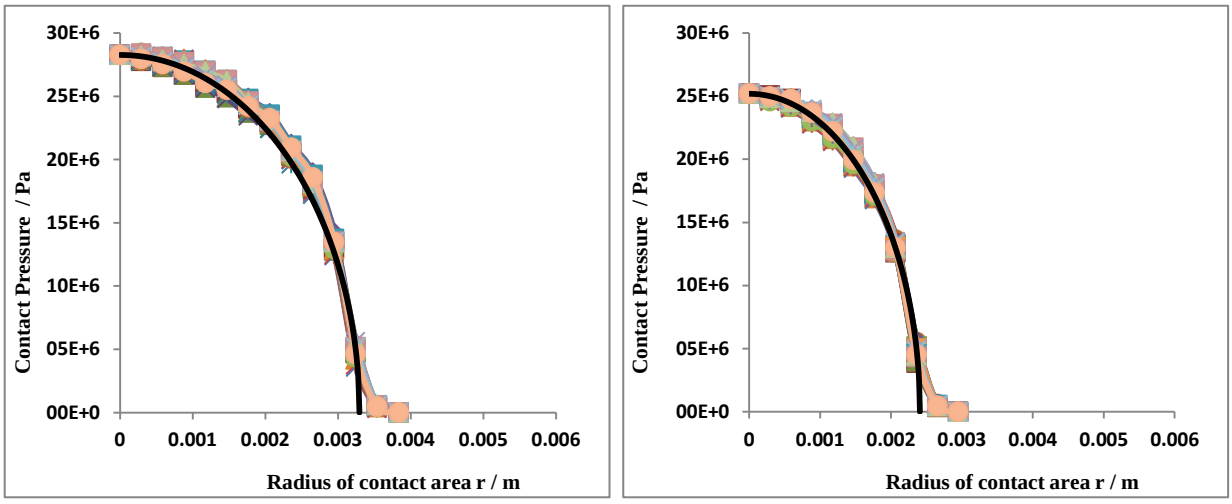

G H

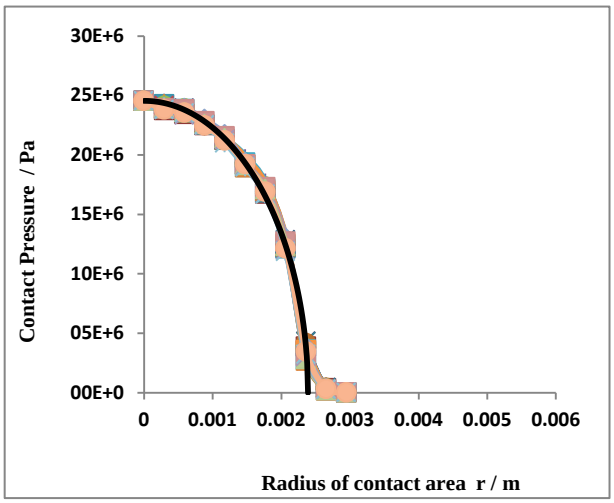

I

Figure 7.1 FEA dry contact pressure distribution of 4 mm cup thickness of the nine contact points A, B, C, D, E, F, G, H, and I compared with the theoretical equivalent Hertzian (black line).

Pressure distribution of 6 mm cup thickness

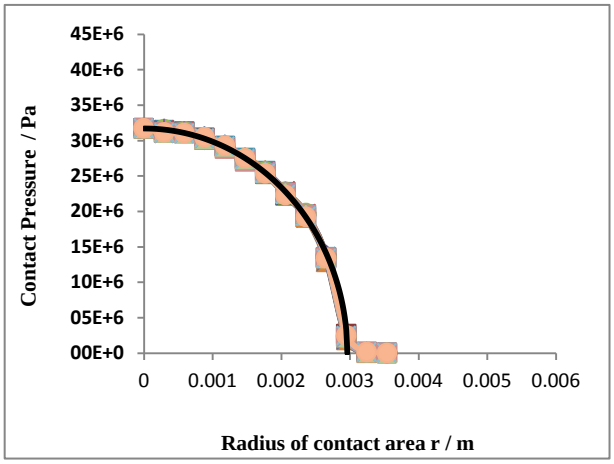

A

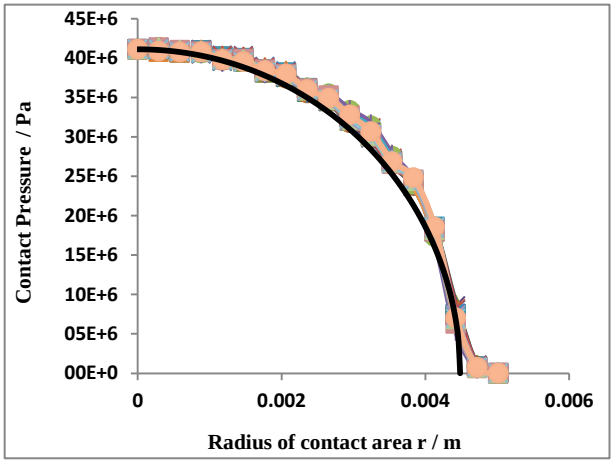

B

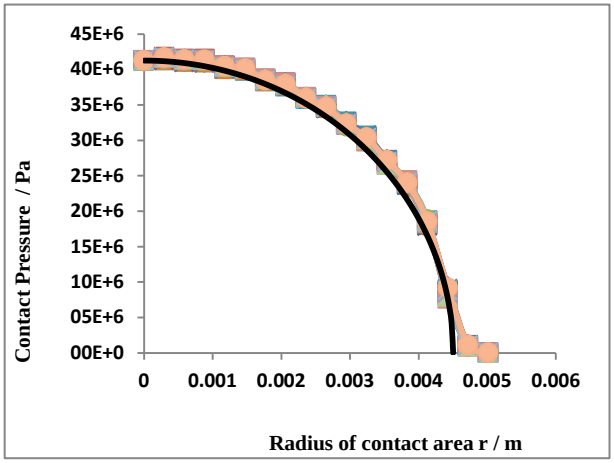

C

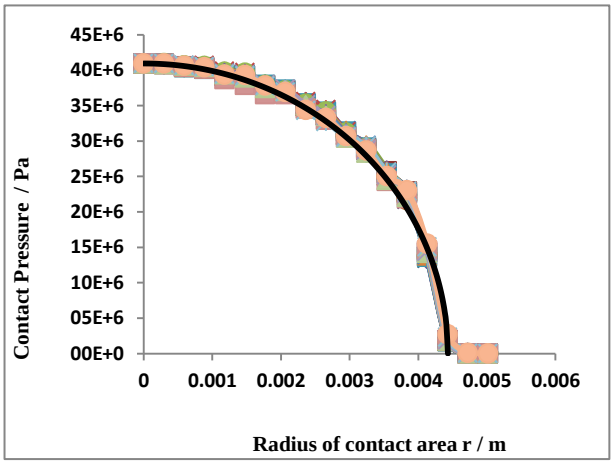

D

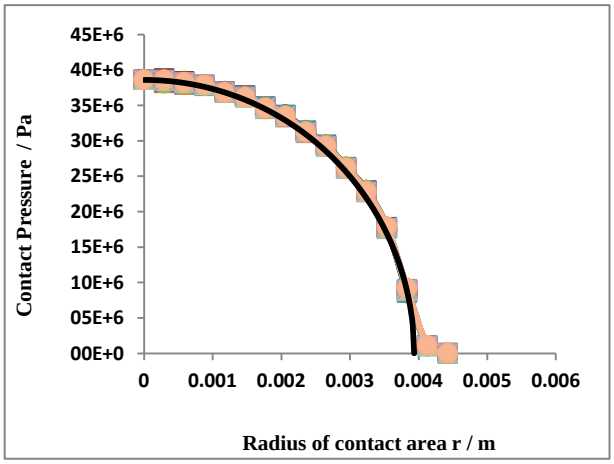

E

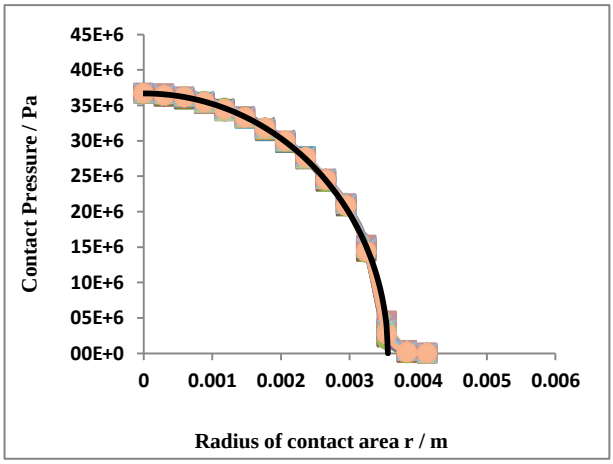

F

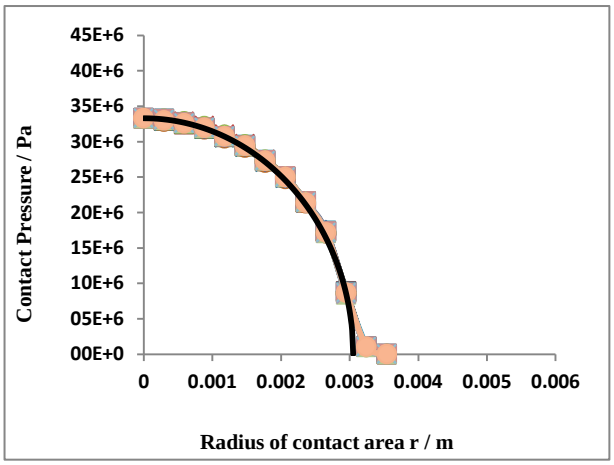

G

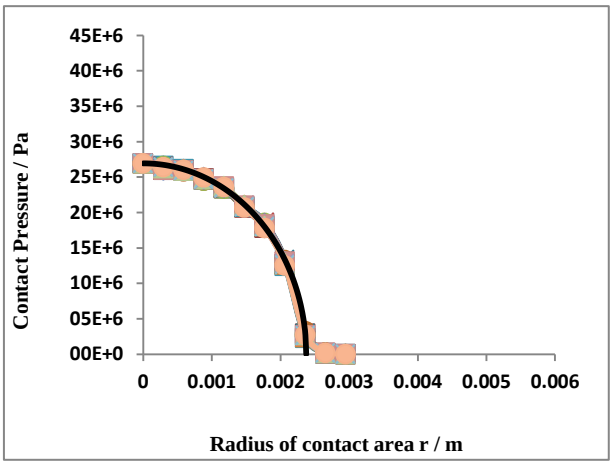

H

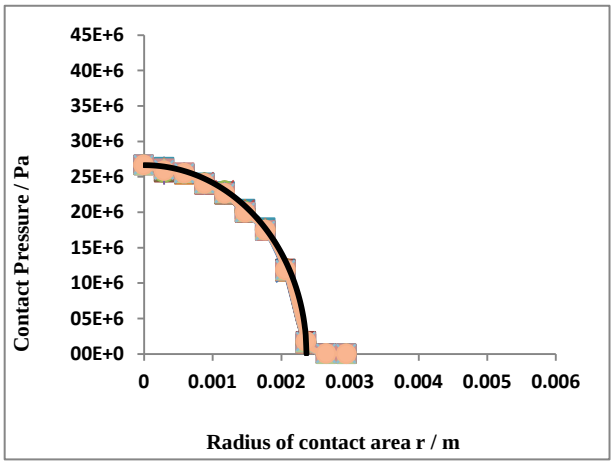

I

Figure 7.2 FEA dry contact pressure distribution of 6 mm cup thickness of the nine contact points A, B, C, D, E, F, G, H, and I compared with the theoretical equivalent Hertzian (black line).

Pressure distribution of 8 mm cup thickness

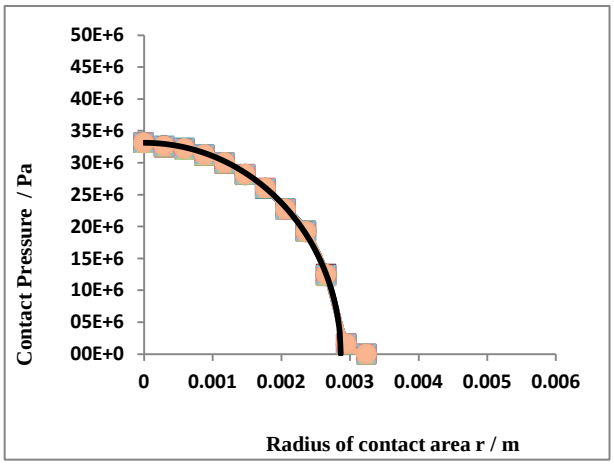

A

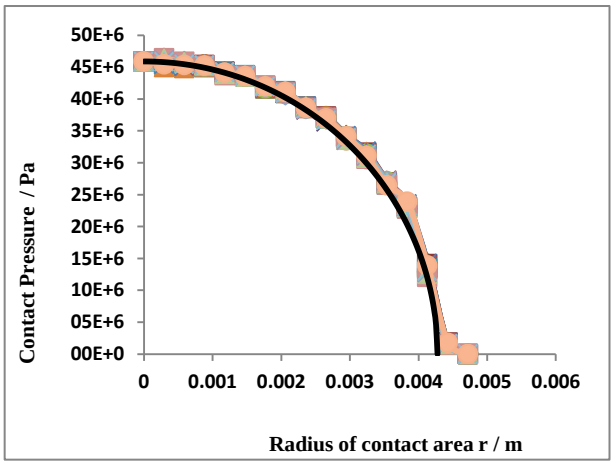

B

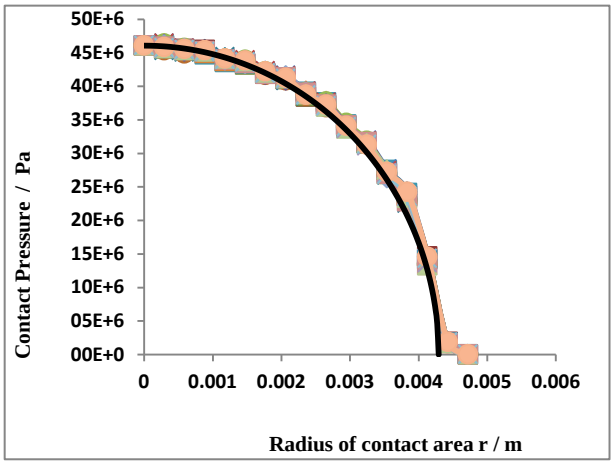

C

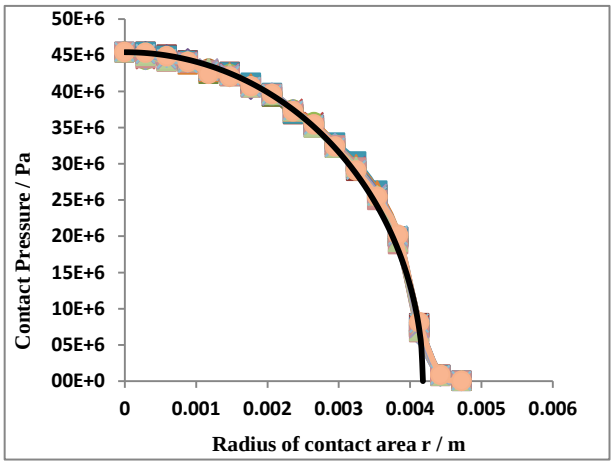

D

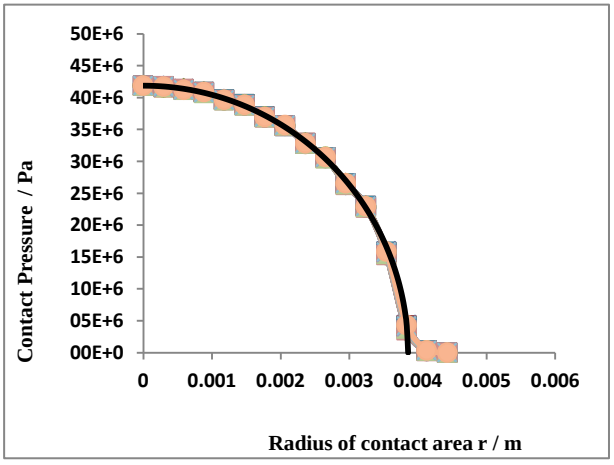

E

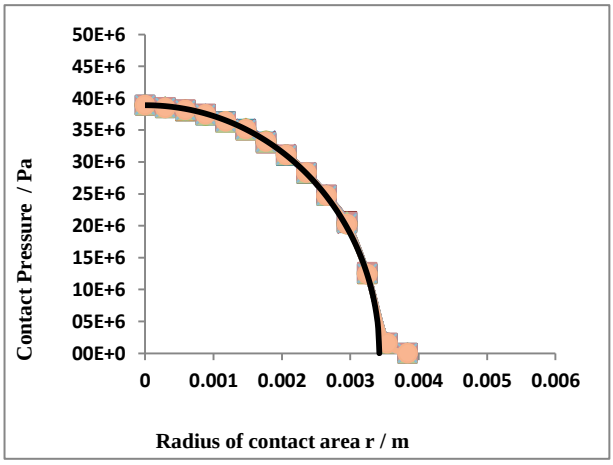

F

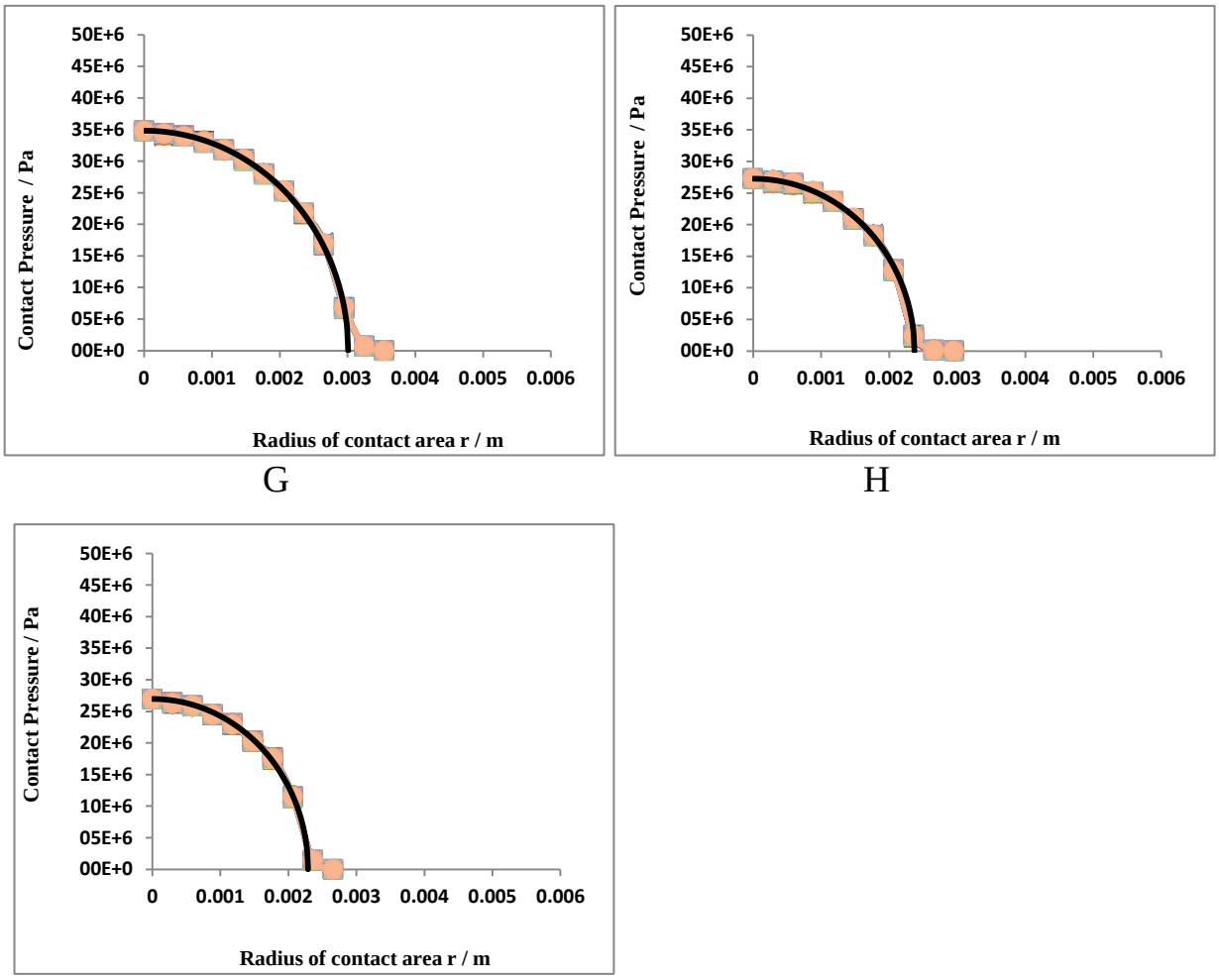

Figure 7.3 FEA dry contact pressure distribution of 8 mm cup thickness of the nine contact points A, B, C, D, E, F, G, H, and I compared with the theoretical equivalent Hertzian (black line).

Pressure distribution of 10 mm cup thickness

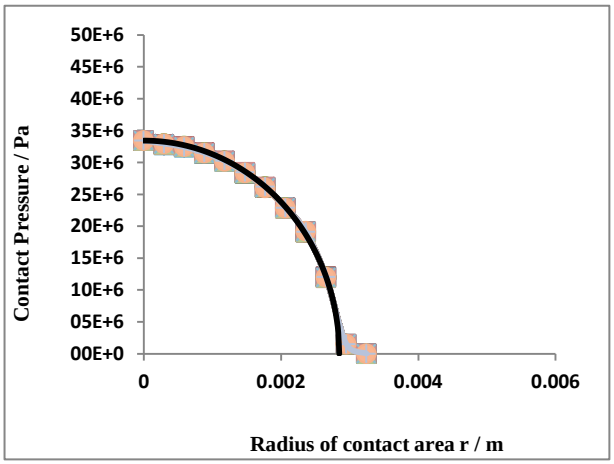

A

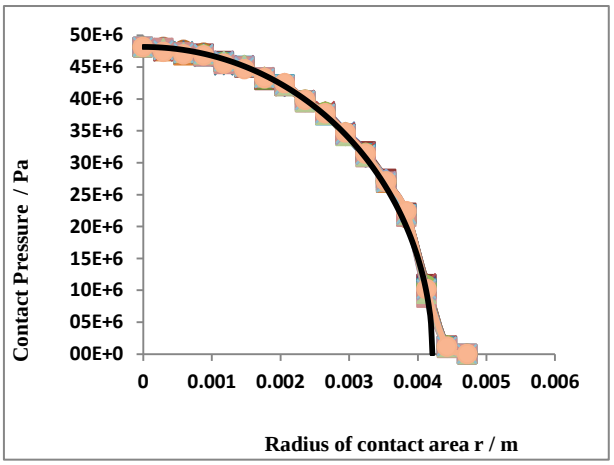

B

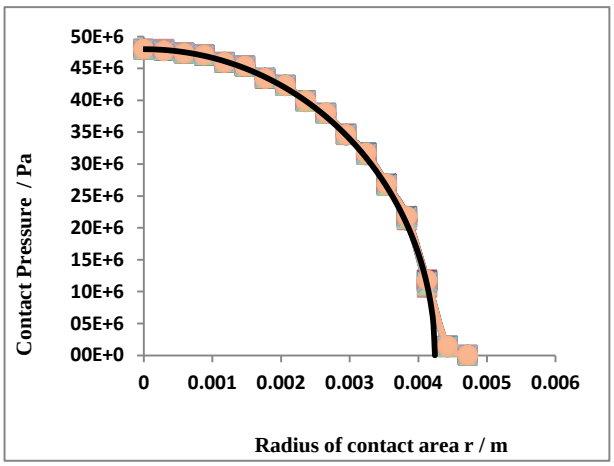

C

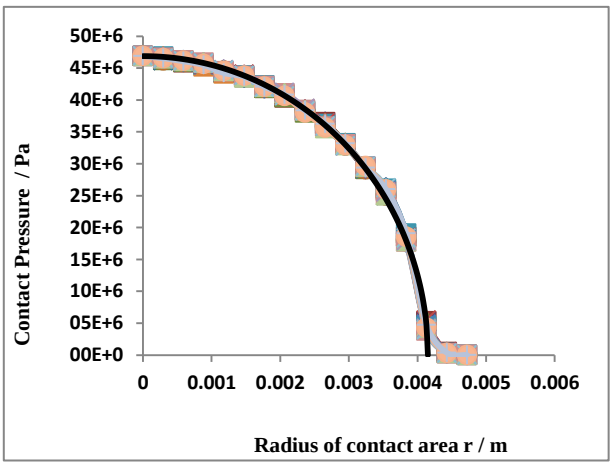

D

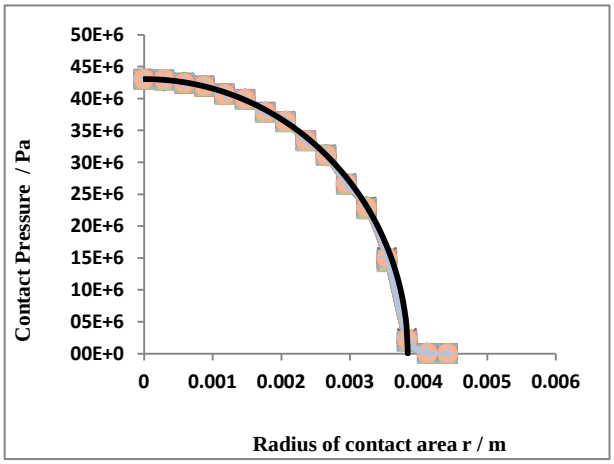

E

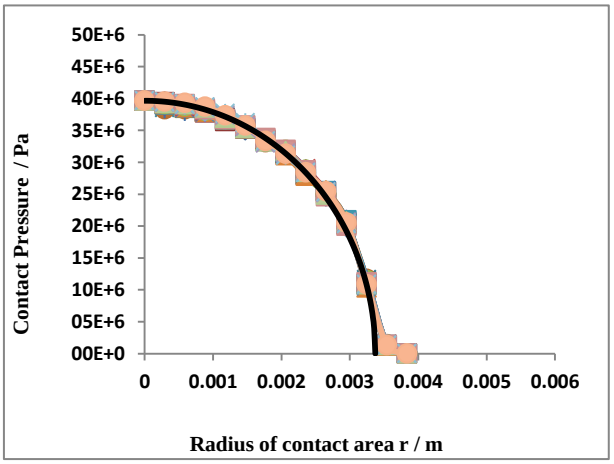

F

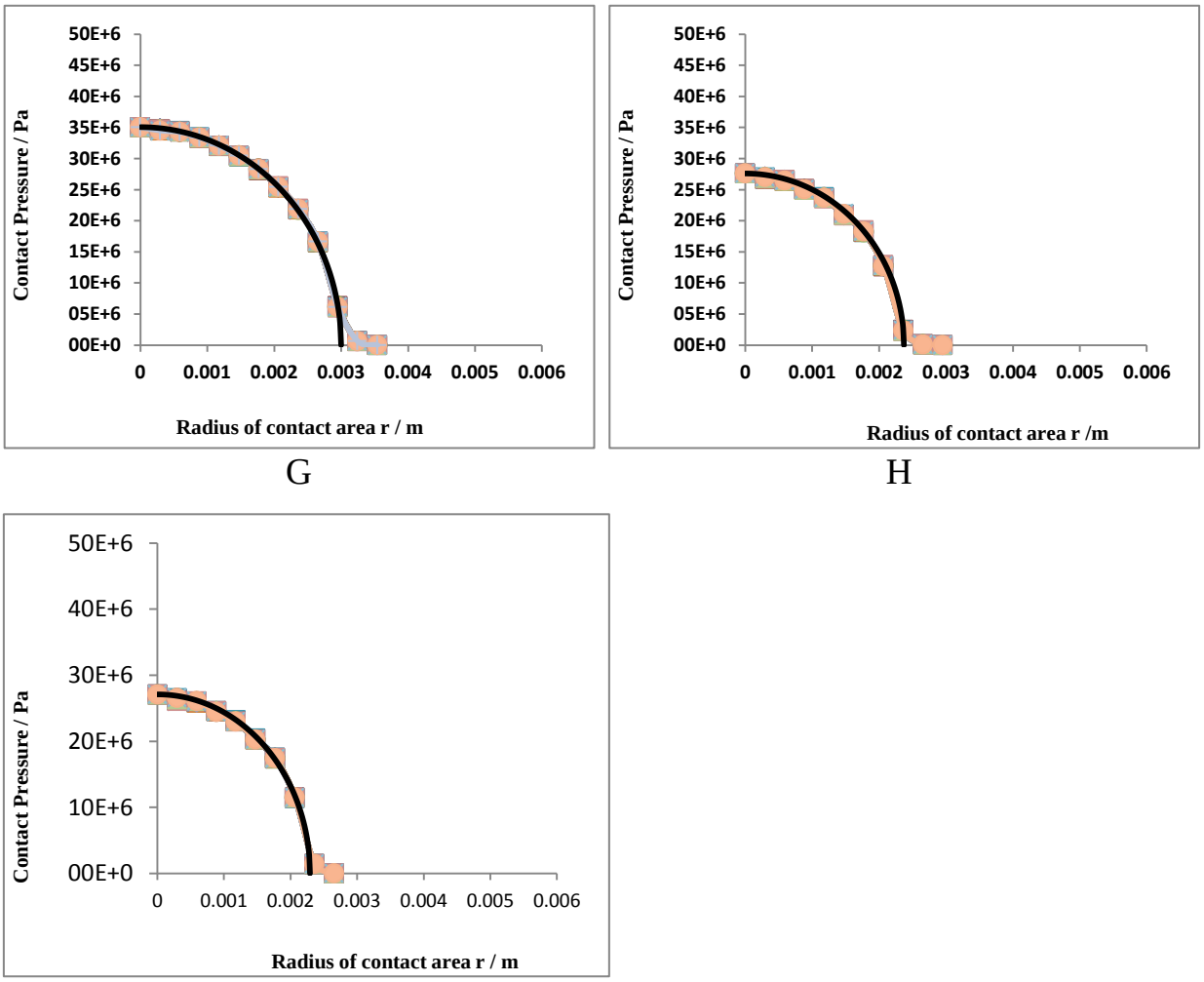

Figure 7.4 FEA dry contact pressure distribution of 10 mm cup thickness of the nine contact points A, B, C, D, E, F, G, H, and I compared with the theoretical equivalent Hertzian (black line).

Table 7.1 Cup wall thickness (*wt*), Measured load (*W*), Equivalent load (W_{equiv}), Calculated contact pressure ($P_{\mathrm{o(f)}}$), Equivalent elastic modulus ($\acute{E}_{\mathrm{equiv}}$), Entrainment velocity($\vec{U}_{\mathrm{i}}$), Equivalent and Hertzian radius of contact area (a_{eq}, a_{h}), ratio of cup thickness to Hertzian radius of contact area (wt/a_{h}).

	wt **(mm)**	***W*** **(N)**	W_{equiv} **(N)**	$\mathrm{P_{o(f)}}$ **(MPa)**	$\acute{E}_{\mathrm{equiv}}$ **(GPa)**	$\vec{\mathrm{U}}_{\mathrm{i}}$ **(m/s)**	a_{eq} **(mm)**	a_{h} **(mm)**	wt/a_{h}
Point A	**10**	**568**	**567.8**	**33.4**	**231.363**	**0.049**	**2.847**	**2.85**	**3.50**
	8	**568**	**569.5**	**33.1**	**227.963**	**0.049**	**2.865**	**2.85**	**2.80**
	6	**568**	**581.8**	**31.7**	**211.161**	**0.049**	**2.96**	**2.85**	**2.10**
	4	**568**	**546.0**	**27.7**	**178.520**	**0.049**	**3.065**	**2.85**	**1.40**
Point B	**10**	**1807**	**1790.3**	**48.2**	**225.401**	**0.032**	**4.212**	**4.192**	**2.38**
	8	**1807**	**1757.2**	**46.4**	**211.558**	**0.032**	**4.276**	**4.192**	**1.90**
	6	**1807**	**1730.7**	**41.3**	**180.727**	**0.032**	**4.483**	**4.192**	**1.43**
	4	**1807**		**28.8**		**0.032**	**5.124**	**4.192**	**0.95**
Point C	**10**	**1819**	**1809.4**	**48**	**223.172**	**0.008**	**4.241**	**4.202**	**2.37**
	8	**1819**	**1777.4**	**46.3**	**211.592**	**0.008**	**4.292**	**4.202**	**1.90**
	6	**1819**	**1752.2**	**41.7**	**180.605**	**0.008**	**4.503**	**4.202**	**1.42**
	4	**1819**		**28.9**		**0.008**	**5.14**	**4.202**	**0.95**
Point D	**10**	**1679**	**1692.4**	**46.8**	**222.618**	**0.028**	**4.151**	**4.085**	**2.44**
	8	**1679**	**1661.4**	**45.5**	**214.210**	**0.028**	**4.179**	**4.085**	**1.95**
	6	**1679**	**1684.5**	**40.9**	**182.111**	**0.028**	**4.432**	**4.085**	**1.46**
	4	**1679**		**28.6**		**0.028**	**5.033**	**4.085**	**0.97**
Point E	**10**	**1276**	**1331.3**	**43.1**	**220.874**	**0.073**	**3.842**	**3.733**	**2.67**
	8	**1276**	**1303.7**	**41.9**	**214.039**	**0.073**	**3.856**	**3.733**	**2.14**
	6	**1276**	**1250.9**	**38.7**	**193.350**	**0.073**	**3.934**	**3.733**	**1.60**
	4	**1276**		**29**		**0.073**	**4.436**	**3.733**	**1.07**

Point F	**10**	**958**	**944.0**	**39.6**	**231.869**	**0.075**	**3.371**	**3.393**	**2.94**
	8	**958**	**955.3**	**38.9**	**223.986**	**0.075**	**3.362**	**3.393**	**2.35**
	6	**958**	**972.5**	**36.6**	**203.264**	**0.075**	**3.557**	**3.393**	**1.76**
	4	**958**		**29.3**		**0.075**	**3.824**	**3.393**	**1.17**
Point G	**10**	**663**	**660.3**	**35**	**230.479**	**0.034**	**2.998**	**3.001**	**3.33**
	8	**663**	**659.8**	**34.8**	**228.192**	**0.034**	**3.008**	**3.001**	**2.66**
	6	**663**	**649.1**	**33.3**	**215.196**	**0.034**	**3.051**	**3.001**	**1.99**
	4	**663**	**642.0**	**28.4**	**169.222**	**0.034**	**3.293**	**3.001**	**1.33**
Point H	**10**	**312**	**325.1**	**27.6**	**229.438**	**0.01**	**2.371**	**2.334**	**4.28**
	8	**312**	**321.0**	**27.2**	**226.698**	**0.01**	**2.371**	**2.334**	**3.42**
	6	**312**	**318.2**	**26.9**	**223.618**	**0.01**	**2.374**	**2.334**	**2.57**
	4	**312**	**305.8**	**25.1**	**206.211**	**0.01**	**2.408**	**2.334**	**1.71**
Point I	**10**	**295**	**297.9**	**27**	**233.098**	**0.029**	**2.291**	**2.291**	**4.36**
	8	**295**	**295.9**	**26.9**	**232.233**	**0.029**	**2.289**	**2.291**	**3.49**
	6	**295**	**312.4**	**26.6**	**221.972**	**0.029**	**2.366**	**2.291**	**2.61**
	4	**295**	**293.2**	**24.5**	**202.658**	**0.029**	**2.388**	**2.291**	**1.74**

In Table 7.1 the value of $\dot{E}_{\mathbf{equiv}}$ is seen to reduce as the cup thickness reduces at each of the nine gait cycle positions. There is a tendency for $\dot{E}_{\mathbf{equiv}}$ to reduce as the load is increased for each value of cup thickness but this is a trend rather than a rule and is also influenced by the position of the contact point on the cup surface. The values of a_{equiv} follow the pattern of the Hertzian results, and can be seen to be larger, and increasingly so as the cup thickness is reduced. The differences between a_{equiv} and a_{h} become large for the 4 mm cup at the heaviest loads (22% for case C). The pattern of W_{equiv} is

less ordered. Its value generally falls as the cup thickness is reduced but points A, D and I have no clear trend.

The equivalent Hertzian models are based on two features of the FE analyses which are not established precisely. The contact dimension is obtained by an extrapolation of the pressure curve to find the position at which it becomes zero. This calculation is made for each axial position in the FEA mesh and an average is used for a_{equiv}. The values obtained at the 24 angular positions are close to each other and are best viewed as consisting of a circle with random errors of radius, rather than a distorted circle with a smooth boundary. The second feature is the contact pressure at the centre of the contact and this has an element of variation, e.g. case C in figure 7.2. It is therefore reasonable to expect same inconsistencies to emerge in the trends for the equivalent model parameters when the different loads and cup positions are considered.

7.3 EHL Film Thickness Contours

Contours of the film thicknesses for the nine contact points, A – I, and four cup thicknesses, 4, 6, 8 and 10 mm are shown in figures 7.5 – 7.8. The black dashed line in each contour plot represents the boundary of the contact area. In these figures the contour key has been kept fixed so that the film thicknesses may be compared. Figure 7.5 for a 4 mm cup thickness shows contours for cases A, G, H and I only because these are the only cases with this cup thickness where the contact can be regarded as Hertzian. All the contours presented here were for the modified equivalent Hertzian case. A typical film shape of the steady state problem for each contact point with the classic horseshoe film thickness can be shown in these figures where the constriction is formed. This is most evident in the contours of figure 7.8 case

D because the fixed contour levels show the horseshoe constriction clearly and the location of the minimum film thickness in the side lobes. The value of central and minimum film thickness is given below the key for each contour plot. Within the Hertzian contact, in the right hand side of each figure the minimum film thickness develops near the contact edges. There is a reduction in the lubricant film thickness for the circular contact points from the central area of the contact as y/a increases. For the contours presented for the three different cup thicknesses, 6, 8 and 10 mm, the lowest value of the film thickness occurs at the contact point C with a value of $h_m = 0.030$ µm.

Comparing the contour plots for the different cup thicknesses, it can be seen that the minimum film thickness which occurs in the side lobes become thinner as the cup thickness increases. Points G and D are good examples to illustrate this as their minimum film thickness value reduces to cross the contour colour boundary at 0.075 μm as the cup thickness increases. This is illustrated by the emergence of the red contour at these points. Although, the load applied and the entrainment velocity are fixed for the same contact point, the minimum and central film thicknesses of point G decrease from 0.160 and 0.112 μm at 4 mm cup to be 0.145 and 0.102 μm at 6 mm cup, 0.141 and 0.100 μm at 8 mm, 0.140 and 0.99 μm at 10 mm cup thickness. It is possible to say that thicker film thickness can be produced by reducing the cup wall thickness because the resulting change to the equivalent contact conditions are determental to the film thickness.

The minimum and central film thicknesses for the contact point I are about double that of the contact point H for all the cup thicknesses, although the difference of the measured load between these two points is no more than 6%. The reason for this variation in the film thickness comes from entrainment velocity, where the velocity for the point I is three times bigger than the velocity for the point H. This case can also be applied for the contact points

B, C and D, where there are relatively small differences between the measured loads of these points as it shown from Table 7.1, but there are large variations in the contour plots due to the changing the entrainment velocities.

Contour of film thickness of 4 mm cup

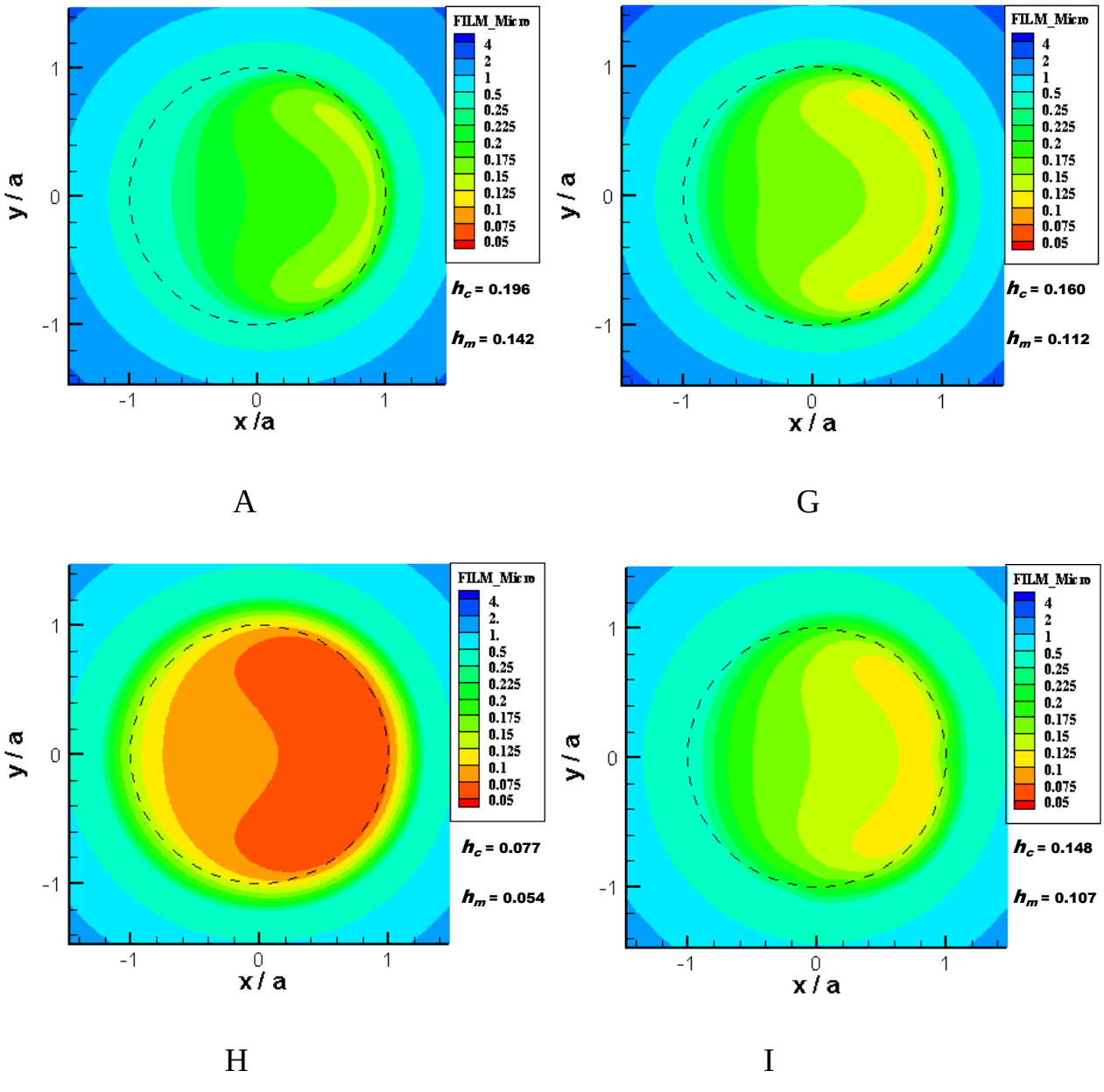

Figure 7.5 film thickness /μm at different contact positions for points A, G, H, I, of the gait cycle for a 4 mm cup thickness.

Contour of film thickness of 6 mm cup

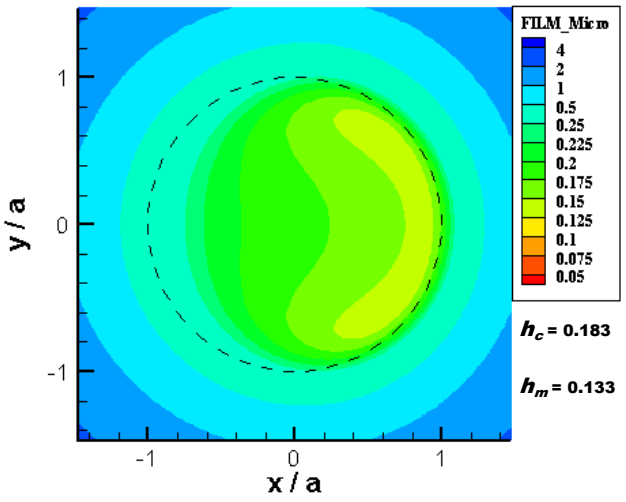

A

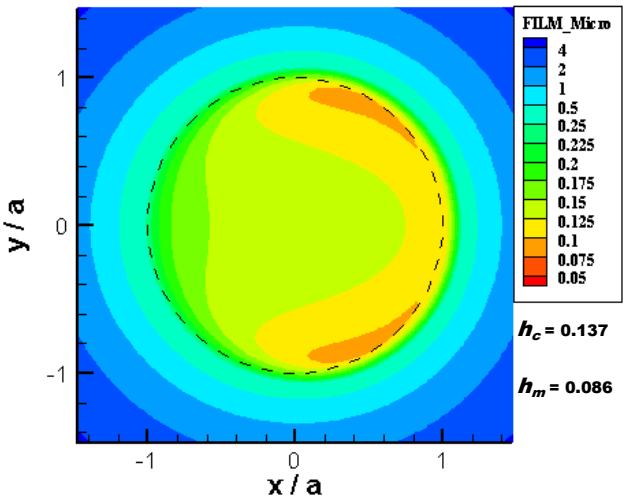

B

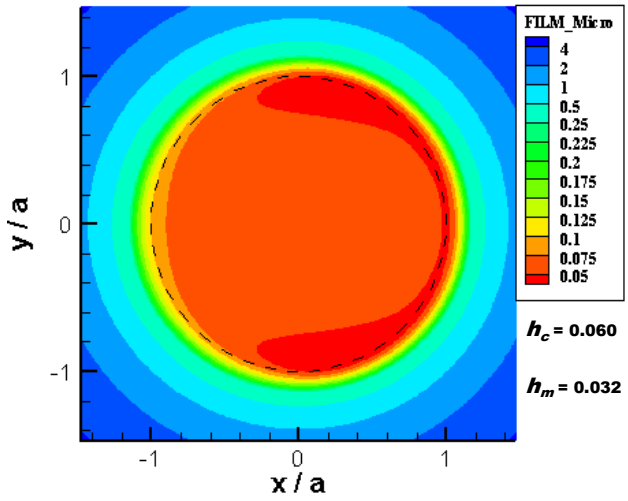

C

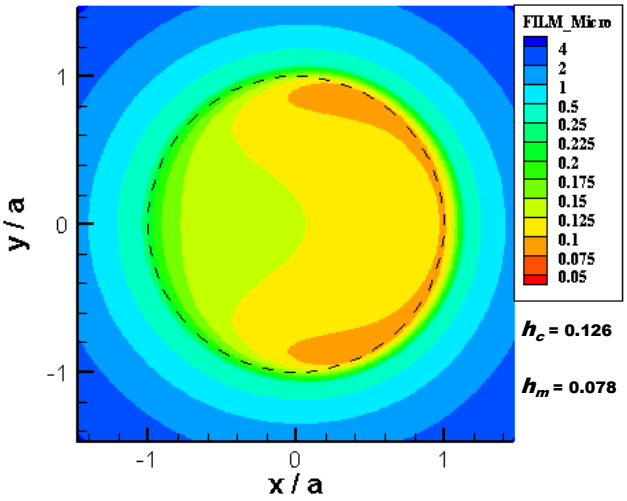

D

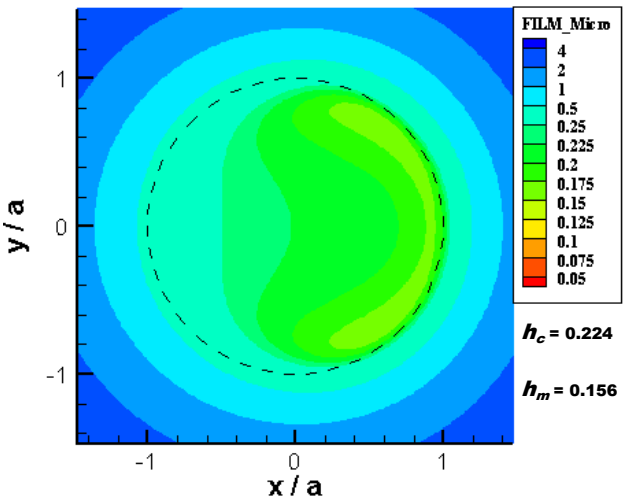

E

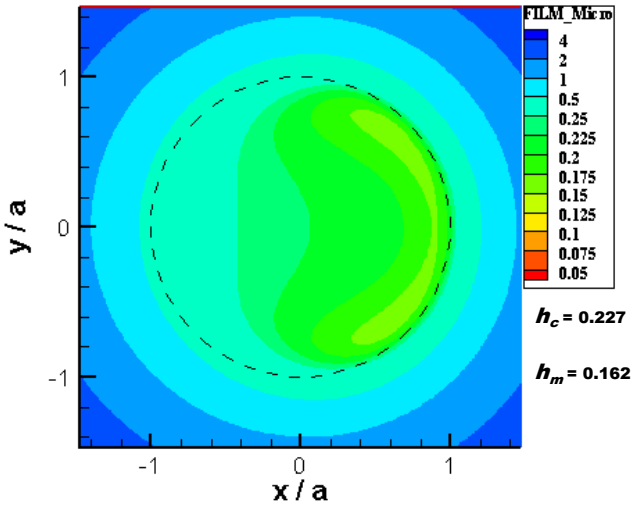

F

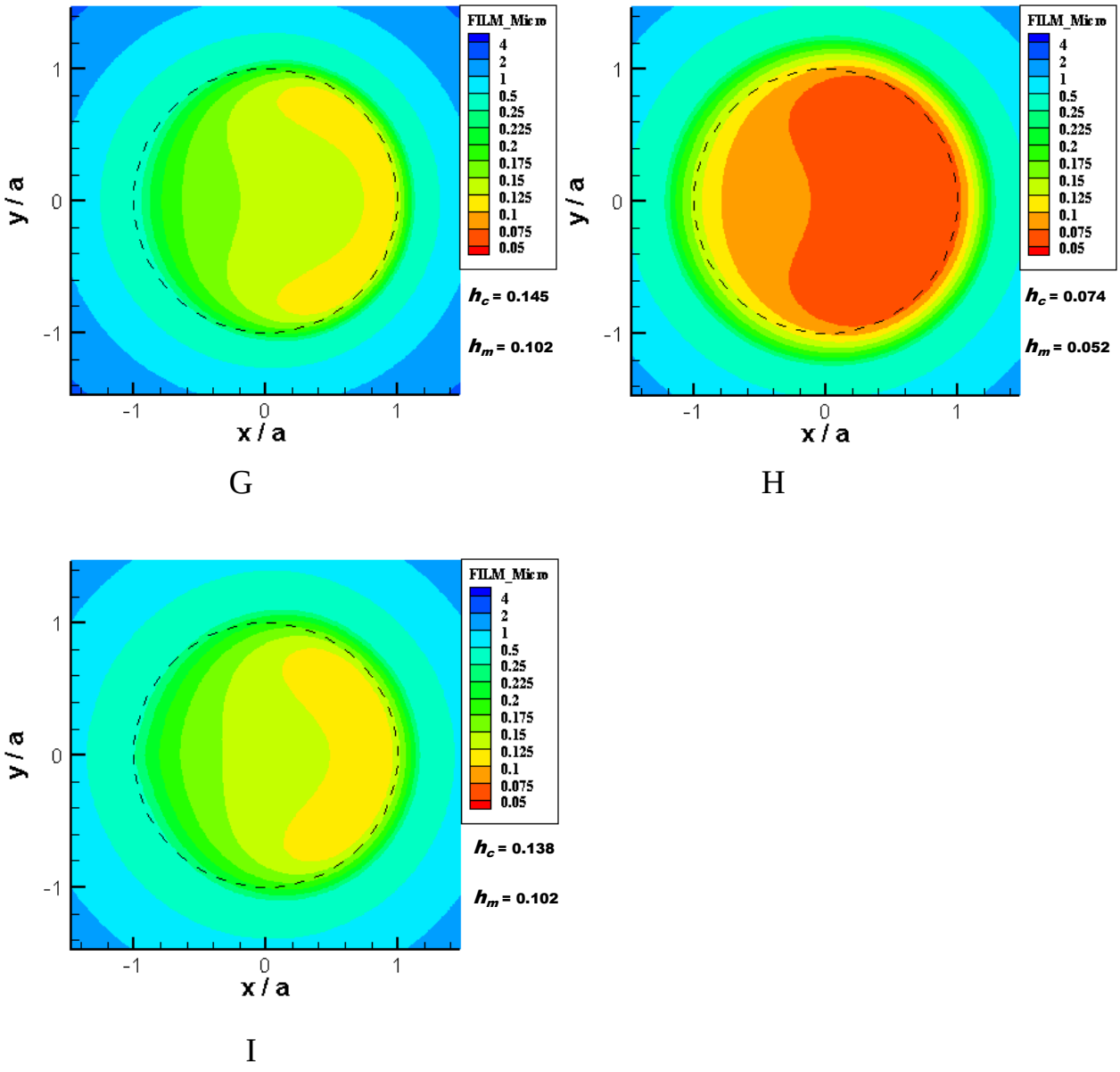

Figure 7.6 film thickness /μm at different contact positions, nine points, of the gait cycle for a 6 mm cup thickness.

Contour of film thickness of 8 mm cup

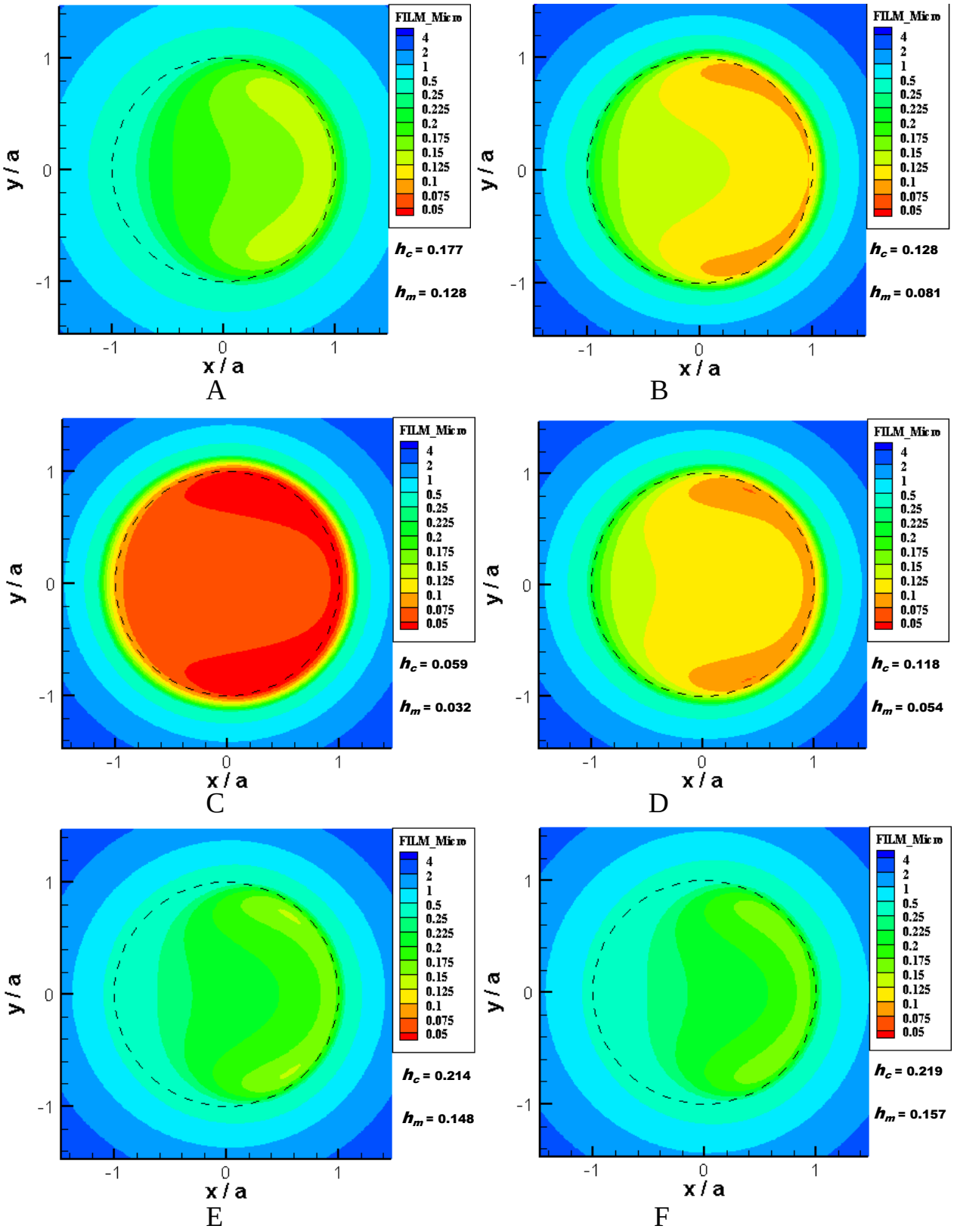

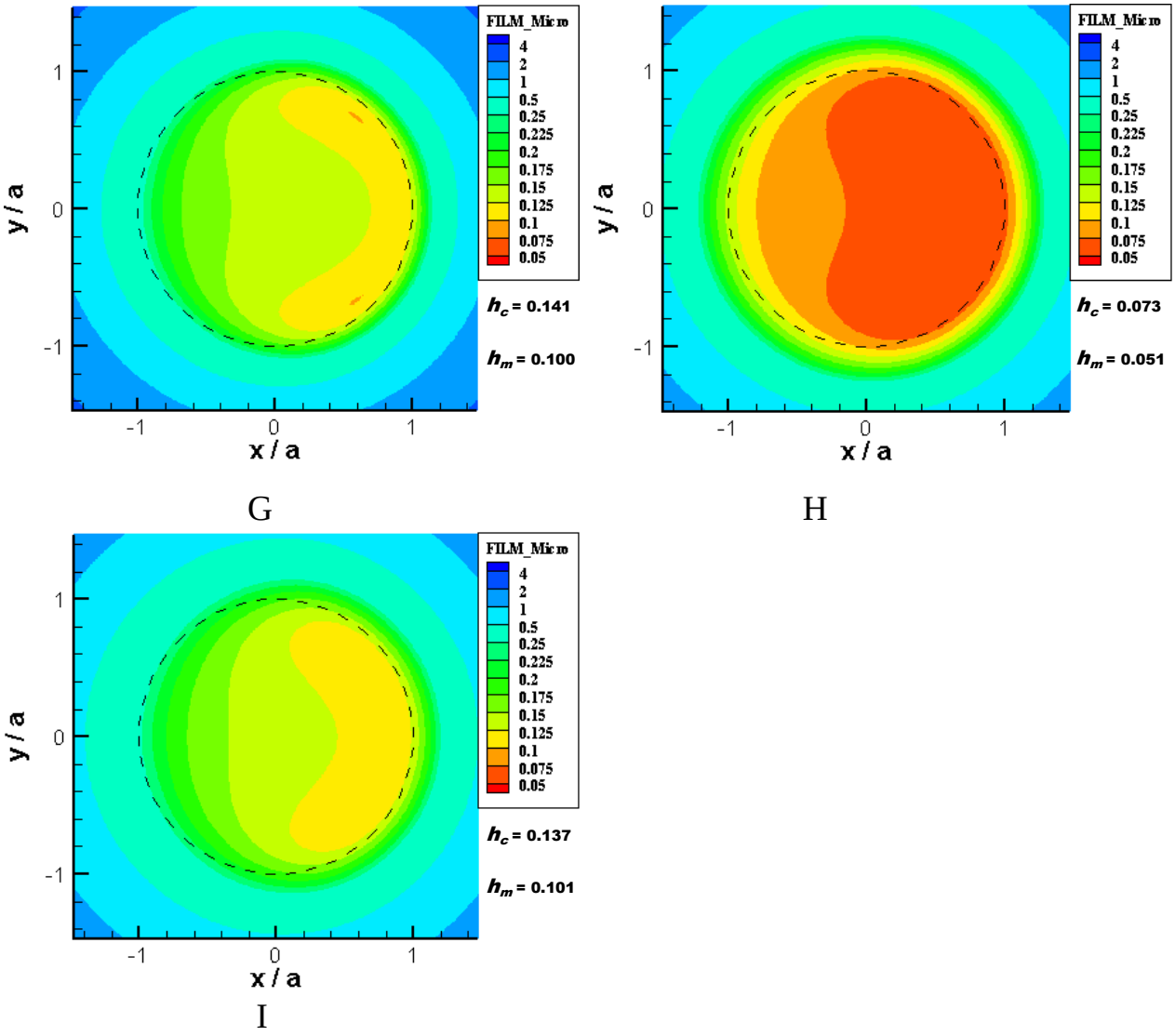

Figure 7.7 film thickness /μm at different contact positions, nine points, of the gait cycle for a 8 mm cup thickness.

Contour of film thickness of 10 mm cup

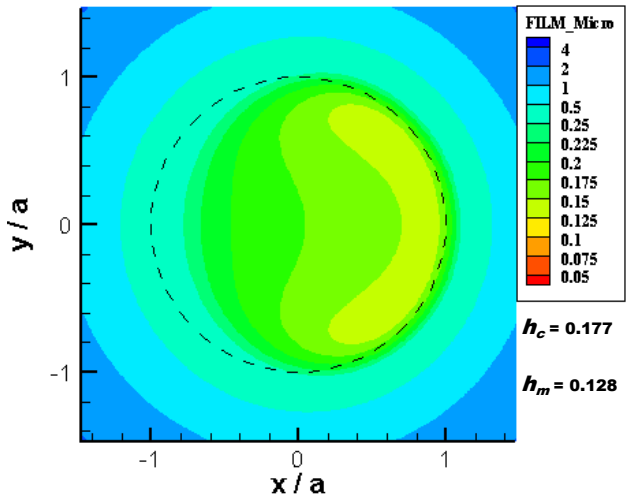

A

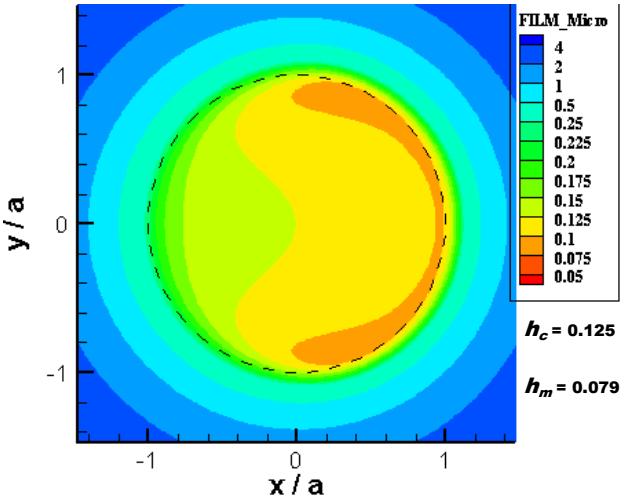

B

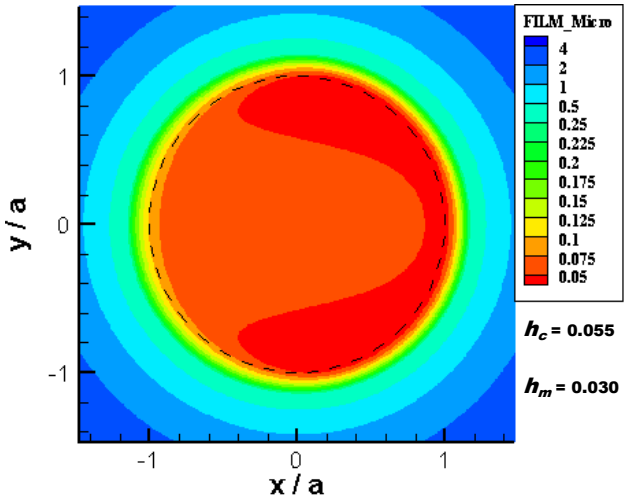

C

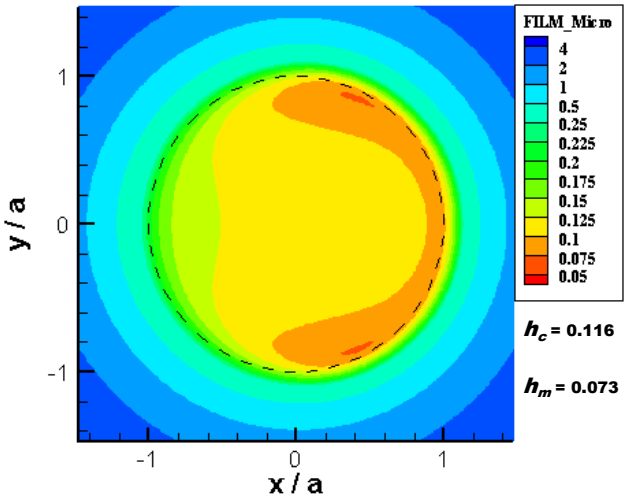

D

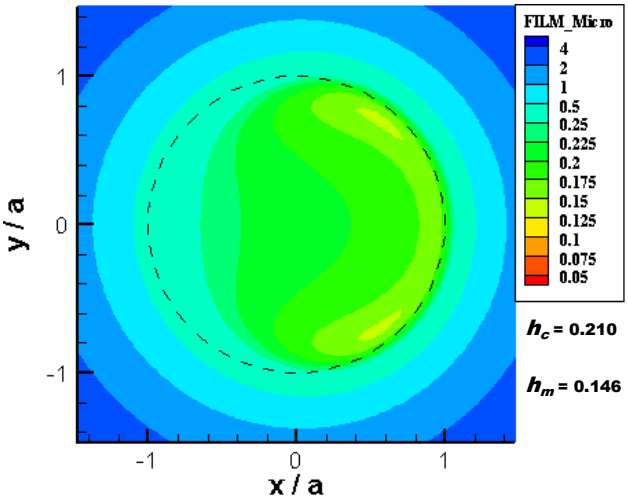

E

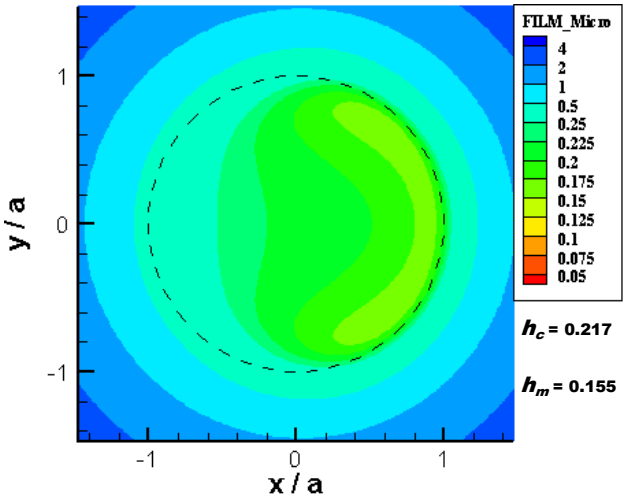

F

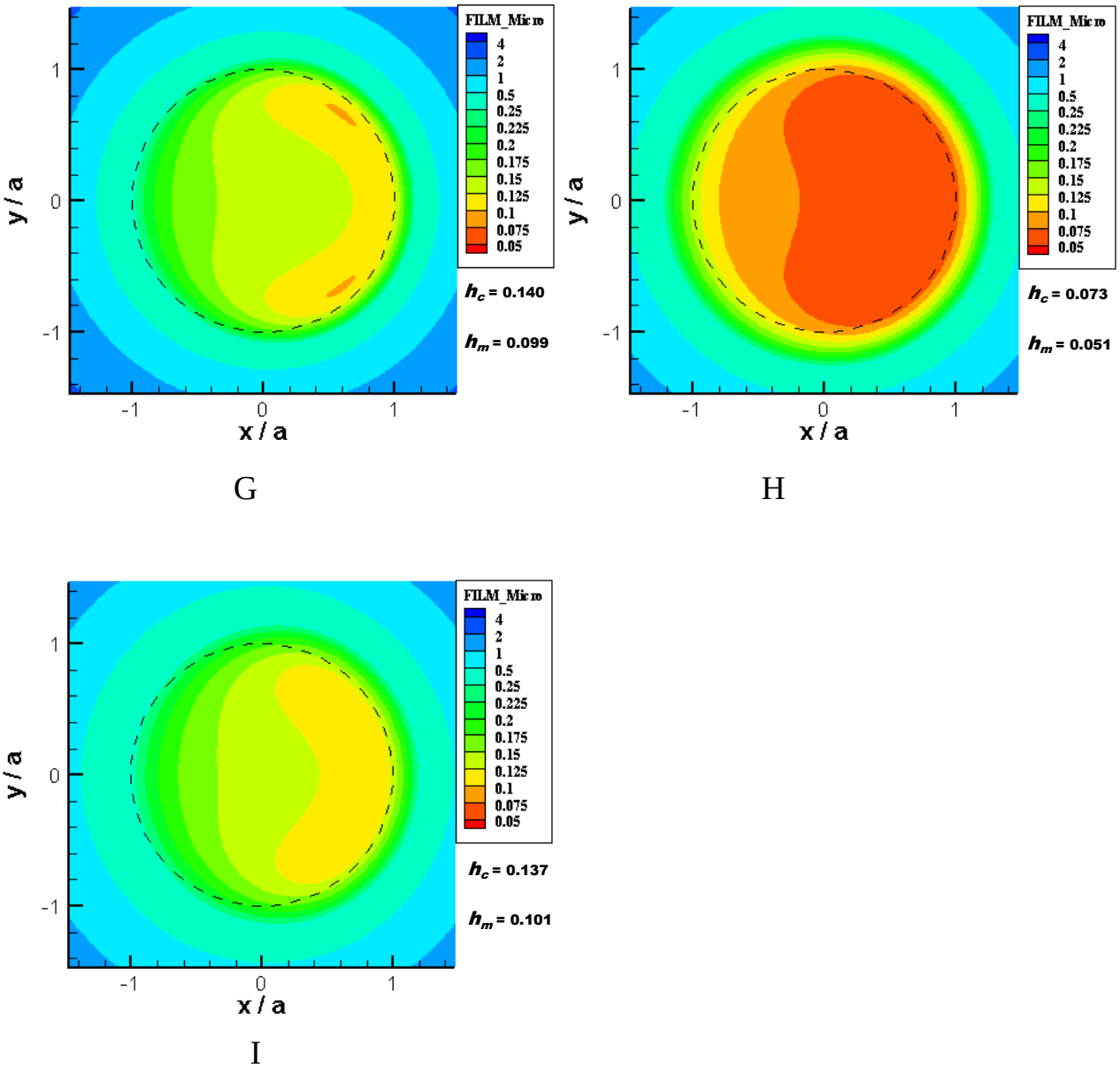

Figure 7.8 film thickness /μm at different contact positions, nine points, of the gait cycle for a 10 mm cup thickness.

Detailed results for each of the cup thickness values examined are given in the next sections taking those for each thickness in turn. For each case, five figures are presented. The first shows the gap factor obtained from the FE contact analysis along each of the radial mesh lines. The next two figures

show sections of pressure and film thickness, respectively, in the contact entrainment direction. The final two figures show the corresponding sections perpendicular to the entrainment direction.

In each of these sections three curves are shown; the result for EHL analysis of the nominal Hertzian contact, denoted Hz; the result for the equivalent Hertzian contact determined according to section 5.5, denoted Hz-equiv; and the result when the gap factor is added to the equivalent Hertzian contact, denoted Hz-equiv-mod.

In comparing the results for the gap factors for the various cup thicknesses and gait cycle positions it was found that the gap factor values decrease when the cup thickness increases for the same contact point. For example, the contact point A has an average gap factor equal to – 0.48 μm, – 0.175 μm, – 0.105 μm, – 0.05 μm at r/a =2.4 for 4, 6, 8, 10 mm cup thickness respectively. When the cup thickness increases the contact pressure also increases and the radius of the contact area decreases at the same applied load. As a result, the gap factor decreases. In other words, when the radius of the contact area decreases, the gap outside the contact zone which is calculated from equation (5.18) for the equivalent Hertzian also decreases. Consequently, the difference between the gap from the FE analysis and Hertzian theory is reduced. The gap factors also have different values for the nine contact points, A to I, for the same cup thickness. In general, it seems that the gap factor depends directly on the radius of the contact area, $\boldsymbol{a}$.

7.4 Detailed EHL results for 4 mm cup thickness

Figures 7.9 – 7.28, show the EHL results for the four contact points, A, G, H and I of the 4 mm cup thickness. In comparison to the nominal Hertzian EHL pressure distribution it was found that the equivalent and modified cases had contact pressures that were lower by 16.3%, 19.6%, 7.8% and 8.8% for the contact points A, G, H and I respectively. Besides the reduction in the maximum contact pressure there is also an increase in the film thickness. Where the percentage ratios of increasing of the central film thicknesses for A, G, H and I are 11.5%, 14%, 5%, and 5.7% respectively. There were very small variations between the results of the equivalent case and the modified case, which means that adding the gap factor value to the undeformed geometry of the equivalent Hertzian case does not make a significant change to the results.

It should be noted that in these sections the position (x or y) is normalised to the contact dimension for the individual model. The reduction in contact pressure occurs in association with an increase in the contact dimension as the load is the same for the cases compared in the sectional figure.

Table 7.2 shows summary for the 4 mm cup of the calculated Hertzian and equivalent radius of contact area, the Hertzian and the equivalent maximum contact pressure and the ratio between them, the Hertzian and the equivalent central film thickness and the ratio between them. Where the pressure and the film ratios were obtained as follows;

$$\text{Percentage of the pressure ratio} = \frac{P_{o(equiv)} - P_{o(h)}}{P_{o(h)}} \times 100\% \quad \text{.....(7.1)}$$

$$\text{Percentage of the central film thickness ratio} = \frac{h_{c(equiv)} - h_{c(h)}}{h_{c(h)}} \times 100\% \text{.....(7.2)}$$

EHL results for 4 mm Cup thickness

Contact Point A

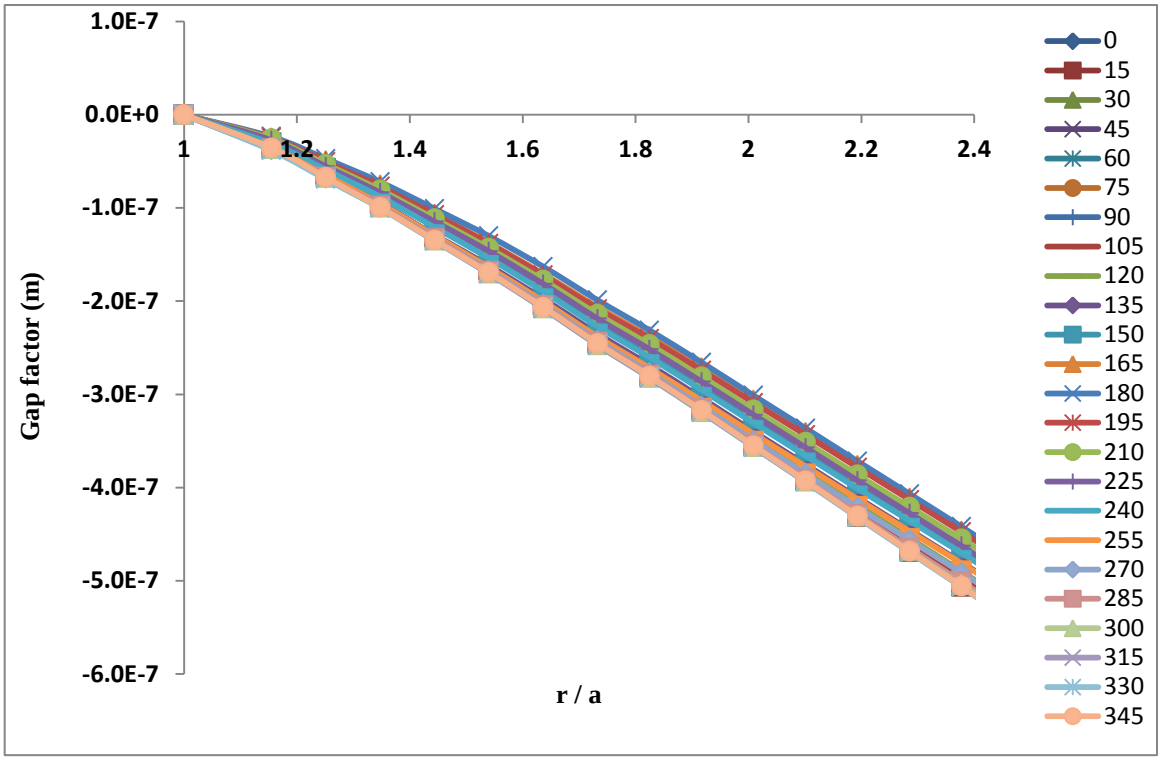

Figure 7.9 Gap factor for point A of 4 mm cup thickness

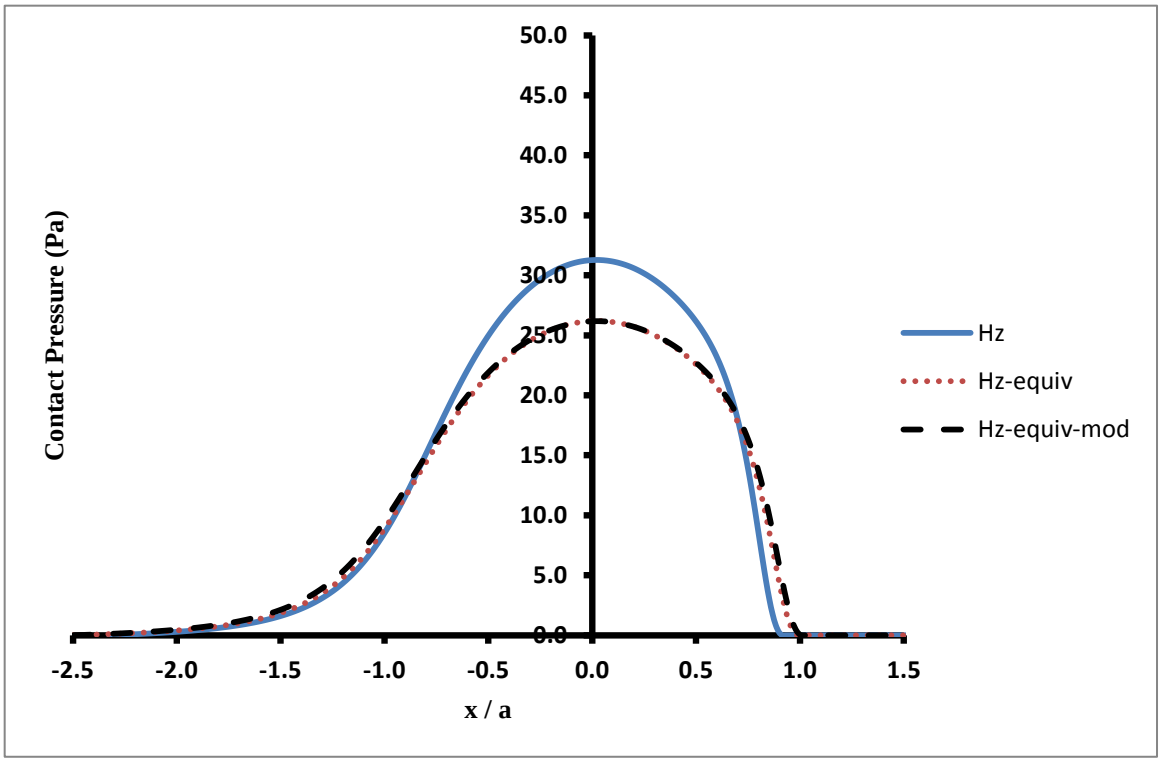

Figure 7.10 Pressure distribution for point A, 4 mm cup thickness, central line in x-direction

where

Equiv : means Equivalent Hertzian.

Mod : means Modified Equivalent Hertzian, which is equal to the Equivalent Hertzian after adding the gap factor.

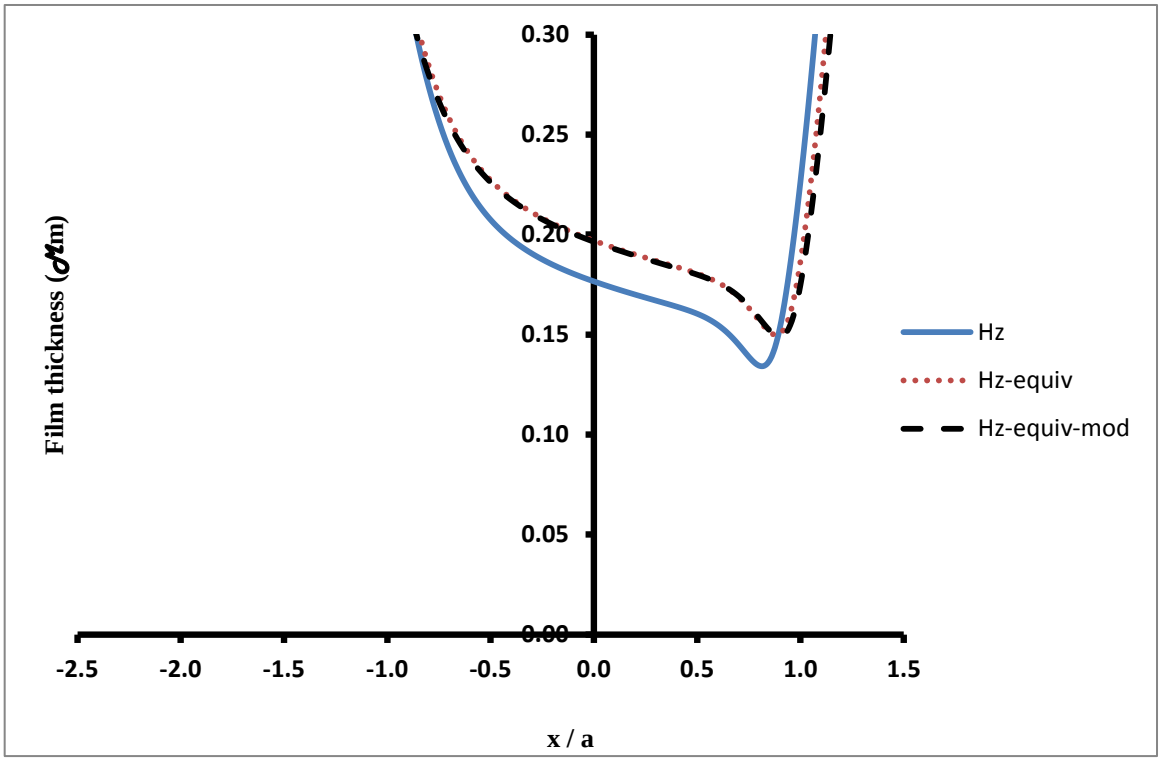

Figure 7.11 Film thickness for point A, 4 mm cup thickness, central line in x-direction

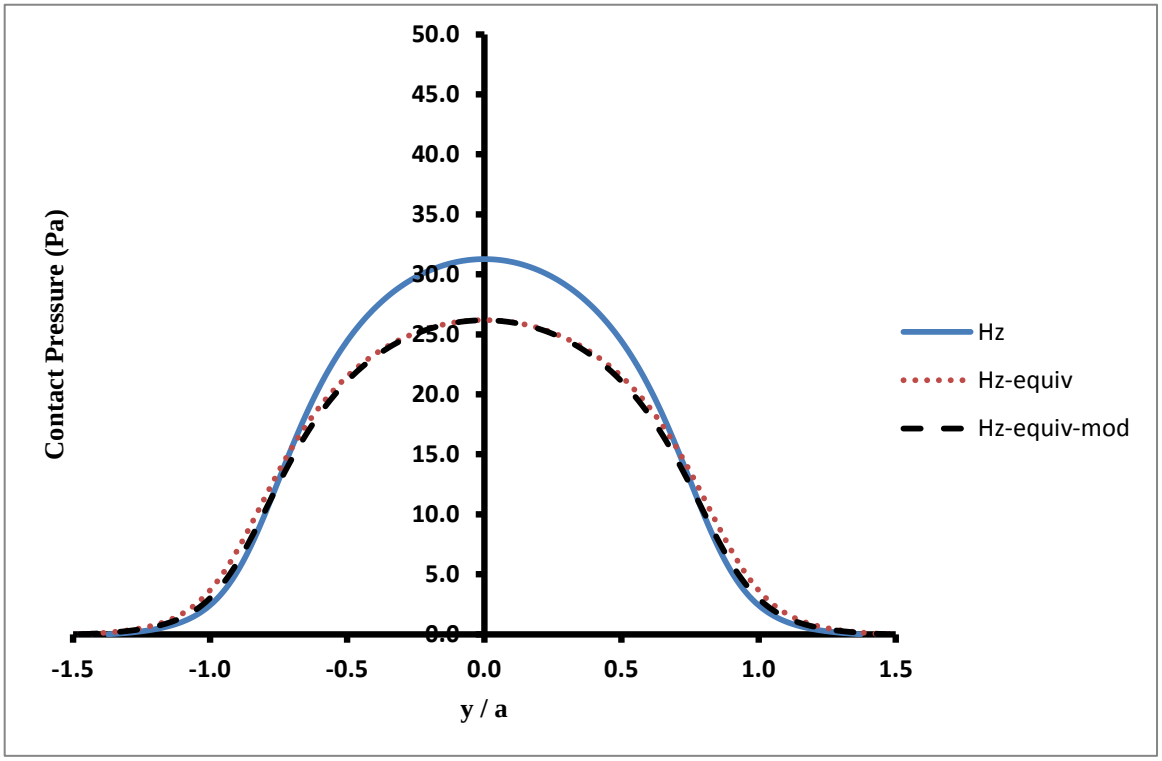

Figure 7.12 Pressure distribution for point A, 4 mm cup thickness, central line in y-direction

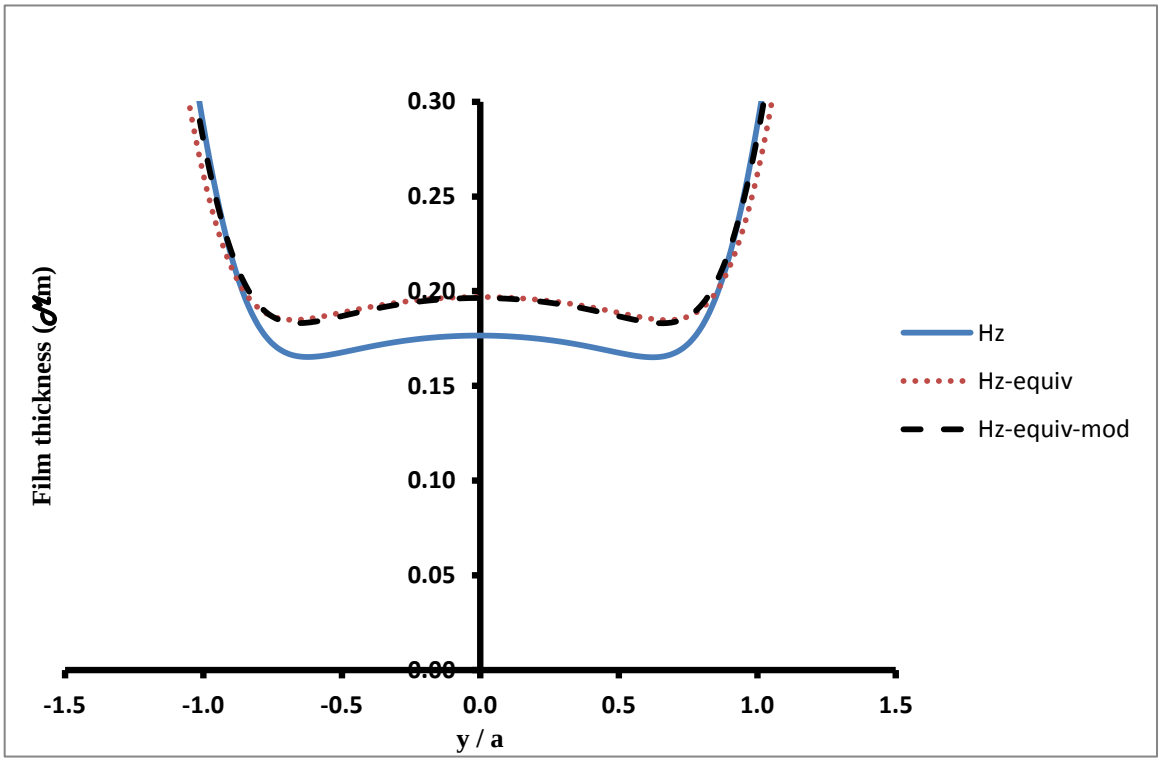

Figure 7.13 Film thickness for point A, 4 mm cup thickness, central line in y-direction

Contact Point G

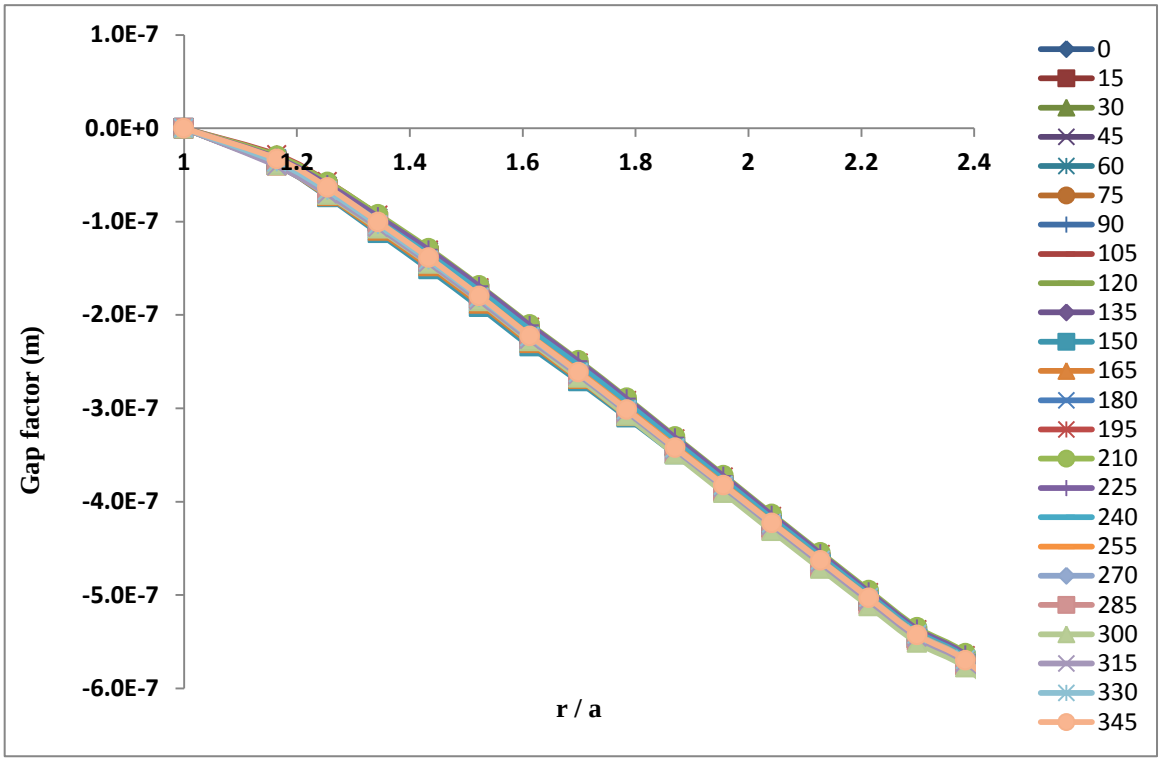

Figure 7.14 Gap factor for point G of 4 mm cup thickness

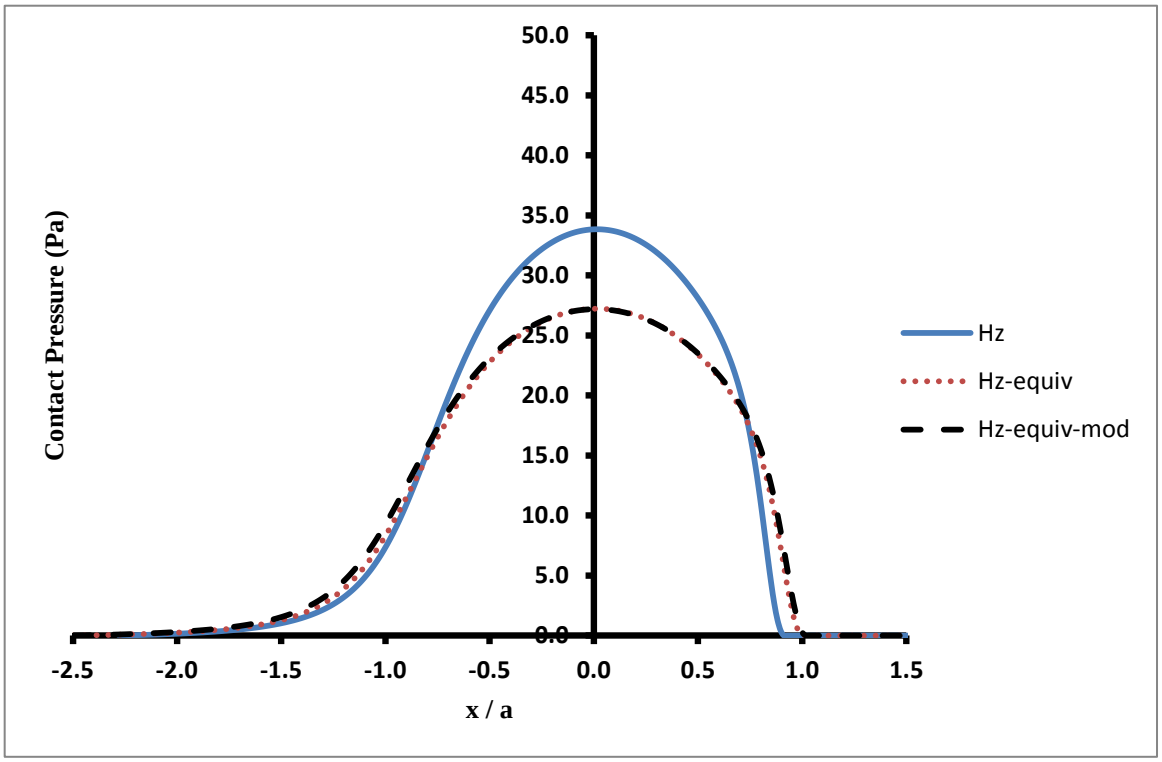

Figure 7.15 Pressure distribution for point G, 4 mm cup thickness, central line in x-direction

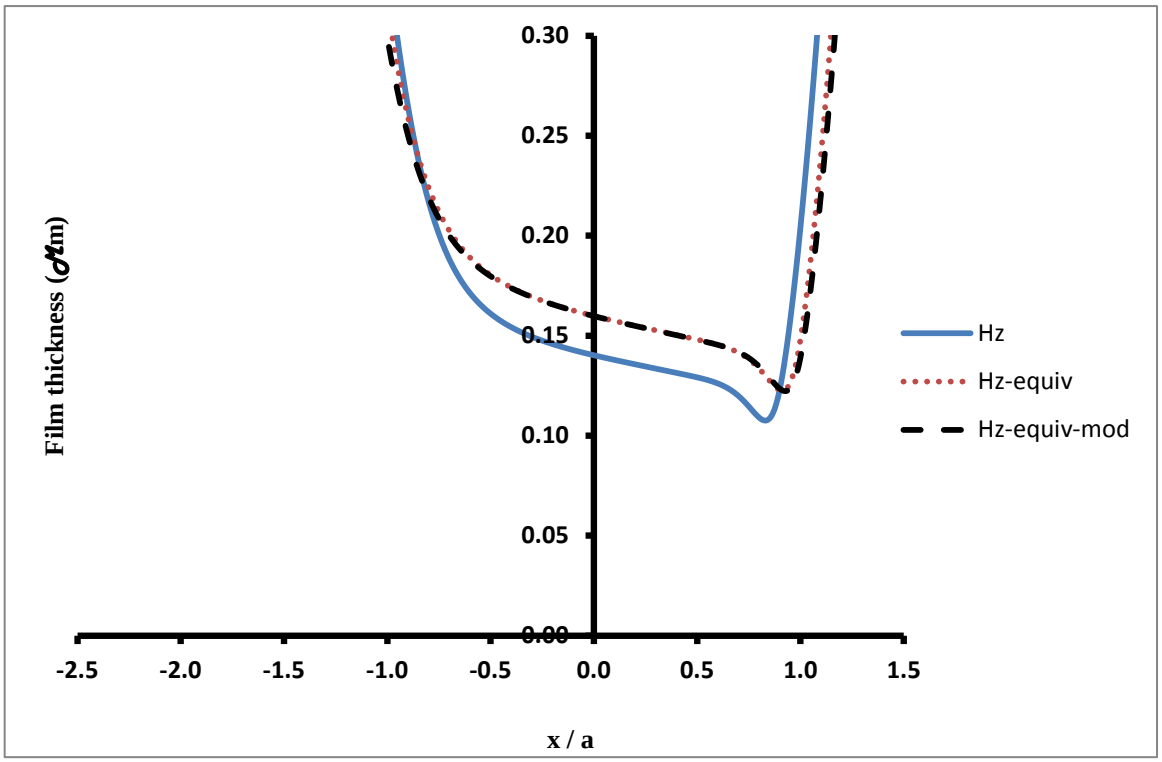

Figure 7.16 Film thickness for point G, 4 mm cup thickness, central line in x-direction

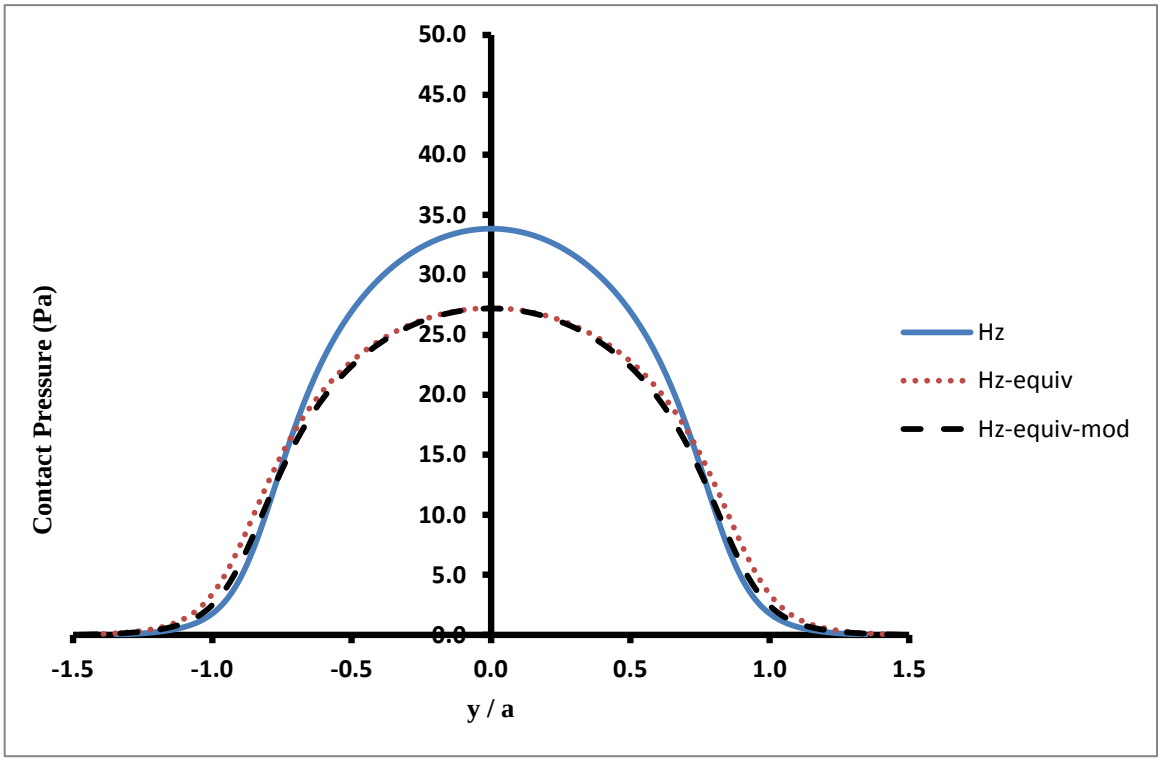

Figure 7.17 Pressure distribution for point G, 4 mm cup thickness, central line in y-direction

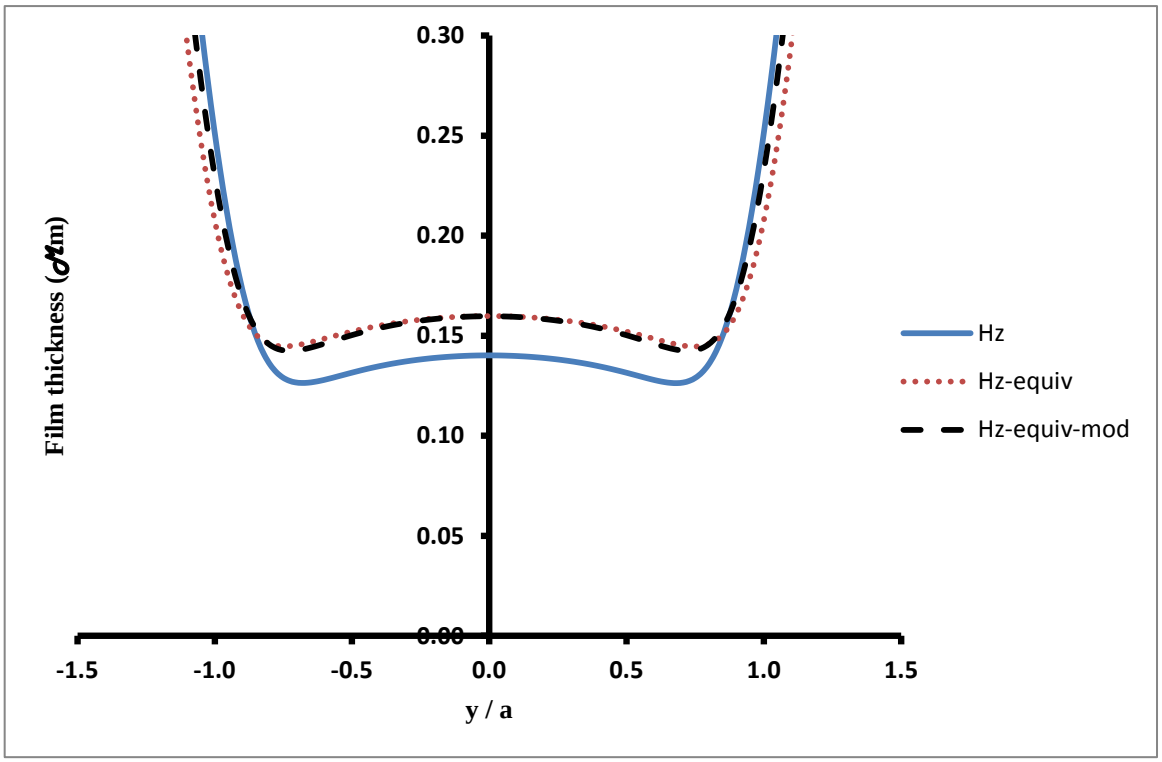

Figure 7.18 Film thickness for point G, 4 mm cup thickness, central line in y-direction

Contact Point H

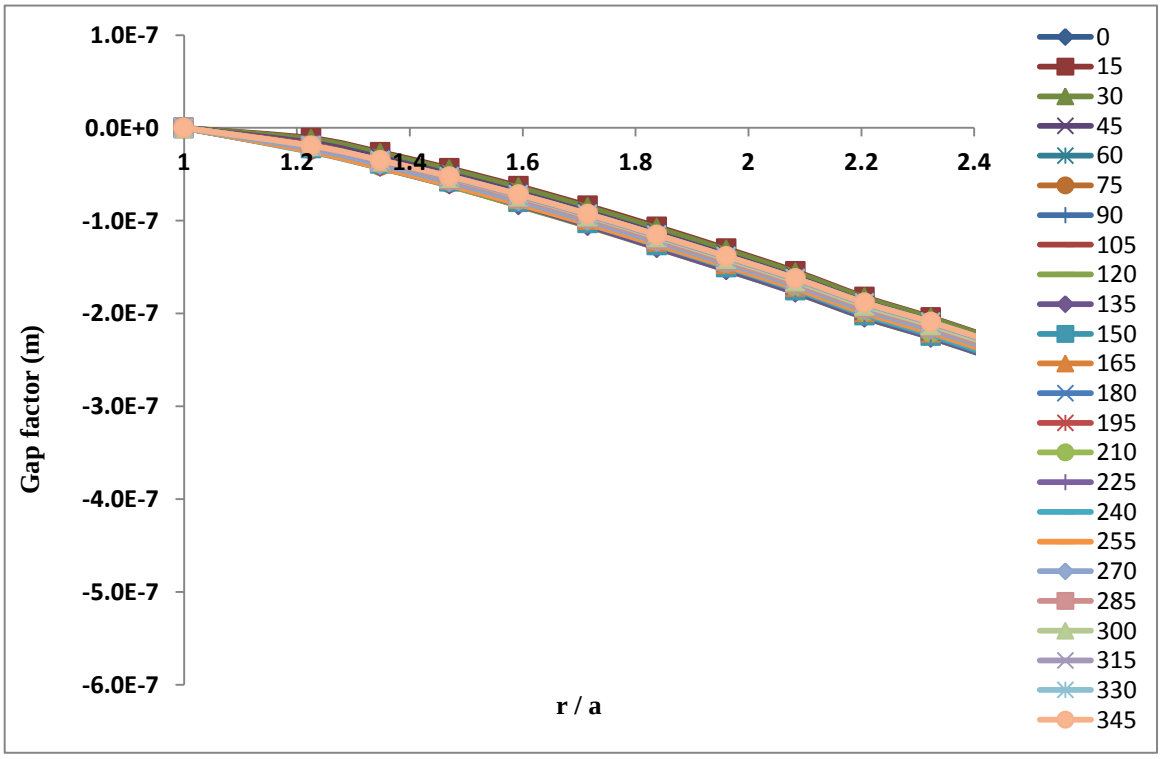

Figure 7.19 Gap factor for point H of4 mm cup thickness

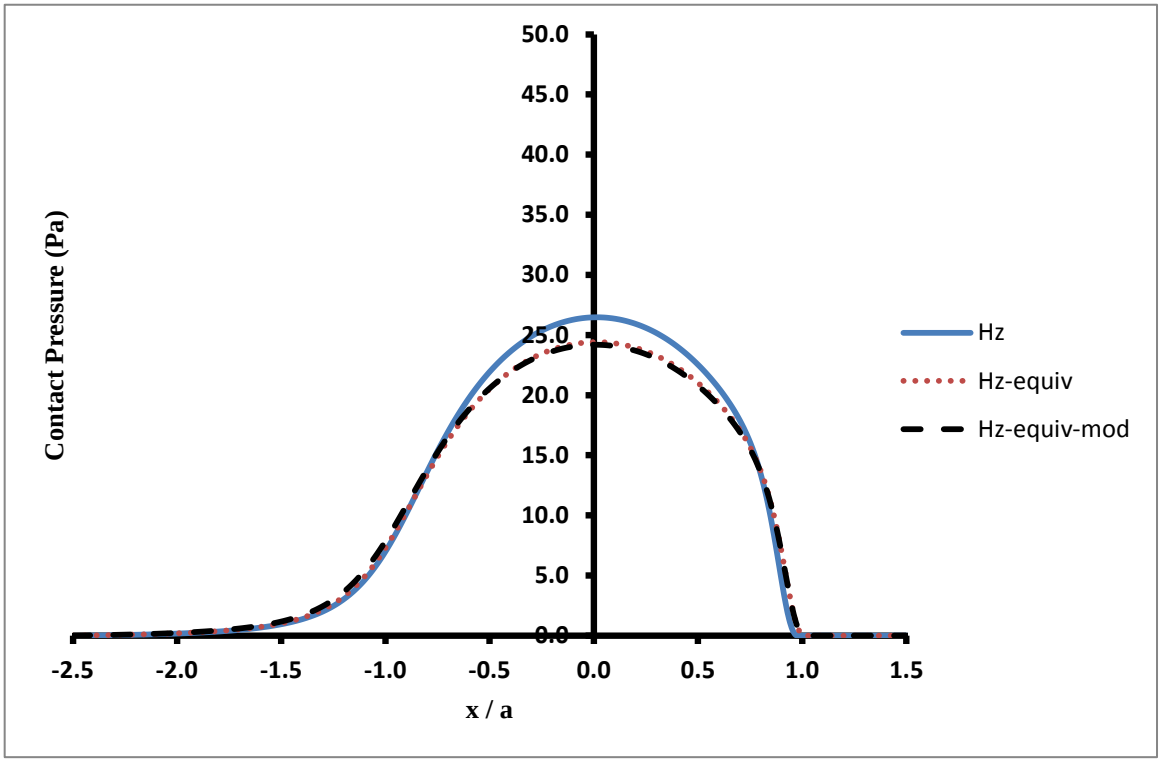

Figure 7.20 Pressure distribution for point H, 4 mm cup thickness, central line in x-direction

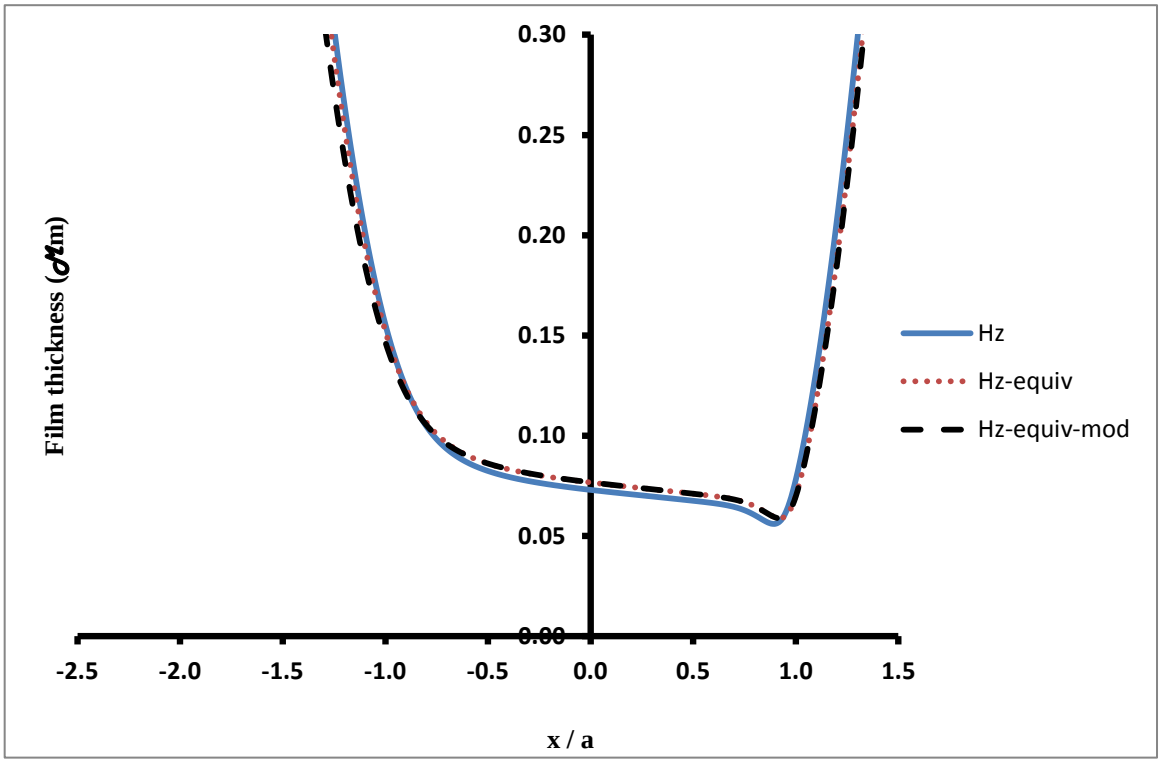

Figure 7.21 Film thickness for point H, 4 mm cup thickness, central line in x-direction

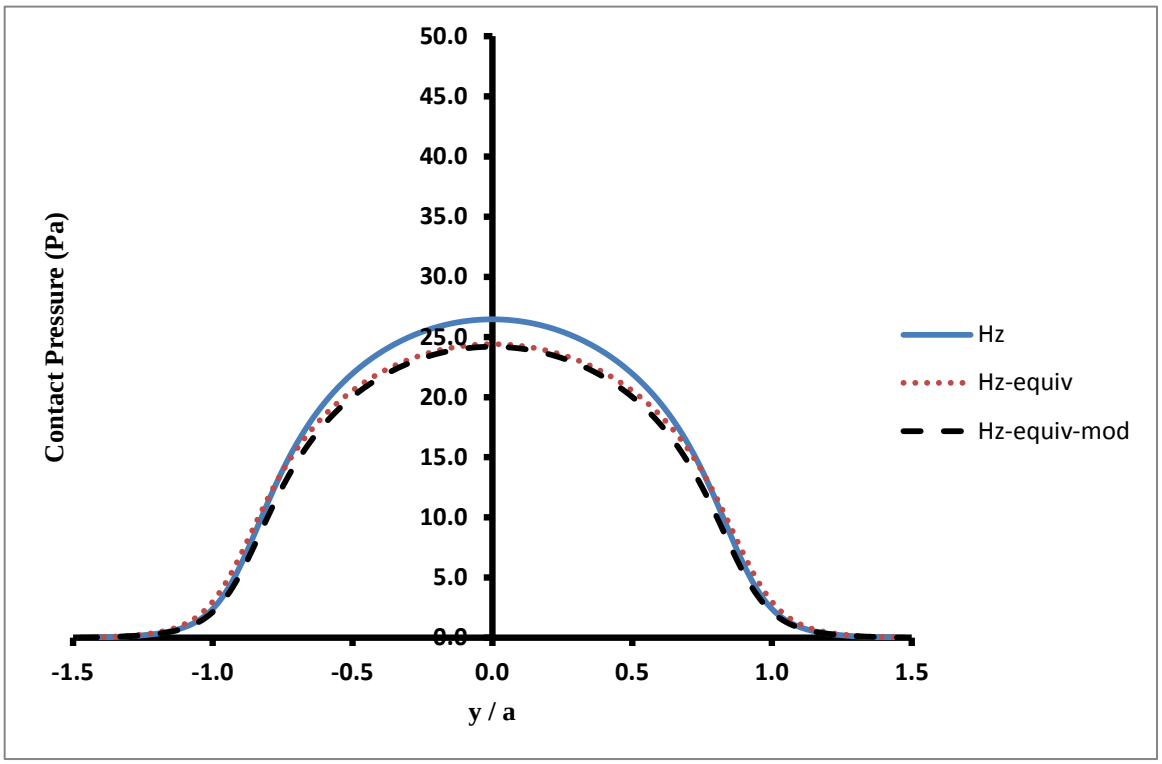

Figure 7.22 Pressure distribution for point H, 4 mm cup thickness, central line in y-direction

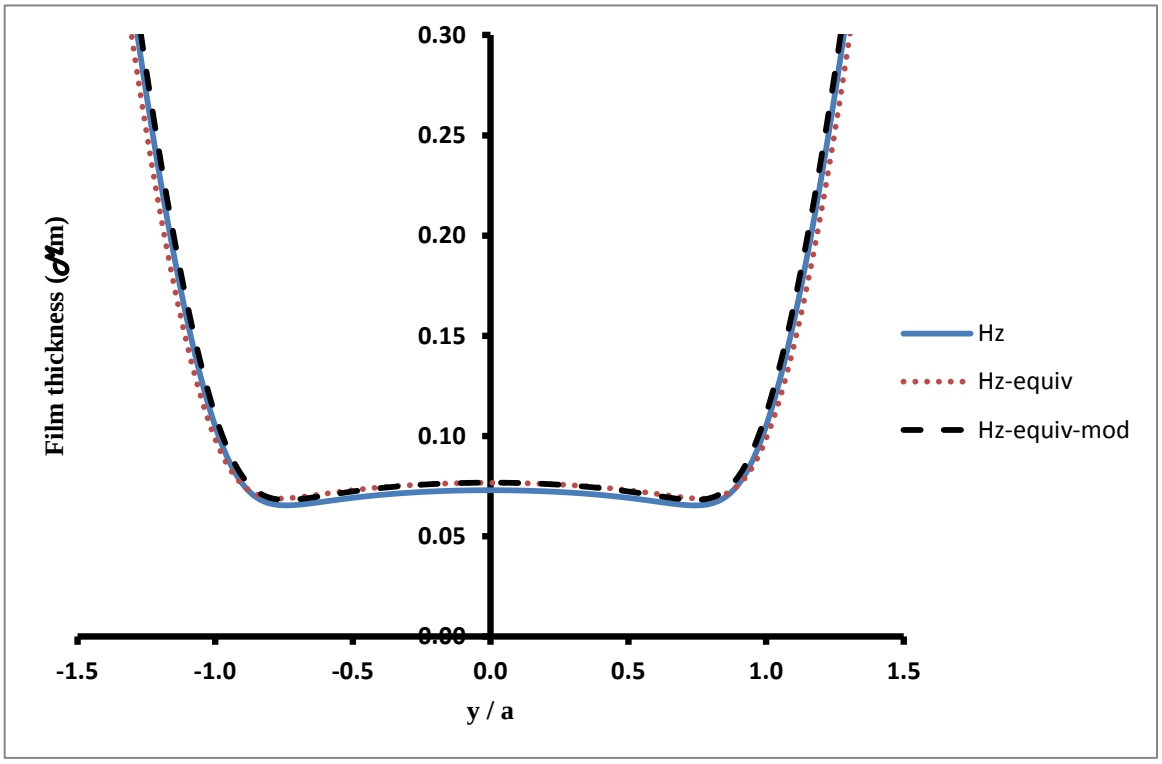

Figure 7.23 Film thickness for point H, 4 mm cup thickness, central line in y-direction

Contact Point I

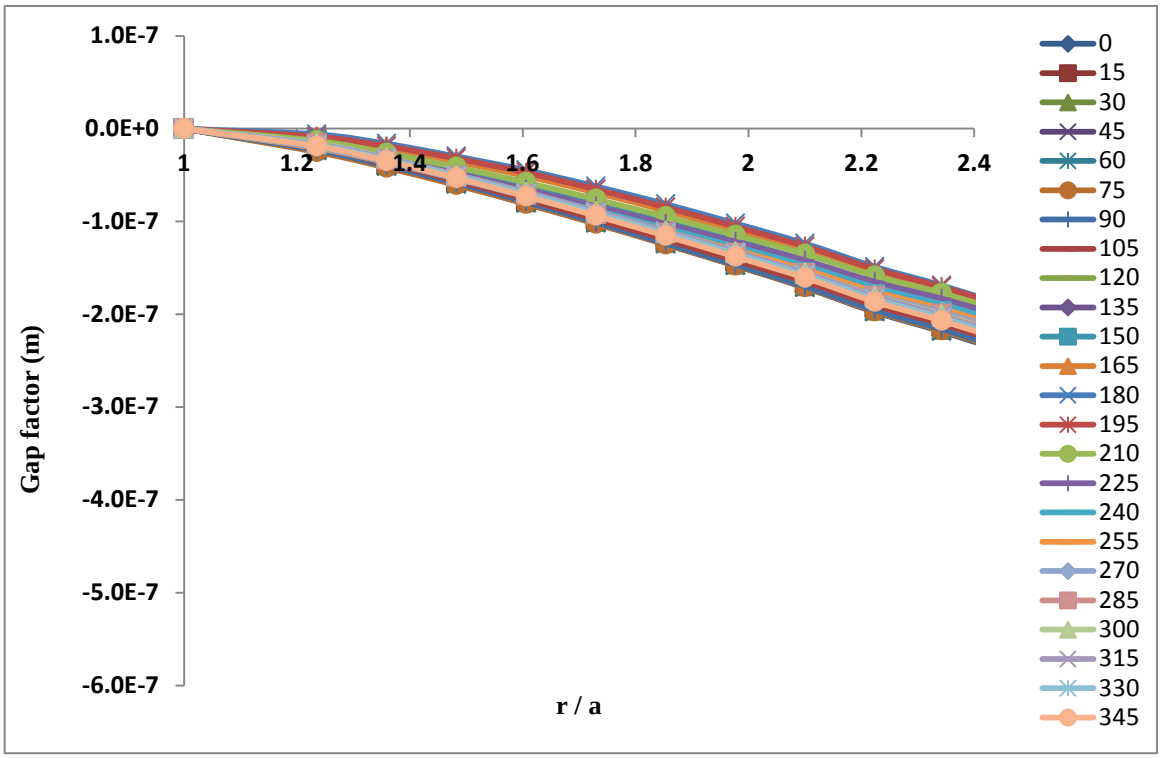

Figure 7.24 Gap factor for point I of 4 mm cup thickness

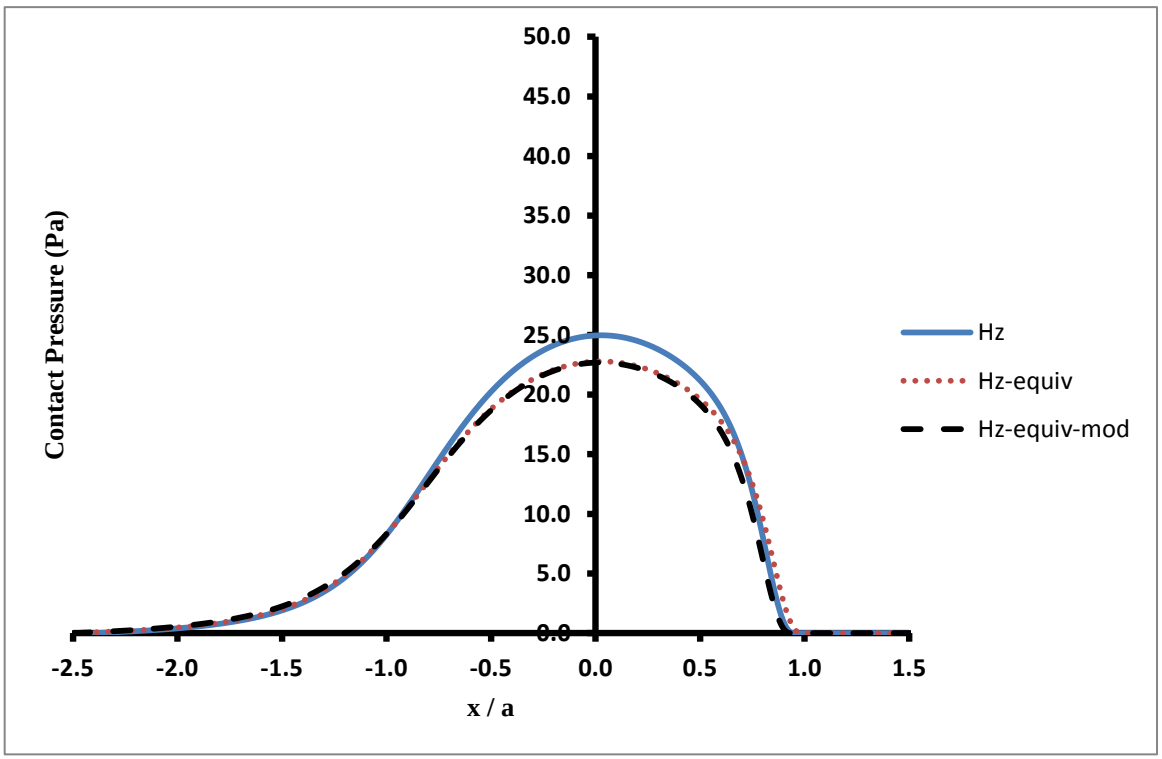

Figure 7.25 Pressure distribution for point I, 4 mm cup thickness, central line in x-direction

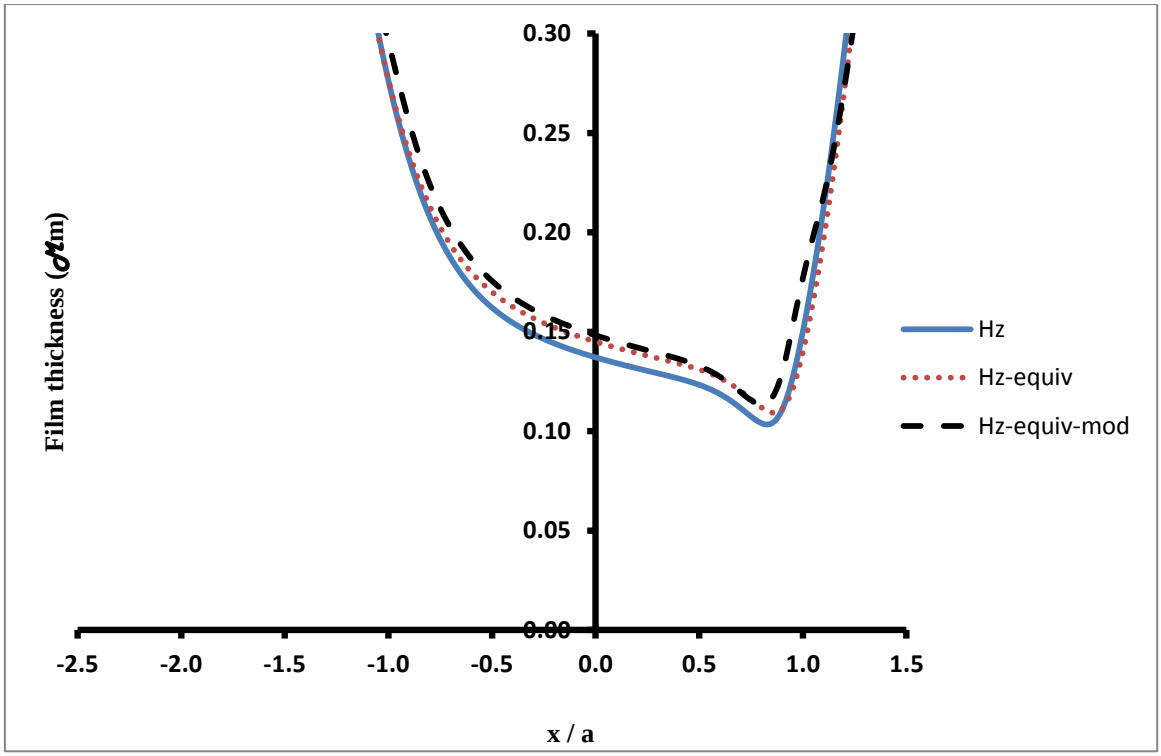

Figure 7.26 Film thickness for point I, 4 mm cup thickness, central line in x-direction

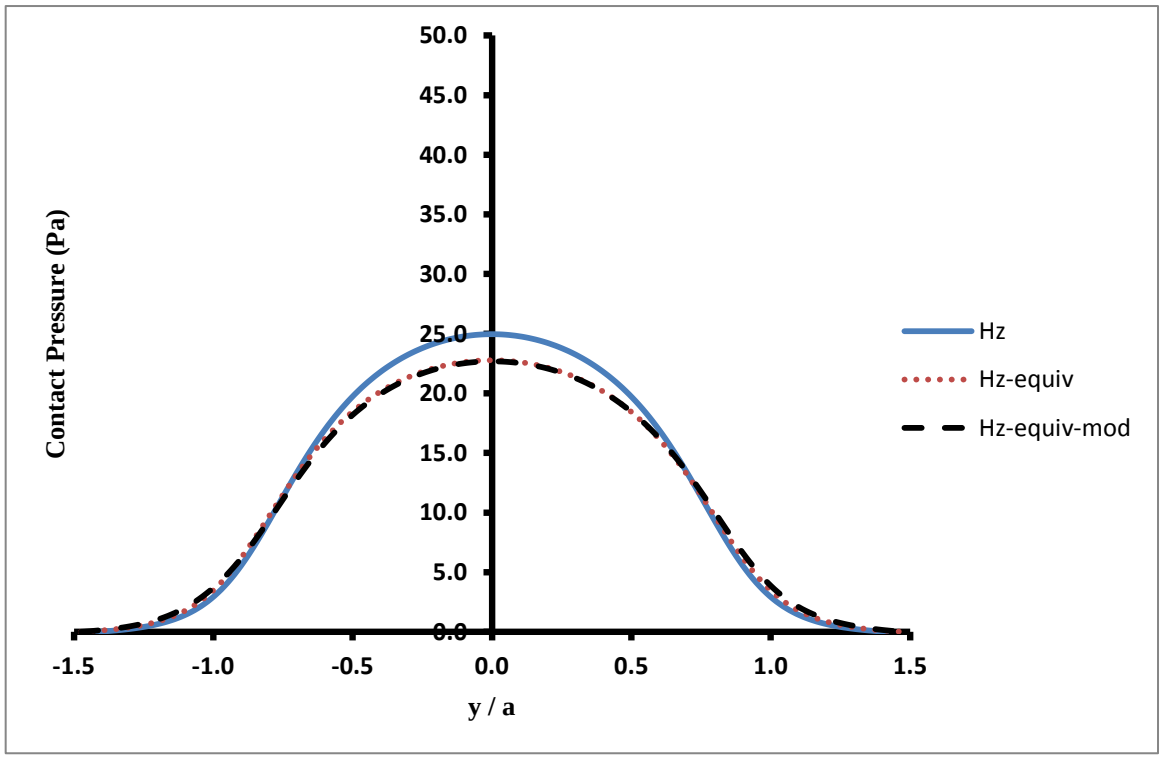

Figure 7.27 Pressure distribution for point I, 4 mm cup thickness, central line in y-direction

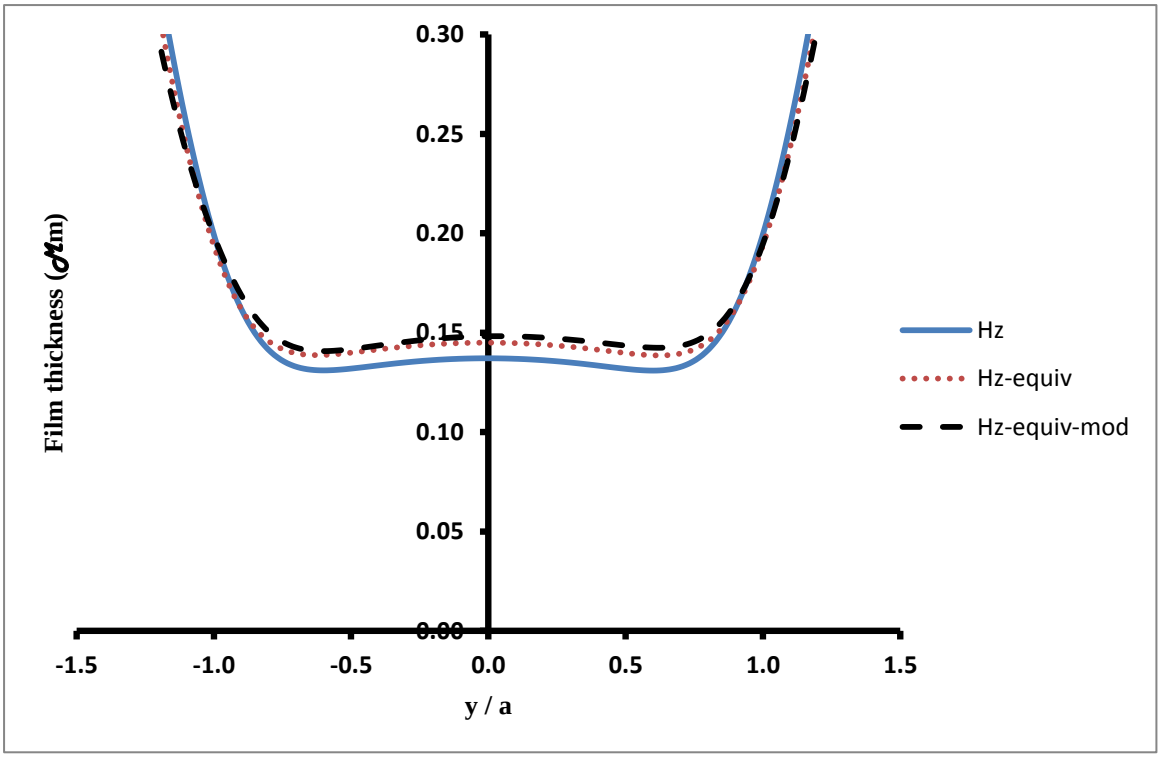

Figure 7.28 Film thickness for point I, 4 mm cup thickness, central line in y-direction

Table 7.2 shows the calculated the Hertzian and the equivalent pressure and the pressure ratio, the Hertzian and the equivalent central film thickness and the film ratio, the Hertzian and the equivalent radius of contact area for the 4 mm cup.

	a_h(mm)	a_{equiv}(mm)	$P_{o(h)}$(MPa)	$P_{o(equiv)}$(MPa)	%	$h_{c(h)}$(μm)	$h_{c(equiv)}$(μm)	%
A	2.852	3.067	31.277	26.192	-16.258	0.177	0.197	11.533
G	3.003	3.295	33.848	27.228	-19.558	0.140	0.160	14.013
H	2.336	2.410	26.471	24.407	-7.797	0.073	0.077	5.068
I	2.293	2.389	24.970	22.779	-8.775	0.137	0.145	5.727

7.5 Detailed EHL results for 6 mm cup thickness

For the results of the 6 mm cup thickness, Figures 7.29 – 7.73, it is possible to categorise the nine contact points into three groups. Firstly, the contact points B, C and D where for these three points the effect of adding the gap factor value to the undeformed geometry can be seen, although there are slight changes in the results relative to the equivalent case. Adding the gap factor to the undeformed geometry with an average value 0.8 μm at r/a =2.4 reduced the film thickness in the inlet zone which made the contact pressure increase to be greater than the pressure produced by the same geometry without the gap factor. Adding the gap factor to the undeformed geometry does not make change to the film thickness within the contact area zone, although it makes the maximum pressure value for the modified model be higher than that for the equivalent model by a maximum of approximately 1.5% considering all cases.

For contact points B, C and D there is a reduction in the maximum contact pressures due to changing the model from the Hertzian to the equivalent model by 16.2%, 16.1% and 14.4%, respectively. This ratio of the variation of the contact pressure comes from the difference between the Hertzian theory which assumed the contacting bodies are semi-infinite bodies, and the changed load and reduced elastic modulus of the equivalent Hertzian contact which replaces the contact of the real model with a specific cup thickness, 6mm in this case. It is expected that lower pressure ratios can be found with increasing the cup thickness and this will be shown in the next sections. In addition to the reduction in the contact pressure there is an increase in the

radius of the contact area by 6.9%, 7.1% and 8.3% for contact points B, C and D respectively.

Secondly, the contact points H and I where there are no differences between the three cases, Hertzian, equivalent and the modified, and the results of the contact pressures and the film thicknesses are similar. Two factors are expected to be the reason for this similarity in the results. The first factor is the low load measured in the hip joint, 295 – 312 N, for these two contact points which represents no more than 40% of the body weight of patient and this can be explained by examining the values of wt/a_h in Table 7.1 which shows values of 2.6 for these two cases. In these circumstances the cup behaves as a semi-infinite body and the equivalent model is essentially the same as Hertzian. Therefore, there is no difference between the equivalent model from one side and the Hertzian model on another side. The second factor is low value of the average gap factor where it is about 0.075 μm at r/a = 2.4 for these two points and this factor is the reason for the similarity between the equivalent and modified models.

The third group of the contact points, A, E, F and G where the average value of the gap factor is 0.18 – 0.55 μm. These values are not high enough to make changes between the equivalent and the modified cases. While there are differences between them and the Hertzian case due to changing the model from the Hertzian to the equivalent. The variation ratios of the central film thicknesses and the maximum contact pressures between the Hertzian case and the equivalent case for the nine contact points are shown in Table 7.3.

EHL results for 6 mm Cup thickness

Contact Point A

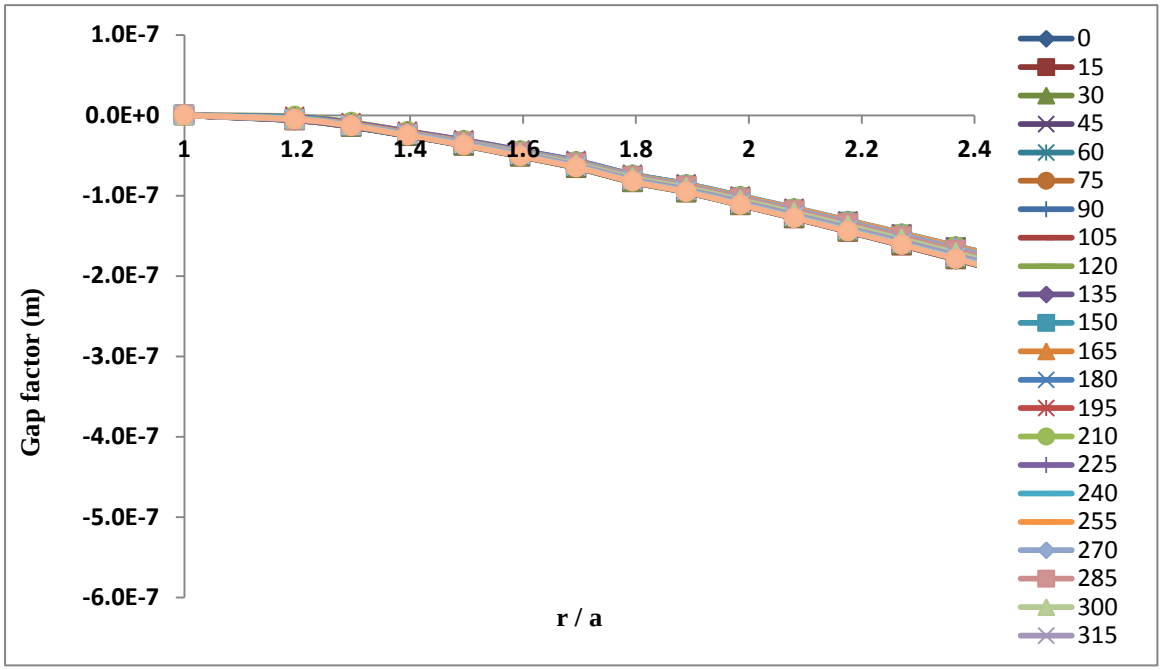

Figure 7.29 Gap factor for point A of 6 mm cup thickness

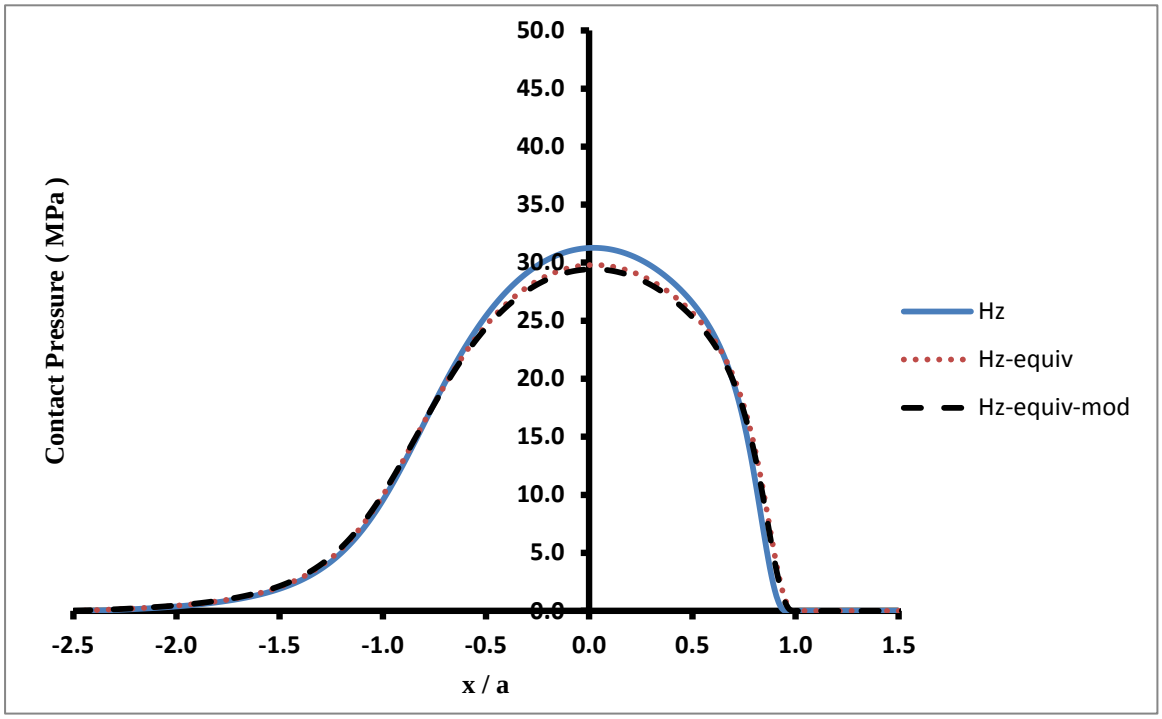

Figure 7.30 Pressure distribution for point A, 6 mm cup thickness, central line in x-direction

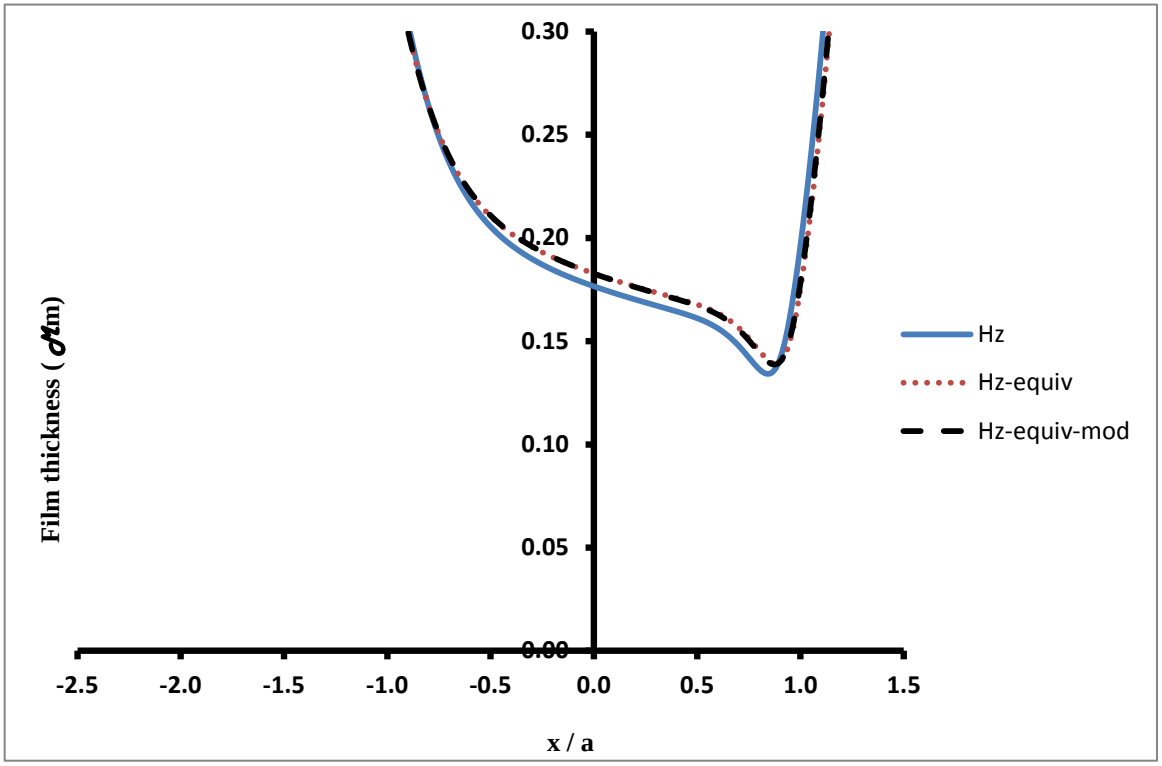

Figure 7.31 Film thickness for point A, 6 mm cup thickness, central line in x-direction

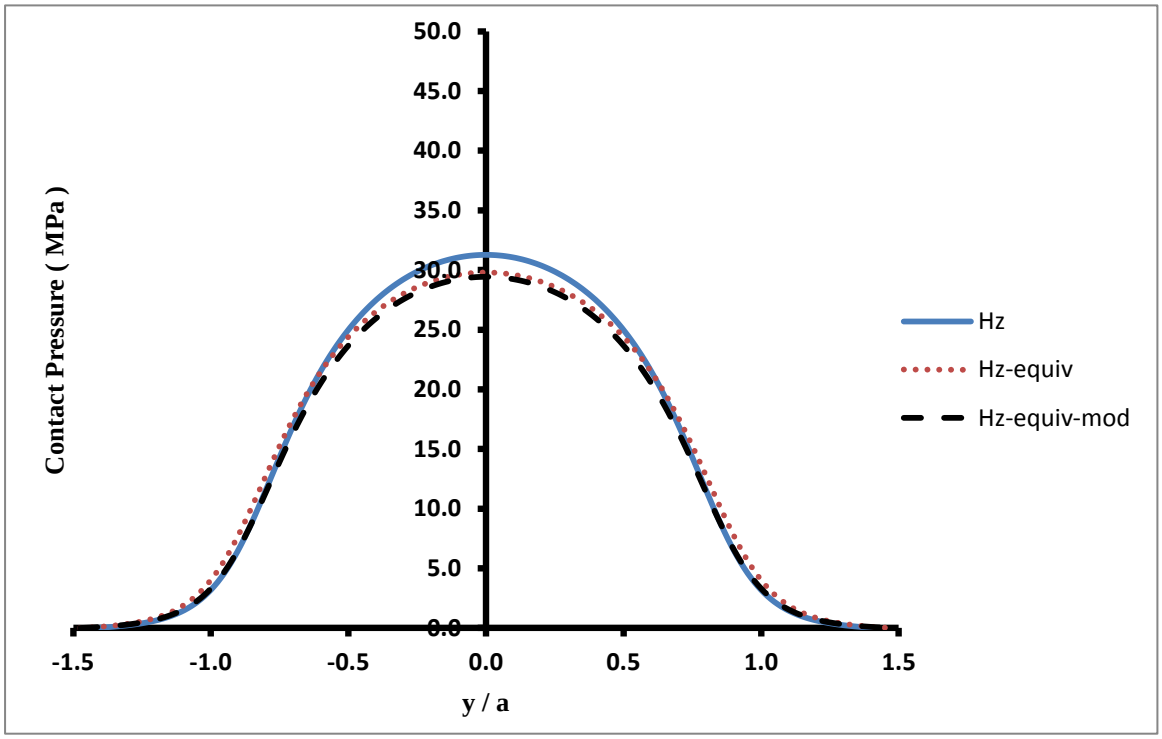

Figure 7.32 Pressure distribution for point A, 6 mm cup thickness, central line in y-direction

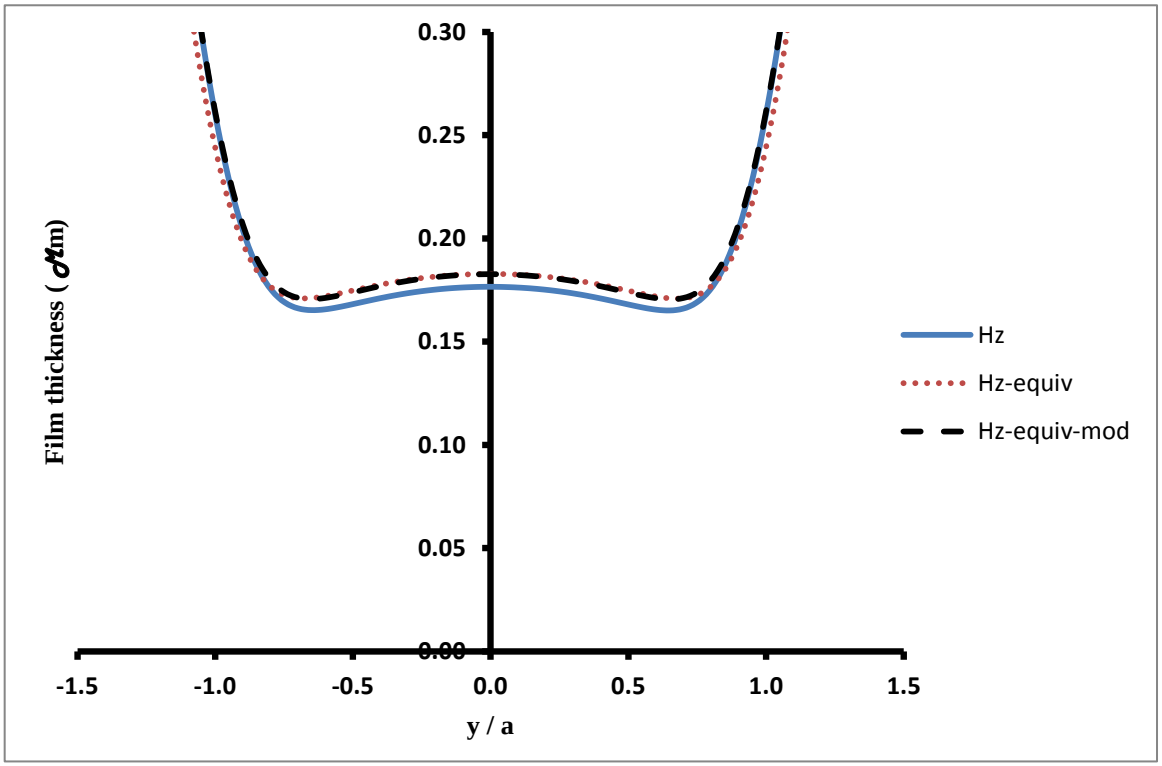

Figure 7.33 Film thickness for point A, 6 mm cup thickness, central line in y-direction

Contact Point B

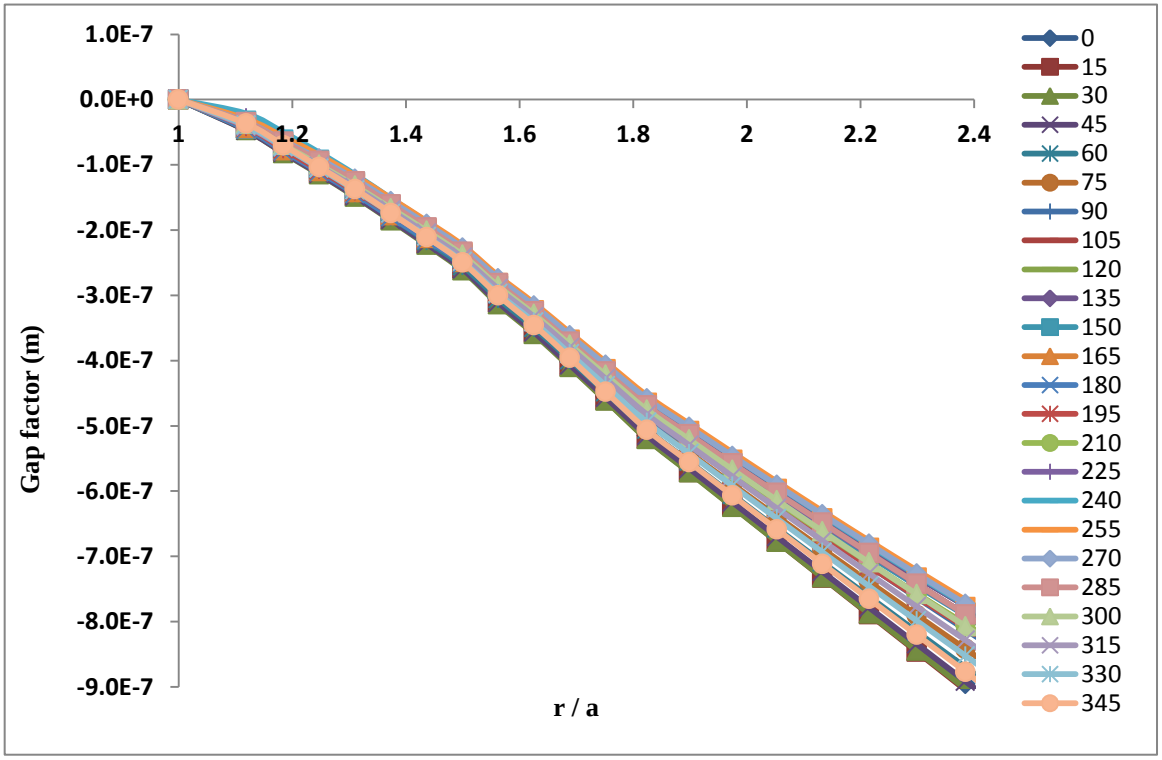

Figure 7.34 Gap factor for point B of 6 mm cup thickness

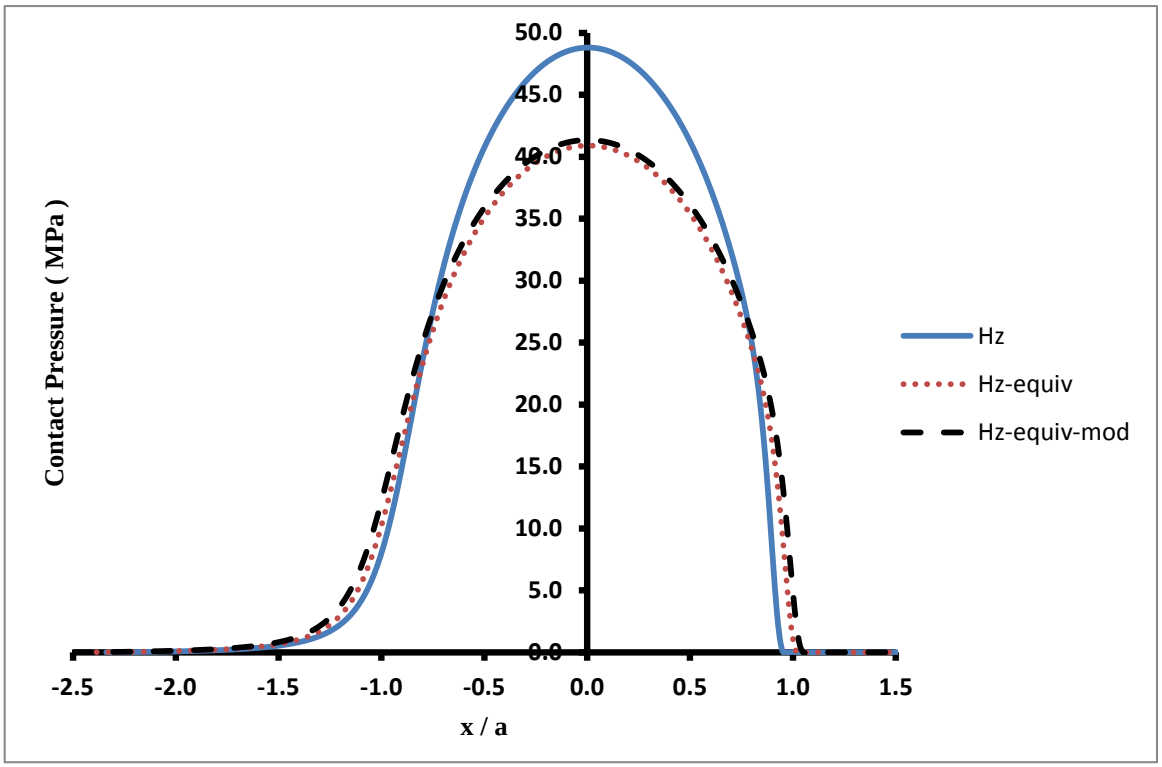

Figure 7.35 Pressure distribution for point B, 6 mm cup thickness, central line in x-direction

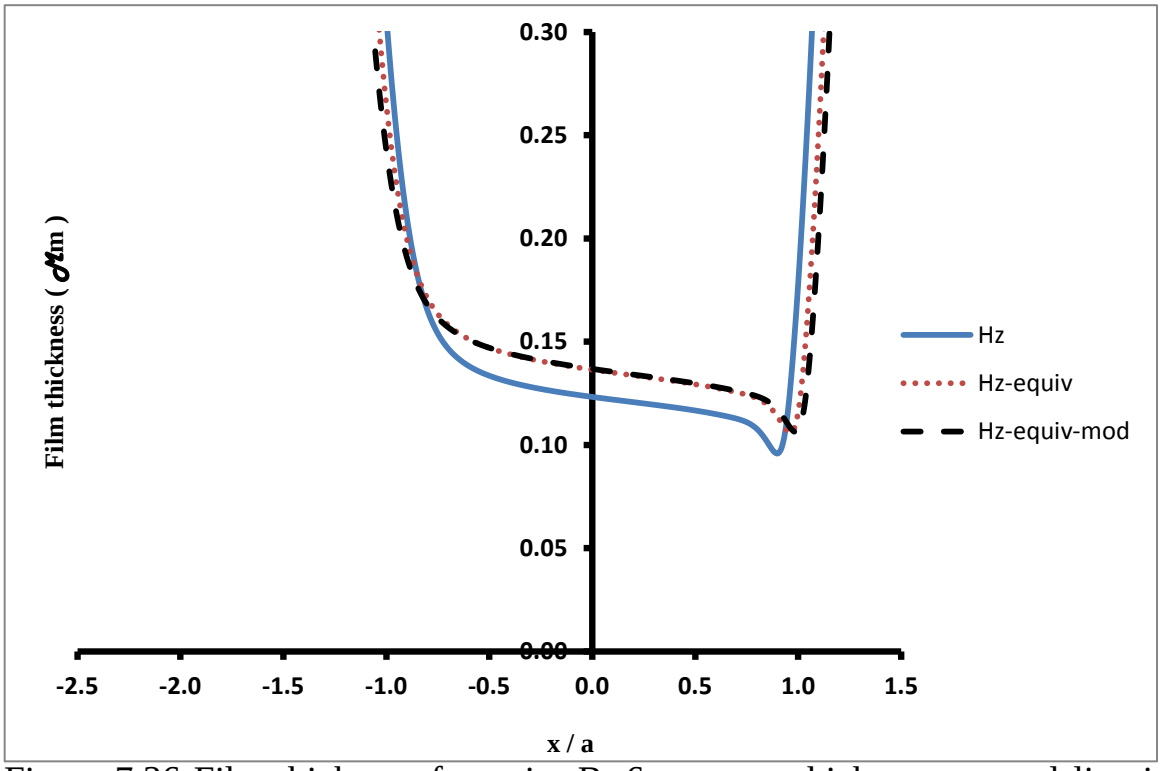

Figure 7.36 Film thickness for point B, 6 mm cup thickness, central line in x-direction

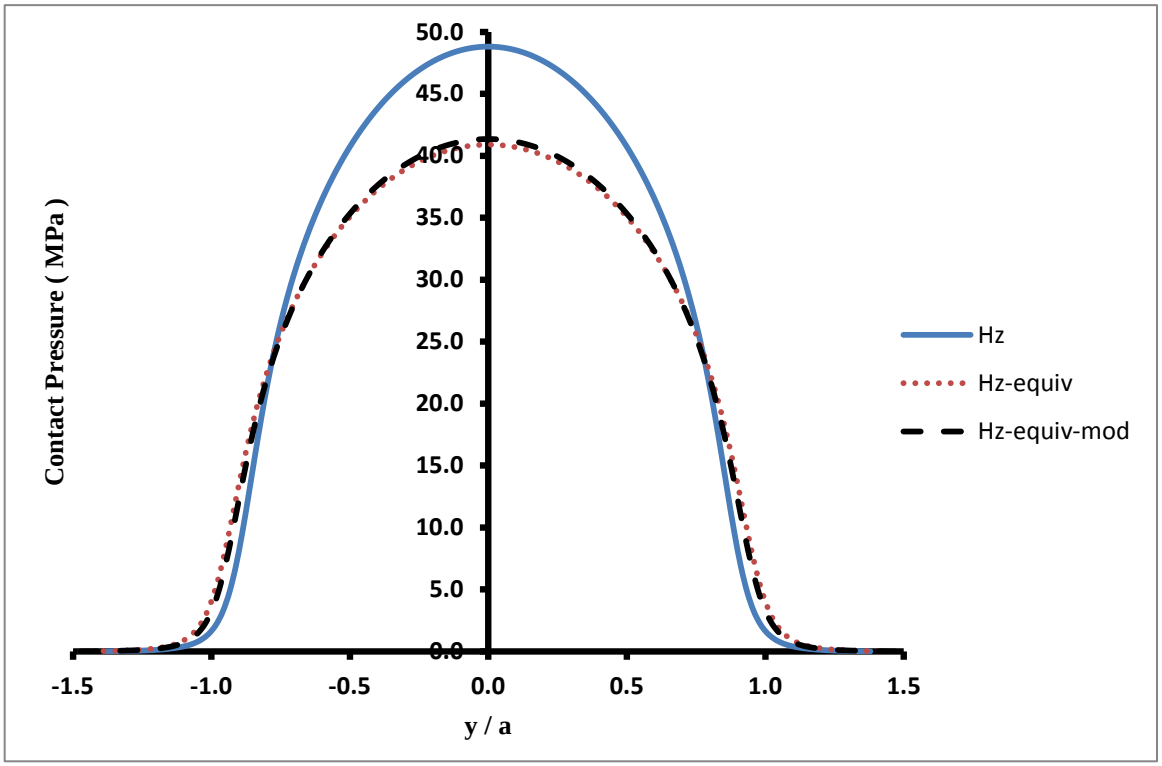

Figure 7.37 Pressure distribution for point B, 6 mm cup thickness, central line in y-direction

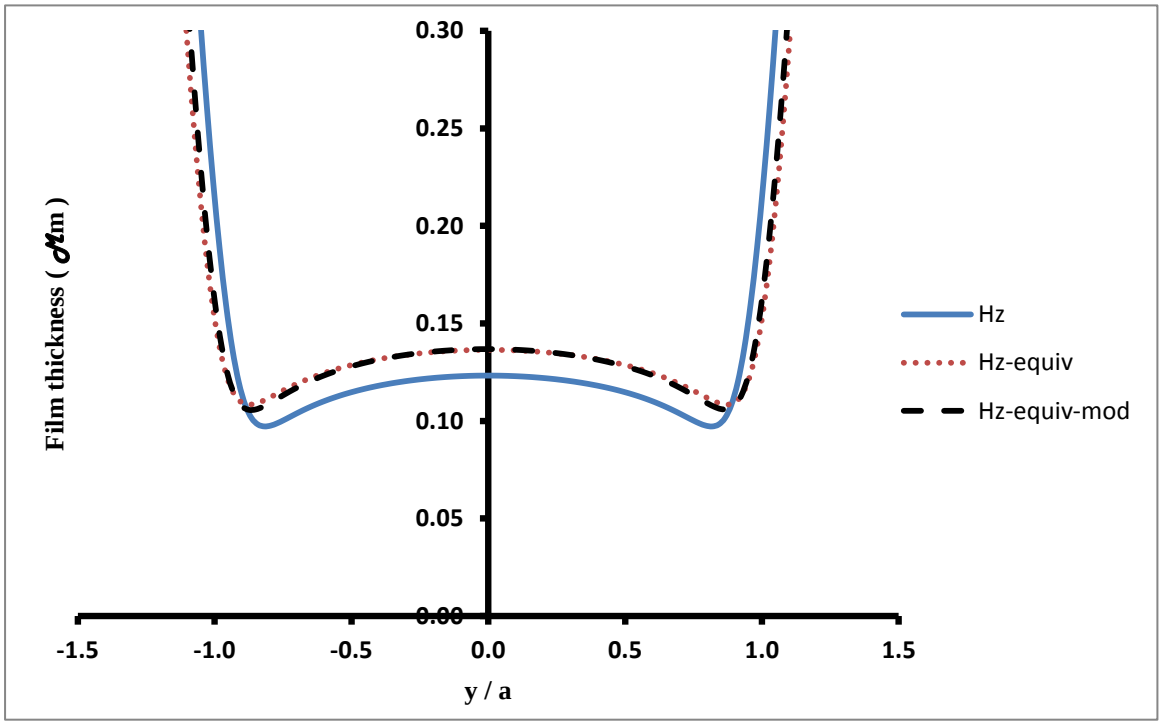

Figure 7.38 Film thickness for point B, 6 mm cup thickness, central line in y-direction

Contact Point C

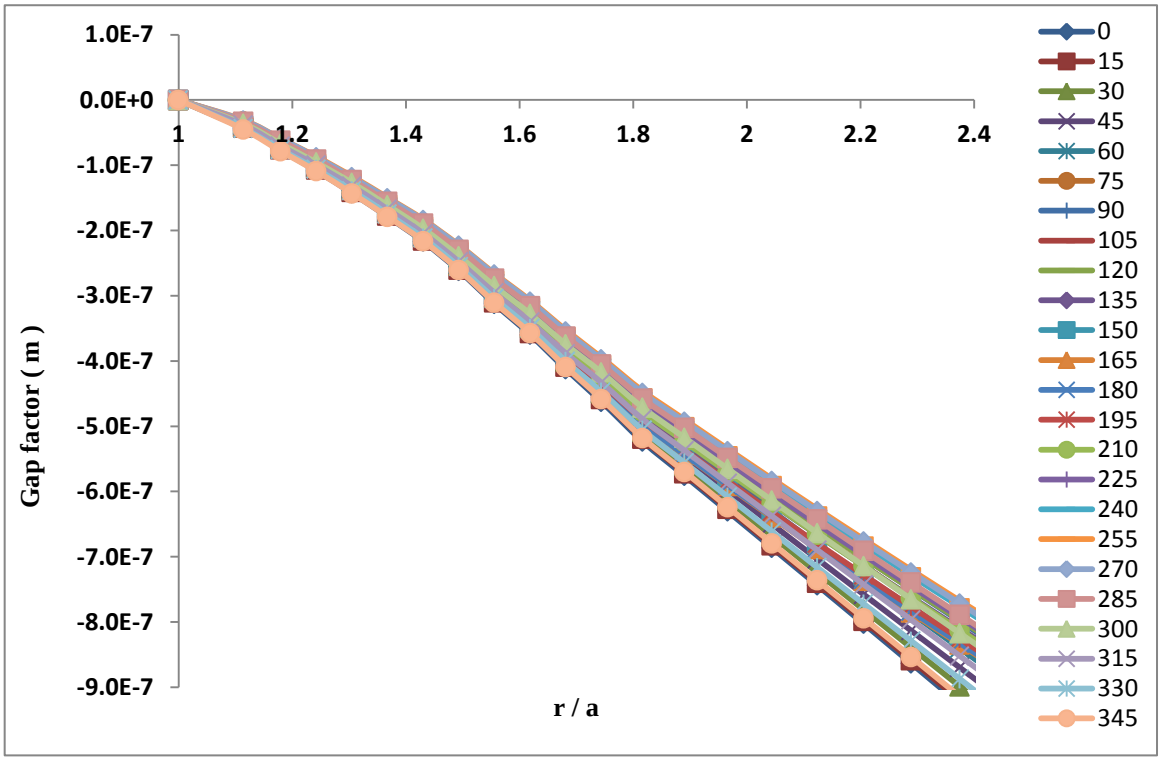

Figure 7.39 Gap factor for point C of 6 mm cup thickness

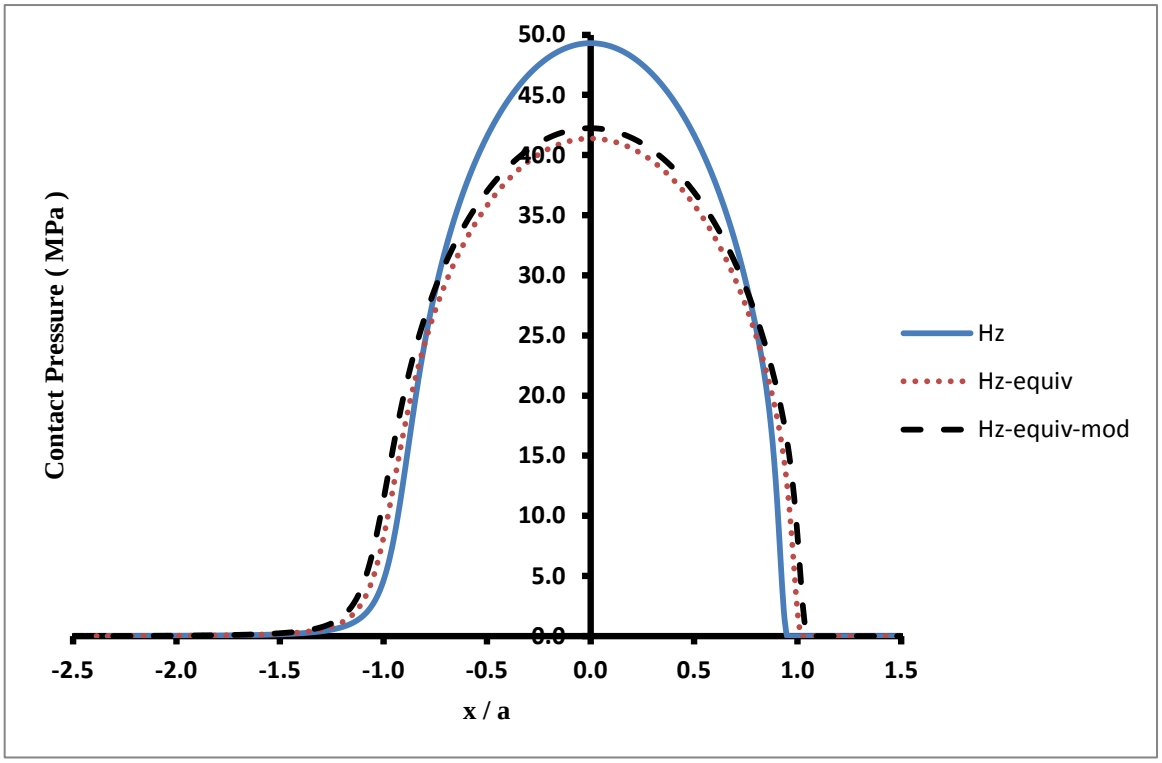

Figure 7.40 Pressure distribution for point C, 6 mm cup thickness, central line in x-direction

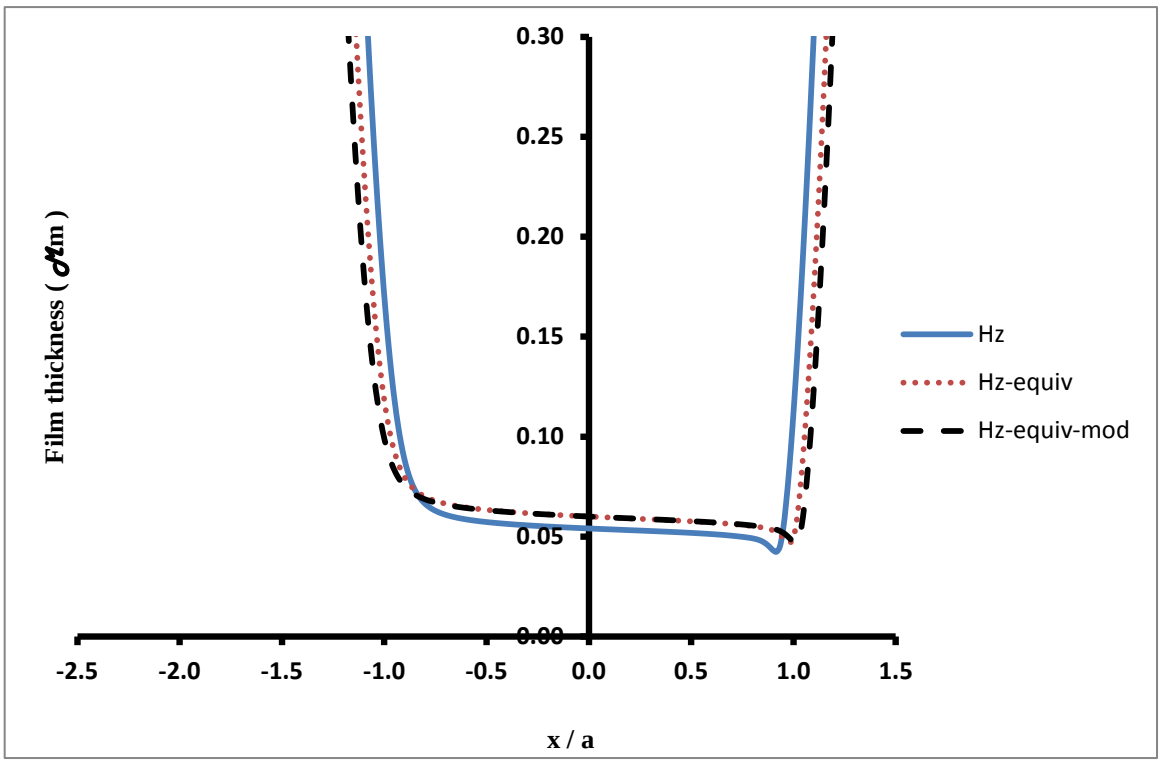

Figure 7.41 Film thickness for point C, 6 mm cup thickness, central line in x-direction

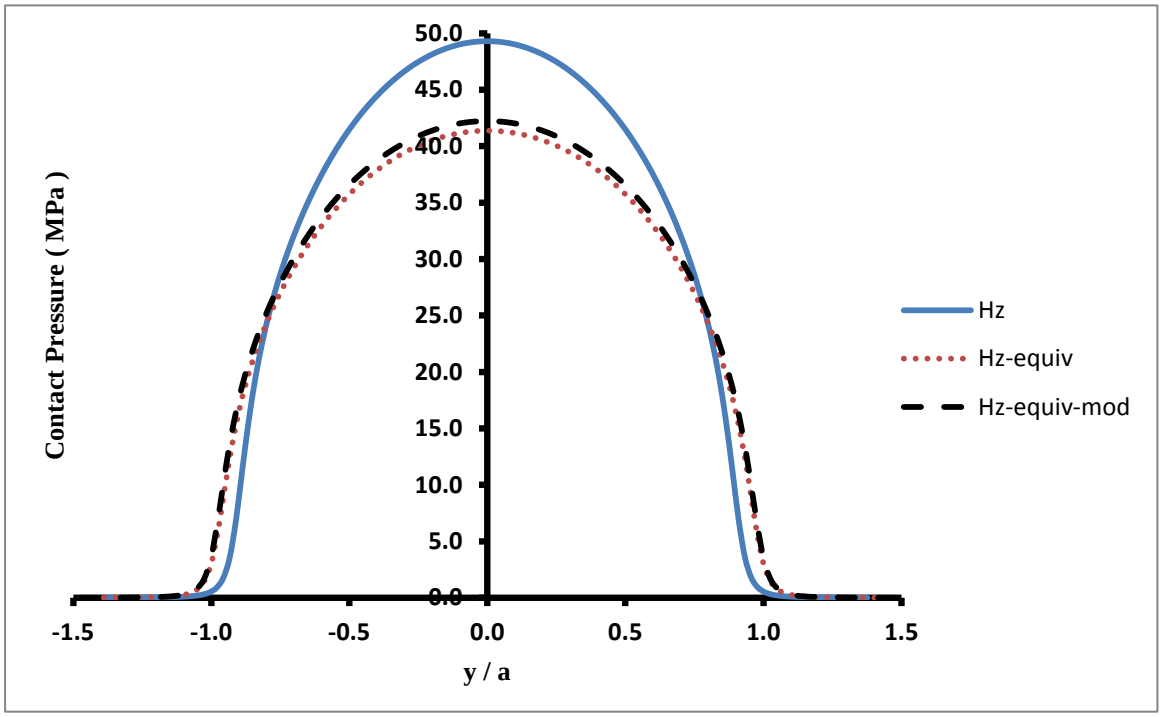

Figure 7.42 Pressure distribution for point C, 6 mm cup thickness, central line in y-direction

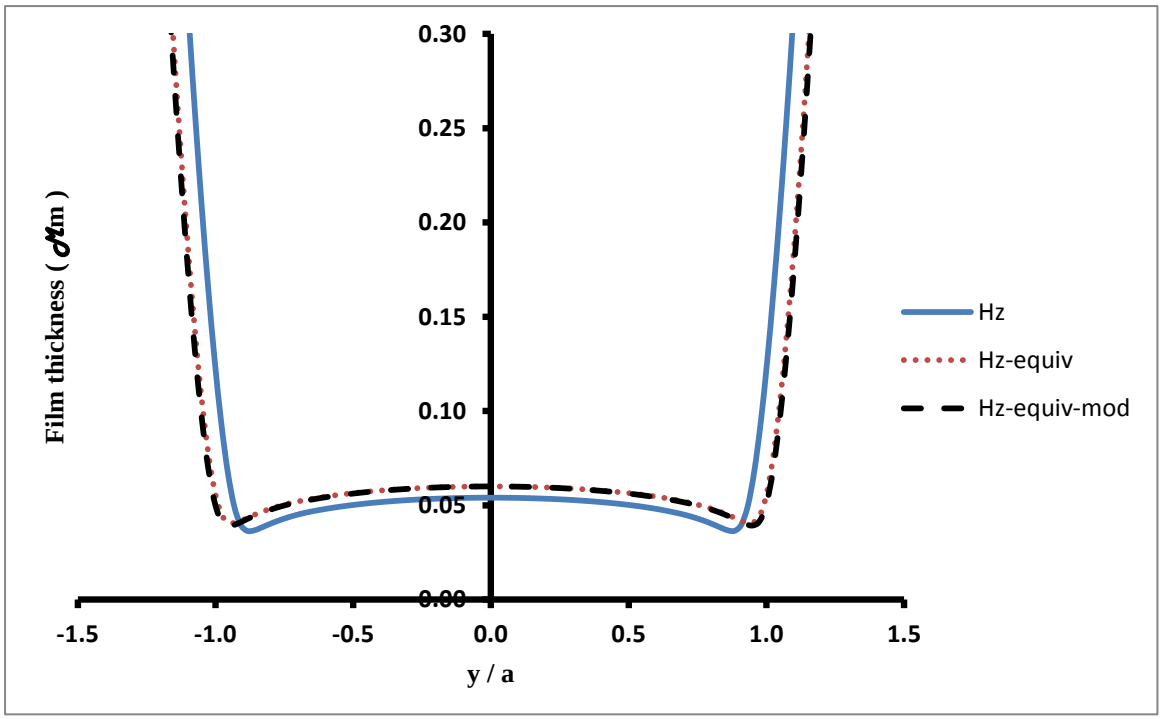

Figure 7.43 Film thickness for point C, 6 mm cup thickness, central line in y-direction

Contact Point D

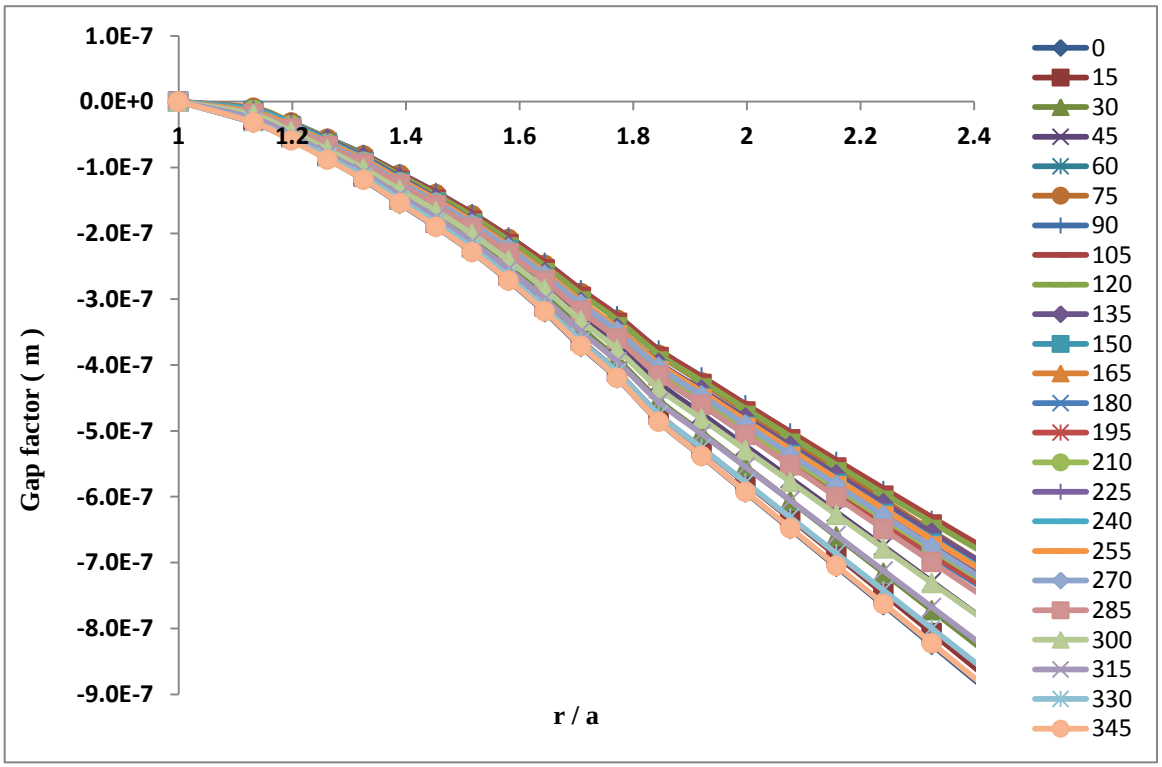

Figure 7.44 Gap factor for point D of 6 mm cup thickness

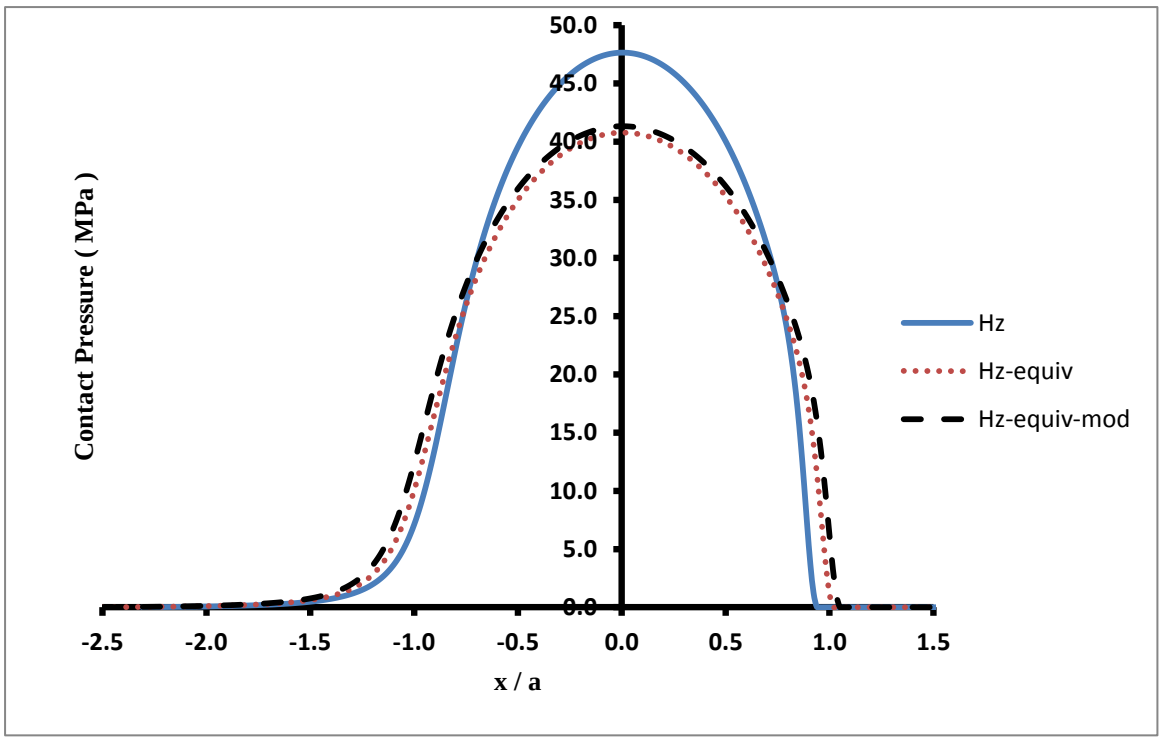

Figure 7.45 Pressure distribution for point D, 6 mm cup thickness, central line in x-direction

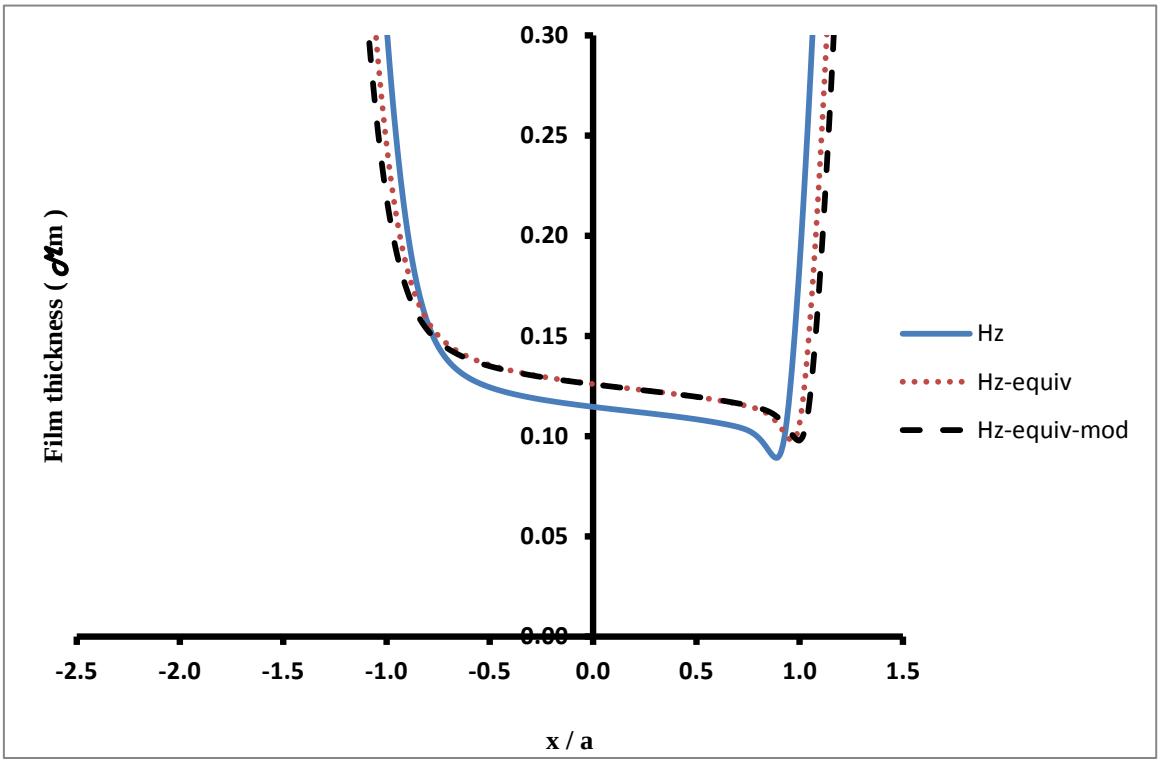

Figure 7.46 Film thickness for point D, 6 mm cup thickness, central line in x-direction

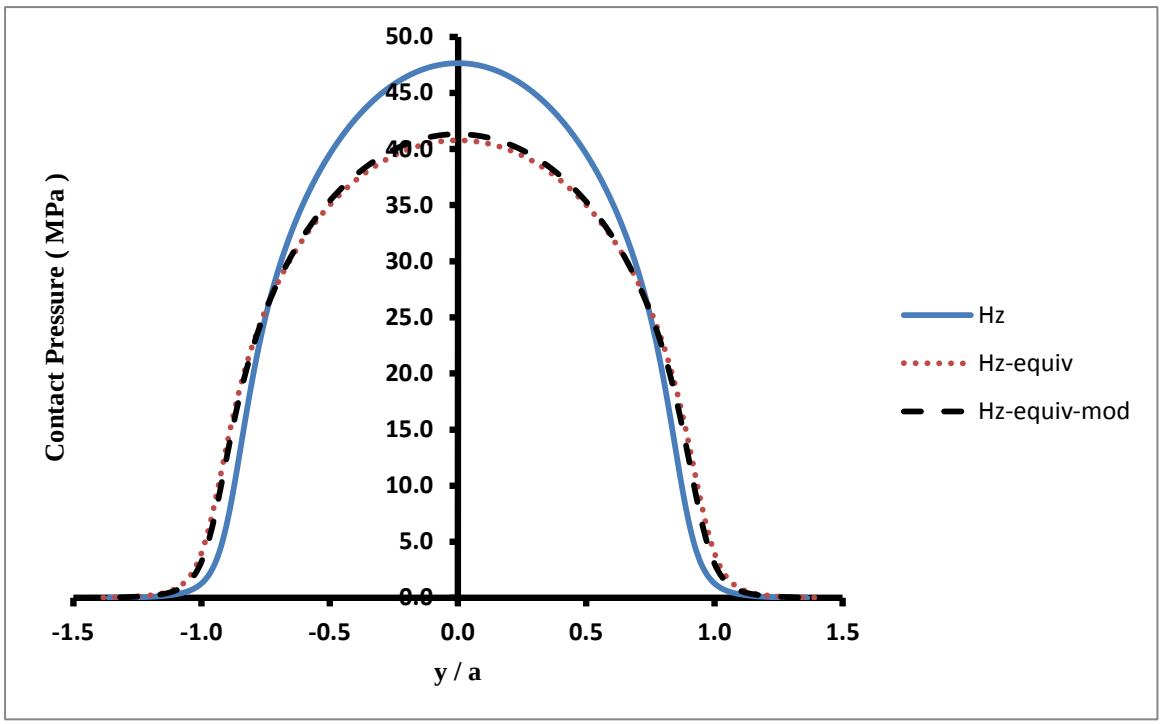

Figure 7.47 Pressure distribution for point D, 6 mm cup thickness, central line in y-direction

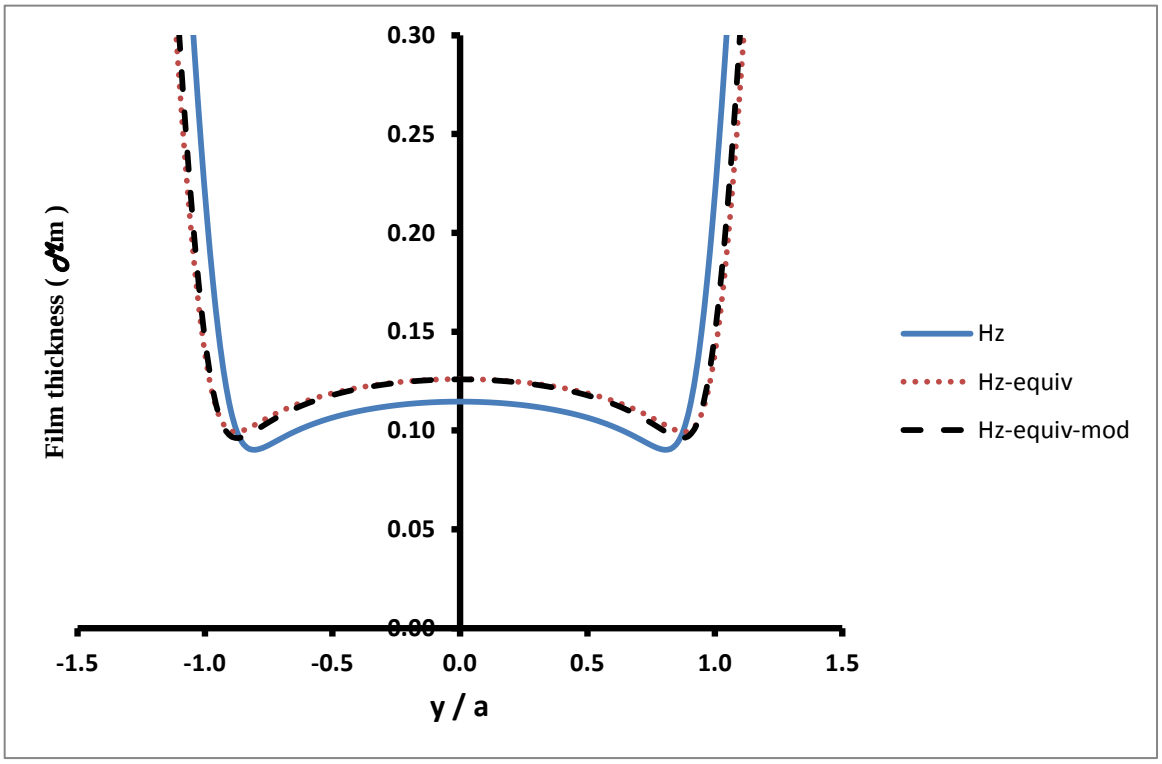

Figure 7.48 Film thickness for point D, 6 mm cup thickness, central line in y-direction

Contact Point E

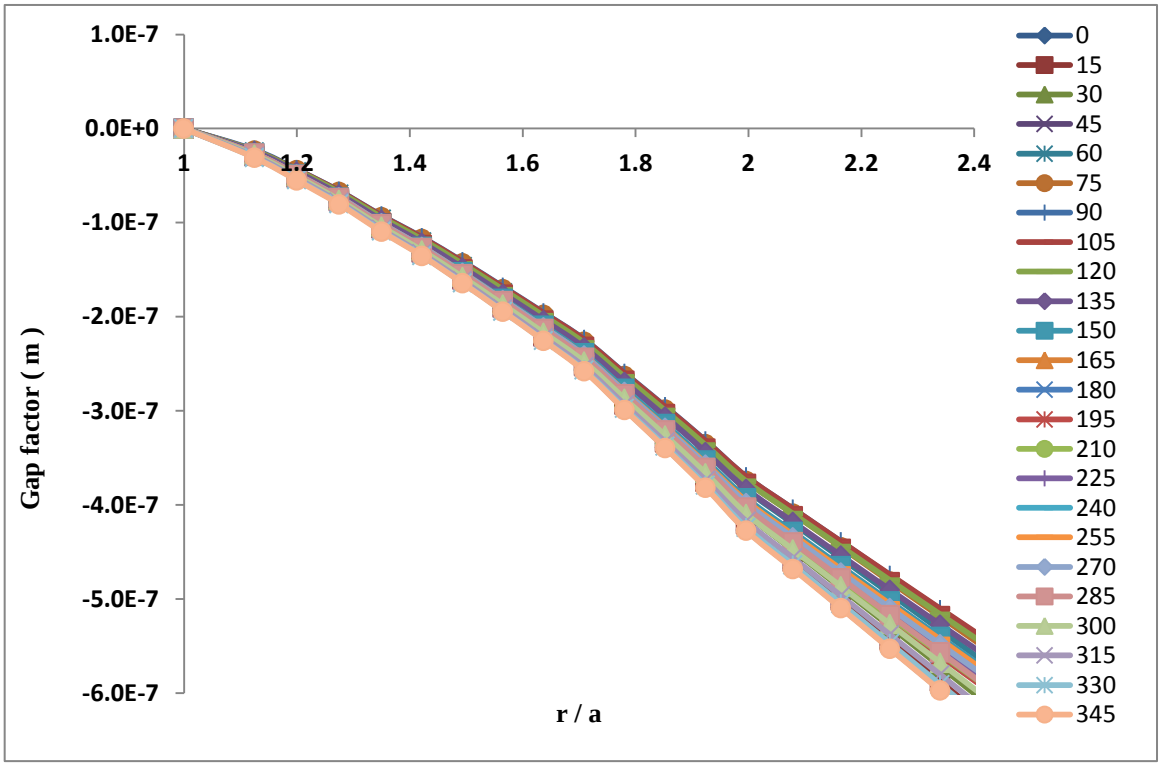

Figure 7.49 Gap factor for point E of 6 mm cup thickness

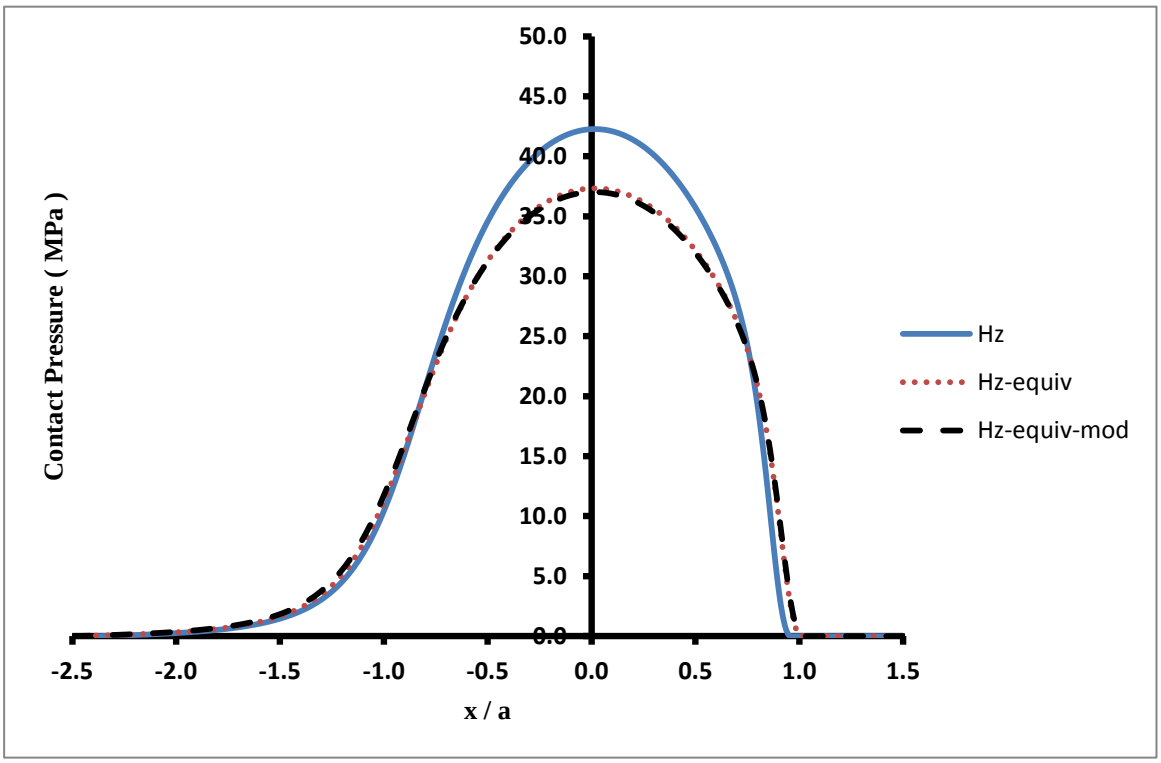

Figure 7.50 Pressure distribution for point E, 6 mm cup thickness, central line in x-direction

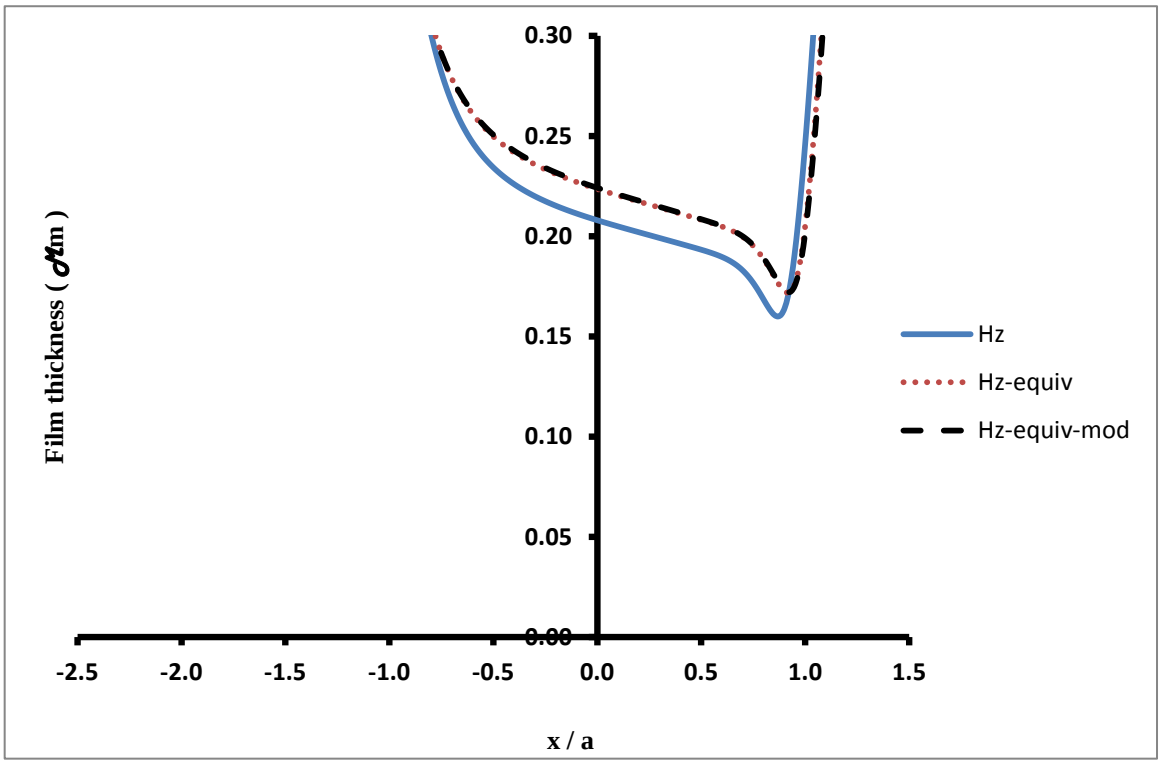

Figure 7.51 Film thickness for point E, 6 mm cup thickness, central line in x-direction

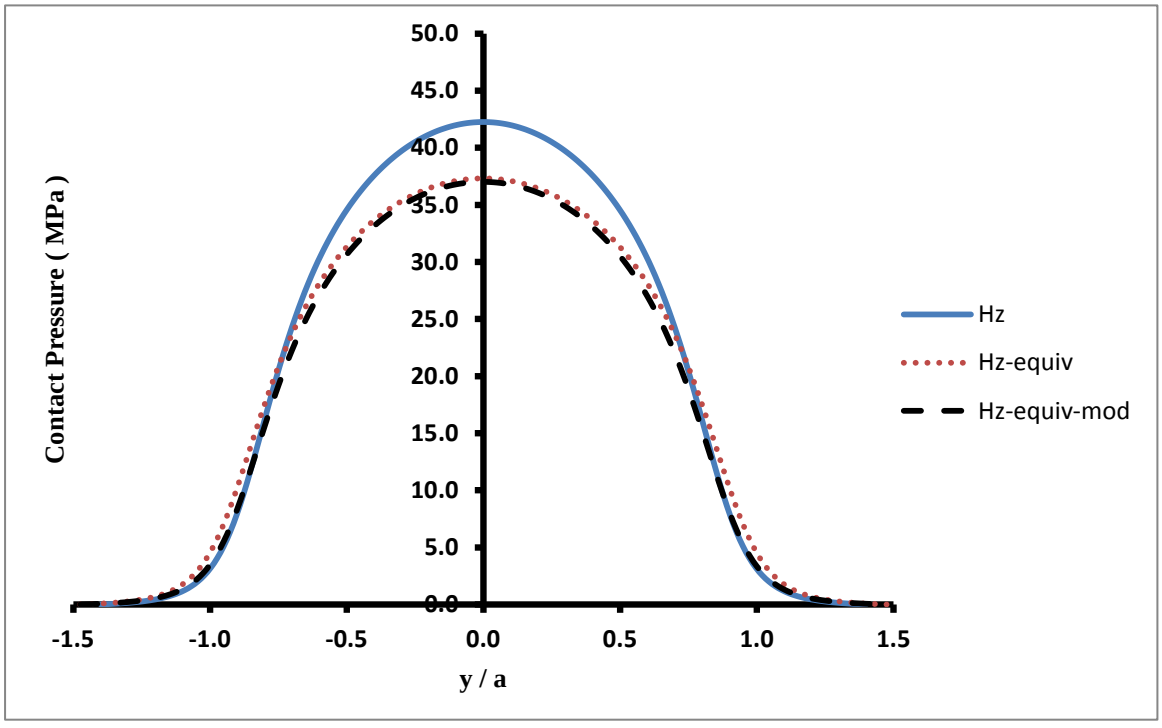

Figure 7.52 Pressure distribution for point E, 6 mm cup thickness, central line in y-direction

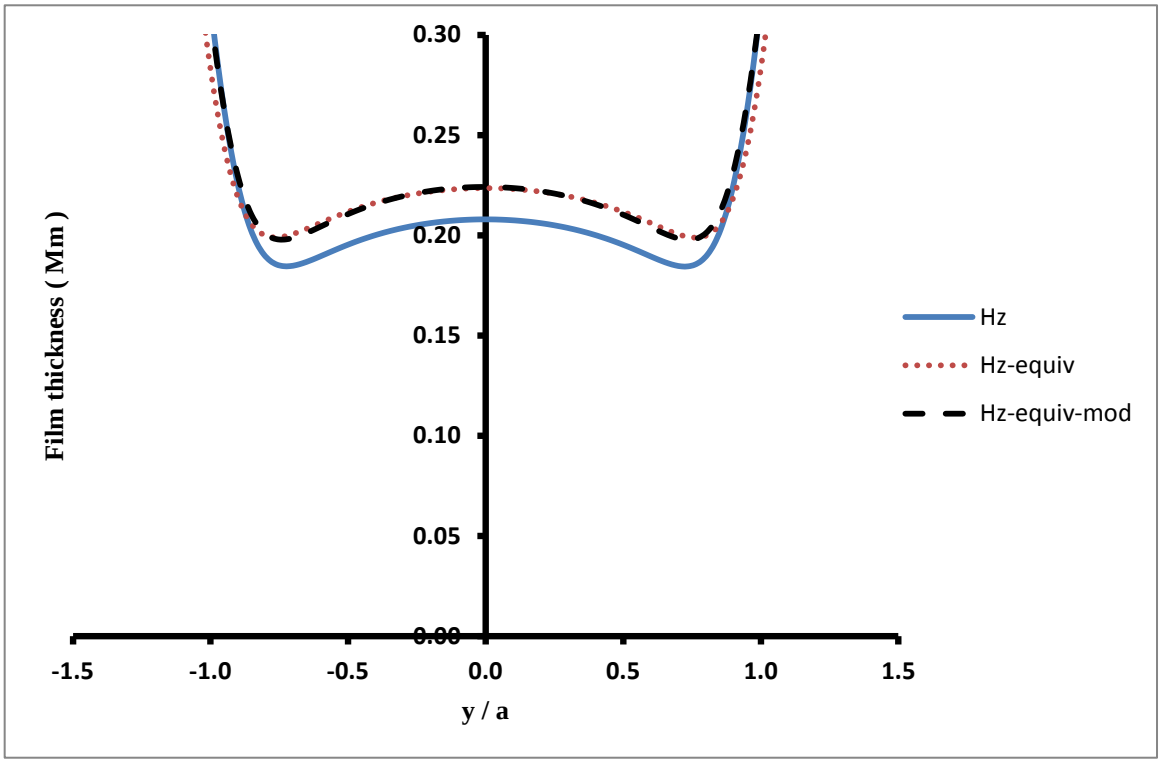

Figure 7.53 Film thickness for point E, 6 mm cup thickness, central line in y-direction

Contact Point F

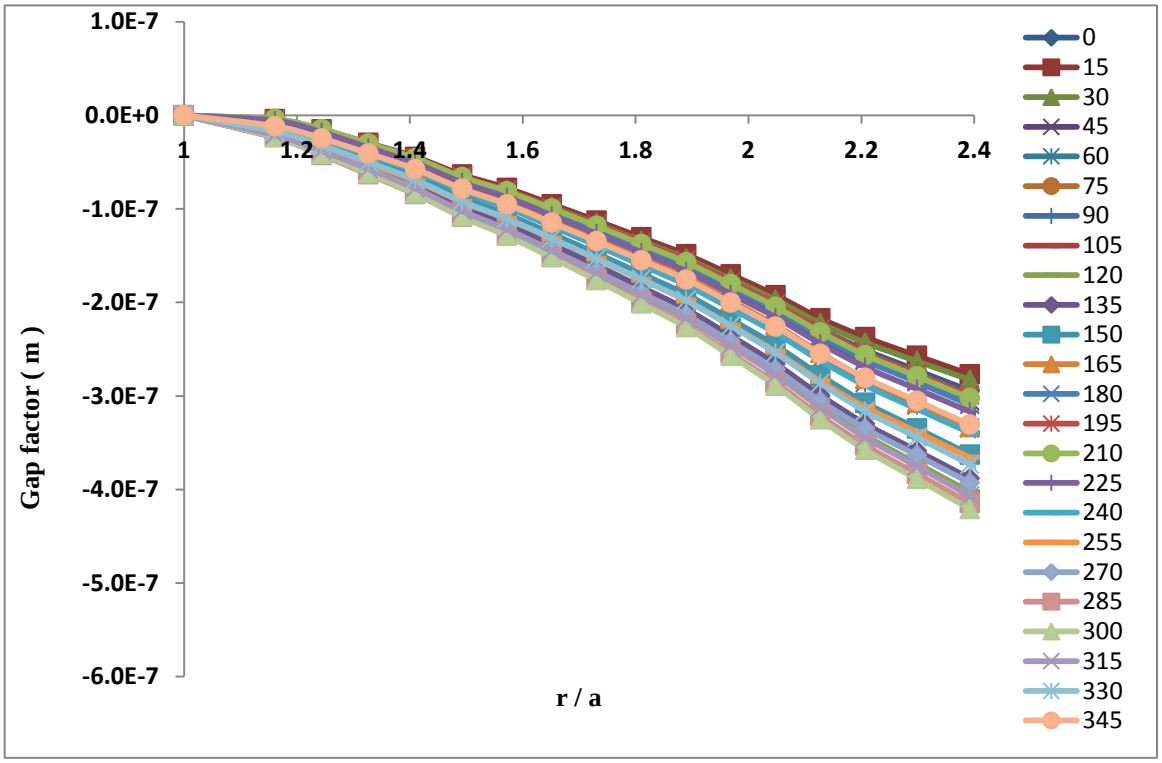

Figure 7.54 Gap factor for point F of 6 mm cup thickness

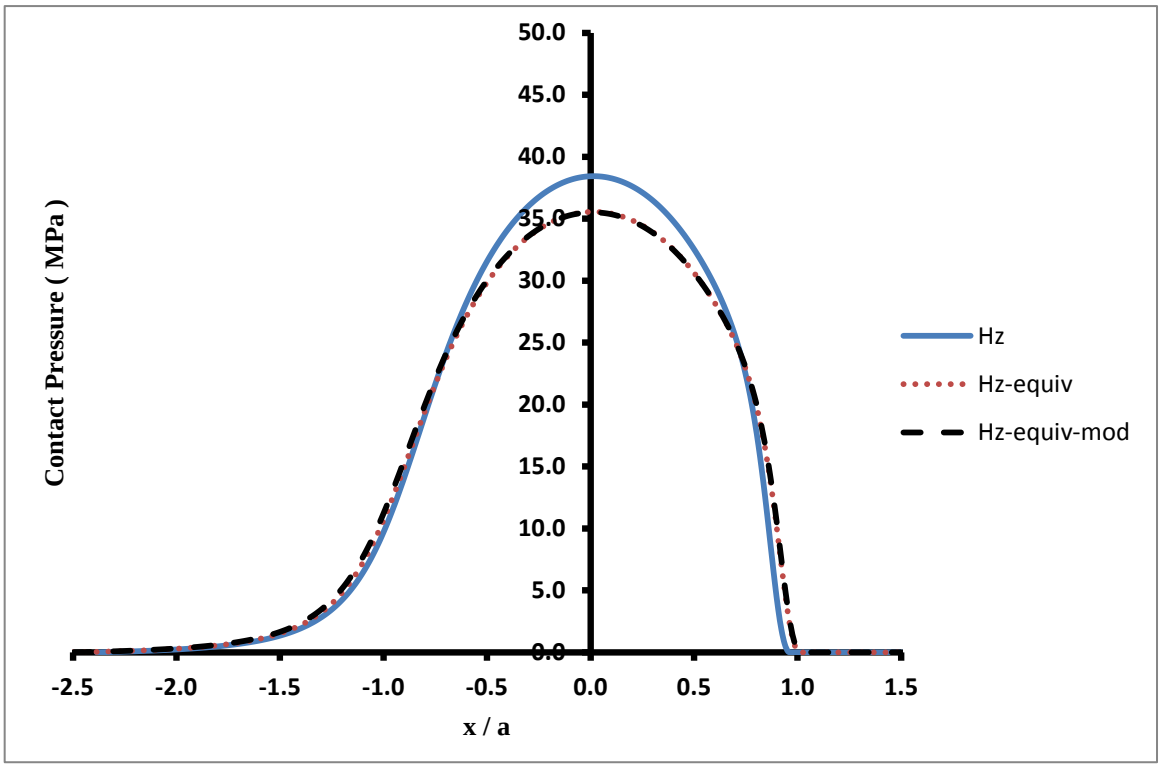

Figure 7.55 Pressure distribution for point F, 6 mm cup thickness, central line in x-direction

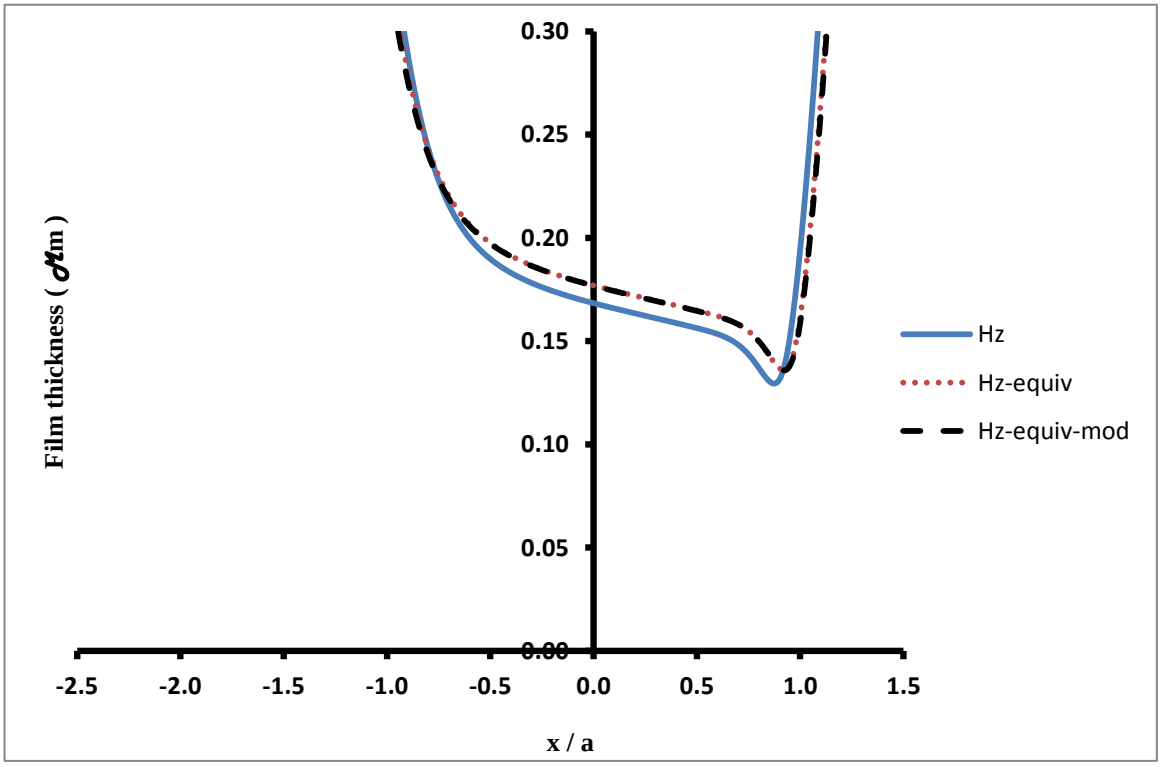

Figure 7.56 Film thickness for point F, 6 mm cup thickness, central line in x-direction

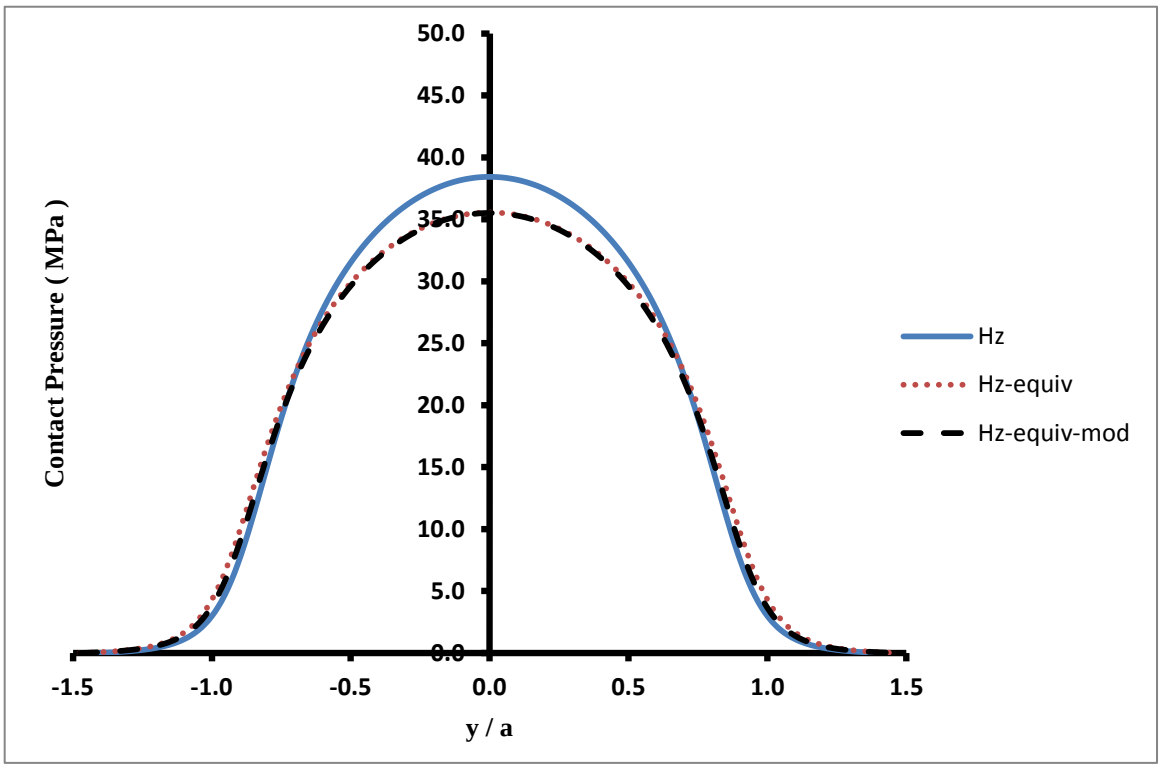

Figure 7.57 Pressure distribution for point F, 6 mm cup thickness, central line in y-direction

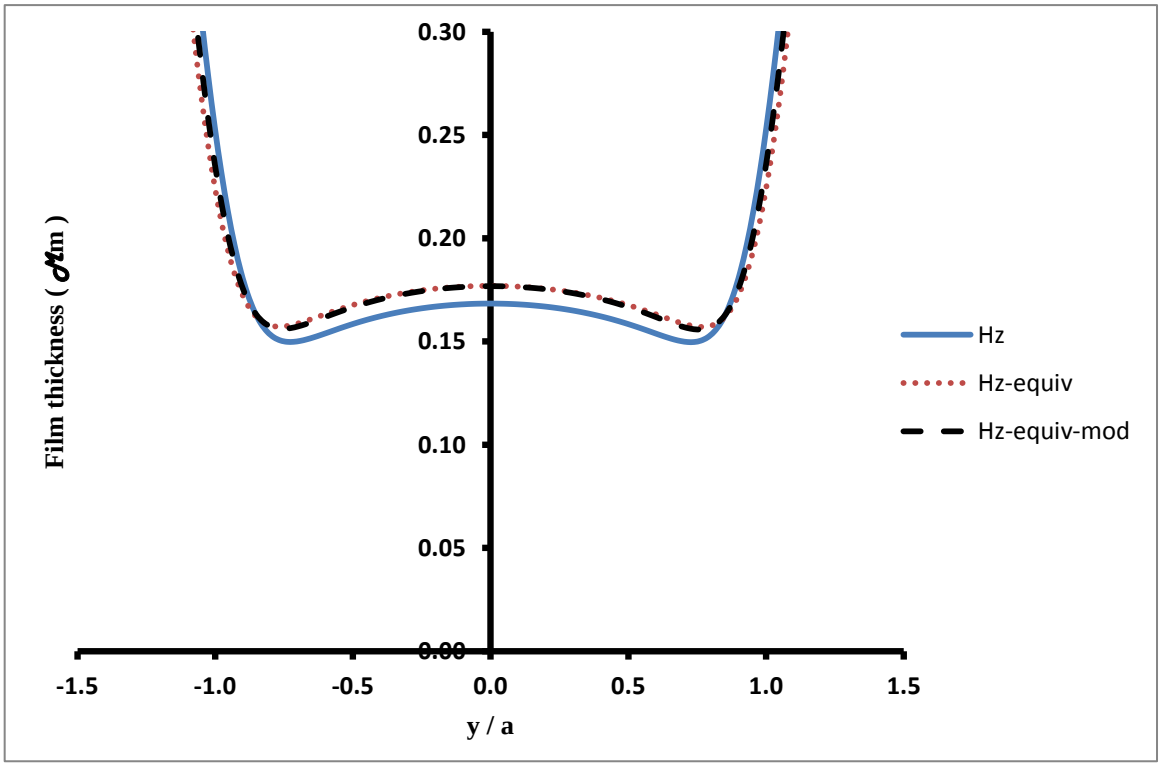

Figure 7.58 Film thickness for point F, 6 mm cup thickness, central line in y-direction

Contact Point G

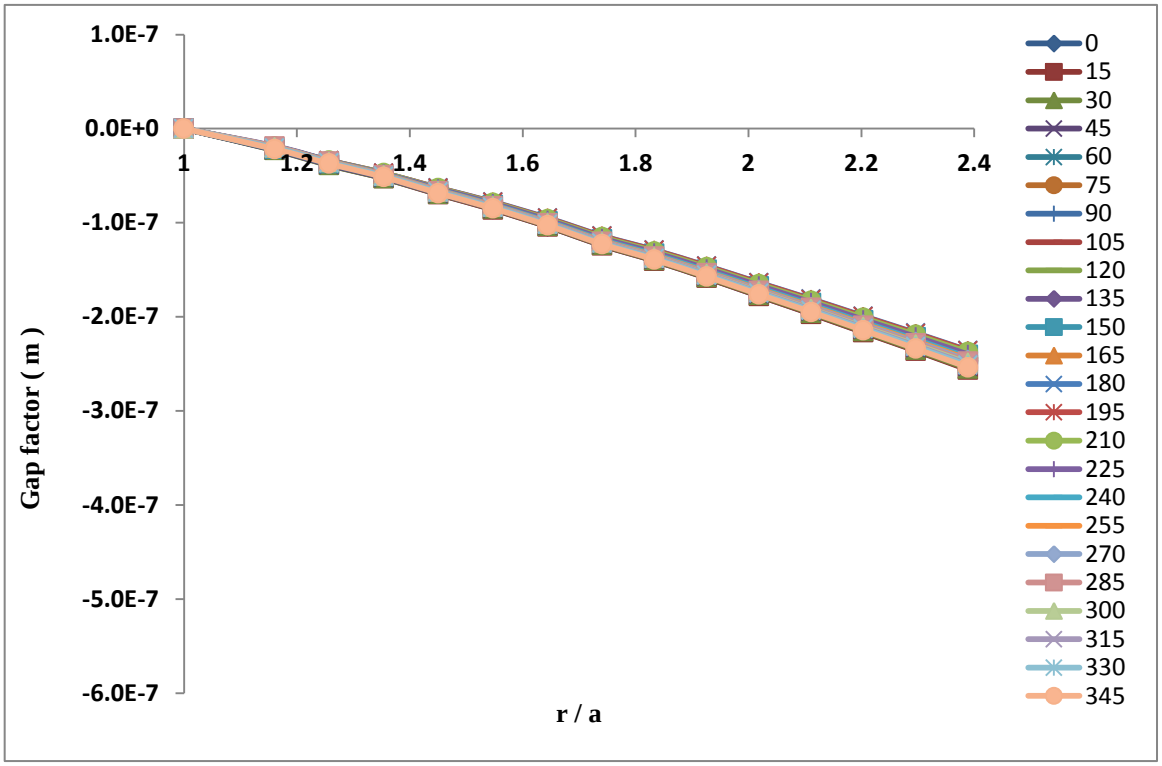

Figure 7.59 Gap factor for point G of 6 mm cup thickness

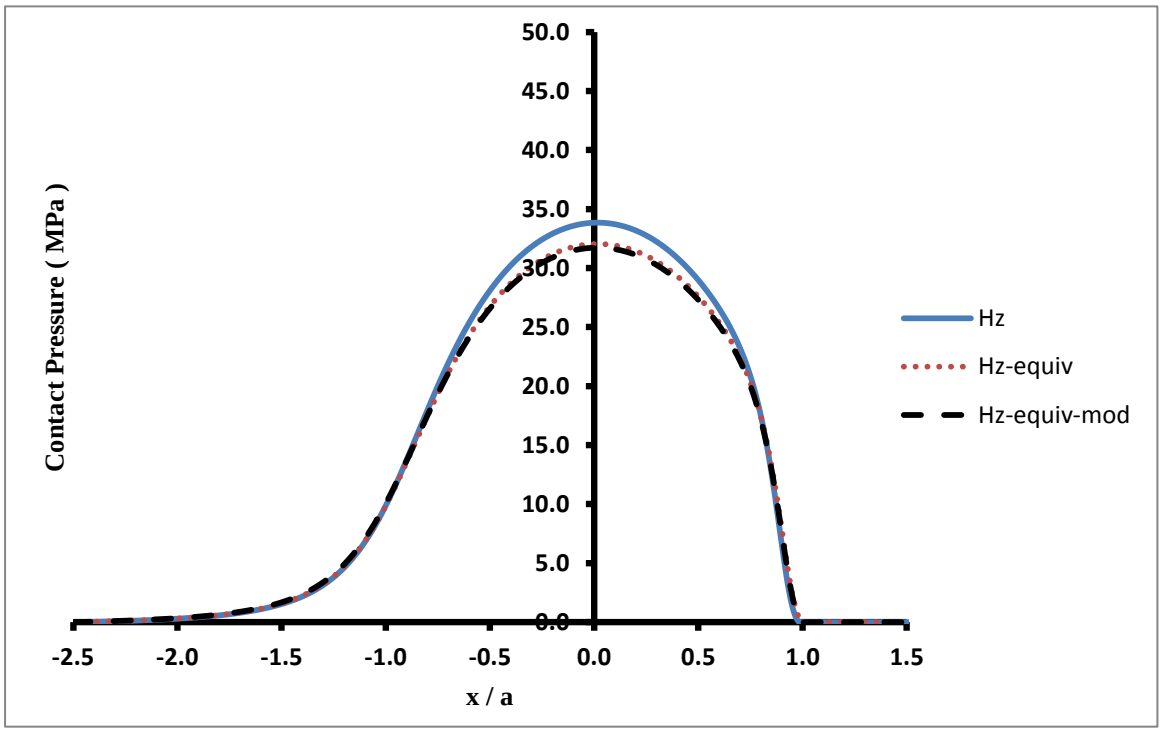

Figure 7.60 Pressure distribution for point G, 6 mm cup thickness, central line in x-direction

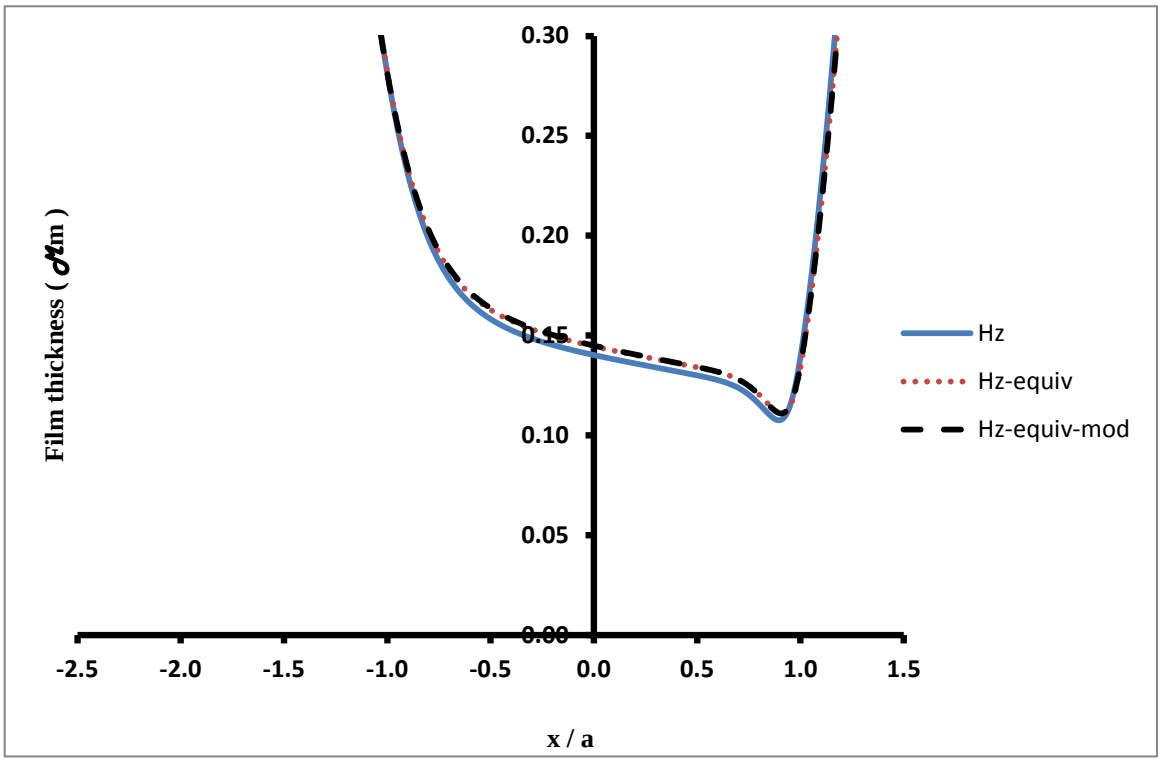

Figure 7.61 Film thickness for point G, 6 mm cup thickness, central line in x-direction

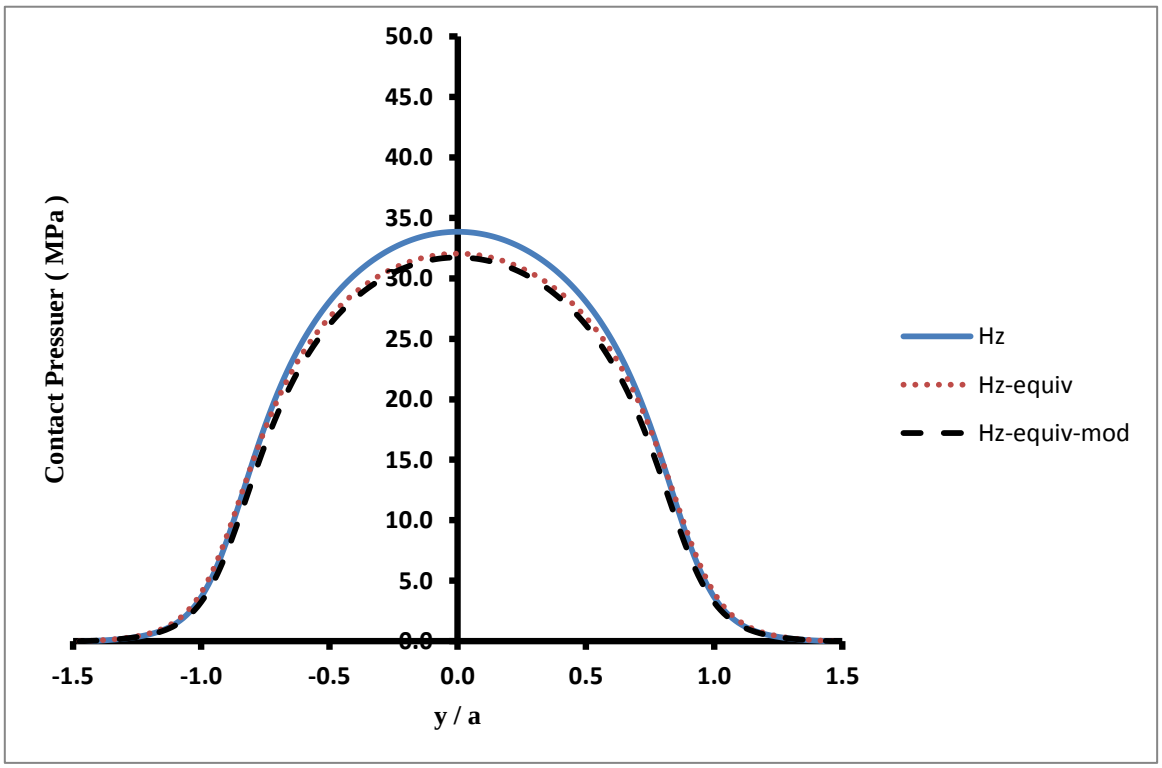

Figure 7.62 Pressure distribution for point G, 6 mm cup thickness, central line in y-direction

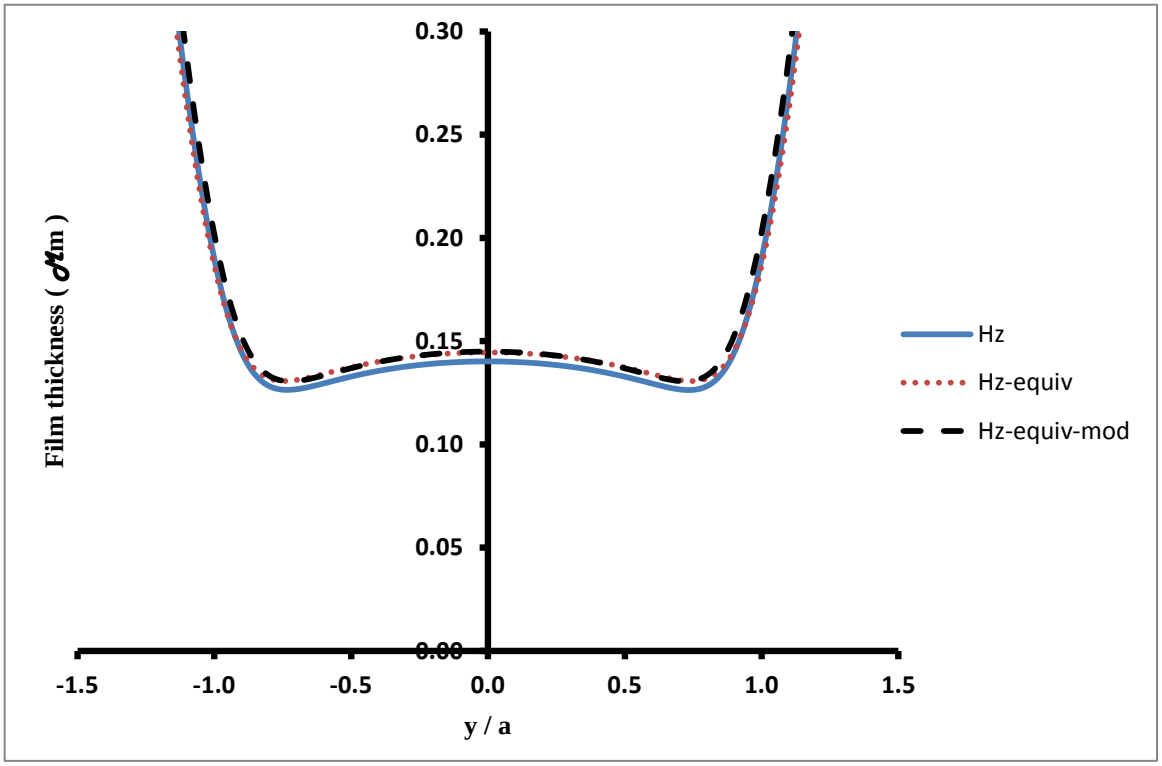

Figure 7.63 Film thickness for point G, 6 mm cup thickness, central line in y-direction

Contact Point H

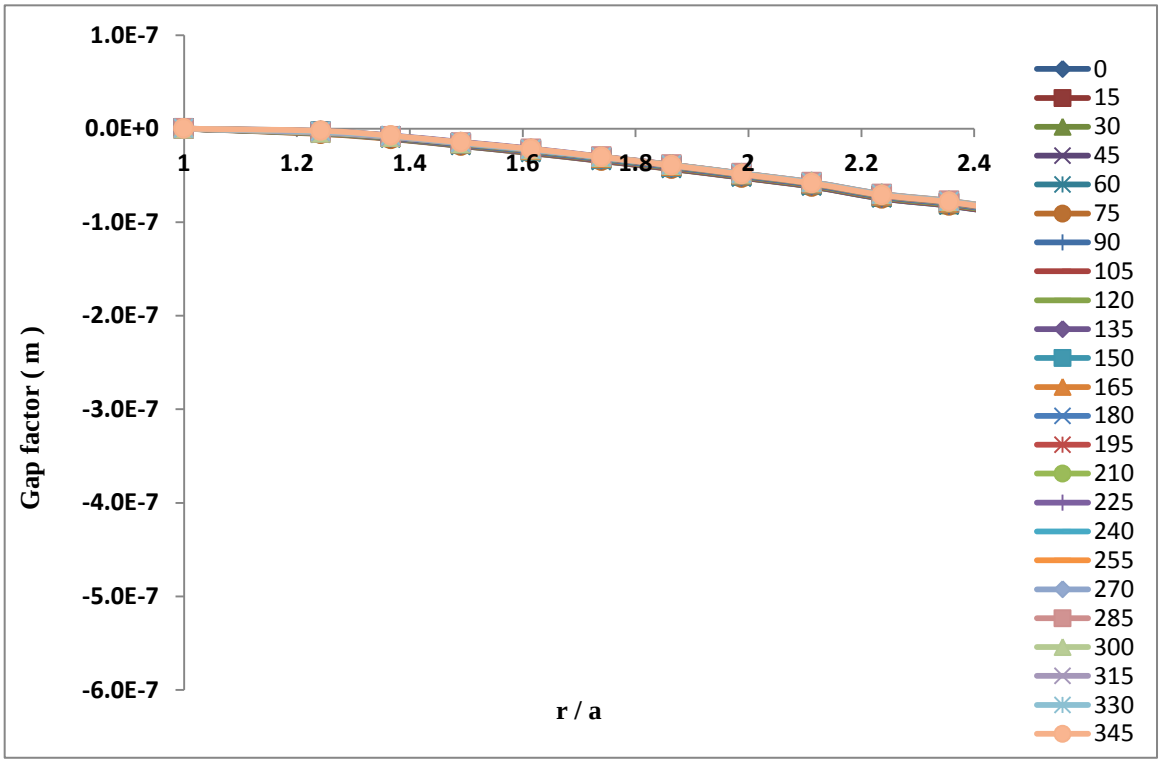

Figure 7.64 Gap factor for point H of 6 mm cup thickness

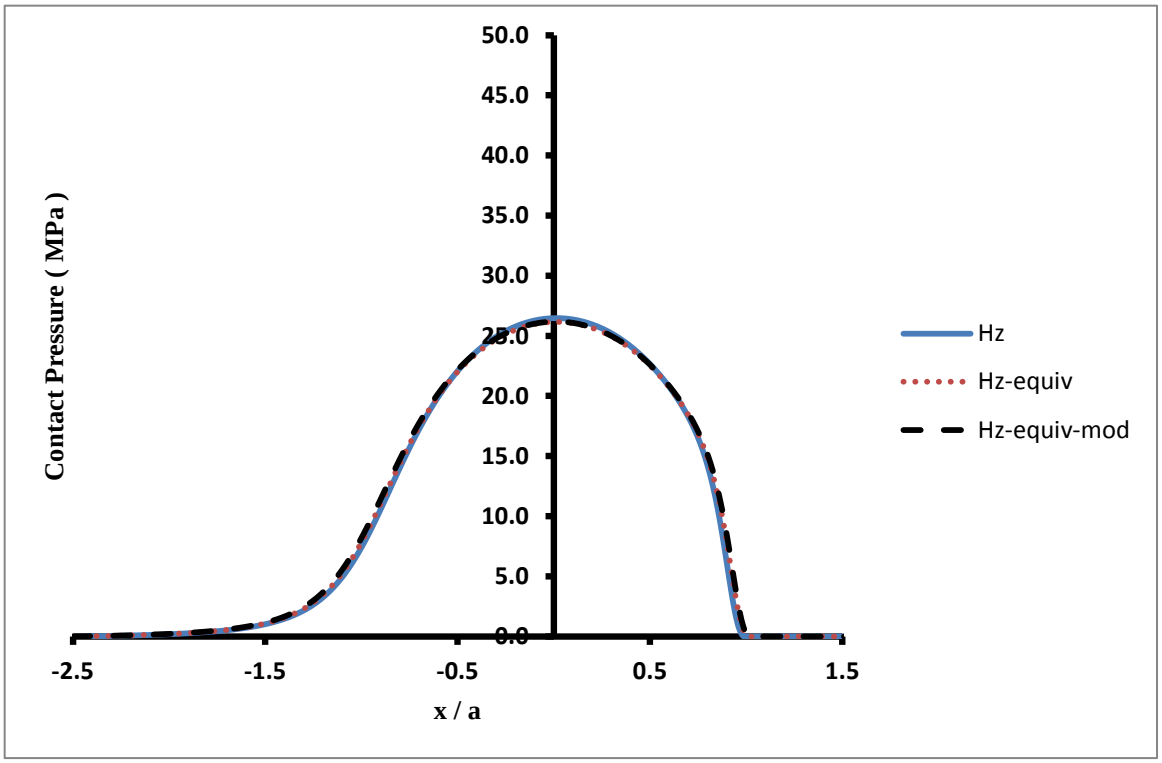

Figure 7.65 Pressure distribution for point H, 6 mm cup thickness, central line in x-direction

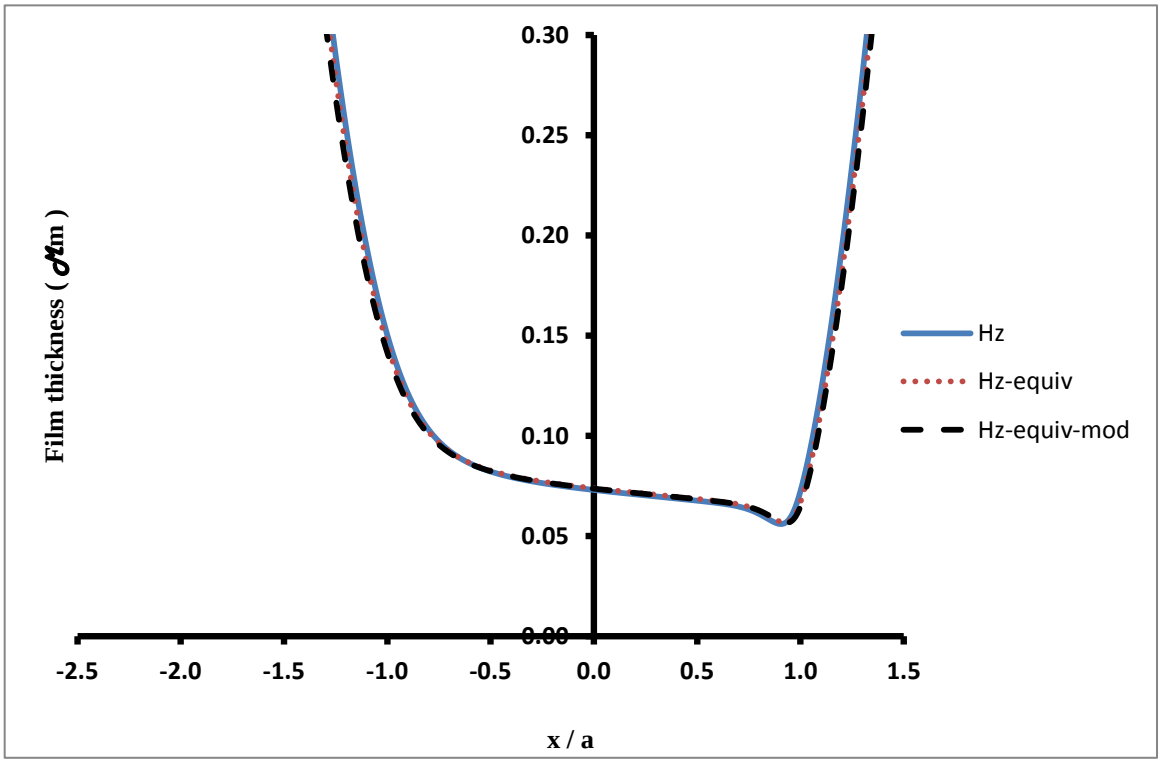

Figure 7.66 Film thickness for point H, 6 mm cup thickness, central line in x-direction

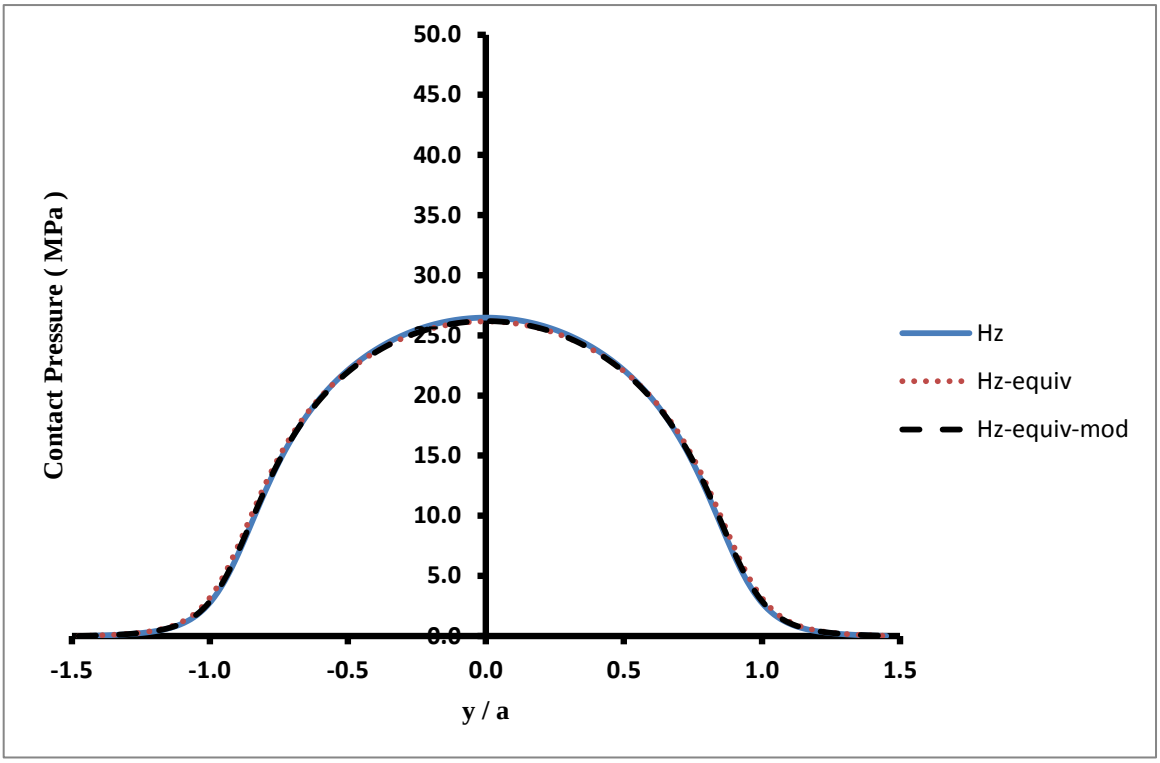

Figure 7.67 Pressure distribution for point H, 6 mm cup thickness, central line in y-direction

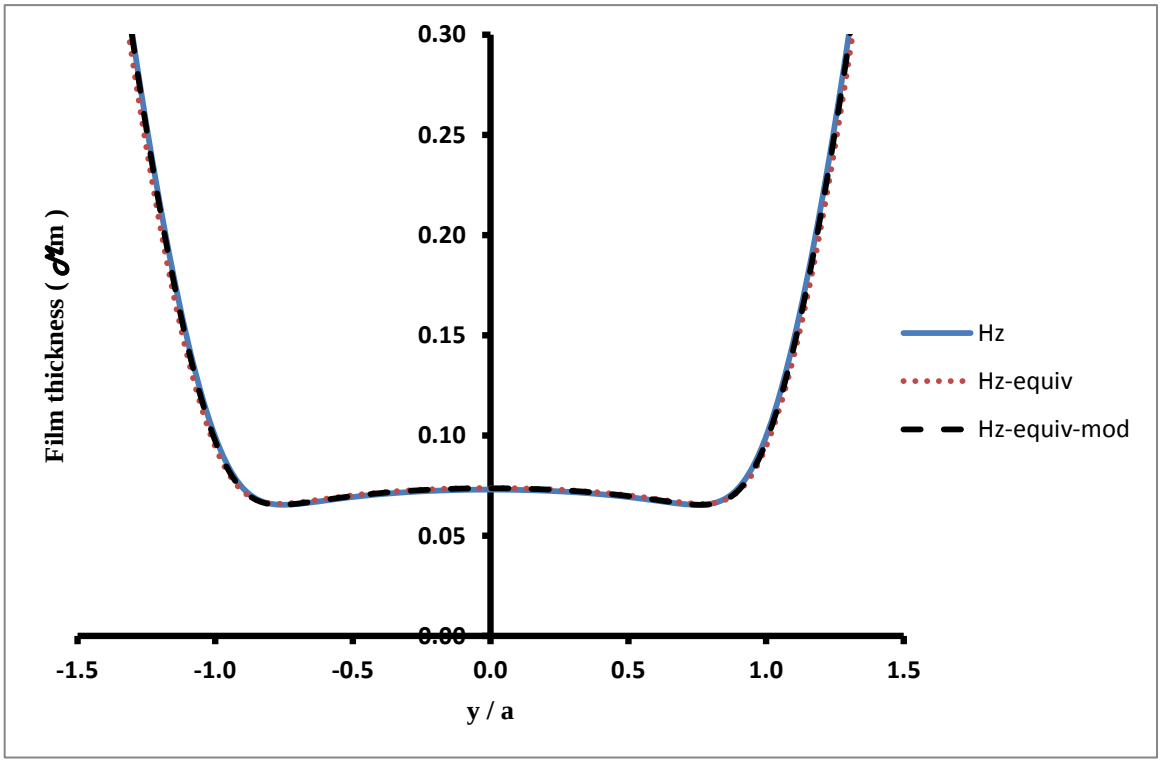

Figure 7.68 Film thickness for point H, 6 mm cup thickness, central line in y-direction

Contact Point I

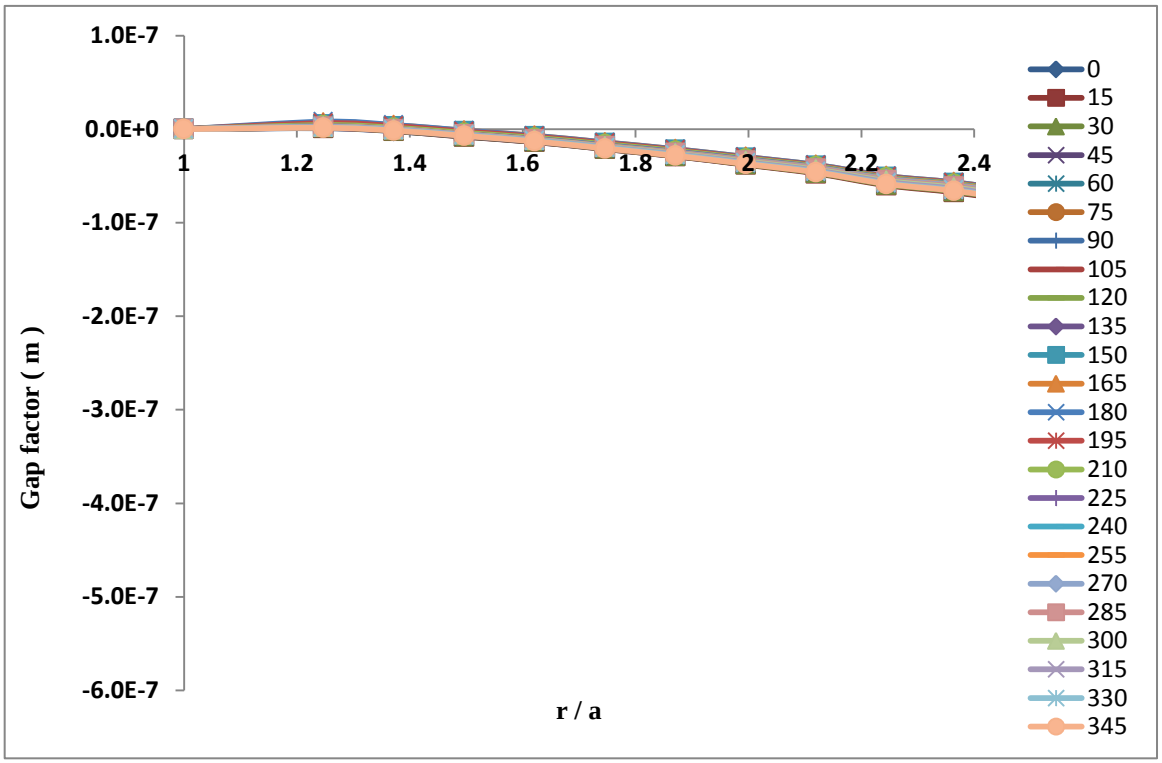

Figure 7.69 Gap factor for point I of 6 mm cup thickness

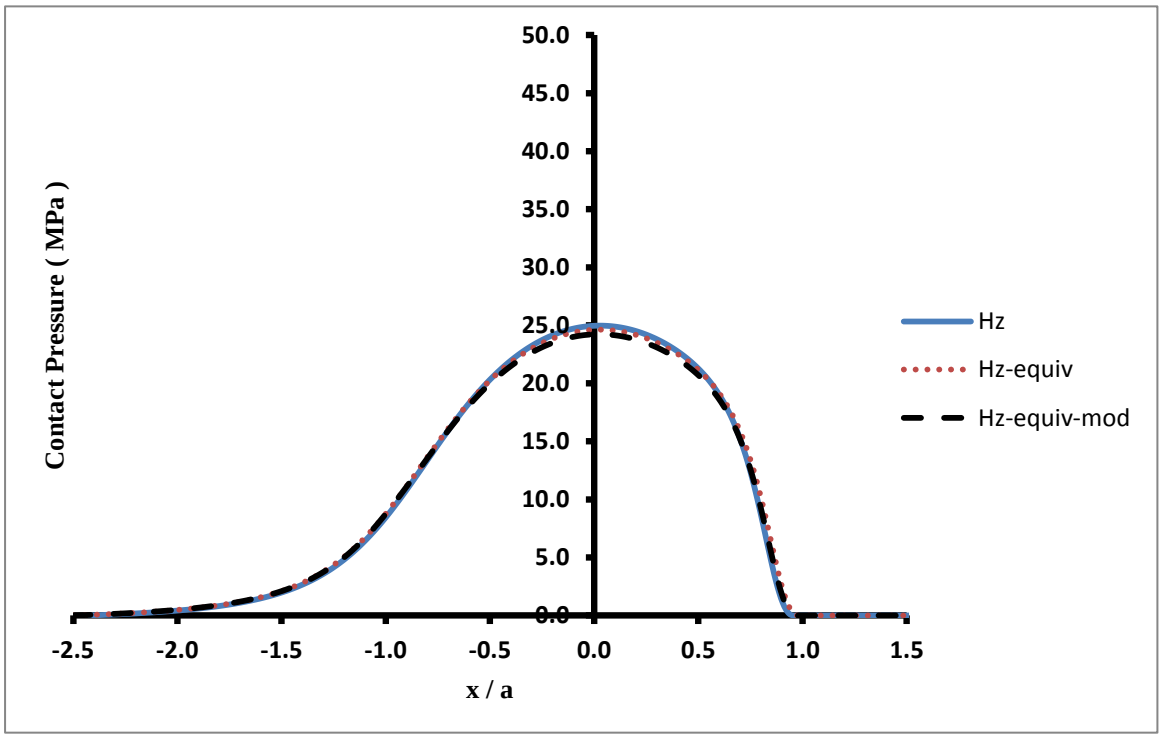

Figure 7.70 Pressure distribution for point I, 6 mm cup thickness, central line in x-direction

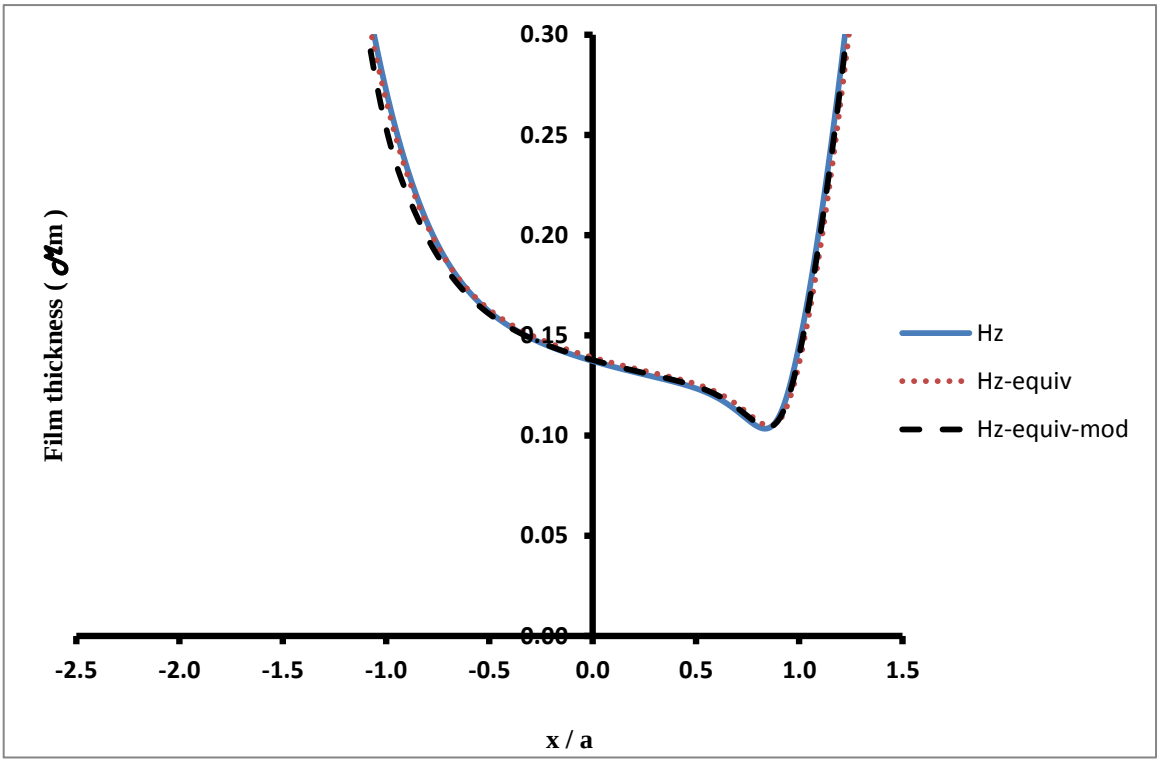

Figure 7.71 Film thickness for point I, 6 mm cup thickness, central line in x-direction

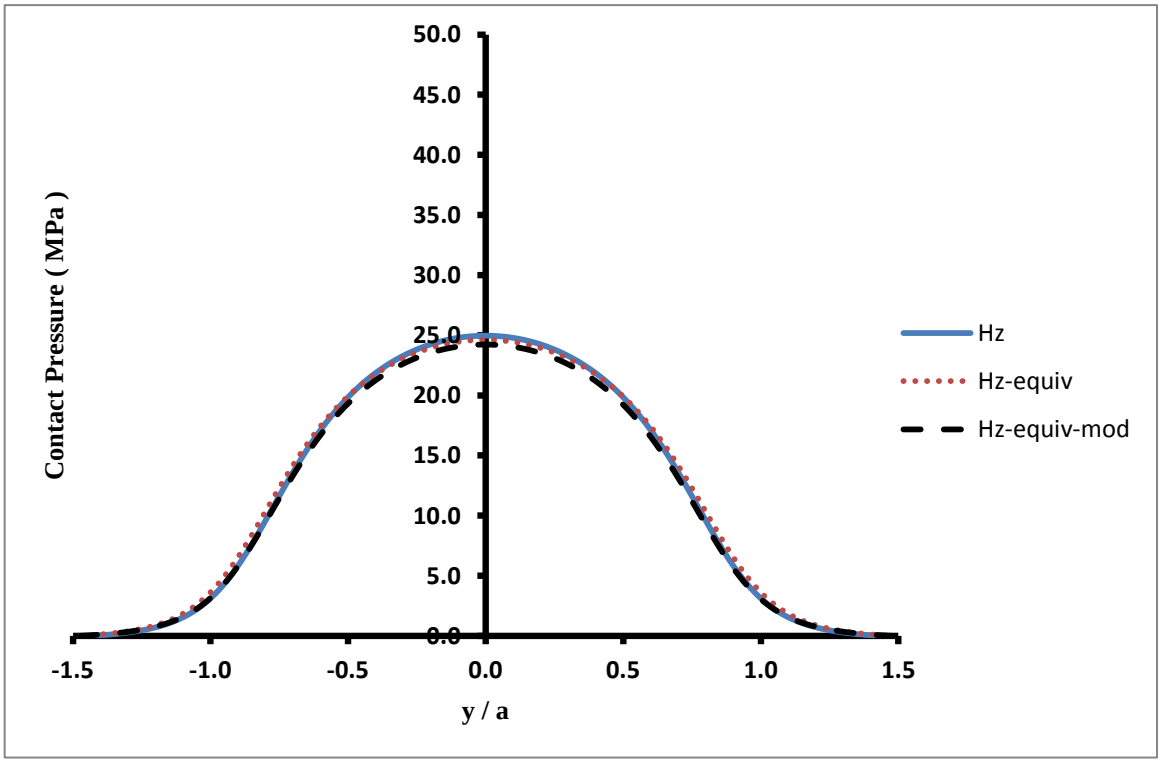

Figure 7.72 Pressure distribution for point I, 6 mm cup thickness, central line in y-direction

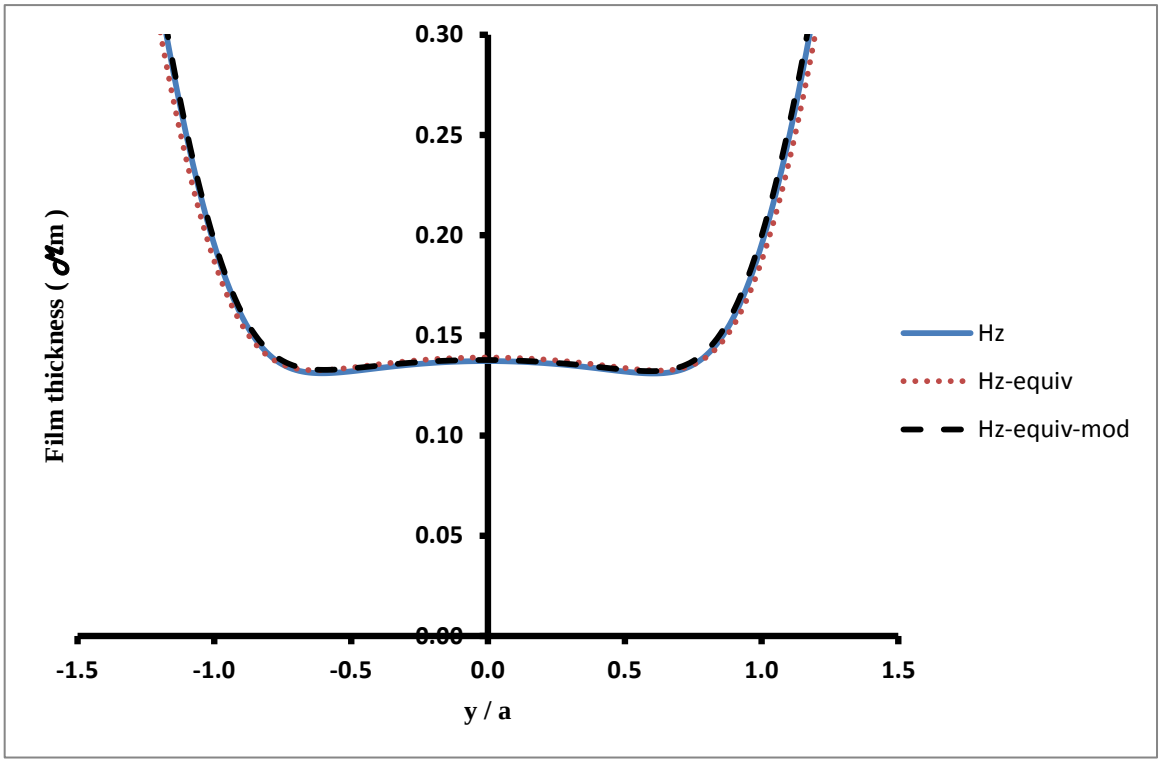

Figure 7.73 Film thickness for point I, 6 mm cup thickness, central line in y-direction

Table 7.3 Calculated Hertzian and equivalent pressure and the ratio between them, Hertzian and equivalent central film thickness and the ratio between them, Hertzian and equivalent radius of contact area for the 6 mm cup.

	a_h(mm)	a_{equiv}(mm)	$P_{o(h)}$(MPa)	$P_{o(equiv)}$(MPa)	%	$h_{c(h)}$(μm)	$h_{c(equiv)}$(μm)	%
A	2.852	2.960	31.277	29.802	-4.716	0.177	0.183	3.523
B	4.195	4.486	48.811	40.900	-16.207	0.123	0.136	10.701
C	4.204	4.506	49.306	41.375	-16.085	0.054	0.060	11.041
D	4.094	4.435	47.649	40.800	-14.374	0.115	0.126	9.941
E	3.736	3.936	42.267	37.326	-11.690	0.208	0.224	7.493
F	3.395	3.559	38.433	35.557	-7.483	0.168	0.177	5.091
G	3.003	3.052	33.848	32.041	-5.339	0.140	0.145	3.096
H	2.336	2.376	26.471	26.151	-1.209	0.073	0.074	1.143
I	2.293	2.367	24.970	24.621	-1.398	0.137	0.139	1.307

7.6 Detailed EHL results for 8 mm cup thickness

The section results for the EHL analyses with an 8 mm cup thickness are given in figures 7.74 to 7.118. Comparing the results of the EHL analysis of 8 mm cup thickness with the 6 mm cup, it can be shown that five contact points, A, F, G, H and I are essentially identical for the Hertzian, equivalent and modified equivalent model cases. As only points H and I had identical results for the 6 mm cup, it can be said that increasing the cup thickness reduces the differences between the Hertzian model and the equivalent model. In other words, the contact pressure, the film thickness and radius of the contact area become closer and closer to the Hertzian case when the cup thickness becomes thicker and thicker. Again this corresponds to increasing values of wt/a_h in Table 7.1.

When the measured load of the hip joint is greater than 150% of the body weight as in the contact points B, C, D and E there are some differences in the values of the contact pressure and the film thickness. Lower values by 6.5%, 6.3%, 5% and 4.1% were found for the maximum contact pressure due to changing from the Hertzian model to the equivalent model for contact points B, C, D and E respectively. Also there was an increase in the lubricant film thickness for these four contact points by 3.8%, 3.9%, 3% and 2.8%.

A summary of the radius of contact area, contact pressure and the film thickness for the Hertzian and equivalent models are given in Table 7.4.

EHL results for 8 mm Cup thickness

Contact Point A

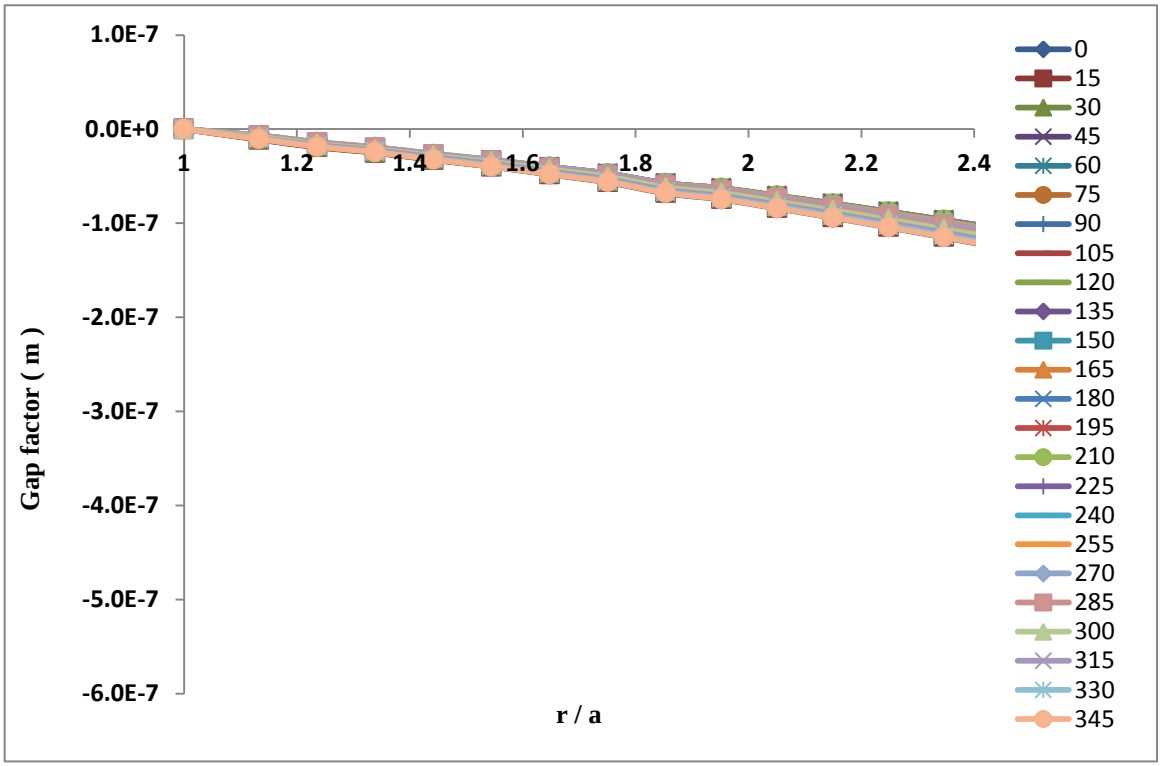

Figure 7.74 Gap factor for point A of 8 mm cup thickness

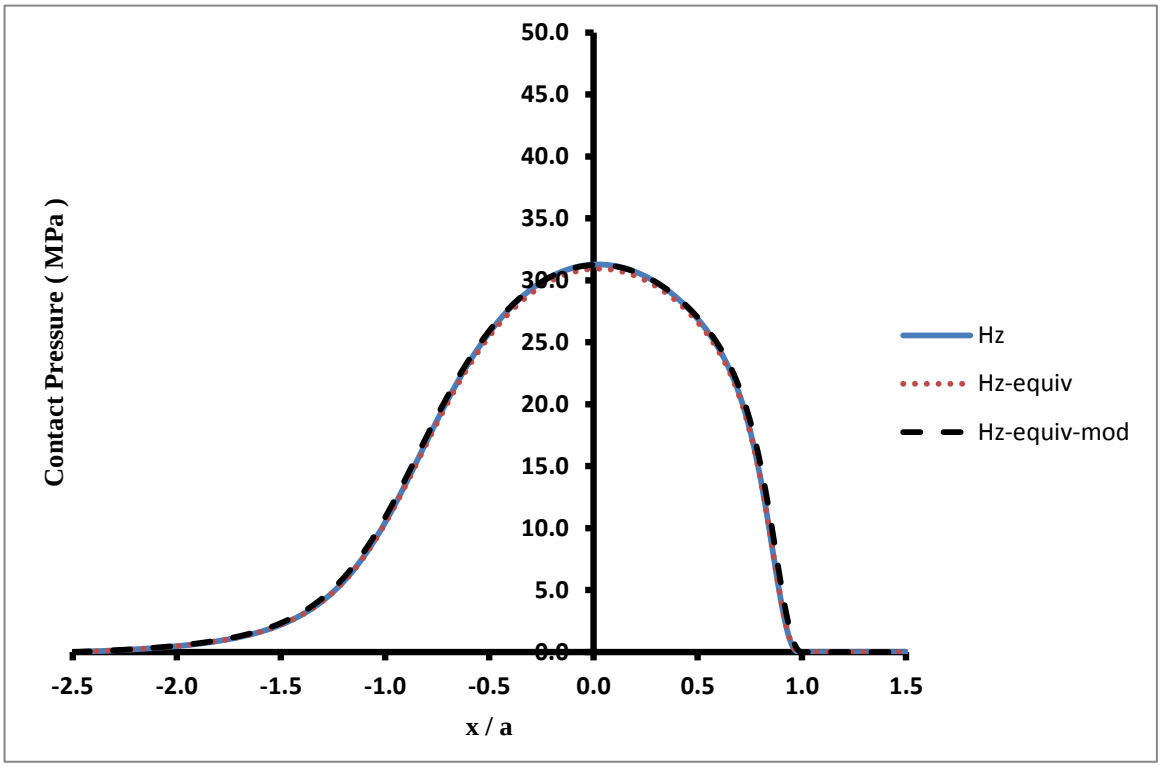

Figure 7.75 Pressure distribution for point A, 8 mm cup thickness, central line in x-direction

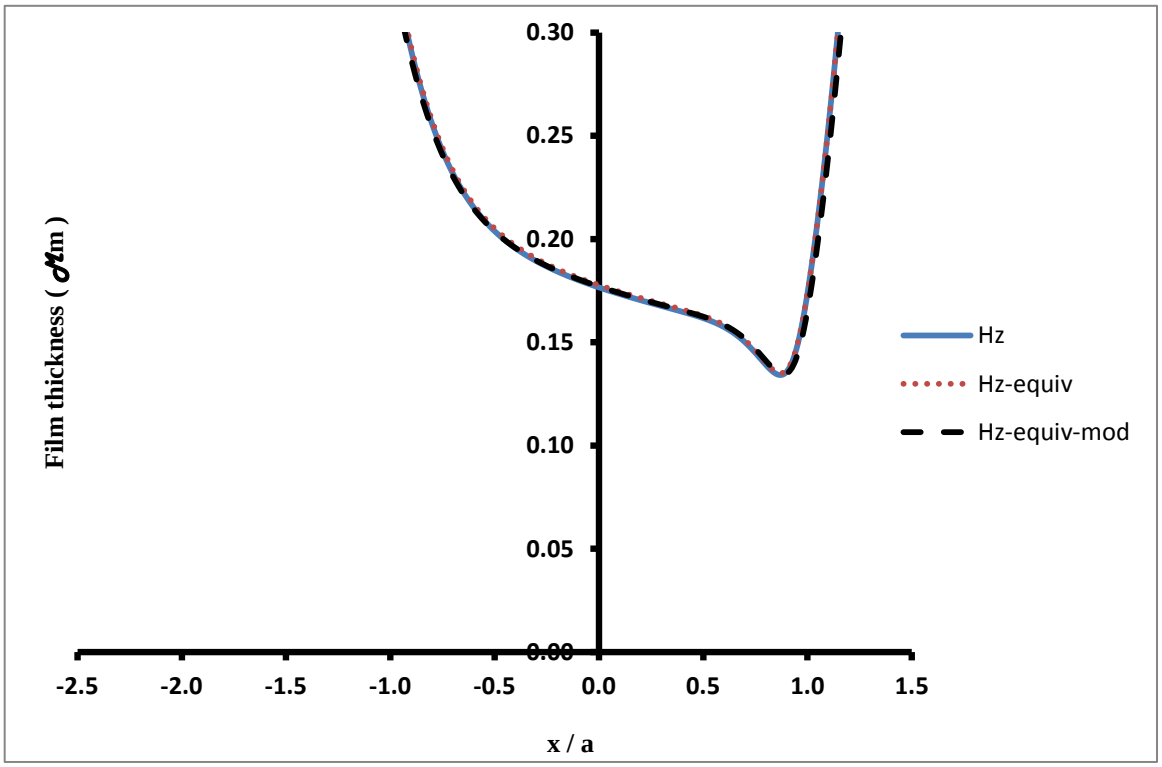

Figure 7.76 Film thickness for point A, 8 mm cup thickness, central line in x-direction

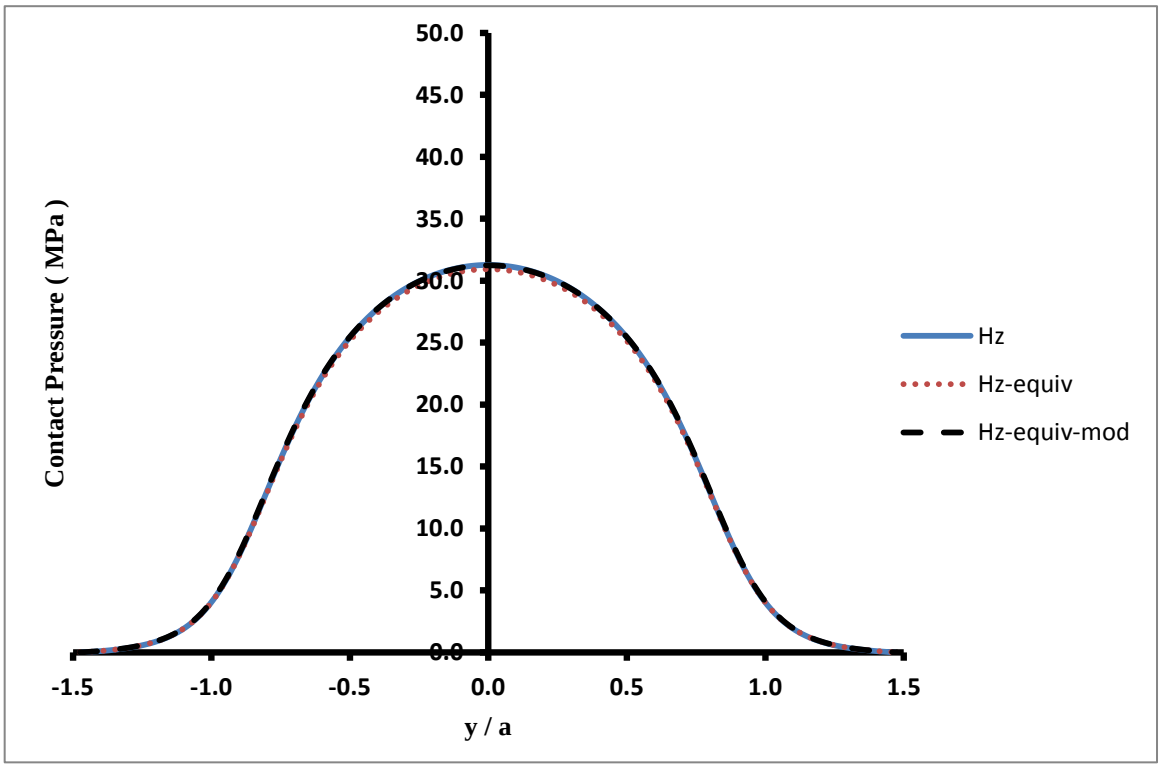

Figure 7.77 Pressure distribution for point A, 8 mm cup thickness, central line in y-direction

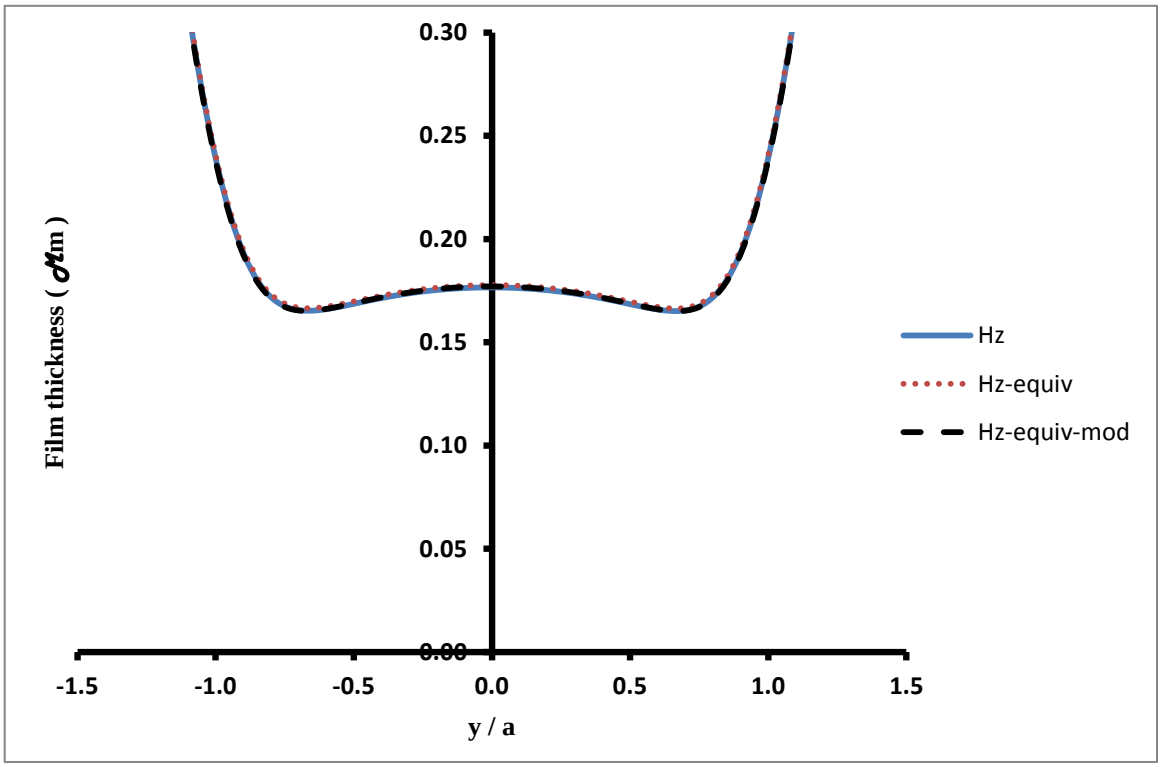

Figure 7.78 Film thickness for point A, 8 mm cup thickness, central line in y-direction

Contact Point B

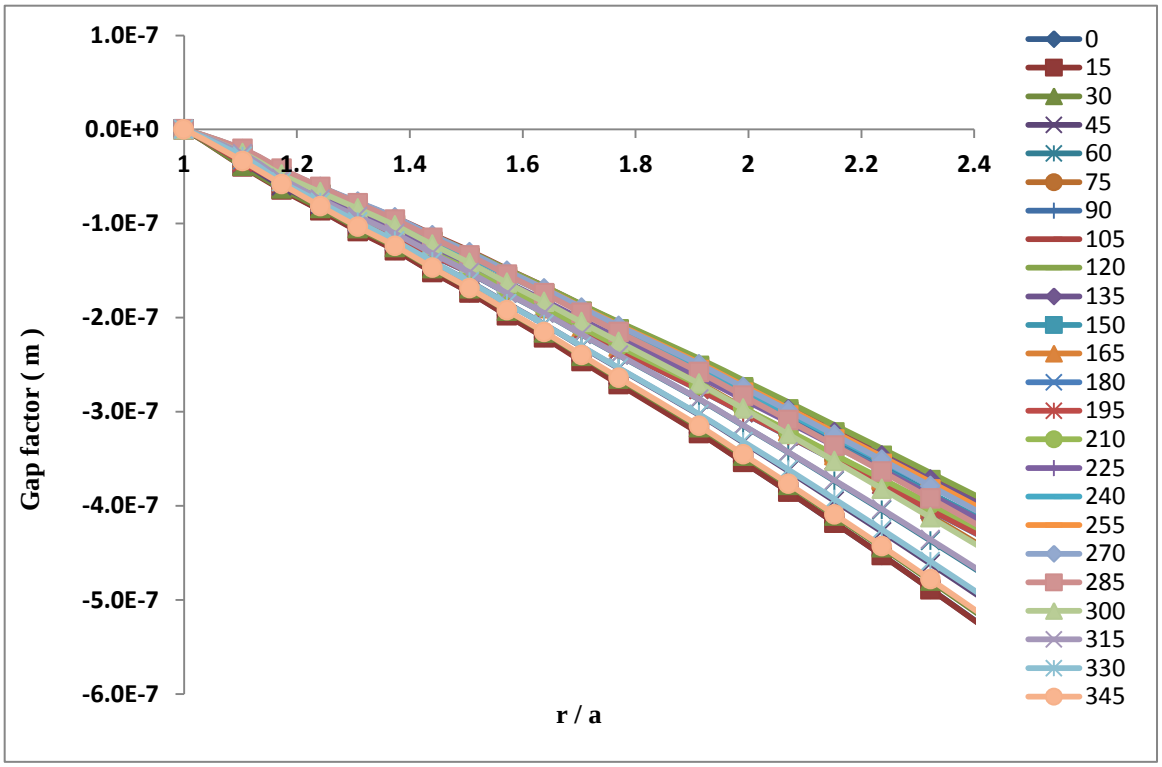

Figure 7.79 Gap factor for point B of 8 mm cup thickness

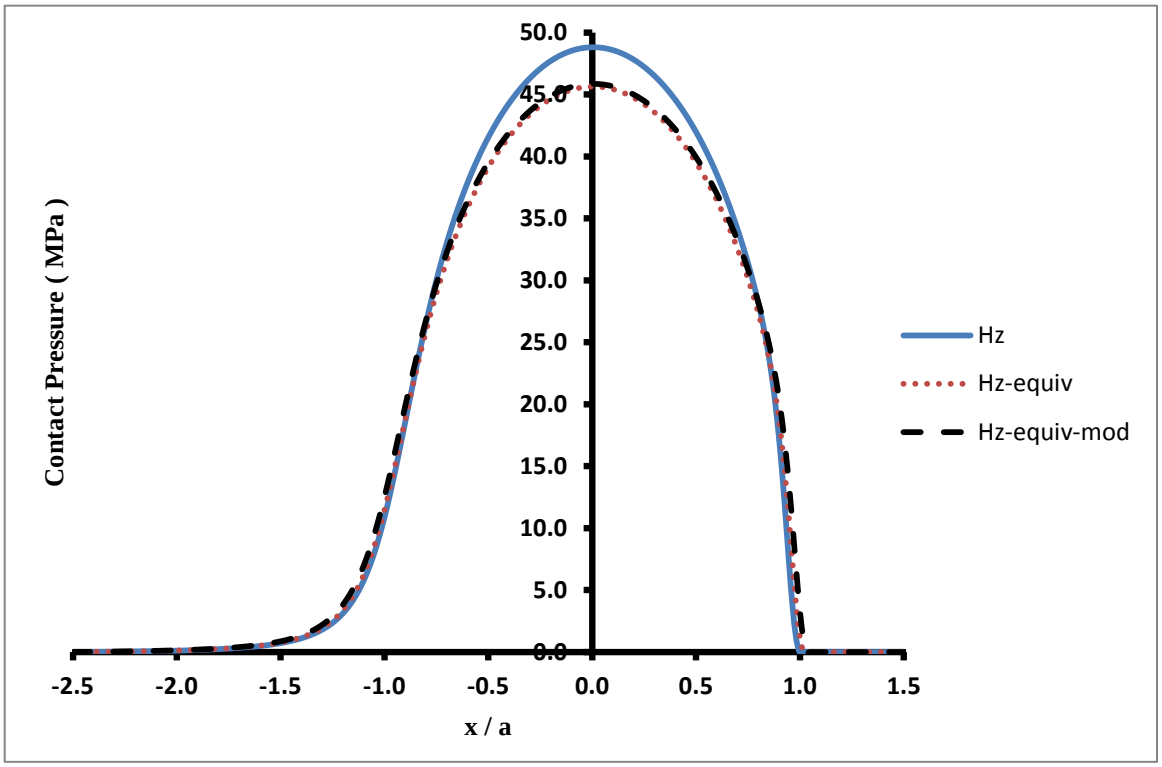

Figure 7.80 Pressure distribution for point B, 8 mm cup thickness, central line in x-direction

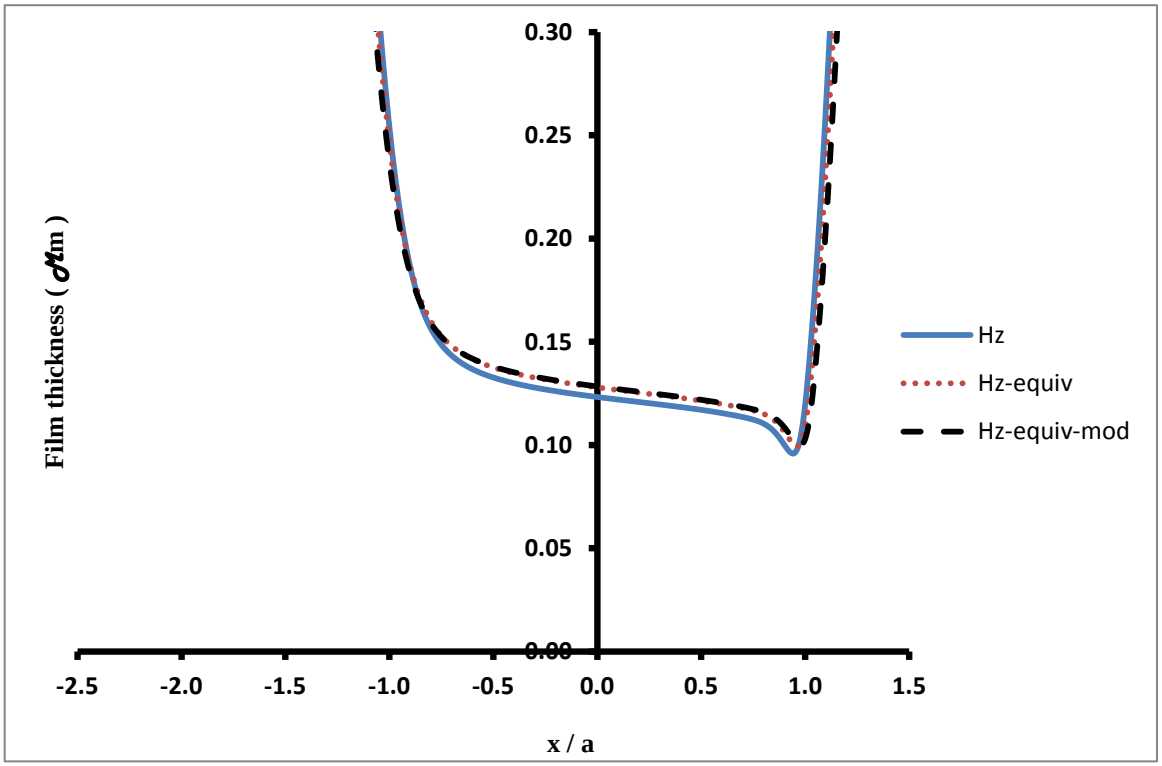

Figure 7.81 Film thickness for point B, 8 mm cup thickness, central line in x-direction

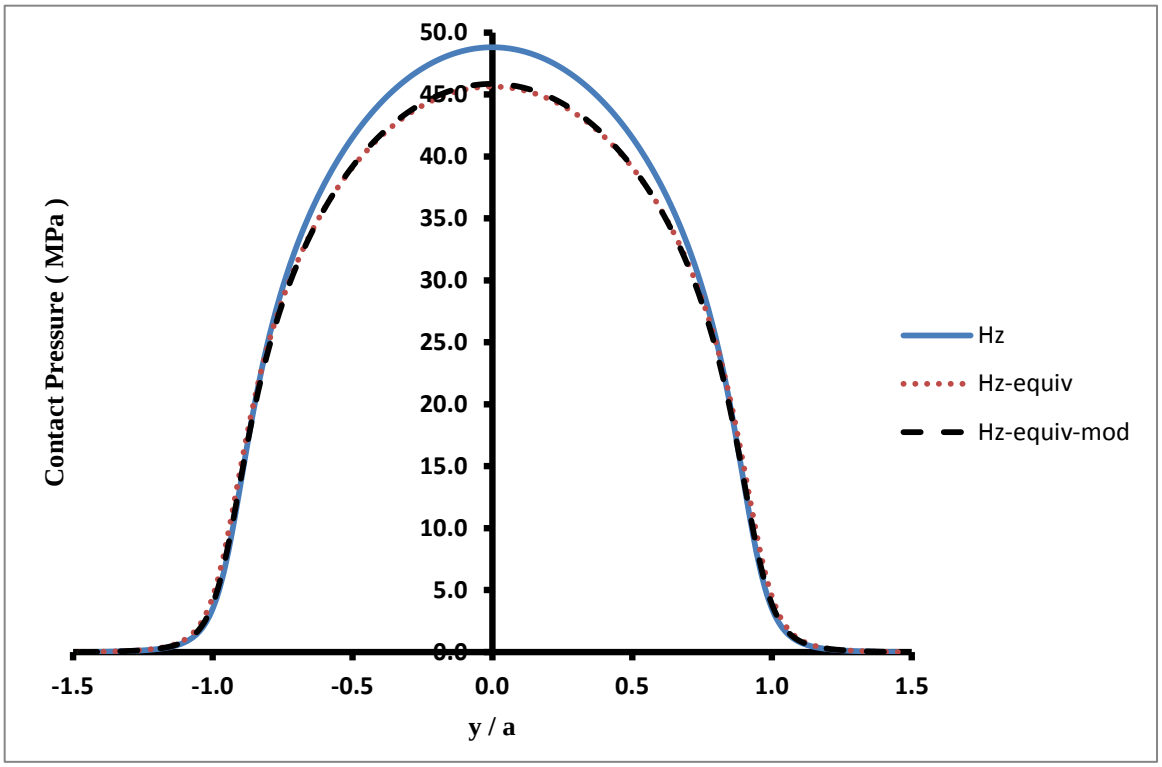

Figure 7.82 Pressure distribution for point B, 8 mm cup thickness, central line in y-direction

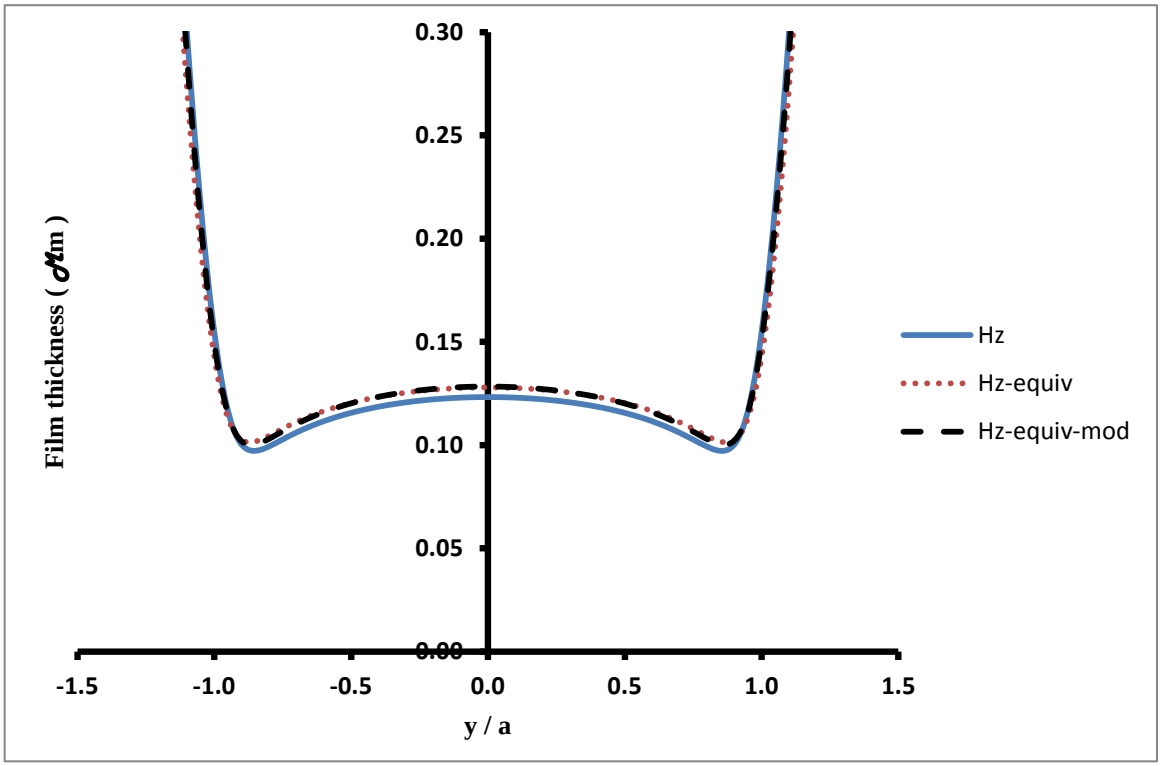

Figure 7.83 Film thickness for point B, 8 mm cup thickness, central line in y-direction

Contact Point C

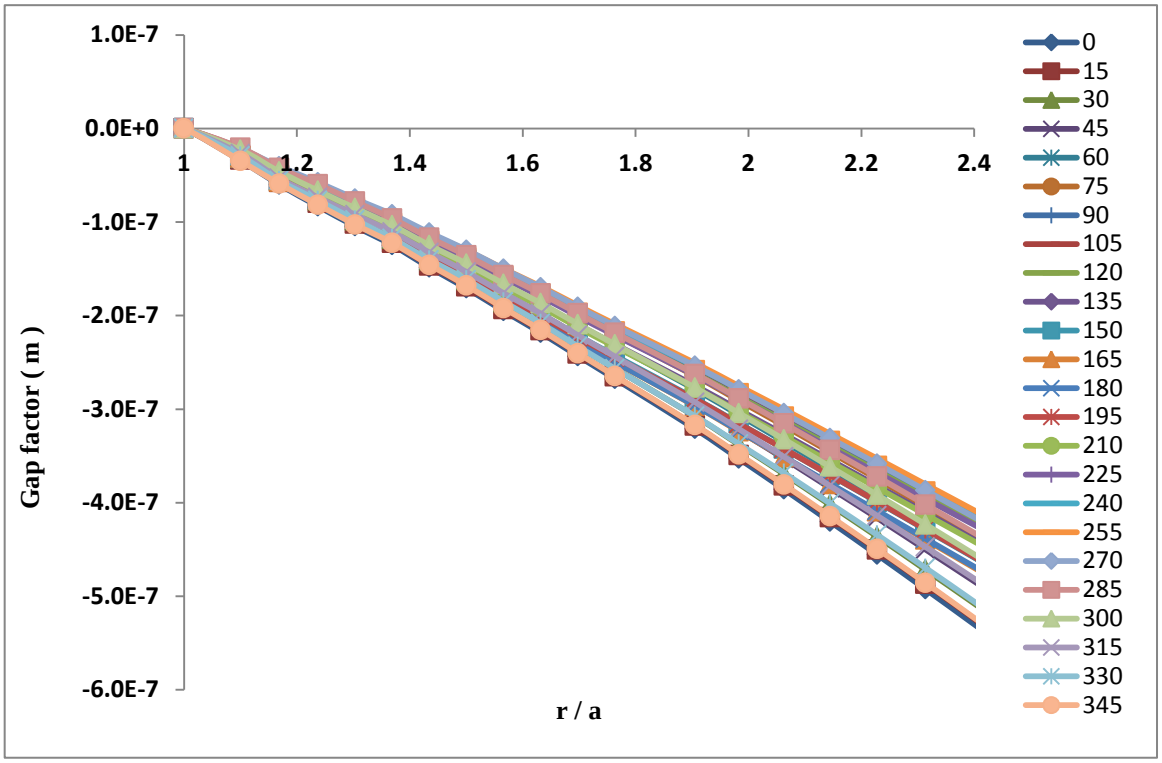

Figure 7.84 Gap factor for point C of 8 mm cup thickness

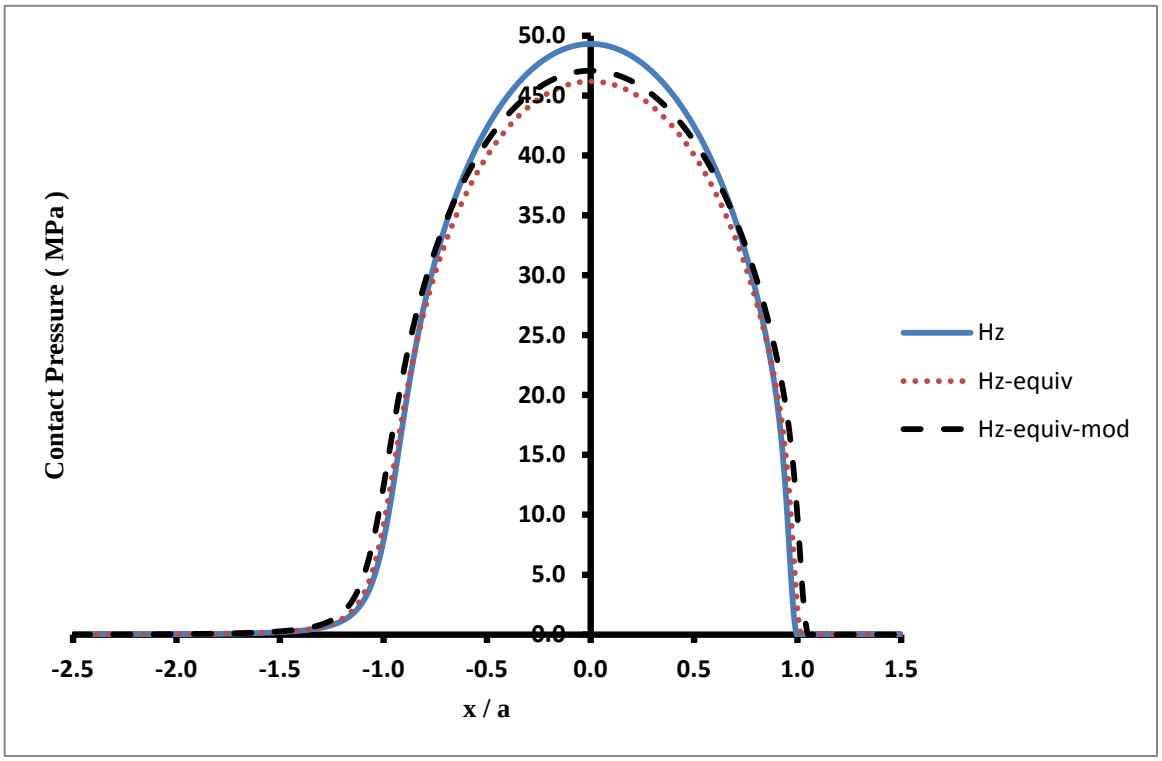

Figure 7.85 Pressure distribution for point C, 8 mm cup thickness, central line in x-direction

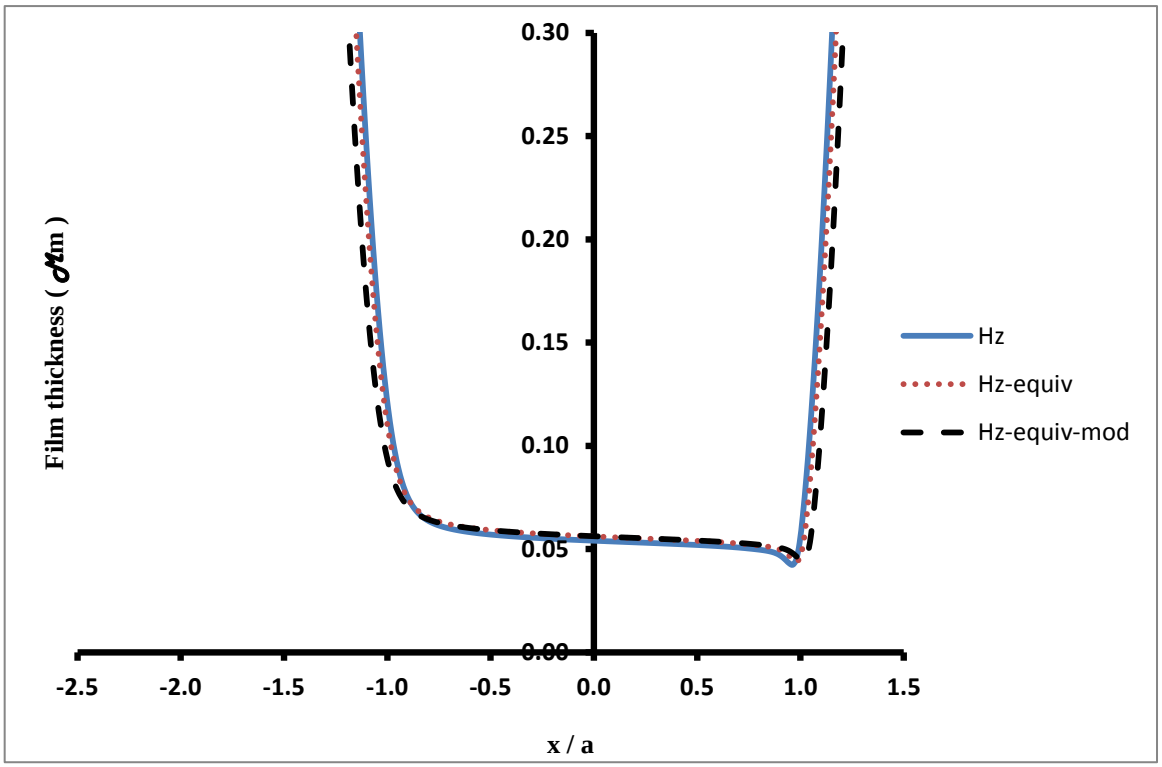

Figure 7.86 Film thickness for point C, 8 mm cup thickness, central line in x-direction

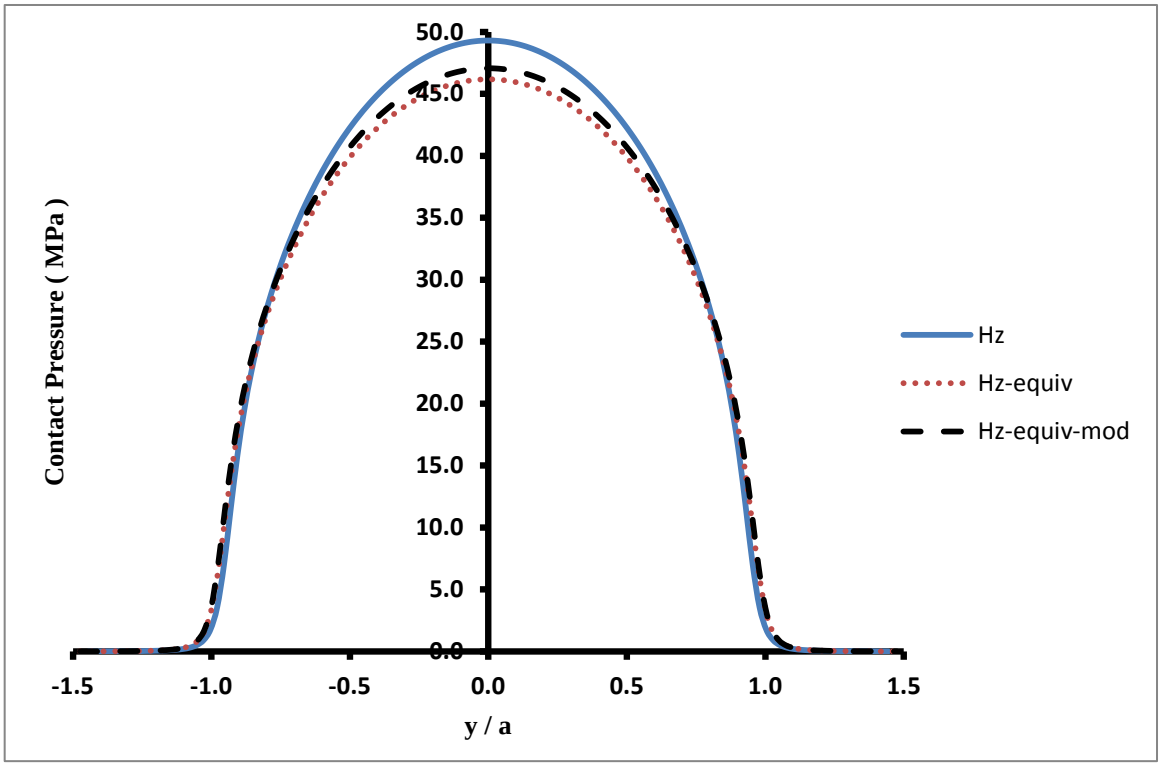

Figure 7.87 Pressure distribution for point C, 8 mm cup thickness, central line in y-direction

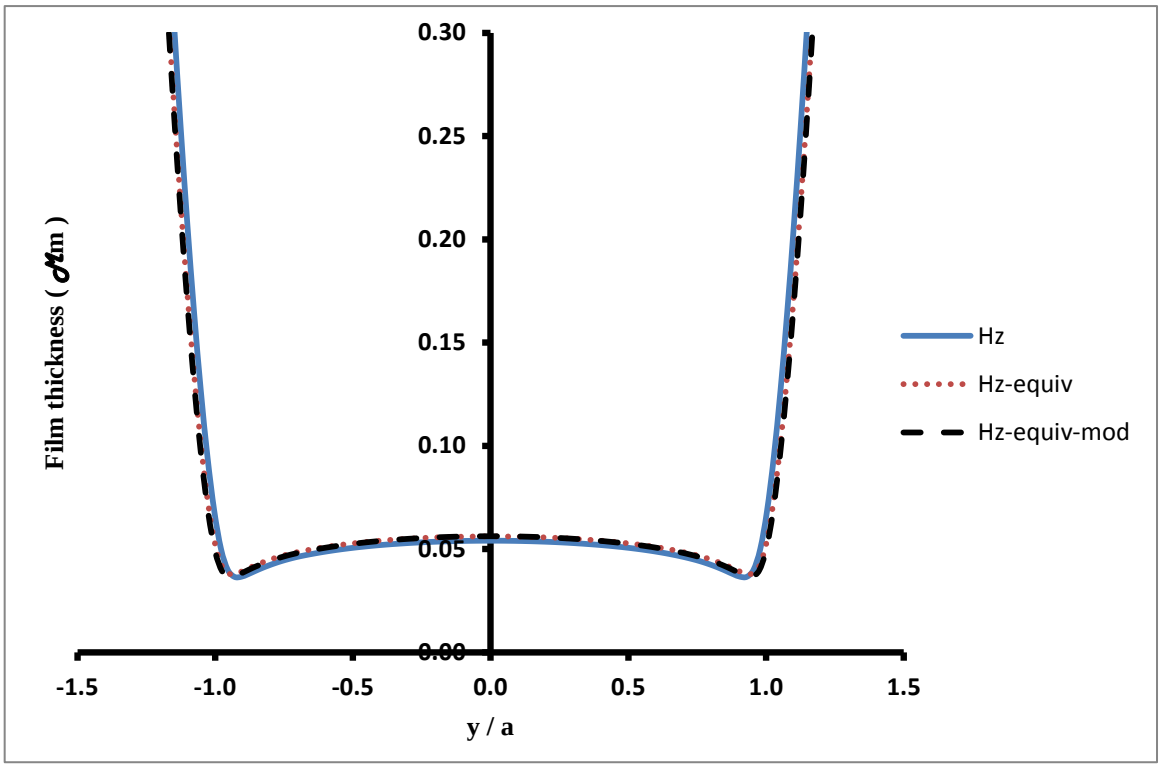

Figure 7.88 Film thickness for point C, 8 mm cup thickness, central line in y-direction

Contact Point D

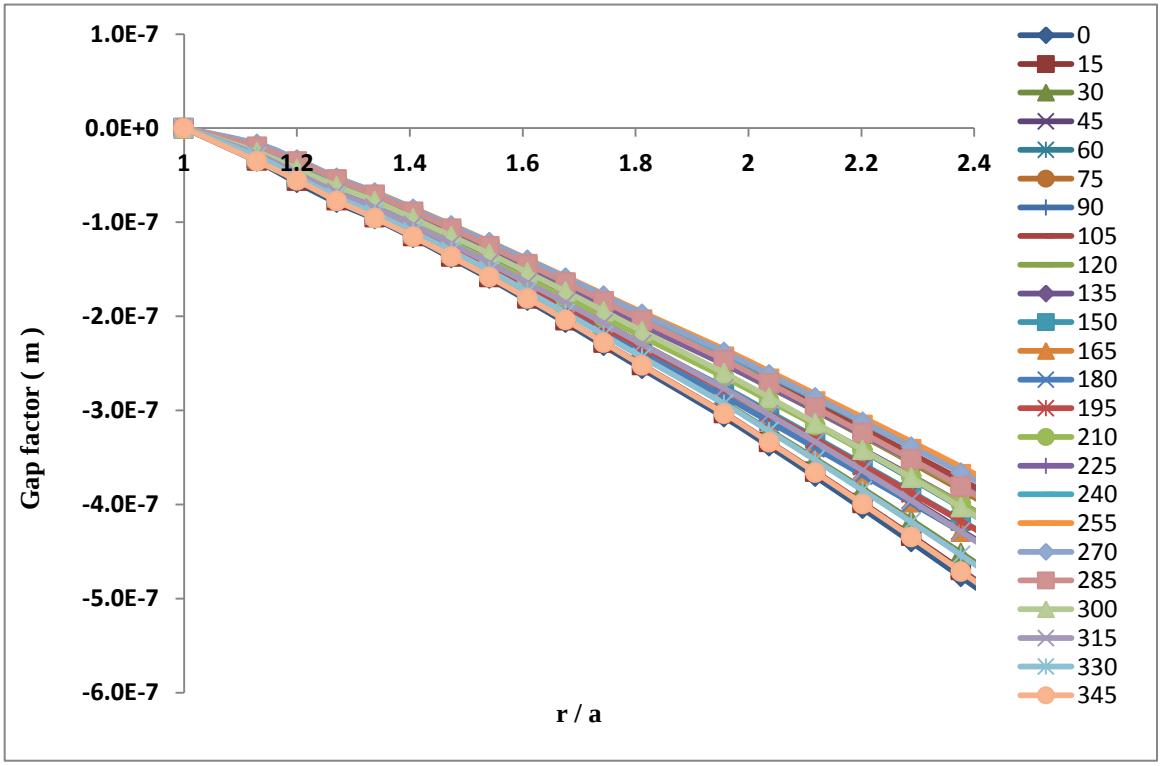

Figure 7.89 Gap factor for point D of 8 mm cup thickness

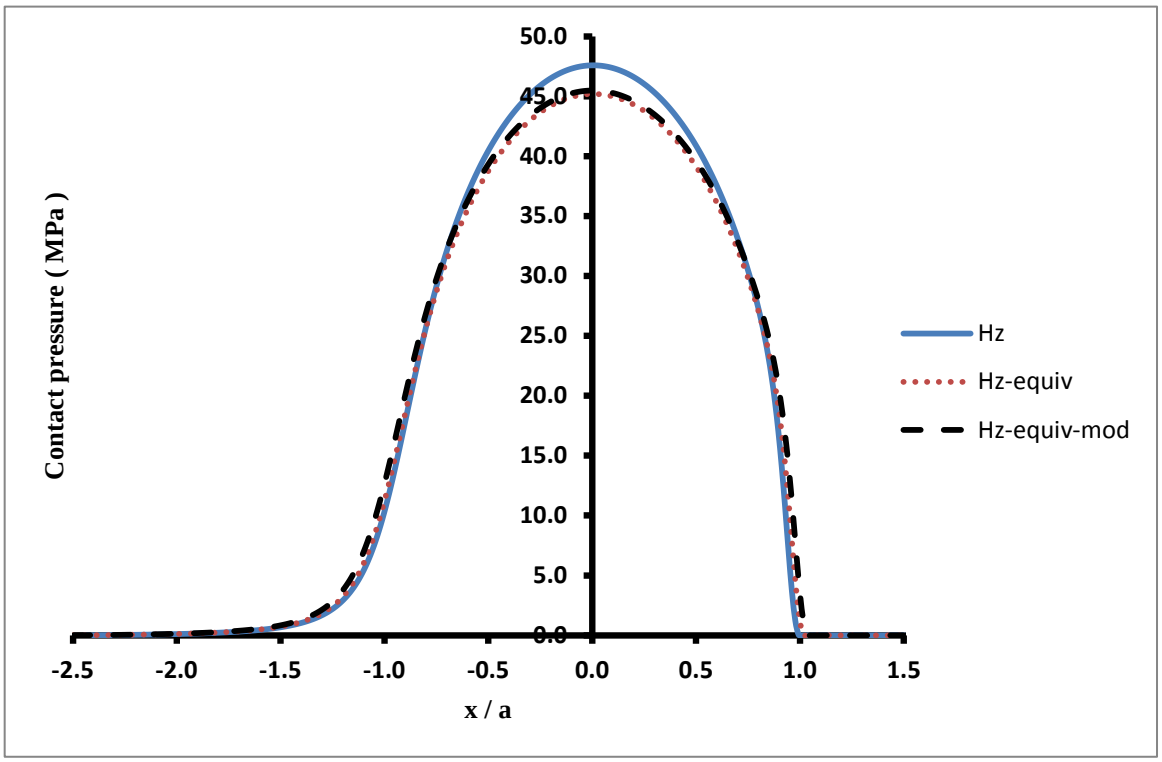

Figure 7.90 Pressure distribution for point D, 8 mm cup thickness, central line in x-direction

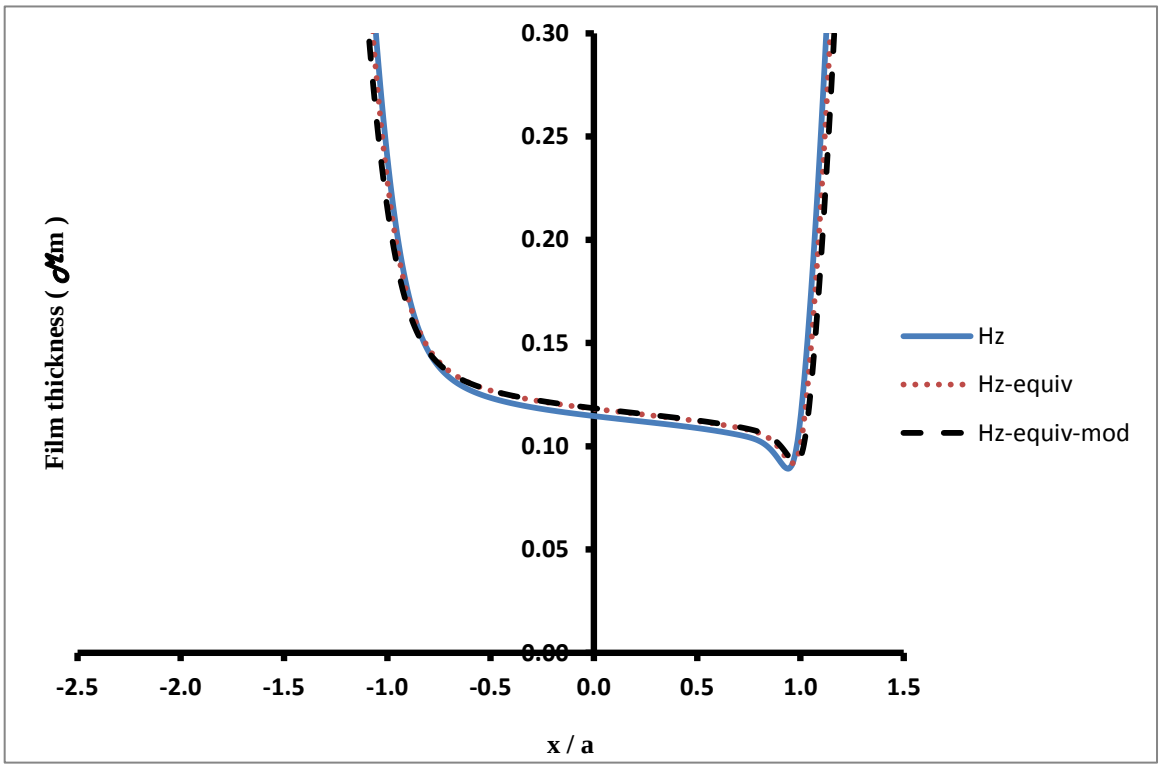

Figure 7.91 Film thickness for point D, 8 mm cup thickness, central line in x-direction

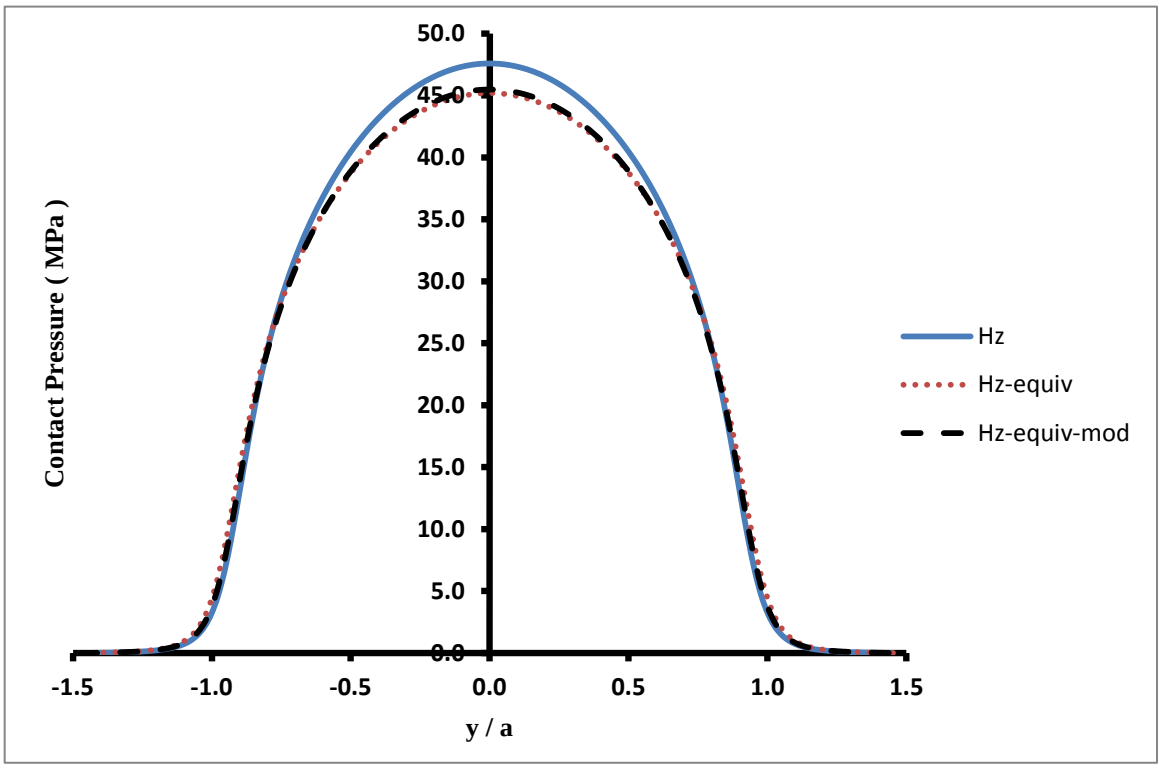

Figure 7.92 Pressure distribution for point D, 8 mm cup thickness, central line in y-direction

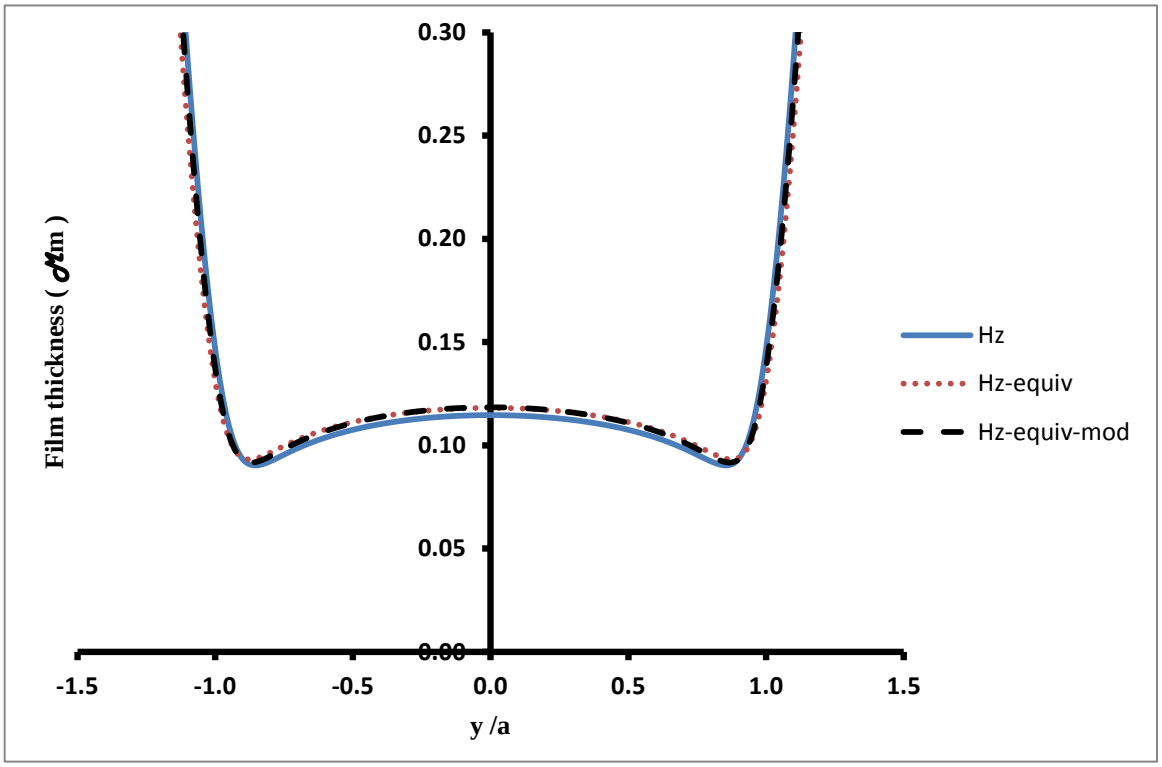

Figure 7.93 Film thickness for point D, 8 mm cup thickness, central line in y-direction

Contact Point E

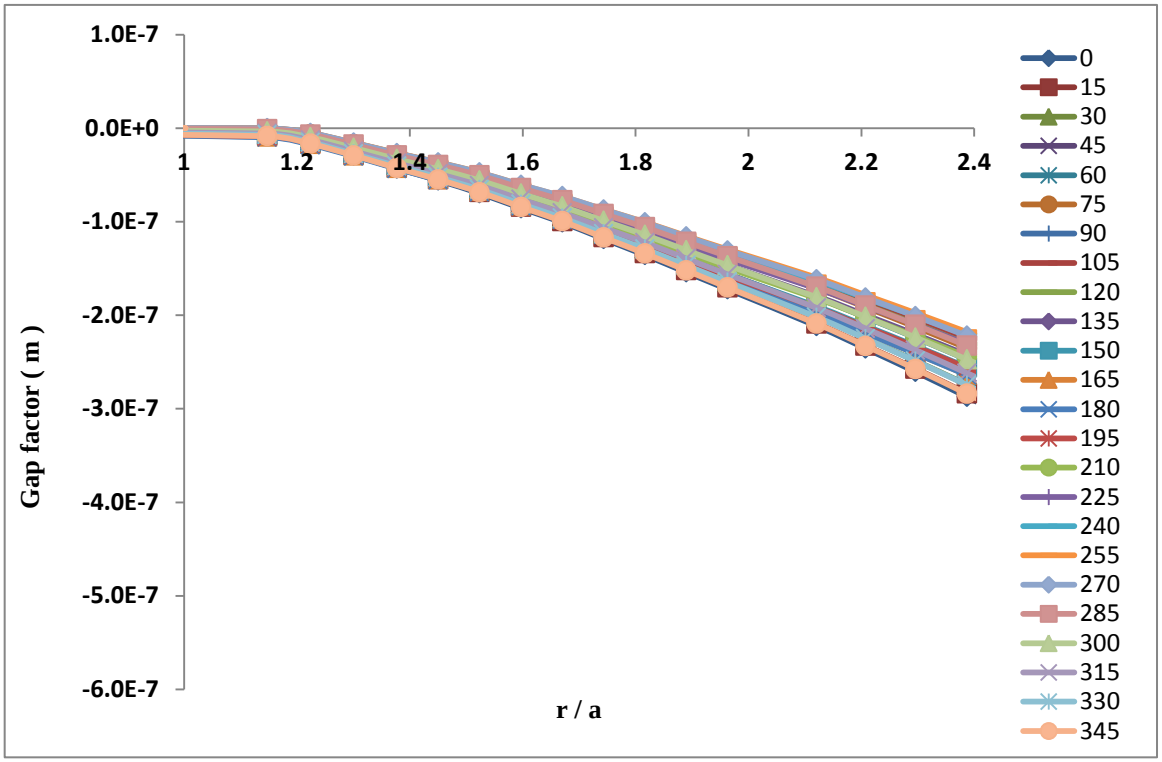

Figure 7.94 Gap factor for point E of 8 mm cup thickness

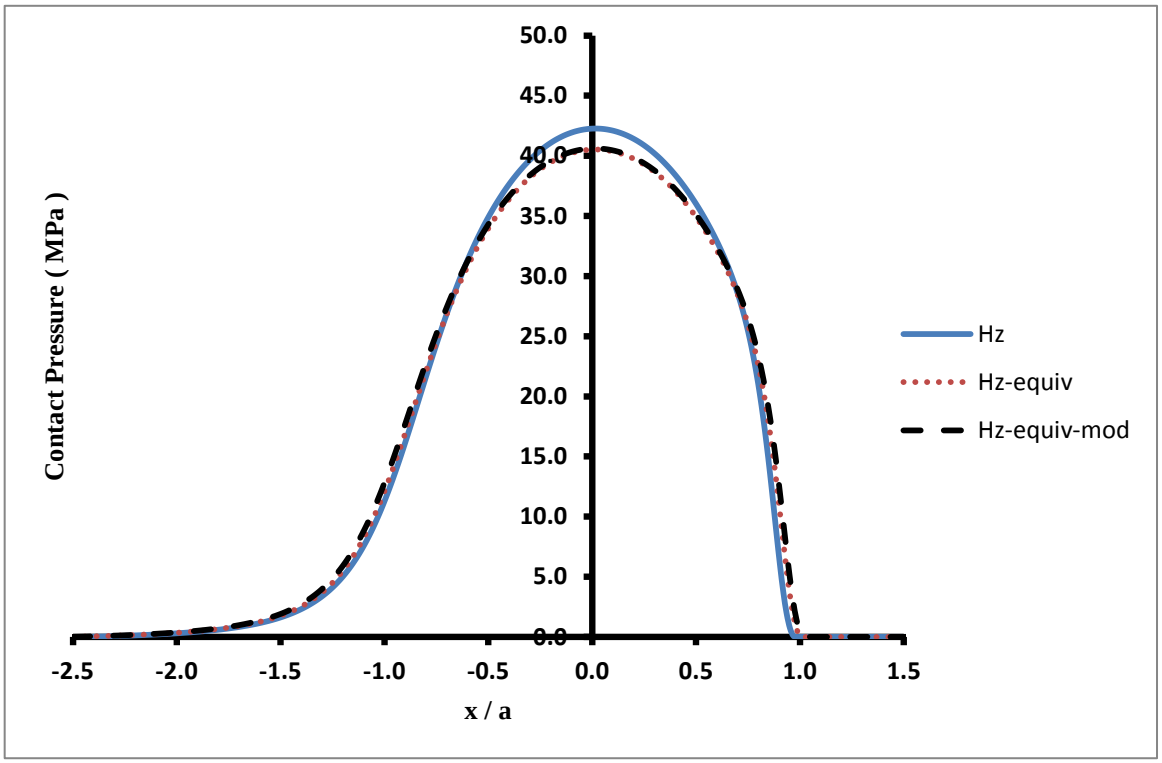

Figure 7.95 Pressure distribution for point E, 8 mm cup thickness, central line in x-direction

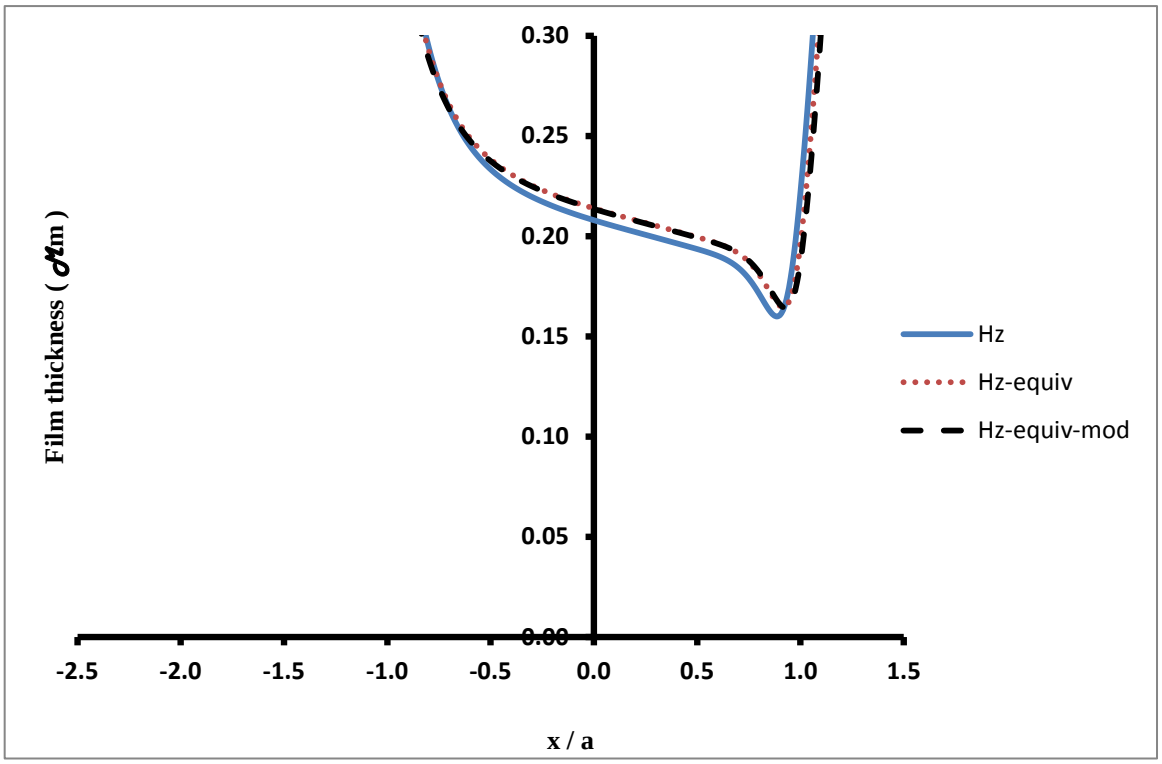

Figure 7.96 Film thickness for point E, 8 mm cup thickness, central line in x-direction

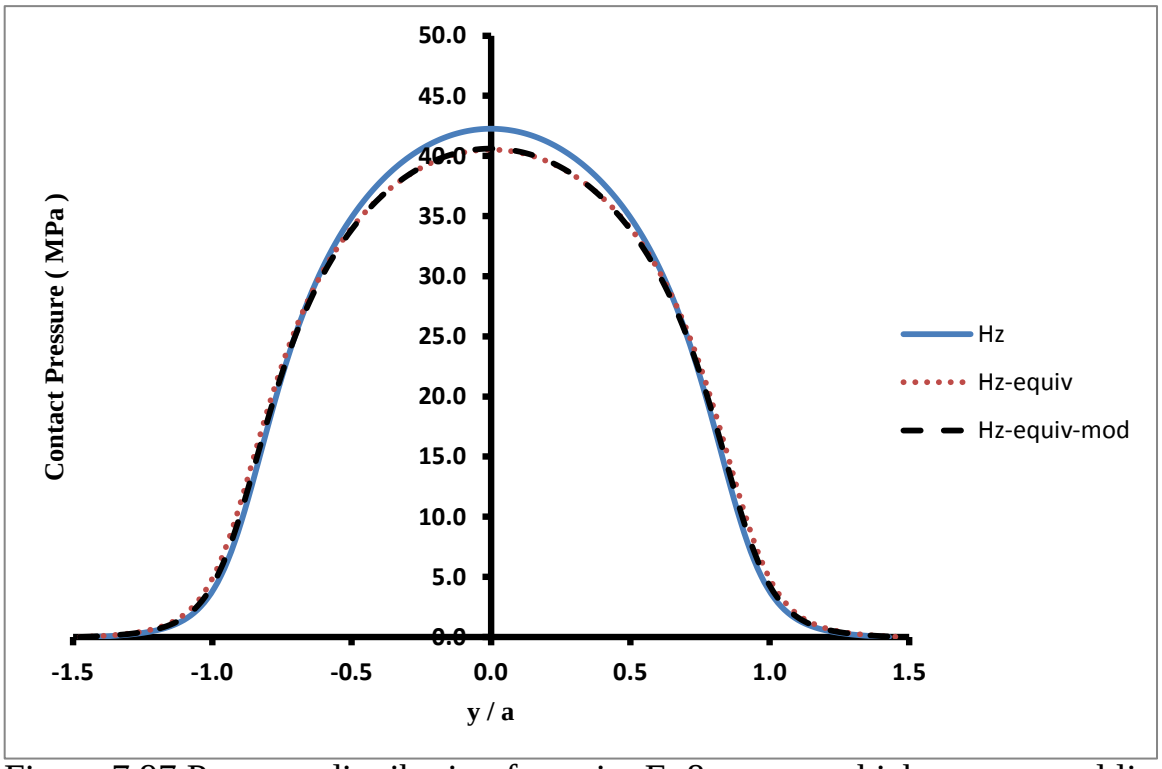

Figure 7.97 Pressure distribution for point E, 8 mm cup thickness, central line in y-direction

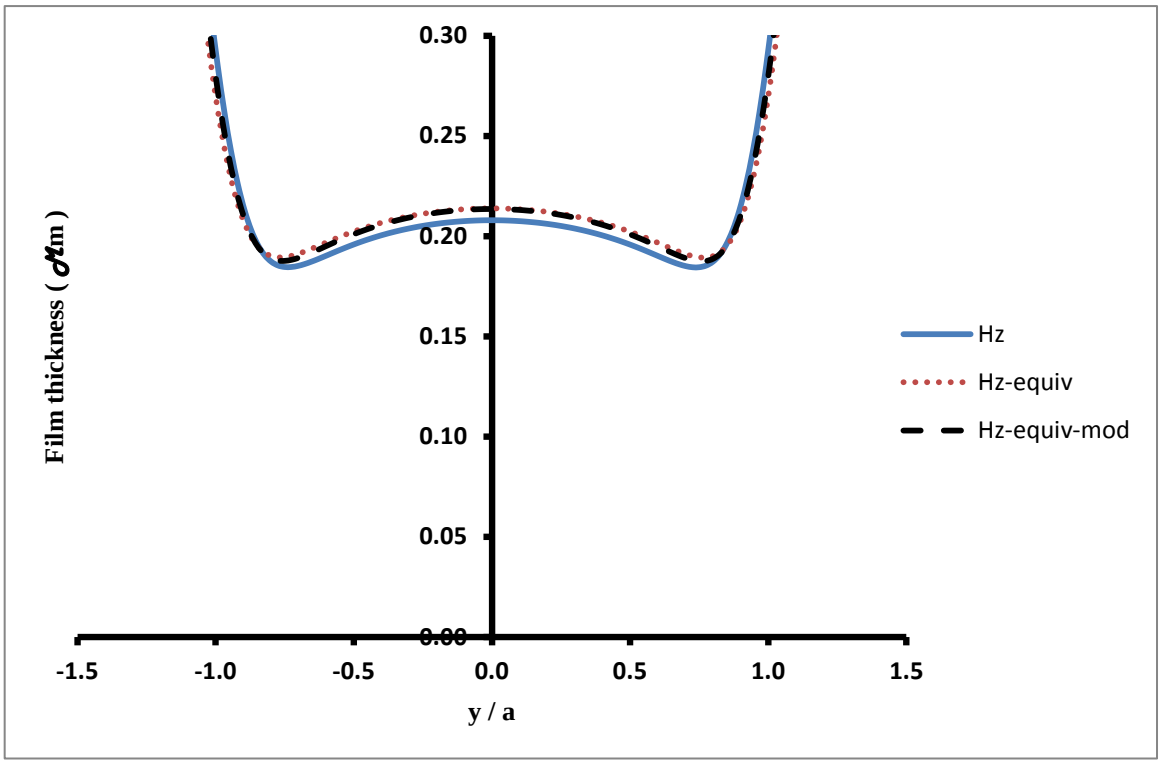

Figure 7.98 Film thickness for point E, 8 mm cup thickness, central line in y-direction

Contact Point F

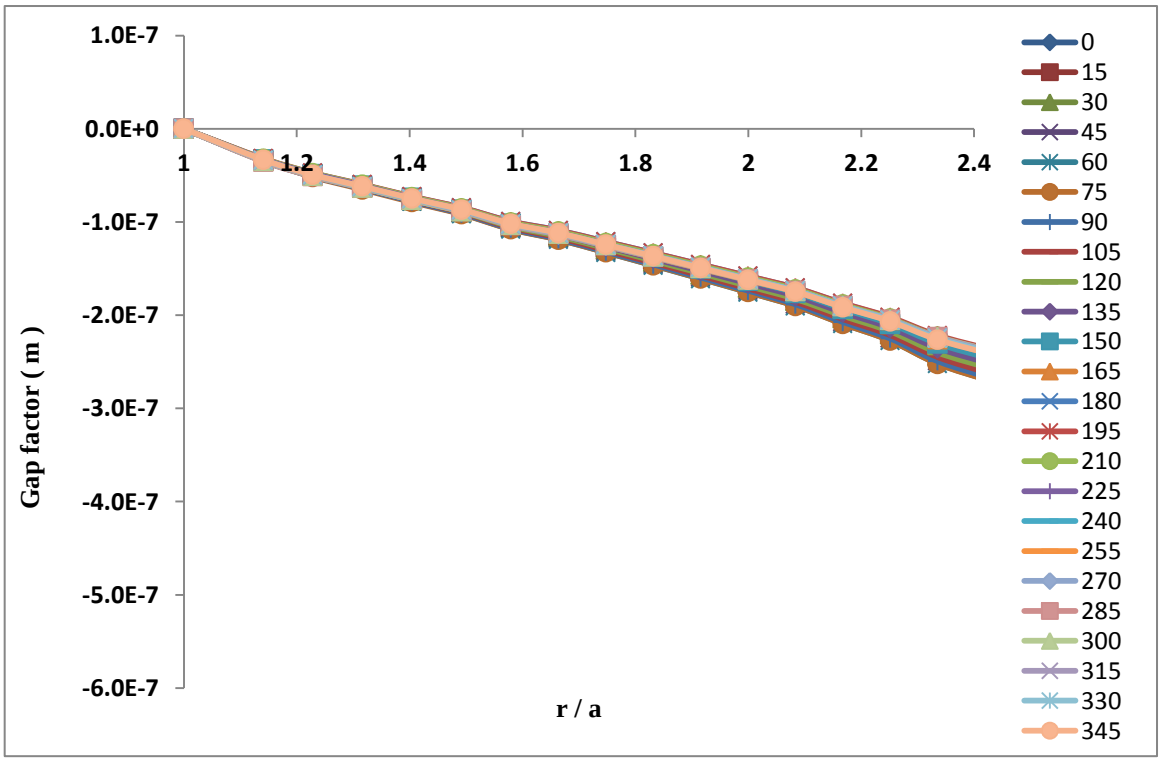

Figure 7.99 Gap factor for point F of 8 mm cup thickness

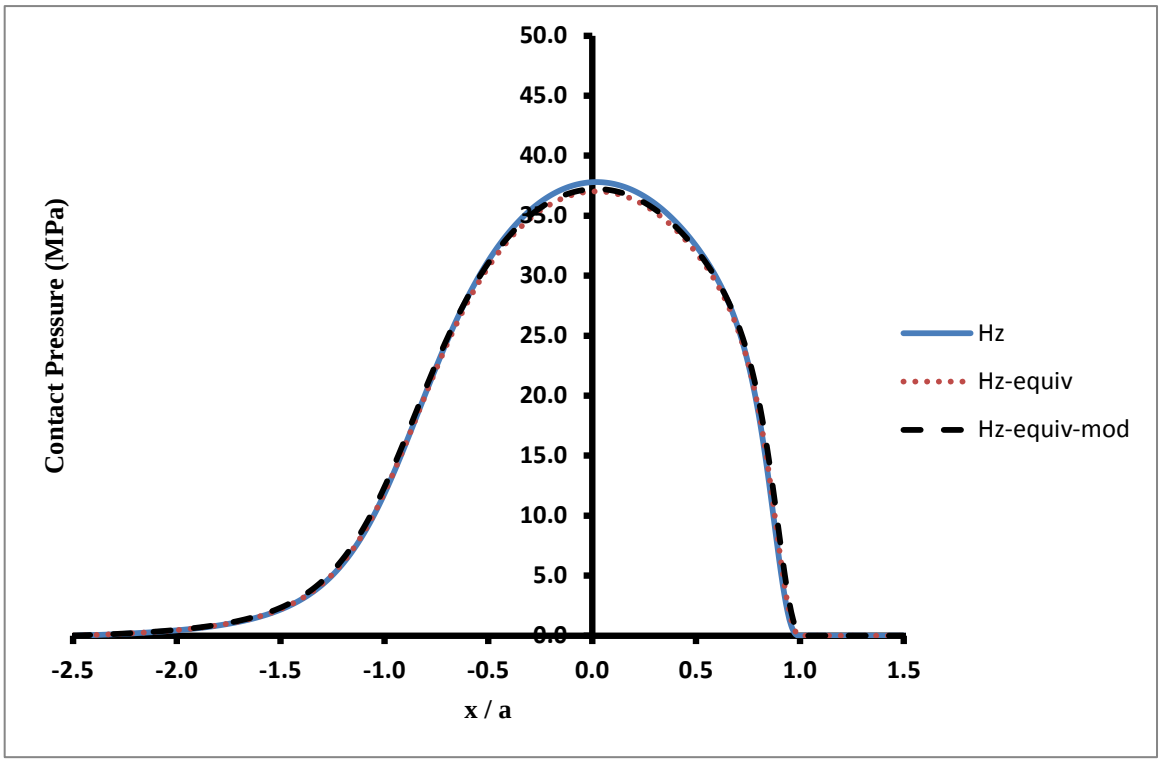

Figure 7.100 Pressure distribution for point F, 8 mm cup thickness, central line in x-direction

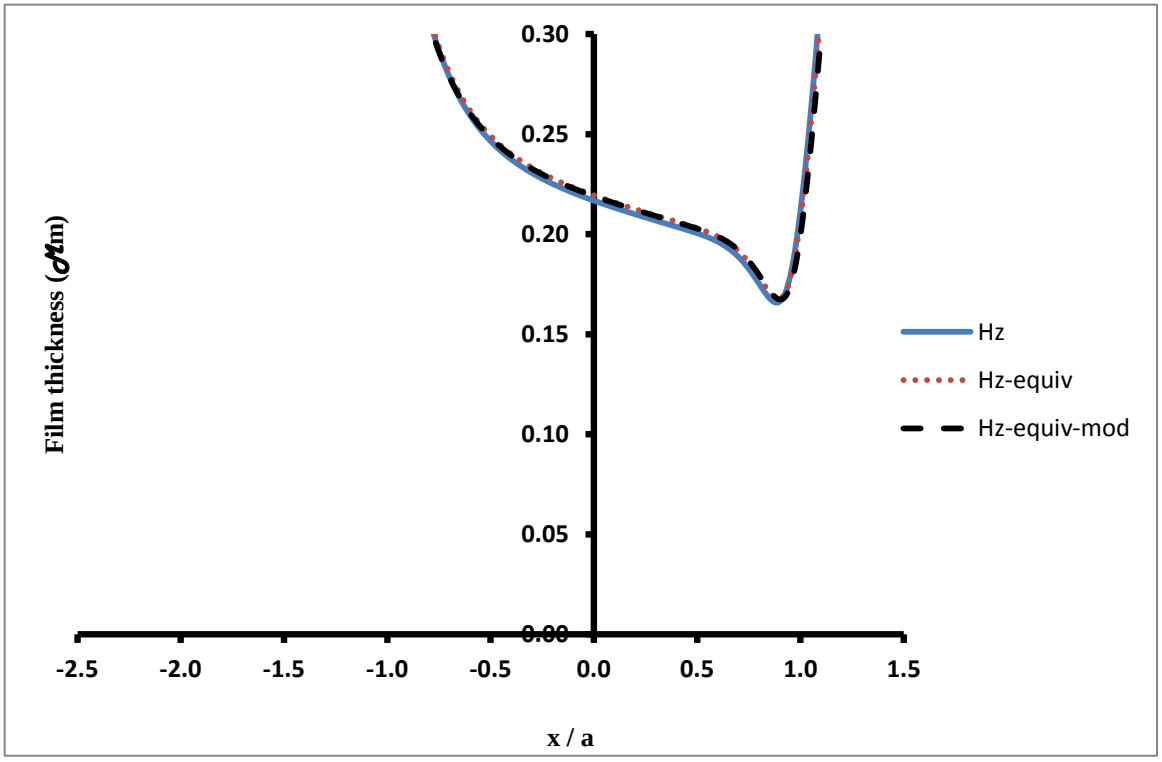

Figure 7.101 Film thickness for point F, 8 mm cup thickness, central line in x-direction

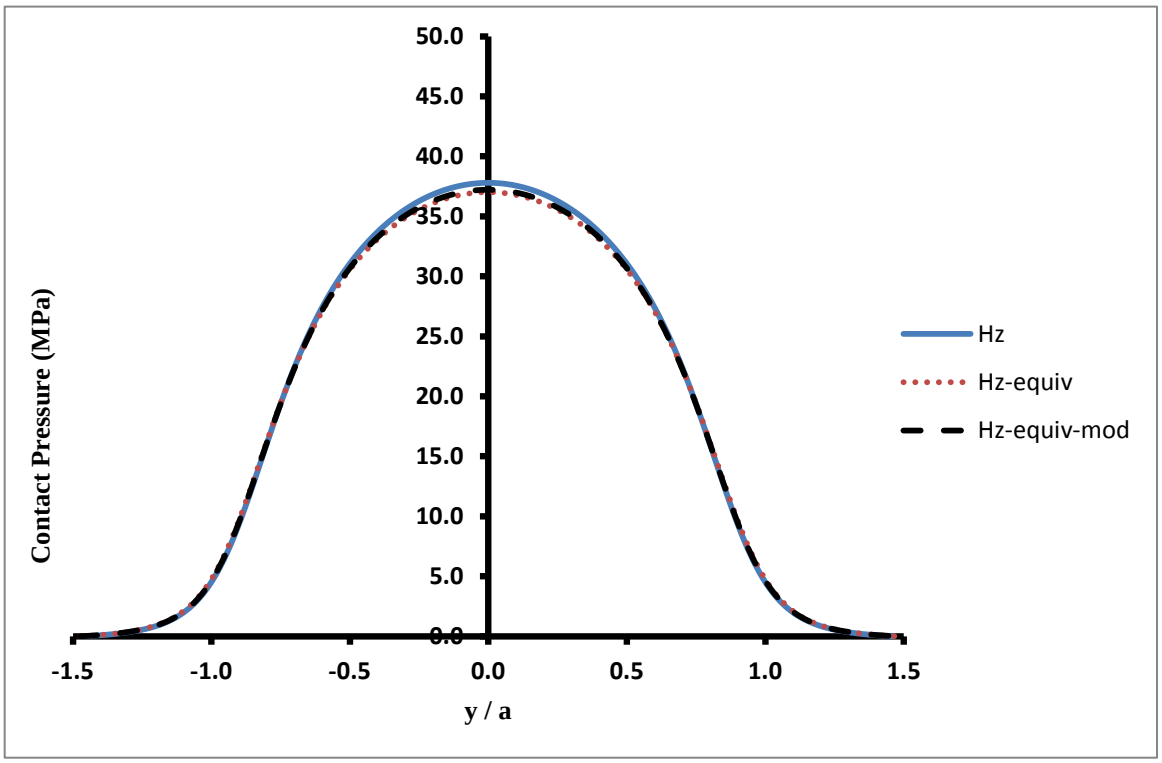

Figure 7.102 Pressure distribution for point F, 8 mm cup thickness, central line in y-direction

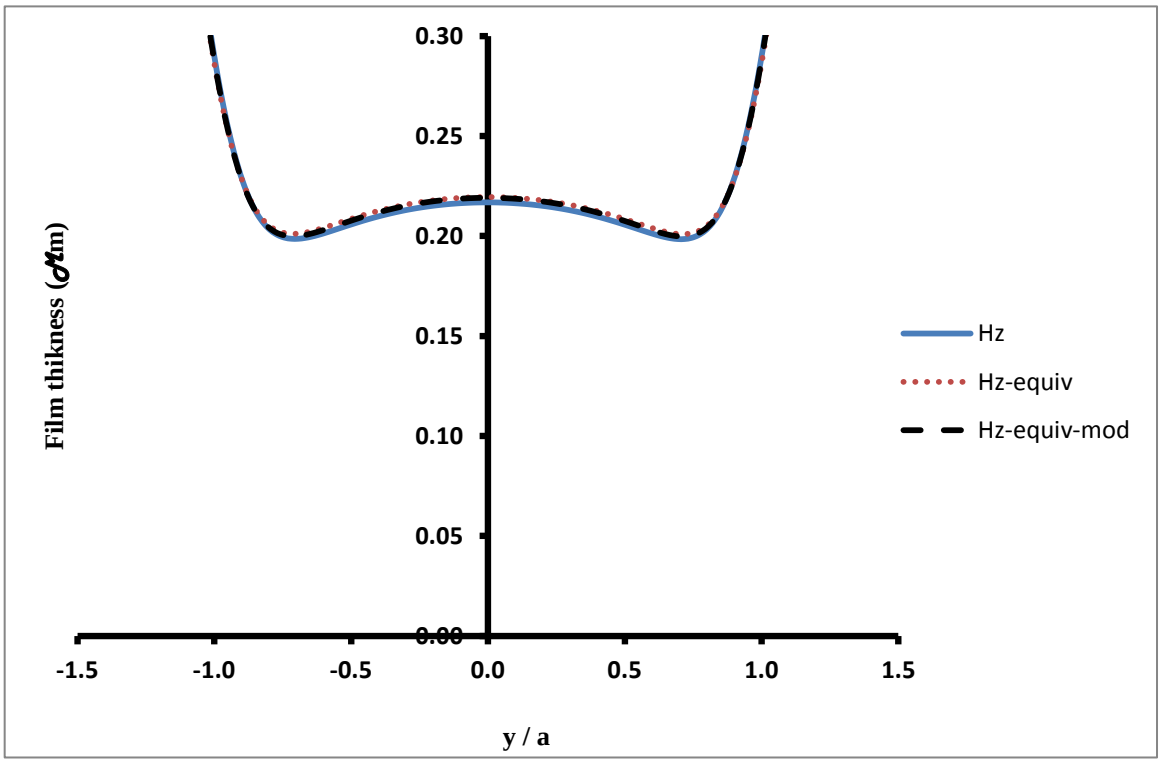

Figure 7.103 Film thickness for point F, 8 mm cup thickness, central line in y-direction

Contact Point G

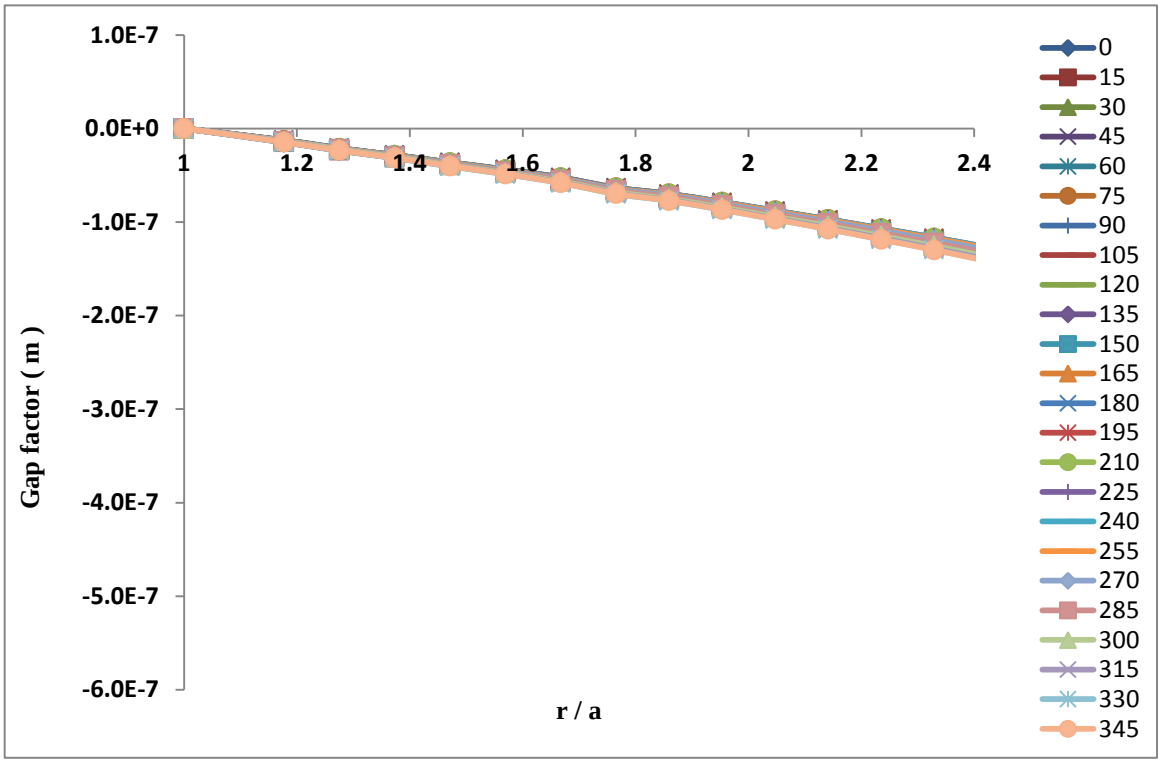

Figure 7.104 Gap factor for point G of 8 mm cup thickness

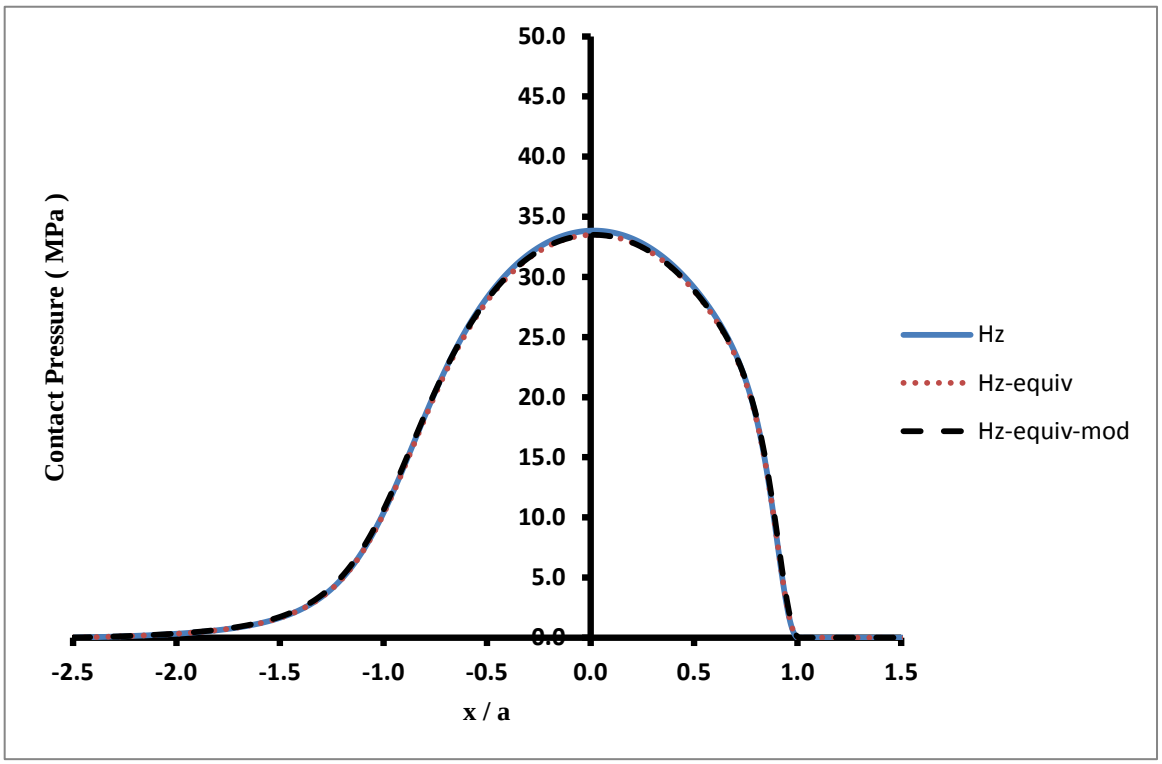

Figure 7.105 Pressure distribution for point G, 8 mm cup thickness, central line in x-direction

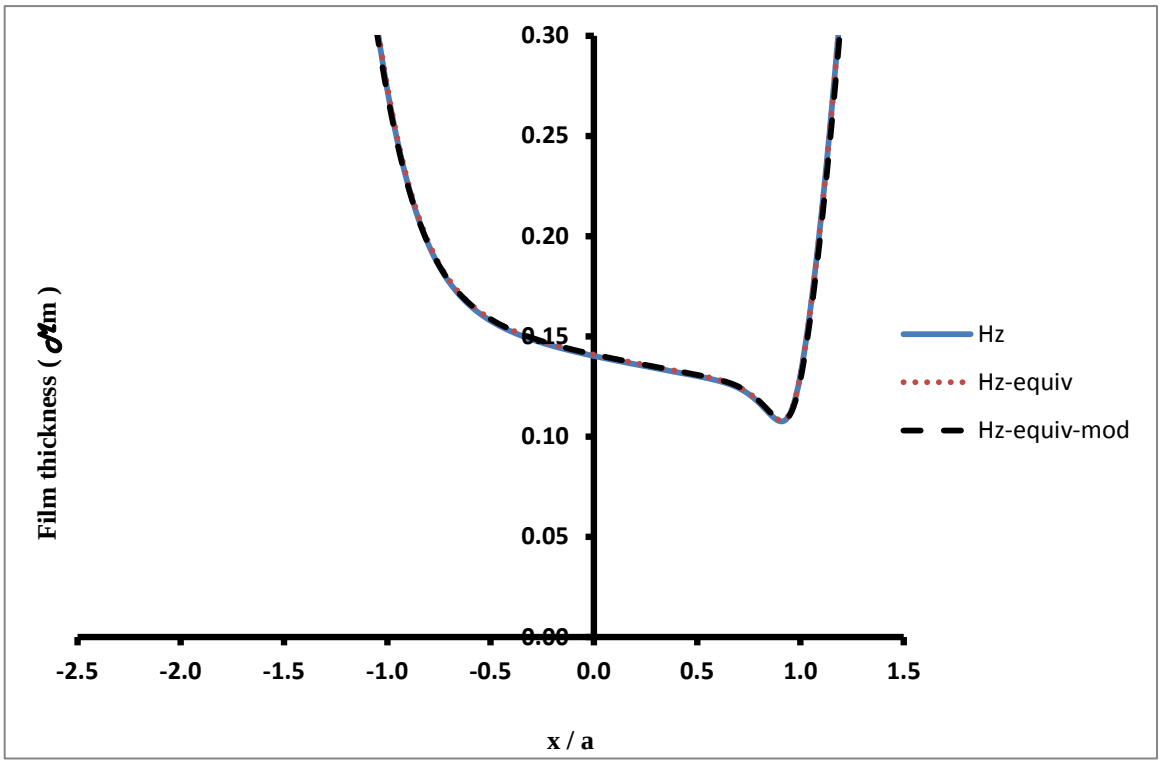

Figure 7.106 Film thickness for point G, 8 mm cup thickness, central line in x-direction

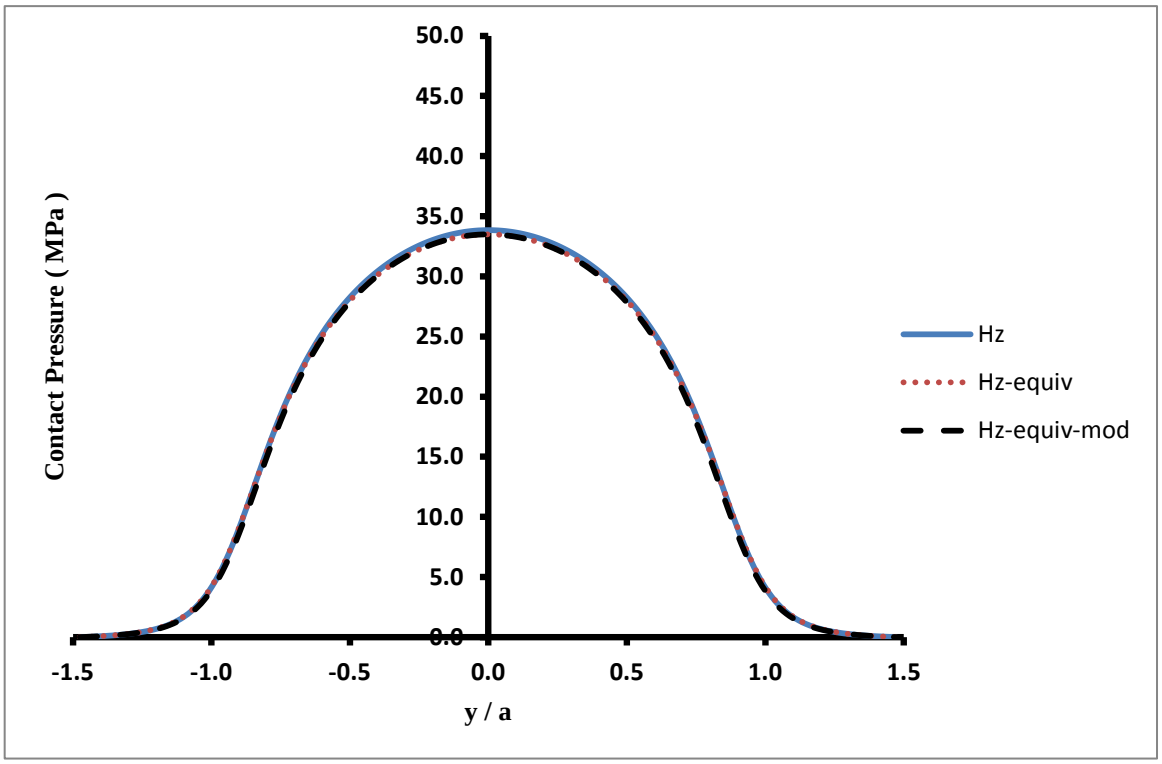

Figure 7.107 Pressure distribution for point G, 8 mm cup thickness, central line in y-direction

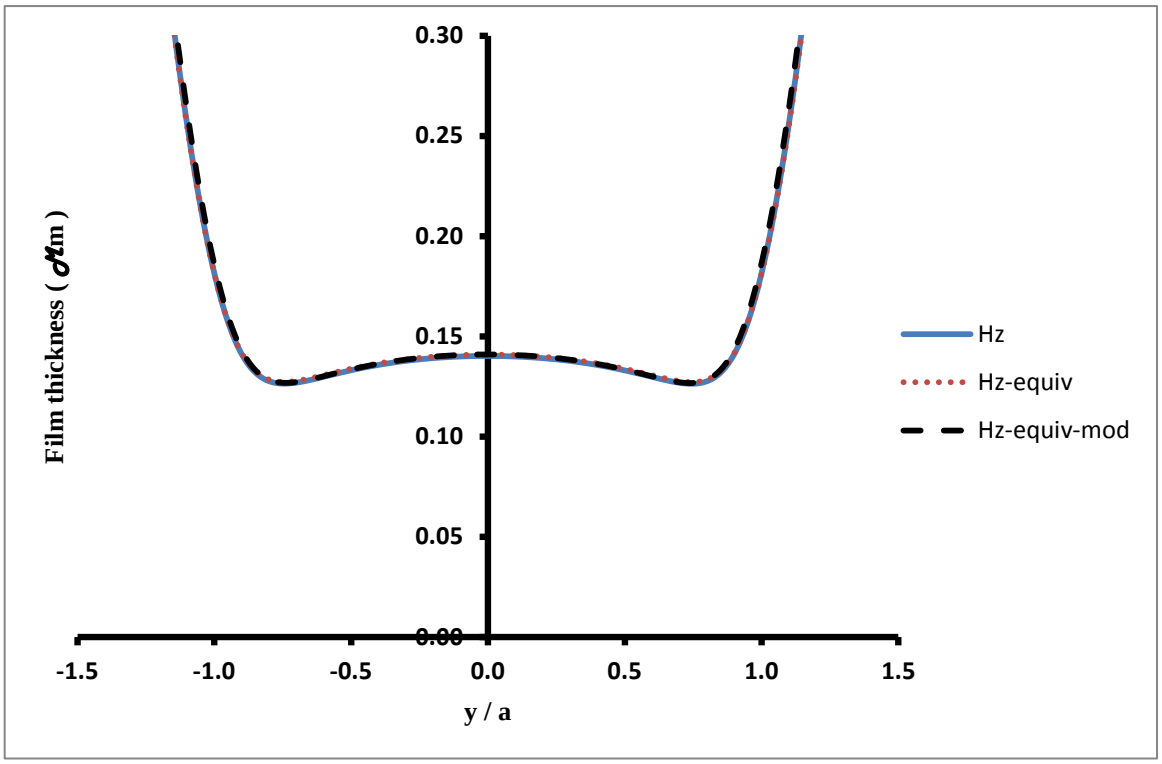

Figure 7.108 Film thickness for point G, 8 mm cup thickness, central line in y-direction

Contact Point H

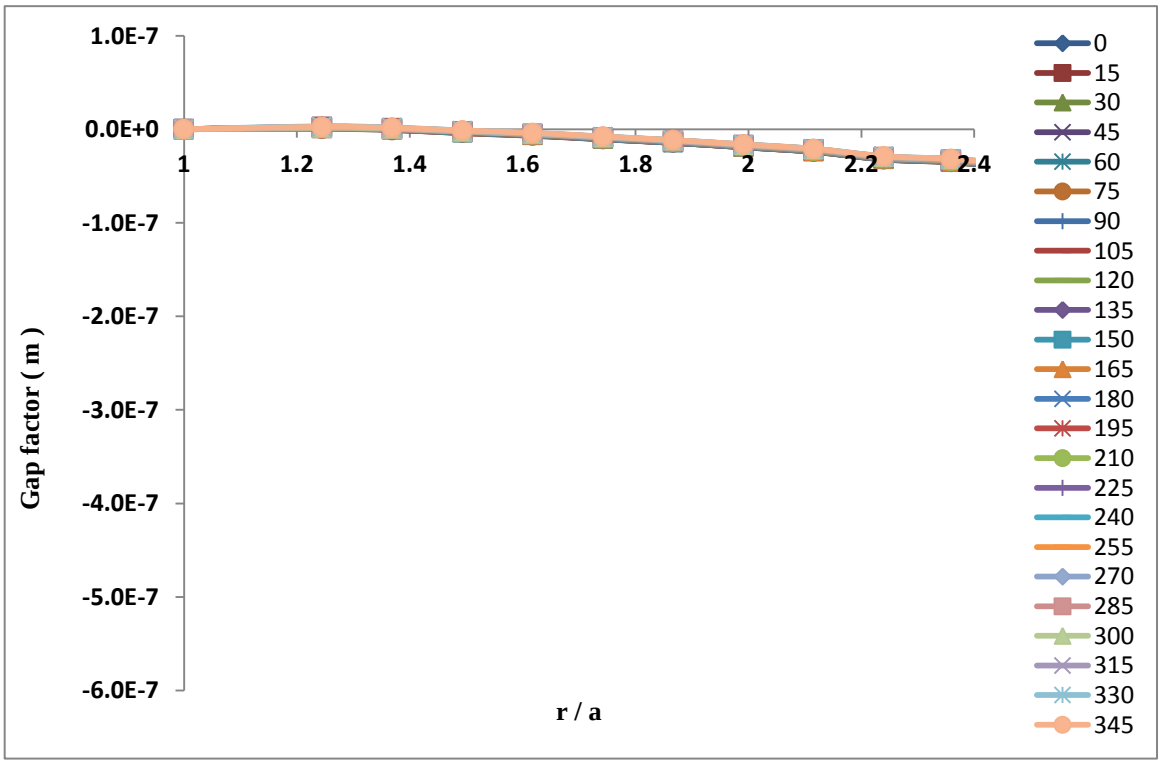

Figure 7.109 Gap factor for point H of 8 mm cup thickness

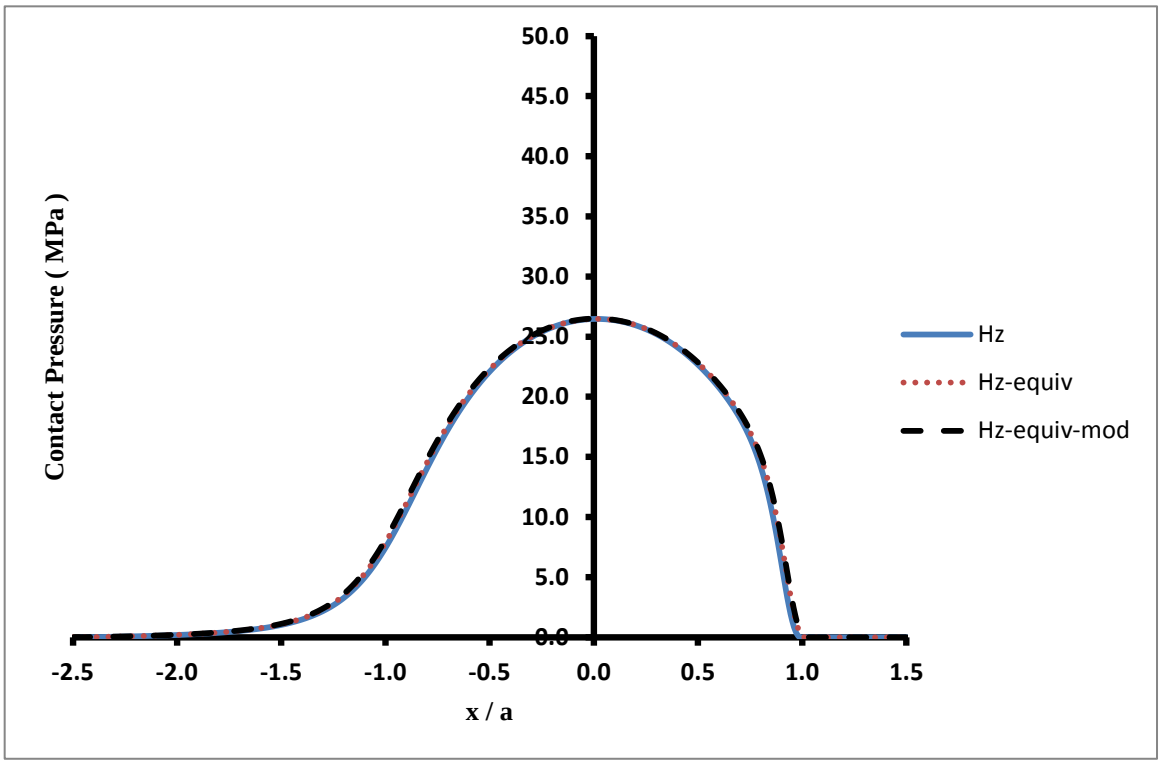

Figure 7.110 Pressure distribution for point H, 8 mm cup thickness, central line in x-direction

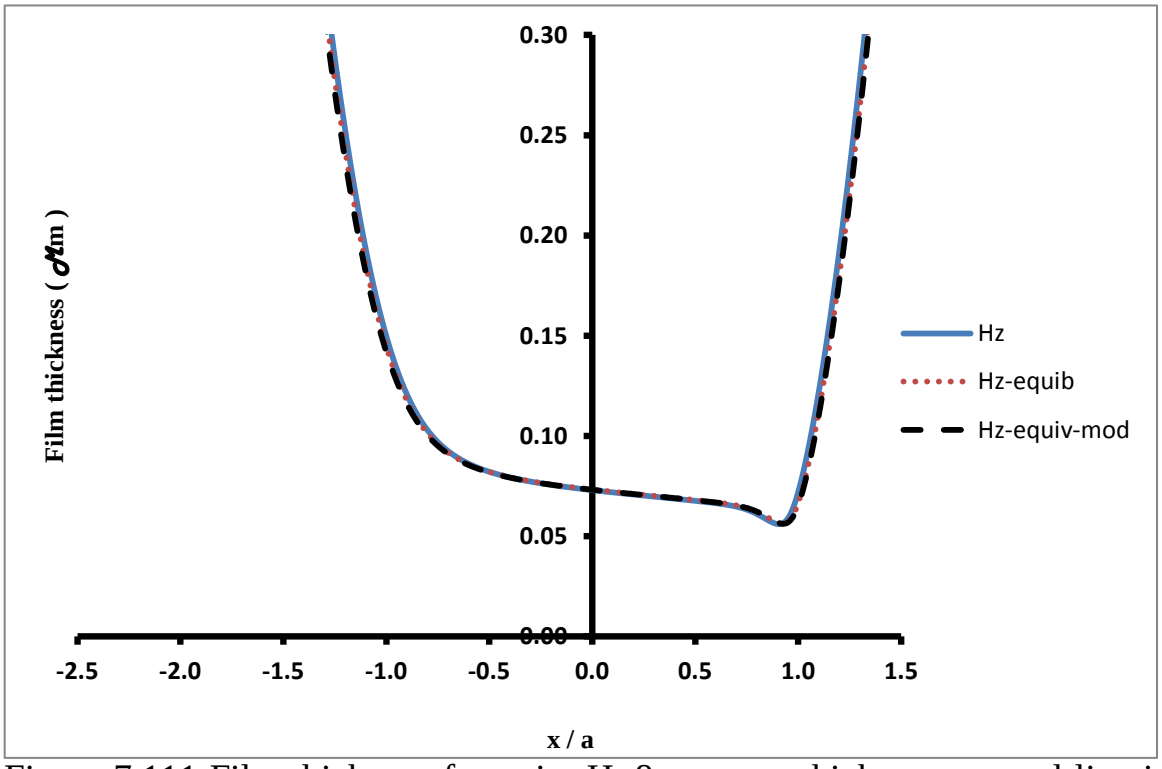

Figure 7.111 Film thickness for point H, 8 mm cup thickness, central line in x-direction

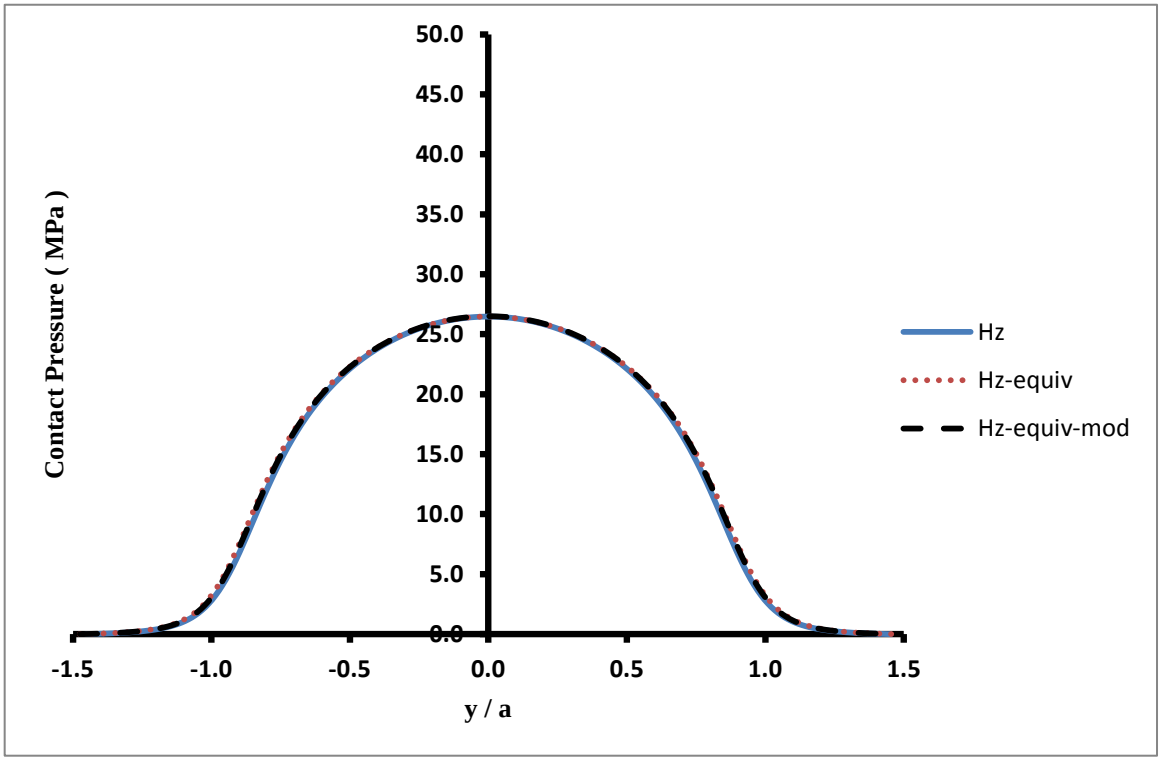

Figure 7.112 Pressure distribution for point H, 8 mm cup thickness, central line in y-direction

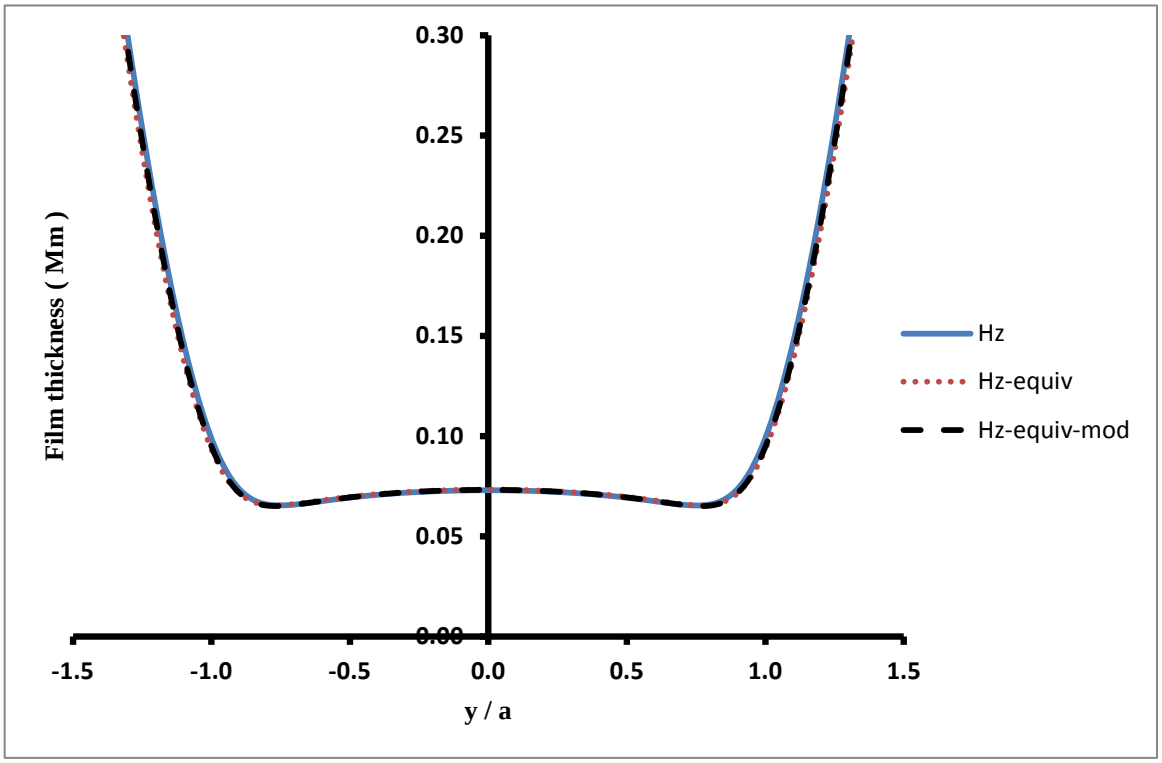

Figure 7.113 Film thickness for point H, 8 mm cup thickness, central line in y-direction

Contact Point I

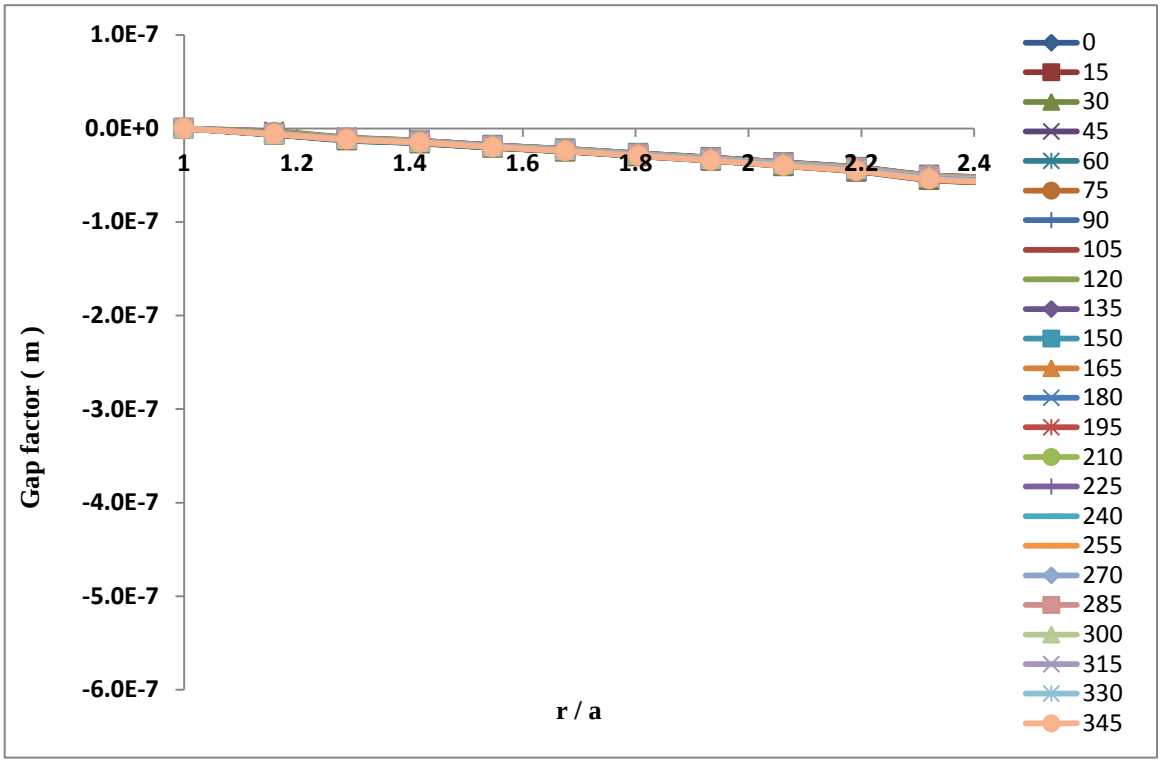

Figure 7.114 Gap factor for point I of 8 mm cup thickness

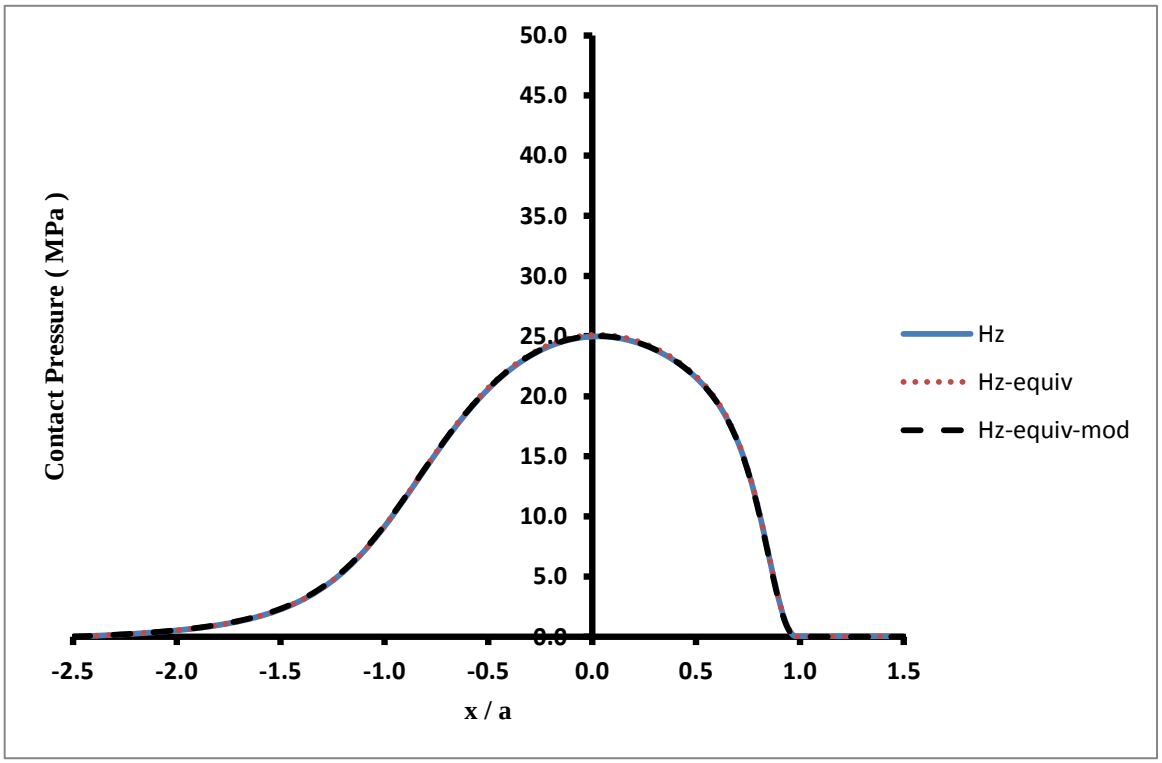

Figure 7.115 Pressure distribution for point I, 8 mm cup thickness, central line in x-direction

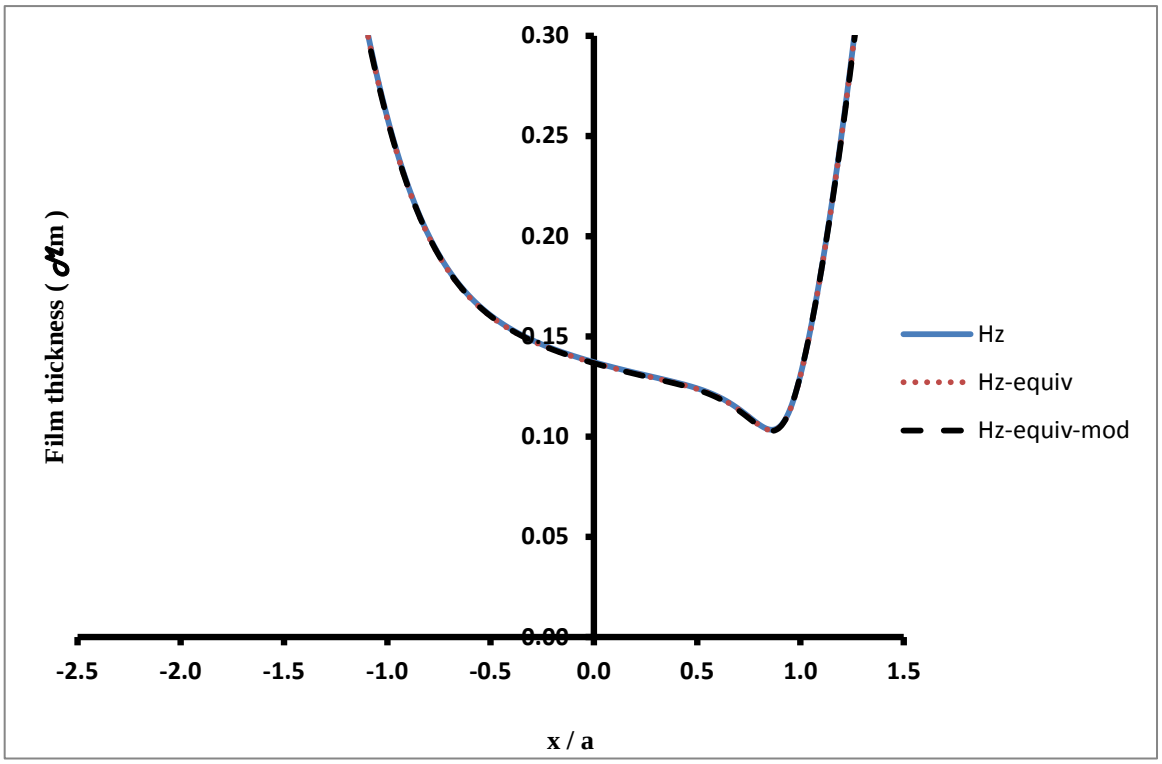

Figure 7.116 Film thickness for point I, 8 mm cup thickness, central line in x-direction

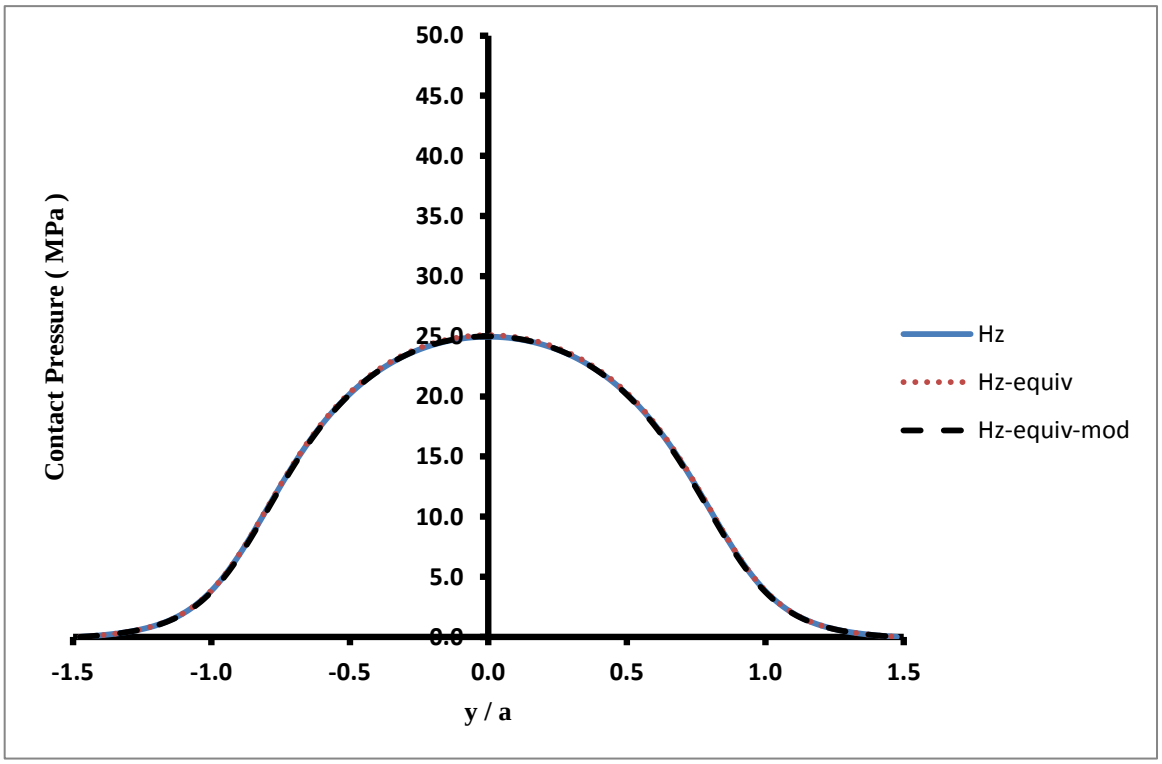

Figure 7.117 Pressure distribution for point I, 8 mm cup thickness, central line in y-direction

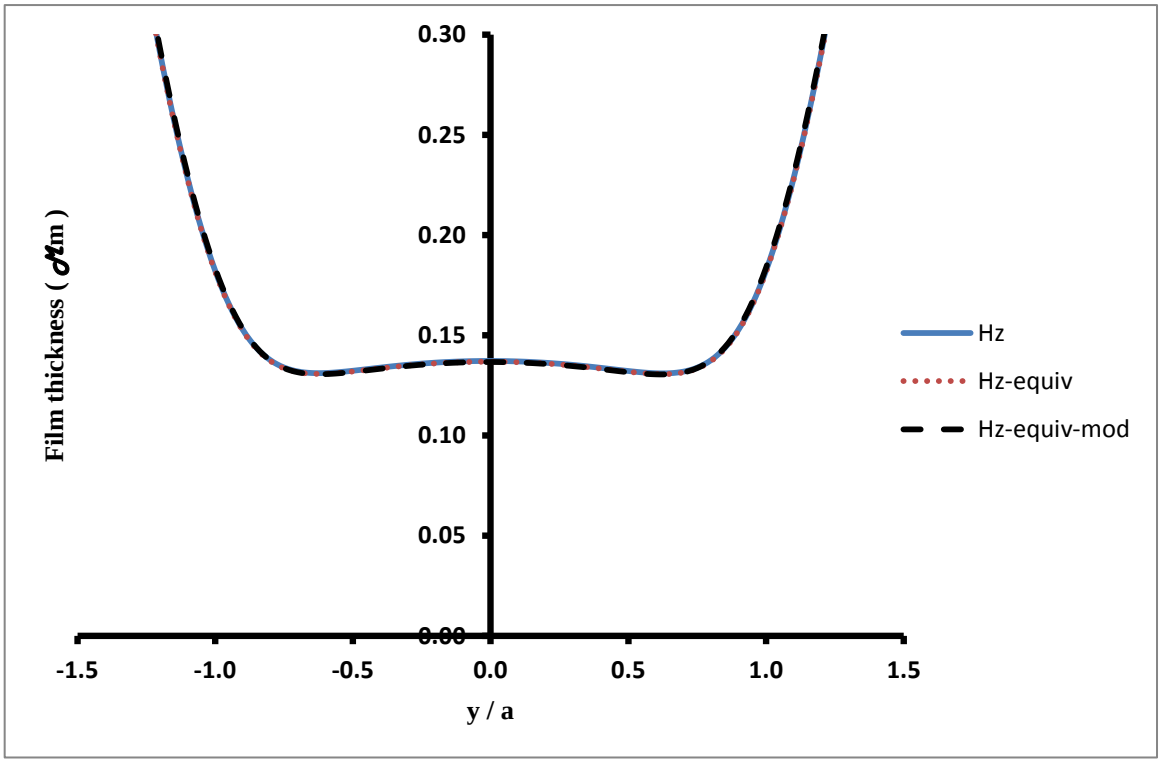

Figure 7.118 Film thickness for point I, 8 mm cup thickness, central line in y-direction

Table 7.4 Calculated Hertzian and equivalent pressure and the ratio between them, Hertzian and equivalent central film thickness and the ratio between them, Hertzian and equivalent radius of contact area for the 8 mm cup.

	a_h(mm)	a_{equiv}(mm)	$P_{o(h)}$(MPa)	$P_{o(equiv)}$(MPa)	%	$h_{c(h)}$(μm)	$h_{c(equiv)}$(μm)	%
A	2.852	2.867	31.277	30.932	-1.103	0.177	0.178	0.643
B	4.195	4.278	48.811	45.635	-6.507	0.123	0.128	3.775
C	4.204	4.295	49.304	46.176	-6.344	0.054	0.056	3.852
D	4.088	4.182	47.581	45.188	-5.029	0.115	0.118	3.064
E	3.736	3.858	42.267	40.524	-4.124	0.208	0.214	2.846
F	3.395	3.426	37.801	37.021	-2.063	0.217	0.219	1.228
G	3.003	3.010	33.848	33.495	-1.043	0.140	0.141	0.508
H	2.336	2.372	26.471	26.477	0.023	0.073	0.073	0.447
I	2.293	2.290	24.970	25.102	0.529	0.137	0.137	-0.287

7.7 Detailed EHL results for 10 mm cup thickness

Results of the EHL analysis for the 10 mm cup thickness are given in figures 7.119 to 7.163 and show that the Hertzian, equivalent and modified equivalent models of all the nine contact points are very similar, except for points B, C and D where there are a small difference between the Hertzian and the equivalent cases. No variation was observed in the film thicknesses. As mentioned in section 7.5, when the cup thickness increases the equivalent case becomes similar to the Hertzian case.

For the contact points B, C and D of the 10 mm cup thickness, the maximum pressure of the equivalent model reduced by 1.8%, 2.4% and 2.1%, as shown in Table 7.5, relative to the Hertzian model pressure, and the variation in the pressure for the other contact points is about 1% or less. Increases in the central film thicknesses were found of 1%, 1.4% and 1.3% for points B, C and D respectively, and less than 1% for the rest of the contact points.

Comparisons were made of the average value of the gap factor for each of the nine contact points. For example, for point G at r/a = 2.4 and cup thicknesses of 4, 6, 8 and 10 mm these values were found to be 0.58, 0.25, 0.12 and 0.08 μm. It can be said that the gap factor depends on the cup thickness used, although within this range of values no significant changes were observed in the results of the contact pressure and film thickness.

A summary of the results for the 10 mm cup thickness cases is given in Table 7.5.

EHL results for 10 mm Cup thickness

Contact Point A

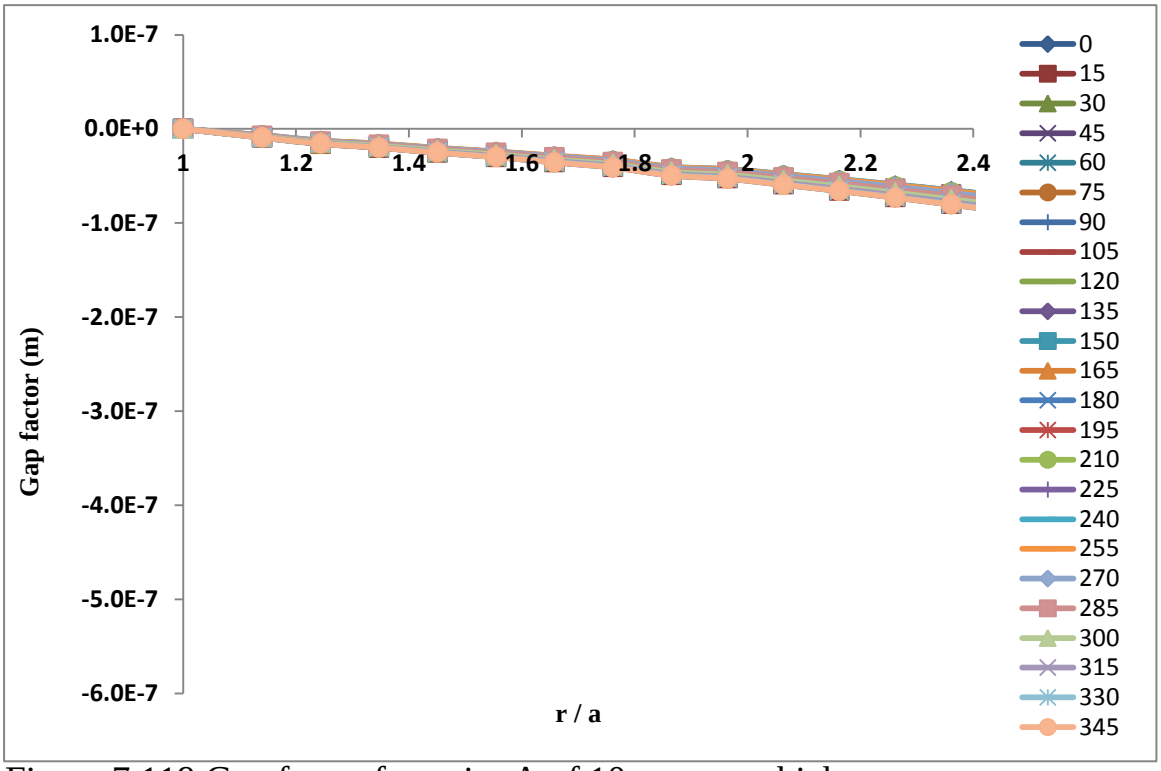

Figure 7.119 Gap factor for point A of 10 mm cup thickness

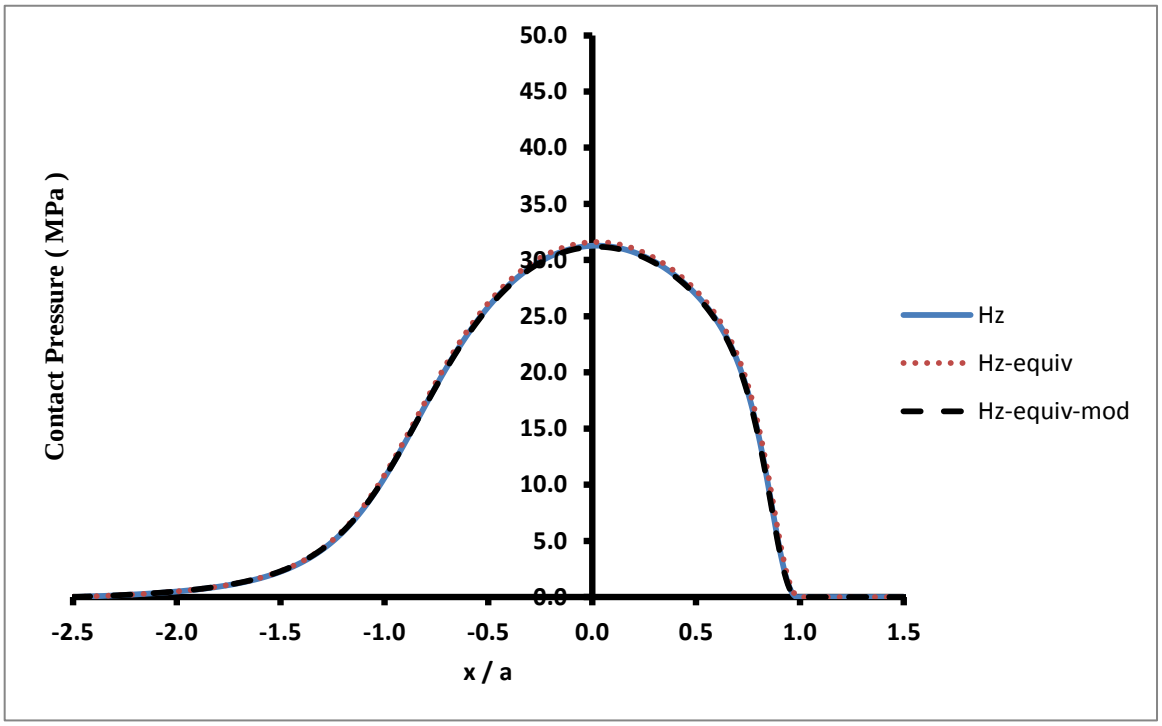

Figure 7.120 Pressure distribution for point A, 10 mm cup thickness, central line in x-direction

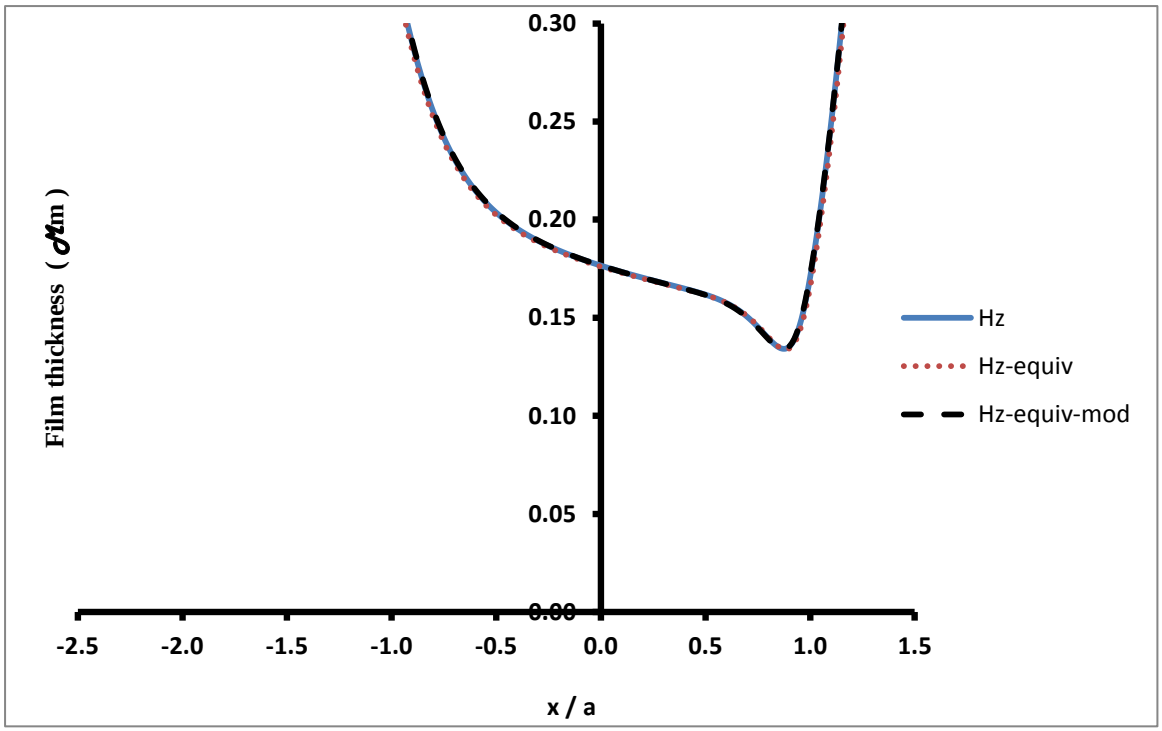

Figure 7.121 Film thickness for point A, 10 mm cup thickness, central line in x-direction

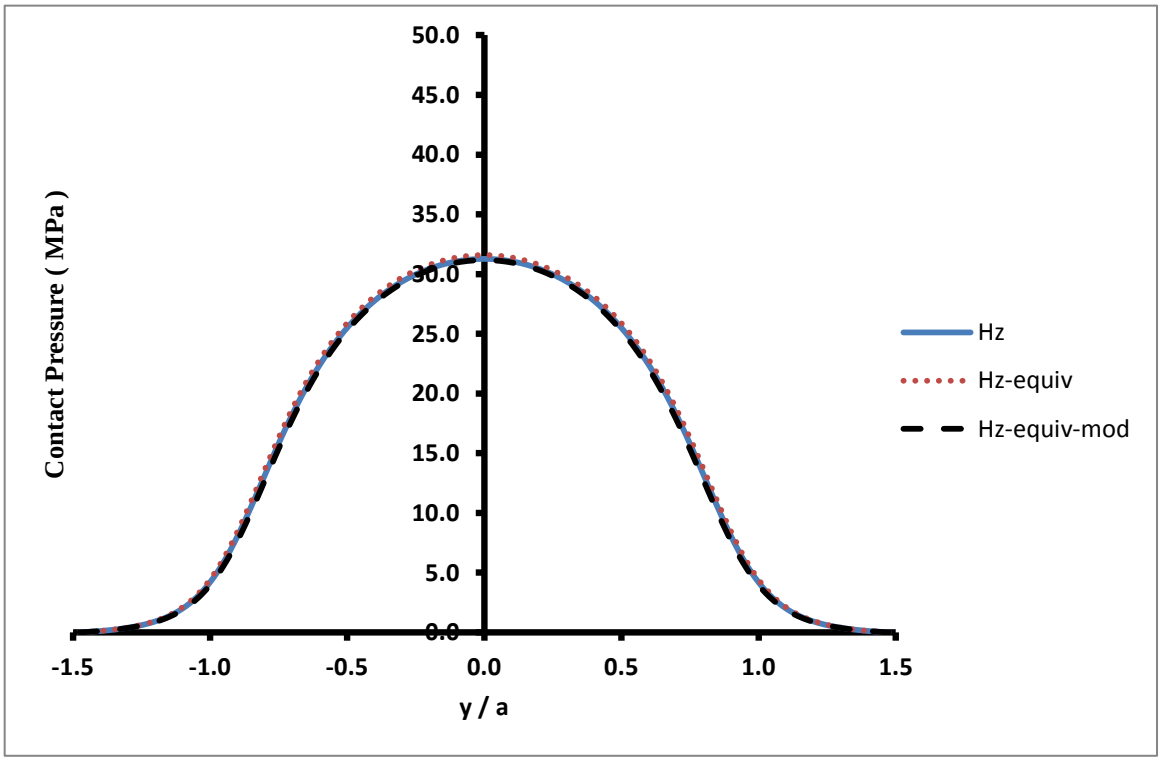

Figure 7.122 Pressure distribution for point A, 10 mm cup thickness, central line in y-direction

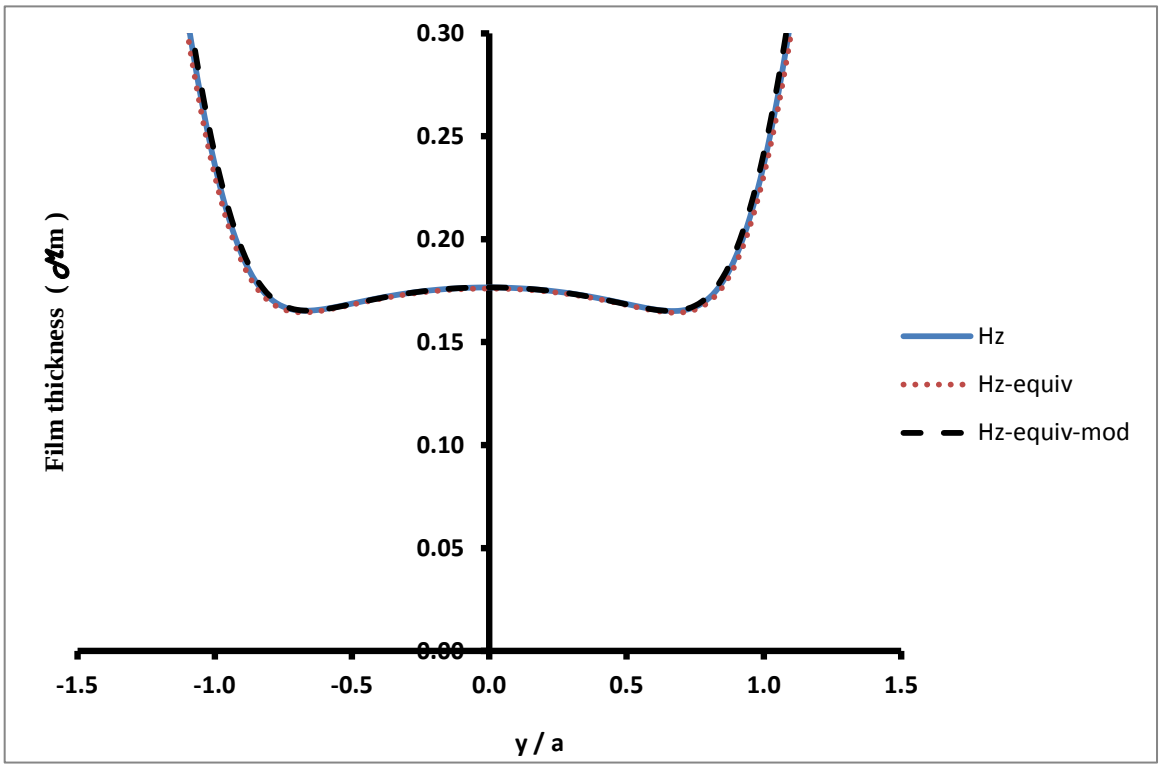

Figure 7.123 Film thickness for point A, 10 mm cup thickness, central line in y-direction

Contact Point B

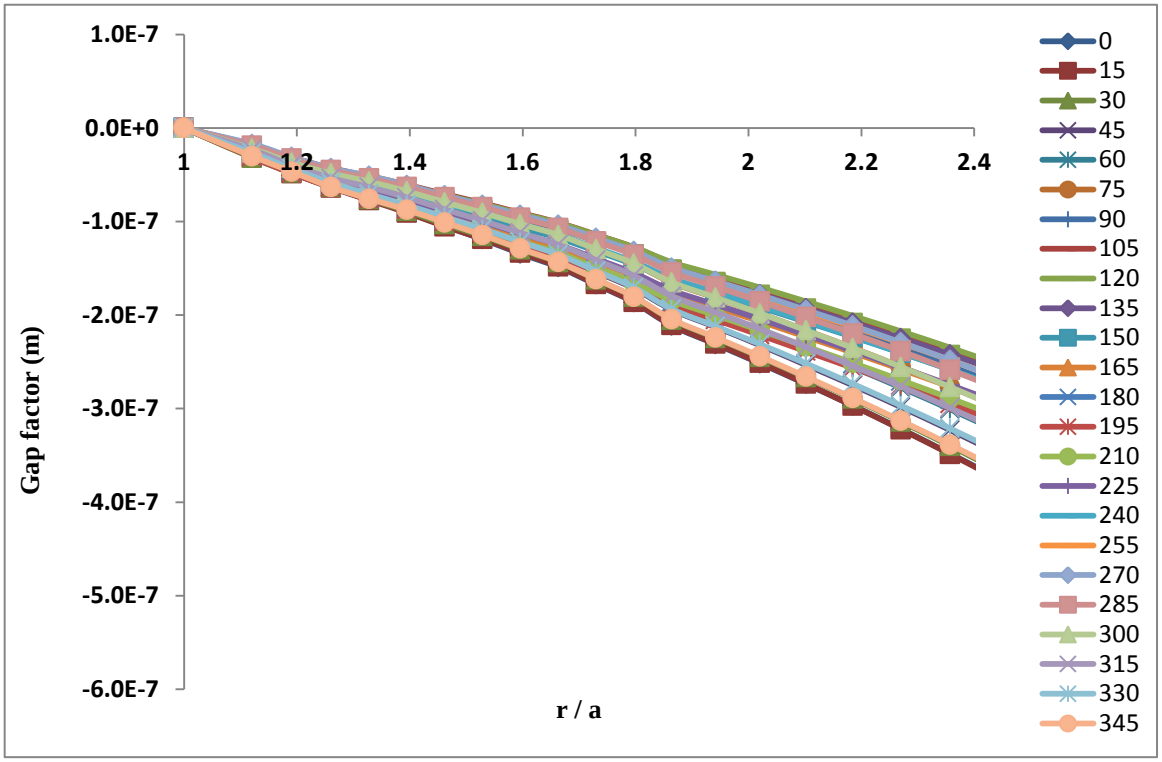

Figure 7.124 Gap factor for point B of 10 mm cup thickness

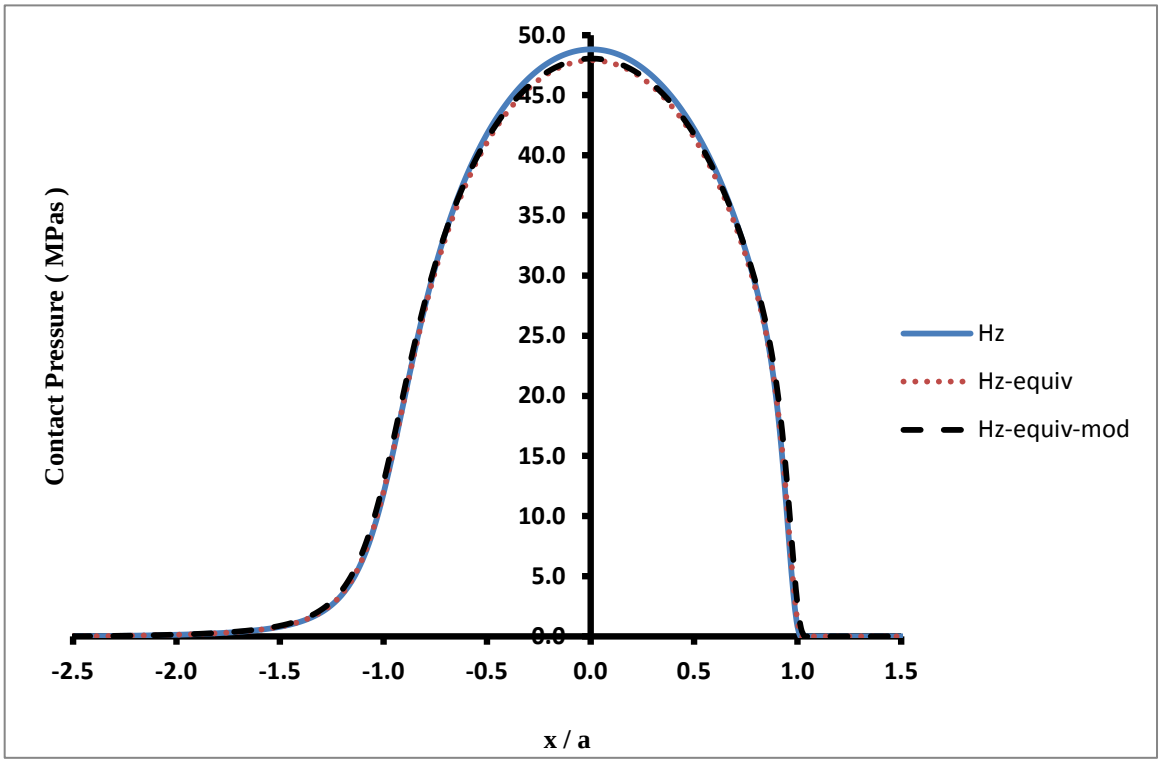

Figure 7.125 Pressure distribution for point B, 10 mm cup thickness, central line in x-direction

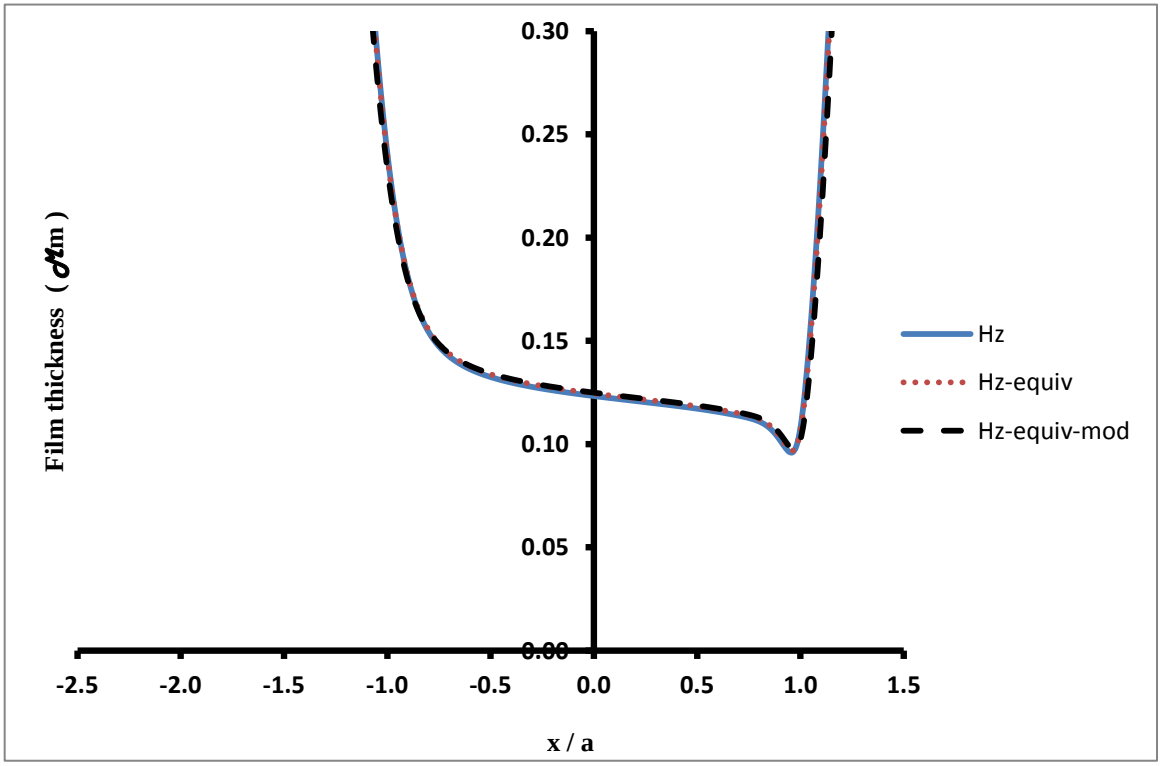

Figure 7.126 Film thickness for point B, 10 mm cup thickness, central line in x-direction

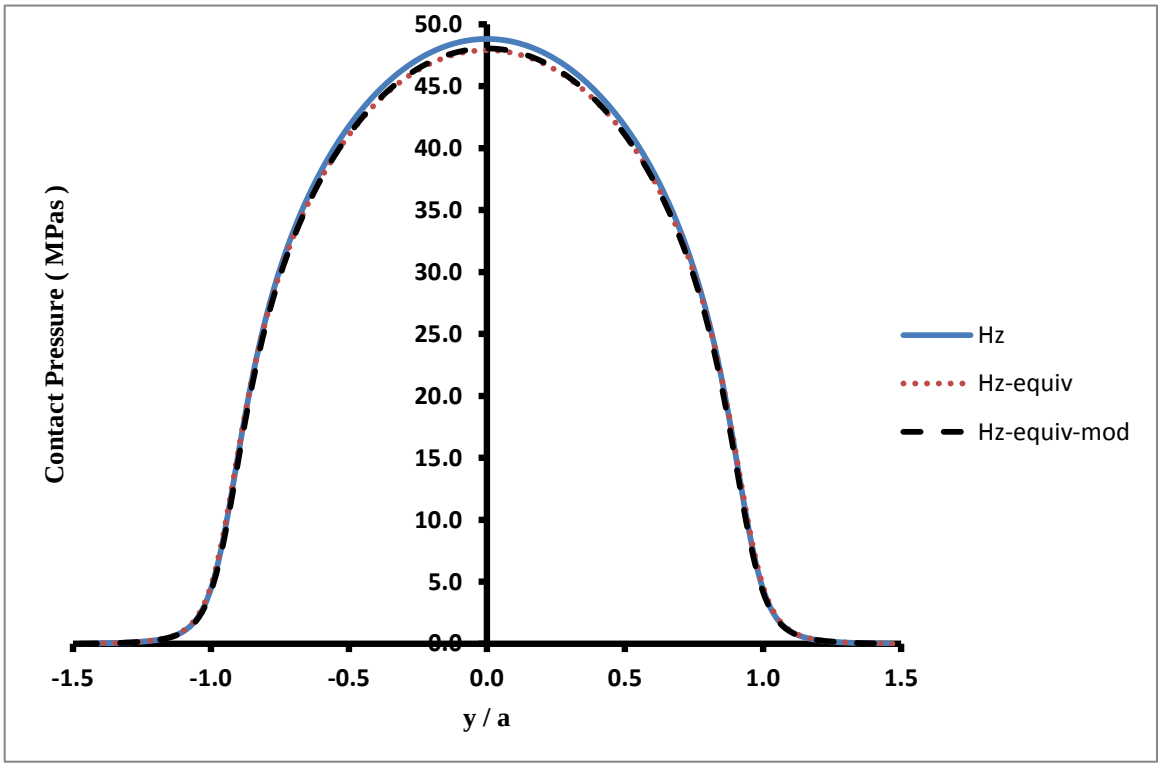

Figure 7.127 Pressure distribution for point B, 10 mm cup thickness, central line in y-direction

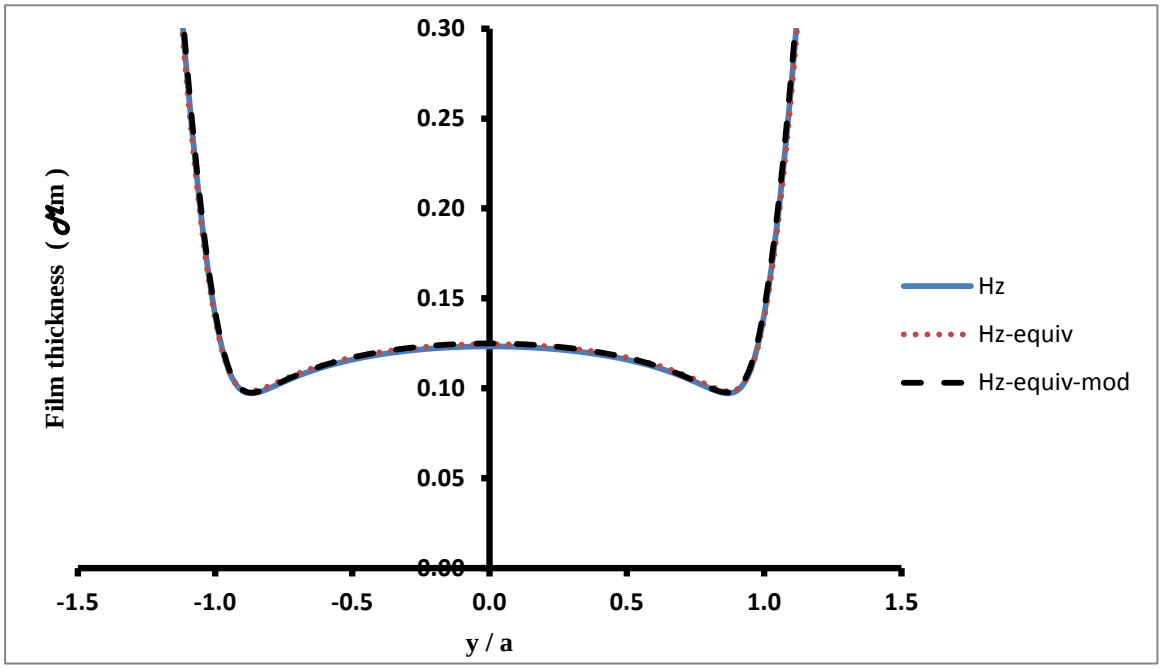

Figure 7.128 Film thickness for point B, 10 mm cup thickness, central line in y-direction

Contact Point C

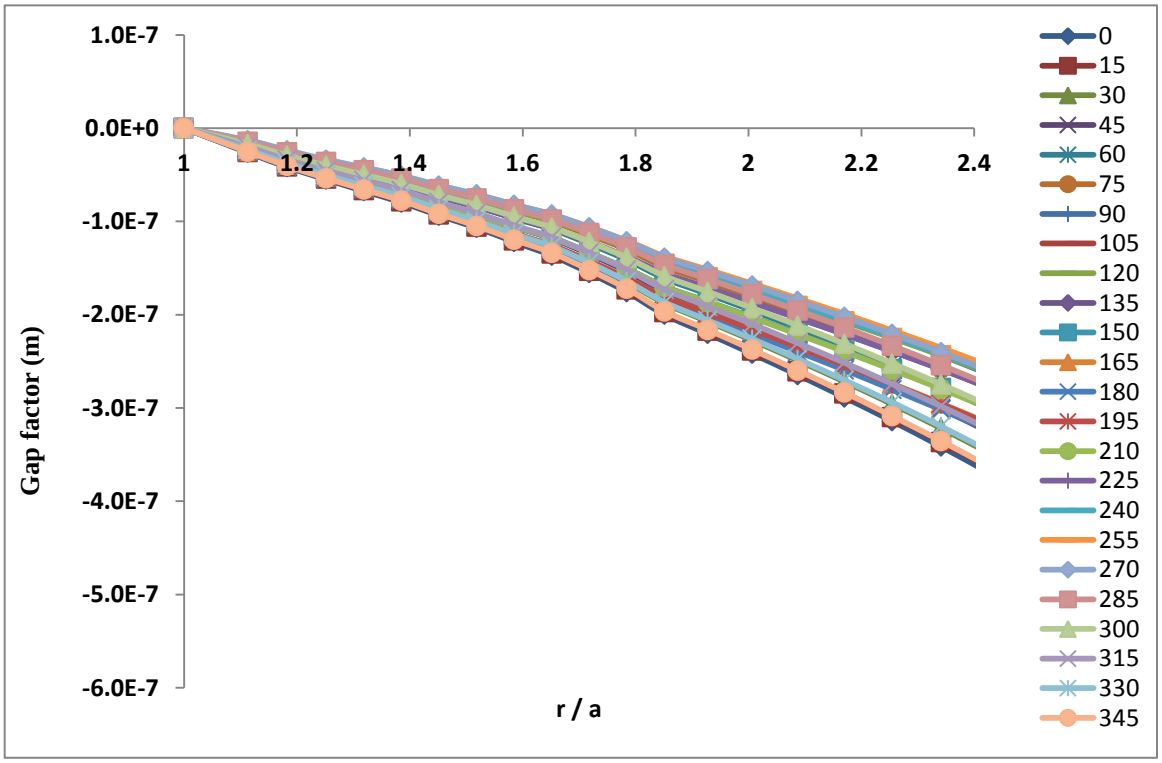

Figure 7.129 Gap factor for point C of 10 mm cup thickness

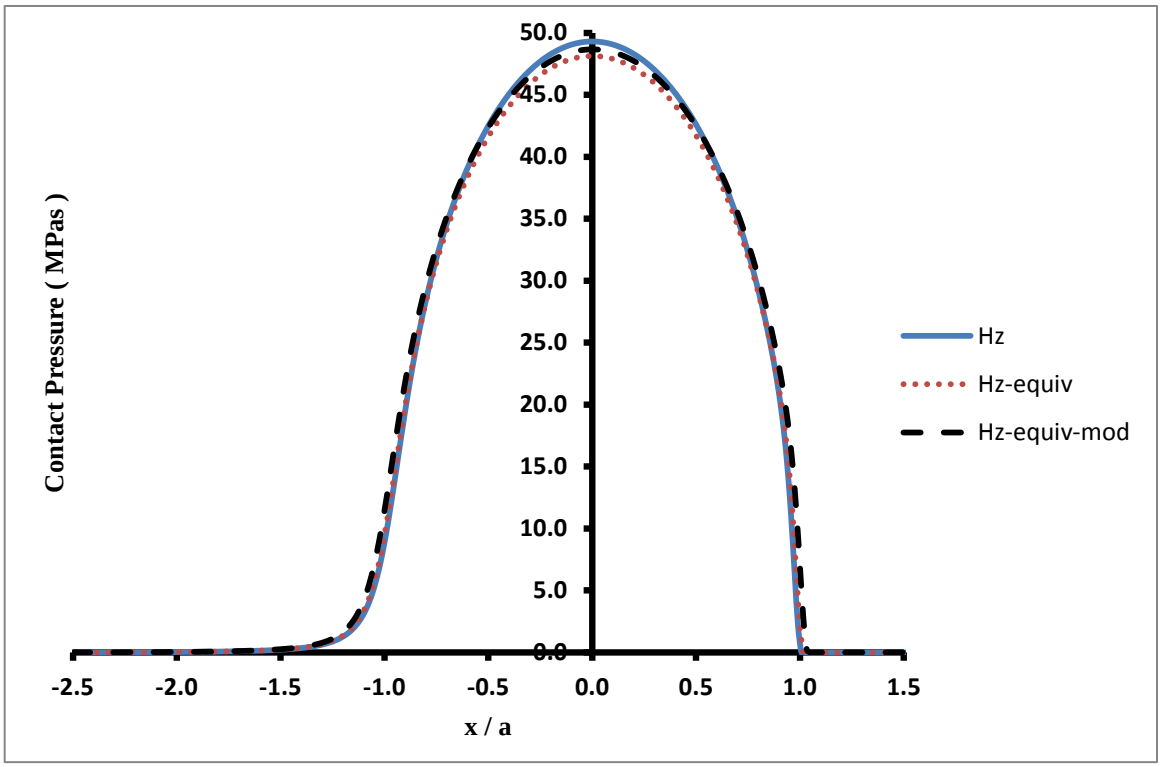

Figure 7.130 Pressure distribution for point C, 10 mm cup thickness, central line in x-direction

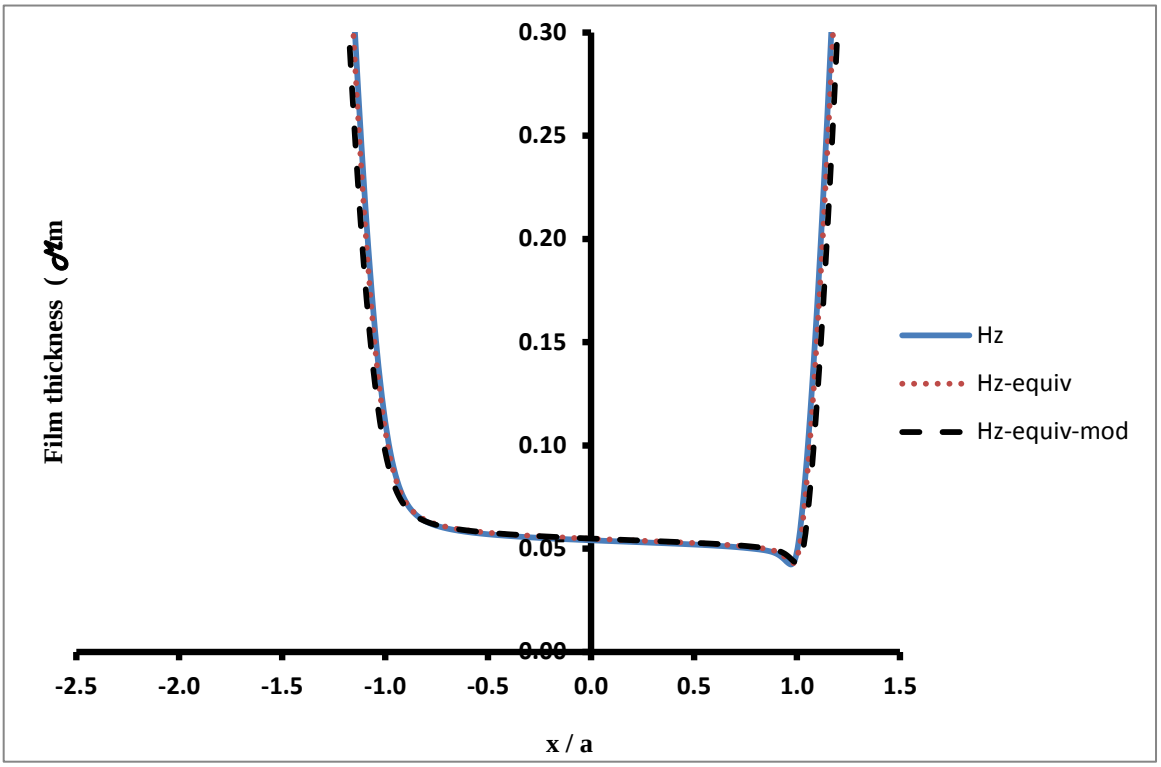

Figure 7.131 Film thickness for point C, 10 mm cup thickness, central line in x-direction

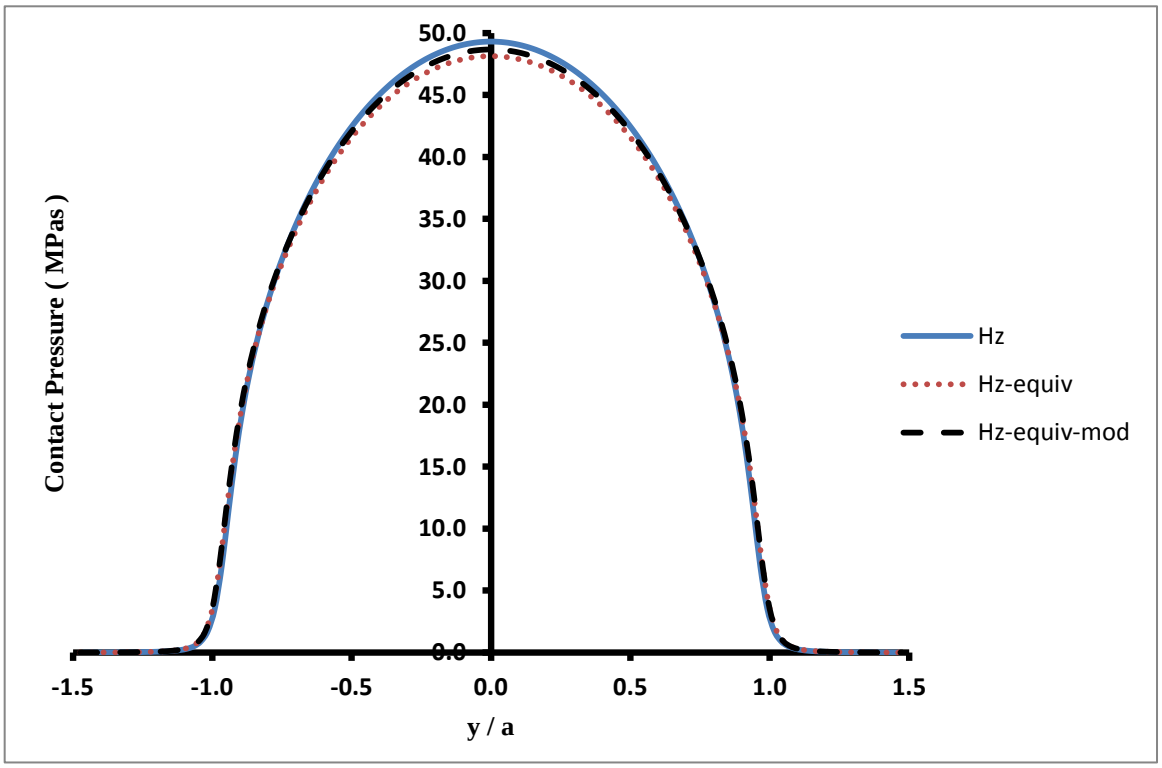

Figure 7.132 Pressure distribution for point C, 10 mm cup thickness, central line in y-direction

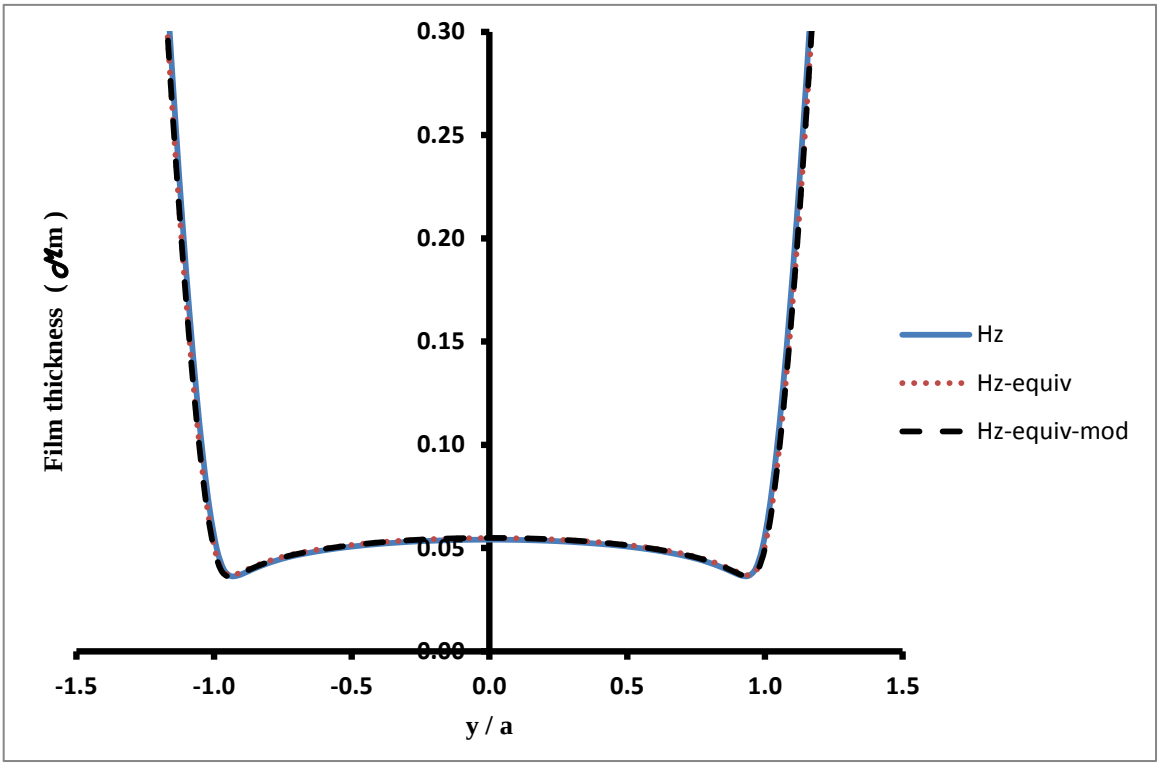

Figure 7.133 Film thickness for point C, 10 mm cup thickness, central line in y-direction

Contact Point D

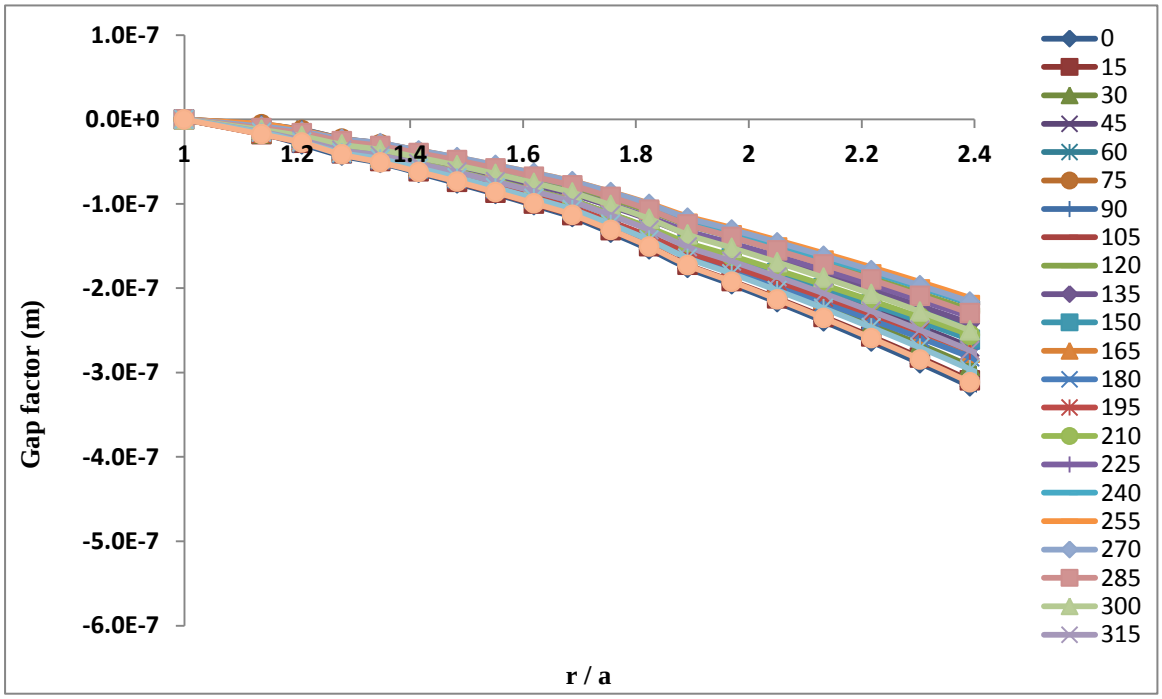

Figure 7.134 Gap factor for point D of 10 mm cup thickness

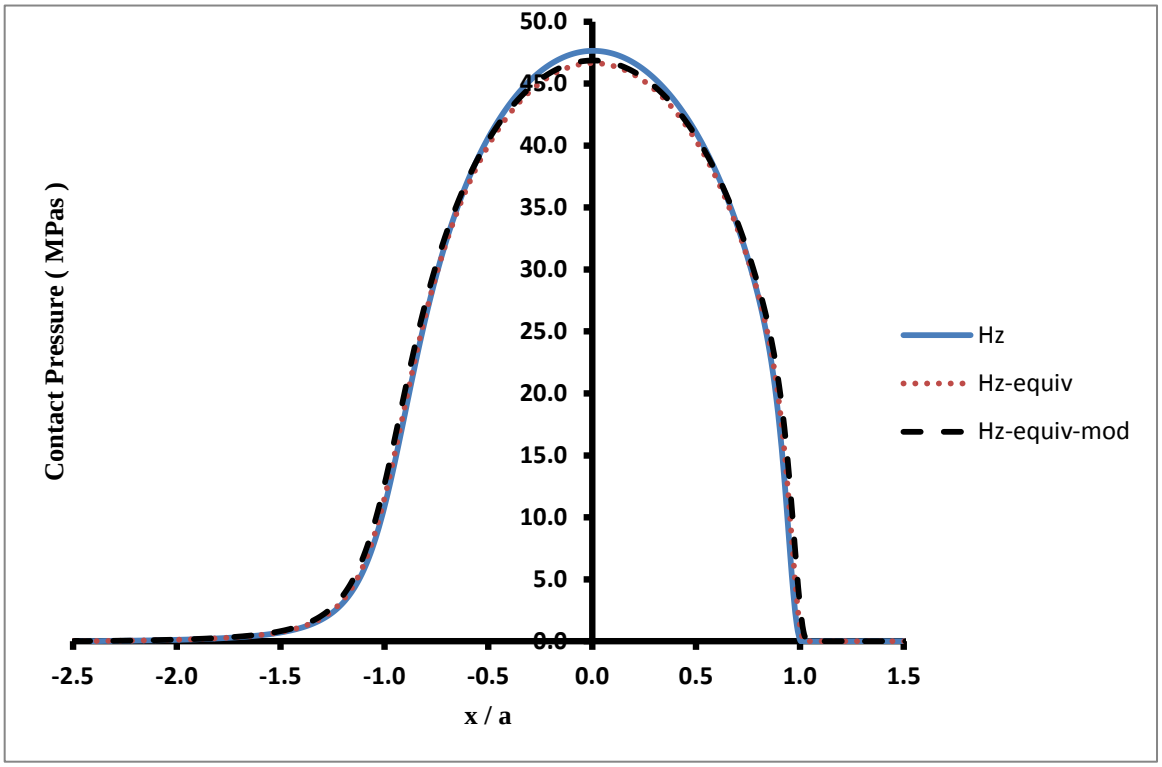

Figure 7.135 Pressure distribution for point D, 10 mm cup thickness, central line in x-direction

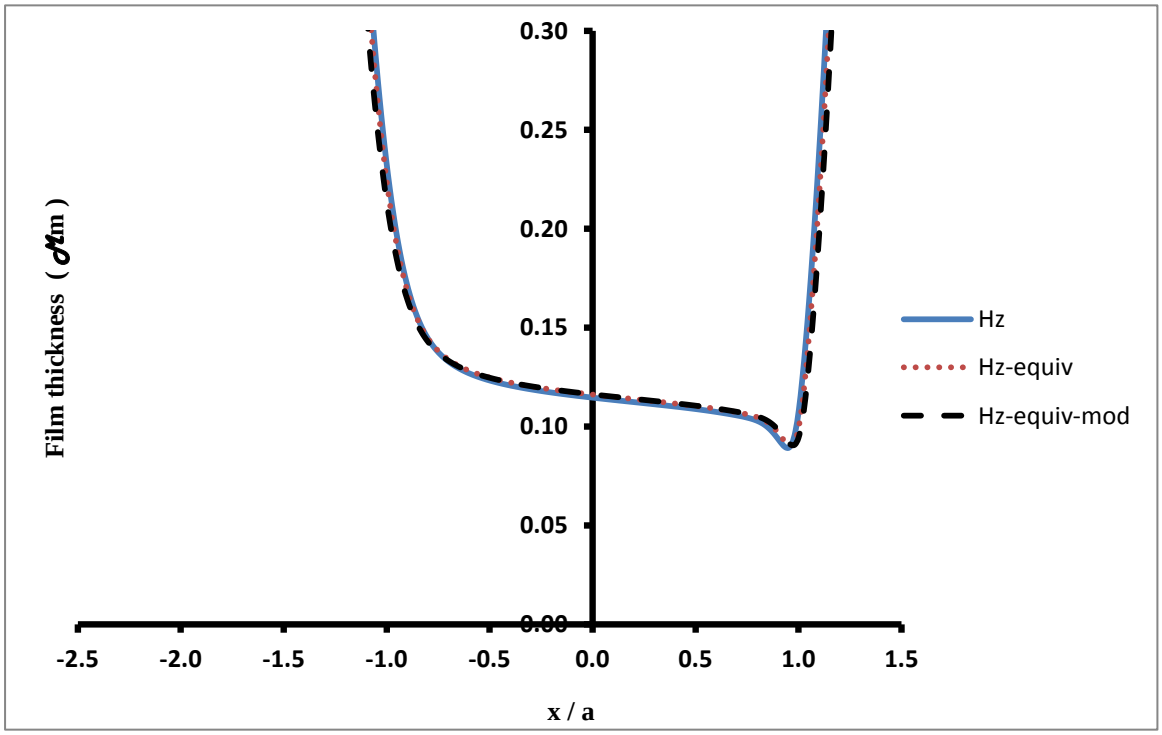

Figure 7.136 Film thickness for point D, 10 mm cup thickness, central line in x-direction

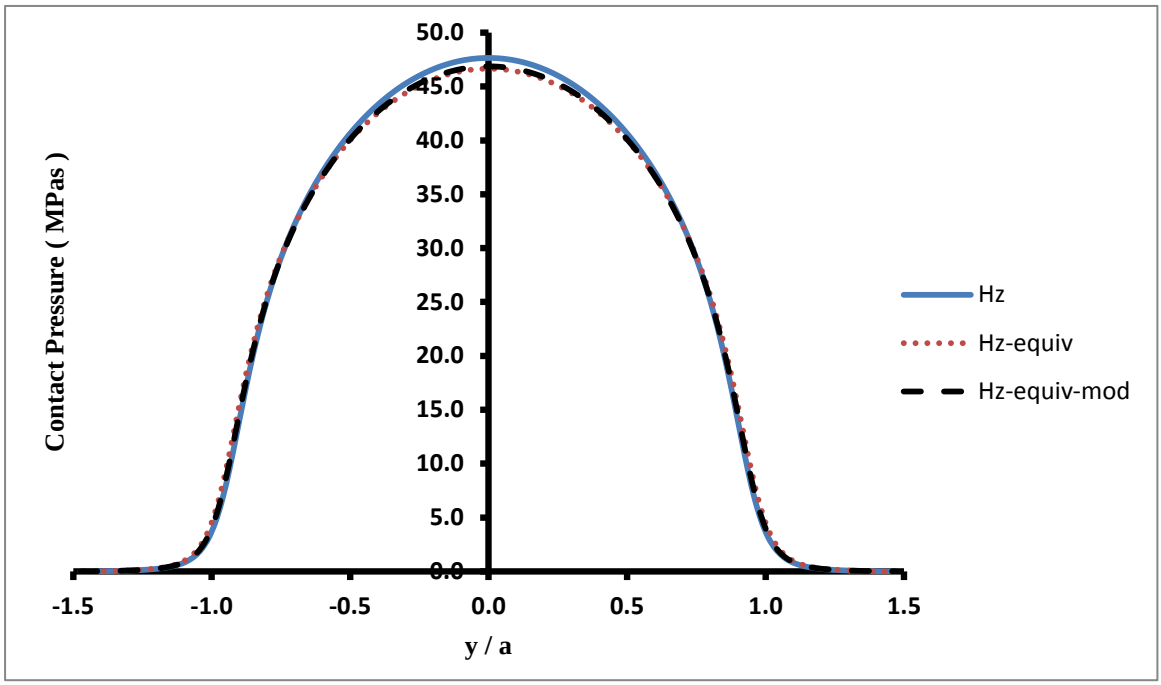

Figure 7.137 Pressure distribution for point D, 10 mm cup thickness, central line in y-direction

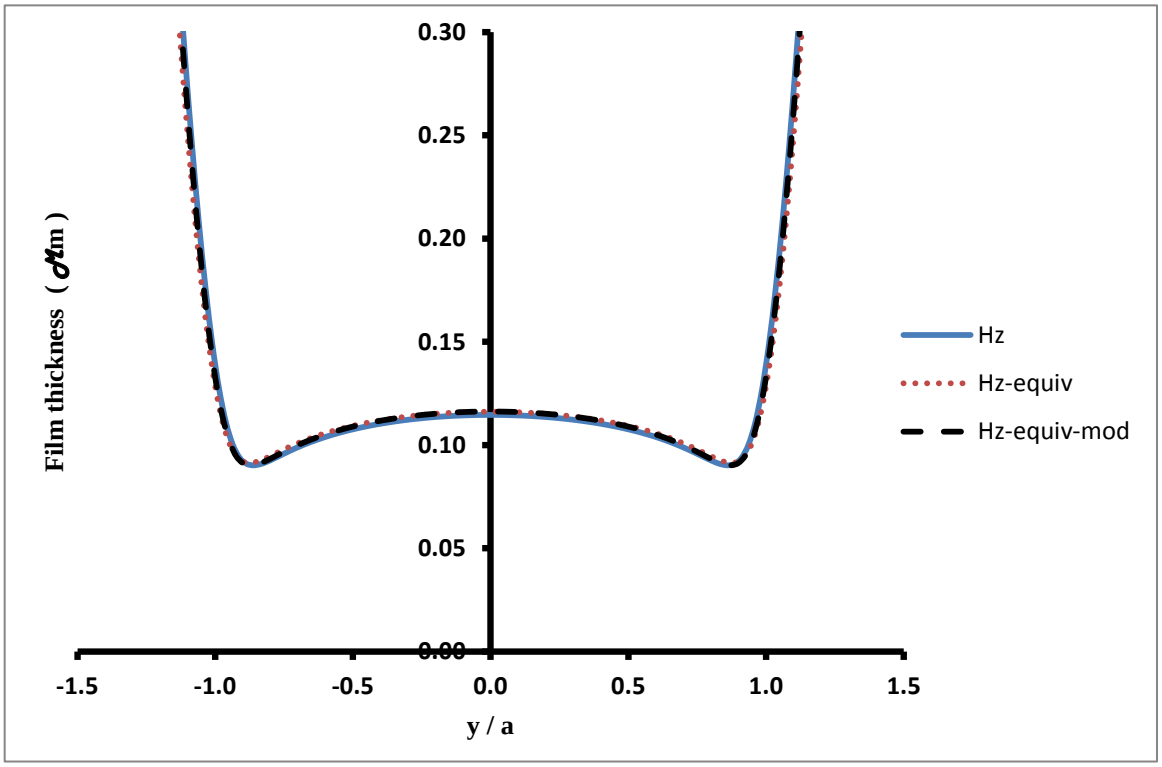

Figure 7.138 Film thickness for point D, 10 mm cup thickness, central line in y-direction

Contact Point E

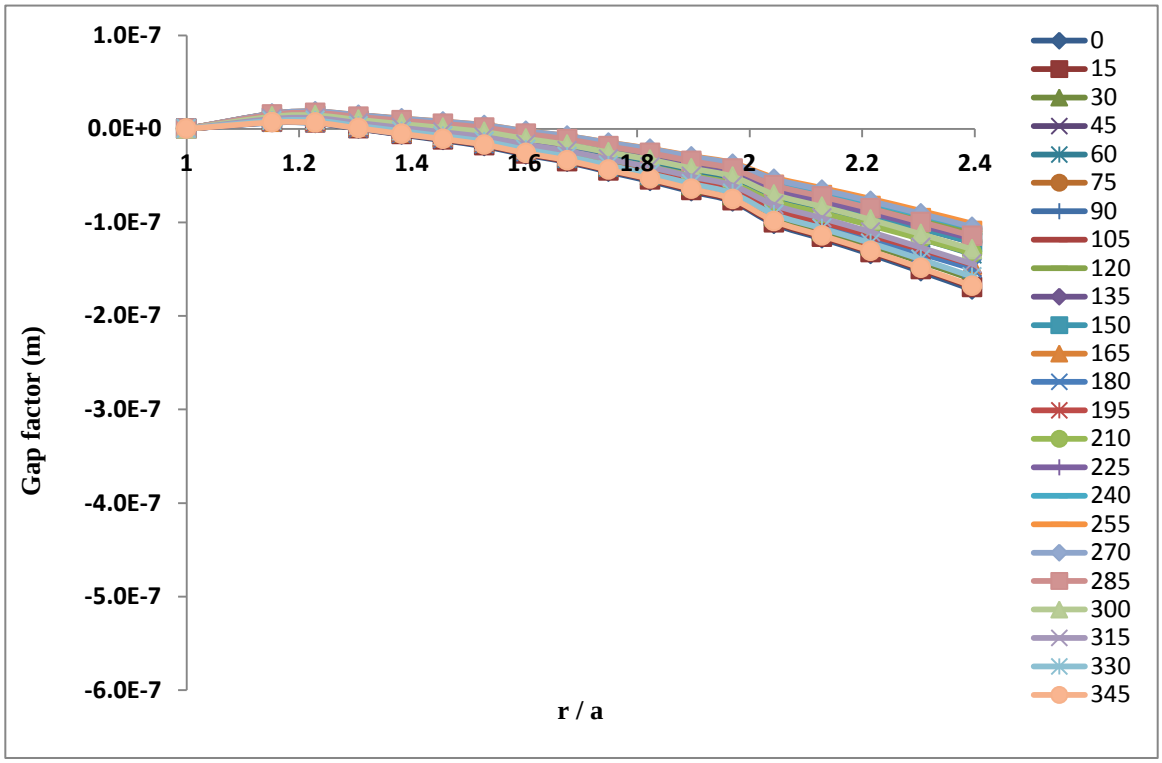

Figure 7.139 Gap factor for point E of 10 mm cup thickness

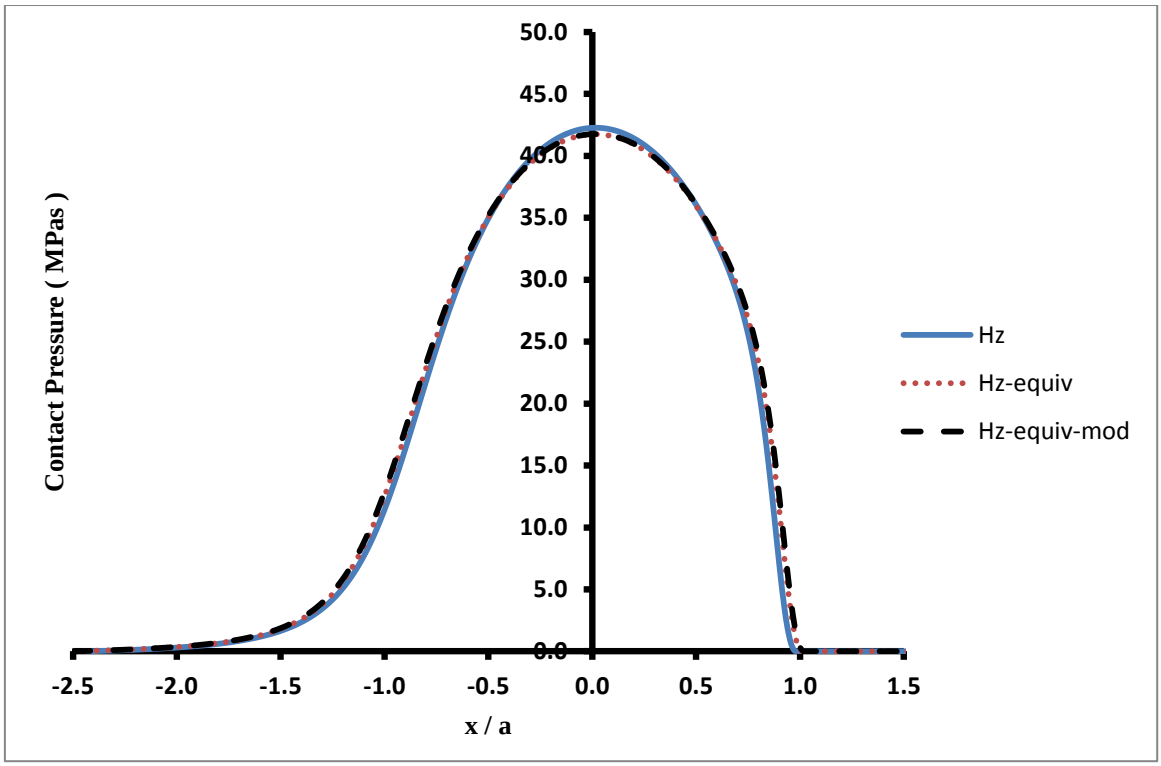

Figure 7.140 Pressure distribution for point E, 10 mm cup thickness, central line in x-direction

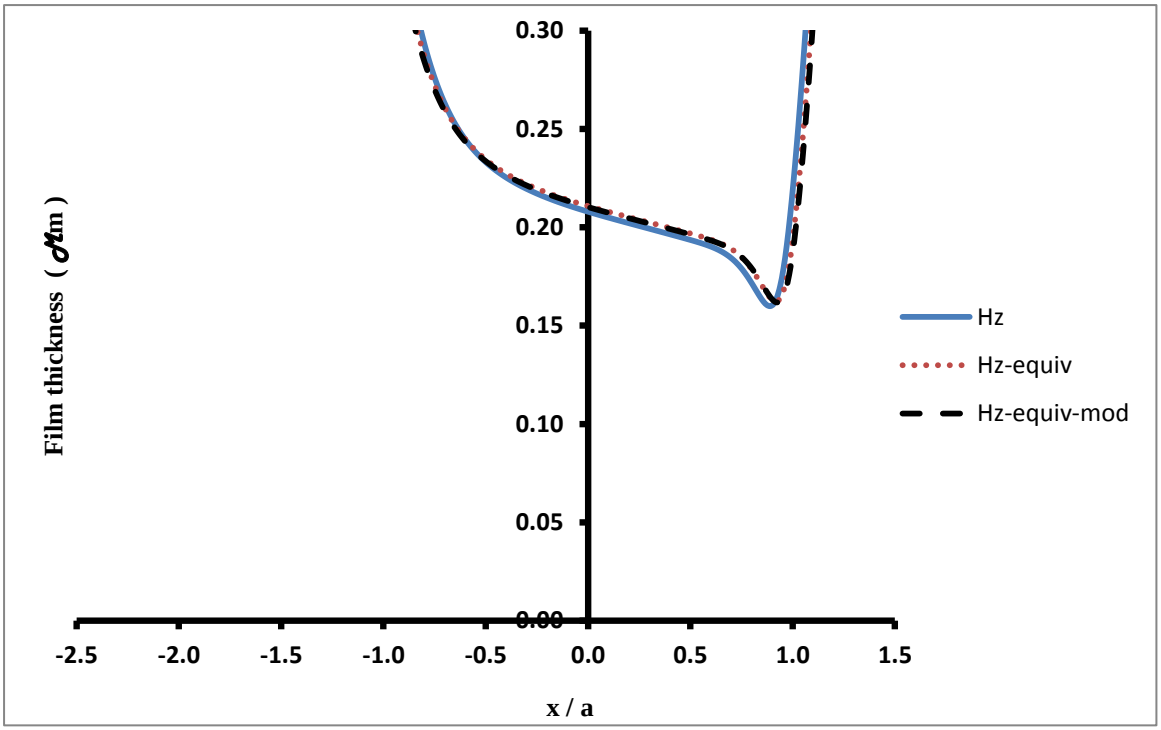

Figure 7.141 Film thickness for point E, 10 mm cup thickness, central line in x-direction

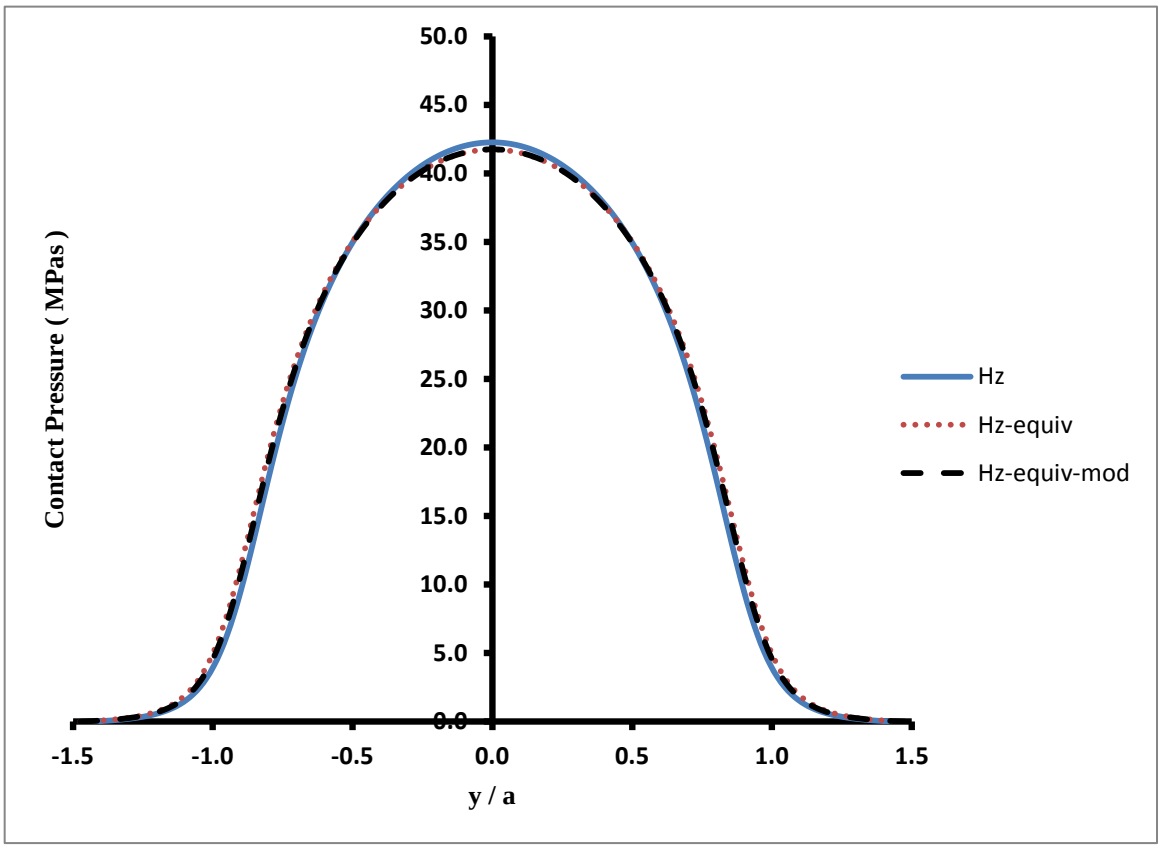

Figure 7.142 Pressure distribution for point E, 10 mm cup thickness, central line in y-direction

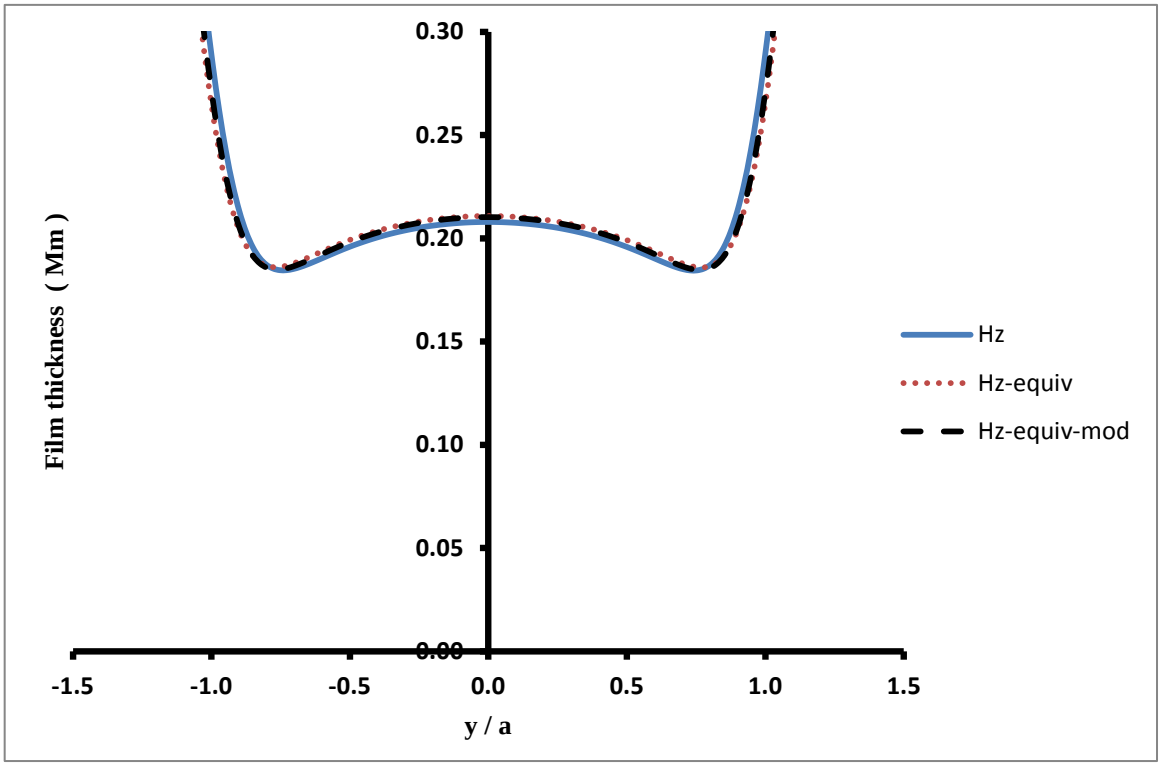

Figure 7.143 Film thickness for point E, 10 mm cup thickness, central line in y-direction

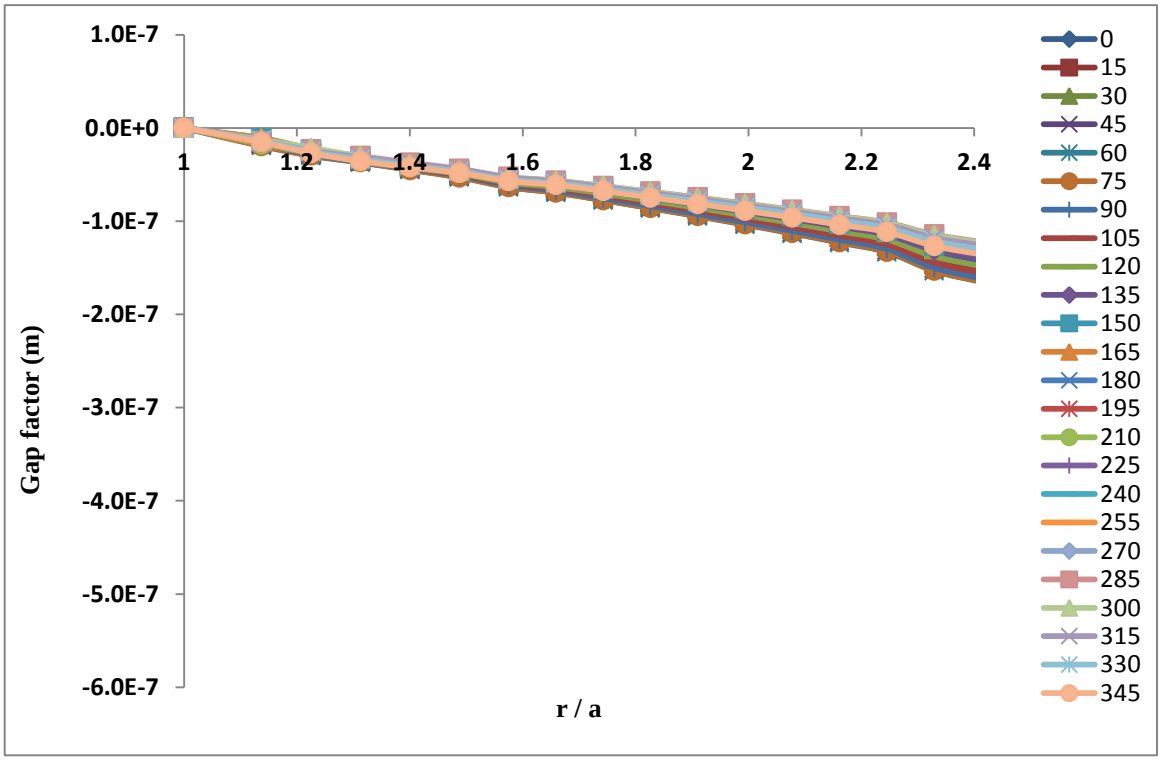

Figure 7.144 Gap factor for point F of 10 mm cup thickness

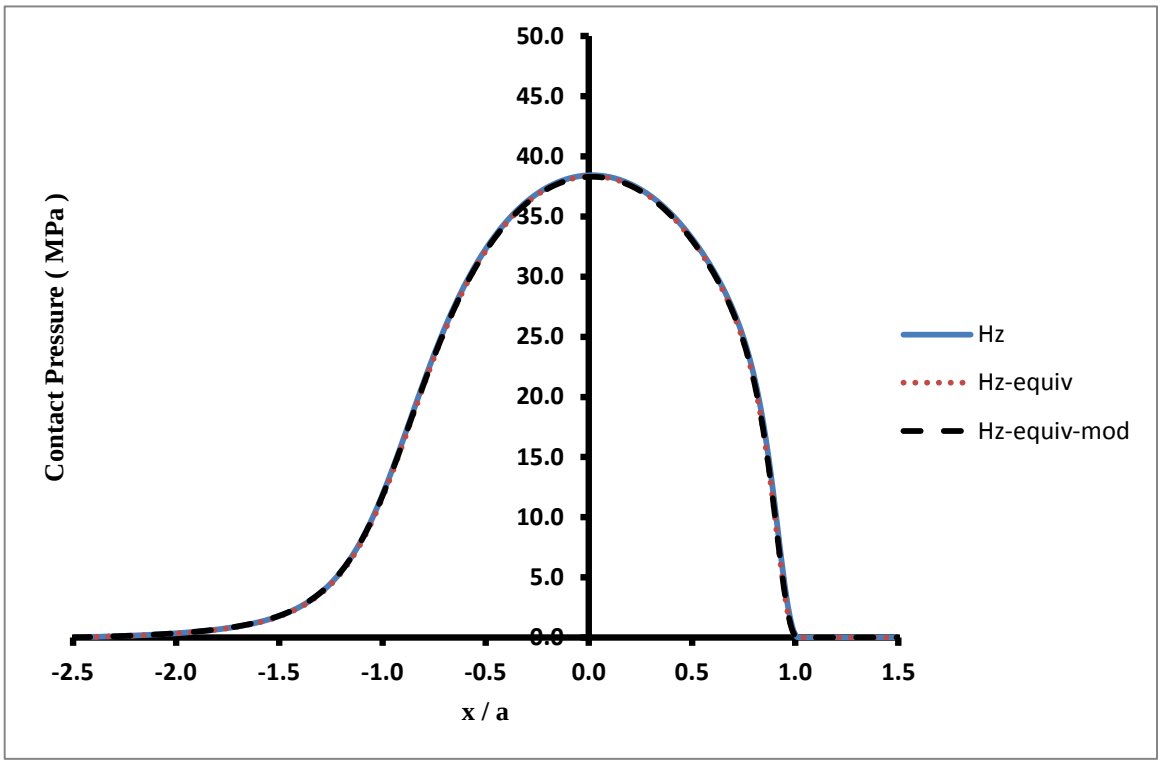

Figure 7.145 Pressure distribution for point F, 10 mm cup thickness, central line in x-direction

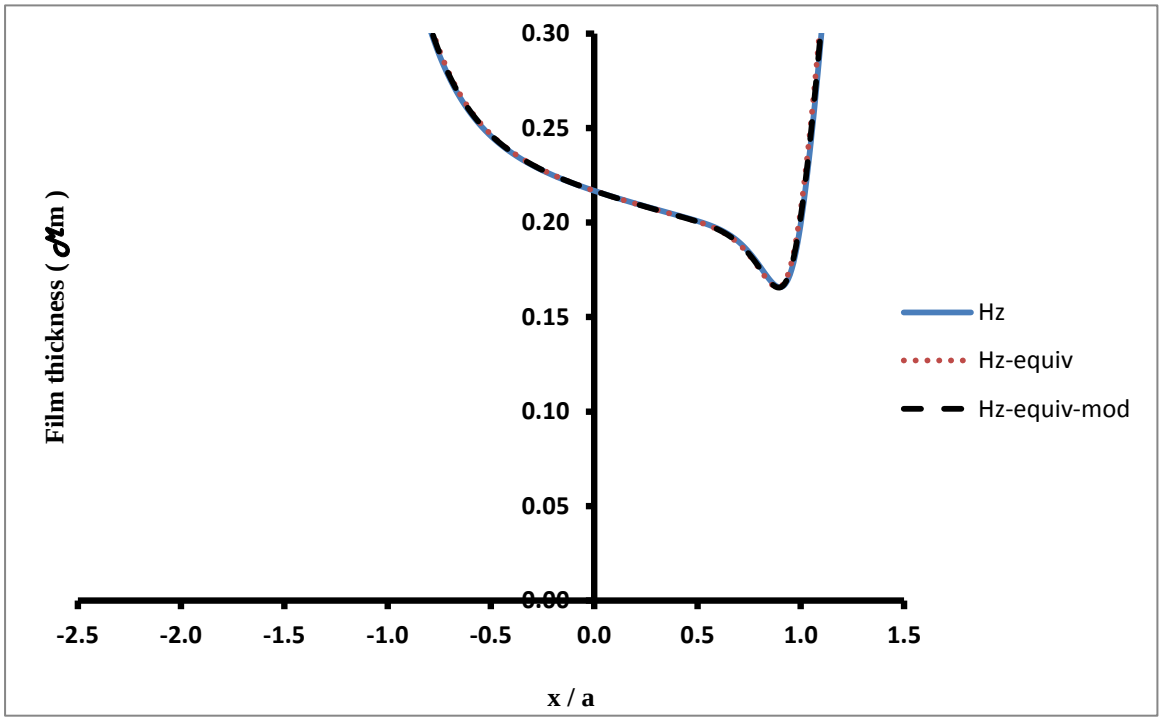

Figure 7.146 Film thickness for point F, 10 mm cup thickness, central line in x-direction

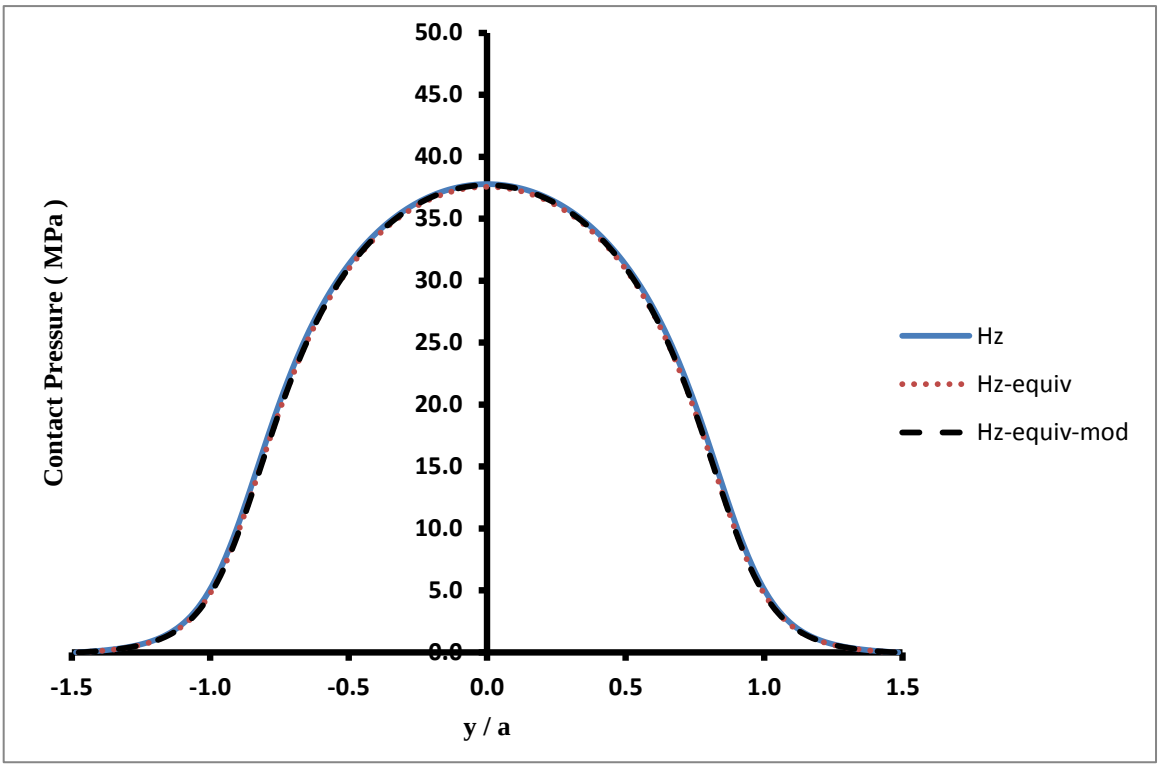

Figure 7.147 Pressure distribution for point F, 10 mm cup thickness, central line in y-direction

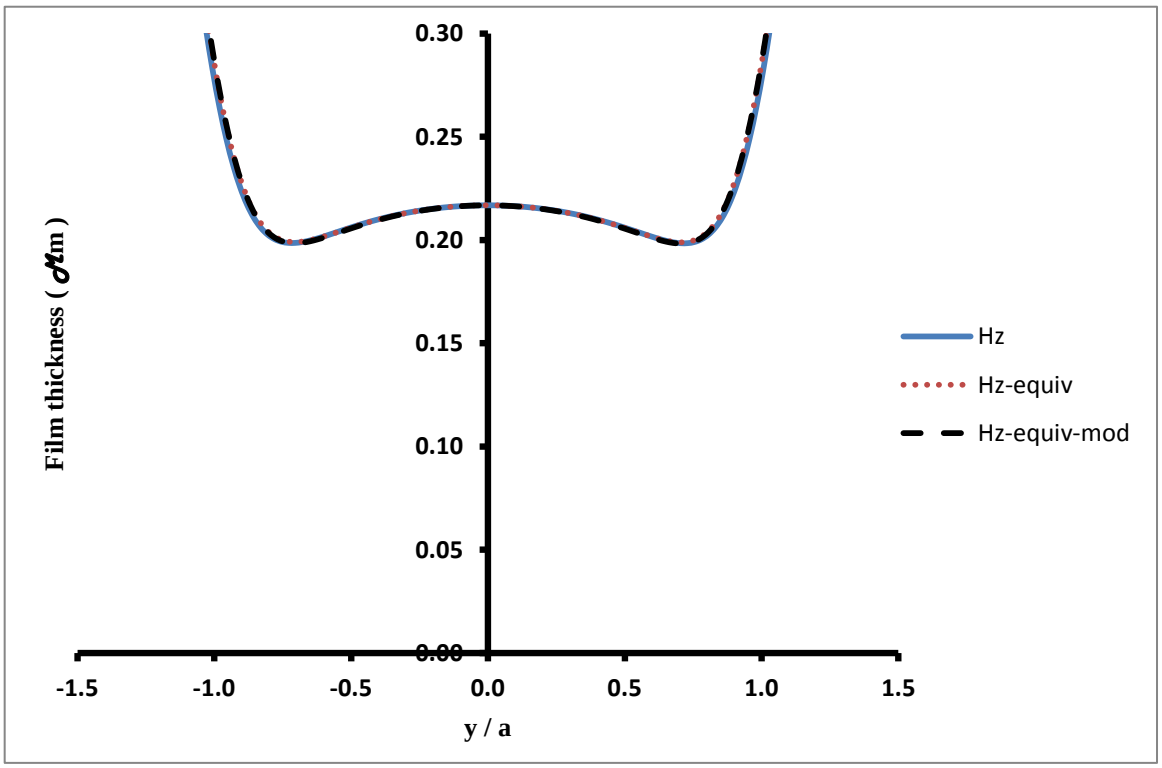

Figure 7.148 Film thickness for point F, 10 mm cup thickness, central line in y-direction

Contact Point G

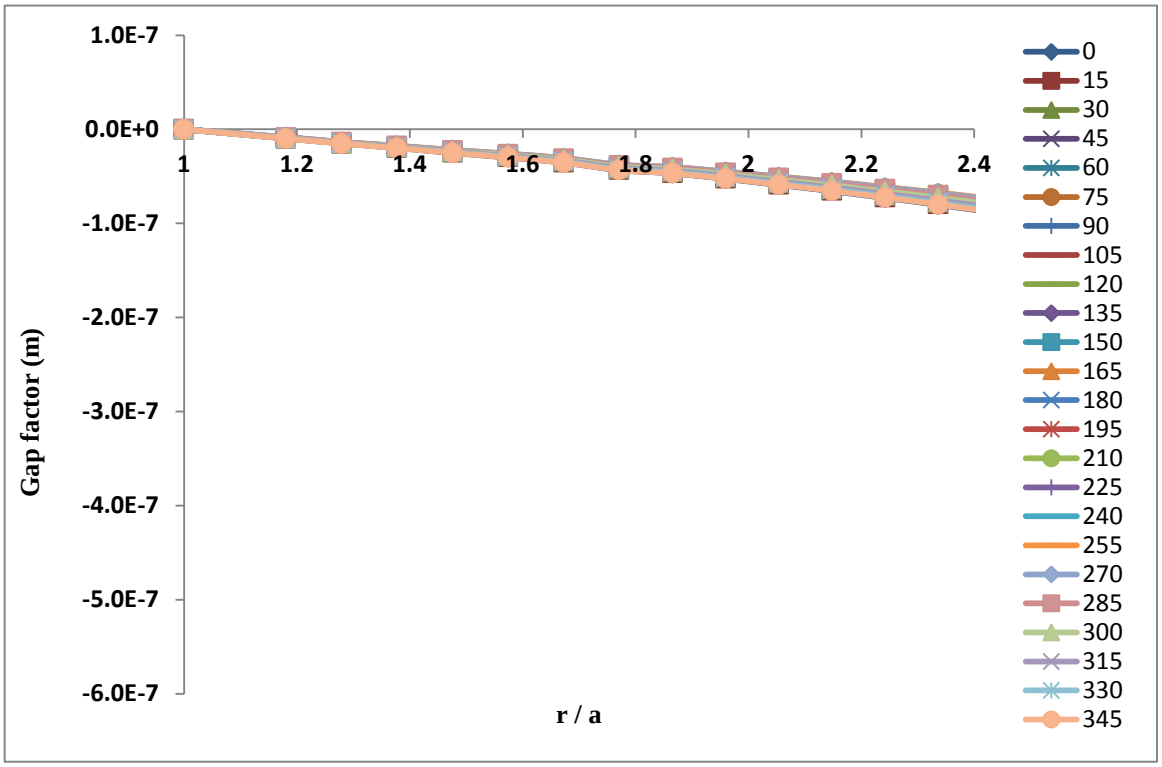

Figure 7.149 Gap factor for point G of 10 mm cup thickness

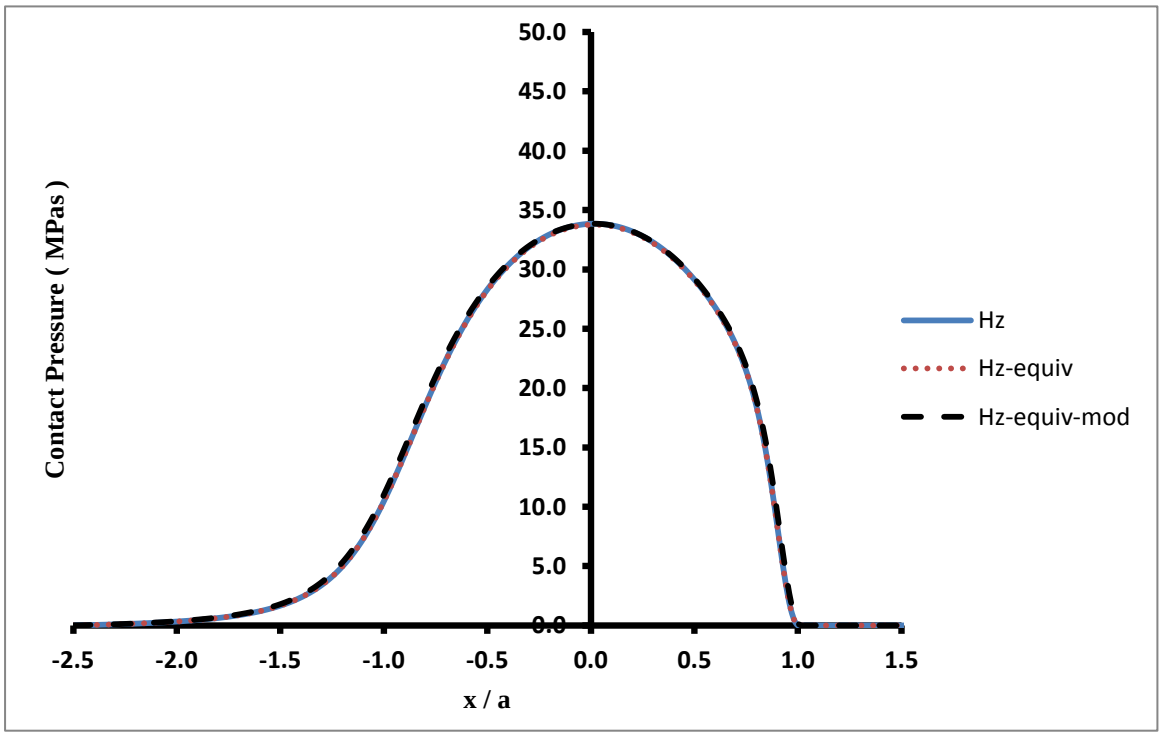

Figure 7.150 Pressure distribution for point G, 10 mm cup thickness, central line in x-direction

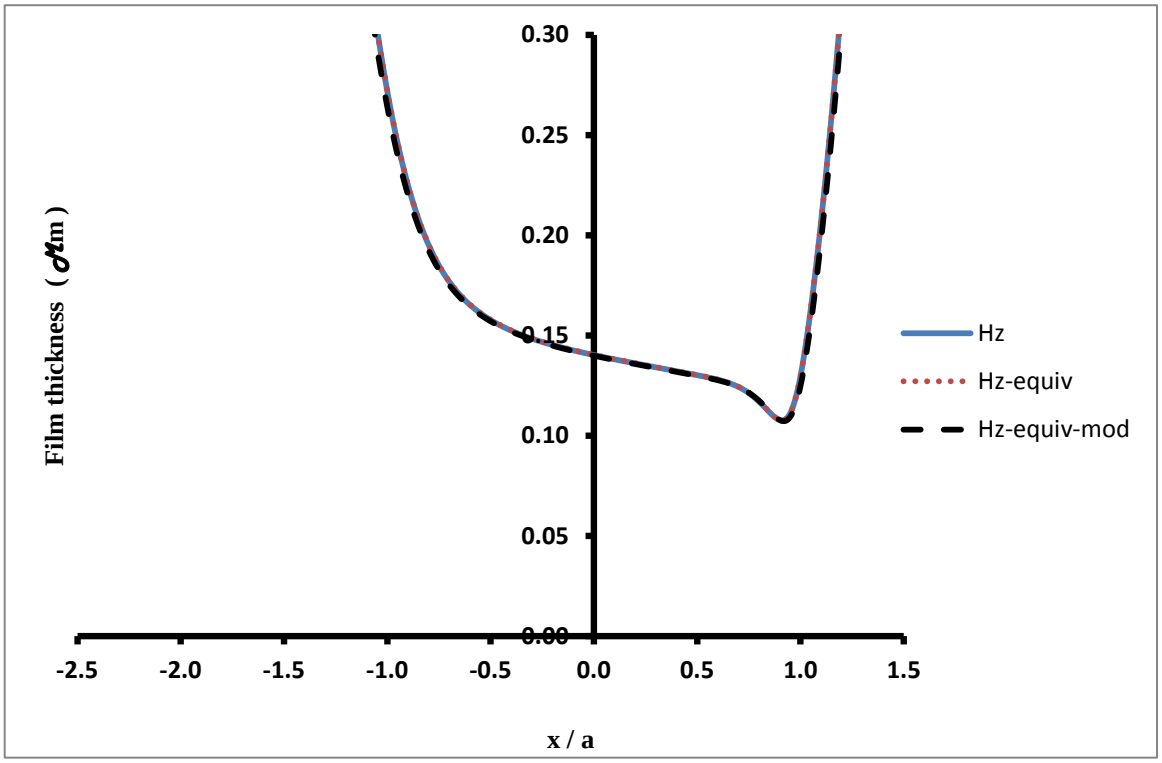

Figure 7.151 Film thickness for point G, 10 mm cup thickness, central line in x-direction

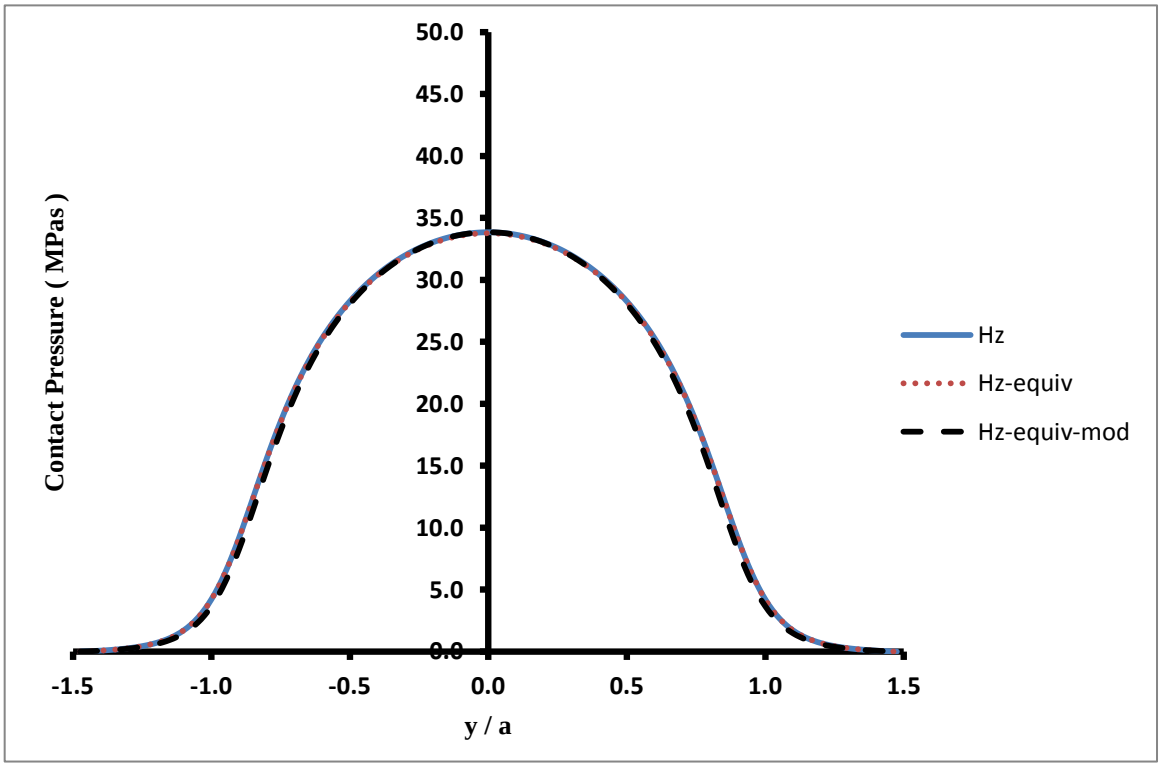

Figure 7.152 Pressure distribution for point G, 10 mm cup thickness, central line in y-direction

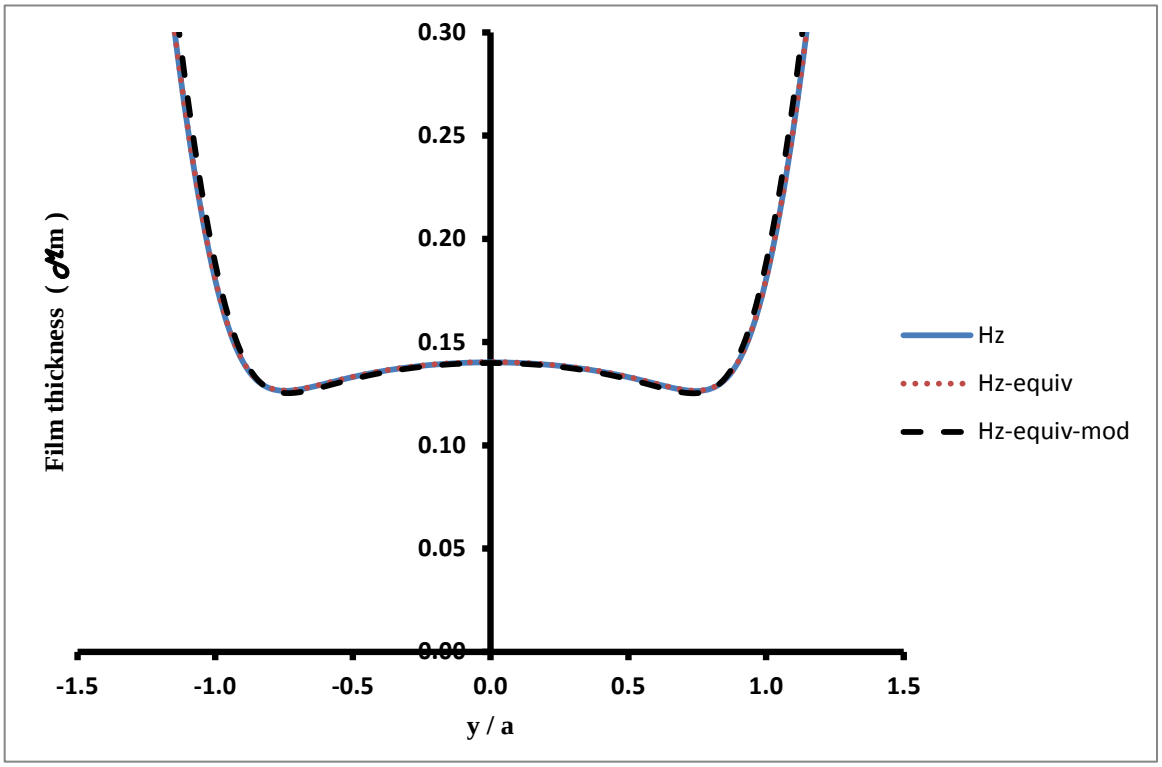

Figure 7.153 Film thickness for point G, 10 mm cup thickness, central line in y-direction

Contact Point H

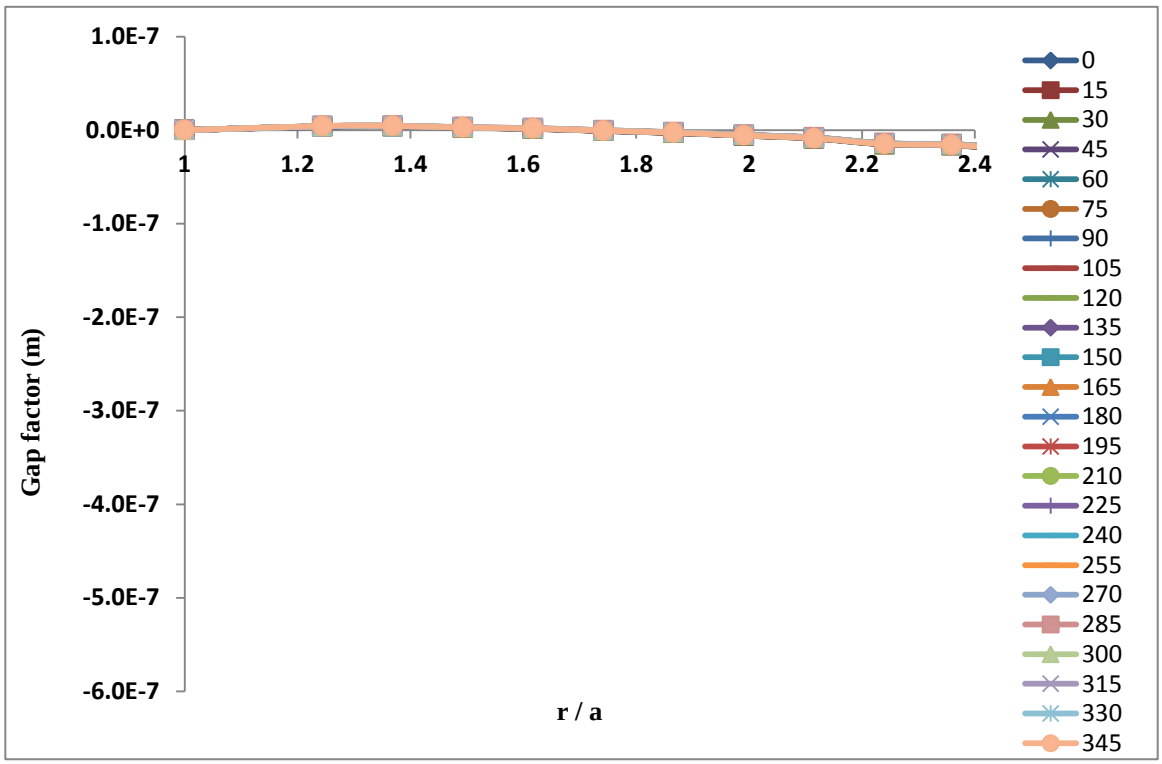

Figure 7.154 Gap factor for point H of 10 mm cup thickness

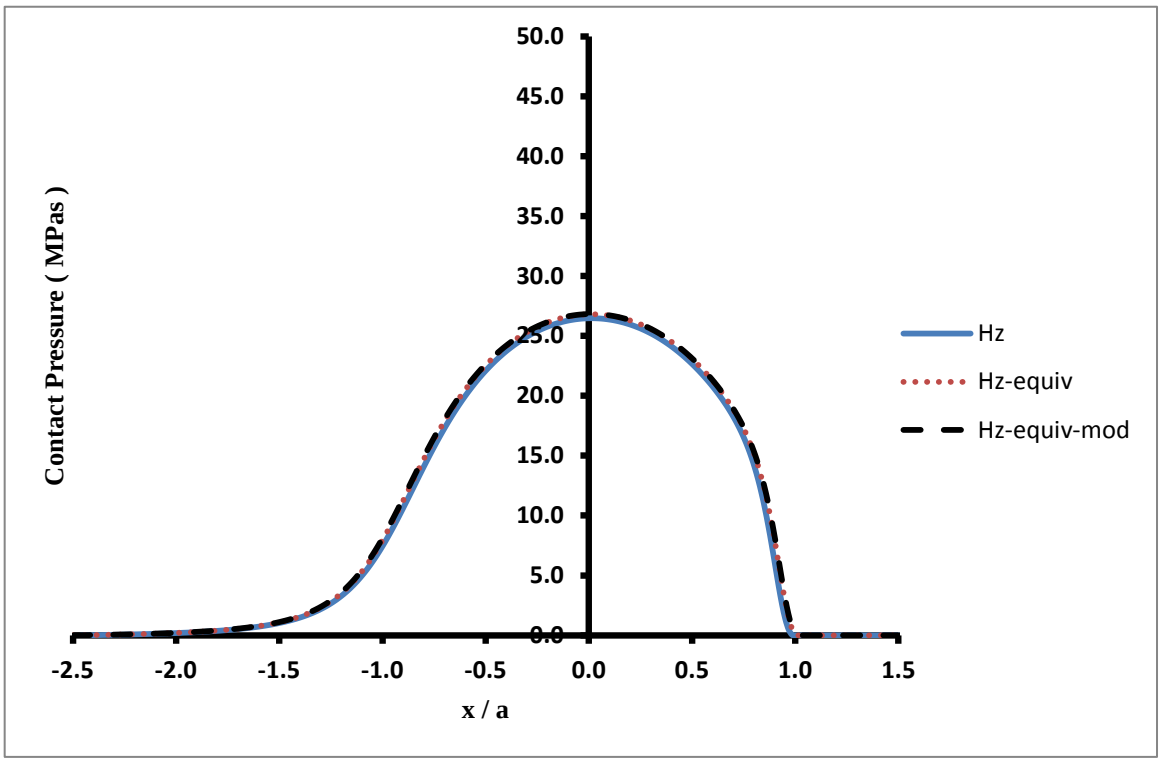

Figure 7.155 Pressure distribution for point H, 10 mm cup thickness, central line in x-direction

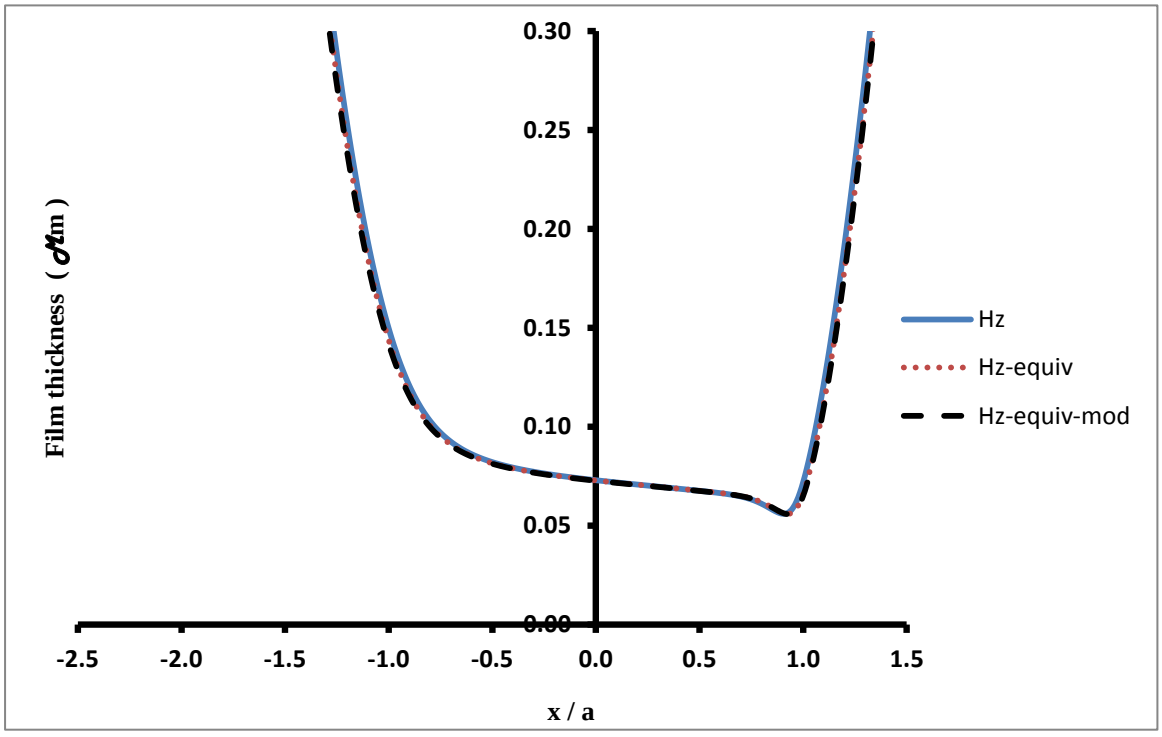

Figure 7.156 Film thickness for point H, 10 mm cup thickness, central line in x-direction

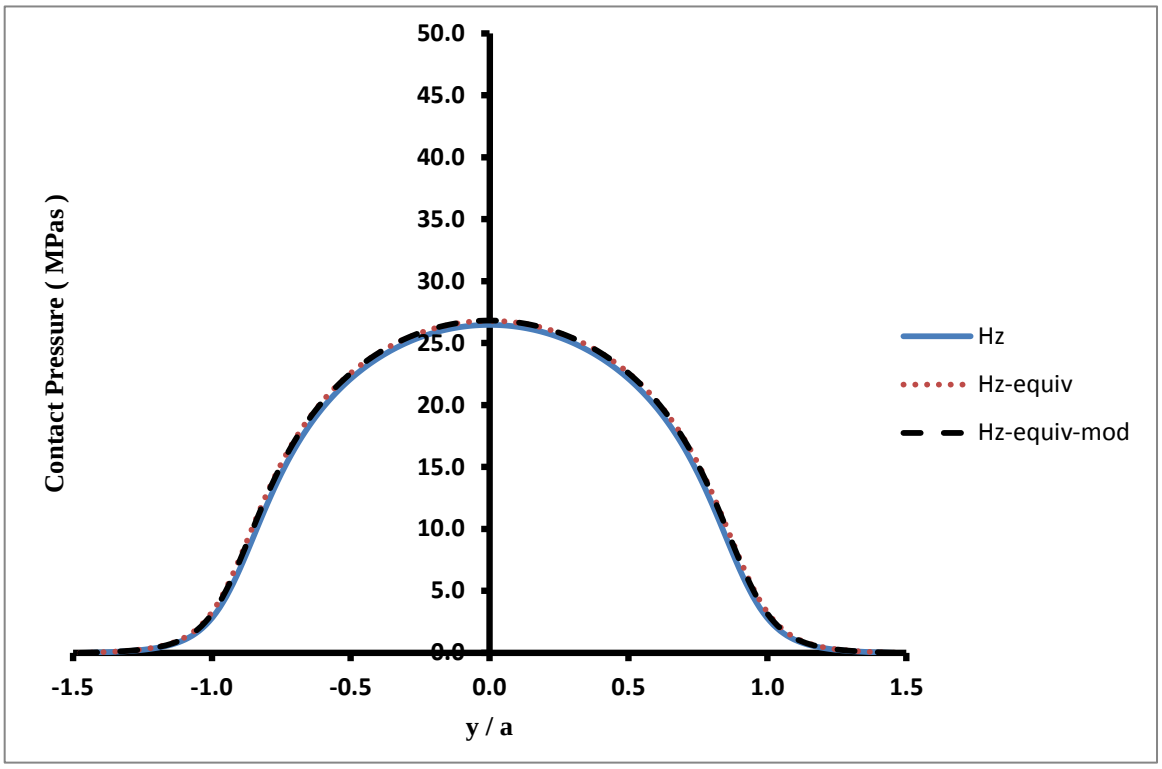

Figure 7.157 Pressure distribution for point H, 10 mm cup thickness, central line in y-direction

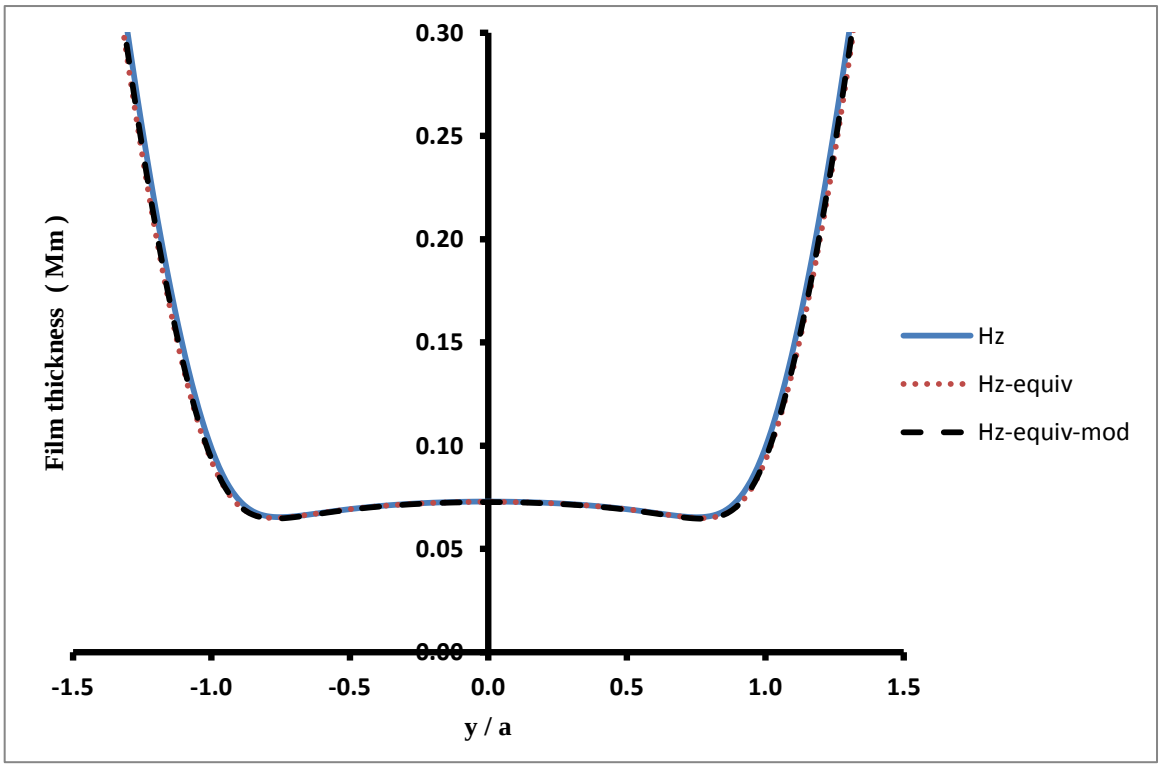

Figure 7.158 Film thickness for point H, 10 mm cup thickness, central line in y-direction

Contact Point I

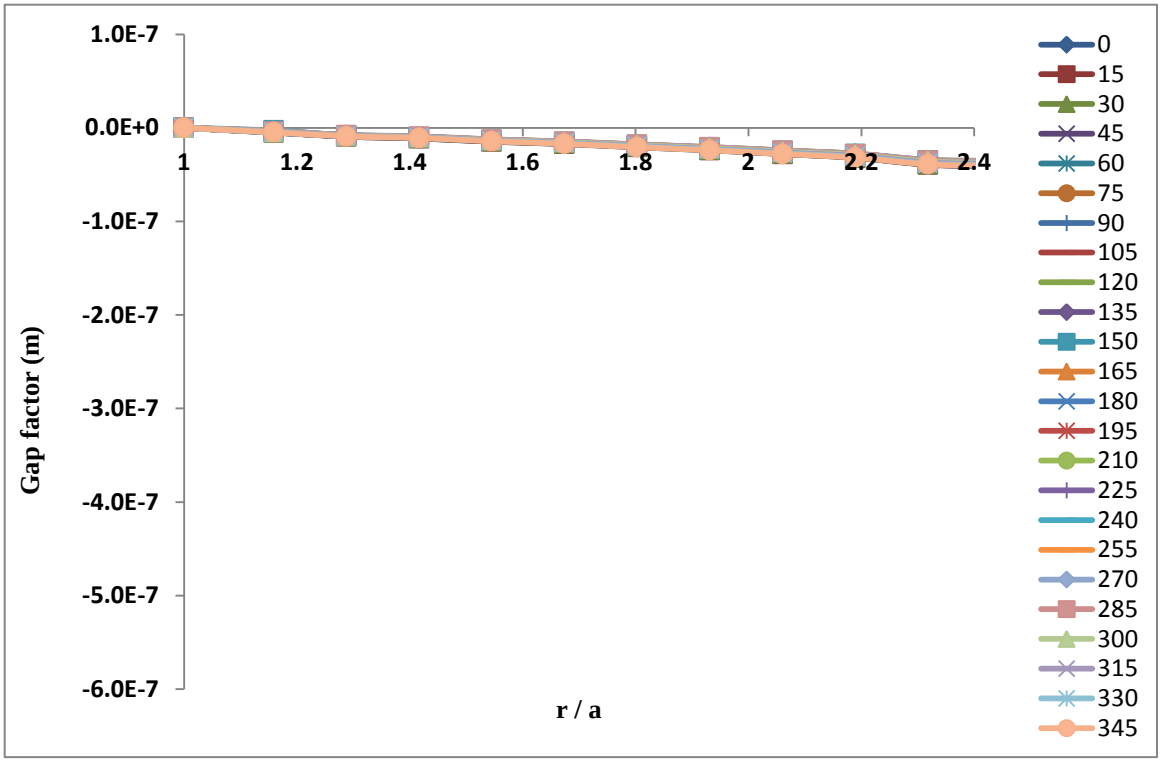

Figure 7.159 Gap factor for point I of 10 mm cup thickness

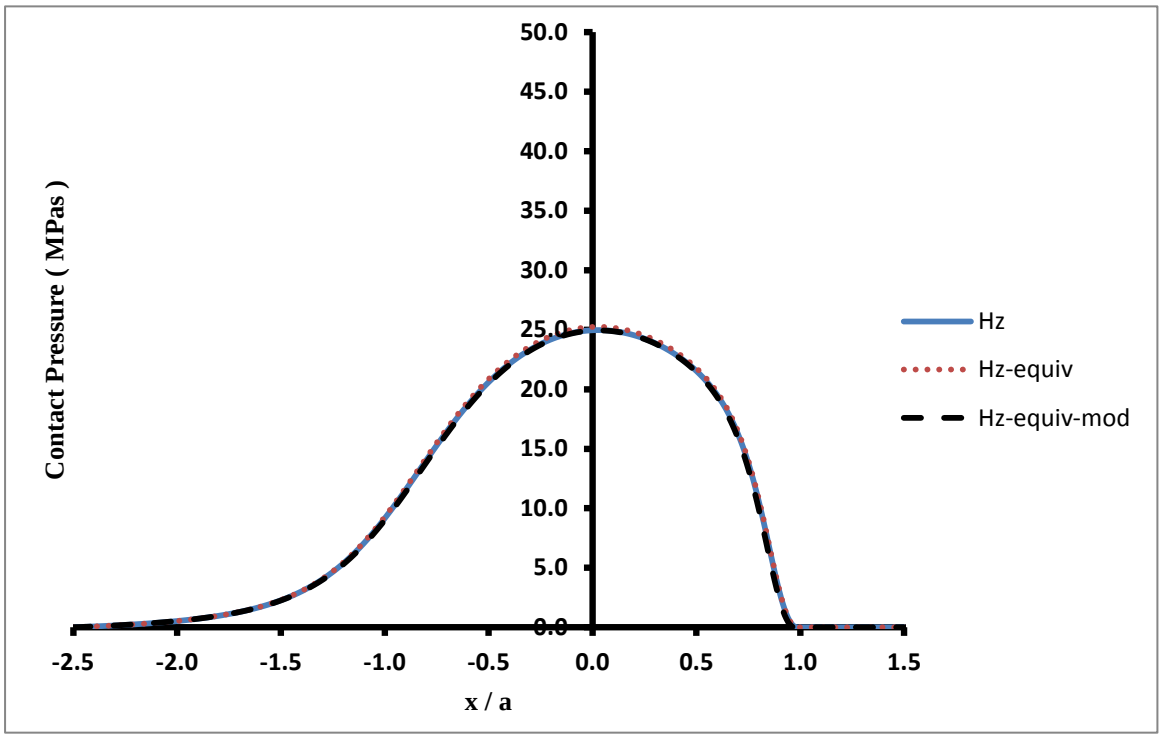

Figure 7.160 Pressure distribution for point I, 10 mm cup thickness, central line in x-direction

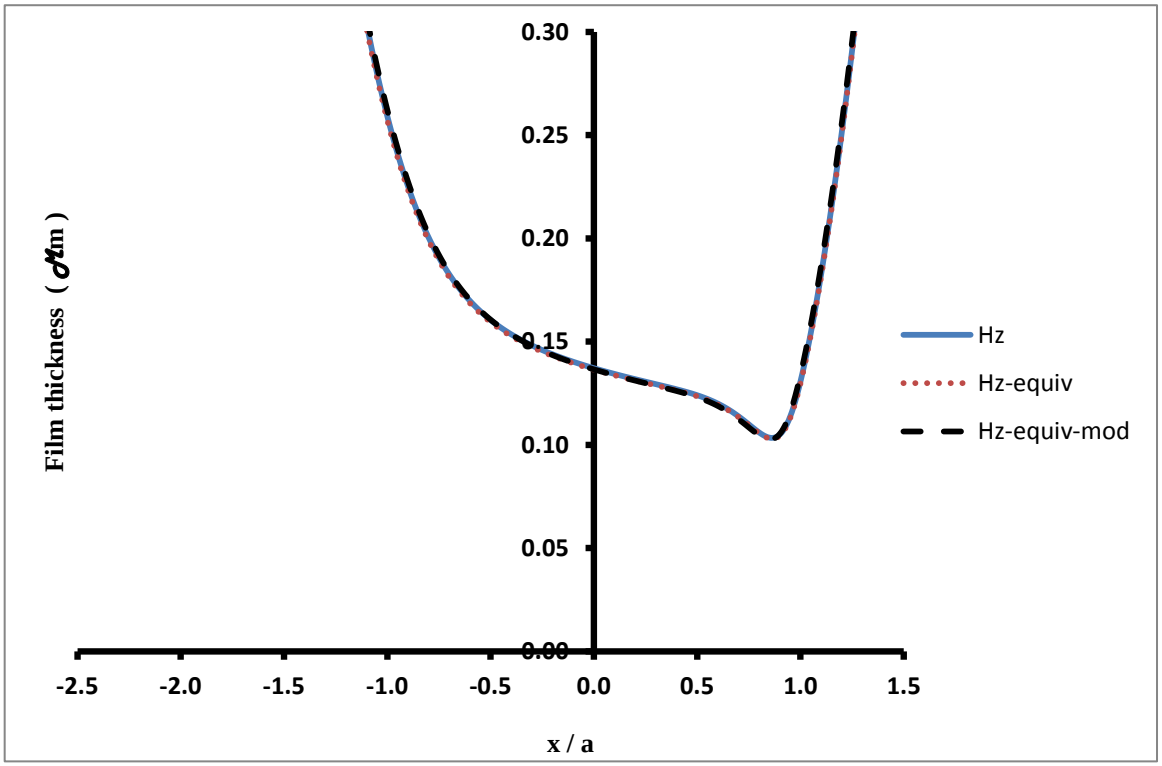

Figure 7.161 Film thickness for point I, 10 mm cup thickness, central line in x-direction

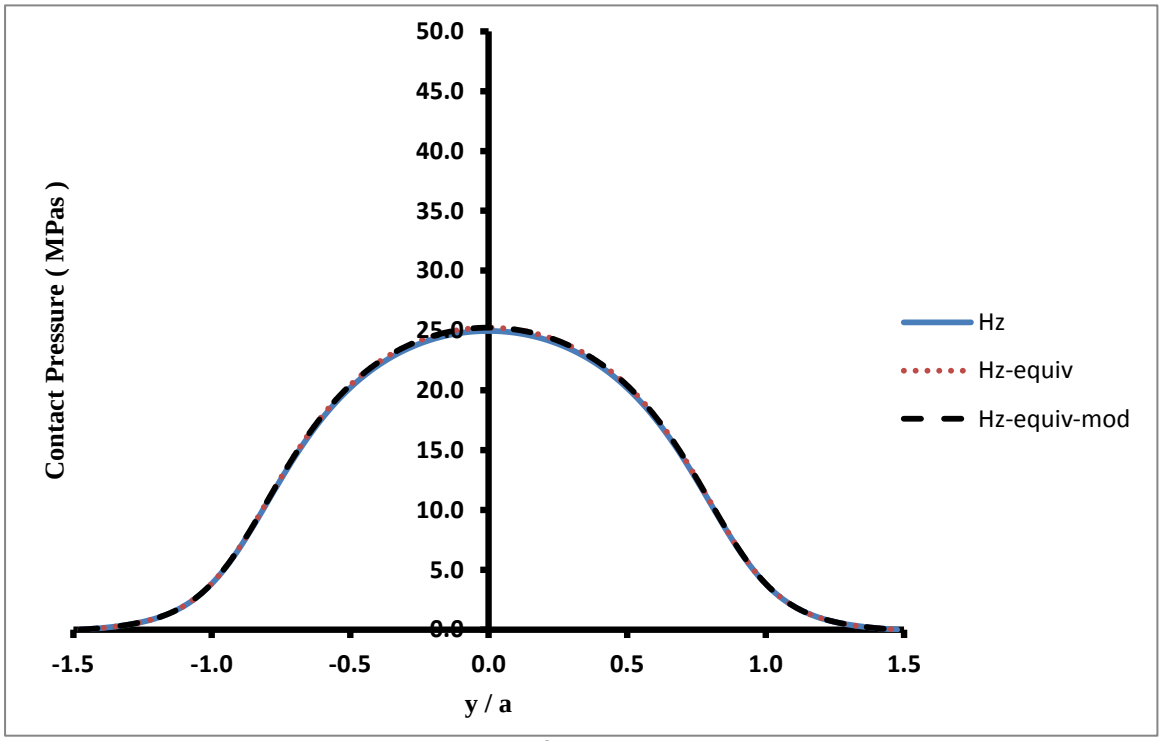

Figure 7.162 Pressure distribution for point I, 10 mm cup thickness, central line in y-direction

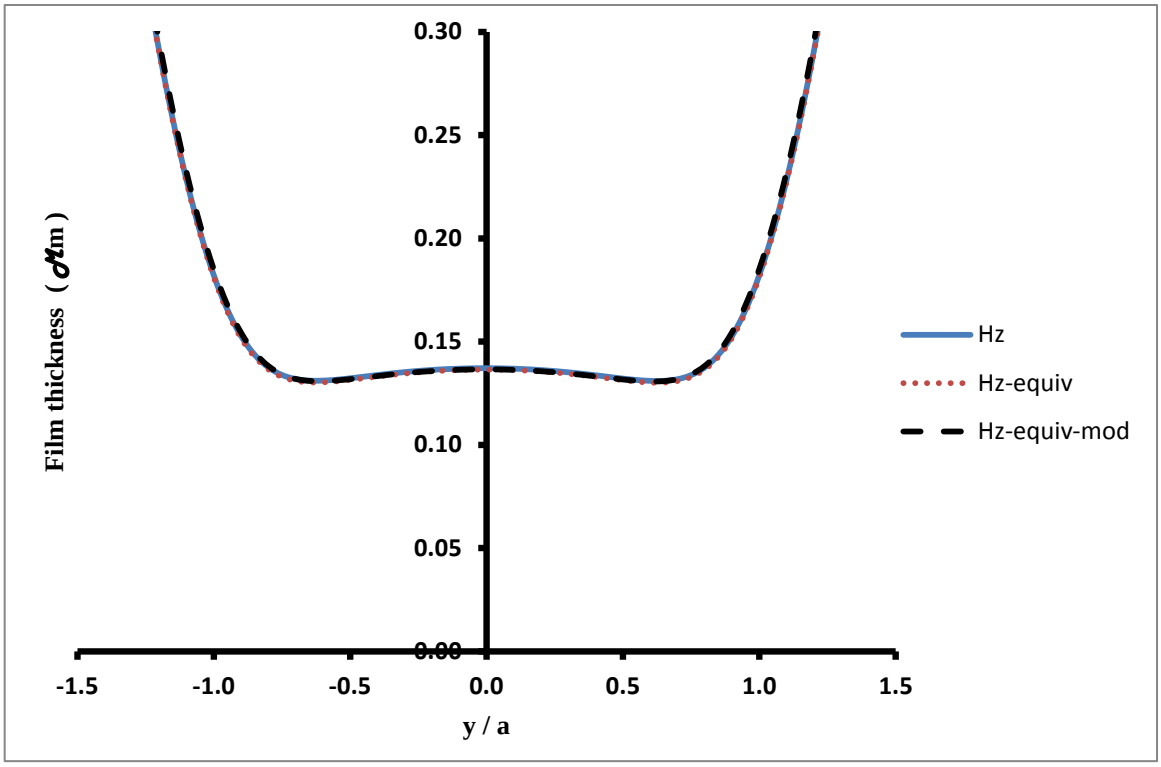

Figure 7.163 Film thickness for point I, 10 mm cup thickness, central line in y-direction

Table 7.5 Calculated Hertzian and equivalent pressure and the ratio between them, Hertzian and equivalent central film thickness and the ratio between them, Hertzian and equivalent radius of contact area for the 10 mm cup.

	a_h(mm)	a_{equiv}(mm)	$P_{o(h)}$(MPa)	$P_{o(equiv)}$(MPa)	%	$h_{c(h)}$(μm)	$h_{c(equiv)}$(μm)	%
A	2.852	2.850	31.277	31.603	1.042	0.177	0.176	-0.307
B	4.195	4.215	48.811	47.898	-1.870	0.123	0.125	1.024
C	4.204	4.244	49.306	48.132	-2.381	0.054	0.055	1.432
D	4.094	4.154	47.649	46.651	-2.094	0.115	0.116	1.362
E	3.736	3.845	42.267	41.738	-1.252	0.208	0.211	1.395
F	3.395	3.373	37.801	37.583	-0.577	0.217	0.217	0.007
G	3.003	3.000	33.848	33.766	-0.242	0.140	0.140	0.093
H	2.336	2.373	26.471	26.801	1.247	0.073	0.073	-0.183
I	2.293	2.293	24.970	25.247	1.109	0.137	0.136	-0.507

7.7 Discussion

The EHL results obtained in this chapter cover all of the equivalent Hertzian contact models. They were obtained using a mesh that was based on the Hertzian contact dimension a (a_{equiv}). The standard computing mesh used covered the rectangular area $-2.5a \le x \le 2a$, $-1.5a \le y \le 1.5a$, and the resolution adopted was $\Delta x = a/60$, $\Delta y = a/40$.

The problems for which solutions are presented were relatively lightly loaded in EHL terms. Peak pressures of 50MPa for point C were just approaching a pressure of $1/\alpha$ = 60.6 MPa, so that the piezo viscous effect was mild and the results could have been obtained with a simpler solution scheme. The radius of the ball used in the study was 25 mm and that of the cup was 25.1 mm, resulting in a radius of relative curvature of 6.275 m. However, any greater mismatch between the radius of the ball and socket would have moved the conditions further into the EHL regime where an EHL solver would be necessary to produce solutions. The contacts are subject to considerable elastic deflection as can be seen from the film thickness sections. For a circular contact the Hertzian deflection at the contact point is a^2/R, where R is the radius of relative curvature, and $a^2/2R$ at the edge of the Hertzian contact zone. Taking contact point C with 10 mm cup thickness as an example this leads to a central deflection that is 50 times the EHL film thickness, and at the other extreme of load, contact I has a contact point deflection that is 6 times the EHL film thickness.

The film thicknesses obtained from the analyses are low with values for central film thickness that vary between 0.055 μm and 0.227 μm. The variation in entrainment speed is clearly influential with cases C and D, which have similar loads differing by a factor of 2 in central film thickness values. The minimum film thicknesses cover the range from 0.030 μm and 0.162 μm. These film thickness values would require extremely smooth surfaces to be unaffected by surface roughness. To obtain Λ values of unity, based on the calculated central film thicknesses would need surface finish with standard deviations of surface height, *Rq*, that are of the order 0.02 μm. This is much finer than is likely to be achieved in practice, so that contacts of the type analysed will operate in the mixed lubrication regime with considerable interaction of the surface asperity features. This will cause pressure fluctuations in the lubricant film at the scale of the roughness features, and will lead to higher friction values than would be the case if the roughness was small compared to the film thickness. It is also likely to be influential in the production of wear particles referred to in the literature review.

Comparison of the three model types for each contact shows that there are clear differences between the equivalent Hertzian model results and those for the Hertzian model based solely on dimensions and material properties. The equivalent Hertzian models have lower lubricant pressures (up to 10% reduction) and higher film thicknesses (by 10 to 20%) but these differences do not change the assessment of the contacts significantly. The complication of adding the inlet gap correction to the equivalent Hertzian model is not justified by the results, which in all cases are indistinguishable from the equivalent Hertzian model results.

Neither of these observations were known before the contacts were analysed in this comparative way. It is also clear that for cups that are thinner than the Hertzian contact radius the contact pressure distribution is non-Hertzian and the FEA results at the higher loads suggest that the cup deflection is tending towards the membrane behaviour that would certainly be expected for thin cups if they were restrained around the lip periphery. To calculate film thicknesses for thin cups would require a different approach to the elastic deflection.

Conclusions and Recommendations

8.1 Conclusions

The main parameter characteristics required to produce an artificial hip joint that is a good alternative to the natural hip joint are to reduce the wear rate to be as small as possible and to improve the lubrication process to develop full fluid film lubrication and avoid asperity contact. A better understanding of the lubrication mechanism is needed to improve future designs and to help understand problems that have occurred with commercial metal–on–metal designs. An MOM ball-in-socket model with a "sawbones" polyurethane foam block supporting system was studied using an FEA contact model. Four different cup thicknesses 4, 6, 8, 10 mm were used. Results of EHL based on the Hertzian analysis geometry were compared with the developed equivalent and modified models. The finite element analysis to simulate the contact between the femoral head and the acetabular cup using measured forces in three directions were considered in this investigation.

The EHL analyses presented in the thesis were limited to steady state conditions at nine points in the walking cycle. The walking cycle analysis was developed to give a detailed picture of the way in which contact position, load, and entrainment velocity vary over the walking cycle. This provides the basis for a transient EHL analysis of the contact and would be a clear candidate for further work built on the foundation of this project. This is envisaged as a process that consists of the following steps. (i) conduct a series of FEA contact analyses for the walking cycle to provide, say, 20 equivalent Hertzian contact models, possibly over a series of loads covering the variation between this point and its neighbours. (ii) Establish the variation of contact

load and entrainment velocity over the walking cycle and introduce smoothing procedures to remove any numerical noise introduced by the experimental data. (iii) construct a transient EHL analysis of walking cycle where the equivalent Hertzian contact is obtained by interpolation between those established from the FEA analyses and the load and entrainment velocity vary according to the smoothed cycle.

Difficulties that will be encountered will be that of the small number of instances where there is a rapid variation in magnitude and/or direction of the entrainment velocity. This occurs naturally at the ends of the swinging motion cycle of the femur relative to the hip where the entrainment magnitude falls to zero and the flow direction within the contact reverses.

A zero entrainment velocity steady state case will have no film generating capability, but a transient analysis will not experience a loss of film as entrainment will grow in a different direction before the lubricant can start to leak away.

The main results of this work are:

- For the 4 mm cup thickness, the pressure distribution was only of Hertzian form when the measured load of the hip joint was less than 30% of the body weight. For the 6, 8 and 10 mm cup thickness the pressure distribution for all the loads cases considered was of Hertzian form. This indicates that by increasing the cup thickness the contact pressure becomes progressively closer and closer to the Hertzian pressure. In general, it was found from the ratio of the cup thickness to the Hertzian radius of contact, wt/a_h, that when this ratio is unity or less the pressure distribution from the FE analysis is non Hertzian, and vice versa.

- The maximum variation ratio of contact pressure of the 4 mm cup thickness for the nine contact points and load range of 295 to 1819 N was 19.5%, while for the 6, 8, 10 mm cup thickness the variations are 56.7%, 72.4% and 78.5 % respectively. With the thinner cup the results obtained have been less affected by varying the applied load because the higher load values were not analysed due to their non-Hertzian behaviour.
- Increasing the cup thickness produces higher contact pressures and smaller contact areas. In addition, it is possible to say that thinner film thicknesses were produced as a result of increasing the cup wall thickness.
- For the four cup thicknesses used in this work and the nine contact points for each cup, adding the gap factor to the undeformed geometry reduced the film thickness in the inlet zone in some of the contact points. This was associated with increased contact pressure but the increase was small when compared to the results for the same geometry without the gap factor with the highest variations being approximately 1.5%. There were no differences in the film thickness within the contact area zone, which means that adding the gap factor value to the undeformed geometry of the equivalent Hertzian case does not make a significant change to the results.

It can be concluded that the equivalent Hertzian model is a valid analysis method for all cases where $wt > a_h$, and that introducing the gap factor to the model has no significant effect on the EHL calculations produced. It can also be say that a thinner, more flexible cup may significantly reduce the contact pressure and increase the film thickness, potentially resulting in reduced wear. Using a thin cup could significantly improve the wear performance,

while also conserving bone stock and allowing a larger head in a given size of acetabulum, reducing the risk of dislocation.

8.2 Future work

In proposing future work on the basis of the results obtained in this research study there are a number of ways in which the current approach could be developed, for example to quantify the effect of different design decisions in terms of ball diameter, contact conformity and cup thickness choices. These are of course dominated by surgical considerations but it would be useful to know how film thickness can be improved by design, if at all. There are also material choices to be made and wear minimisation may well be best approached by seeking better materials.

The research in the thesis has focussed on modelling the film forming ability of the contacts taking the particular nature of the ball cup contacts into account by detailed FE contact analysis. There are two significant factors that emerge as a result of this study which were not investigated in the present study due to time constraints and ways to approach these factors are discussed as follows:

8.2.1 Transient Effects

The EHL analyses presented in the thesis were limited to steady state conditions at nine points in the walking cycle. More accurate results could be obtained to calculate the film thickness if the effect of the squeeze film was taken into account. The walking cycle analysis was developed to give a detailed picture of the way in which contact position, load, and entrainment velocity vary over the walking cycle. This provides the basis for a transient EHL analysis of the contact and would be a clear candidate for further work built on the foundation of this project. . The equivalent Hertzian approach can be used in a transient analysis by plotting the variation of W_{equiv} and $\dot{E}_{\text{equiv}}$

over the walking cycle. The transient load can be replaced by the transient equivalent load, W_{equiv}, and the value of $\dot{E}_{\text{equiv}}$ regarded as a time varying parameter to be varied from time step to time step. The effect of including the gap factor could be evaluated but is unlikely to be significant as the squeeze film term will be dominated by the film thickness variation due to the transient load changes. The transient model envisaged would be a process that consists of the following steps.

(i) Conduct a series of FEA contact analyses for the walking cycle to provide, say, 20 equivalent Hertzian contact models, possibly over a series of loads covering the variation between this point and its neighbours.

(ii) Establish the variation of contact load and entrainment velocity over the walking cycle and introduce smoothing procedures to remove any numerical noise introduced by the experimental data.

(iii) Construct a transient EHL analysis of walking cycle where the equivalent Hertzian contact is obtained by interpolation between those established from the FEA analyses and the load and entrainment velocity vary according to the smoothed cycle.

Difficulties that will be encountered will be that of the small number of instances where there is a rapid variation in magnitude and/or direction of the entrainment velocity. This occurs naturally at the ends of the swinging motion cycle of the femur relative to the hip where the entrainment magnitude falls to zero and the flow direction within the contact reverses.

A zero entrainment velocity steady state case will have no film generating capability, but a transient analysis will not experience a loss of film as entrainment will grow in a different direction before the lubricant can start to leak away.

8.2.2 Roughness Effects

The film thickness results obtained in chapter 7 show that the contacts between MoM cups and balls are likely to operate well into the mixed lubrication regime and as such are influenced considerably by surface roughness. To gain an appreciation of the roughness effects they need to be added to the surface geometry to form a mixed lubrication model. To do this in a deterministic way where roughness is measured and included in the analysis is extremely challenging from a computational perspective. The problem requires resolution at the spatial scale of the roughness features, which are very fine, and transient consideration at the timescale of the motion of the roughness features within the contact. As a general rule this requires the surfaces to move through no more than half a spatial mesh point in each time step to include the roughness effects correctly.

The difficulties presented by these constraints are compounded by the fact that the contact areas are very large in comparison with the spatial separation of the roughness features. In the current work contact circle diameters of up to 10 mm occur and the roughness features of the fine surfaces can be expected to have width dimensions of the order 5 μm. These numbers are in the ratio of 2000 so to resolve the full rough surface problem at this resolution is problematic.

To make progress in this direction would require roughness investigations to characterise the roughness effect in parametric form obtained under different EHL circumstances such as a small concentrated contact operating under similar conditions of film thickness, entrainment velocity and sliding speed. There may be scope for such an investigation to be coupled with experimental evaluation using interferometry techniques, and this would be a challenging and very worthwhile endeavour for a future investigation.

References

1. S. Pramanik, A. K. Agarwal, K. N. Rai, Chronology of Total Hip Joint Replacement and Materials Development, Trends Biomater. Artif. Organs, 19(1), (2005) 15-26.
2. A. Unsworth, Tribology of artificial hip joints, J. Engineering Tribology, IMechE (220) part J, (2006), 711-718.
3. N. K. Arden, A. Kiran, A. Judge, L.C. Biant, M.K. Javaid, D.W. Murray, A.J. Carr, C. Cooper, R.E. Field, what is a good patient reported outcome after total hip replacement, Osteoarthritis and Cartilage, 19 (2011) 155-162.
4. R. Pivec, A.J. Johnson, S. C. Mears, M. A. Mont, Hip arthroplasty, www. Thelancet.com, Vol.(380), November 17(2012).
5. D. Kluess, J. Wieding, R. Souffrant, W. Mittelmeier, R. Bader, Finite Element Analysis in Orthopaedic Biomechanics, www.intechopen.com
6. A. Ramos, J. A. Simoes, The influence of cement mantle thickness and stem geometry on fatigue damage in two different cemented hip femoral prostheses, Journal of Biomechanics 42 (2009) 2602-2610.
7. D. S. Garbuz, M. Tanzer, N. V. Greidanus, B. A. Masri, C. P. Duncan, Metal-on-metal hip resurfacing versus large-diameter head metal-on-metal total hip arthroplasty, Clinical Orthopaedics and Related Research, Vol. 468, (2) February (2010).
8. http://www.zimmernederland.nl/producten/heup/alternative-bearing-solutions/metasulr-ldh-large-diameter-head/.
9. http://earlsview.com/2011/10/07/total-hip-replacement-short-review/.
10. H. Malchau, P. Herberts, T. Eisler, G. Garellick, P. Soderman, The Swedish total hip replacement Register, Journal of Bone and Joint Surgery, Vol. 84-A, supplement 2, (2002), 2-20.
11. T. J. S. Puolakka, K. J. J. Pajamaki, P. J. Halonen, P. O. Pulkkinen, P. Paavolainen, J. K. Nevalainen, The Finnish arthroplasty register, Acta Orthop Scand 72 (5), (2001) 433-441.
12. S. S. Jameson, D. J. Langton, S. Natu, T. V. F. Nargol, The influence of age and sex on early clinical results after hip resurfacing, the Journal of Arthroplasty, Vol. 23 (6), 2008, 50-55.
13. R. Ramakrishnan, W. L. Jaffe, W. R. Kennedy, Metal-on-Metal Hip Resurfacing, The Journal of Arthroplasty Vol. 23 (8), (2008), 1099-1104.
14. B. Tins, Dislocation and spontaneous reduction of the femoral implant against the femoral neck in an infected metal on metal hip resurfacing with complex collection, European Journal of Radiology 79 (2011) 136-139.
15. P. F. Lachiewicz, Metal-on-metal hip resurfacing, Clinical Orthopaedics and related Research, 465 (2007) 86-91.
16. B. M. Wroblewski, B. Purbach, P.D. Siney, P.A. Fleming, Charnley low-friction arthroplasty in teenage patients, The Journal of Bone and Joint Surgery, Vol. 92-B (4), April (2010), 486-488.

17. A. H. Hosman, H. C. Mei, S. K. Bulstra, H. J. Busscher, D. Neut, Effects of metal-on-metal wear on the host immune system and infection in hip arthroplasty, Acta Orthopaedics 81(5), (2010) 526-534.
18. M. Topolovec, A. Cor, I. Milosev, Metal-on-metal vs. Metal-on-polyethylene total hip arthroplasty tribological evaluation of retried components and periprosthetic tissue, Journal of the mechanical behavior of biomedical materials, 34 (2014) 243-252.
19. G. M. Keegan, I. D. Learmonth, C. P. Case, Orthopaedic metals and their potential toxicity in the arthroplasty patient, The Journal of Bone and Joint Surgery, Vol. 89-B (5), May (2007), 567-573.
20. J. Lazennec, P. Boyer, J. Poupon, M. A. Rousseau, C. Roy, P. Ravaud, Y. Catonne, Outcome and serum ion determination up to 11 years after implantation of a cemented metal-on-metal hip prosthesis, Acta Orthopaedica 80 (2), (2009) 168-173.
21. D. Dowson, A comparative study of the performance of metallic and ceramic femoral head componenets in total replacement hip joints, wear, 190 (1995) 171-183.
22. B. Weisse, C. Affolter, G.P. Terrasi, G. Piskoty, S. Kobel, Failure analysis of in vivo fractured ceramic femoral heads, Engineering Failure analysis 16 (2009) 1188-1194.
23. http://evertsmith.com/innovations/#masthead.
24. C. Esposito, W. L. Walter, P. Campbell, Squeaking in metal-on-metal hip resurfacing arthroplasty, Clinical orthopaedics and Related Research Vol. 468 (9), September (2010), 2333-2339.
25. D. Hannouche, A. Zaoui, F. Zadegan, L. Sedel, R. Nizard, Thirty years of experience with alumina-on-alumina bearings in total hip arthroplasty, International Orthopaedics 35, (2011) 207-213.
26. M. A. Germain, A. Hatton, S. Williams, J. B. Matthews, M. H. Stone, J. Fisher, E. Ingham, Comparison of the cytotoxicity of clinically relevant cobalt-chromium and alumina ceramic wear particles in vitro, Biomaterials 24 (2003) 469-479.
27. A. S. Greenwald, J. P. Garino, Alternative bearing surfaces: the Good, the Bad, and the Ugly, The Journal of Bone and Joint Surgery, Vol. 83-A (2), (2001), 68-72.
28. A. Race, M. A. Miller, D. C. Ayers, K. A. Mann, Early cement damage around a femoral stem is concentrated at the cement/bone interface, Journal of Biomechanics 36, (2003) 489-496.
29. R. G. H. H. Nelissen, E. Garling, E. R. Valstar, Influence of cement viscosity and cement mantle thickness on migration of the Exeter total hip prosthesis, The Journal of Arthroplasty, Vol. 20 (4), (2005), 521-528.
30. J. Stolk, N. Verdonschot, L. Cristofolini, A. Toni, R. Huiskes, Finite element and experimental models of cemented hip joint reconstruction can

produce similar bone and cement strains in pre-clinical tests, Journal of Biomechanics 35, (2002) 499-510.
31. C. M. Bellini, F. Galbusera, R. G. Ceroni, M. T. Raimondi, Loss in mechanical contact of cementless acetabular prostheses duo to post-operative weight bearing: A biomechanical model, Medical Engineering and Physics 29, (2007) 175- 181.
32. Z. M. Jin, M. Stone, E. Ingham, J. Fisher, Biotribology, Current orthopaedics, 20 (2006) 32-40.
33. D. Jalali-Vahid, M. Jagatia, Z.M. Jin, D. Dowson, Predication of lubrication film thickness in UHMWPE hip joint replacements, Journal of Biomechanics, 34 (2001) 261-266.
34. A. Charles, H. Henry, Metal-on-Metal Hip Arthroplasty, Clinical Orthopaedics and Related Research, 468 (2010) 406-412.
35. B. Tins, Dislocation and spontaneous reduction of the femoral implant against the femoral neck in an infected metal on metal hip resurfacing with complex collection, European Journal of Radiology Extra, 74 (2010) e13-e16.
36. B. Theruvil, N. Vasukutty, N. Hancock, D. Higgs, D. G. Dunlop, J. M. Latham, Dislocation of large diameter Metal-on-metal bearings, the Journal of Arthroplasty, 26 (2011) 6, 832-837.
37. C. Shahrdar, Pseudotumor in large diameter Metal-on-metal total hip articulation, the Journal of Arthroplasty, 26 (2011) 4, 665.e21-665.e23.
38. W. P. Barrett, K. A. Kindsfater, J. P. Lesko, Large diameter modular metal-on-metal total hip arthroplasty, the Journal of Arthroplasty, 27 (2012) 6, 976-983.
39. Y. M. Kwon, S. J. Ostlere, P. M. Smith, N. A. Athanasou, H. S. Gill, D. W. Murray, Asymptomatic Pseudotumors after metal-on-metal hip resurfacing arthroplasty, the Journal of Arthroplasty, 26 (2011) 4, 511-518.
40. M. D. Earll, P. G. Earll, R. S. Rougeux, Wound drainage after metal-on-metal hip arthroplasty secondary to presumed delayed hypersensitivity reaction, the Journal of Arthroplasty, 26 (2011) 2, 338.e5-338.e7.
41. M. Hasegawa, K. Yoshida, H. Wakabayashi, A. Sudo, Pseudotumor with dominant B-lymphocyte infiltration after metal-on-metal total hip arthroplasty with a modular cup, the Journal of Arthroplasty, 27 (2012) 3, 493.e5-493.e7.
42. M. Lavigne, E. L. Belzile, A. Roy, F. Morin, T. Amzica, P. VendittoliF, Comparison of whole blood metal ion levels in four types of Metal-on-metal large diameter femoral head total hip arthroplasty: the potential influence of the adapter sleeve, the Journal of Bone and Joint Surgery, 93 (2011) 2, 128-136.
43. R. E. Andrews, K. M. Shah, J. M. Wilkinson, A. Gartland, Effects of cobalt and chromium ions at clinically equivalent concentrations after metal-on-metal hip replacement on human osteoblasts and osteoclasts: implications for skeletal health, Bone, 49 (2011) 717-723.

44. P. A. Vendittoli, T. Amzica, A.G. Roy, D. Lusignan, J. Girard, M. Lavigne, Metal ion release with large diameter metal-on-metal hip arthroplasty, the Journal of Arthroplasty, 26 (2011) 2, 282-288.
45. K. Maezawa, M. Nozawa, T. Yuasa, K. Aritomi, K. Matsuda, K. Shitoto, Seven years of chronological changes of serum chromium levels after metasul metal-on-metal total hip arthroplasty, the Journal of Arthroplasty, 25 (2010) 8, 1196-1200.
46. M. Porat, J. Parvizi, P.F. Sharkey, K.R. Berend, A.V. Lombardi, R.L. Barrack, Causes of failure of ceramic-on-ceramic and metal-on-metal hip arthroplasty, Clinical Orthopaedics and Related Research, February 470 (2012) 2, 382-387.
47. T. Bernasek, D. Fisher, D. Dalury, M. levering, K. Dimitris, Is metal-on-metal squeaking related to acetabular angle of inclination, Clinical Orthopaedics and Related Research, September 469 (2011) 9, 2577-2582.
48. P. Damm, J. Dymke, R. Ackermann, A. Bender, F. Graichen, A. Halder, A. Beier, G. Bergmann, Friction in total hip joint prosthesis measured in vivo during walking, PLOS ONE, www. Plosone.org, Vol. 8, Issue 11, Nov. 2013.
49. F. Liu, I.J. Udofia, Z.M. Jin, F. Hirt, C. Rieker, P. Roberts, P. Grigoris, Comparison of contact mechanics between a total hip replacement and a hip resurfacing with a metal-on-metal articulation, IMechE vol.219 Part C, 2005, 727-732.
50. A. Yew, Z. M. Jin, A. Donn, M. M. Morlock, G. Issac, Deformation of press-fitted metallic resurfacing cups. Part2: finite element simulation, J. Engineering in medicine, vol. 220 Part H, IMechE 2006, 311-319.
51. I. R. Spears, M. Pfeiderer, E. Schneider, E. Hille,G. Bergmann, M. M. Morlock, Interfacial conditions between a press-fit acetabular cup and bone during daily activities: implications for achieving bone in-growth, Journal of Biomechanics, 33 (2000) 1471-1477.
52. I. R. Spears, M. Pfeiderer, E. Schneider, E. Hille, M. M. Morlock, The effect of interfacial parameters on cup-bone relative micromotions A finite element investigation, Journal of Biomechanics, 34 (2001) 113-120.
53. A. Hothan, G. Huber, C. Weiss, N. Hoffmann, M. Morlock, Deformation characteristics and eigenfrequencies of press-fit acetabular cups, Clinical Biomechanics, 26 (2011) 46–51.
54. F. Liu, Z. Chen, Y. Gu, Q. Wang, W. Cui, W. Fan, Deformation of the Durom Acetabular Component and It Impact on Tribology in a Cadaveric Model—A Simulator Study, PLOS ONE, www.plosone.org, October 2012, Vol. 7, Issue 10, e45786.
55. E. Sariali, T. Stewart, Z. Jin, J. Fisher, Effect of cup abduction angle and head lateral microseparation on contact stresses in ceramic-on-ceramic total hip arthroplasty, Journal of Biomechanics, 45 (2012) 390-393.

56. I.J. Udofia, Z.M. Jin, Elastohydrodynamic lubrication analysis of metal-on-metal hip resurfacing prostheses, Journal of Biomechanics, 36 (2003) 537-544.
57. D. Dowson, C. Hardaker, M. Flett, G. H. Isaac, A hip joint simulator study of the performance of metal-on-metal joints, the Journal of Arthroplasty, Part II, 19 (2004) 8, 124-130.
58. S. L. Smith, D. Dowson, A. A. J. Goldsmith, The lubrication of metal-on-metal total hip joints: a slide down the Stribeck curve, Proc Instn Mech Engrs, Vol. 215, part J, IMechE 2001, 483-493.
59. Z. M. Jin, D. Dowson, J. Fisher, Analysis of fluid film lubrication in artificial hip joint replacements with surfaces of high elastic modulus, Proc Instn Mech Engrs, Vol. 211, part H, IMechE 1997, 247-256.
60. F. Liu, J. Fisher, Z. M. Jin, Computational modelling of polyethylene wear and creep in total hip joint replacements: Effect of the bearing clearance and diameter, J of Engineering Tribology, Proc IMechE part J, 226(6), 2012, 552-563.
61. F. Liu, Z. M. Jin, F. Hirt, C. Rieker, P. Roberts, P. Grigoris, Transient Elastohydrodynamic lubrication analysis of metal-on-metal hip implant under simulated walking conditions, Journal of Biomechanics, 39 (2006) 905-914.
62. L. Gao, F. Wang, P. Yang, Z. M. Jin, Effect of 3D physiological loading and motion on Elastohydrodynamic lubrication of metal-on-metal total hip replacements, Medical Engineering and Physics, 31 (2009) 720-729.
63. Q. Meng, L. Gao, F. Liu, P. Yang, J. Fisher, Z. M. Jin, Contact mechanics and Elastohydrodynamic lubrication in a novel metal-on-metal hip implant with a aspherical bearing surface, Journal of Biomechanics, 43 (2010) 849-857.
64. L. Gao, P. Yang, I. Dymond, J. Fisher, Z. M. Jin, Effect of surface texturing on the Elastohydrodynamic lubrication analysis of metal-on-metal hip implants, Tribology International, 43 (2010) 1851-1860.
65. N. E. Bishop, F. Waldow, M.M. Morlock, Friction moments of large metal-on-metal hip joint bearings and other modern designs, Medical Engineering and Physics, 30 (2008) 1057-1064.
66. D. Dowson, Tribological principles in metal-on-metal hip joint design. Journal of Engineering in Medicine, Part H, 220 (2006) 161-171.
67. K. L. Johnson, Contact Mechanics, Cambridge University Press, 1985.
68. B. J. Hamrock, Fundamentals of fluid film lubrication, McGRAW-HILL International Edition, 1994.
69. A. Cameron, The principles of lubrication, Longmans Green and Co LTD, 1966.
70. S. P. Timoshenko, J. N. Goodier, Theory of Elasticity, Third Edition, McGraw-Hill Book Company, 1970.

71. H. P. Evans, T. G. Huges, Evaluation of deflection in semi-infinite bodies by a differential method, Proc Instn Mech Engrs Vol. (214) Part C, IMechE (2000).
72. J. M. Elkins, K. M. Kruger, D. R. Pedersen, J. J. Callaghan, T. D. Brown, Edge loading severity as a function of cup lip radius in metal-on-metal total hips-A finite element analysis, Journal of Orthopaedic Research, February (2012), 169-177.
73. Z. K. Hua, J. H. Zhang, A new simulator for Bio-tribology study, Journal of Bionic Engineering, (2008) 143-147.
74. Z. M. Jin, S. Meakins, M. M. Morlock, P. Parsons, C. Hardaker, M. Flett, G. Isaac, Deformation of press-fitted metallic resurfacing cups. Part1: Experimental simulation, J. Engineering in Medicine, Vol. 220 Part H, IMechE, (2006), 299-309.
75. J. B. Grimes, Does Deformation of Metal-On-Metal Acetabular Components Contribute to Early Failure?, The journal of Arthroplasty, 25 (3) e21, (2010).
76. A. Fritsche, K. Bialek, W. Mittelmeier, M. Simnacher, K. Fethke, A. Wree, R. Bader, Experimental investigations of the insertion and deformation behaviour of press-fi t and threaded acetabular cups for total hip replacement, journal of Orthopaedic science, 13 (2008), 240–247.
77. K. L. Ong, S. Rundell, I. Liepins, R. Laurent, D. Markel, S. M. Kurtz, Biomechanical modelling of acetabular component polyethylene stresses, fracture risk, and wear rate following press-fit implantation, Journal of Orthopaedic Research, November (2009), 1467-1472.
78. G. Schmidig, A. Patel, I. Leipins, M. Thakore, D. C. Markel, The effects of acetabular shell deformation and liner thickness on frictional torque in ultrahigh molecular weight polyethylene acetabular bearings, The Journal of Arthroplasty, Vol. 25 (4), (2010), 644-653.
79. http://www.sawbones.com/ products/bio/composite.aspx.
80. I. R. Spears, M. M. Morlock, M. Pfleiderer, E. Schneider, E. Hille, The influence of friction and interference on the seating of a hemispherical press-fit cup: a finite element investigation, Journal of Biomechanics, 32 (1999) 1183-1189.
81. Z. M. Jin, Theoretical studies of Elastohydrodynamic lubrication of artificial hip joints, J. Engineering Tribology, Vol. 220 Part J, IMechE, (2006), 719-727.
82. V. Saikko, T. Ahlroos, H. Revitzer, O. Ryti, P. Kuosmanen, The effect of acetabular cup position on wear of a large diameter metal-on-metal prosthesis studied with a hip joint simulator, Tribology International, 60 (2013) 70-76.
83. S. G. Clarke, A. T. M. Phillips, A. M. J. Bull, J. P. Cobb, A hierarchy of computationally derived surgical and patient influence on metal-on-metal press-fit acetabular cup failure, Journal of Biomechanics, 45 (2012) 1698-1704.

84. P. Campbell, E. Ebramzadeh, S. Nelson, K. Takamura, K. Smet, H. C. Amstutz, Histological features of Pseudotumor like tissues from metal-on-metal hips, Clinical Orthopaedics and related research, Vol. 468 (9), September (2010), 2321-2327.
85. G. Bergmann, G. Deuretzbacher, M. Heller, F. Graichen, A. Rohlmann, J. Strauss, G.N. Duda, Hip contact forces and gait patterns from routine activities, Journal of Biomechanics, 34 (2001) 859-871.
86. P. Damm, F. Graichen, A. Rohlmann, A. Bender, G. Bergmann, Total hip joint prosthesis for in vivo measurement of forces and moments, Medical Engineering & Physics, 32 (2010) 95-100.
87. G. Lenaerts, W. Bartels, F. Gelaude, M. Mulier, A. Spaepen, G. Perre, I. Jonkers, Subject specific hip geometry and hip joint centre location affects calculated contact forces at the hip during gait, Journal of Biomechanics, 42 (2009) 1246-1251.
88. http://www.orthoload.com/.
89. Q. E. Meng, F. Liu, J. Fisher, Z. M. Jin, Transient Elastohydrodynamic lubrication analysis of a novel metal-on-metal hip prosthesis with a non-spherical femoral bearing surface, J. Engineering in Medicine, Vol. 225 Part H, IMechE, (2011), 25-37.
90. F. Liu, Z. M. Jin, P. Roberts, P. Grigoris, Effect of bearing geometry and structure support on transient Elastohydrodynamic lubrication of metal-on-metal hip implants, Journal of Biomechanics, 40 (2007) 1340-1349.
91. https://www.ncbi.nlm.nih.gov/pmc/articles/PMC3593048/
92. http://cal.vet.upenn.edu/projects/saortho/chapter_86/86mast.htm
93. http://downloads.lww.com/wolterskluwer_vitalstream_com/sample-content/9781582558752_Mundt/samples/Chapter_11.pdf
94. http://www.ccg.msm.cam.ac.uk/images/FEMOR_Lecture_1.pdf
95.http://www.sv.vt.edu/classes/MSE2094_NoteBook/97ClassProj/num/midkiff/theory.html
96. L E Goodman, L M Keer, The contact stress problem for an elastic sphere indenting an elastic cavity, Int. J. Solids structure 1965. Vol I. pp. 407 to 415. Pergamon press Ltd, printed in Great Britain
97. M J A Holmes, H P Evans, T G Hughes, R W Snidle, "Transient Elastohydrodynamic point contact analysis using a new coupled differential deflection method, Part 1: theory and validation", Proc IMechE, Part J, Jn Engng Tribol, Vol 217, pp 289-303. "Part 2: results", pp 305-321, 2003.

A.1 The Abaqus software package

Abaqus is an influential engineering simulation software package based on the finite element analysis method. It contains a wide range of element types that can be used to model any geometry. It is used in a large number of research institutions and industries due to its capabilities to address linear and non-linear applications. Abaqus can be used to simulate different engineering materials including metals, polymers, reinforced concrete, composites, and others. It is also able to import input data files from a number of different engineering software packages (AutoCAD, Nastran, ANSYS, and other software). A complete Abaqus analysis consists of three stages: pre-processing (Abaqus/ CAE), Simulation (Abaqus Standard, Abaqus Explicit, Abaqus CFD and Abaqus Electromagnetic) and post-processing (Abaqus Viewer).

A.2 Pre-processing stage

The pre-processing stage is the first stage of a finite element analysis program. In this stage the model of the physical problem is created, usually using graphical tools available within the system, the material properties are specified, and the loads and the boundary conditions applied to the model are defined. The parts or components that make up the model of the physical problem are also subdivided into finite elements by meshing the geometry at this stage using Abaqus/CAE.

A.3 Simulation

The second stage in the simulation is where the numerical problem of the model defined in the pre-processing stage is solved. It is achieved either by using the Abaqus Standard solver or the Abaqus Explicit solver. When the solution has been obtained, the output data files will be ready for post-processing to view the results of the analysis. The running time may take from a few minutes, to hours or days to complete the analysis of the job according to the complexity of the problem being submitted. It also depends on the specifications of the computer being used to carry out the analysis.

A.4 Post-processing

In the final post-processing stage the results of the model analysed can be viewed using Abaqus Viewer. It allows the results database to be interrogated to provide tabulated output together with a wide range of plots that can be generated, including X-Y plots, colour contour plots, deformed shape plots and animations.

A.5 Abaqus / CAE

Abaqus/CAE is a Complete Abaqus Environment. It provides an easy, consistent interface for creating a job, submitting and monitoring the Abaqus results model. The components of the Abaqus main window as shown in the screenshot presented in Figure A.1 are denoted: **Title bar, Menu bar, Toolbars, Context bar, Model Tree, Toolbox area, Viewport, Message area and Prompt area**.

Title bar

The title bar shows the name of the current model as well as the version of Abaqus/CAE which is running.

Menu bar

In the menu bar all the available menus are presented, and within the menus all the functionality in the Abaqus software system can be reached. Depending on the module which is selected (see **context bar** below), different menus can be seen in the menu bar.

Toolbars

A quick access to items available in the selected menu is provided by the toolbars which consists of icons for each of the items.

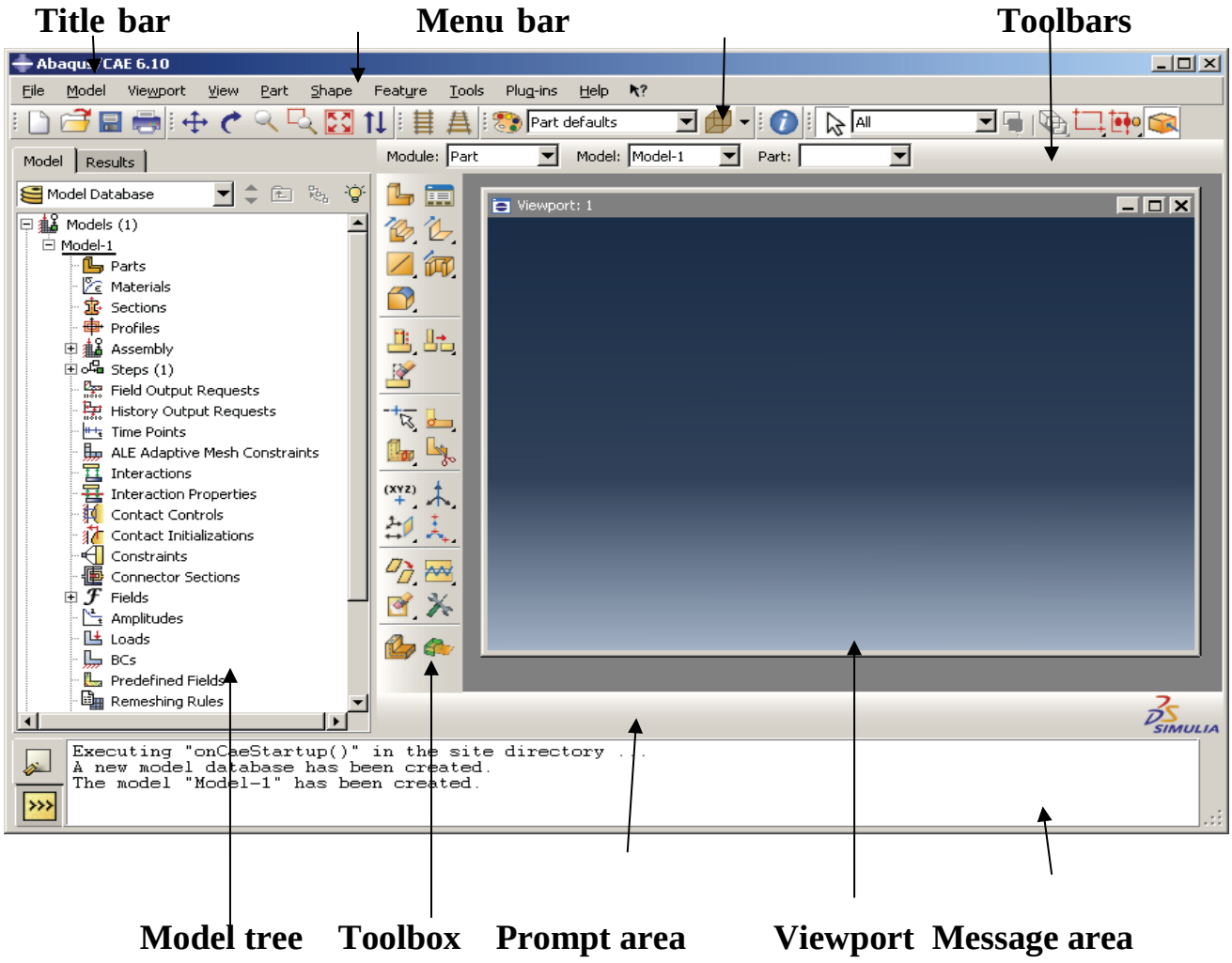

Figure A.1, Components of the main window of Abaqus CAE

Context bar

Abaqus/CAE is composed of a set of modules, where each module permits work to be carried out on one aspect of the model. In the context bar there is a **Module** list which allows the user to select between these modules. A number of icons in the context bar are a function of the module that is currently selected. For example, the context bar allows an existing part to be retrieved while creating the geometry of the model, or for the output database associated with the current viewport to be changed. Similarly, in the Mesh module it is possible to choose whether to display a particular part or an assembly.

Model Tree

The Model Tree supplies a graphical description of the model and the objects that it contains, such as parts, properties of the materials, analysis steps, loads, and output requests. In addition, the Model Tree supplies an appropriate, centralised tool for changing between modules and for dealing with objects. If the model database contains more than one model, the Model Tree can be used to move between models.

Toolbox area

When a module is entered, the toolbox area displays tools that are suitable for that module as a series of icons. The toolbox permits rapid access to many of the module functions which are also obtainable from the menu bar.

Viewport

Viewport is the area where Abaqus / CAE exhibits the model which is being created.

Message area

In the message area Abaqus/CAE provides brief messages about warnings and the status information, for example.

Prompt area

The prompt area shows the essential commands for the user to be followed during the procedure of modelling.

Abaqus/CAE consists of modules as shown in Figure A.2, where each module describes a logical aspect of the modelling procedure as follows:

The ***Part*** module is used for creating, drawing and managing the geometry in the current model. Individual parts can be created. The entire model will represent the assembly process for all the parts together.

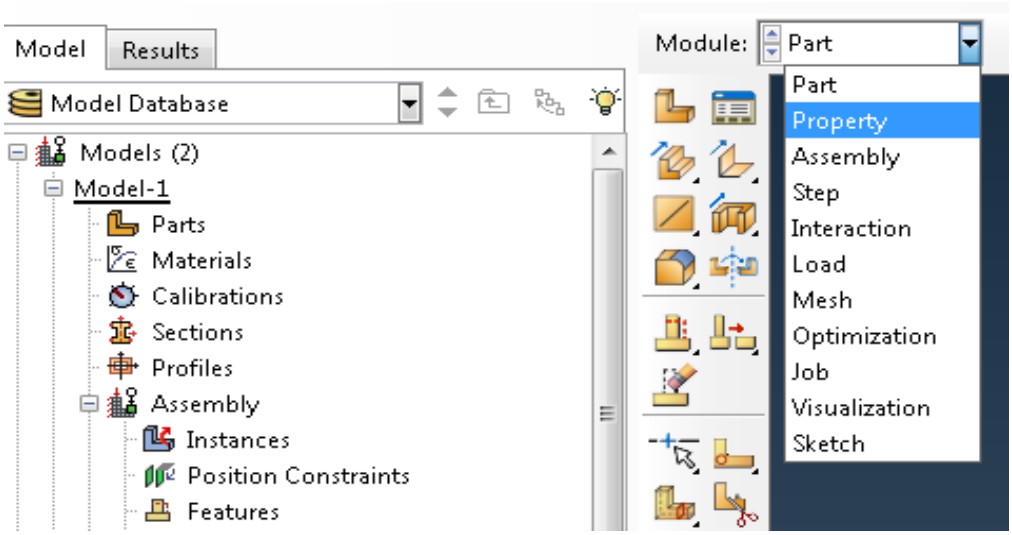

Figure A.2 Module in Abaqus/ CAS

The ***Property*** module is utilised to specify the material properties of the model parts. Five categories, **General, Mechanical, Thermal, Electrical/ Magnetic and Other,** of material behaviours are available in the current Abaqus version as shown in Figure A.3.

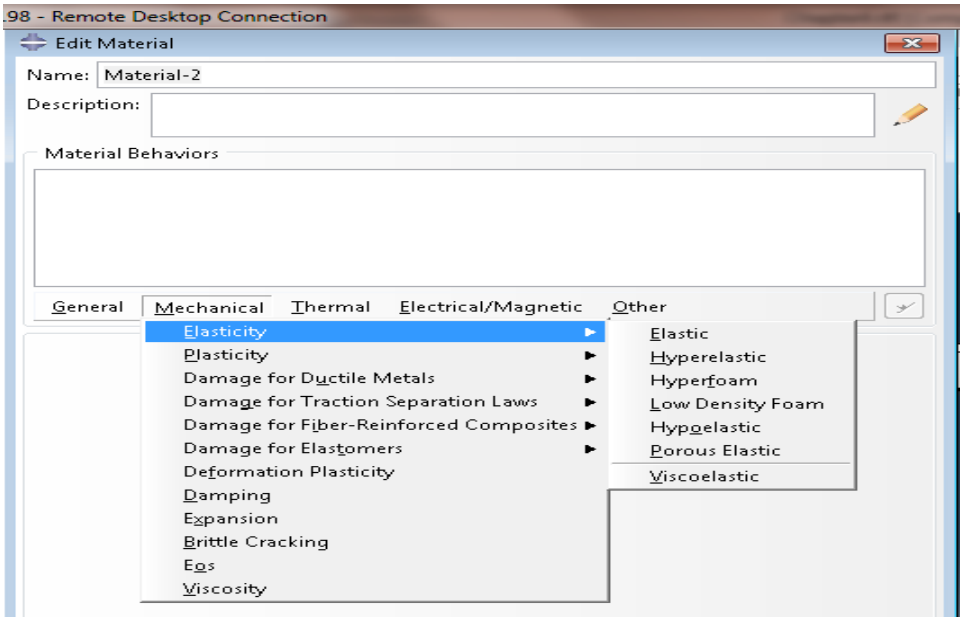

Figure A.3 Elasticity behaviours under the Mechanical menu

All the parts have the local coordinate systems in which they have been created. A copy of each part, which is called an "instance", is used by the ***Assembly*** module to assemble them together in a global coordinate system. It is possible to use the same part more than once. The assembly module includes functions to rotate, translate, cut, merge and create constraints in order to assemble all the instances together.

In the ***Step*** module it is possible to create analysis steps and to request the files of output information to be prepared. Static or dynamic behaviour can be chosen within this module. In this module different types of field output

requests can be saved after the analyses have completed, this option enables the user to control the size of the results files.

The ***Interaction*** module is used to manage the interaction within the model. When there are multiple parts in the model then the relationship between these parts like surface-to-surface contact, for example, will be controlled and specified by using the interaction module.

In the ***load*** module the applied load and boundary conditions are defined and managed. Multi-types of loads and boundary conditions are available to apply at specific regions, surfaces or nodes. By using the step module the user can specify the load and boundary conditions as being active in one step and inactive in another one.

One of the most important modules is the ***Mesh*** module as the accuracy of the results is dependent on the meshing process. In this module the user can specify the element shape (hexahedron, tetrahedron or wedge), type (linear or quadratic) and size.

After finishing all of the tasks involved in defining the model such as creating the geometry, defining the properties, applying the loads and boundary conditions, making the assembly and meshing the parts, the model becomes ready for submitting and performing the analysis and monitoring its progress. These steps are achieved using the ***Job*** module.

The ***Visualization*** module (Abaqus Viewer) is used to view and plot the results of the model analysis. It supplies a graphical display of the finite element results. The user can view the results by plotting the deformed shape, contours, symbol, X-Y data and other methods.